TENTH EUROPEAN CONFERENCE ON

CONTROLLED FUSION

AND

PLASMA PHYSICS

X
FUSION
MOSCOW
1981

Vol. I

CONTRIBUTED PAPERS

TENTH EUROPEAN CONFERENCE ON

CONTROLLED FUSION
AND
PLASMA PHYSICS

X
FUSION
MOSCOW
1981

Vol. I

CONTRIBUTED PAPERS
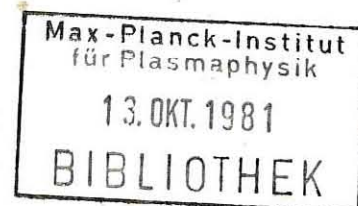
Moscow, September 14—19, 1981

PREFACE

This volume contains 204 Contributed Papers, which have been selected by International Programme Committee of the X European Conference on Controlled Fusion and Plasma Physics, held in Moscow from May 13 to May 15, 1981. A number of papers (B-6, B-10, C-11, F-2a, F-8, F-13, G-2a, L-4, M-5) the presentation of which was supposed to be not really adequate will be published in the second volume together with the Invited papers and the urgent papers supplemented by the new results obtained after the deadline date.

Since the papers in this volume have been printed by photo-offset directly from material provided by the authors the content of the papers remains their own responsibility.

We sincerly thank the authors for carrying out the instructions for preparing papers. We wish also to thank the members of the International Programme Committee and concerned scientific Institutions for their help and cooperation.

The Organizing Committee

August 1981
Moscow

CONTENTS

TOKAMAK EXPERIMENTS

MAGNETIC CONFINEMENT

OPEN-END SYSTEMS

PLASMA FOCUS DEVICES, Z- AND Q-PINCHES

STELLARATORS AND BUMPY-TORUS

INERTIAL CONFINEMENT

REACTOR PROBLEMS

HEATING AND CURRENT DRIVE

IMPURITY CONTROL

WAVE-PLASMA INTERACTION

COMPACT TORI AND TOROIDAL PINCHES

RELATIVISTIC PLASMA ELECTRONICS

A

TOKAMAK EXPERIMENTS

HIGH DENSITY DISCHARGES WITH NEUTRAL INJECTION IN DITE TOKAMAK

P.J. Lomas, K.B. Axon, J.E. Bradley, R.D. Gill, J. Hugill,
P.C. Johnson, B.A. Powell, A.J. Wootton.

Culham Laboratory, Abingdon, Oxon., OX14 3DB, UK
(Euratom/UKAEA Fusion Association)

Abstract

High density discharges have been produced in DITE by gas puffing during neutral beam injection. The general behaviour of these discharges, a power balance for a discharge near the density limit and the scaling of β and τ are discussed.

Behaviour of a typical discharge

Discharges with mean line of sight densities, $\bar{n}_e$ up to 1×10^{20} m^{-3} have been produced in DITE by strong gas puffing during injection of $\leq$ 1MW of 24keV neutrals. The density is ramped until disruption occurs at $\bar{n}_e$ Rq/$B_T \leq 2\times10^{20}$m^{-2}T^{-1} [1]. Figure 1 shows the time behaviour of the main discharge parameters for a low-q D$_2$ discharge with Ti limiters, and Figure 2 the electron density, $n_e(r)$ and electron temperature, $T_e(r)$ profiles measured at four times. In this case there is no disruption until after the 100ms injection pulse. No density clamp is seen. T_{e0} and T_{i0} remain about 800eV and 600eV respectively as the density is increased. The density profile broadens as $\bar{n}_e$ is increased, and at the highest density it is flat out to r/a $\sim$ 0.5. Strong sawteeth can be seen on the soft X-ray signals. Figure 3 shows the evolution of $\bar{\beta}_T$ (from diamagnetic loop measurements) as a function of plasma density for various injection powers, P_{inj} into similar discharges. For $0 < P_{inj} < 600$kW both the maximum density reached, $\bar{n}_e$(max) and $\bar{\beta}_T$(max) increase with P_{inj}, $\bar{\beta}_T$(max) being reached somewhat earlier. For $P_{inj} > 600$kW, neither $\bar{n}_e$(max) nor $\bar{\beta}_T$(max) increase further.

Power balance for high density low-q discharge

Power balances have been evaluated for high density discharges in DITE using the Hermes transport analysis code [2] together with an ion transport code [3], and the Stott neutral transport code [4]. The profile of total radiation, $P_{rad}(r)$, $n_e(r)$, $T_e(r)$ and the central ion temperature, $T_i(0)$ are measured. $T_i(r)$ and the corresponding neutral density profile, $n_D(r)$ are calculated assuming neoclassical ion conduction of the form given by Hazeltine and Hinton [5] but enhanced by some anomaly factor. This is chosen to give a T_i profile which does not diverge at the plasma boundary.

The radial power balance for the discharge illustrated in Figures 1 and 2 is shown in Figure 4. Two different assumptions have been made for $n_D(0)$ and the analysis has been carried through for each case. Firstly, n_D has been assumed negligible so that charge exchange losses can be ignored. Secondly, $n_D(0) = 5 \times 10^{13}$ m^{-3} has been taken; the value required to produce the observed rate of increase in central electron density by ionisation alone. This is consistent with the empirical scaling of $n_0(0)$ with $\bar{n}_e$ observed for DITE. Since the neutrals are assumed cold in the ion transport calculations, this will provide an upper limit to the charge exchange losses. The shaded regions in the power balance indicates the uncertainty in the charge exchange losses and the effects of these losses on the detailed form of the calculated T_i profile at the edge. The ion conduction is then 3-3.5 above the Hazeltine-Hinton values.

Within r/a $\sim$ 0.5 these uncertainties are small, and the strongest loss mechanism is ion conduction which transports $\sim$ 220kW. The power input to the ions comes directly from the beam $\sim$ 140kW, and from the electrons by equipartition, $\sim$ 90kW. Electron conduction is significant at this radius, $\sim$ 140kW, but smaller than the ion losses. Radiation accounts for only 70kW.

The density profile is broad so that electrons and ions are closely coupled by equipartition in the outer regions of the plasma. The effect of charge exchange is to keep $T_i < T_e$ so that power conducted from the plasma centre is lost by charge exchange rather than electron conduction. In this case the product $n_e X_e$ is more nearly constant than the case where neutrals are neglected. Although charge exchange losses have a significant effect on T_e-T_i, T_i does not change very much, so that the power conducted by the ions in the outer regions is insensitive to the assumption about n_D. Thus the dominant loss channels at the edge are ion conduction, radiation and either electron conduction or charge exchange.

The power balance analysis for a lower current, I $\sim$ 110kA (q = 3.5) lower density, $\bar{n}_e \simeq 3.7\times10^{19}$ discharge which is also close to the DITE density limit shows a somewhat different picture. As expected from the variation of electron and ion thermal diffusivity with density, electron losses are more important and ion losses less important than in the discharge just described. In addition the density profile is much less broad so that electron-ion coupling is weak. As a result charge exchange loss from the edge is fed by ion conduction from the centre rather than by equipartition. The ion conduction is a similar factor of 3-4 above the Hazeltine-Hinton neoclassical values.

Scaling of τ_E and β at high density

A wide range of discharges have been examined with $B_T \approx 0.9$ to 2.7T, ohmic current, I = 40 to 260kA, P_{inj} = 0 to 1MW, $\bar{n}_e = 2\times10^{19}$m^{-3} to 9.5×10^{19}m^{-3} using titanium limiters at r = 26cm and carbon limiters which can be used to set the minor radius between 12 and 22.5cm. In most of these discharges the density is ramped throughout the injection pulse or until the plasma disrupts. At higher q values, q $\gtrsim$ 3, density clamping usually occurs where, with constant gas feed, the density stops rising upon injection. A two to threefold increase in gas feed rate is usually required to restore the density ramp. β values, as measured by the diamagnetic loop, exhibit a broad maximum as a function of density similar to the example in Figure 3. Although in ohmically heated discharges the energy confinement time is well represented by $\tau_E = 10^{-20}$ na^2, in injection dominated discharges at high density τ_E can be a factor $\sim$ 3 less.

We have fitted the diamagnetic estimates of $\bar{\beta}_T$ to a power law in the other discharge parameters over the ranges given above, to give

$$\bar{\beta}_T(\%) = \frac{4\times10^{-5}I(kA)^{1.5}\,\bar{n}_e(10^{19}m^{-3})^{0.12}P_{TOT}(MW)^{0.27}R(m)^{0.2}}{B_T(T)^{2.2}\,a(m)^{2.0}} \qquad ...(1)$$

High β data from ISX, T11 and JFT2 [6,7,8] have been included in this fit, but this does not affect the result appreciably except for the introduction of the weak dependence on R. This fit is illustrated in Figure 5. Note that the T11 and low power ISX data agree very well with this scaling and even the highest β data from ISX and JFT2 is not significantly further from the fit than the best DITE data. The dependence on $\bar{n}_e$ and P_{TOT} indicate a tendency to saturation in $\bar{\beta}_T$ at high densities and injection powers.

We can express the fit of equation (1) as

$$\tau_E \sim \frac{I^{1.5}\,n_e^{0.12}\,R^{1.2}}{B_T^{0.2}\,p^{.7}}$$

where the increase in τ_E with current and the reduction with increased injection power are the most notable effects. Although the power balance of Figure 4 shows that ion conduction is important, the dependencies on $\bar{n}_e$ and power in equation (1) are weaker than would be expected assuming an ion conduction loss of the form $\sim nT^{\gamma 2}$. The strong dependencies on I, B_T and a suggest that we are observing a soft limit on β_p which scales as $\sim 1/\sqrt{I}$.

Conclusions

Ion and electron conduction, radiation and charge exchange are all significant loss mechanisms for discharges in DITE at high density. The general behaviour of these discharges and the scaling of discharge parameters is consistent with T11, ISX, JFT2. This scaling is more complicated than na^2 scaling because electron conduction plays a minor role in the power balance at these densities, and although the underlying physics appears straightforward it has not proved possible to explain the scaling on simple transport arguments.

Acknowledgements

References

[1] Axon, K.B. et al. Plasma Phys. and Contr. Nucl. Fus. Res. IAEA-CN-38/N-4, 1980

[2] Cordey, J.G., Start, D.F. Details available on request.

[3] Johnson, P.C. Details available on request.

[4] Stott, P.E. Plasma Physics 1976, 18, p251.

[5] Hazeltine, R.D., Hinton, F.L. Phys. Fluids 1973, 16, p1883.

[6] Murakami, M. et al. Plasma Physics and Contr. Nucl. Fus. Res. Brussels 1980, IAEA-38/N-1.

[7] Mukhovatov, V.S., Proc. 2nd Joint Grenoble-Varenna Int. Symp. on Heating in Toroidal Plasmas. Como 1980.

[8] Nagashima, T., Proc. 2nd Joint Grenoble-Varenna Int. Symp. on Heating in Toroidal Plasmas. Como 1980.

$B_T = 1.35$, R = 1.17m, a = 0.26m
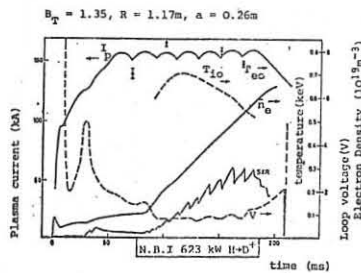
Fig 1. Time behaviour of discharge parameters for a high density low-q deuterium discharge with injection
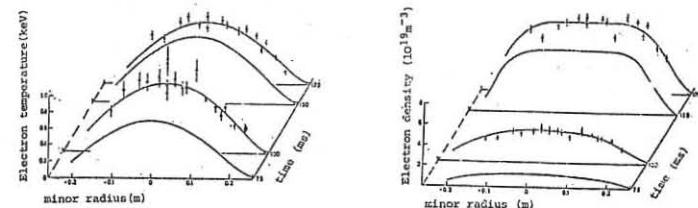
Fig 2. Temperature and density profiles for discharge in Fig 1.
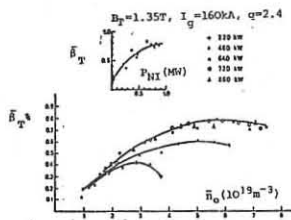
$B_T=1.35$T, $I_g=160$kA, q=2.4

Fig 3. Behaviour of $\bar{\beta}_T$ as a function of density for discharges with $B_T = 1.35$T, I = 160kA, q = 2.4 for different neutral beam powers.
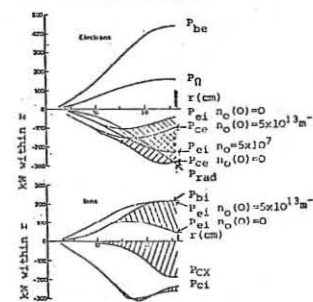
Fig 4. Ion and electron radial power balance for discharge illustrated in Figs 1 and 2. The curves show the powers in the various channels integrated out to minor radius r. The labels refer, P_Ω to ohmic power, P_{be} the beam input to electrons, P_{rad} the radiation loss, P_{ce} the electron conduction and convection loss, P_{ei} the equipartition from electrons to ions, P_{bi} the beam input to ions, P_{ci} the ion conduction and convection loss and P_{cx} the charge exchange loss. Inputs are shown positive and losses negative.

$$\bar{\beta}_T \quad 4.1\ 10^{-5}\ \frac{I^{1.5}\,n_e^{0.12}\,P_{TOT}^{0.27}\,R^{0.2}}{B_T^{2.2}\,a^{2.0}}$$

x – Fig 1 case
Δ – ISX
○ – T11
□ – JFT2
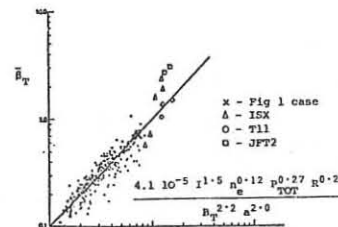
Fig 5. Best fit of $\bar{\beta}_T$ to discharge parameters. I(kA), $n_e(10^{19}m^{-3})$, total input power P_{TOT}(MW), B_T(T), R(m), a(m).

IMPURITY RADIATION IN DITE DURING NEUTRAL INJECTION

W H M Clark, J G Cordey, M Cox, S J Fielding, R D Gill,
R A Hulse*, P C Johnson, J W M Paul, N J Peacock, B A Powell,
M F Stamp+ and D F H Start
Culham Laboratory, Abingdon, Oxon, OX14 3DB, UK
(Euratom/UKAEA Fusion Association)
*Princeton Plasma Physics Laboratory, +University of Oxford

ABSTRACT   The large increase in radiation during neutral
injection in DITE is identified as being primarily due to the
charge exchange recombination of the impurities by the fast
neutrals. The scaling of the radiation increase with inject-
ion power and density has been determined and the signific-
ance of its toroidal asymmetry is discussed.

INTRODUCTION   A large and rapid increase in impurity line
emission and total radiation is observed in the DITE experi-
ment during neutral injection. In a previous paper[1],
charge exchange recombination of the impurities by the in-
jected fast neutrals has been suggested as the primary cause
of the enhanced radiation. Experiments to obtain the scaling
of this process with injection power and density have recently
been completed on DITE, and compared with theory. A brief
account of this study is given below.

THEORETICAL MODEL   The 'average ion' model developed by
Post et al[2] is used to describe the atomic physics. The
main theoretical difficulty is that the profile of the in-
jected neutrals is three dimensional (r, θ, ϕ); previous
treatments have usually neglected the θ and ϕ dependence
arguing that the transit time of an impurity around the
torus is short compared to the atomic physics timescales.
This approximation is not satisfied in DITE, since the imp-
urities are actually collisional and their diffusion time
around the torus can, in some conditions, be longer than their
ionisation time. In this case the full transport equation
for the impurity density n^q of the qth charge state

$$\frac{\partial n^q}{\partial t} + \nabla \cdot D^q \nabla n^q = S^{q-1} n^{q-1} - S^q n^q + R^{q+1} n^{q+1} - R^q n^q \quad (1)$$

has to be used. In the above S^q is the ionisation rate and
R^q is the recombination rate, which includes radiative and
dielectronic recombination as well as charge exchange re-
combination on both injected fast and thermal neutrals.

The component of the diffusion coefficient along the
field lines in eq(1) is assumed to be classical, $D_{\parallel}^q = v_i^2/v^q$,
with v^q the collision frequency of the impurity ion in charge
state q. If the ionisation time is longer than the diffusion
time, $\tau_{ion} > v^q R^2/v_i^2 i^2$ (i rotational transform), the impurity
density n^q is symmetric in ϕ and θ, and a field line averaged
form of eq(1) is appropriate. Both the line average and non-
averaged rate equations were solved numerically and the non-
averaged solution used in comparisons with experiment when
toroidal asymmetry was important.

EXPERIMENTAL RESULTS   Radial profiles of carbon, oxygen
and titanium line emission during neutral injection, obtained
from photographic grazing in-
cidence measurements are
shown in Fig.1 for a low den-
sity case ($\bar{n}_e = 10^{19} m^{-3}$).
These profiles, which are
peaked on axis due to cx
recombination, have been
compared with solutions of
the averaged-rate equation.
Taking the impurity profile
proportional to the density
profile ($n_z \approx n$) is found
to give a good fit.

The time history of
the line intensity during
neutral injection, measured
by grazing and normal in-
cidence photoelectric spec-
trometers, is shown in
Fig.2 along with the theo-
retical curves. The CVI,
CV, OVIII, OVII and
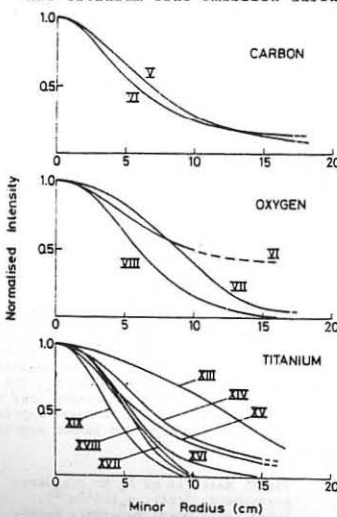
Fig.1 Normalised line intensity
versus radius during injection.

Ti XIII lines
increase by an order
of magnitude during
injection with rise
and fall times of
the order of 2 ms,
in contrast to the
Ti XVIII line which
initially falls due
to the recombination
of Ti^{17+} by the beam
neutrals. The theo-
retical curves (dotted
in Fig.2.) show a
similar time behaviour
and absolute increase.

The scaling of the
ratio of line intensity
during injection to
that before injection
with injection power
is shown in Fig.3 for
two different densities.
For both densities the
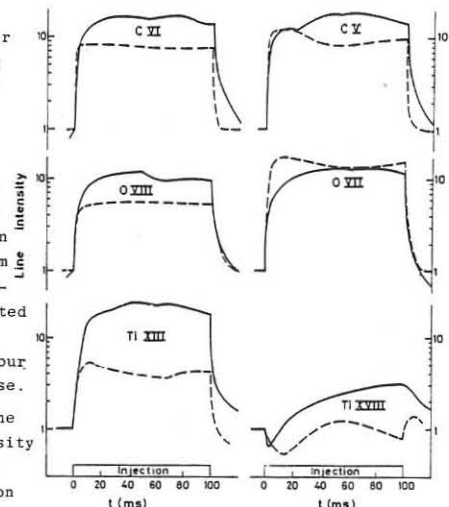
Fig. 2 Line intensity versus time during
neutral injection, dotted curve is the
theory (field line averaged).
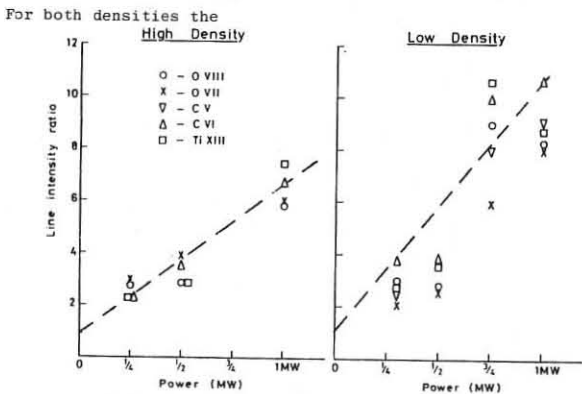
Fig.3 Ratio of line intensity during injection to value before injection
versus power.

scaling is linear with power. The lower density case has a
larger slope due to the increased importance of charge
exchange recombination relative to ionisation.

The toroidal asymmetry of the radiation is shown in Fig.4,
where the line emission and total radiation in the vicinity
of an injector is compared with that from a region on the
opposite side of the torus. Typically there is a factor of
2-3 difference in the intensity of the radiation between the
two measurements. The theoretical solution of the non-
averaged rate equation has a similar asymmetry.

The asymmetry of the radiation makes precise power bal-
ance calculations very difficult. Present indications are
that at low densities, the enhanced radiation (x 5) due to charge
exchange recombination of the impurities does play a signif-
icant role in the power balance, and is responsible for the
poor electron heating at low densities in DITE.

REFERENCES

[1] AXON K B et al,
Proc. 8th Int. Conf.
Plasma Physics and
Nuclear Fusion Research,
Brussels 1980, IAEA
Vienna, IAEA-CN-38/N-4.
[2] POST D E et al,
Atomic Data and Nuclear
Tables 20 397 (1977).
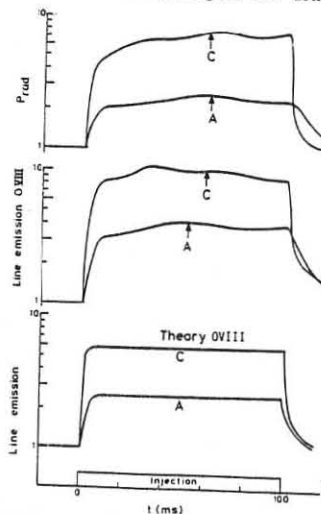
Fig.4 Line emission and total radiation
versus time seen by detectors close to the
injector (C), and 180° around the torus (A).

ENERGY CONFINEMENT OF HIGH DENSITY PLASMAS IN THE FT TOKAMAK

F. Alladio, G. Bardotti, R. Bartiromo, G. Buceti*, P. Buratti[•],

F. Crisanti*, A. De Angelis, F. De Marco, M. De Pretis, M. Gasparotto,

R. Giannella, M. Grolli, G. Maddaluno*, G. Mazzitelli[•], L. Pieroni,

G.B. Righetti, F. Santini, S.E. Segre, A. Tanga, O. Tudisco*, V. Zanza

Associazione EURATOM-CNEN sulla Fusione, Centro di Frascati, C.P. 65,
00044 Frascati, Rome, Italy

INTRODUCTION

Energy confinement studies have been performed on FT in the parameter range 60 kG $\leq B_T \leq$ 80 kG, $I_p \leq$ 550 kA, $\bar{n}_e \leq 4.5 \times 10^{14}$ cm^{-3}. At low densities the confinement time increases roughly linearly with density. However at densities greater than $\bar{n} = 2.5 \times 10^{14}$ cm^{-3} the rate of increase seems slower. The maximum peak density obtained is $\hat{n} = 7.5 \times 10^{14}$ cm^{-3} with an energy confinement time τ_E = 55 ms and a corresponding value of the Lawson parameter $\hat{n}\tau$ of 4×10^{13} cm^{-3} sec.

The main characteristics of the machine and of its operation are described in Ref. 1. For the discharges considered in this work FT operated in deuterium with a s.s. limiter having a radius a = 20 cm.

DISCHARGE EVOLUTION

The evolution of a high density discharge is shown in Fig. 1.

The density is increased by puffing gas with a piezoelectric fast valve. In most discharges the main gas pulse was during the last phase of the current build-up. Typical values of fluxes were 20 ÷ 30 torr-liters sec^{-1} lasting 100 milliseconds. If the amount of gas is increased substantially, a major disruption occurs. Non thermal effects are present during the current rise. A strong enhancement of the D_α radiation occurs abruptly at high densities. The correlation of the start of this enhancement with the discharge parameters is unclear and it can not be
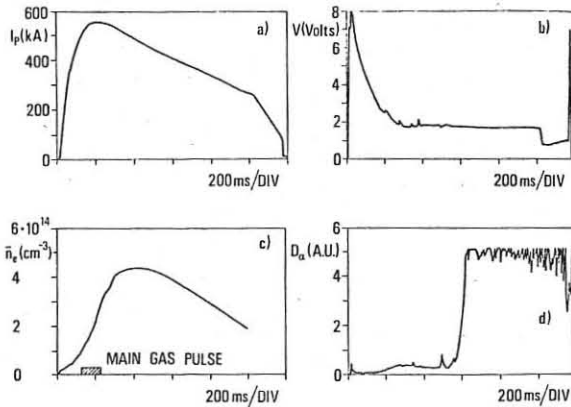
Fig. 1 - a) Plasma current; b) Loop voltage; c) Linear average density
d) D_α emission at a port different from the puffing gas

easily controlled. Sawtooth oscillations are well developed for most of the duration of high density discharges. Their period varies from 3.5 ms for $\bar{n} \sim 2 \times 10^{14}$ cm^{-3} up to 9 ms for $\bar{n} \sim 7 \times 10^{14}$ cm^{-3}.

ENERGY CONFINEMENT

The electron density and temperature profiles were measured with Thomson scattering. Peak ion temperatures, as determined by neutron yeld, turned out to be about .9 $\bar{T}_e$. Energy confinement times were calculated by assuming the same temperature profiles for electrons and ions.

Figure 2 shows τ_E vs $\bar{n}$, the straight line is the Alcator law τ_E(ms) = $4 \times 10^{-16} \bar{n}$ a^2(cm^{-1}). The scatter in the data is large, but some trends are visible. For densities lower than 2.5×10^{14} cm^{-3} the points are above the Alcator line while for higher densities their are below the line and the increase with density, if present, seems slower.

Figure 3 shows the effect of high densities on the temperature profiles. $\bar{T}_e$ is the cross section average electron temperature.

* CNEN Fellow
• Guest
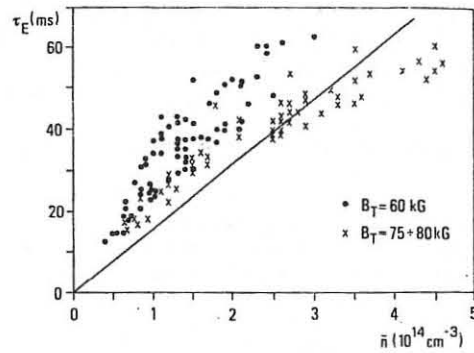
Fig. 2 - Energy confinement time vs linear average density
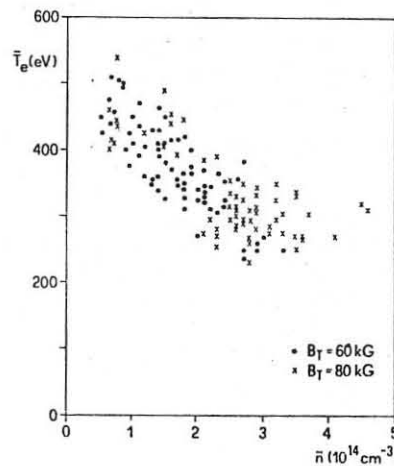
Fig. 3 - Cross section average electron temperature vs average density

Figure 4 shows the electron density profiles for one of the highest densities discharges.
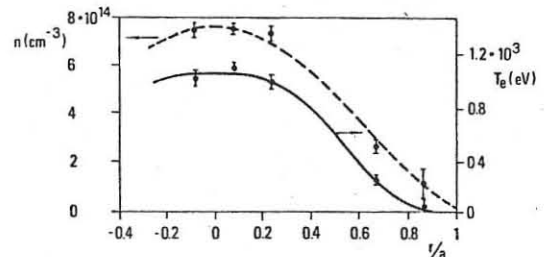
Fig. 4 - Electron density and temperature profiles for a high density discharge

The influence of ion transport on energy confinement at high densities has been considered. At half radius the neoclassical ion heat flux of the discharge shown in Fig. 4, calculated with the theory of Hazeltine and Hinton [2] gives a loss of about 150 kW compared with an ohmic input power at the same radius of about 750 kW.

REFERENCES

[1]   U. Ascoli-Bartoli, G. Bardotti, R. Bartiromo, M. Brusati, P. Buratti, A. De Angelis, F. De Marco, R. Giannella, M. Grolli, M. Martone, L. Pieroni, G.B. Righetti, M. Samuelli, A. Tanga, V. Zanza, Proc. of 9th European Conference on Controlled Fusion and Plasma Physics (Oxford, September 1979)

[2]   F.L. Hinton, R.D. Hazeltine, Rev. of Modern Physics, 48, 239 (1976)

INVESTIGATION OF FT-1 TOKAMAK PLASMA BY MEANS
OF PELLET INJECTION

A.P.Zhilinsky[*], B.V.Kuteev[*], M.M.Larionov, A.D.Lebedev,
S.S.Mikheikin[*], V.A.Nikiforov[*], V.A.Rozhansky[*]

A.F.Ioffe Physico-Technical Institute, Leningrad, USSR
[*] M.I.Kalinin Polytechnical Institute, Leningrad, USSR

In Ref.[1] a method of plasma diagnostics, based upon the investigation of the impurity, ablated from the pellet's surface was proposed. It is possible by this method to determine the velocity of poloidal rotation [2] and the impurity confinement time [3]. The ablation rate can give information on some of the plasma parameters[4]. The magnitude and the direction of poloidal rotation may influence transport processes both for the main plasma component [5] and for the impurities [6]. Meanwhile, the data concerning poloidal rotation are dissimilar for different tokamaks. In TM-2, T-3 [7] and T-10[4] plasma had a positive charge, but in ST [8] and LT-3 [9] a negative one. The direction of the radial electrical field in [2] was not determined. We present below the data on the direction and the radial profile of the poloidal rotation velocity $v_o(r)$ and on the impurity confinement time in FT-1 tokamak.

When the poloidal rotation having been investigated, the 0.7 mm carbon pellets were injected in plasma upwards along the central vertical chord or along the chord shifted outward on 7.5 cm (for sign determination). The spatial distribution of ablating impurities was detected in different spectral lines (CIII, CV) by the rapid scanning optical system. The discharge was synchronised with the moment when the pellet reached the upper point of the trajectory. The data concern the 5÷10 ms from the beginning of the discharge. The undisturbed plasma parameters at 15-th ms are follows: $T_e(0) = 200÷300$ eV, $T_i(0)=70÷100$eV, $n_e(0) \sim 10^{13}$ cm^{-3}, B = 6÷12 kG, I = 20÷60 kA. Limiter radius a = 15 cm.

The measurements were made at t ≃ 6-th ms, when the ablating impurity did not disturb the discharge essentially. In the case of injection along the shifted chord the radial profiles of CIII line were measured. Typical profiles of CIII for direct and reversed directions of toroidal field are shown in Fig.1. The profiles are asymmetrical and the asymmetry reverses with the reversion of B_T. This fact indicates on the drift character of the slowly decaying wing of the profile. The line intensity decreases exponentially with the distance from the pellet to the point of observation x , see Fig.2. It means, that the spreading of C^{2+} ions along the magnetic field is insignificant. The absence of spreading along the magnetic field can be connected with the low level of ion temperature at the initial stage of tokamak discharge. In this case the ion-impurity collisional frequency is high enough. The poloidal rotation velocity was obtained from expression:

$$I^\lambda \sim \dot{N}_r \exp\left(-\frac{x}{v_o \tau_{ion}}\right) \qquad (1)$$

where $\dot{N}_r$- ablation rate, τ_{ion} - ionization time for CIII. The values of v_o for r = 8 cm are shown in Fig.3.

When the injection was made along the central chord, we used the same method for v_o measurements as in Ref.[2]. The value v_o was calculated from the expression:

$$V_o = \frac{\pi \tau_o}{\tau_{ion} \ln \frac{2A_1}{A_2}} \qquad (2)$$

where r_o – radius of the magnetic surface, on which the pellet was ablating, A_1 – intensity of the main maximum of spectral line emission, A_2 – intensity of the "satellite", appearing on the opposite side of the magnetic surface due to poloidal rotation. The expression (2) differs from the expression (2) in Ref.[2], where the significant spreading velocities of the impurity ions along the magnetic field were supposed. Therefore the v_o values in [2] seems to be overstated. The $v_o(r)$ profile, obtained by this method, is also shown in Fig.3.

The direction of poloidal rotation could be measured only by injection along the shifted chord. The sign of poloidal rotation corresponds to the direction of the radial electrical field from the periphery to the centre. This sign did not change during the stage of intensive ablation, when the plasma parameters were strongly disturbed. At this stage the CIII line intensity decrease was also exponential with the same characteristic $length$ as at the initial stage (t ≤ 5÷6 ms).

Impurity transport was studied by means of injection of the very small pellets (0.1 mm). Such pellets did not influence the macroscopic parameters, but yielded the perturbation of the electron density and the impurity radiation. From the relaxation of this perturbation one can obtain the impurity confinement time τ_I . For the large set of impurities from Li to W (see[3] for details) it was shown, that the impurities did not accumulate in plasma of relatively small electron density $n_e \sim 10^{13}$ cm^{-3}. Impurity confinement time was independent of the kind of impurity and could be approximated by expression:

$$\tau_{teor} = 0.5 \cdot 10^{-2} \frac{R a^2 B^2}{T_i^{3/2}} \left(\frac{cm^3 \kappa G^2}{e V^{3/2}}\right) \qquad (3)$$

shown in Fig.4.

DISCUSSION. The direction of the radial electrical field in FT-1 tokamak was measured at the initial stage of the discharge, when the ion temperature was low and the ions were in Pfirsch-Schlüter regime. In this regime the ion thermal conductivity must exceed the electron one, and the electrical field confines ions, as the most rapid component. The sign of the electrical field in FT-1 is the same as in LT-3 [9], where ions were in hydrodynamical regime. At the intensive ablation stage the collisional frequency increased due to the input of impurities and plasma cooling, so the Pfirsch-Schlüter regime maintained and the sign of the electrical field did not change. The magnitude of the electrical field, as pointed in [2], is close to $E = (T_e/en)dn/d\tau$ It does not contradict the conceptions of electrical field in the Pfirsch-Schlüter regime [10].

The impurity transport was studied at the stationary stage of the discharge. In this case electrons were more rapid than ions: $\tau_{Ee} \sim 1$ ms, $\tau_{Ei} \sim 5÷6$ ms. The impurity confinement time observed here is in good agreement with the expression (3) , obtained from the neoclassical theory [6] in assumption that the plasma had a positive charge.

It is possible that the discrepancy in the directions of poloidal rotation in different tokamaks can be connected with the different relations between transport coefficients of electrons and ions.

REFERENCES

1. V.E.Golant, et al. Pis'ma Zh.Tech.Fiz., 3, 1035, 1977.
2. A.P.Zhilinsky, et al., Pis'ma Zh.Ehksp.Teor.Fiz., 30, 405, 1979.
3. A.P.Zhilinsky, et al., Pis'ma Zh.Ehksp.Teor.Fiz., 32, 412, 1980.
4. S.M.Egorov, et al., X Europ.Conf.on Contr.Fus. and Plasma Phys., Moscow, 1981.
5. A.A.Galeev, R.S.Sagdeev. In: "Voprosy Teorii Plasmy", ed. by M.A.Leontovich, v.7, Moscow, 1973.
6. V.A.Rozhansky, Fiz.Plasmy, 6, 850, 1980.
7. S.V.Mirnov, I.B.Semenov, Atomnaya Energiya, 30, 20, 1971.
8. F.C.Jobes, S.C.Hosea, VI Europ.Conf.on Contr.Fus. and Plasma Phys., Moscow, 1, 199, 1973.
9. M.S.Bell, Nucl.Fusion, 19, 30, 1979.
10. V.A.Rozhansky, L.D.Tsendin, Fiz.Plasmy, 6, 1258, 1979.

Fig.1
Fig.2
Fig.3
Fig.4
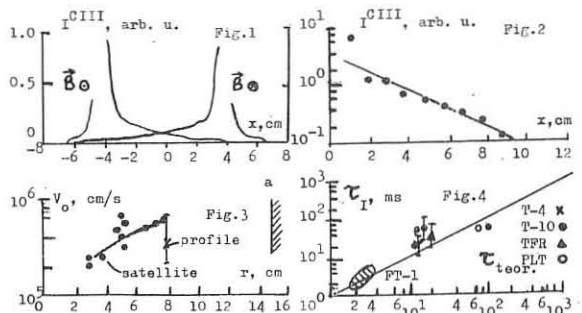
PELLET DIAGNOSTICS EXPERIMENTS IN T-10 TOKAMAK

S.M.Egorov,A.P.Zhilinsky,V.A.Krupin[x], B.V.Kuteev,V.A.Nikiforov,
V.A.Rozhansky,L.D.Tsendin

Kalinin Polytechnical Institute,Leningrad,USSR
[x]Kurchatov Institute of Atomic Energy,Moscow,USSR

In virtue of the short duration of pellet heating and ablation in large tokamaks, it is necessary to use fast pellets for diagnostic purposes /1/.This method has some additional advantages with respect to the method of immovable pellets /2/.Pellets can be injected at the arbitrary stage of the discharge.So it is possible to create almost instantaneous impurity source in any point of tokamak.The possibility arises for detailed investigation of transport phenomena in plasma.It is essential,that one can get the information about distribution of examined characteristics during one impulse.

Experimental scheme is shown in Fig.1.Pellet radius and velocity were 100-300μm and 100 m/s,respectively.In first (I) case pellets were injected along the vertical chord 20 cm shifted to the inner side of the torus.In second (II) one the trajectory formed $30°$angle with the equator plane.Observation on the pellet ablation and impurity cloud was carried on with the optical system.It provided spatial distribution of impurity line intensity with the resolution ~1 cm and periodicity ~ 300μs.Investigations were fulfilled in the discharges with the following parameters:magnetic field B_t=15-17kG,discharge current I=200 kA,safety factor q=2,mean electron density $\langle n_e \rangle$=(1÷3)10^{13} cm^{-3},electron T_e and ion T_i temperatures 1 keV and 0.5 keV,respectively,limiter radius a=29 cm.

The investigation of fast high-melting pellets interaction with plasma is of interest both for further development of diagnostics and for elucidation of heat transport mechanism on the hydrogen pellet used for refueling/3/.Dependences of the ablation rate $\dot{N}_I$ from radius in two variants of injection are shown in Fig.2,3.In the experiment lines of CII (AlI,TiI) were observed.Line intensity was supposed to be proportional to $\dot{N}_I$.Absolute calibration of $\dot{N}_I$ and evaluation of pellet size carried out by the total electron density increase after injection.It was supposed,that the final ionization state of C was total. Intensive carbon ablation started near r=26 cm.It was in good agreement with the model of pellet heating up to the temperature ≳2500°K under the heat flux Γ=9/4 $S n_e T_e^{3/2} m_H^{-1/2}$ (s-surface area).This expression was derived with the account of negatively charged pellet surface. In the case I $\dot{N}_I$ varied with radius proportionally to ~$nT^{3/2}$ (see Fig.2).In the case II line intensity sharply increased at r=20 cm. At lesser radii $\dot{N}_I$ did not change until the total extinction of the pellet.The pattern of Al and Ti ablation was similar.The expression for the ablation rate with the account of dense plasma cloud formation around the pellet states

$$\dot{N}_I = 10^{18} S n_e T_e^{3/2}/\mathcal{E}_o \qquad (1)$$

$\mathcal{E}_o$~50 eV-being the ionization energy to ion C^{+1}.Possibly,the discrepancy at r=20 cm is caused by the observed group of fast electrons on the outer side of the torus,which may lead both to the shift of $nT^{3/2}$ maximum outside and to the additional heat flux on the pellet. From the obtained it data it follows,that for the next-step tokamak pellet diagnostics velocities about ~1 km/s will be sufficient.

The injection of small pellets did not lead to the loss of stability and discharge disruption.For the investigated low-q regime the critical sizes are about 300μm for C and 100μm for Al and Ti.Maximum density increase for C at $\langle n_e \rangle$=10^{13} cm^{-3} mounted up to 100%,but for Al and Ti was less than 10%.After injection there were observed relatively fast changes in n_e,bolometric and soft X-ray(SXR,E≳2 keV) signals and subsequent signal relaxation to the undisturbed level (Fig.4).Decay time of these signals may be interpreted as the impurity life-time τ_I.In the case of carbon injection the main contribution to n_e gave nuclei C^{+6}.By the n_e signal relaxation it was possible to determine τ_I.It increased with electron density (see Fig.5). τ_I values obtained from relaxation of n_e,SXR and bolometric signals are close to each other.The situation is different in case of Al and Ti injection.Density increase is small in this case and bolometric signal rapidly (with the ionization time to He-like ions) relaxes to the undisturbed level.Pellet injection most affected the SXR-signal. If the SXR-signal is proportional to the central Al density ,the Al transport time from r=20 cm,where the pellets were ablated,to the centre was about ~ 50 ms (for $\langle n_e \rangle$=$3\cdot10^{13}$ cm^{-3}).The relaxation of SXR signal is caused by the impurity outflow.Al and Ti ions remain in plasma a little longer than C.The τ_I values for C in a factor of 1.5 exeed the Ar^{+16} transport time /4/.The question of τ_I dependences

from the impurity species requires more detailed investigations.

For theoretical analysis of plasma and impurity transport it is necessary to know the magnitude and the direction of poloidal rotation velocity V_o /5/.These characteristics were determined by the method described in /2/.The dependences of CII line intensity I at carbon injection along the vertical chord are shown in Fig.6.The profile maximum shift corresponds to pellet movement.The profile asymmetry is caused by the plasma rotation.It reverses with the magnetic field reversal.On the profile wing the striations in $\vec{E} \times \vec{B}$ direction were observed.The similar ones are observed in the active cosmic experiments /6/.The values of V_o were determined according to $I=I_o exp(-x/(V_o \tau_{ion}))$,where τ_{ion}.- ionization time.The striation must be formed at the distance Δl~$V_o \tau_{ion}$. from the impurity source /6/.V_o values calculated from I(x) decay and from the first striation position are shown in Fig.7.The poloidal rotation direction corresponds to the positive charge of the plasma centre.Its value considerably exeeds the electron diamagnetic drift velocity. $u_{ne} \sim (\frac{cT_e}{eBn})\frac{dn}{dr}$. According to/5/ the neoclassical convective impurity flux must depend on the radial electric field magnitude and be directed outward, if plasma is charged positively.Transport velocities values $\langle V_r \rangle$calculated according to /5/ with measured V_o were about ~10^3 cm/s.This velocity corresponds to τ_I~$a/\langle V_r \rangle$≳30 ms.However,dependece of $\langle V_r \rangle$ from V_o in the V_o range from V_o=u_{ne} to the experimental values turned to be weak.So scaling /2/ corresponding to V_o~u_{ne} gives $\tau_I(ms)=0.5\cdot10^{-2}$ $Ra^2B^2q^{-1}(0)T_i^{-3/2}$ $(cm^3 kG^2 eV^{-3/2})$≳20 ms. In low density regime these values are in quite good agreement with measured ones.

REFERENCES

1. V.E.Golant,et al.Pis'ma Zh.Tech.Fiz.,3,1035,1977.
2. A.P.Zhilinsky,et al.Pis'ma Zh.Ehks.Teor.Fiz.,32,412,1979.
3. C.T.Chang,L.W.Jørgensen,R.Nielsen,L.L.Lengyel,Nucl.Fus.,20,859,1980
4. A.B.Berlizov,et al.,8th Int. Conf. on Plasma Phys. and Contr. Nucl. Fus. Res.,Brussels,1980,IAEA, Rep. CN 38/A-2.
5. V.A.Rozhansky, Fiz.Plasmy,6,850,1980.
6. V.A.Rozhansky, Fiz.Plasmy,7,Noo.3,1981.
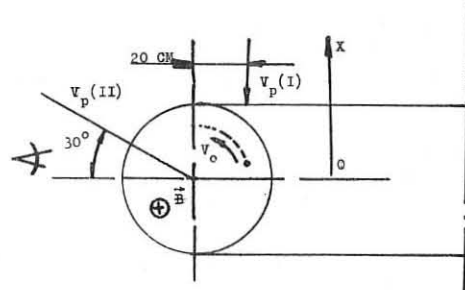
Fig.1
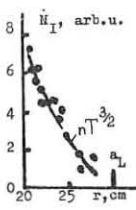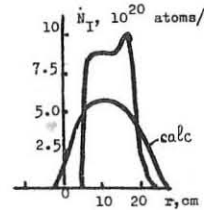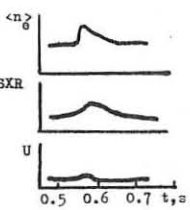
Fig.2   Fig.3   Fig.4
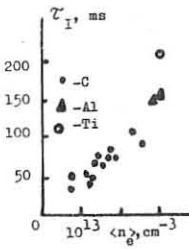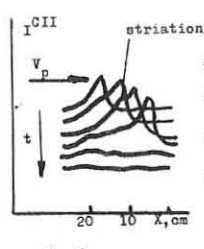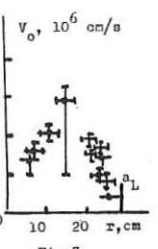
Fig.5   Fig.6   Fig.7

HIGH BETA STUDIES WITH BEAM-HEATED, NONCIRCULAR PLASMAS IN ISX-B*

E. A. Lazarus, S. C. Bates, J. D. Bell, C. E. Bush, B. A. Carreras,
J. L. Dunlap, G. R. Dyer, P. H. Edmonds, J. H. Harris, H. C. Howe,
D. Hutchinson, R. C. Isler, H. E. Ketterer, L. L. Lao, J. F. Lyon,
C. H. Ma, J. T. Mihalczo, M. Murakami, L. E. Murray, G. H. Neilson,
D. R. Overbey, V. K. Paré, M. J. Saltmarsh, S. D. Scott, K. A. Stewart,
D. W. Swain, C. E. Thomas, R. M. Wieland, J. R. Wilgen, W. R. Wing, and
A. Wootton
Oak Ridge National Laboratory
Oak Ridge, Tennessee 37830, U.S.A.

Introduction

In this paper we describe some preliminary results of high beta studies on ISX-B in mildly D-shaped discharges. ISX-B is a modest size tokamak (R_o =93 cm, a =27 cm) equipped with two tangentially aligned neutral beam injectors giving a total power up to 3 MW. The poloidal coil system (Fig. 1) allows choice of plasma boundary shapes from circular to elongated ($\kappa \leq 1.8$), with D, elliptical, or inverse D cross sections. The noncircular work discussed here is for $\kappa \sim 1.5$.

In brief, the major results of high beta experiments in circular discharges ($\kappa < 1.2$) are as follows:[1] (a) with injection powers up to 2.5 MW, we have achieved β (=$<\beta>_{vol}$) $\sim2.5\%$, β^* (=$\sqrt{<\beta^2>}$) $\sim3.5\%$, $\beta_p \sim2.5$, and q_ϕ (=$d\phi/d\psi$) ~3; (b) β increases more slowly with beam power above ~1.5 MW and it is the quantity $\beta_p \cdot \sqrt{I_p}$ that saturates, rather than β per se; and (c) the saturation results from a degradation of energy confinement, primarily due to decreasing electron energy confinement time as beam power increases. A possible mechanism for the decreasing confinement is enhanced electron heat conduction due to mixing of magnetic islands at high β_p equilibria,[2] a mechanism consistent with the observed MHD activity. However, beam-specific effects (e.g., plasma rotation) may be involved.

Noncircular Discharge Characteristics

Typical discharge characteristics for a sequence at B_T =0.91 T are shown in Fig. 2. The plasma current is programmed to rise slowly, leading to a q value that decreases to $q_\phi \gtrsim 3$ at the end of the discharge. Titanium gettering has been used to facilitate low q operation. The injectors are turned on at 80 and 120 ms. A slowly rising beam current is used to improve plasma position control. The time behaviors of β and β_p derived from the magnetic measurements are shown in Fig. 2d.

Analysis of Noncircular Discharges

The data analysis procedure has recently been expanded to determine the internal magnetic configuration consistent with MHD equilibrium theory using a moment analysis method.[3] The shift, elongation, and triangularity (Fig. 5) of the internal flux contours are derived from (a) the experimental pressure profile, based on the midplane Thomson scattering profiles and ion temperature measurements supplemented by neoclassical ion power balance and beam slowing-down equations; (b) the plasma current profile, modeled to be consistent with the radius of the q=1 surface observed with the soft x-ray array; and (c) the form of the outermost magnetic surface, determined from the coil currents and the array of magnetic probes shown in Fig. 1. As a further self-consistency check, predictions are made of experimentally determined quantities not used as input to the analysis, such as T_e and n_e profiles 10 cm above the midplane (Figs. 3a, 3b) and multichord line integral densities obtained by vertically oriented far-infrared (FIR) interferometry (Fig. 3c). The example shown in Fig. 3 shows little difference in the Thomson scattering profiles on and above the midplane, an indication of the substantial internal elongation observed in the lower q discharges. A further check on the self-consistency is illustrated in Fig. 4 where the value of β computed from the magnetic analysis is compared with the value obtained from the energy analysis. Agreement is excellent.

Experimental Results and Discussion

Due to the apparent β_p saturation observed in circular plasmas, the high β studies with elongated plasmas have emphasized low q operation. This results in operation at current levels close to the machine limit (for low β_p) and low toroidal field (for high β and low q). However, no significant penalty is incurred by low B_T operation. This can be seen in Fig. 6, which shows that β_p remains constant as B_T is reduced to 0.75 T at constant plasma current, beam power, and line density. Although the total energy content remains a constant, significant changes in profiles are occurring, as evidenced by an almost linear decrease in $T_e(0)$ from 1.35 keV to 0.65 keV as B_T decreases from 1.4 T to 0.75 T.

The results for elongated plasmas have been similar to those for circular plasmas. For example, a similar dependence of β values and confinement time on beam power has been observed. Figure 7 shows that the electron energy confinement time (evaluated at a/2) normalized to $\bar{n}_e$ decreases with P_b as it did in circular plasmas, data for which are represented by the curve shown. These similarities are perhaps not surprising because the internal elongation ($\kappa \sim 1.3$ compared with $\kappa \sim 1.1$ in circular discharges; see Fig. 5) has not increased greatly.

The power balance in these plasmas is similar to that in circular plasmas. There is a large unidentified electron energy loss in the plasma core. Two possible mechanisms for this loss are being investigated: resistive MHD modes characteristics of high β_p plasmas and beam-specific effects such as plasma rotation. The MHD activity is being studied with a new 32-unit array of soft x-ray detectors viewing the plasma from the side, as well as an array of Mirnov coils. The signals confirm that the MHD instability is dominantly m=1. The m/n=2/1 response of the Mirnov coils is not a "separate" mode localized near q=2. Experimental waveforms are similar to those generated by a simulated x-ray diagnostic applied to instability structures obtained from resistive MHD calculations.[2] From these calculations the more unstable toroidal eigenmode is the n=1, which has m=1 as the dominant component and an m=2 component that peaks near the q=1 surface (as opposed to the q=2 surface, as would be expected if the m=2 mode were dominant). The distorted mode nonlinearly generates many overlapping magnetic islands that may enhance heat conduction loss. The beam-specific effects, such as plasma rotation and beam-driven current, are being studied.

In conclusion, we have expanded the high β experiment to include elongated, moderate q plasmas and developed profile analysis methods consistent with both MHD equilibrium theory and details of other supporting measurements. Measurements to date have not resulted in higher β values than those achieved in circular plasmas; however, we are not prepared to conclude that further experiments cannot demonstrate improvement due to elongation.

REFERENCES

1. D. W. Swain et al., "High Beta Injection Experiments on ISX-B," to be published.
2. J. A. Holmes, B. A. Carreras, H. R. Hicks, and K. E. Rothe, paper presented at the Annual Controlled Fusion Theory Conference, University of Texas, Austin, Texas, U.S.A, April 8-10, 1981.
3. L. L. Lao, S. P. Hirshman, R. M. Wieland, ORNL/TM-7616 (accepted by Phys. Fluids).
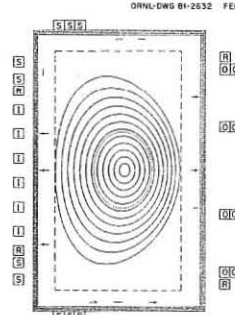
FIGURE 1. SHOWN ARE THE INNER (I), OUTER (O), SHAPING (S), AND RADIAL FIELD (R) WINDINGS ENERGIZED IN SEQUENCE #040711; ALSO, THE $B_R(-)$ AND $B_Z(|)$ PROBES USED FOR THE MAGNETIC ANALYSIS. THE DASHED RECTANGLE REPRESENTS THE LIMITER POSITIONS. THE INNER FLUX CONTOURS ARE THOSE DETERMINED FROM THE ENERGY ANALYSIS WITH THE OUTER BOUNDARY AS DETERMINED FROM POLOIDAL FIELD MEASUREMENTS. THE DASHED CONTOUR IS THE q=1 SURFACE.
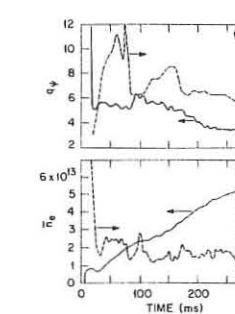
FIGURE 2. DISCHARGE CHARACTERISTICS: (a) LINE AVERAGE DENSITY AND LOOP VOLTAGE, (b) PLASMA CURRENT, ELONGATION, AND NEUTRAL BEAM POWER, (c) q_ϕ AND FRACTION OF INPUT POWER RADIATED, (d) β and β_p. SHAPING WINDINGS ARE ENERGIZED AT 80 ms.
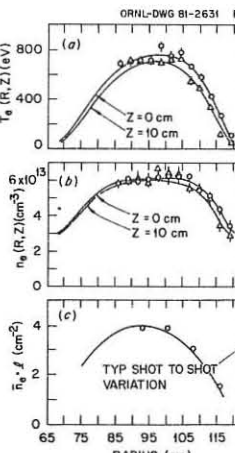
FIGURE 3. (a) T_e AND (b) n_e PROFILES AT Z=0 (CIRCLES) AND Z=10 cm (TRIANGLES) AND (c) LINE INTEGRATED VERTICAL DENSITY INFERRED FROM ENERGY ANALYSIS COMPARED TO MEASURED VALUES.
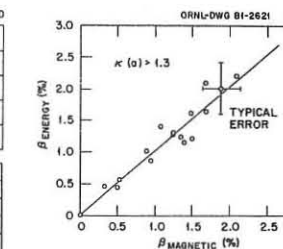
FIGURE 4. A COMPARISON OF β VALUES FROM MAGNETIC ANALYSIS AND THOSE FROM ENERGY ANALYSIS.
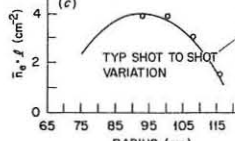
FIGURE 5. SHIFT, ELONGATION, AND TRIANGULARITY vs ρ FROM ENERGY ANALYSIS.
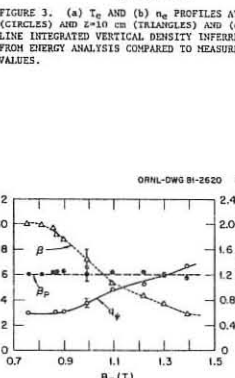
FIGURE 6. TOROIDAL FIELD SCAN AT FIXED BEAM POWER (1.9 MW), PLASMA CURRENT (170 KA), ELONGATION (1.45), AND LINE DENSITY ($n_e \cdot \ell_{vertical} = 4.2 \times 10^{13}$ cm^{-2}). SHOWN ARE β, β_p, AND q_ϕ.

FIGURE 7. ELECTRON ENERGY CONFINEMENT (WITHIN a/2) NORMALIZED TO LINE AVERAGE DENSITY vs BEAM POWER. THE LINE REPRESENTS MEASUREMENTS IN CIRCULAR PLASMAS.

EXPERIMENTAL OBSERVATIONS OF TOROIDAL DISCHARGES IN RINGBOOG II

L.Th.M. Ornstein, R.W. Polman, E.P. Barbian, C.J. Barth,
W. van den Boom, G.J. Boxman, J.J. Busser, R. Eppenga, W.J. Goedheer,
C.A.J. Hugenholtz, O.G. Kruyt, H.A. van der Laan, J. Lok,
B.J.H. Meddens, J.H.H.M. Potters, W.J. Schrader, D.A. van Wezep.
Association Euratom-FOM, FOM-Instituut voor Plasmafysica,
Rijnhuizen, Nieuwegein/Jutphaas, The Netherlands

ABSTRACT. Measurements on toroidal arcs with $n_e \simeq 2 \times 10^{20}$ m^{-3} and q_{wall} ranging from 1.5 to 8 are presented. Plasma profiles are found to extend beyond the limiter radius. A persistent outward shift in the H_α-emission is observed. The power input needed to sustain the discharge is high. This may partly be due to oxygen line radiation and, in some regimes, the losses may be enhanced because of the observed magnetically unstable behaviour of the plasma.

In RINGBOOG II [1], a tokamak-like device with B_T up to 3.2 T, R = 0.56 m and a = 0.08 m, toroidal discharges can be produced in a wide range of filling pressures. In this paper a description is given of the behaviour of discharges with various values of q_{wall}, produced at a filling pressure of 6.8 mtorr, resulting in plasma densities $\sim 2 \times 10^{20}$ m^{-3} throughout the duration of the discharge. The purpose of the experiment is to study cold-plasma and gas blankets which may surround a hot plasma core and provide shielding from plasma-wall interaction as well as fuelling and helium exhaust by diffusion through these blankets.

In earlier reports a description was given of the behaviour of the plasma in regimes which were characterized by different initial filling pressures, resulting in electron densities ranging from $\sim 10^{19}$ m^{-3} to 3×10^{21} m^{-3} [2,3]. The measured radial profiles of n_e, T_e, and the H_α- and H_β-emission were compared with results from numerical computations based on a 1-d, three-fluid, steady-state model for cylindrically symmetric cases [4]. The energy loss of the discharges could not be explained by means of the model when applied to pure hydrogen plasmas. Therefore, we assumed that the major part of the power input is lost through line radiation of impurities, mainly oxygen. This assumption leads to an upper estimate for the oxygen density of $n_{ox} \simeq 2 \times 10^{18}$ m^{-3} (cf. $n_e \simeq 2 \times 10^{20}$ m^{-3}) when the pertinent radiative energy losses are taken into account [5]. When a small amount of oxygen was introduced into the code, broader profiles were calculated in reasonable agreement with experimental observations.

Recently, profiles have been measured by simultaneous horizontal and vertical scanning. In all discharges studied, plasma profiles, such as $\int n_e d\ell$, H_α- and OIV-emission, are found to extend far beyond the limiter radius, in contrast with usual tokamak results. Furthermore, it may be observed that although the discharge is well centred, as is evident from the cosine-belt and from the $\int n_e d\ell$-profile (see Fig. 1), an outward shift is found in the $H_\alpha(R)$-emission. This asymmetry persists for all positions of the discharge, even if it is shifted over 20 mm towards the inside. This phenomenon is, as yet, not understood. The asymmetry makes our earlier comparisons of symmetrized experimental profiles with the numerical results questionable.
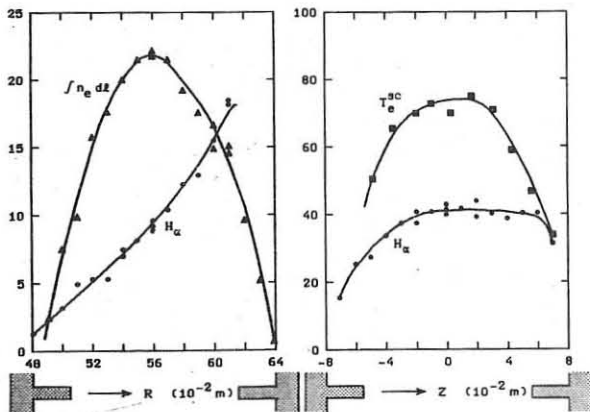
Fig. 1. Radial profiles of $\int n_e d\ell$ (in 10^{18} m^{-2}) obtained from CO_2-laser interferometry, T_e^{SC} (in eV) obtained by Thomson scattering, and H_α-emission (arb. units) for discharges with p_{fill} = 6.8 mtorr, I_p = 29.5 kA, B_T = 2.35 T, limiter aperture 0.11 m. Values are taken at t = 4.4 ms.

To study toroidal arcs in a wider parameter space, I_p was varied from 7 to 35 kA and B_T from 0.7 to 3.2 T; p_{fill} was kept constant at 6.8 mtorr. As shown in Fig. 2, the temperatures depend strongly on the value of q_{wall} and on the discharge current.

In Fig. 3 the power input per particle, P^*, is plotted as a function of T_e^σ. A number of observations can be made:

a. For low discharge currents, I_p = 7, 15, and 22 kA, the values of T_e^σ and P^* are limited to narrow ranges (regimes labeled a, a', a''). The values of q_{wall} for these regimes are high: ranging up to q_{wall} = 8. In these regimes the fluctuations in the poloidal magnetic field are low. We may again assume that the power loss is mainly due to oxygen line radiation as stated earlier [2,3]. The evolution in time of characteristic O IV-O V-O VI-lines in the VUV range has been studied. The temperature on axis as deduced from this evolution ($\sim$ 20 eV) compares well with the Thomson-scattering data, where $T_e^{SC} \simeq 16$ eV for rather flat profiles.

b. Regimes (b) and (b') at I_p = 15 and 22 kA, are characterized by higher values of P^* at lower values of $q_{wall} \simeq 3$ to 4. Small magnetic fluctuations with f $\simeq$ 10 kHz occur, corresponding to vertical oscillations of the plasma column; possibly some interaction of the plasma with the walls and the limiter leads to increased power losses.

c. At low values of q_{wall} ($\lesssim 2$), plasma regimes (c,c',c'') exist (see Fig. 2) with a strongly increased P^*. Irregular high-amplitude high-frequency ($\sim$ 50 kHz) magnetic oscillations on all magnetic pick-up belts and coils, accompanied by positive voltage spikes, indicate strongly unstable behaviour. In this regime the $\int n_e d\ell$-profiles are wider than in the standard regime a'.

d. For $I_p \gtrsim 25$ kA (regimes d,d',d'') with q_{wall} ranging from 3 to 6, strong vertical oscillations of the plasma column are found (f $\simeq$ 10 kHz). Occasionally, fast horizontal displacements of the discharge are observed, accompanied by negative voltage spikes. These occur at rather regular intervals: $\sim$ 1 ms in regime d and $\sim$ 0.3 ms in regime d'. This loss-of-equilibrium phenomenon may cause enhanced power dissipation.

In regime d the temperature profile $T_e^{SC}(z)$ has been determined by Thomson scattering. The profile is peaked rather than uniform with T_e^{SC} = 75 eV on axis (see Fig. 1). Furthermore, the $\int n_e d\ell$-profile is found to be narrower than usual.
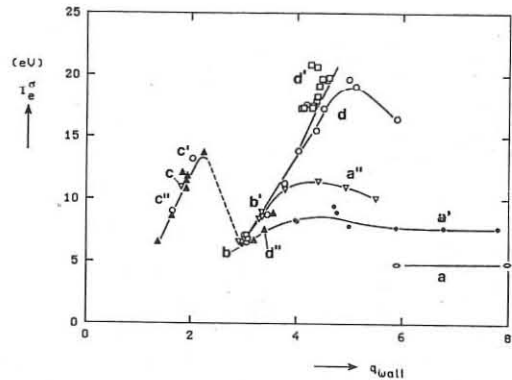
Fig. 2. Conductivity temperature, T_e^σ (calculated for uniform current density distributions extending throughout the discharge chamber, a = 0.08 m, and for Z_{eff} = 1) as a function of q_{wall} with I_p as a parameter:

-○-	7 kA	-▽-	22 kA	-□-	30 kA
-●-	15 kA	-○-	25 kA	-▲-	35 kA

Values at t = 4.4 ms.
(Labels a, b, c, d refer to different regimes as described below.)
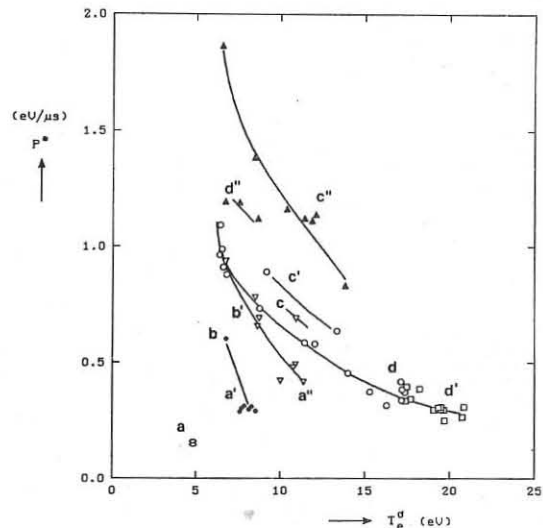
Fig. 3. Power input per particle, P^* (in eV/μs) versus T_e^σ with the discharge current I_p as a parameter (cf. Fig. 2). Labels as before. Values at t' = 4.4 ms.

REFERENCES

1. RINGBOOG-Team, Proc. 10th Symp. on Fusion Technology, Padova, 1978, Vol. 1, p. 49.
2. RINGBOOG-Team, Proc. 9th Eur. Conf. on Contr. Fusion and Plasma Phys., Oxford, 1979, paper D 2.6, p. 92.
3. Goedheer, W.J. et al., Proc. 8th Int. Conf. on Plasma Phys. and Contr. Nucl. Fusion Res., Brussels, 1980, IAEA-CN-38/Z-1.
4. Goedheer, W.J., Rijnhuizen Report 78-111 (1978).
5. Jacobs, V.L. et al., JQRST 19 (1978) 591.

DISCHARGE INITIATION WITH AN IN-SITU HYDROGEN PELLET IN DOUBLET III

F. B. Marcus, D. R. Baker, F. P. Blau, R. P. Chase, E. S. Fairbanks,
G. L. Jahns, J. L. Luxon, R. T. Snider

General Atomic Company, San Diego, California, USA

Abstract: The results of the in-situ pellet experiments in Doublet III
are summarized, with particular attention to the recent measurements of
the electron temperature and density during the early phase of the dis-
charge when large vertical elongations are achieved.

Introduction: Experiments are described in which a 2-mm diameter
cylindrical pellet of solid hydrogen is injected at low velocity (9
m/s) to the central region of the discharge column in the Doublet III
tokamak, immediately prior to initiation of the plasma discharge. The
pellet provides a source of high purity hydrogen on axis which forms a
dense, cold plasma when ionized. The cold plasma regulates the pellet
ablation rate, allowing a relatively slow buildup of plasma density.
The in-situ gas source results in a plasma with higher density, lower
impurity levels, and a persistent broadened current density profile.
The recently obtained electron temperature data reported here provide
important information for understanding the evolution of this broadened
current density profile.

Experimental Apparatus: High-purity solid hydrogen is extruded and cut
into a 2-mm diameter rod approximately 3 mm long [1]. The pellet is
accelerated vertically upwards at velocities up to 14 m/s, and is timed
to arrive at the discharge magnetic axis immediately prior to discharge
initiation.

The Doublet III tokamak [2] has the following parameters: major
radius R_0 = 1.43 m, plasma width $2a_0 \leqslant 0.94$ m, plasma height $2z_0 \leqslant 2.90$
m, and toroidal field = 2.4 T. Feedback control of the magnetic flux
linking the 24 field shaping coils allows the shape and position of
many types of discharge to be controlled [3]. For pellet experiments,
the power supplies are programmed to produce an elliptical plasma in
the upper half of the vessel with a nominal external vertical elonga-
tion of 1.3-1.4 for discharges with a typical ohmic current profile.

Experimental Results: The results common to the earlier [4] and more
recent experiments are summarized as follows. The in-situ pellet
ablates in the presence of a neutral shielding cloud over a period of
6-9 ms after breakdown, providing a high purity source of hydrogen on
axis which is retained in the plasma with 80% efficiency. The line-
averaged density is increased from 2×10^{13} cm^{-3} by a factor of 2 to 3
up to a maximum of 5×10^{13} cm^{-3}. Electron density profiles are
obtained by inverting the measurements from a CO_2 laser interferometer
array. Electron density profiles of discharges with pellet initiation
(type P) are flat, whereas normal discharges with no pellet (type NP)
have hollow profiles for the first 50 ms. Both types have identical
levels of gas prefill and power supply programming. Both types are quies-
cent, accept gas puffing beginning at 50 ms, and last over 800 ms.
With moderate gas puffing (20 torr·litres/sec, vessel volume 27 m^3),
type P discharges have lower electron temperatures and impurity levels
for at least 450 ms.

Pellet initiation produces current profiles which are initially
hollow and then peak very slowly. These profiles allow a large
increase in the vertical elongation of the plasma. MHD equilibria [5]
were calculated at several times for type P and type NP discharges.
The flux surfaces of a type P discharge at 30 ms after discharge initi-
ation are shown in Fig. 1. The inner and outer flux surfaces have very
high height-to-width ratios $\kappa(0)$ = 2.4 and $\kappa(a)$ = 2.1, and safety fac-
tors of $q(0)$ = 11.0 and $q(a)$ = 9.8, respectively. The plasma current
is I_p = 450 kA, and the major and minor horizontal radii are R = 1.42
m, a = 0.39 m. The current density profile is hollow, and the internal
inductance is ℓ_i = 0.26 (a flat profile gives ℓ_i = 0.5). The high
elongation is confirmed by the presence of a large electron density at
the vessel midplane. Type P discharges maintain broader current pro-
files, lower values of internal inductance (Fig. 2) and larger height-
to-width ratios than type NP for up to 250-350 ms.

The lower current density in highly-elongated type P discharges is
accompanied by lower electron temperature. The electron temperature T_e
and density n_e were measured 20 ms after initiation, by laser Thomson
scattering at two points. Both points are at major radius R = 1.49 m,
one on the vessel midplane (M) and the other on the upper (U) diagnos-
tic port axis at a height z = 0.89 m. In type P, the temperatures were
T_e(U) = 36 ± 10 eV and T_e(M) = 48 ± 13 eV, indicating a hollow temper-
ature profile, and the densities were n_e(U) = $(4.4 \pm 1.5) \times 10^{13}$ cm^{-3}
and n_e(M) = $(1.2 \pm 0.4) \times 10^{13}$ cm^{-3}. In type NP, the upper temperature
increased and the density decreased to T_e(U) = 54 ± 15 eV and n_e(U) =
$(1.9 \pm 0.6) \times 10^{13}$ cm^{-3}. No midplane density was observed in type NP
due to decreased elongation. Within these errors, the point measure-
ments of electron density confirm CO_2 array measurements for type P,
but imply that density profiles may be somewhat less hollow in type NP
discharges than indicated by interferometer array measurements. Very
recent studies of circular type NP plasmas with an additional CO_2 array
channel at an intermediate position support the earlier finding that
these discharges are hollow during the first 50 ms.

The temporal evolution of the electron temperature profiles for
type P and type NP was observed with a scanning Michelson interfero-
meter which measures $2\omega_{ce}$ (twice the electron cyclotron frequency)
radiation along the diagnostic chord at z = 0.89 m. The maximum tem-
perature of each profile is shown in Fig. 3 for both types, and the
first few profiles for type P and NP are shown in Figs. 4 and 5. The
interferometer was calibrated by the Thomson scattering measurements at
high temperatures. The electron temperature calculation assumes that
the plasma is blackbody for $2\omega_{ce}$ radiation. Even at the lowest tem-
peratures, the optical depth is approximately one, so when a wall
reflectivity of = 0.9 is assumed, then the $2\omega_{ce}$ radiation is blackbody.
Each scan lasts 14-16 ms, and the time of each scan after discharge
initiation is shown. In type P, the electron temperature is initially
lower and increases more slowly than in type NP. The first scan at 28
ms in type P shows a hollow temperature profile corresponding to the
hollow current profile for the equilibrium at 30 ms (Fig. 1). At R =
1.49 m, z = 0.89 m, the $2\omega_{ce}$ temperature at 30 ms is 60 eV, which is a
reasonable increase from the laser temperature at 20 ms. At later
times, the peak electron temperatures in type P continue to be lower
than type NP.

The slower rate of temperature rise in type P discharges is also
observed by a fast far-infrared radiation detector which continuously
monitors $2\omega_{ce}$ radiation from the entire plasma width. During the
first 100 ms, the signal, which is proportional to an average of the
electron temperature, is half as large in type P as in type NP.

Initially, soft X-ray signals are very low. At later times (after
300 ms), the peak electron temperature is measured by a soft X-ray
spectrometer averaging over 50 ms intervals. The soft X-ray spectro-
meter temperatures are typically 85% ± 10% of the $2\omega_{ce}$ values and con-
firm that type P discharges are colder than type NP. The soft X-ray
enhancement factor over pure hydrogenic radiation at 325 ms is ζ = 4 in
type P and ζ = 10 in type NP, indicating that type P discharges have a
lower impurity level. After 500 ms, both types exhibit large decreases
in soft X-ray diode signals, after which sawtooth oscillations
appear [6].

Discussion: The electron temperature measurements show that type P
discharges have lower electron temperatures and a slower temperature
rise than type NP, which is consistent with a larger area and therefore
a lower current density. The properties of these equilibria (flat cur-
rent profile and high-elongation), are all favorable for stability to
ballooning modes at high β [7]. The electron density is high enough at
early times to allow auxiliary heating by high-energy neutral atom
beams, yet low enough for wave heating by ECRH.

References

[1] E. R. Johnson, General Atomic Report GA-A16090 (1980), to be pub-
    lished in Proc. 4th ANS Topical Mtg. on the Tech. of Cont. Nuc.
    Fusion (1980).
[2] R. W. Callis, General Atomic Report GA-A13996 (1976).
[3] J. C. Wesley, et al., General Atomic Report GA-A15951, to be pub-
    lished in Proc. IAEA 8th Int. Conf. on Cont. Nucl. Fus. Res.
    (1980), Brussels.
[4] F. B. Marcus, D. R. Baker, J. L. Luxon, General Atomic Report
    GA-A16060 (1980). Submitted to Nuclear Fusion.
[5] J. L. Luxon, B. B. Brown, General Atomic Report GA-A15970 (1980).
[6] Doublet III Groups, Journal of Nucl. Mat. 93 & 94 (1980) 259.
[7] R. W. Moore, et al., General Atomic Report GA-A15899, to be pub-
    lished in Proc. IAEA 8th Int. Conf. on Cont. Nucl. Fus. Res.
    (1980) Brussels.
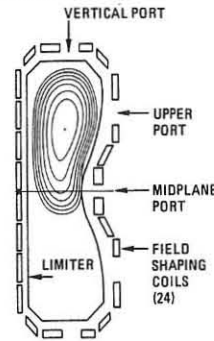
Fig. 1. MHD equilibrium.
Type P, 30 ms.
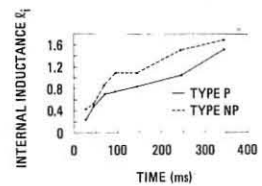
Fig. 2. Internal inductance vs
time.
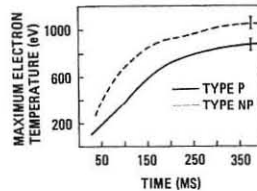
Fig. 3. Maximum electron tem-
perature vs time for
for type P and type
NP
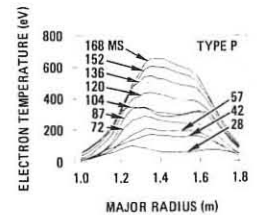
Fig. 4. Type P. Electron tem-
perature at z = 0.89 m
vs major radius at
several times.
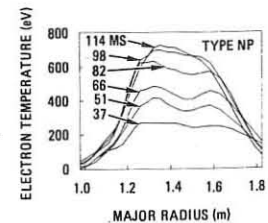
Fig. 5. Type NP. Electron
temperature at z =
0.89 m vs major radius
at several times.

DEE-SHAPED PLASMA EXPERIMENTS IN DOUBLET-III

H. Yokomizo, M. Nagami, M. Shimada, H. Yoshida, M. Maeno, K. Ioki,
S. Izumi, K. Shinya, N. Fujisawa, S. Konoshima, S. Seki, A. Kitsunezaki

Japan Atomic Energy Research Institute

Tokai, Ibaraki, JAPAN

and

GA Doublet III Group

General Atomic Company

San Diego, California, USA

Abstract: Dee-shaped plasmas are obtained stably with a surface elongation of K = 1.0 - 1.8. The maximum elongation of K = 1.9 is limited by the appearance of axisymmetric instability. The energy confinement time with an elongated plasma is improved by its geometrical effect.

Experimental Procedure: The details of an active and passive plasma control in Doublet III are described in another report [1]. The 17 field shaping coils among the 24 coils are used to produce dee-shaped plasmas [2] in the upper half of Doublet III. The rest of the lower coils are left open to decrease the power supply requirement and eliminate the production of runaway electrons. Since these coils are located just outside the vacuum vessel and are connected in parallel with each other, they are expected to work like a conducting shell and stabilize MHD instability. The plasmas discussed here have a major radius of $R \simeq 141$ cm, and a width $2a \simeq 90$ cm with an elongation of K = 1.0 - 1.8. Figure 1 shows the three kinds of plasma shapes which are sustained to be stable during the flattop of the plasma current. The diagnostics used in this study are: 5-channel tangential CO_2 laser interferometer for $n_e(r)$, scanning soft X-ray energy spectrometer for $T_e(r)$, 5-channel bolometer array for $P_r(r)$, charge exchange energy analyzer for $T_i(o)$, 10-channel tangential and 19-channel vertical PIN diode arrays for MHD activity, and 24 magnetic flux loops and 12 Rogowski coils for MHD equilibrium calculations.

Vertical Stability of Elongated Plasma: Vertically elongated plasmas are sustained to be stable with an active feedback control with an elongation of K = 1.0 - 1.8. MHD behavior measured by PIN diode array shows no drastic difference in shape. The plasma becomes vertically unstable with elongations above K = 1.8. Figure 2 shows the growth rates of the vertical displacement in hydrogen plasma without active feedback control of the vertical position. The growth rate increases rapidly around the decay index of the external field $n \left(= -\frac{R}{B_r} \frac{\partial B_r}{\partial R} \right) = -1.5$. Since ideal MHD theory in the shell-less tokamak predicts a growth rate of $\sim 10^6$ sec^{-1}, the difference between the growth rates in theory and experiment is caused by the passive feedback effect from the field shaping coils. The wall stabilization effect estimated by numerical calculation produces a stabilizing field with a decay index of $n_s = \sim 1.5$. The instability of the present experiment agrees well with this calculation. A plasma with a larger growth rate than $\gamma = 200$ sec^{-1} fails to be stabilized because the response time of the vertical position control system is ~ 5 ms. Figure 3 shows one example of a positionally unstable discharge which is controlled to increase the elongation gradually during discharge. The vertical position becomes unstable after 0.6 sec and oscillates up and down. When the vertical position finally runs out of control, the plasma current begins to decrease. It is interesting to note that the plasma motion is not a rigid movement during positional oscillation.

Improvement of Energy Confinement Time by Elongation: Figure 4(a) shows the experimental results of gross electron confinement time under three conditions. $T_{E_e}G$ is defined as the following:

$$T_{E_e}G = \int \frac{3}{2} n_e T_e \, dV \Big/ \int\int P_{OH} \, dV$$

where n_e, T_e, P_{OH} denote electron density, electron temperature and ohmic input, respectively. Volume integration is carried out inside r = a/2 because energy transport is dominant at $r \lesssim a/2$ and radiation loss is dominated at $r \gtrsim a/2$. The experimental conditions in Fig. 4 (a) are: ① K = 1.0, I_p = 350 kA, ② K = 1.4, I_p = 520 kA, ③ K = 1.7, I_p = 650 kA of deuterium plasmas at a toroidal field of B_T = 24 kG. Under the assumption of $n_e T_e = n_i T_i$, T_{E_eG} is expressed as:

$$T_{E_eG} \simeq \frac{T_E}{2} = \left(1 - \frac{P_r}{P_{OH}}\right) \frac{T_{E_e} T_{E_i}}{T_{E_e} + T_{E_i}}$$

$$T_{E_e} = \int \frac{3}{2} n_e T_e \, dV \Big/ \int\int \left(P_{OH} - P_r - P_{ei}\right) dV$$

$$T_{E_i} = \int \frac{3}{2} n_i T_i \, dV \Big/ \int\int P_{ei} \, dV$$

where P_r, P_{ei} indicate radiation loss power and heat transfer from electrons to ions. Because the ratio of P_r/P_{OH} is almost constant in these discharges, the saturation behavior of T_{E_eG} at the high density region is caused mainly by the electron and ion confinement properties. One of the best expressions to explain the present experiments has the following scalings:

$$T_{E_e} = \frac{n}{I} \frac{1 + K^2}{2} \quad (\propto nq*)$$

$$T_{E_i} = \frac{I^2}{\left(\frac{1+K^2}{2}\right)^2} \frac{K^2}{n} \quad \left(\propto \frac{K^2}{q* {}^2 n}\right)$$

where n and I are non-dimensional electron density and plasma current. Figure 4(b) shows the model calculations which simulate the actual experimental conditions shown in Fig. 4(a). The comparison of experimental results and model calculations shows good agreement at n, I normalized to the case of ① where T_{E_i} takes two times neoclassical confinement time. K in the model calculation takes the values of an elongation at $r = \frac{a}{2}$. At the high density region, T_{E_eG} with K = 1.7 is improved $\sim 65\%$ compared to that with K = 1.0 under the same q*.

[1] R. Stambaugh, H. Yokomizo, et al., General Atomic Report GA-A 16049, 11th Symposium on Fusion Technology (1980) Oxford.

[2] JAERI team, Nuclear Fusion 20 (1980) 1455.
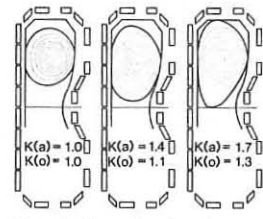
Fig. 1 Three dee-shaped plasmas

K(a)=1.0, K(o)=1.0   K(a)=1.4, K(o)=1.1   K(a)=1.7, K(o)=1.3

Fig. 5 A positionally unstable plasma.

K = 1.8   K = 1.9   K = 1.6   K = 1.9
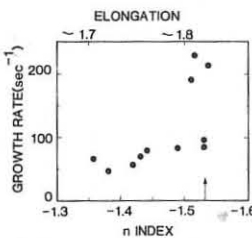
Fig. 2 Vertical movement growth rates

(a) experimental results   (b) transport calculations
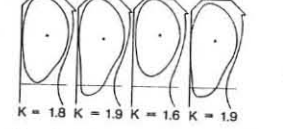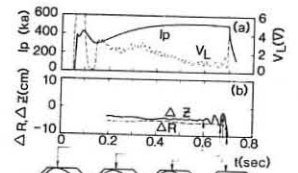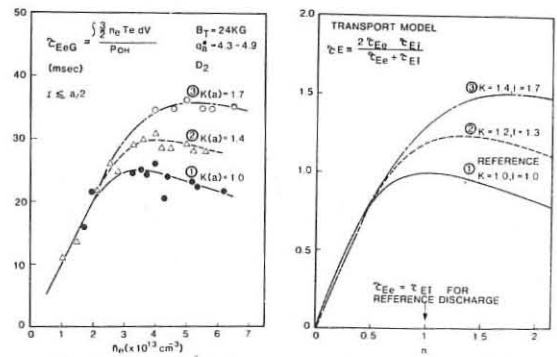
Fig. 4 Gross electron confinement time

INVESTIGATION OF PLASMA CONTAMINATION IN THE MT-1 TOKAMAK
AND MODEL EXPERIMENTS ON HIGH ENERGY EXFOLIATION

F. Pászti, G. Mezey, L. Pogány, E. Kótai, A. Manuaba, L. Pócs,
T. Lohner, J. Gyulai, G. Bürger, P. Kostka, E. Klopfer

Central Research Institute for Physics
Budapest, Hungary

To check the plasma contamination in the MT-1 tokamak [1],
single-crystal silicon probes were placed into the limiter
shadow in a configuration where the probes were facing either
to the electron or to the ion drift. This way one can measure
the radial distribution of foreign atoms. The probes were ex-
posed in two series in 203 and 751 plasma discharges
RBS and channeling measurements were carried out to investi-
gate the lateral distribution of impurities. As probing
beams. 2 MeV $^4He^+$ and $^{14}N^+$ ions served.

On each spot C, O, P, Fe, Cr, Cu, Ca. Mo and Cd /or Ag/ atoms
were found. The difference between the most abundant C and
the rarest Cd was five order of magnitude. The Fig. 1.
summarizes the observations during 751 discharges. It is re-
markable that besides impurities, serious radiation damage
was observed both on the electron and the ion side. The inter-
pretation of the results is difficult. First of all, the
sticking coefficients of different impurity atoms are un-
known. The second problem follows from the long-time collec-
tion. One can not predict the effect of subsequent discharges
on species which are already on the surface.

As a first step to study the blistering and exfoliation
processes due to plasma-wall interaction, exfoliation on cold
-rolled gold was produced by 3.52 MeV $^4He^+$ bombardment. To
study the inner morphology of the formations, they were open-
ed mechanically. The summary of the observations is the
following:

- The formation have more than one level, dome-like structure
  and their diameter increased with the bombarding dose.
- After opening, regions bordered by zones were observed both
  on the bottom and inner side of lid.
- The size of regions were highly independent of the dose,
  only the number of them increased with higher bombarding
  dose.
- The borders of regions consisted of splitted up lamellas
  that were bent outward on the bottom and inward on the
  inner side of the cover.
- The regions had different degree of surface roughness.
- The network of cracks due to the radiation hardening can be
  observed both on the bottom and the inner side of the cover.
- On the bottom of exfoliations several dips of quasi-circular
  shape in the diameter range of 10-90 /um were found.
  The material missing from them was found on the inner side
  of the lid.
- On the bottom regions several secondary blisters were found.
- The skin of the exfoliations consisted of a soft and a
  radiation hardened layer respectively.

The gold served as a model material. Similar phenomena were
observed on INCONEL and stainless steel samples, too, but this
investigations are still in progress.

References

1. G. Bürger, G. Hrehuss, B. Kardon, P. Kostka, Z. Mészáros,
   A. Montvai, L. Pócs, I. Szentpétery and L. Vályi; see this
   proceedings
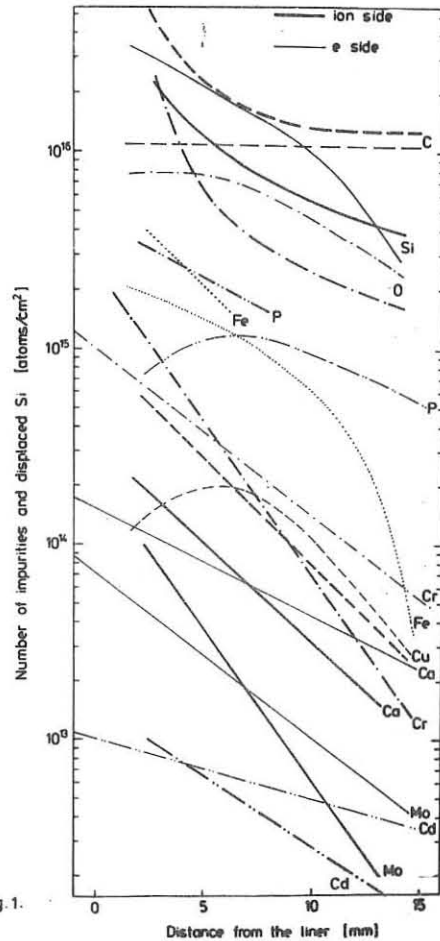
fig.1.

PLASMA PROPERTIES OF THE MT-1 TOKAMAK

G.Bürger,G.Hrehuss,B.Kardon,P.Kostka,Z.Mészáros,A.Montvai,
L.Pócs,I.Szentpétery,L.Vályi

Central Research Institute for Physics
Budapest, Hungary

The MT-1 tokamak, a recently installed machine, provided with copper shell, has a major radius R=0.4 m and the radius of the Mo limiter is a=0.09 m. A toroidal magnetic induction of 1.2 T is attainable by discharging a condenser bank of 250 kJ through the 20 toroidal coils. The maximum plasma current without major disruptions is I_p=35 kA with a duration of 8.5 ms and stable operation can be achieved with q(a)≥2.6.

The surface MHD activity pattern has been mapped by means of a set of Mirnov probes over the whole region of gross stability in the I_p - gas pressure(cont.) plane (Fig.1). A more detailed analysis [1] of the MHD resonances and also that of the frequency-amplitude patterns revealed characteristic figures for the derivatives $|d(nkT)/dr|_{r=a} \approx 2 \times 10^3$ J.m^{-4} and $|d /dr|_{r=a} \approx 10^{-7}$kg.m^{-4}, being the mass-density of the plasma. The volume averaged transverse kinetic pressure as given by diamagnetic flux measurements ranges up to the order of 1 kJ.m^{-3} and yields maximum energy confinement times approximating 1 ms (at B_{tor}=1 T, see Fig. 2). This does not contradict to Alcator-scaling, even for our relatively low B_{tor} values.

Special attention was paid to the soft- and hard x-ray spectrometry of the plasma. The soft spectra (Fig.3) are measured both with a windowless Kevex Si(Li) spectrometer and a gas-proportional scintillation counter [2]. The peak electron temperature reaches a value of 500 eV for regimes with I_p>30 kA, in agreement with Spitzer conductivity estimates assuming $Z_{eff} \leq$ 3. For gas pressure corresponding to the middle of the stability pattern (Fig.1) the hard x-ray spectra consist of one dominant exponential term only with an energy parameter $\varepsilon \approx$ 0.3 MeV (Fig.4). The energy integrated intensity oscillates in a fairly regular way being similar to and in phase with the soft x-ray sawteeths off the resonant surface q(r_s) = 1. For the lowest possible gas pressures, however, the time dependence becomes mostly irregular fluxtuating around an increased intensity level and the usual runaway spectra appear as a roughly exponential additional term with ε = 1.4 - 1.7 MeV.

The soft x-ray sawtooth oscillations as measured by means of a 5-channel pinhole camera have a repetition time of about 0.2 ms (following Launois's scaling). These are analysed in terms of the called model [3] yielding χ_e (0) $\simeq$ 10^{4}cm^2/s for the electron heat conductivity at the center, a value incompatible with the energy confinement time measured. This suggests that the radiation losses should dominate over heat conductivity in our small machine.

An extension of the diagnostics (including Thomson-scattering, charge exchange measurement of ion temperature, electron density measurement by microwave interferometry, etc.) and further investigations are in progress.

References

1. G. Bürger, G. Hrehuss, P. Kostka: Investigation of surface waves of tokamak plasmas, submitted to Nucl. Fusion
2. N.D. Vinogradova, Yu.V. Esipchuk, R.E. Kovrov, K.A. Razumova and I. Szentpétery, G. Hrehuss, B. Kardon and G. Hordósy, Plasma Physics and Controlled Nuclear Fusion Research (Proc. 7th Int. Conf., Innsbruck, 1978) IAEA-CN-37/N-3
   G. Hordósy, G. Hrehuss, Nuclear Instruments and Methods 177 (1980), 449
3. J.D. Callen, M. Soler, Nuclear Fusion 19 (1979), 703
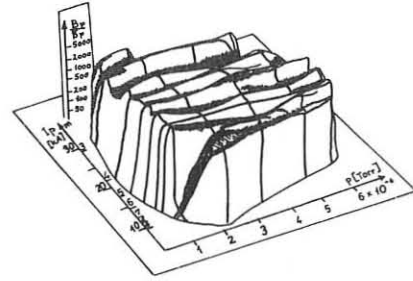
Figure 1. The inverse MHD activity $(\tilde{B}_\varphi/B_\varphi)^{-1}$ as a function of the plasma current I_p and gas pressure p.
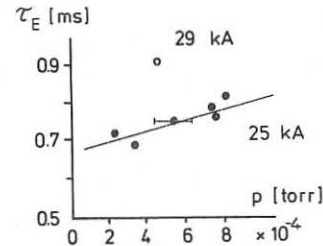
Figure 2. The energy confinement time τ_E vs. gas pressure p.
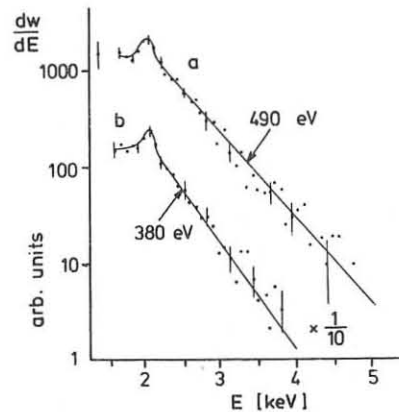
Figure 3. The soft x-ray spectra for regimes with I_p=32 kA (a) and 22 kA (b), respectively.
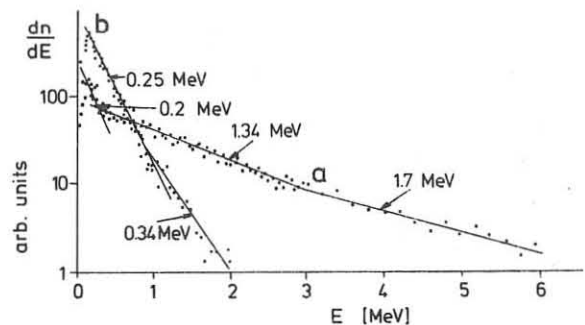
Figure 4. The hard x-ray spectra for regimes with 2x10^{-4} torr and 23 kA (a) and 5x10^{-4} torr and 30 kA (b).

THE PECULIARITIES OF THE T_e-PROFILE INTO THE T-10

Bobrovskii G.A., Vasin N.L., Vinogradova N.D.,
Gorbunov E.P., Yesiptchuk Yu.V., Kovrov P.E.,
Lyadina E.S., Notkin G.E., Odinjov A.N.,
Razumova K.A., Fyachretdinov A.N.

I.V.Kurchatov Institute of Atomic Energy,
Moscow, USSR

Possible reasons of the X-ray intensity profile asymmetry with regard to magnetic surface were investigated systematically on the T-10 Tokamak.

The analogous feature of the chord profile of the X-ray intensity $I_x(h)$ was observed previously /1/. The data presented in this paper were received in a good reproducible regime with $H_z=1.5$ T, $I_p=240$ kA, $a_L=29$ cm (bottom carbon limiter), $q(a_L)=1.8$, $\bar{n}_e=2.2.10^{13}$ cm^{-3}. As in /1/, the plasma column was scanned by Si(Li)-detectors along X and Y axes (Fig.1). Along the Y axis the column was scanned by a triple-crystal detector with different filters and diaphragms. For the observation of the sawtooth oscillations surface-barrier detectors were used which registrated soft X-ray radiation along different vertical chords. For the two-dimensional inversion the method was used analogous to the one described in /1/. The method makes possible the solutions in cases when a distribution is not symmetric to the X and Y axes. It takes into account the exponential drop in the $I_x(h)$-value at the column periphery. The T_{ex}-value was then calculated both from the slope of the spectra $I_x(E)$ and by the filter method. In the first case the T_{ex}-value is averaged over the time interval 0.3 ... 0.7 s of the discharge. The filter method had time resolution of about 20 ms. Figure 1 shows the T_{ex}-profiles determined both from $I_x(h)$ (without inversion, curve 1) and from $I_x(x,y)$ (with inversion, curve 2). It is clearly seen on the figure that the T_{ex}-profile is shifted outwards and therefore there is no symmetry in it at the radii of sawtooth inversion, $\pm r_s$, which are believed to correspond to a magnetic surface. The asymmetry can be seen also on the $n_e(x)$-profile (Fig.2). This profile was obtained as a result of the "two-dimensional" inversion of the phase shift profile measured along vertical chords.

We made it clear that the T_{ex}-profile could not be ascribed to the bulk of electrons, i.e. the electron distribution function was not a Maxwellian one, but contained also suprathermal electrons. The distortion is more essential on the outer side of the torus and may be explained by the toroidal drift of locally trapped fast electrons ($E_e > 2$ keV) which are walking from the center of the column to its periphery. This mechanism leads to the appearance of the "overheated" toroidally trapped particles outside /2/. The amount of those electrons is not less than 2.10^{11} cm^{-3} at the radius $r=+15$ cm where the effect is maximal. This density is in agreement with the value which can be estimated using the results of /2/. Pressure of those electrons is not uniform around the magnetic surface as it is pointed out by Fig.1 and 2. The energy loss due to the convective flow of such electrons is not more than a few percents of the heat conductivity losses.

We then calculated Z_{eff} and current density profiles taking into account the suprathermal electrons. The calculations showed: 1) the safety factor in the center of the plasma column was as small as 0.5 ... 0.7; 2) the $Z_{eff}(x)$-profile was nonsymmetric and

had the maximum on the outer side of the torus ($r \simeq +15$ cm). The asymmetry of the profile can be explained by the electrostatic well formed by the energetic toroidally trapped electrons. Our estimations showed that the well depth should be a few tens volts and could trap ions. For example, the asymmetry of the carbon ion density profile due to this well is estimated to be several tens of percents.

In conclusion, the electron distribution function is enriched by suprathermal particles at the periphery of the column, its amount is of order of 10^{11} cm^{-3}, their energy transport is negligible compared with heat conductivity, the $Z_{eff}(x)$-profile appears to have a maximum outside ($r \simeq +15$ cm).

References

/1/ Yesiptchuk Yu.V., Vinogradova N.D. et al. Fizika Plazmy, 7, 5 (1981).

/2/ Gurevich A.V., Dimant Ya.S. Nucl. Fusion, 18, 629 (1978).
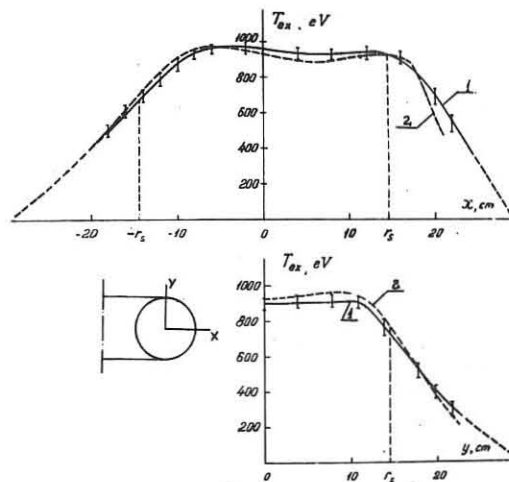
Fig.1
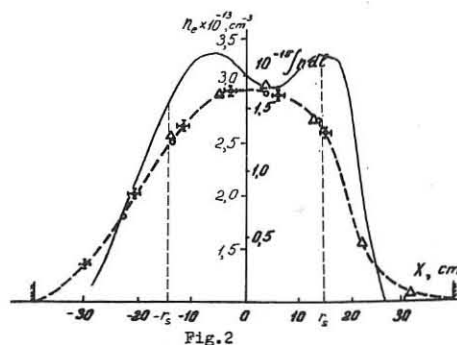
Fig.2

PECULIARITIES OF THE ION DISTRIBUTION FUNCTION IN THE T-10 TOKAMAK

E.L.BEREZOVSKY, S.L.EFREMOV [x)], A.B.IZVOZCHIKOV,

M.P.PETROV, S.Ya.PETROV

A.F.IOFFE PHYSICAL-TECHNICAL INSTITUTE,LENINGRAD,USSR

[x)]I.V.KURCHATOV INSTITUTE OF ATOMIC ENERGY

Formerly the investigation of ion energy distribution function on tokamaks has been carried out several times by scanning plasma cross-section with neutral particle analyzers up and down according to the machine equatorial plane.Ion temperature profiles obtained were,as a rule, asymmetric because of the drift of localized ions [1,2].

This work is dedicated to the scanning of the plasma cross-section in the meridional plane(inward-outward)of T-10.It was achieved by using the methods of active and passive neutral particle diagnostics(the experimental set-up is shown on Fig.1).Two neutral particle analyzers (A1 and A2 on Fig.1) and diagnostic injector of atomic beam I [3], were used in these experiments.This injector made it possible to perform active diagnostic experiments on the charge-exchange of hydrogen beam atoms with plasma deutrons(deuterium had been used as working gas in T-10). The plasma was scanned by the beam along the sight line of A1 analyzer and by the beam with A2 analyzer simultaneously along the horizontal line.Experiments were carried out in the discharge regime with low safety factor q (discharge current I=220 kA,toroidal magnetic field H=15kG, mean plasma density $\bar{n} \approx 2,5.10^{13} cm^{-3}$).

Ion temperature profile $T_i(r)$ obtained by active charge-exchange is shown on Fig.2.Ion temperature values were deduced from the slope of neutral atom spectra in (2-8)· $T_i(o)$ energy range.It is seen that the shape of $T_i(r)$ profile is asymmetric.Calculated profile $T_i(r)=600(1-r/29)^{2,5})^2$ eV corresponding to the neoclassical energy balance for this discharge conditions is shown on Fig.2 by a dotted line.On Fig.3 the density profiles for ions with two definite energies are shown.These profiles were obtained by active charge-exchange technique along the sight line of A1 analyzer.Calculated distributions $n_i(E,r)$ with $n_i(r)=$ $4.10^{13}(1-(r/39)^4)^4 cm^{-3}$ and $T_i(r)$ mentioned above are shown on the same figure.It is clearly seen that experimental curves on the plasma periphery are shifted outward comparatively to the calculated ones and that this shift grows with energy.This effect is the cause of the asymmetry of measured distribution $T_i(r)$ shown on Fig.2.

Fig.4 presents the distributions of passive charge-exchange atomic fluxes obtained by plasma scan with analyzer A2 for direct and reversed toroidal magnetic field.Again there are shifts of atomic fluxes outward which are more evident if compared with Fig.3 because of the increase of neutral atom density within the plasma edge.

Presented experimental data have proved the displacement of energetic ions to the outer side of plasma torus cross-section.The explanation of the given effect may be that observed ions have rather small longitudinal velocities($v_{\parallel}/v_{\perp} \leq 10^{-2}$).Such velocity ratio is characteristic for instance of the ions located near the tips of the banana orbits.These ions can be active in the convective transport,which was described in [4]. The transport takes place because of high probability for the ions located near the tips of bananas to be trapped by the local magnetic wells and to receive drift displacement $\Delta\Gamma_\delta \sim \delta.E^{5/2}$ $/(n_i.Z_{eff})$ (δ —the depth of the magnetic field ripple, E-ion energy,Z_{eff}-plasma effective charge).Then these ions might leave the local trap because of soft collisions and continue their movement along the banana orbits appear to be shifted outside(the value of this shift will be about $\Delta\Gamma_\delta$).This phenomena is the most evident in the outer plasma regions with the largest values of the magnetic field ripple.Here a noticeable"overheating" of ion velocity distribution function takes place as a result of combined drift of trapped and localized ions.Calculated ion drift displacements are presented on Fig.3 by horizontal chords.

The curves presented on Fig.4 show the role of the magnetic field ripple in observed ion displacement.The reversity of magnetic field H leads the changing of toroidal ion drift direction.As a result atomic fluxes detected by A2 analyzer changes considerably while the atomic fluxes asymmetry direction remains permanent.

Thus the displacements of energetic ions to the outer region of the torus are experimentally detected which are probably the effect of the superposition of drift displacements of localized and trapped ions.

References

1. A.A.Bagdasarov et al. Plasma Phys.and Control.Nucl.Fusion Research, Vienna 1979, IAEA, 1, 35.
2. Equipe TFR. Nuclear Fusion 18, 647 (1978).
3. V.I.Davydenko,I.I.Morozov,G.V.Roslyakov.Fyzica Plasmy, 7, 2, 464 (1981).
4. A.V.Gurevich,Ya.S.Dimant,Yu.N.Dnestrovsky.Doklady Acad. Nauk, 244, 1, 71, (1979).
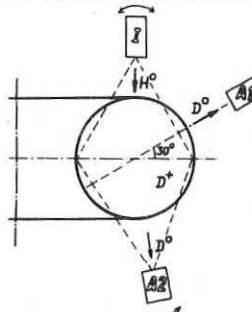
FIG. 1
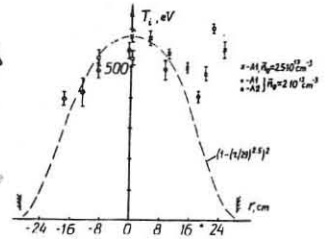
FIG. 2
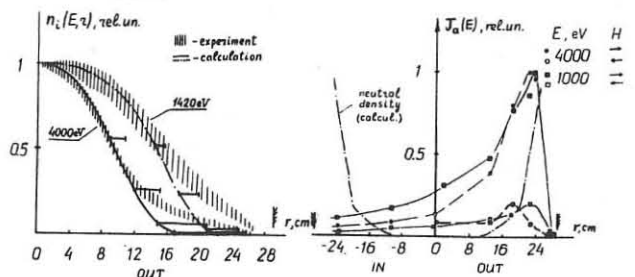
FIG. 3

FIG. 4

SPECTROSCOPY RESEARCH OF LIGHT IMPURITIES IN T-10 DEVICE

V.I.Bugarya, N.L.Vasin, N.M.Gegechkori,
Yu.N.Dnestrovsky, A.G.Zhidkov, V.A.Krupin,
S.Yu.Lukyanov, A.B.Pimenov, V.F.Strizhov

I.V. Kurchatov Institute of Atomic Energy,
Moscow, USSR

The present research concerns the experimental investigation and numerical simulation of the light impurity behaviour on the periphery of plasma column, which were carried out in T-10 standard discharge. With the help of the optical system, which consists of monochromator and rotating mirror, the time and spatial profiles of CIII ($\lambda_1 = 4647 Å$, $\lambda_2 = 2297 Å$), CV ($\lambda = 2271 Å$) and OV ($\lambda = 2781 Å$) lines were obtained. The use of this system gave an opportunity to record four profiles of the stable discharge phase. Record duration was 10 ms, space resolution was 10-15 mm, relative pulse duration ~ 100 ms.

Spatial profiles of OVIII ion ($\lambda = 19 Å$) were obtained with an X-ray monochromator, according to the Woolf-Bregg scheme with plane crystal KAP. Space resolution was approximately 20 mm, spectral one – $\frac{\Delta\lambda}{\lambda} \simeq 5 \cdot 10^{-3}$. Absolute calibration of optical and X-ray systems and Abel inversion allowed us to determine the radiation density for all the above-mentioned lines in energy units.

At the beginning of the discharge, the profiles of radiation of all lines were dome-shaped. While increasing T_e, their maxima intensities were transfered from column axis to periphery and then they occupied stable positions in the course of the whole plateau stage of discharge current. The amplitude of maxima was practically invariable. A typical case of space-time evolution of the ion CV line intensity is given in Fig.1. The examples of radial distributions of C and O ion lines in steady state of standard T-10 discharge (I=230 kA, H_z=16 kGs, $\bar{n}_e$= 1.9 . 10^{13}cm^{-3}, a_L=29 cm, $q(a_L) \approx 2$) are presented in Fig.2a,b.

Simulation of impurity ion radial distributions was done by numerical solution of the following equations:

$$\frac{\partial n_\kappa}{\partial t} = \frac{1}{\tau}\frac{\partial}{\partial \tau}\left(\tau \Gamma_\kappa\right) + S_\kappa - \frac{n_\kappa}{\tau_\kappa^\kappa} , \qquad \kappa = 1,2\ldots z$$

where k is the ion charge, z the charge of impurity nucleous, s_k describes the following atomic processes: ionization, recombination, and charge transfer, $\tau_\kappa^\kappa \simeq \frac{\pi q R}{v_s^\kappa}$ is the time of particle loss to limiter with ion-sound velocity v_s^κ. The ion flux Γ_κ was presented in the form of $\Gamma_\kappa = \Gamma_\kappa^{NC} + \Gamma_\kappa^A$, where Γ_κ^{NC} and Γ_κ^A were neoclassical /1/ and anomalous fluxes with plasma diffusion coefficient defined experimentally /2/.

The population of the excited levels of the types of ions in question, were defined by the stationary coronal model, which helps to consider the collisional population of these levels from metastable state.

T_e profile used for simulation was taken from Ref./2/, but its values in the range $20 \leq r \leq a_L$ were reduced. Additional experimental results underline this. They are as follows: the value of T_i, obtained from Doppler broadening of CV and OV lines, and the value of T_e obtained from the recombination jump of ion Ar^{+17}. Experimental profile of n_e was given by the approximate equation: $n_e = 3 \cdot 10^{13}/ 1 - (\frac{r}{37})^4/^4$. Calculated profiles of radial intensities of the lines under consideration are presented in Fig.2a, b. The chosen model gives good description of the maxima positions but describes not so well their absolute values.

The calculated halfwidths of profiles were found to be narrower than the experimental ones. Probably this is connected with the fact that it was necessary to take into account the space resolution of spectrometer (~ 1.5 cm).

The calculated total concentrations of carbon and oxygen ions are $N_c = 2.5 \cdot 10^{11}$cm^{-3} and $N_0 = 0.8 \cdot 10^{11}$cm^{-3}.

Recent experiments with fast hydrogen atom injection and the following record of line intensity of H-like oxygen ion /3/ allowed us to get the radial distribution of of oxygen nuclear concentration. Calculated radial profiles of some carbon and oxygen ions and experimental density values of nuclei 0^{+8} are shown in Fig.4. It is clearly seen that the calculations agree with the experimental results.

It should be mentioned that the Z_{eff} (~ 2) values, which is possible to get from the results of the calculations, are lower than the value of Z_{eff} (~ 4) obtained from the absolute intensity of continuous spectrum in the X-ray range and plasma conductivity. The fact, that the ion-type impurities were taken into account, doesn't improve the present state of affairs to a great extent. The reason of such divergence lies, perhaps, in the presence of some unidentified impurities in plasma.

References

1. R.J.Hawriluk, S.Suckewer, S.P.Hirshman, Nuclear Fusion, v.19, p.607, 1979.
2. A.B.Berlizov et al. Plasma Physics and Controlled Nuclear Fusion Research. 1980. Report CN-38/A-2.
3. Зиновьев А.Н.и др.Письма в ЖЭТФ, том 32, вып.9, стр.557-560, 1980г.

Fig.1. Space and time evolution of the ion CV line intensity (λ = 2271 Å).

Fig.2. Radial distributions of line intensities of ions: 1. – CV (2271 Å); 2. – CIII(2297 Å); 3.–CIII(4647 Å); 4.–OVIII(19 Å); 5–OV(2781Å). Calculation-dashed curves, experiment-solid curves.

Fig.3. Radial distribution of n_e and T_e.

Fig.4. Radial profiles of C and O ions
I - /3/.

Fig. 1.

Fig. 2a

Fig. 2β
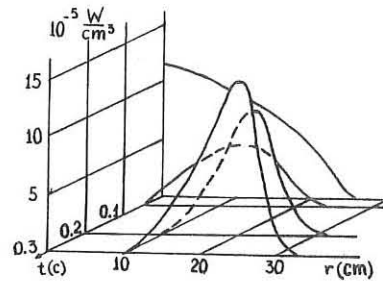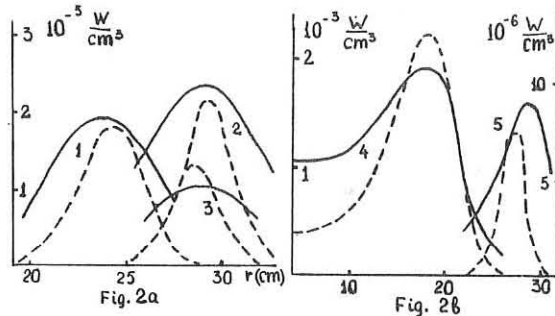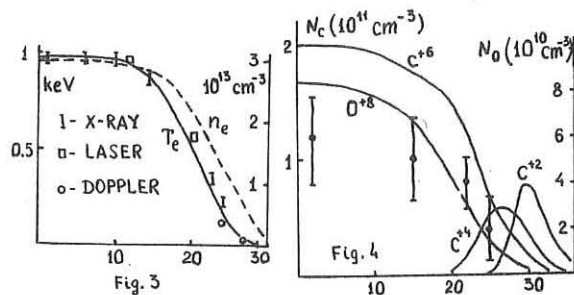
Fig. 3

Fig. 4

OHMIC HEATING IN "TUMAN-3" TOKAMAK AT LOW MAGNETIC FIELD

Golant V.E., Gornostaev S.V.[*], Grigoriev A.V.,
Gryaznevich M.P., Evtushenko T.P., Kislyakov A.I.,
Lebedev S.V., Lipin B.M., Litunovskij R.N.[*], Minyaev O.A.[*],
Rozhdestvenskij V.V., Sakharov N.V., Fedorov A.A.,
Shakhovetz K.G., Shchemelinin S.G.

A.F.Ioffe Physico-Technical Institute, Leningrad, USSR

[*]D.V.Efremov Scientific Research Institute for
Electrophysical Equipment, Leningrad, USSR

Ohmic heating regime at toroidal fields B_t= 3 kG and B_t= 4.5 kG with plasma current I_p= 70 kA and I_p= 100 kA, respectively and safety factor $q \simeq 2.5$ is described. Low value of ion collisionality parameter ($\vartheta_i^* < 1$) characterises the regimes. High average toroidal beta (up to 1÷2%) is obtained at B_t= 3 kG.

It's very important for the adiabatic compression programme, which is being carried out at "Tuman-3" [1], to obtain an effective ohmic heating at low magnetic field. In connection with the beta limit problem study of such regimes in a small aspect ratio tokamak is also of particular interest.

An experimental run followed the cleaning of the vacuum chamber with a glow hydrogen discharge and low T_e induction discharges in the mixture of hydrogen and argon. Plasma density is controlled by the puffing. Plasma column equilibrium is provided by vertical and horisontal feedback systems. Horisontal feedback has 1 kHz operating frequency and 1 MW power. At the stationary stage of the discharge the maximum shift is equal to 0.5 cm in horisontal direction and 0.2 cm in vertical direction.

Using of discharge cleaning, feedback control and puffing allows one to obtain MHD-stable regimes with low values of safety factor. The main parameters of two regimes are shown in Table 1. Fig.1 shows typical oscillograms for the first regime. Loop voltage oscillations appear due to operation of control system.

Table 1.

	R cm	a_c cm	a_1 cm	B_t kG	I_p kA	q_1	$\frac{P_{rad}}{P_{oh}}$ %	$\overline{n}_e$ 10^{13}cm^{-3}	T_i eV	$\overline{\beta}_t$ %	$\mathcal{T}_{E_i}$ ms
I	55	25	24	2,3–3,1	70	2,4–2,9	15–20	0,5–1,5	100–125	≤2	5
II				3,5–4,6	100			1–3,5	140–200	≤1	10

Ohmic heating at low magnetic field has some peculiarities. At first, plasma critical density (see Tabl.1) is not high. Increasing density above critical value results in appearance of MHD-activity and then disruption occurs. Another peculiarity of the low field discharge is the high value of $\overline{\beta}_t$.

Fig.2 presents ion temperature, measured from the slope of charge-exchange neutral spectrum by 5-channel analiser (energy interval 0.5-1.5 keV). Fig.2 also shows density profile obtained by 8-channel interferometer with λ = 2 mm. Spectral line space distributions are shown in Fig.3. Measured $T_i(r)$, $n_e(r)$ and estimated T_e allow one to calculate $\overline{\beta}_t$, which is equal to 1.5÷2% in regime I. High value of $\overline{\beta}_t$ is mainly because of the low toroidal field B_t.

Another distinction of the regimes is low ion collisionality parameter $\vartheta_i^* \sim \frac{R}{T_i^2} r q \left(\frac{R}{r}\right)^{3/2}$ due to the small aspect ratio (R/a = 2.3) and low q (see also T-11 data [2]). In considerable part of the plasma column ϑ_i^* is lower than unity and its minimum value is equal to 0.3. Ion temperature in regime II reaches 200 eV at $\overline{n}_e \simeq 1 \times 10^{13}$ cm^{-3}. This value is higher than the value calculated in assumption of neoclassical "plato" (" Artsimovich formula"). In the stationary stage of discharge ion energy lifetime estimated from the balance equation is equal to 5 ms in regime I and 10 ms in regime II. These values are

2-3 times larger than estimations, based on neoclassical plato heatconductivity, and correspond to banana heatconductivity. T_i dependence on $\overline{n}_e$ (Fig.4) is another confirmation of the considerable role the trapped particles play in the ion energy balance. If the plato regime existed one would expect T_i increase proportional to $\overline{n}_e^{1/3}$, but experimental curve has considerable decrease, which can be explained by collision frequency growth or by T_e decrease.

In both regimes one can see sawtooth oscillations, they are characteristic of low-q discharges [3]. Oscillations appear on the interferometer signal, its amplitude reaches 8-12% of $\overline{n}_e l$ value and decreases with $\overline{n}_e$ growth. Oscillation period is equal to 0.5÷1.0 ms (Fig.5). Multichannel ($\overline{n}_e l$) scan shows that phase inversion radius ($q(r_s)=1$) is equal to 7÷8 cm. "Ware" pinch seems to be an explanation of the density rise in sawtooth oscillations. Possibly, this mechanism (particularly strong in the small aspect ratio tokamak) also results in contraction of current density profile. Fig.5 shows corresponding poloidal field oscillations, registered by magnetic probe (γ = 0 outside of torus).

Thus high value of $\overline{\beta}_t$ and low collisionality parameter are obtained in the ohmic heating regimes at low magnetic field. The regimes studied can be used for the experiments on compression [4].

REFERENCES

1. Vorobiev G.M. et al. Proc. II Joint Grenoble-Varenna Int.Symp.on Heating in Toroidal Plasmas, Como, Italy, 1980.
2. Leonov V.M. et al. Proc. VIII Int.Conf.on Plasma Phys. and Contr.Nucl.Fus.Res., Brussels, 1980, Paper CN-38/N-2.
3. Equipe TFR. Nucl.Fusion, 1980, v.20, p.1227.
4. Vorobiev G.M.et al., this conference.

Fig. 1

Fig. 4

Fig.2

Fig.5

Fig.3
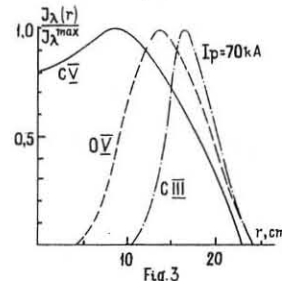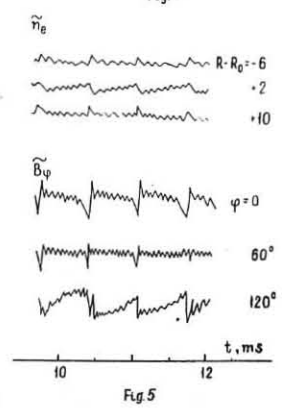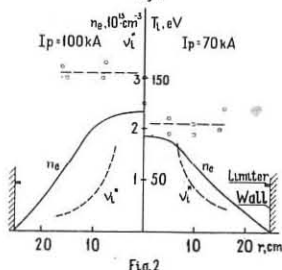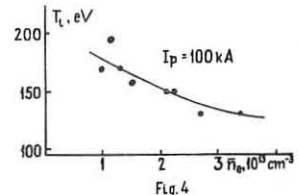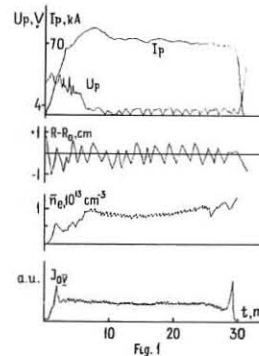
TRANSPORT PHENOMENA INVESTIGATION IN THE TOKAMAK WITH MAGNETIC COMPRESSION "TUMAN-2A"

M.I.Vil'dzhyunas,V.I.Gladushchak,S.G.Goncharov, V.K.Gusev,
V.A.Ipatov, S.G.Kalmykov, S.I.Lashkul, B.M.Lipin,
S.V.Lebedev, G.T.Razdobarin, V.V.Rozhdestvenskij,
V.V.Semenov, A.I.Smirnov, I.D.Shprits
Physical-Technical Institute, Leningrad, USSR

1. For some years a magnetic compression of plasma in minor radius is being investigated on small tokamak in Physical-Technical Institute in Leningrad /1-2/. It is considered not only as a method of plasma heating but also as a method to form actively space distribution of plasma parameters. From this point of view the study of the tokamak confinement properties in the compression experiments is of interest. The aim of the present work was to obtain heat diffusion coefficient radial profiles both for the quasistationary ohmic heating and for the maximum of compression.

2. The main experimental parameters for chosen regime are listed in the table as well as some data on transport processes for ohmic heating.

Typical discharge oscillograms are given in Fig.1. The dashed line corresponds to the discharge without compression. Electron temperature $T_e(z)$, density $n_e(z)$ and radiation losses $q_{rad}(z)$ radial profiles before compression and for the moment of maximum compression are shown in Fig.2. To obtain them microwave interferometer, ruby laser and scanning collimated pyroelectric bolometer (Fig.1, U_{bol1}) together with the stationary wide-angle one (Fig.1, U_{bol2}) were used.

Comparing Δt_c and τ_{eE}^{OH} listed in the table, one can see that the compression is much slower than the adiabatic one. As it can be seen from Fig.2 there are no significant changes in the outer discharge regions for such a slow compression. But the total particle number in the

Fig.1

Fig.2

Major radius, R	40 cm
Limiter radius, a_ℓ	8 cm
Plasma current, $I_\rho \simeq const$	11 kA
Safety factor at the limiter for the ohmic heating, $q^{OH}(a_\ell)$	5
Z_{eff} (taking into account trapped particles)	1
Compression ratio, $\alpha = B_T^c/B_T^{OH}$	2
Compression time, Δt_c	0,5 ms
Relative level of radiation losses, P_{rad}/P_{OH}	0,3
Particle life time, τ_ρ^{OH}	2,5 ms
Averaged over cross section diffusion coefficient, $D_{eff}^{OH} = a_\ell^2/(6\tau_\rho^{OH})$	$4 \cdot 10^3$ cm²/s
Energy life-time for electrons; total, τ_{eE}^{OH}	0,25 ms
transport, τ_{tr}^{OH}	0,35 ms
Averaged over cross section electron heat diffusion coefficient, $\bar{\chi}_{eff}^{OH} = a_\ell^2/(6\tau_{tr}^{OH})$	$3 \cdot 10^4$ cm²/s

plasma column $N = 4\pi^2 R \int n_e(z) z dz$ increases during compression time Δt_c, indicating confinement improvement. It follows from Fig.1 (oscillogram of $\bar{n}_e l$) that plasma density remains at a stationary level during postcompression in spite of B_T and neutral hydrogen influx (see Fig.1, spectral line $L_\perp$ oscillogram) decrease. Particle life-time estimate gives $\tau_\rho^c = 4 \div 6$ ms and $D_{eff}^c = a_\ell^2/(6\tau_\rho^c) \simeq 2 \cdot 10^3$ cm²/s.

In spite of low compression rate the temperature increase in the center of the plasma corresponds to adiabatic law $T_e^c(0)/T_e^{OH}(0) \simeq 1,6 \simeq \alpha^{2/3}$. This implies that energy confinement improves too during compression. From the solution of the power balance equation for the moment of maximum compression

$$\frac{dW_e(t)}{dt} = I_\rho U_{\rho z} + P_{magn} - \frac{W_e(t)}{\tau_{eE_c}}, \quad (1)$$

where $W_e(t) = \int 1{,}5 n_e T_e \, dV$, $P_{magn} = \frac{2}{3}\frac{B_T(t)}{B_T(t)} W_e(t)$ toroidal magnetic field power input, $I_\rho U_{\rho z}$ - ohmic power input, one obtaines $\tau_{eE}^c \simeq 0,4$ ms. The bolometric measurements made it possible to evaluate transport losses of energy
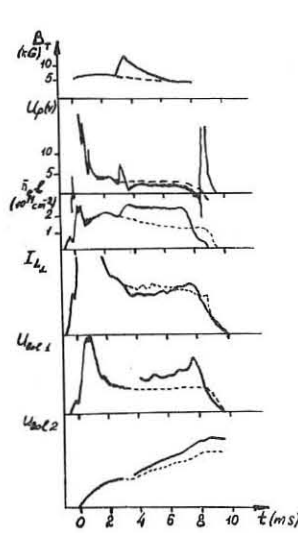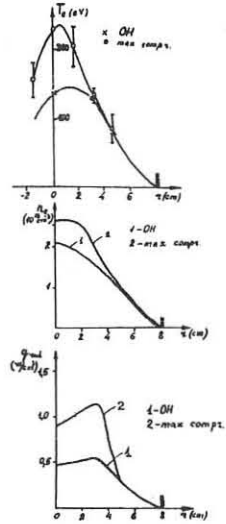
for electrons both for ohmic heating and compression. For the moment of maximum compression the transport energy life time was $\tau_{tr}^c \simeq 1,6$ ms and $\bar{\chi}_{eff}^c \simeq 7 \cdot 10^3$ cm²/s.

To obtain local values of effective heat transport coefficients $\chi_{eff}(z)$ and $æ_{eff}(z) = 1{,}5 n_e(z)\chi_{eff}(z)$ for electrons the local heat balance equation was used:

$$4\pi^2 R z \, æ_{eff}\left|\nabla T_e(z)\right| = P_{OH}(z) + P_{magn}(z) - P_{rad}(z) - P_{ei}(z) - \frac{dW_e(z)}{dt} \quad (2)$$

$$P_{OH}(z) = 2\pi U_{\rho z} \int_0^z j(z) z \, dz, \qquad P_{magn}(z) = 2\pi^2 R \frac{B_T}{B_T} \int_0^z |\nabla(n_e T_e)| r^2 dz.$$

The results of calculation are presented in Fig.3. The strong decrease of transport coefficient values in central and outer parts of the discharge column might be connected with MHD activity n=1, m=2 damping. But the decrease of the total
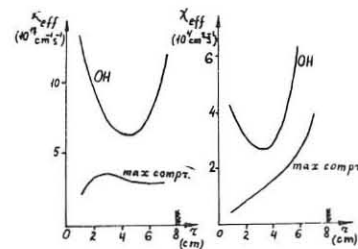
Fig.3

transport level during compression needs more explanation. Plasma parameter variations could lead to changes in confinement as in conventional stationary tokamaks (see, for example, /3/), but they are not large enough in our case.

3. The results of the present paper support and extend results of /2/.

It was shown that in "Tuman-2A" machine the confinement of heat and particles was significantly improved even under conditions of slow ($\Delta t_c > \tau_E$) compression in minor radius. One of the reasons for confinement improvement might be contraction of the current channel - heat source. The second reason is the transport coefficient decrease. For the case of fast compression a formation of a rarefied layer near the wall is possible, thus leading to further thermoinsulation improvement. The confinement improvement due to compression can result in an additional superadiabatic heating during the time of Δt_c, it is an advantage of minor radius compression.

References:
1. M.G.Kagansky, S.G.Kalmikov, S.V.Lebedev et al.. Plasma Phys. and Controlled Nucl. Fusion Research (Proc. of 6 th Int. Conf., Berchtesgaden, 1976), IAEA, Vienna, 1977, 1, 387.
2. E.L.Berezovskij, M.I.Vil'dzhyunas, V.I.Gladushchak et al.. Nucl. Fusion Supplement Plasma Phys. and Controlled Nucl. Fusion Research (Proc. of 7 th Int. Conf., Innsbruck, 1978), IAEA, Vienna, 1979, 1, 349.
3. E.Apgar, B.Coppi, A.Gondhalekar et al.. Plasma Phys. and Controlled Nucl. Fusion Research (Proc. of 6 th Int. Conf., Berchtesgaden, 1976), IAEA, Vienna, 1977, 1, 247.

THE DISTRIBUTION OF THE LOCAL VALUE OF DIFFUSION COEFFICIENT MEASUREMENT IN TOKAMAK FT-1 BASED ON PLASMA FLUORESCENCE DIAGNOSTICS

V.S.Burakov[*], I.P.Folomkin, M.M.Larionov, P.Ya.Misakov[*],
P.A.Naumenkov[*], G.T.Razdobarin, V.V.Semenov

A.F.Ioffe Physico-Technical Institute, Leningrad, USSR

[*]Institute of Physics, Minsk, USSR

ABSTRACT. The distribution of the local value of the diffusion coefficient in the tokamak FT-1 was obtained using the data on the hydrogen atoms ionization rate and the electron density profile time evolution.

The absolute density profile of hydrogen atoms measured by the resonance fluorescence method [1] was used to obtain the radial distribution of the diffusion coefficient in tokamak FT-1 (R = 62.5 cm, $\mathcal{J}$ = 27 kA, $n_e \leqslant 10^{13}$cm^{-3}, $T_e \leqslant 350$ eV, H = 7.5 kG). The local values of the diffusion coefficient were calculated using the electron surface flux outside the cylinder of radius r .

$$\Gamma_\perp = -2\pi r \; D_{eff}(r) \cdot \frac{\partial n_e}{\partial r} \qquad (1)$$

The electron surface flux $\Gamma_\perp$ was taken from the particle transport equation

$$\Gamma_\perp = \dot{I} - \frac{\partial N_e}{\partial t} \qquad (2)$$

using the experimentaly measured hydrogen atom ionization rate I and the rate of electron number change $\frac{\partial N_e}{\partial t}$ in the volume enclosed by the cylindrical surface of radius r and unit length.

$$\dot{I} = \int_0^r n_e n_a \langle \delta_i \upsilon \rangle 2\pi r' dr' \qquad (3)$$

$$\frac{\partial N_e}{\partial t} = \int_0^r \frac{\partial n_e}{\partial t} 2\pi r' dr' \qquad (4)$$

The radial distribution of ionization rate $n_e \cdot n_a \langle \delta_i \upsilon \rangle$ in formula (3) was determined from the fluorescence emission intensity on the Balmer H_α line. The fluorescence emission intensity may be written as

$$G(r) = n_e n_a \beta \qquad (5)$$

with the coefficient β calculated in paper [1].

The radial profiles of the coefficient β and the ionization rate coefficient $\langle \delta_i \upsilon \rangle$ received from experimentaly measured electron density and temperature profiles [2] are shown in Fig.1. In the condition that both coefficients indicate very similar temperature dependence and essential independence on electron density in the n_e range 10^{12}–10^{13}cm^{-3} the ratio $\frac{\langle \delta_i \upsilon \rangle}{\beta}$ is nearly constant over the column cross-section up to the wall region .

As a result the ionization rate $n_e n_a \langle \delta_i \upsilon \rangle$ and the fluorescence emission intensity G(r) have the similar dependence on radius r. The radial distribution of ionization rate $n_e n_a \langle \delta_i \upsilon \rangle$ calculated from the fluorescence emission intensity is shown in Fig.2.

The electron density was determined by multichanel microwave 4 mm wavelength interferometer. The measured line average electron density $n_e(t)$ on central chord decreased from 8.10^{12}cm^{-3} down to 2.10^{12}cm^{-3} during the time interval $\Delta t \approx 30$ ms after the maximum of the discharge current. There was no seen any significant change of the electron density profile form. In this case the rate of the

electron number fall $\frac{\partial N_e}{\partial t}$ inside the cylinder of radius r could be obtained using the formula

$$\frac{\partial N_e}{\partial t} = \frac{1}{n_e} \cdot \frac{\partial \bar{n}_e}{\partial t} \cdot 2\pi \int_0^r n_e(r') r' dr' \qquad (6)$$

Both terms $\dot{I}$ and $\frac{\partial N_e}{\partial t}$ appear to give compareable contribution to the electron surface flux (at the distance r=2/3a $\dot{I} = 3.5 \times 10^{16}$cm^{-1}sec^{-1}, $\frac{\partial N_e}{\partial t} = -7.10^{16}$cm^{-1}sec^{-1}).

The hatched area in Fig.3 represent the determined local values of the diffusion coefficient. As can be seen the diffusion coefficient increases from 10^3 cm^2/sec on axis of discharge up to 2.6×10^3 cm^2/sec in outside region. The experimental error in plotting the radial distribution of the diffusion coefficient is associated mainly with inaccurate specification of the radial distribution of electron density $n_e(r)$. In the estimates of D_{eff} the influence of impurities (Z_{eff}= 2) was not taken into account. Electron density increase due to impurity ionization might be resulted in higher values of D_{eff}. The increase of D_{eff} in the outside region due to impurities could not exceed 30%. On the discharge axis the correction of D_{eff} should be lower. Curves 1-3 in Fig.3 represent the diffusion coefficients calculated on the basis of theoretical predictions according to neoclassical transport (curve 1) and anomalous transport theory (curve 2 – pseudoclassical diffusion, curve 3 – diffusion due to dissipative trapped-electron instabilities) [3].

REFERENCES
1. G.T.Razdobarin et al. Nucl.Fusion, 19, 1439, 1979.
2. V.K.Gusev et al. Fizika Plasmi, 4, 269, 1978.
3. S.O.Dean et al. USAEC Rep.Wash.,1295, U.S.At.Energy Comm., Washington D.C. 1974.
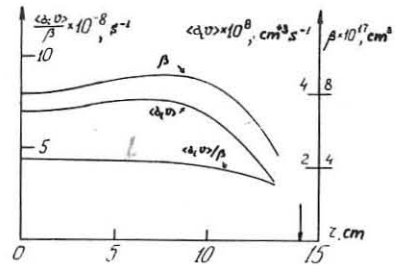
FIG.1.
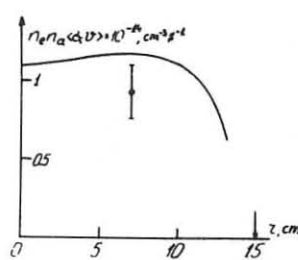
FIG.2.
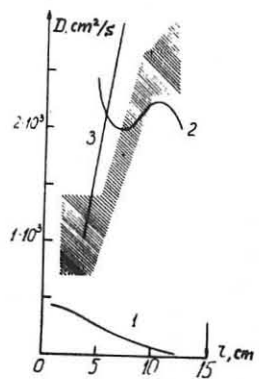
FIG.3.

THE STUDY OF SUBWALL PLASMA PARAMETERS IN THE TM-4 TOKAMAK WITH DIFFERENT METHODS OF THE CHAMBER WALL CLEANING

V.I.Bugarya, A.V.Gorshkov, S.A.Grashin, V.F.Denisov, K.A.Razumova, V.V.Sanni-kov, Yu.A.Sokolov, V.M.Trukhin, V.V.Hilil

Kurchatov Institute of Atomic Energy

I.S.Bondarenko, L.I.Krupnik, I.S.Nedzelsky

Charkov Physical Technical Institute

The comparison of the TM-4 tokamak plasma parameters was performed with the discharge chamber temperatures $T_L=20°C$ and $T_L=300°C$. Such experiments are of interest because INTOR-like tokamaks will operate at the first wall temperature about $300°C$. The experiments were performed in the TM-4 tokamak /R=53 cm, a_L=8.5 cm/ in the following regime: H_z=20 KOe, J=35-36 kA, $\bar{n}_e$ = 3-3.5 . 10^{13} cm^{-3}, q_L=3.6. The discharge chamber with molibdenium limiter is made of stainless steel. The parameters of discharges with $T_L=20°C$ and $T_L=300°C$ are given in Fig.1. The main data is in Table 1.

Table 1

	$T_e(0)$, eV	$Z_{eff}(0)$	$\bar{\bar{Z}}_{eff}$	$\tilde{Z}_{eff}$	n_{ew}, 10^{12}cm^{-3}	T_{ew}, eV	β	$\tilde{\tau}$, ms	W_R/W_J
$T_L=20°C$	650	1.36	3.1	3.6	5	8	0.56	1.6	10%
$T_L=300°C$	700	2.3	4.8	5.5	5	12	0.56	2.2	20%

The impurities' income /C,O,Mo,Fe/ was controlled with visible spectra observations. The impurity fluxes increased by 30-100% at $T_L=300°C$. This increase may be the consequence of the higher chamber wall pollution, increase of the sputtering yield factor or the limiter shadow plasma parameters' variation. As $T_L=300°C$ Langmuir probe measurements showed, electron temperature T_{ew} in the shadow of the limiter approximately increases 1.5 times at constant density n_{ew}. The increase of T_{ew} may lead to the higher impurity influx because of the sheath potential increase /1/. Namely this mechanism, to our opinion, can explain the increase of the impurity income at $T_L=300°C$. No notable change of the impurity content determining Z_{eff} happened at passing to $T_L=300°C$ temperature. According to the soft X-ray measurements, $Z_{eff(0)}$ value is mainly determined by light impurities in both cases, although 2.5 times increase of Mo L-line was observed at $T_L=300°C$. No lines of iron were detected in the spectra. There is a discrepance in the determination of Z_{eff} using different methods. The average effective charge $\bar{Z}_{eff}$ calculated from $j(r) \sim T_e^{3/2}(r)$, V_{loop}, J assuming uniform profile of the electric field is higher then $Z_{eff}(0)$. Such discrepance was previously observed in the TM-3 experiments /2/. The calculation of $\tilde{Z}_{eff}$ inside q < 1 region gives a value close to $\bar{Z}_{eff}$. Following the /2/ assumption about nonuniform electric field profile it is needed to decrease the electric field in the center of plasma in 2.3-2.5 times.

Interaction of hydrogen with the chamber wall was considered from the view of hydrogen deposit. The deposit of hydrogen was determined using thermodesorbtion method at the increase of the temperature up to $450°C$. The experiments were performed with $T_L=20°C$ and $T_L=300°C$. The total

deposit of hydrogen is given in Fig.2 after operation at $T_L=20°C$ versus the number of discharge pulses. Hydrogen is deposited 10 times slower at $T_L=300°C$. The consideration of the particle confinement time and the amount of the injected cool hydrogen makes it possible to assume 2-3 times circulation of particles between wall and plasma in the experiments with $T_L=20°C$ before the particles are locked by the wall. The same factor at $T_L=300°C$ increases up to 5-7. Such recycling factor makes it possible to explain the observed hydrogen deposit on the chamber wall.

Core plasma density fluctuations were studied in the TM-4 by Cs^+ /3/ ion beam probe. Local plasma density was determined at q < 1 region. Secondary beam ions $C_s^{2+}(a)$, proportional to the local electron density, and soft X-ray oscillations (b) are given in Fig.3.* The estimation of local density fluctuations gives the value close to 1-2%. Interferometric measurements of the plasma density also show the existence of relaxation oscillations in the central region (Fig.4). Just before the inner disruption there are oscillations obviously connected with m=1 mode development. Fluctuations connected with m=2 peripheral mode are also observed in the density curve. Typical characteristic parameters are the following: $T_{m=1}$ = 50 μs, $T_{m=2}$ = 36 μs, $\tilde{T}$ = 500-800 μs. Phase shifts $\tilde{\Phi}_{i+1-i}=\pi$, $\tilde{\Phi}=\frac{\pi}{4}$, total phase shift Φ =12π. Density fluctuations estimations give $\tilde{n}_{m=1}$ = 3-8.10^{12}cm^{-3}, $\tilde{n}$ = 1-2.10^{12}cm^{-3}, n(0) = 4.5 . 10^{13}cm^{-3}.

References

1. H.Maeda, S.Sendoka, 7th Intern.Conf. on Plasma Phys. and CTF, Innsbruck, 1978, v.1, 377.

2. G.A.Bobrovskij, K.A.Razumova, V.V.Sannikov, Sov.Fysica Plasmy, 2, 898 (1976).

3. F.C.Jobes, J.C.Hosea, 6th European Conf. on Plasma Physics, Moscow, 1973, v.1, 199.
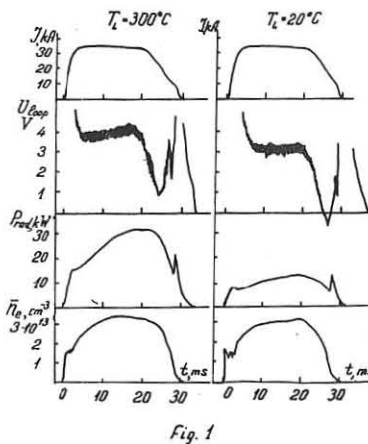
Fig. 1
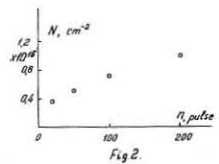
Fig.2.
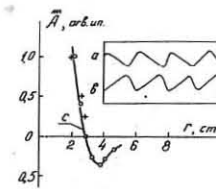
Fig. 3
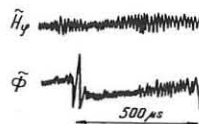
Fig. 4

---
* Fig.3 (c). Space beam Cs^{++} oscillations.

THE ROLE OF TRAPPED PARTICLES IN DISTORSION OF A TEMPERATURE PROFILE MEASURED BY MEANS OF CHARGE-EXCHANGE NEUTRALS

Yu.V.Gott, E.I.Yurchenko

I.V.Kurchatov Institute of Atomic Energy,
Moscow, USSR

Abstract. In the paper tokamak plasma ion temperature radial distributions measured by means of corpuscular diagnostics are shown to be anomalously broad. This is due to the effect of ions moving along banana trajectories. A method to reconstruct a true radial temperature distribution from charge-exchange particle spectra is described.

Corpuscular diagnostics is currently widely used for tokamak ion temperature measurements /1-4/. This technique records fast atom spectra resulting from charge-exchange of a small fraction of the plasma ion component on neutral gas atoms. Measurements start generally with a minimal charge-exchange atom energy exceeding a maximal plasma ion temperature (T_o) by a factor of 2-3. Hence, any distortions of the distribution function of these fast particles, which do not affect the bulk of the ions, can cause experimental errors.

For example, the particles trapped in longitudinal magnetic field ripples cause essential asymmetry in the radial temperature profile measured by charge-exchange /1,2/.

The recent T-10 experiments have given anomalously broad ion temperature radial distribution profiles. These cannot be associated with the effects of particles trapped in the magnetic field ripples. In this case, the temperature in the vicinity of a limiter was about 400 eV, that in the column centre being about 600 eV.

We show that the temperature profile distortion can be attributed to the effect of particles moving along banana trajectories, i.e. of those trapped in the toroidal field mirrors.

The expression for a charge-exchange atom flux reaching the analyser is:

$$\Phi(E) \sim \int \frac{n_o(z)}{\sqrt{E}} f_i(z,E) \langle \partial_{cx} v_i \rangle e^{-l} dz \qquad (1)$$

where n_o is the neutral gas density, f_i the ion distribution function, ∂_{cx} the resonant charge-exchange cross-section, the French quotes mean averaging over the neutral gas particle distribution, l -the plasma optical thickness for charge-exchange atoms.

With an experimental value of $\Phi(E)$ one can find the plasma temperature by the formula:

$$T = -\left(\frac{d\ln\Phi(E)}{dE}\right)^{-1}, \quad E > T_o \qquad (2)$$

It is seen from (1) and (2) that an experimentally measured temperature depends on the ion energy distribution function f_i. We take the distribution function appearing in (1) and taking into account the ion motion along banana trajectories in the form:

$$f_{ib}(z^*) = \frac{R(z^*)}{T(z^*)^{3/2}} exp\left(-\frac{E}{T(z^*)}\right) \qquad (3)$$

where $\partial^* = \partial - \Delta z - \gamma\Delta z_{max}$ (4)

$$\Delta z_{max} = \frac{\rho_i q}{\sqrt{E}}\sqrt{1-\cos\theta_o}, \qquad \Delta z = \partial\frac{\rho_i q}{E v_i} v_{\parallel}$$
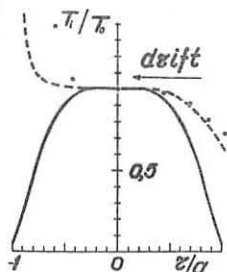
ρ_i is the ion Larmor radius in the toroidal field B_o. $q = \partial B_o/B_s$ — the safety factor, $\mathcal{E} = \ell/R$ the toroidality, θ_o the azimuthal angle of the reflection point of the trapped ion, B_s the current magnetic field, $v_{\parallel}$-the ion velocity component in the direction of the resulting magnetic field, $\partial = \pm 1$.

The design of the analyser and the tokamak defines the values of $v_{\parallel}$ and ∂ for the particles that can be recorded. Distribution function (3) differs from that of the banana guiding centres /5/ because when deriving (3) we have taken into account the plasma temperature gradient over the banana width. The parameter $\gamma < 1$ arises from averaging of the locally-Maxwellian function over the banana trajectory and depends on the particle energy and plasma temperature gradient. To include the effect of particles trapped in the magnetic field ripples we have used the distribution function in the form:

$$f_{iz}(z) = \frac{R(z-\Delta z)}{T^{3/2}(z-\Delta z)} exp\left(-\frac{E}{T(z-\Delta z)}\right) \qquad (5)$$

where z is the coordinate along which drift trapped ions, $\Delta z = \frac{v_d}{v_{ii}}(2\delta - \sin^2\psi)$, $v_d = \frac{m v_i^2}{2B_o R}$ the drift velocity, $2\delta = \frac{B_{max} - B_{min}}{B_o}$ — the measure of the ripple magnetude, $\psi = v_{\parallel}/v_i$ — the ion pitch-angle.

In numerical simulation of the radial temperature distribution measured by charge-exchange particles we look for temperature profiles in the form:

$$T = T_o\left(1 - (z/a_1)^\beta\right)^\alpha \qquad (6)$$

where a_1 is the radius at which the plasma temperature equals 0, α and β the parameters to be found from the condition of agreement between numerical calculations and experimental data. When calculating the model charge-exchange particle flux we substitute into (1) a calculated neutral gas distribution n_o /6/, ion distribution function f_i in the form (3) and (4) with a temperature distribution in the form (6).

Particular calculations have been performed for the conditions when the particles getting into the analyser are those with $v_{\parallel} = 0$, $\psi = 0$ (for the T-10 device $v_{\parallel}/v_i \sim 1/250$). The results of calculations for the T-10 low q (q(a) $\approx$ 2) operation are shown in the figure. Here a solid curve is a true temperature profile (6): $\alpha = 2$, $\beta = 4$, a dotted curve represents numerical simulation results, points correspond to experimental results /3/. It is seen that experimental and simulation results are in good agreement, and a true profile is reasonably peaked. The performed calculations show that it is possible to determine true tokamak temperature profiles by means of corpuscular diagnostics provided the trapped particles are taken into acount.

References

1. М.П.Петров, ЖЭТФ, письма, 17, 1973, 110.
2. В.С.Заверяев, А.Б.Извозчиков, С.Е.Лысенко, М.П.Петров, Физика плазмы, 4, 1978, 1205.
3. А.В.Берлиозов и др., Доклад IAEA-38/A-2, Брюссель,1980.
4. V.S.Vlasenkov et al., Plasma Phys. Control. Nucl. Fus. Res., 1978, Vienna, 1979, 1, 211.
5. А.А.Галеев, Р.З.Сагдеев, В сб. "Вопросы теории плазмы", Атомиздат, М., т.7, 1973, 205.
6. Yu, N.Dnestrovsky, S.E.Lysenko, A.I.Kyslyakov, Nucl. Fus.19, (1979), 293.

PARTICLE BALANCE IN T-11 TOKAMAK

V.M.Leonov, V.G.Merezhkin, V.S.Mukhovatov
and V.V.Sannikov

I.V.Kurchatov Institute of Atomic Energy,
Moscow, USSR

Abstract. Total particle loss rate Γ_e as a function of line-averaged electron density $\bar{n}_e$ in ohmically heated discharges at different limiter radii a_L and safety factors $q(a_L)$ have been measured. The values of Γ_e and $n_e D$ are found to rise with an increase in a_L and with a decrease in $q(a_L)$.

In Refs /1-3/ it has been shown that the gross particle confinement time τ_p increases with rising density, $\tau_p \sim \bar{n}_e$, and the particle diffusion coefficient scales as $D \sim \bar{n}_e^{-1}$. In the recent experiments on T-11 we attempted to determine the dependence of the total particle loss rate, $\Gamma_e = N_e/\tau_p$ (N_e is the total number of electrons in the plasma column), on the limiter radius a_L and the safety factor $q(a_L)$. The measurements were performed at $B_T = 8.7 - 11.5$ kG, $I_p = 50 - 100$ kA, $a_L = 20$ cm and 15 cm, $q(a_L) = 2.5$ and 4.1 in the density range $\bar{n}_e = (0.9 - 3.6) \times 10^{13}$ cm^{-3}. The value of Γ_e is determined from the equation $\Gamma_e = \Gamma_{tot} - dN_e/dt$, where $\Gamma_{tot} = \Gamma_W + \Gamma_L + \Gamma_{GP}$ is the volume ionization rate for neutrals incoming from the chamber wall (Γ_W), from the limiter (Γ_L) and from the pulsed valve (Γ_{GP}). The value of Γ_e is obtained from a change in the time derivative of the mean plasma density, $d\bar{n}_e/dt$, just after closing the pulsed valve. The ratio $\Gamma_L : \Gamma_{GP} : \Gamma_W$ is determined from the ratio of H_β intensities near the limiter (H_β^L), near the pulsed valve (H_β^{GP}), and in the region away from them (H_β^W), taking into account effective lengths (along the torus) of neutral-influx inhomogeneities in the vicinity of the limiter and of the valve. These lengths are evaluated from the measurements of tangential charge-exchange neutral fluxes in the region where the valve and the limiter are located and far away from them as well. In the present experiments, the typical ratio Γ_{GP}/Γ_{tot} is found to be about 0.35. The ratio Γ_L/Γ_{tot} measured at $\bar{n}_e \simeq 2.10^{13}$ cm^{-3} increases from ~ 0.1 to ~ 0.35 with a_L decrease from 20 cm to 15 cm.

Fig.1 shows the typical oscillograms of the line-averaged electron density $\bar{n}_e$ and H_β intensities in the discharge at $a_L = 20$ cm and $q(a_L) \simeq 2.5$. Usually, the discharge is initiated at low initial hydrogen pressure, $P_0 \sim 7.10^{-5}$ torr. The pulsed valve is switched on shortly after the discharge initiation. Gas is injected at an approximately constant rate ($\sim 1.10^{21}$ atom/s) during ~ 50 ms resulting in a nearly constant rate of density rise. It was possible to change the density achieved by the end of the gas pulse from $\sim 1.10^{13}$ cm^{-3} up to $\sim 4.10^{13}$ cm^{-3} by a relatively small ($\sim 30\%$) increase in the gas injection rate. At the same time, an increase in the total ionization rate was no more than $\sim 10\%$. After termination of the gas-puffing, an almost linear decay of density, corresponding approximately to the same value of $dN_e/dt \simeq 1.10^{21}$ s^{-1} at different plasma densities, is observed.

Fig.2 shows an electron loss rate Γ_e as a function of $\bar{n}_e$ for two values of $q(a_L)$ at two different radii of the plasma column. One can see that Γ_e practically does not depend on $\bar{n}_e$, and it drops with a decrease in a_L and with an increase in $q(a_L)$. These data show that τ_p is proportional to $\bar{n}_e$, weakly depends on a_L, $\tau_p \sim a_L^{0.4}$, and rises with an increase in $q(a_L)$. These trends are similar to those obtained in
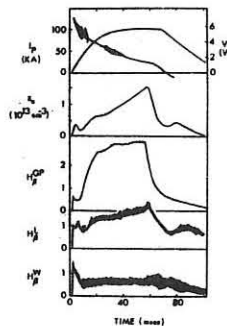
FIG. 1
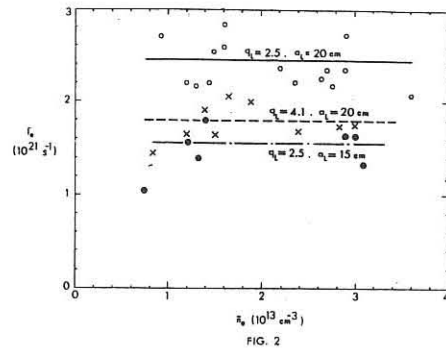
FIG. 2

Ref./4/ for the electron energy confinement time, namely $\tau_{Ee} \sim \bar{n}_e q(a_L) a_L^{0.3}$. The absolute values of τ_p and τ_{Ee} were found to be close to each other.

Using the calculated radial profiles of neutral density and taking into account the neoclassical pinch effect, we evaluate the particle diffusion coefficient D. In the calculations, the energy of incoming neutrals was varied in the range 2-5 eV. In Fig.3 we plotted the values of $n_e D$ - deduced from these experiments- and the values of $n_e \chi_e$ (χ_e being the electron heat diffusivity) obtained in our previous measurements /4/. A variation in $n_e D$ with plasma parameters appears to be similar to that in $n_e \chi_e$ giving an approximately constant ratio $\chi_e/D \simeq 4 \div 5$.
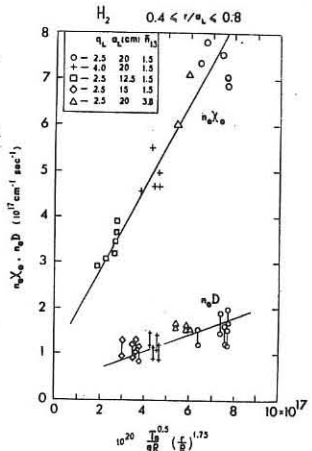
FIG. 3

Assuming $n_e D \simeq 2.10^{19} (\sqrt{T_e}/qR)(r/R)^{1.75}$, which does not contradict our findings for hydrogen plasma, one should expect the particle loss to be important in the ion energy balance at an electron collisionality factor $\nu_e^* \lesssim 1$ in ohmically heated plasma, and at $\nu_e^* \lesssim 0.1$ in the discharges with high-power additional heating, $P_{ADD}/P_{OH} \sim 10$.

References

/1/ E.Apgar, B.Coppi, et al., in Plasma Physics and Controlled Nuclear Fusion Research (Proc. 6th Int. Conf., Berchtesgaden, 1976) Vol.1, IAEA, Vienna (1977) 247.

/2/ J.W.Paul, in Proc. of 9th European Conf. on Contr. Fusion and Plasma Physics, Vol.II, Oxford (1979) 13.

/3/ R.J.Goldston et al., in Proc. of 2nd Joint Grenoble-Varenna Int. Symposium on Heating in Toroidal Plasmas, Como, Italy, 1980.

/4/ V.M.Leonov et al., in Proc. of 8th Int. Conf. on Plasma Physics and Contr. Nuclear Fusion Research, Brussels, 1980, IAEA-CN-38/N-2.

THE FIRST EXPERIMENTS ON THE TO-2 TOKAMAK WITH DIVERTOR

L.I.Artemenkov, E.V.Grodzinsky, A.A.Gurov,
P.I.Melikhov, P.A.Mukhin, L.N.Papkov,
A.P.Poprjadukhin, N.N.Shwindt

I.V.Kurchatov Institute of Atomic Energy,
Moscow, USSR

The different types of tokamak divertors are investigated in recent years. It would be interesting to investigate experimentally a possibility of using a classical toroidal divertor /1/ for tokamaks /2/. The race-track tokamak TO-2 with two toroidal divertors has been built for this goal (fig.1).

Table I

TO-2 tokamak parameters

Large radius of the toroidal sections	– 0.6 M
Length of racetrack sections	– 0.72 M
Separatrix radius	– 0.12-0.14 M
Toroidal magnetic field	– 1,0÷1.6 T
Plasma current /q(a) = 3/	– 30÷55 kA
Inductor magnetic flux	– 0,8 T sec
Divertor chamber volume (one unit)	– 1.5 M^3
Asotite surface of divertors (total)	– 5 M^2
Pumping speed for two divertors	– 10^6 L sec^{-1}

The basic discharge regimes

There is possible to run experiments in the next regimes (see table II).

Table II

	Continuous gas leakage 2.10^{-4} torr,H_2	Start pulse gas injection	Puffing	Asotite gettering in the divertors	$\bar{n}_e$ om^{-3}	Discharge duration in msec
1	+	–	–	–	5.10^{+12}	250÷300
2	–	+	–	–	4.10^{12}	-"-
3	–	+	–	+	2.10^{12}	-"-
4	–	+	+	–	$1.5 .10^{13}$	100÷150
5	–	+	+	+	$1.0 .10^{13}$	-"-

In these regimes the plasma current is I_p=24÷30 kA with B_0=1 T. The stationary state of discharge is become settled after 15÷20 msec. The typical oscillograms of the plasma current I_p, discharge voltage U, plasma density n, H_β, Fe II, hard X-rays are presented on the figures 2 and 3. One may note the important feature of the divertor tokamak discharges. The pulse time length is diminished drastically by a small changes of the divertor coil currents. In particular it isn't possible to obtain a long stable discharge when the divertor currents are switched off.

It is measured the radial profiles of some spectral lines /CIII(4647 Å), CV (2271 Å)/ (fig.4). From these profiles one could see, that plasma discharge is isolated from the wall (a metal limiter was not used) and is limited by the separatrix. Comparison the mentioned profiles with the one's obtained on the nondivertor tokamak TO-1 (at nearly the same plasma parameters) is indicated on some broadening of the hot plasma region in TO-2.

The divertor layer probe measurements

It is placed two probes on the toroidal part for a measuring of plasma parameters. One probe could be shifted in the vertical direction and another in the horizontal one.It is possible to use each probe or for the electric current measuring or for the measuring of the thermoelectomotive force, arising in the result of the probe heating by a plasma flux. Combining these data one could obtain the plasma density n_e and the ion temperature T_i. Using the probe characteristics (obtained for many identical pulses) one could determine the electron temperature T_e also. In the regime N 1 (see table II) the electron temperature T_e is 8÷12 eV. The ion temperature in the same regime is turned out significantly

higher, i.e. 60÷70 eV. The plasma density across the divertor layer is presented on the fig.5. On the separatrix this density is 7.10^{10} om^{-3} and decreases in ten times over 1.0 om. One could see the assymetry of this dependence on the fig.5a (co and counter current directions). The reason of this effect may be disturbances of the magnetic field, which were detected by electron beam method is special measurements of the magnetic field quality. It was shown that the separatrix of one divertor does not transit continuously into the separatrix of the other one.

The divertor probe measurements

The four probes are placed near the divertor plate of a one divertor. The probe construction was analogous to the mentioned one. Two probes are adopted the cocurrent particles (N 1 and N 2) and two others one – the counter-current particles (N 2 and N 4). The plasma density profiles are presented on the fig.6 a and the heat flux profiles are presented on the fig.6 b. The average maximum density in the plasma flux near the divertor plate equals $2.2 . 10^{10}$ cm^{-3}, and the average ion temperature equals T_i=70 eV. The halfwidth of the plasma flux on the divertor plate equals ~ 1 om.

The measurement of energetic balance

It was measured the heat flux over the pulse length transported by plasma on the divertor plates $Q_{p\ell}$. This was done in the regime N 1 (see table II) for plasma current I_p= 14 kA. We define the divertor energetic efficiency as relation the total heat on the divertor plates to the ohmic energy input, W_{OH}, $\eta = \frac{Q_{p\ell}}{W_{OH}}$. In the process of this measurement it was discovered the existence of two kinds of discharges with different η -value. We name them stable and unstable mode. The second case we relate with so-called transverse runaway electron instability, which characterized by numerous short positive pulses of the discharge voltage. In this operation mode η equals 70% ($Q_{p\ell}$=4.0 кJ, W_{OH}=5.7 кJ). Energetic efficiency equals 50% in the stable mode ($Q_{p\ell}$=2.7 кJ, W_{OH} = 5.2 кJ).

References

1. Spitzer L., Proceedings of the Second UN International Conf. on the PVAE, v.32, p.181 (1958).
2. Л.И.Артеменков, Ю.Н.Петренко, А.П.Попрядухин, А.И.Чудковский. Препринт ИАЭ-294I (1978).
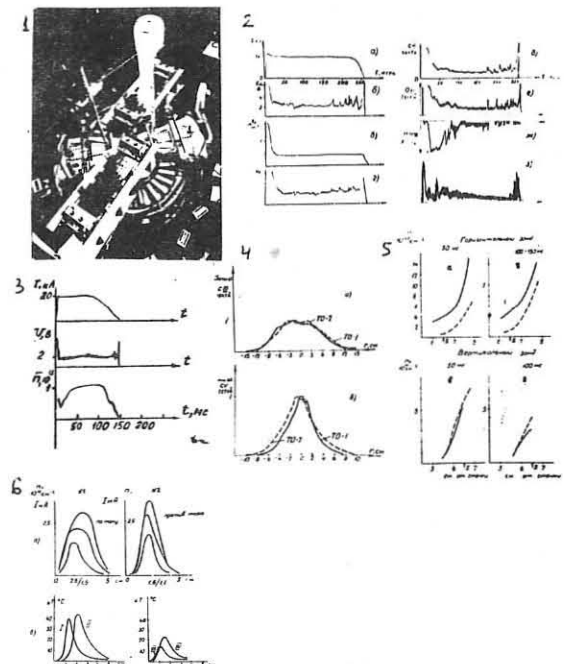
B

MAGNETIC CONFINEMENT
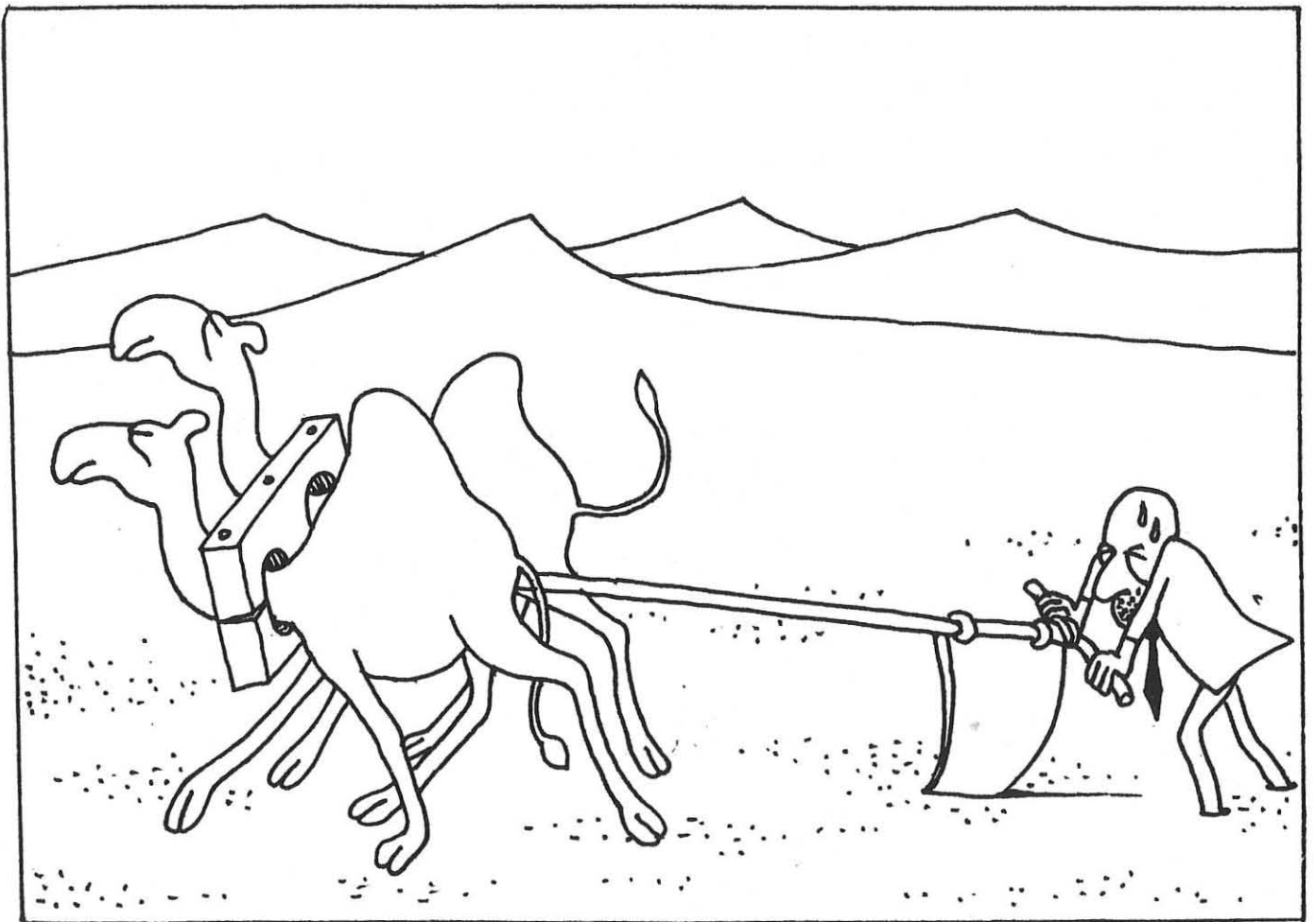
ROTATION AND ISLAND EFFECTS IN TOKAMAKS WITH
HIGH-POWER NEUTRAL BEAM HEATING*

J. Hogan
Oak Ridge National Laboratory
United States of America

I. **Introduction:** The study of β limits in tokamaks with neutral injection has disclosed a slower-than-hoped-for growth in β as injected power is raised. While attention is focused on the stimulation of new modes to explain this possible saturation (e.g. hybrid tearing/ballooning) it should be re-emphasized that neutral injection can introduce important new effects at high power level which are unrelated to β. We discuss two of these:

1) the effect of toroidal flow on equilibrium and stability.

2) New MHD behavior resulting from large beam-produced temperature gradients,

and present results for typical parameters of the ISX/B tokamak.

II. **Toroidal flow effects:** The possible influence of rotation on β-limits has been noted earlier [1]. While υ_ϕ has not been measured in the ISX/B experiments, charge exchange and MHD loop signals suggest estimates of 10^6cm/s $\leq \upsilon_\phi \leq 10^7$cm/s.

II.1 **Analytic solutions for equilibrium:** The analytic equilibria of Maschke and Perrin [2] are trivially generalized to account for $\beta_p \neq 1$. With this exact solution, and the solution expanded near the magnetic axis

$$\psi = \lambda_1 Z^2 + \lambda_2 X^2 + \lambda_3 XZ^2 + \lambda_4 X^3$$

$$\lambda_1 = -[1 + \upsilon_\phi^2/c_s^2](1 - \beta_p)/\beta_p \qquad \lambda_3 = (\varepsilon_a - 1)/2R$$

$$\lambda_2 = -(1 + \varepsilon_a + 2\upsilon_\phi^2/c_s^2)/4 \qquad \lambda_4 = -(1 + \varepsilon_a + 10\upsilon_\phi^2/3c_s^2)/4R$$

we are able to evaluate flow effects on stability.

II.2 **Local interchange criterion:** The generalized interchange criterion of Solov'ev [3] is applied to tokamak geometry with purely toroidal flow. The criterion in this case is: (for $\omega^2 = c_s^2$)

$$\frac{1}{4}(V')^6 S^2 = P_T'\left\{f^2[U'Q* - V'Q_2\frac{Q_0^*}{V*^2} + P_T'(Q_2 Q_3^{**} - Q_1^{*2})]\right.$$

$$+ U'[ff' + P_T' Q_3^{**} - \frac{Q_0^*}{V*^2}]\right\} - \left\{f^2[\frac{n}{c_s^2}\omega^4(Q_3^* - Q_4^*)Q_2\right.$$

$$+ Q_2 \langle B_\perp \rangle n'\omega^2] + U'[\frac{n\omega^2}{c_s^2}(Q_3^* - Q_4^*) + \langle B_\perp \rangle n'\omega^2] \geq 0$$

$$\text{e.g., } Q_2 \equiv \left\langle \frac{1}{r^2|\nabla\psi|^2} \right\rangle, Q_3^* \equiv \left\langle \frac{e^{r^2\omega^2/2c_s^2}}{r^2|\nabla\psi|^2} \right\rangle$$

Considering the neighborhood of the magnetic axis, and expressing the criterion in geometric variables (ellipticity E, triangularity, τ) the modified "Mercier" criterion is:

$$\frac{1}{q^2(o)} < \frac{F(E^2)}{1 + E^2} - \frac{4\beta_p(o)(1 - 2\upsilon_\phi^2/c_s^2)}{E(E + 1)} \quad ; E^2: \text{ELLIPTICITY}$$

$$\text{TRIANGULARITY: } \tau = \frac{1}{2}\frac{E_o^2}{E_o^{*2}} - 2\frac{E^2}{E_o^{*2}} + \frac{5}{3}\frac{1 + E_o^2}{E_o^{*2}}\frac{\upsilon_\phi^2}{c_s^2}$$

The flow velocity enters through changes in the equilibrium, and we have used an expansion in υ_ϕ^2/c_s^2.

As seen in Fig. 1, the toroidal flow increases the triangularity, thus lowering the tolerable q-value. $q(o) \sim .9$ could be interchange stable for estimated ISX/B parameters.
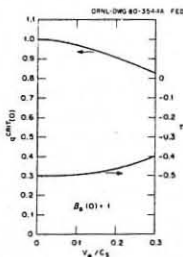
Figure 1

Effect of toroidal flow on interchange criterion near the magnetic axis. $q_{(o)}^{crit}$ drops as the triangularity is increased with increasing υ_ϕ/c_s.

II.3 **Numerical results:** Solving the Grad-Shafranov equation numerically with flow added (assuming temperature constant on a flux surface)

$$\Delta^*\psi = -ff' - r^2[P_T' + P_T(\frac{\omega^2}{2c_s^2})'r^2] e^{r^2\omega^2/2c_s^2}$$

$$\text{PRESSURE} \qquad P = P_T(\psi)e^{r^2\omega^2/2c_s^2}; \omega = \frac{\upsilon_\phi}{r} = \omega(\psi)$$

and modifying the Grad-Hu-Stevens [4] generalized differential equation to account for flow, we calculate the self-consistent evolution of the

1½-D transport [5]. Evaluating ideal (and resistive) interchange criteria, we see the stabilizing effect for a typical ISX/B case, expected from previous analytic calculations [Fig. 2].

III. **Periodic MHD behavior:** High power injection experiments evidence a variety of new MHD behavior [6]. Some of this may be due to higher temperature gradients produced by the increased heat source, and due to finite island width effects on transport.

Figure 2

Generalized ideal and resistive interchange criteria for two limiting ISX-B cases: momentum lifetimes of 30 msec (upper curves) and 5 msec (lower curves). $-D_I$ $-D_R$ are displayed, with $D < 0$ required for stability.

Calculating saturated tearing mode island evolution with the quasi-linear model

$$\frac{dW}{dt} = \eta\Delta'(w)$$

we find a periodic alternating 2/1, 3/2 behavior to result, under some conditions, without a priori assumptions about periodicity. [Figs 3a,b]. Transport modelling of the "sawtooth" process has been hampered by the need to specify an ad hoc trigger parameter (typically the $q_{(o)}^{min}$ allowed before reconnection). A periodic 1/1 oscillation has been discovered [7] which does not require this assumption. The 2/1, 3/2 alternation is similar in nature to the oscillation reported in [7]. The q-profile required to produce such activity is restricted, and this "pre-spike" behavior (with mild positive voltage spikes) should occur in the near-disruptive regime.

References

[1] H. P. Furth, Proc. 9th Europ. Conf. on Controlled Fusion and Plasma Physics, Oxford, 1979, V. 2, p. 309.
[2] E. Maschke, F. Perrin, Plasma Physics 22 (579) 1980.
[3] L. S. Solovev JETP 54 (666) 1968.
[4] H. Grad, P. N. Hu, D. C. Stevens, Proc. Natl. Acad. Sci. 72 (3789) 1975.
[5] J. T. Hogan, Nucl. Fusion 19 (753) 1979.

References cont'd.

[6] M. Murakami, D. Swain, J. Dunlap, Proc. IAEA, Brussels, 1980.
[7] V. V. Parail, G. V. Pereversev, Fiz. Plaz. 6 (27) 1980).
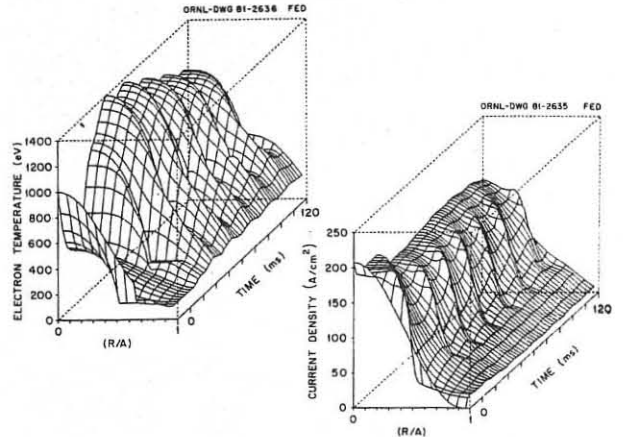
Figure 3a

Figure 3b

Evolution of a calculated ISX/B case with 1.9 MW injected power. Injection is assumed to begin at 20 msec.

a. Electron temperature oscillations, with period $\sim$ 16 msec.

b. Oscillation in the toroidal current density, driven by alternating 2/1 and 3/2 islands.

The behavior is sensitive to assumptions about transport across the island: enhanced χ_e will not produce this activity, T_e(out) = T_e(in) boundary conditions are required.

THE THEORY OF DISRUPTIVE INSTABILITY IN TOKAMAKS

Zakharov L.E.

I.V.Kurchatov Institute of Atomic Energy,
Moscow, USSR

Conditions of helical equilibrium give an opportunity to understand the cause for the kink and tearing instabilities, to formulate invariant (independent of the plasma model) requirements for a steady state regime, to give an estimation of the possible results in the development of kink instabilities.

I. Conditions for the helical equilibrium with free boundary /1/.

In case of a rectilinear plasma column, which has an elliptical cross-section with helical symmetry characterized by a poloidal wave number m=2 and by a toroidal n at the uniform plasma current j_{pl}=const, one needs an external maintaining field to be produced with the helical windings:

$$\psi_{ext} = \frac{\pi}{c}(x^2 - y^2)\frac{\lambda^2 - 1}{\lambda^2 + 1}\left[\frac{2\lambda}{(\lambda+1)^2}\dot{j}_{pl} - \dot{j}_B\right]. \quad (1)$$

Here, $\psi_{ext}(\rho,\theta)$ is the flux function through a helical surface $\theta \equiv \omega - \varkappa S$ =const, $\varkappa = n/mR$ is the helical symmetry index, R is the radius of an equivalent torus, $\lambda = \ell_y/\ell_x$ is the cross-section semiaxes ratio, $\frac{4\pi}{c}\dot{j}_B \equiv \frac{2n}{mR}B_S$, B_S is a longitudinal field.

Presence of a term $\sim \dot{j}_B \sim B_S$ shows the role of a longitudinal field B_S in the maintainance of a non-circular cross-section of the plasma column.

Eq.(1) shows, that a cross-section of the helical plasma column is determined by a balance of three forces: a) selfcontraction /$\vec{j}_{pl} \times \vec{B}_{pl}$ /, b) interaction of the plasma current, flowing along the helical lines, with longitudinal field /$\vec{j}_{pl} \times \vec{B}_S$ / c) interaction of $\dot{j}_{pl}$ with an maintaining field /$\dot{j}_{pl} \times \vec{B}_{ext}$/.

The relative value of the first two forces is determined by the sign of brackets (1): if $\frac{2\lambda}{(\lambda+1)^2}\dot{j}_{pl} - \dot{j}_B > 0$, then $\vec{j}_{pl} \times \vec{B}_{pl} > \vec{j}_{pl} \times \vec{B}_S$, and $\vec{j}_{pl} \times \vec{B}_{pl} < \vec{j}_{pl} \times \vec{B}_S$ in opposite case.

2. Cause of kink and tearing modes.

The kink instabilities are caused by the disruptive force /$\vec{j}_{pl} \times \vec{B}_S$ /, when it is greater than /$\vec{j}_{pl} \times \vec{B}_{pl}$ /. For a mode m=2,n at $\lambda \to 1$ this,condition is satisfied when

$$\dot{j}_{pl} \leq 2\dot{j}_B \quad (2)$$

that corresponds to nq $\geq$ 1. In general case, this condition is substituted by nq $\geq$ nq$_{cr}$, where q$_{cr}$ corresponds to the left boundary of kink modes (nq $\geq$ m - 1 for uniform current).

For resonance surface inside the current channel, the helical equilibrium will be violated on the boundary of a tearing mode, where $\Delta' < 0$. The tearing mode is also caused by a disbalance between the selfcontraction force and that of interaction between the current flowing through the cross-section nq $\leq$ m and a longitudinal field. The current beyond the resonance surface helps to stabilize helical perturbations, as it follows from a general structure of the tearing-mode configuration with magnetic islands.

3. The surface currents on a boundary of the current channel act as a linear stabilizing mechanism /3/ and give the right boundary nq = m. The second linear mechanism includes the eddy currents through a casing. Later, the second mechanism will not be taken into account. The third linear stabilization mechanism is the eddy currents through the liner in the presence of sufficiently fast plasma rotation. In this case, the liner becomes equivalent to a perfectly conducting casing.

4. Quasi-linear mechanism of stabilization /4/ is a current redistribution near the resonant surface in such a way that an increased current density is produced across the magnetic islands. Thus, the currents through the magnetic islands produce a maintaining field like helical conductors.

5. A non-linear mechanism for stabilizing the kink and tearing modes is generation of a negative surface current $\dot{\iota}$ on the boundary of a current channel or in the region of large jump in the current density /2/ which produces a stabilizing force /$\vec{\iota} \times \vec{B}_S$/. The reason of $\dot{\iota}$ generation is the increase in the bulk current due to flux conservation. For a plasma column with a uniform current and with elliptical cross-section the μ-value ($\mu = 1/q$) is

$$2\mu = 1 + \left(\frac{\dot{j}_{pl}}{\dot{j}_B} - 1\right)\frac{2\lambda}{\lambda^2 + 1} \quad (3)$$

With an increase in λ, $\dot{j}_{pl}$ as well as the bulk current should rise to conserve μ.

6. The disbalance between the disruptive force /$\vec{j}_{pl} \times \vec{B}_S$ / and /$\vec{j}_{pl} \times \vec{B}_{pl}$ / does not disappear at a non-linear stage. When the linear conditions of stability are violated, the only stationary mechanism of stabilization is a quasi-linear one which is applicable in this case only to a tearing mode and only near the marginal stability.

Therefore, a requirement for a steady-state discharge in a tokamak is to meet the linear conditions of stability for the kink-modes and for the tearing modes (quasi-linear mechanism of stabilization should be taken into account).

In particular, at nq(α) $\leq$ m on the boundary of a current channel, it is necessary to satisfy the following unequality on the axis:

$$nq(o) \leq m - 1 \quad (4)$$

This is the necessary stability criterion for a falling-down current profile.

7. A drop in the current density at the centre of a plasma column (broadening in the current profile) results in a disruptive instability so that either the conditions for the kink instability /2/ are violated (when nq $\leq$ m on the border of a current channel) or a quasi-linear mechanism of stabilization stops to work (transition of a magnetic island beyond the boundary of a current channel indicates this: thus, the tearing-mode is actually converted into a kink-mode with a free-boundary).

8. A disruptive instability is being actually developed as a kink-mode with a free boundary. Then, it is necessary to discern two cases.

a) The linear conditions of stability are violated, but the necessary criterion (4) is met. In this case, a kink mode can rearrange only the periphery of a current channel without touching its centre. It is a minor disruption.

b) The necessary criterion (4) is violated (considerable drop in the current density at the centre). In this case, the instability completely turns out the plasma column. It is a major disruption. An increment in the total current $\delta I/I$ (negative voltage spike) is determined by a relationship:

$$\frac{\delta I}{I} = \frac{2\ell_i - \frac{n}{m}q(d)}{\ln \delta/d^2}, \quad \ell_i = \frac{1}{d \cdot B_\theta(d)}\int_0^d B_\theta(\rho)d\rho \quad (5)$$

d is the radius which is reached by a magnetic axis after a complete turning out. In some cases, d is the radius of a limiter.

After a complete turning out with a mode m, n, the value of nq (0) becomes equal to nq(0)=m/5/and, thus, the conditions for a disruption with the next mode (m+1) are provided. This fact explains a consecutive development of modes in the process of disruption.

References

1. Goedbloed J.P., Nucl.Fusion, 20, 1515 (1980).
2. Zakharov L.E. Fisika plasmy, 7, 18 (1981).
3. Shafranov V.D. Zh. Techn. Fiz. 40, 241 (1970).
4. White R.B., Monticello D.V. et al. Phys. Fluids, 20, 800 (1977).
5. Kadomtsev B.B. In plasma Phys. and Contr.Nucl. Fusion Res. 1976, v.I, IAEA, Vienna, 1, 555 (1977).

IDEAL MHD STABILITY OF A FORCE-FREE MAGNETIC FIELD
AND THE RESISTIVE FLUID FORCE-FREE FIELD

M. BINEAU

ASSOCIATION EURATOM-CEA SUR LA FUSION
Département de Recherches sur la Fusion Contrôlée
Centre d'Etudes Nucléaires
Boîte Postale n° 6. 92260 FONTENAY-AUX-ROSES (FRANCE)

ABSTRACT

The variational problem is discussed with examples in cylindrical symmetry. Self consistency conditions are associated with some hypothesis in the model of a diffusive force-free field.

I - THE VARIATIONAL PROBLEM

With no pressure term the potential energy of a mhd fluid has the form

$$W = \frac{1}{2} \int_{\mathcal{D}} B^2 \, d\tau$$

($\mathcal{D}$ is a simply connected domain with boundary S).

Let the field B be equal to $B_0 + \varepsilon B_1$ and $W(B) = W_0 + \varepsilon \int B_0 . B_1 \, d\tau + \frac{1}{2} \varepsilon^2 \int B_1^2 \, d\tau$. The field B has locally three degrees of freedom if the constraints have one of the following types :

a) $\nabla \times B = 0$ ($B_0 = \nabla \psi_0$, $B_1 = \nabla \psi_1$) $\psi_1 =$ const. on S. The associated variational equation is $\nabla . B = 0$.

b) $\nabla . B = 0$ ($B_0 = \nabla \times A_0$, $B_1 = \nabla \times A_1$) $A_1 = \nabla_S \psi$ on S. The associated variational equation is $\nabla \times B = 0$.

In both cases the solution of the variational problem gives an absolute minimum W_0 of $W(B)$.

A force-free field is a solution of a modified type b problem where the varied potential A_1 has two degrees of freedom with the constraint $A_1 . B_0 = 0$ (this observation is taken from H.Grad's work).

c) $B_0 = \nabla \gamma \times \nabla \beta$, $B_1 = \nabla \times A_1$ with $A_1 = u \nabla \gamma - v \nabla \beta$ and $u = 0$, $v = 0$ on S. These conditions imply that the magnetic lines have tied ends on S.

Now the potential energy $W(u,v)$ has terms in ε, ε^2, ε^3, ε^4. The first order variation is $\varepsilon \int_{\mathcal{D}} B . (\nabla u \times \nabla \beta + \nabla \gamma \times \nabla v) \, d\tau = \varepsilon \int_{\mathcal{D}} J . (u \nabla \beta - v \nabla \gamma) \, d\tau$. It is identically zero iff $J \times B = 0$. When $J \times B = 0$ the potential energy is stationary. The field is called stable when the second order variation is positive and unstable in the opposite case. An example of an unstable force-free field with cylindrical symmetry is obtained in ref. (1). An example of an unstable field and of a stable field is given in the next section.

If the field B_0 is stable, W_0 is a minimum of W for any field B in a functional neighborhood of B_0. Under what condition the field B_0 makes $W(B_0)$ an absolute minimum of $W(B)$ is an open question.

II - STABLE AND UNSTABLE CYLINDRICAL FORCE-FREE FIELD

Let B_0 be a force-free field and $J_0 = \nabla \times B_0 = \alpha(x) B_0$. The second variation of W can be written in terms of a vector field A such that $A . B_0 = 0$.

$$W_2 = \frac{1}{2} \int \left[(\nabla \times A)^2 - \alpha A . \nabla \times A \right] d\tau \quad \text{or equivalently}$$
$$W_2 = \frac{1}{2} \int \left[(\nabla \times A - \alpha A)^2 + \alpha A . (\nabla \times A - \alpha A) \right] d\tau$$

If $B_0 = B_\theta(r) e_\theta + B_z(r) e_z$ is a force-free field we have $J_0 = \nabla \times B_0 = \alpha(x) B_0$.

The field A can be written in terms of two arbitrary functions/u, v : $A = u \, e_r \times B_0 + v \, e_r$. A Fourier transform in z and θ gives $u(r,\theta,z) = \sum_m e^{im\theta} \int e^{ikz} u_m(r,k) \, dk$; $v = ...$

The minimum with respect to v is obtained algebraically and W_2 is a sum of terms :

$$W_m^{\pm} = \int_0^\infty \frac{r \, dr}{1+k^2 r^2} \left\{ (f^{\pm})^2 \left[u'^2 + \left(\frac{m^2-1}{r^2} + k^2 m^2 \right) u^2 \right] - \frac{2 k^2}{1+k^2 r^2} (B_\theta^2 - k^2 r^2 B_z^2) u^2 \right\}$$

where u is written for $u_m(r,k)$, u' for $\frac{\partial}{\partial r} u_m(r,k)$ and $f^{\pm} = B_\theta \pm kr B_z$.
This formula is used in the two next examples

a) The "solid" force-free field (the magnetic lines satisfy the equation $\theta - \lambda z =$ const.), $B_z = \frac{1}{1+\lambda^2 r^2}$, $B_\theta = \frac{\lambda r}{1+\lambda^2 r^2}$, is locally unstable for any r ($r \neq 0$) (with a k value close to λ)

b) The one-parameter family of force free fields $B_z = r^{-n}$, $B_\theta = r^{-n} \sqrt{\frac{n}{1-n}}$, $o < n < 1$, $o \leq r \leq R$, has a total current inside the tube of radius r :

$I(r) = \sqrt{\frac{n}{1-n}} r^{1-n}$ and a magnetic energy per unit length equal to $\frac{\pi r^{2(1-n)}}{(1-n)^2}$. These force-free fields are all stable for any value of R. The following inequality is used for bounding W :

$$\int_0^{r_o} \frac{r \, dr}{1+k^2 r^2} f^2 u'^2 > \int_0^{r_o} \frac{r \, dr}{1+k^2 r^2} h^2 u^2$$

where $f = (kr - \sqrt{\frac{n}{1-n}}) r^{-n}$, $r_o = \frac{1}{k} \sqrt{\frac{n}{1-n}}$,

$$h = \frac{1+k^2 r^2}{f} \cdot \frac{1}{C + \int_0^r \frac{1+k^2 x^2}{x \, f^2(x)} dx}$$

(C is an arbitrary constant).

The energy W_m is bounded by a term $\int_0^{r_o} \psi(n,k,r) u^2 \, dr$ with some function $\psi(n,k,c)$ which is computed by numerical means.

III - THE RESISTIVE FORCE-FREE FLUID

In this section we consider a system of equations combining premaxwell equations, fluid momentum equation with no inertia and no pressure $J \times B = 0$ and ohm's law $E + v \times B = \eta J$.

v is interpreted as a velocity. The question of the consistency of this system is related to constraints on the v field.

For example : does a field v exist such that $\frac{\partial B}{\partial t} = 0$, or is $v = 0$ compatible with $\frac{\partial}{\partial t} J \times B = 0$.

In case of a negative answer the system is somehow a singular limit. This type of question is similar to the problem of the Pfirsch-Schlüter diffusion velocity : in order to compute $< v_\perp >$ one assumes a stationary equilibrium and the meaningfull effect, observed for $J.B \neq 0$, imply a non-stationary equilibrium (ref. 2).

We introduce some hypothesis for the discussion :

1) The initial variational problem assumes that magnetic lines have tied ends. It is therefore natural to associate a condition like $v = 0$. It follows however from $\frac{\partial B}{\partial t} = - \nabla \times (\eta J)$ that $\frac{1}{\sqrt{B}} \frac{\partial \sqrt{B}}{\partial t} = - \eta \alpha^2$. We conclude that $v = 0$ is not compatible with $\frac{\partial B}{\partial t} = 0$.

2) More generally does a field v allow $\frac{\partial B}{\partial t} = 0$?
If $\frac{\partial B}{\partial t} = 0$ is used to compute v with the field $B_z = r^{-n}$, $B_\theta = \sqrt{\frac{n}{1-n}} r^{-n}$ contradictory conditions are obtained. Therefore such a field cannot be stationary.

3) Is it possible to have $v = 0$ and a varying force-free field (such that $\frac{\partial}{\partial t} J \times B = 0$) ?
In case of cylindrical symmetry it is found that $v = 0$ and $\frac{\partial}{\partial t} J \times B = 0$ imply $\frac{d}{dr}(\eta \alpha) = 0$.
The constraint $\nabla \alpha = 0$ is therefore related to the resistive time scale.

4) With the force-free field of section II b does the constraint $\frac{\partial}{\partial t} J \times B = 0$ determine a field v ?
There is a solution to this equation with a radial velocity given by $v = \frac{1-n}{2(1+n)} \frac{\eta}{r}$.
This discussion presents the force-free field as a singular limit of the low β resistive equilibrium.

(1) D. Voslamber and D. Callebaut
The Phys. Rev. 128, 5, 2016, 1962.

(2) M. Bineau
Phys. of Fl. 10, 9, 2026, 1967.

EXACT ANALYTICAL FORCE-FREE THREEDIMENSIONAL TOROIDAL EQUILIBRIA OF ARBITRARY CROSS SECTION

Ferdinand F. Cap, University of Innsbruck, Austria

Force-free equilibria which are described by

$$\operatorname{curl} \vec{B} = \gamma \vec{B}, \quad \operatorname{div} \vec{B} = 0 \tag{1}$$

became recently again of interest /1/ since analytical solutions of (1) can be found. In circular cylindrical coordinates r, ϕ, z the solution of (1) is given by

$$B_\phi = \sum_{m,k,1} A_{mk1} e^{im\phi+ikz}\left[-\frac{mk}{r}Z_m\left(\sqrt{\gamma_1^2-k^2}\,r\right) - \gamma Z_m'\left(\sqrt{\gamma_1^2-k^2}\,r\right)\right] \tag{2}$$

$$B_r = \sum_{m,k,1} A_{mk1} i e^{im\phi+ikz}\left[\frac{my}{r}Z_m\left(\sqrt{\gamma_1^2-k^2}\,r\right) + kZ_m'\left(\sqrt{\gamma_1^2-k^2}\,r\right)\right] \tag{3}$$

$$B_z = \sum_{m,k,1} A_{mk1} e^{im\phi+ikz}\left[(\gamma^2-k^2)Z_m\left(\sqrt{\gamma_1^2-k^2}\,r\right)\right], \tag{4}$$

where γ_1 is the l-th eigenvalue and Z_m a superposition of Bessel's and Neumann's functions. First, we investigate axisymmetric toroidal equilibria $(m=0)$ of arbitrary cross section. In this case we have /2/ $B_\phi = -\gamma Z_0'$, $B_r = -\frac{1}{\gamma r}\frac{\partial}{\partial z}B_\phi r =$ $= ikZ_0'$, and $B_z = \frac{1}{\gamma r}\frac{\partial}{\partial r}(rB_\phi) = (\gamma^2-k^2)Z_0$. On the other hand, the differential equations for the magnetic field lines read $(m=0)$

$$\frac{dr}{B_r} = \frac{dz}{B_z} = \frac{dr}{-\partial B_\phi r/\partial z} = \frac{dz}{\partial B_\phi r/\partial r}. \tag{5}$$

Integration of (5) yields $rB_\phi = \text{const}$. This means that the magnetic field lines (along which the normal component of $\vec{B}$ vanishes) are described by $rB_\phi = \text{const}$. On a wall made of a perfect conductor, the normal component of $\vec{B}$ vanishes too. Thus, the wall of an axisymmetric toroidal chamber may be described by $(m=0, k=0, k_1, 1=0)$

$$z(r) = \frac{1}{k_1}\arccos\left[\frac{-x_1 rJ_1(\gamma r) - x_2 rY_1(\gamma r) + x_5}{x_3 rJ_1\left(\sqrt{\gamma^2-k_1^2}\,r\right) + x_4 rY_1\left(\sqrt{\gamma^2-k_1^2}\,r\right)}\right]. \tag{6}$$

By choosing for a given γ (or k_1) a set of 5 coordinates $z_i = z(r_i)$, $i = 1\ldots5$, we may generate various arbitrary cross sections. For $i = 1\ldots5$ equation (6) represents five homogenous equations for the five unknown constants x_i. In order to obtain a non-trivial solution, the determinant of the linear equations (6) must vanish. This condition yields the eigenvalue k_1 (or γ). Then the equations (6) are solved for the x_i. If the x_i, γ and k_1 are known, appropriate initial conditions may be assumed and the numerical integration of the magnetic field lines (5) yields the field. Arbitrary cross sections of the toroidal vessel may be obtained by appropriate choice of the r_i, z_i, see Figs. 1-4.

In the *threedimensional* (non-axisymmetric) case we have $m \neq 0$. Now we may use $x_1\ldots x_5$, γ and $k = 0$, k_1 from the axisymmetric case, but now new constants x_6, x_7 etc appear. They may be chosen arbitrarily or in such a manner to determine a special helical structure. The differential equations to be integrated are now

$$\frac{dz}{d\phi} = \frac{rB_z}{B_\phi}, \quad \frac{dr}{d\phi} = \frac{rB_r}{B_\phi} \tag{7}$$

They yield $z(\phi)$, $r(\phi)$. The expressions to be inserted into (7) for the field components are e.g.

$$B_\phi(r,z,\phi) = x_1 J_1(\gamma r) + x_2 Y_1(\gamma r) + \left[x_3 J_1\left(\sqrt{\gamma^2-k_1^2}\,r\right) + x_4 Y_1\left(\sqrt{\gamma^2-k_1^2}\,r\right)\right]\cos k_1 z + $$
$$+ \left[-x_6 J_0(\gamma r) - x_7 Y_0(\gamma r) + \frac{x_6}{r}J_1(\gamma r) + \frac{x_7}{r}Y_1(\gamma r)\right]\cos\phi$$

$$B_r(r,z,\phi) = k_1\left[x_3 J_1\left(\sqrt{\gamma^2-k_1^2}\,r\right) + x_4 Y_1\left(\sqrt{\gamma^2-k_1^2}\,r\right)\right]\sin k_1 z - $$
$$- \frac{1}{r}\left[x_6 J_1(\gamma r) + x_7 Y_1(\gamma r)\right]\sin\phi$$

$$B_z(r,z,\phi) = x_1 J_0(\gamma r) + x_2 Y_0(\gamma r) + (\gamma^2-k_1^2)\left[x_3 J_0\left(\sqrt{\gamma^2-k_1^2}\,r\right) + \right.$$
$$\left. + x_4 Y_0\left(\sqrt{\gamma^2-k_1^2}\,r\right)\right]\cos k_1 z + \left[x_6 J_1(\gamma r) + x_7 Y_1(\gamma r)\right]\cos\phi.$$

If more modes m, k (and more eigenvalues γ_0 $\gamma_1, \gamma_3 \ldots$ are chosen, many arbitrary cross sections may be produced /3/. In order to obtain the cross section of the torus for various ϕ, it is necessary to follow (by integrating (7)) a field line going around and around the torus, i.e. for $0 \leq \phi \leq n\cdot2\pi$. For $n = 50$ we obtain 51 crossing points of a field line in the meridional cut at ϕ_0. Repeating the same procedure for $\phi_0 = 0$, $\pi/4$, $\pi/2$ etc we obtain a series of meridional cuts, see Figs. 5 and 6.

References

/1/ F.Cap,, Proceed.Int.Conf.Plasma Phys. Nagoya, April 7-11, 1980, Vol 1, paper 7a-I-01 and Beitr.Plasmaphysik Vol 18, no 4, pp 207-216 (1978)

/2/ F.Cap, R.Deutsch, IEEE Transact.Microwave Theory and Techniques, Vol MTT 28, Nr.7, 700-703 (1980)

/3/ D.Lortz, W.Lotz, J.Nührenberg, F.Cap, Three-dimensional Analytical Force-free MHD Equilibria, submitted Zeitschr. f.Naturforschung.
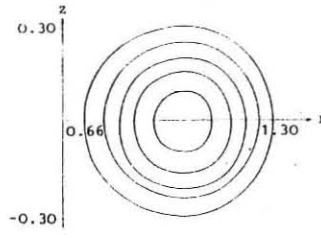
Fig.1 Nearly circular cross section
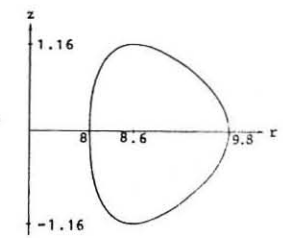
Fig.2 D-shaped cross section
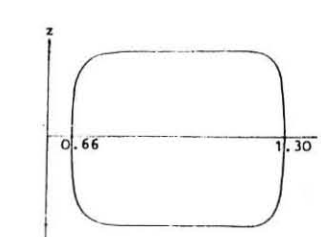
Fig.3 Nearly rectangular cross section
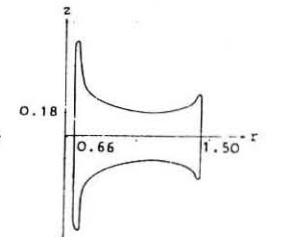
Fig.4 Hollow cross section
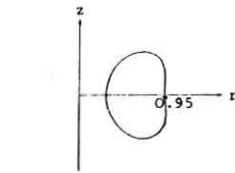
Fig.5 Toroidal 3-d field meridional cut at $\phi_0 = 2\pi$
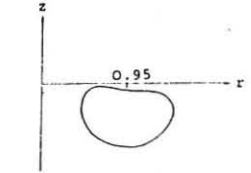
Fig.6 Toroidal 3-d field meridional cut at $\phi_0 = 3\pi/2$

WEAK FLUIDOMAGNETIC EQUILIBRIA ABOUT A SURFACE

C. Lo Surdo

Associazione EURATOM-CNEN sulla Fusione, Centro di Frascati, C.P. 65, 00044 Frascati, Rome, Italy

Despite its relevance to thermonuclear research, the question as to the existence of general global magneto-fluidostatic (MFS) fields remains essentially unanswered. Confining ourselves to nowhere force-free MFS fields in a bounded, connected Ω with (smooth) boundary $\delta\Omega$, the problem is that of proving the existence of C^1 solutions ($\underline{B}$, P) to the PDE system

(1) $\nabla \cdot \underline{B} = 0$, $\nabla \times \underline{B} \times \underline{B} = \nabla P$ in Ω, with

(2) $\nabla P \neq 0$ in $\Omega \cup \partial\Omega$ and under the boundary conditions

(3) $P = \text{const}_i$ on $\partial\Omega_i$, the i-th connected part of $\partial\Omega$ (i = 1, ..s).
Standard characteristic analysis shows that (1) has the $\underline{B}$-lines counted twice as characteristics. Since these lines cannot cross $\partial\Omega$ nor have singular points they must be closed or unending. This global-hyperbolic nature of the problem gives rise to peculiar difficulties.

As a matter of fact, only two special classes of C^1 MFS configurations are presently known, the axisymmetric and the plane-(pseudo) symmetric classes. On the other hand, no significant attempts have been made to date of constructing (not to say of defining) *weaker* (in a convenient sense) MFS fields. This is rather surprising, on considering that by now for several decades the generalized-solution standpoint has played a major role in PDE research, especially linear.

A classical theorem [1] states that Ω must be a toroidal annulus (and so s = 2) in order that a C^1 solution to (1) exists. This induces us to study the MFS problem in weakened sense, where a larger solution space is allowed by definition, in a Ω with the above topological structure.

A step toward the possible solution of a local version of this problem - that is, about a given (smooth) toroidal surface, assumed isobaric - has been recently contributed by the author [2]. What follows is an outline of some new ideas related to and inspired by that previous analysis.

By using P as first common Euler potential and (C_1, C_2) as second (monotone) potentials of $\underline{J} \equiv \nabla \times \underline{B}$ and respectively $\underline{B}$, one puts
(4) $\gamma \equiv \hat{n} \cdot \nabla' C_1 \times \nabla' C_2$, where $\hat{n}$ is the normal unit vector (for instance, pointing outwards) on the initial surface $\mathcal{S}_o$ (say, $P = 0$), and ∇' means surface gradient. The requirement that the surface differential form $\gamma^{-1} d\underline{x} \cdot \hat{n} \times \nabla' C_2$ be integrable is an initial constraint. To first order in P, the neighbouring surface $\mathcal{S}$ can be determined by displacing $\underline{x}_o \in \mathcal{S}_o$ by the amount $P \nabla \hat{n}$. The $\partial_n C_1$'s one needs to compute the $(\underline{J}, \underline{B})$ surface fields on $\mathcal{S}$ are then given by the following global-hyperbolic linear equations (read alternately upper or lower indices):
$(5_{\frac{1}{2}})$ $\hat{n} \times \nabla' C_2 \cdot \nabla' \partial_n C_1 + \nabla' C_1 \cdot [\nabla' (\hat{n} \times \nabla' C_2) \cdot \hat{n} + \nabla' C_1] = 0$.
Finally, one goes on to next (and higher) order Eqs (4, $5_{\frac{1}{2}}$) by replacing ∂_n by $-\gamma^{-1} \nabla' \gamma$. Eqs ($5_{\frac{1}{2}}$) (and n-derivatives) both have the $\underline{B}$-lines as characteristics. The main difficulties - and, ultimately, the need of making recourse to generalized solutions - are tied to these equations. In fact the relevant unknowns must be periodic on $\mathcal{S}_o$ up to arbitrary monotone summands. General questions of existence/uniqueness under these conditions cannot be reasonably put - for the equations of concern - but in some averaged sense; typically, on allowing the (periodic part of the) unknowns to be only L^2 - summable over $\mathcal{S}_o$ (w.r.t., $d_2\mathcal{S}_o$). Unfortunately the simplest and best-known (sufficient) existence/uniqueness criteria appear of hard application, or unsuitable, to the present case.

An interesting alternative to the above formulation is allowed by a sort of inversion between the independent and dependent variable spaces.

Precisely, one puts
(6) $C_{\frac{1}{2}} \equiv C_{\frac{1}{2}\alpha} z^\alpha$ (α, etc. = 1, 2), and

(7) $\gamma^{-1} \equiv (\det \hat{C})^{-1} \partial_n z^3$, where $C_{\frac{1}{2}\alpha}$ are the (surface invariant) increments of $C_{\frac{1}{2}}$ the long ($\alpha = 1$) or short ($\alpha = 2$) way around $\mathcal{S}_o$, and $\hat{C} \equiv (C_{\alpha\beta})$, ($\det \hat{C}$ turns out to be $\neq 0$ in view of (2)). Then one looks for a mapping $z \equiv (z^1, z^2, z^3) \longmapsto \underline{x}$, periodic with unit periods w.r.t. z^1 and z^2, such that $\underline{x}(z^1, z^2, z^3 = \text{const})$, with const about zero, are the isobaric surfaces about $\mathcal{S}_o$. The equations to be solved can now be written in terms of the metric $g_{ik} \equiv \partial_i \underline{x} \cdot \partial_k \underline{x}$ (i, k, etc. = 1, 2, 3, $\partial_i \equiv \partial_{z^i}$) as
(8) $T^{2\alpha} \mathcal{E}_{\alpha\beta} = 2\partial_{\llcorner\beta} (g_{3\rfloor\alpha} - T^2{}^\alpha)$,
(9) $g \equiv \det(g_{ik}) = 1$, together with the initial integrability constraint:
(10) $T^{2\alpha} \partial_1 g_{2\frac{1}{2}} - T^{2\alpha} \partial_1 g_{2\frac{3}{2}}|_o = 0$. Here $T^{\frac{1}{2}\alpha} \equiv \mathcal{E}^{\beta\alpha} C_{\frac{1}{2}\beta} (\det \hat{C})^{-1}$, $\mathcal{E}^{\alpha\beta}, \mathcal{E}_{\alpha\beta}$ are the unit antisymmetric density and capacity, and $\llcorner \lrcorner$ means alternation. The problem has thus been entirely geometrized. The order of the differential PDE system (8, 9) in $\underline{x}(z^1, z^2, z^3)$ can be lowered by one by taking the g_{ik}'s as unknowns together with the second fundamental form $q_{\alpha\beta}$ on $\mathcal{S}$ via:
(11) $q_{\alpha\beta} = \Gamma^3{}_{,\alpha\beta} p^{-1/2}$, with $\Gamma_{i,k}$ being the usual connection coefficients and $p \equiv \det (p_{\alpha\beta} \equiv g_{\alpha\beta})$. Of course one needs three more equations. These are provided via a long manipulation starting from the Gauss-Weingarten formulas on $\mathcal{S}$ together with
(12) $\partial_3 \underline{x} = \overset{\circ}{g}{}_3^\alpha \partial_\alpha \underline{x} + \partial_1 \underline{x} \times \partial_2 \underline{x} p^{-1}$, where $\overset{\circ}{g}{}_3^\alpha \equiv g_{3\beta} p^{\alpha\beta}$. The result is (with; meaning surface covariant derivative)
(13) $\partial_3 q_{\alpha\beta} = (p^{-1/2})_{;\alpha\beta} - p^{-1/2} q_\alpha^\gamma q_{\gamma\beta} + \overset{\circ}{g}{}_3^\gamma q_{\gamma\alpha;\beta} + 2q_{\gamma(\alpha} \overset{\circ}{g}{}_3^\gamma{}_{;\beta)}$,
where ( ) means symmetrization. Note that the third term on the RH is symmetric w.r.t. α, β in virtue of Codazzi's equations. Equations (13) can be shown to be solutions of the z^3-derivative of Gauss-Codazzi's system, as it must be. Finally, Eqs (8, 11) can be restated as
(14) $\partial_3 p_{\alpha\beta} = 2(g_{3(\alpha;\beta)} - p^{-1/2} q_{\alpha\beta})$ and
(15) $T^{2\alpha} g_{3\beta;\alpha} = - T^{1\alpha} \mathcal{E}_{\alpha\beta} - \dot{T}^{2\alpha} p_{\alpha\beta} + 2p^{-1/2} T^{2\alpha} q_{\alpha\beta}$, with the dot $\equiv z^3$-(ordinary) derivative. Note that the $\partial_i \underline{x}$'s disappear from Eqs (13, 14), in agreement with Gauss-Bonnet's theorem. System (15), which has the inverse image of the $\underline{B}$-lines on the (z^1, z^2) plane as (straight) characteristic lines, is the global-hyperbolic counterpart of system $(5_{\frac{1}{2}})$. If the (linear) operator on the left is invertible (in the weak sense), we are thus in position to obtain $\underline{x}$ via Eq. (12) (by means of similar recursive procedures) as a formal power series $\underline{x} (z^3)^i \partial_3^i \underline{x}|_o$, with L^2-summable coefficients over the unit (z^1, z^2) square. To each order m(m = 0, 1, ..) the four constants $d_1^m T^{\alpha\beta}$ are prescribed arbitrarily. The above series might quite converge (for instance, in norm) in the associated Hilbert space. Contrary to the case of Eq. $(5_{\frac{1}{2}})$, the classical Friedrichs (sufficient) criterion [3] for the invertibility of a 1st-order symmetric operator can be applied to Eqs (15), requiring that the matrix $\Phi_{\alpha\beta}$ with (α, β) elements $p^{\beta\delta} \Gamma_{\delta, \alpha\gamma} T^{2\gamma}$ be definite (positive or negative) in the integral sense; namely, that:

$\text{Inf} (\Phi h, h) > 0$ or $\text{Sup} (\Phi h, h) < 0$, where
$\|h\|=1$ $\qquad$ $\|h\|=1$

$(f, g) \equiv \int_o^1 \int_o^1 dz^1 dz^2 f_\alpha g^\alpha$ for any 2-column f_α and 2-row g^α, (periodic over the unit square), and $\|h\|^2 \equiv (h, h)$. What is lacking is rather an intuitive interpretation of such a condition. Finally, Eqs (15) can be shown unconditionally and classically solvable in the usual symmetric cases, as expected.

REFERENCES

[1] V.I. Arnold, Mathematical Methods of Classical Mechanics, p. 331, Springer (1978).

[2] C. Lo Surdo, Annali Mat. Pura Appl., Vol. CXXII, pp. 199-244 (1979).

[3] K.O. Friedrichs, Commun. Pure Appl. Math., Vol. XI, pp. 333-418 (1958.

ERRATUM

In the L.H.S. of eq. 15 a term

$- T^{2\alpha} \overset{\circ}{g}{}_3^\gamma \Gamma_{\gamma,\alpha\beta}$ is missing.

NONLINEAR EVOLUTION OF IDEAL MHD INSTABILITIES NEAR
THE THRESHOLD OF MARGINAL STABILITY

E. Rebhan

Institut für Theoretische Physik, Universität Düsseldorf
4000 Düsseldorf, Federal Republic of Germany

Abstract: A one parameter family of toroidal ideal MHD equilibria is considered assuming, that an increase of the parameter λ beyond a certain threshold λ_0 leads the plasma from stable to unstable. λ may be equal to β, a shape parameter or something else. Using reductive perturbation theory, the nonlinear MHD equations are expanded near $\lambda - \lambda_0$ with respect to a small parameter ε. To second order in ε, a nonlinear equation for the amplitude of the first order perturbation is found, yielding either explosive instability or a nonlinear oscillation about a neighbouring stable equilibrium.

We consider a one parameter family of ideal MHD equilibria

$$\underline{B}_0 = \underline{B}_0(\lambda) \quad , \qquad p_0 = p_0(\lambda). \tag{1}$$

In the neighbourhood of λ_0, we expand

$$\underline{B}_0(\lambda) = \underline{B}_{00} + \tau \underline{B}_{01} + \frac{\tau^2}{2}\underline{B}_{02}, \quad p_0(\lambda) = p_{00} + \tau p_{01} + \frac{\tau^2}{2}p_{02} \tag{2}$$

where $\underline{B}_{00} = \underline{B}_0(\lambda_0)$, $\underline{B}_{01} = d\underline{B}_0/d\lambda|_{\lambda_0}$ etc. and where $\tau = \lambda - \lambda_0$.

With eqs. (2) and $\underline{j} = \nabla \times \underline{B}$, we have the equilibrium conditions

$$\left.\begin{aligned}
\underline{j}_{00} \times \underline{B}_{00} &= \nabla p_{00}, \quad \underline{j}_{00} \times \underline{B}_{01} + \underline{j}_{01} \times \underline{B}_{00} = \nabla p_{01} \\
\underline{j}_{00} \times \underline{B}_{02} + \underline{j}_{02} \times \underline{B}_{00} + 2(\underline{j}_{01} \times \underline{B}_{01}) &= \nabla p_{02}.
\end{aligned}\right\} \tag{3}$$

Now, we consider a timedependent equilibrium perturbation

$$\left.\begin{aligned}
B(\underline{r},t) &= \underline{B}_0(\lambda) + \varepsilon \underline{B}_1 + \varepsilon^2 \underline{B}_2 \\
p(\underline{r},t) &= p_0(\lambda) + \varepsilon p_1 + \varepsilon^2 p_2 \\
\varrho(\underline{r},t) &= \varrho_0(\lambda) + \cdots.
\end{aligned}\right\} \tag{4}$$

Since near the threshold of marginal stability all quantities change slowly (in ideal MHD theory there is no overstability), we may assume that $\underline{B}_1$, $\underline{B}_1$ etc. depend on a slow time $T(t): \underline{B}_1 = \underline{B}_1(\underline{r},T)$ etc. The correct linear stability results are obtained with

$$T = \sqrt{\varepsilon}\, t \tag{5}$$

and with the "slow velocity"

$$\underline{v} = \sqrt{\varepsilon}\,(\varepsilon \underline{v}_1 + \varepsilon^2 \underline{v}_2). \tag{6}$$

Inserting eqs. (2) into (4) and eqs. (4)-(6) into the nonlinear equations of motion

$$\varrho\left(\frac{\partial \underline{v}}{\partial t} + \underline{v} \cdot \nabla \underline{v}\right) = \underline{j} \times \underline{B} - \nabla p \tag{7}$$

$$\frac{\partial \underline{B}}{\partial t} = \nabla \times (\underline{v} \times \underline{B}) \tag{8}$$

$$\partial p/\partial t = -(\underline{v} \cdot \nabla p + \tfrac{5}{3} p\,\mathrm{div}\,\underline{v}) \tag{9}$$

and expanding also

$$\tau = \varepsilon \tau_1 + \varepsilon^2 \tau_2, \tag{10}$$

with proper care of the equilibrium equations (3) we obtain

$$\left.\begin{aligned}
0 &= \underline{j}_{00} \times \underline{B}_1 + \underline{j}_1 \times \underline{B}_{00} - \nabla p_1 \\
\partial \underline{B}_1/\partial T &= \nabla \times (\underline{v}_1 \times \underline{B}_{00}) \\
\partial p_1/\partial T &= -(\underline{v}_1 \cdot \nabla p_{00} + \tfrac{5}{3} p_{00}\,\mathrm{div}\,\underline{v}_1)
\end{aligned}\right\} \tag{11}$$

to first order in ε. Setting

$$\underline{v}_1 = \dot{A}(T)\,\underline{\xi}_1(\underline{r}) \tag{12}$$

where $\dot{} = d/dT$, with

$$\tilde{\underline{B}}_1 = \nabla \times (\underline{\xi}_1 \times \underline{B}_{00}), \qquad \tilde{p}_1 = -(\underline{\xi}_1 \cdot \nabla p_{00} + \tfrac{5}{3} p_{00}\,\mathrm{div}\,\underline{\xi}_1) \tag{13}$$

system (11) is solved by

$$\underline{B}_1 = \dot{A}(T)\,\tilde{\underline{B}}_1, \qquad p_1 = \dot{A}(T)\,\tilde{p}_1 \tag{14}$$

if $\underline{\xi}_1$ is a solution of

$$\underline{F}_0(\underline{\xi}_1) = 0. \tag{15}$$

Here, $\underline{F}_0$ is the usual MHD stability operator $\underline{F}$ taken at $\lambda = \lambda_0$. To second order in ε, we obtain the set of equations

$$\left.\begin{aligned}
\varrho_{00}\frac{\partial \underline{v}_2}{\partial T} &= \underline{j}_{00} \times \underline{B}_2 + \underline{j}_2 \times \underline{B}_{00} - \nabla p_2 + \tau_1(\underline{j}_{00} \times \underline{B}_1 + \underline{j}_1 \times \underline{B}_{00}) + \underline{j}_1 \times \underline{B}_1 \\
\frac{\partial \underline{B}_2}{\partial T} &= \nabla \times (\underline{v}_1 \times \underline{B}_{00}) + \tau_1 \nabla \times (\underline{v}_1 \times \underline{B}_{00}) + \nabla \times (\underline{v}_1 \times \underline{B}_1) \\
\frac{\partial p_2}{\partial T} &= -(\underline{v}_1 \cdot \nabla p_{00} + \tfrac{5}{3}p_{00}\,\mathrm{div}\,\underline{v}_2) - \tau_1(\underline{v}_1\cdot\nabla p_{00} + \tfrac{5}{3}p_{00}\,\mathrm{div}\,\underline{v}_1) - (\underline{v}_1\cdot\nabla p_1 + \tfrac{5}{3}p_1\,\mathrm{div}\,\underline{v}_1)
\end{aligned}\right\} \tag{16}$$

If the first of the eqs. (16) is differentiated with respect to T and the other two are then inserted in the first, we obtain with (12)

$$\varrho_{00}\,\ddot{A}\,\underline{\xi}_1 = \underline{F}_0(\underline{v}_2) + \tau_1\dot{A}\underline{F}_0'(\underline{\xi}_1) + A\dot{A}\,\underline{B}_0(\underline{\xi}_1) \tag{17}$$

where

$$\underline{F}_0' = d\underline{F}/d\lambda|_{\lambda_0} \tag{18}$$

and

$$\underline{B}_0(\underline{\xi}_1) = \underline{j}_{00} \times [\nabla \times (\underline{\xi}_1 \times \tilde{\underline{B}}_1)] + \{\nabla \times [\nabla \times (\underline{\xi}_1 \times \tilde{\underline{B}}_1)]\} \times \underline{B}_{00}$$
$$+ \nabla(\underline{\xi}_1\cdot\nabla\tilde{p}_1 + \tfrac{5}{3}\tilde{p}_1\,\mathrm{div}\,\underline{\xi}_1) + 2(\nabla\times\tilde{\underline{B}}_1)\times\underline{B}_1 \tag{19}$$

Since $\underline{F}$ is a Hermitean operator, we have

$$(\underline{\xi}_1, \underline{F}_0(\underline{v}_2)) := \int \underline{\xi}_1 \cdot \underline{F}_0(\underline{v}_2)\,d^3r = (\underline{v}_2, \underline{F}_0(\underline{\xi}_1)) = 0,$$

and with the normalization $(\underline{\xi}_1, \underline{\xi}_1) = 1$ we thus get from eq. (17)

$$\varrho_{00}\ddot{A} = \tau_1\dot{A}(\underline{\xi}_1, \underline{F}_0'(\underline{\xi}_1)) + \left(\frac{A^2}{2}\right)\cdot(\underline{\xi}_1, \underline{B}_0(\underline{\xi}_1)). \tag{20}$$

Integrating eq. (20) with respect to T and returning from T to t we obtain

$$d^2A/dt^2 = \gamma^2 A + \delta A^2 \tag{21}$$

where an integration constant is chosen such as to yield exponential instability for small A and where we have set

$$\gamma^2 = \frac{1}{\varrho_{00}}(\underline{\xi}_1, \varepsilon\tau_1\underline{F}_0'(\underline{\xi}_1)), \quad \delta = \frac{\varepsilon}{2\varrho_{00}}(\underline{\xi}_1, \underline{B}_0(\underline{\xi}_1)). \tag{22}$$

Integrating eq. (21) once again, we get

$$(dA/dt)^2 = \gamma^2 A^2 + \tfrac{2}{3}\delta A^3. \tag{23}$$

a) If $\delta < 0$, the amplitude at $A = -\tfrac{3}{2}\gamma^2/\delta$ reverses, the motion is a nonlinear oscillation around the "minimum potential" at $A = -\gamma^2/\delta$, where a stationary amplitude is possible. After some oscillations, friction may lead the plasma to settle down in this neighbouring equilibrium which bears the spatial structure of the marginal perturbation $\underline{\xi}_1$. This situation is expected to be possible e.g. for axisymmetric instabilities of tokamaks due to the existence of neighbouring axisymmetric equilibria.
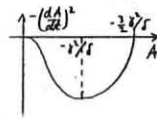
b) If $\delta > 0$, the solution of eq. (21) is given by

$$A = \frac{3\gamma^2}{2\delta}\left[(1+e^{\gamma(t-t_0)})^2/(1-e^{\gamma(t-t_0)})^2 - 1\right]. \tag{24}$$

This is an explosive type of instability, since starting with finite amplitude A_0 at $t = 0$, an infinite amplitude is reached already after the finite time

$$t_0 = -\frac{1}{\gamma}\ln\left[(\sqrt{1+\tfrac{2}{3}\tfrac{\delta}{\gamma^2}A_0} - 1)/(\sqrt{1+\tfrac{2}{3}\tfrac{\delta}{\gamma^2}A_0} + 1)\right] \tag{25}$$

This situation is expected e.g. for nonaxisymmetric instabilities like kinkmodes in tokamaks, due to the nonexistence of nonaxisymmetric neighbouring equilibria.

NUMERICAL STUDIES OF MHD-PLASMA EQUILIBRIUM
IN TOKAMAK BY THE VARIATIONAL METHOD

V.D.Khait, V.K.Kolesnikov
Institute of High Temperature of the USSR Academy
of Sciences, Moscow, USSR

The variational method of approximate solution of the equilibrium equation in axisymmetric toroidal systems is offered in Ref.[1]. This method (as the method of moments[2,3]) enables the two-dimensional problem to be reduced to the system of ordinary differential equations for parameters u_i determining the shape and position of magnetic surface (m.s.) cross-section. This system is:

$$\left(\frac{\partial T}{\partial u_i'}\right)' - \frac{\partial T}{\partial u_i} = 0 \qquad (1)$$

Here $T = \mathcal{J}^2(\zeta)M(\zeta,u_i,u_i') - c^2\rho V(\zeta,u_i) - II'L(\zeta,u_i)$, where ζ is a some surface function choosed as an independent variable, and the prime indicates the ζ derivative, $\mathcal{J}(\zeta)$ and $\rho(\zeta)$ are the longitudinal current and plasma pressure profiles considered as to be prescribed, $V = 2\pi\iint \tau d\tau d\bar{z}$ is the volume of a given m.s., $L = 2\iint \tau d\tau d\bar{z}$ is inductance of the solenoid that coincides with m.s. $M^{-1} = \oint |\nabla\zeta| \tau^{-1} d\ell/4\pi$ is the integral along the cross-section contour of m.s. (τ and $\bar{z}$ are cylindrical coordinates), I is the external poloidal current connected with $\mathcal{J}$ and ρ by the eq. $2M\mathcal{J}\mathcal{J}' + c\rho V' + II'L = 0$. The external poloidal and toroidal fluxes are defined by $\Psi = -2M\mathcal{J}/c$, $\Phi' = IL/c$.

The boundary conditions for (1) are determined by the shape and position of the boundary cross-section: $u_i(\zeta_\Sigma) = u_{i\Sigma}$. Furthermore the regularity of solution on the magnetic axis is required.

Taking into account ellipticity and triangularity is required for adequate solution of a some problems. One can show that arbitrary cubic curve required to describe the cross-section contour in this cases is determined by

$$\zeta = e^\eta(\tau-R)^2 + e^{-\eta}\bar{z}^2[1+\tau_1(\tau-R)]/[1+\tau_2(\tau-R)] \qquad (3)$$

or in parametric form $\tau = R + \sqrt{e^{-\eta}\zeta}\cos t$, $\bar{z} = \sqrt{e^\eta\zeta}(\tau_1^*\cos t +1)/(1+\tau_2^*\cos t)\sin t$, $\tau_1^*/\tau_1 = \tau_2^*/\tau_2 = \sqrt{e^{-\eta}\zeta}$. Here R is the position of m.s., η is the ellipticity parameter, τ_1 and τ_2 are the triangularity parameters. Eq.(3) enables to find easily the functions of the problem $|\nabla\zeta| = \tau\sqrt{g_{22}/g}$, $d\ell = \sqrt{g_{22}}\,dt$ where $g_{22} = \left(\frac{\partial\tau}{\partial t}\right)^2 + \left(\frac{\partial\bar{z}}{\partial t}\right)^2$ is the metric coefficient, $g = Det g_{ik} = \tau^2\left(\frac{\partial\tau}{\partial\zeta}\frac{\partial\bar{z}}{\partial t} - \frac{\partial\tau}{\partial t}\frac{\partial\bar{z}}{\partial\zeta}\right)^2$ is the determinant of metric tensor g_{ik} defining an element of length in the coordinate system ζ, t, φ (azimuthal angle).

The boundary conditions for $\zeta = 0$ is obtained by expanding with respect to ζ in the vicinity of axis. Let present here only the expressions for R_o' and η_o' on the magnetic axis (expressions for τ_{1o}' and τ_{2o}' are fairly unwieldy):

$$\delta = R_o R_o' e^{\eta_o} = (\eta + th\eta_o)^{-1}[\pi c^2\rho_o' i_o^{-2} - (1+th\eta_o)/4 + \gamma_o(1-th\eta_o)/4]$$

$$\eta_o' = \{-(i_o'/i_o)R_o^2 e^{\eta_o}th\eta_o + \tfrac{1}{4}th\eta_o[1-2\gamma_o + \tfrac{1}{4}\gamma_o R_o(\tau_{1o}-2\tau_{2o})] + \tfrac{1}{2}th^2\eta_o(1+\tfrac{1}{4}\gamma_o + \tfrac{1}{4}\gamma_o^2) - 3\delta(1+\gamma_o) - 2\delta th\eta_o(1+\tfrac{1}{2}\gamma_o) + \delta th^2\eta_o(1+\gamma_o) + 2\delta^2(th^2\eta_o - 4th\eta_o - 6) - \tfrac{3}{4}\}/3 R_o^2 e^{\eta_o}(2-th^2\eta_o), \qquad (4)$$

$i_o = \mathcal{J}_o'$, $\gamma_o = R_o(\tau_{1o} - \tau_{2o})$.

Numerical realization of the method had been accomplished so far only for the scheme with two parameters R and η ($\tau_1 = \tau_2 = 0$). In this case $f = \pi\zeta$ (m.s. cross-section area).

Eq.(1) was written in the form of linear equations system, coefficients of that were however functions of u_i and u_i'. This system was being solved on each iteration by the method of factorization as linear one with coefficients calculated from two previous iterations with some "weight". The typical computations take 5-10 iterations for convergence that requires 1-2 sec machine time of BESM-6 computer.

As known there is a limit of the parameter $\beta_y = 2c^2 x \int_o^* \rho d f/\mathcal{J}^2(f_\Sigma)$ above that equilibrium is impossible. Fig.1

presents results of two parametric scheme computatuins limiting $\beta_y = \beta_y^{lim}$ — aspect-ratio A dependence ($\eta_\Sigma = 0$) for two cases: uniform current density $\mathcal{J}' = const$, parabolic pressure $\rho = \rho_o(1 - f/f_\Sigma)$(I) and sharp profiles (II): $\rho = \rho_o(1 - f/f_\Sigma)/(1 + 3,46 f/f_\Sigma)$, $\mathcal{J} = j_o f/(1 + 4 f/f_\Sigma)$ in accordance with data of T-II device[4].

For the same profiles (A=3.5; $\eta_\Sigma =0$) Fig.2 shows magnetic axis shift (normalized to the minor radius of the plasma) and semiaxis ratio V of near-axes cross-section in dependence on β_y.

Fig.3 represents α as function of β_y (1-A=2.5; 2-A=3.0; 3-A=3.5) where α is the ratio of poloidal current I_Σ needed to creat given value of safety factor q_Σ on the plasma boundary to such a value of this current $qA^2\mathcal{J}/e^{\eta_\Sigma}ch\eta_\Sigma$ as required for case of small $(1+\beta_y)/A$. This value characterizing distortion or magnetic configuration is $\alpha = A^2\oint\frac{d\ell}{\tau B_p}\oint B_p d\ell/2\pi^2(1+v_\Sigma^2)$, where B_p is poloidal magnetic field and the integrals are taken along plasma boundary contour. As it rollows from this formula α increases with β_y when zero of B_p approaches the plasma boundary. Fig.3 shows that α can visibly exceed 1. The dependence $\alpha(\beta_y, A)$ turns out to be slightly sensitive to the value of v_Σ as well as to current and pressure profiles at least in the region where α visibly exceeds 1. Such a behaviour of $\alpha(\beta_y)$ leads to the essential quantity $\beta_T = 8\pi\langle\rho\rangle/B_{T\Sigma}^2 = \beta_y\alpha^2 e^{\eta_\Sigma}ch^2\eta_\Sigma/A^2 q^2$ is strongly increasing nonlinear function of β_y (with q fixed) as Fig.4 shows. The equilibrium turns out to be possible at rather high β_T.

1. Хаит В.Д., Физика плазмы, 6, 871, 1980.
2. Захаров Л.Г., Шафранов В.Д., ЖТФ, 225, 1973.
3. Захаров Л.Г., Шафранов В.Д., Препринт ИАЭ-3075, М., 1978.
4. Mukhovatov V.S., Second Joined Grenoble-Varenna International Symposium on Heating of Torroidal Plasma, Italia 1980.

Fig.1

Fig.2

Fig.3

Fig.4
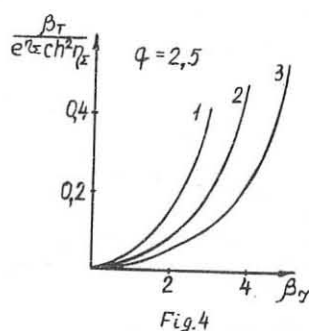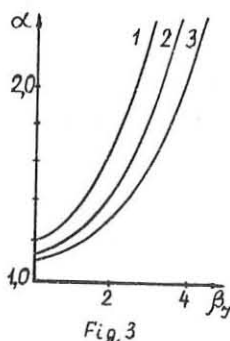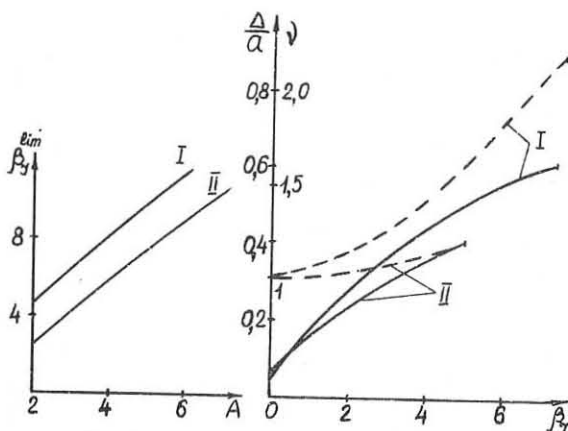
TOKAMAKS WITH A FREE BOUNDARY

J.M. Akkermans and J.P. Goedbloed
Association Euratom-FOM, FOM-Instituut voor Plasmafysica
"Rijnhuizen", Nieuwegein, The Netherlands

ABSTRACT. The free-boundary problem for a high-β tokamak is discussed.
Analytical results for free-boundary equilibria are presented. With re-
spect to external kink mode stability it is suggested that the Kruskal-
Shafranov limit is no longer a strict limit at high beta.

INTRODUCTION. Previously, high-β tokamaks have been mainly investigated
within the context of fixed-boundary models in which the plasma cross-
section is prescribed (e.g., [1]). This leads to a linear, but ill-posed,
problem. An approach closer to experimental reality is to ask for the
shape of the plasma cross-section inside a given conducting shell. This
free-boundary problem is well-posed, but non-linear. In this work we em-
ploy a surface-current model, together with the high-β tokamak ordering
$\beta \sim \varepsilon$. An exposition of this model is given in Refs. [2] and [3]. Due to
the high-β tokamak ordering the free-boundary problem can be reduced to
a two-dimensional problem in which Laplace's equation has to be solved
in the vacuum region subject to the condition that the cross-section of
the wall and the (unknown) cross-section of the plasma are both curves
of constant flux. The influence of the wall shape is investigated by em-
ploying the techniques of conformal mapping. These techniques, combined
with fast Fourier transforms, yield highly accurate numerical solutions
for the equilibrium; examples are found in Ref. [3]. Here, we demonstrate
that the high-β tokamak approach provides the opportunity for fruitful
analytical work on the free-boundary problem. Furthermore, preliminary
results of the stability analysis are shown.

EQUILIBRIUM. Analytical solutions for the free-boundary equilibrium can
be found by combining conformal mapping and Fourier analysis with a pow-
er series expansion in terms of Δ, the toroidal plasma shift. In this
way solutions up to third order in Δ were obtained. For circular walls
the solution is a shifted circle in first order in Δ; in second order it
is a shifted ellipse. In third order the plasma becomes D-shaped. An ex-
ample is given in Fig. 1, where the numerical solution (full line) is
compared with the first-order (dot-dashed line) and second-order (dashed
line) analysis. The maximum deviation of the third-order result from the
numerical result is about 2% (for clarity the third-order result is not
shown here). In Fig. 2 a comparison of numerical and analytical results
for the poloidal beta as a function of the plasma shift is given for two
different plasma half-widths a. The straight dot-dashed line represents
both the first-order and second-order results. It turns out that the el-
lipticity of the plasma does not influence the poloidal beta directly.
Furthermore, it is seen that the analytical results are particularly
good for fat plasmas.

For non-circular walls we have considered shapes slightly deformed
from a circle (where the deformation must be small, but is otherwise ar-
bitrary), for which a simple conformal transformation onto the circle is
known. As expected, the wall deformation influences the plasma shape in
leading order. For elliptical walls there is the following simple ana-
lytical result for the poloidal beta:

$$a \varepsilon \beta_p = \frac{2\Delta a}{1-a^2} \left[1 + \frac{1}{2} E_{wall} (1+a^2) \right] , \qquad (1)$$

where E_{wall} is the ellipticity of the wall ($|E_{wall}| \ll 1$; $1 + E_{wall}$ is the
ratio of major and minor axis). It appears that elongation of the wall
(and, hence, of the plasma) increases the poloidal beta in combination
with the toroidal shift. With respect to the plasma shape it can be re-
marked that for fat plasmas the ellipticity of the plasma is larger than
that of the wall, even when neglecting finite-beta effects.

We have also investigated the influence of surrounding the plasma by
a region with force-free currents instead of a vacuum region. In this
case one has to solve Poisson's equation in the region between plasma
and wall rather than Laplace's equation; the inhomogeneous part repre-
sents the strength of the force-free currents. It turns out that the po-
loidal beta of the equilibrium is strongly increased by the introduction
of force-free currents. For a circular wall the result is

$$a \varepsilon \beta_p = \frac{\Delta}{1-a^2} \left[2a + \Gamma(1-a^2) \right] , \qquad (2)$$

where Γ is a constant representing the strength of the force-free cur-
rents ($\Gamma \sim 1$; for vacuum $\Gamma = 0$). Regarding the plasma shape, force-free
currents provide a stronger coupling between wall and plasma shape than
a vacuum does.

STABILITY. Stability results for the free-boundary equilibrium of a
plasma surrounded by vacuum inside a wall of circular cross-section are
compared with previous results of the fixed-boundary model [4] in Fig. 3.
Through the influence of the wall the unstable region for external kink modes

is restricted to the range $a^2 < nq^* < 1$ at low β. When β is raised this re-
gion shrinks, as opposed to the situation in the fixed-boundary model
where the stability becomes worse at higher β. In the latter model this
leads to a well-defined maximum value of β where the stability boundary
intersects the equilibrium boundary associated with the incidence of a
separatrix at the plasma. In the free-boundary model complete stability
obtains above a certain minimum value of β, which is well below the equi-
librium limit associated with the development of a region of vanishing
poloidal field. We conclude that the Kruskal-Shafranov limit is no long-
er a strict limit for stability with respect to external kink modes when
β is sufficiently high.

REFERENCES
[1] D.A. D'Ippolito, J.P. Freidberg, J.P. Goedbloed, and J. Rem, Phys.
    Fluids 21 (1978) 1600.
[2] J.P. Goedbloed, Proceedings of the IXth European Conference on Control-
    led Fusion and Plasma Physics (Oxford, 1979) p. 171.
[3] R.M.O. Galvão et al., 8th IAEA Int. Conf. on Plasma Physics and
    Controlled Nuclear Fusion Research (Brussels, 1980) paper IAEA-CN-
    38/L-4-1.
[4] D.A. D'Ippolito, J.P. Freidberg, J.P. Goedbloed, and J. Rem, Proceed-
    ings of the Finite Beta Theory Workshop, Varenna, Sept. 1977, ed. B.
    Coppi and W. Sadowski (US Dept. of Energy, Washington DC, 1977) p. 75.
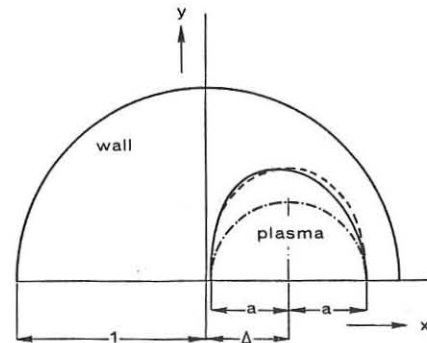
Fig. 1. Numerical (full line), first-order (dot-dashed line) and second-
order (dashed line) results for the equilibrium. Circular wall,
$\Delta = .42$, $a = .40$.
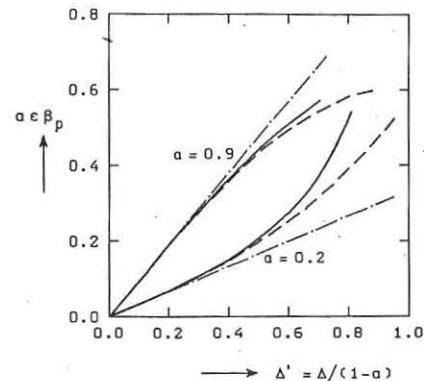
Fig. 2. Numerical (full line), first/second-order (dot-dashed line) and
third-order (dashed line) for $a \varepsilon \beta_p$; circular wall.
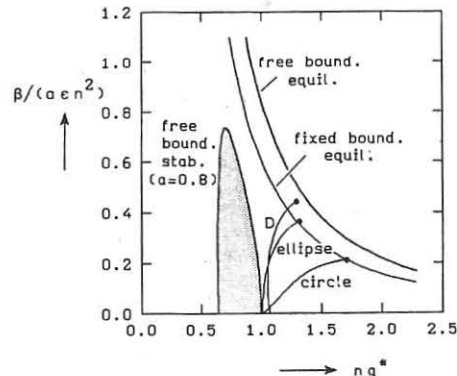
Fig. 3. Equilibrium and stability boundaries for the fixed- and free-
boundary models. Equilibrium below the curves $a \varepsilon \beta_p = .617$ for
fixed-boundary (circle) and $a \varepsilon \beta_p = .859$ for free-boundary (a = .8).
Instability to the left of the curves for fixed-boundary model (circle,
ellipse, D-shape) and in the shaded area for free-boundary model.

THE SHEAR EFFECT ON STABILITY OF BALLOONING MODES IN CLOSED MAGNETIC TRAPS

A. B. MIKHAILOVSKII

KURCHATOV INSTITUTE OF ATOMIC ENERGY,
MOSCOW, USSR

V. V. DEMCHENKO

INSTITUTE OF PHYSICS & TECHNOLOGY,
UKR. ACAD. SCI., KHARKOV, USSR

In paper/1/ideal ballooning MHD-modes of a tokamak were investigated to an approximation of a null shear. In the given report, as opposed to/1/, we shall assume the shear to be a finite one and investigate the influence of the shear on stability of ballooning modes both in tokamaks and in more intricate toroidal traps, including the traps with spatial magnetic axis. In this report we apply the methods of analyzing ballooning modes in the tokamak with shear proposed in paper/2/ and then improved for the case of the tokamak with a finite shear and moderate plasma pressure in paper/3/. We generalize the method of paper/2/ for the case of traps with an arbitrary form of magnetic axis.

Similarly to paper/2/, instead of angular variable θ (as in /4,5/, the coordinate system α, θ, ψ is used with straightened magnetic field lines) we introduce the variable y whose meaning was explained in /2/. Then we shall present radial displacement ξ in eiconal form $\xi = e^{in(qy-\psi)}\bar{\mathcal{F}}(\alpha,y,\psi)$, where $\bar{\mathcal{F}}(\alpha,y,\psi)$—slowly changing function of angular variables, q is a safety factor.

1. Tokamak with circular magnetic surfaces(MS).

According to averaging scheme for the equation of small oscillation proposed in paper/4/for an average part of function $\bar{\mathcal{F}}(\alpha,y,\psi)$, similar to equation(5.21)of paper/5/, we derive

$$\frac{\partial}{\partial y}\left[(1+t^2)\frac{\partial\bar{\mathcal{F}}}{\partial y}\right] - S^2\bar{\mathcal{F}}\left[U_0 + \frac{U_1}{1+t^2} + \frac{4U_2 t^2}{(1+t^2)^2}\right] = 0, \quad (1)$$

$$U_0 = \frac{2p'}{\alpha\mu'^2 B_s^2}\left[\mu^2 - 1 - \frac{3}{2}\cdot\frac{\xi'}{\varepsilon}\left(\frac{3}{2}\xi'^2 - \bar{\alpha}' + \frac{\bar{\alpha}}{\alpha}\right)\right],$$

$$U_1 = \frac{2p'}{\alpha\mu'^2 B_s^2}\left\{\frac{8\pi^2 R^2 \alpha p'}{S'^2}\left[\frac{\xi'^2}{2} + \frac{3}{8}(\alpha\xi''-\xi')(\alpha\xi''+3\xi') + \frac{\alpha\mu'}{\mu} - \frac{(\alpha\xi''-\xi')^2}{32}\right] - \frac{\alpha\mu'}{\mu}\cdot\frac{\alpha\xi''-\xi'}{\varepsilon}\right\},$$

$$U_2 = -\frac{2p'}{\alpha\mu'^2 B_s^2}\left\{\frac{4\pi^2 R^2 \alpha p'}{S'^2}\left[\frac{3}{2}\left(\frac{\bar{\alpha}}{\alpha} - \bar{\alpha}'\right) + \frac{3}{8}\xi'^2 + \frac{\alpha\xi''}{8}(\xi' + 2\alpha\xi'')\right] - \frac{\alpha\mu'}{2\mu}\cdot\frac{\alpha\xi''-\xi'}{\varepsilon}\right\},$$

$t = \frac{\alpha}{R}S\cdot\frac{\alpha q'}{q}$, the prime is the derivative on α, $\bar{\alpha}$—the value characterizing the ellipticity of MS, ξ is the equilibrium displacement of MS. From equation(1)it follows the required criterion of ballooning modes stability:

$$\frac{1}{2}\left(S-\frac{\alpha'}{\bar{\alpha}}\right)^2 + \frac{}{}\varepsilon(1-\mu^2-\Delta) > 0, \quad \alpha = -\frac{2p'Rq^2}{B_s^2}, \quad \Delta = \frac{d^3}{8\varepsilon} - \Delta_1, \quad (2)$$

$$\Delta_1 = \frac{3}{2}\cdot\frac{\xi'}{\varepsilon}\left(\frac{3}{2}\xi'^2 - \bar{\alpha}' + \frac{\bar{\alpha}}{\alpha}\right) - \frac{S}{4}\cdot\frac{\alpha\xi''-\xi'}{\varepsilon} + \frac{\alpha}{2\varepsilon}\left[\frac{5}{16}\xi'^2 - \frac{3}{4}\left(\frac{\bar{\alpha}}{\alpha} - \bar{\alpha}'\right) + \frac{3}{8}(\alpha\xi''-\xi')(\alpha\xi''+3\xi') - \frac{(\alpha\xi''-\xi')^2}{32} - \frac{\alpha\xi''}{16}(\xi' + 2\alpha\xi'')\right]$$

In the case of parabolic pressure profile we have/5/:

$$\xi' = k\alpha\beta_3, \quad \alpha = 4k\alpha\beta_3, \quad \bar{\alpha}/\alpha = (k\alpha)^2\beta_3^2/4, \quad \Delta = 6(k\alpha)^2\beta_3^3,$$

where $\beta_3 = p_0/B_{\theta}^2(\alpha_0)$, p_0—plasma pressure at the centre, $B_\theta(\alpha_0)$—poloidal magnetic field at the shell. From inequality(2) at $q \gg 1$ it follows that instability arises at $\beta_3 \overset{-1/3}{6}(k\alpha)^{-2/3}$.

2. Ballooning modes in the traps with a spatial magnetic axis.

There are some experimental results/6/attesting realization of theoretically predicted effects/7-9/ of plasma self-stabilization. In paper/7/a helical column was discussed, in papers/8,9/—the traps with an arbitrary form of magnetic axis. Both in/7/and/8,9/the perturbation of Mercier type were investigated. In our report the stability of three-dimensional ballooning modes is being examined.

According to our calculations, in the case of simple plasma configurations with a spatial magnetic axis—a helical column—the criterion of ballooning modes stability takes the form:

$$\frac{S^2}{2} + \frac{}{}\varepsilon\left[(k_0 R)^2\frac{\mu_3-\mu_0}{\mu_3+\mu_0} - \mu_3^2 + \Delta_1\right] - \frac{1}{2}\alpha^2 S(k_0 R)^2 > 0, \quad (3)$$

$$\Delta_1 = \frac{3k_0 R^2 \xi'}{2\alpha}\left(\frac{3}{2}\xi'^2 - \bar{\alpha}' + \frac{\bar{\alpha}}{\alpha}\right) - \frac{S}{4\alpha}R(k_0 R)(\alpha\xi''-\xi') + \frac{\alpha R}{2\alpha}(k_0 R)^2\left[\frac{5}{16}\xi'^2 + \frac{3}{8}(\alpha\xi''-\xi')(\alpha\xi''+3\xi') - \frac{(\alpha\xi''-\xi')^2}{32} - \frac{3}{4}\left(\frac{\bar{\alpha}}{\alpha} - \bar{\alpha}'\right) - \frac{\alpha\xi''}{16}(\xi' + 2\alpha\xi'')\right],$$

$\mu_0 = -z_0 R$, $\mu_3 = JR/2B_s^2$, $k_0 = r_0/R^2$, $z_0 = h/R^2$, $R^2 = r_0^2 + h^2$, r_0 and h—radius and step of magnetic axis which has a form of a helical line. At parabolic pressure profile we derive from(3):

$$\frac{S^2}{4} + \frac{}{}4\beta_0(\alpha^2/R^2)\left[(k_0 R)^2\frac{\mu_3-\mu_0}{\mu_3+\mu_0} - \mu_3^2 + \frac{5}{2}k_0^4 R^2\alpha^2\beta_0^2\right] - 8S(k_0 R\alpha)^2 > 0, \quad (4)$$

where $\beta_0 = \frac{4\pi^2 p_0}{S^2(\alpha_0)}$. In the absence of longitudinal current $(\mu_3 = 0)$ we have $\beta_0 \overset{}{\left(\frac{8}{5}\right)}(k_0\alpha)^{-2/3}$. Mercier criterion in this case gives $\beta_0 \overset{}{\left(\frac{6}{25}\right)}(k_0\alpha)^{-2/3}$. Thus, for currentless traps with a spatial magnetic axis the ballooning modes are more dangerous than Mercier-type perturbations. However, due to plasma self-stabilization effect these modes are also found to be stable if plasma pressure is rather high.

REFERENCES

1. A. B. Mikhailovskii. Fizika Plasmy(USSR), 4, 1226, 1978.

2. J. W. Connor, R. J. Hastie, J. B. Taylor. Phys. Rev. Lett., 40, 396, 1978.

3. O. P. Pogutse, E. I. Yurchenko. Fizika Plasmy(USSR), 5, 786, 1979.

4. A. B. Mikhailovskii. Zh. Exper. Teor. Fiz. (USSR), 64, 536, 1973

5. A. B. Mikhailovskii. Nucl. Fusion, 14, 483, 1974.

6. K. Harafuji, N. Sasaki et al., J. Phys. Soc. J., 48, 1323, 1980.

7. A. B. Mikhailovskii, V. D. Shafranov. Zh. Exper. Teor. Fiz. (USSR), 66, 190, 1974.

8. A. B. Mikhailovskii, Kh. D. Aburdzhanija. Plasma Physics, 21, 109, 1979.

9. C. Mercier. Proc. Intern. Symposium on Stellarators with three-dimensional magnetic axis. Sendai, Japan, 1979, p. 29.

THE RESPONSE OF ELECTRONS TO LOW-FREQUENCY MODES

T.J.Schep, A.Abels-van Maanen, B.Braams, F.Pegoraro[*]
Association Euratom-FOM, FOM-Instituut voor Plasmafysica "Rijnhuizen"
Nieuwegein, The Netherlands

We discuss analytic approximations to the non-adiabatic responses of trapped and circulating electrons to unstable, low-frequency modes in an axisymmetric, toroidal configuration and compare them with numerical calculations. We employ flux coordinates (ψ,θ,ζ) with Jacobian J. For large toroidal wave-numbers, any perturbed quantity can be written as[1,2] $\xi = \xi(S,\theta) \exp[-i\omega t + in^\circ(\zeta - \int_0^\theta qd\theta')]$, with

$$\xi(S,\theta) = \int_{-\pi}^{+\pi} \frac{d\alpha}{2\pi} \sum_{-\infty}^{+\infty} \hat{\xi}_\alpha(\theta+2\pi m)\exp i(-2\pi m + \alpha)S , \qquad (1)$$

n° being the toroidal mode number, $S(\psi) = n^\circ(\bar{q}-\bar{q}_0)$, $\bar{q} = (2\pi)^{-1}\oint d\theta q$, $q = JB_\zeta/R$, $\bar{q}_0$ a reference rational surface and α a continuous eigenvalue. Employing this mode representation, the perturbed electron density is[1]

$$\frac{n'_{ea}(\hat{\theta})}{n} = \frac{e\hat{\phi}_\alpha(\hat{\theta})}{T_e} + \left(1 - \frac{\omega_*}{\omega}\right)\hat{\psi}_\alpha(\hat{\theta}) + \frac{e}{T_e}\left[\hat{N}_{aT}(\hat{\theta}) + \hat{N}_{aC}(\hat{\theta})\right], \qquad (2)$$

where ω_* is the drift-frequency. The potential Ψ is related with the parallel component of the perturbed vector potential according to $(-i\omega/c)A_\parallel = (\underline{B}/B)\cdot\nabla\Psi$. The responses $\hat{N}_{T,C}$ are obtained by expanding the distribution function in harmonics of the orbit periodicity and by integrating over velocity space. Collisions will be ignored. Although, this is not correct near the boundary between trapped and circulating particles, a consistent and continuous description of the responses can be given. response of trapped particles is[3]

$$\hat{N}_T(\hat{\theta}) = A(\omega)\int_{-\pi}^{+\pi} d\theta' J' \int_{\Lambda_b}^{\bar{\Lambda}} d\Lambda \frac{BB'}{LL'B_0}\left[\hat{\chi}(\theta'+2\pi m)\frac{\partial}{\partial\delta}I_T(\beta) + \hat{\chi}(-\theta'+2\pi m)\frac{\partial}{\partial\delta}I_T(\beta+\frac{1}{2})\right]_{\delta=1} \quad (3)$$

where $A(\omega) = -[\omega/(2\pi^{3/2}V_{th})][1 - (\omega_*/\omega)(1-3/2n) + (\omega_*/\omega)\partial/\partial\delta]_{\delta=1}$, prime quantities are taken at $\theta=\hat{\theta}'$, Λ is the pitch angle variable, $B_0=B(\frac{1}{2}\pi)$, $\Lambda_b = B_0/B(\pi)$, $\bar{\Lambda} = \min(B_0/B,B')$, $L = (1-\Lambda B/B_0)^{1/2}$, $\hat{\chi} = \hat{\phi} + \hat{\Psi}$, and

$$I_T(\beta) = -\bar{\omega}_b\int_0^\infty dt \exp(-\delta t^2)\sum_{-\infty}^{+\infty} 2(\omega-p\bar{\omega}_b t)^{-1}\cos 2\pi p\beta \qquad (4)$$

Here, $\beta = (\tau-\tau')/\tau_b$, $\tau=\tau(\theta)$ is the parametric time along a particle orbit and $\tau_b = 2\pi/t\bar{\omega}_b(\Lambda)$ the bounce period. The response of circulating particles is

$$\hat{N}_c(\hat{\theta}) = A(\omega)\int_{-\pi}^{+\pi} d\theta' J' \sum_{-\infty}^{+\infty} \int_0^{\Lambda_b} d\Lambda \frac{BB'}{LL'B_0}\hat{\chi}(\theta+2\pi\ell)\frac{\partial I_c(\hat{\beta})}{\partial\delta} , \qquad (5)$$

where

$$I_c(\hat{\beta}) = -\bar{\omega}_t\int_{-\infty}^{+\infty} dt \exp(-\delta t^2)\sum_{-\infty}^{+\infty}\int_{-\frac{1}{2}}^{\frac{1}{2}} dS \frac{\exp[i2\pi(S+p)\hat{\beta}]}{\omega-(S+p)\bar{\omega}_t t} \qquad (6)$$

with $\hat{\beta} = \beta+m-\ell$, $\beta = (\tau-\tau')/\tau_t$, $\tau_t = 2\pi/t\bar{\omega}_t(\Lambda)$ being the transit time. In Eqs. (3)-(6) we dropped the index α and neglected the magnetic drift frequency. I_T and I_c can be evaluated by summing over the orbit periodicities. This brings them in a form suitable for both numerical and analytical calculations. Using $x = (S+p)t$ instead of S, and performing the x-integral by contour integration, I_c can be written as

$$I_c(\hat{\beta}) = 2\pi i\int_0^\infty dt\, t^{-1}\exp(-\delta t^2 + ia|\beta+m-\ell|t^{-1}), \quad a = 2\pi\omega/\bar{\omega}_t \qquad (7)$$

Using Fourier transforms, the sum over the resonant denominators in I_T can be converted into a sum over exponentials,

$$I_T(\beta) = 2\pi i\sum_{-\infty}^{+\infty}\int_0^\infty dt\, t^{-1}\exp(-\delta t^2 + ia|\beta+n|t^{-1}), a = 2\pi\omega/\bar{\omega}_b \qquad (8)$$

Small values of n correspond to large p in Eq.(4) and viceversa. At the boundary between trapped and circulating particles, i.e. at $\Lambda = \Lambda_b$, $a \to \infty$ and $\beta \to 0$, provided θ' and/or $\hat{\theta}' = \pm\pi$ are excluded. The quantity $a|\beta|$ remains finite and is continuous. An application of the saddle-point method shows that the terms with $m \neq \ell$ and $n \neq 0$, in Eqs.(7) and (8) respectively, as well as all terms in the series for $I_T(\beta+1/2)$, vanish exponentially with $a \to \infty$ even for real frequencies. We conclude that the trapped and circulating responses are continuous over the boundary layer and are given there by the $n = 0$ term in Eq.(8).

In the limit of infinite aspect ratios, i.e., $\varepsilon_0 \to 0$, $a \propto \varepsilon_0^{-\frac{1}{2}}$ but remains finite for trapped particles for all values of Λ. Consequently, the trapped particle response vanishes exponentially as $\varepsilon_0 \to 0$. By continuity, the circulating particle response vanishes at $\Lambda = \Lambda_b$. In this limit $a|\beta| = (\omega/\hat{\omega}_t)|\theta - \theta'|(1-\Lambda)^{-1}$ where $\hat{\omega}_t = \bar{\omega}_t(\Lambda=0)$. Since $I_c(\beta)$

depends only on $\delta^{\frac{1}{2}}a|\beta|$, $\partial/\partial\delta$ can be converted into $\partial/\partial\Lambda$. Then the integration over Λ in Eq.(6) can be performed and yields

$$\hat{N}(\hat{\theta}) = \frac{\omega}{2\pi^{3/2}\bar{\omega}_t}\left[1 - \frac{\omega_*}{\omega}\left(1 - \frac{3}{2}n\right) + n\frac{\omega_*}{\omega}\frac{\partial}{\partial\delta}\right]_{\delta=1}\frac{1}{\delta}\int_{-\infty}^{+\infty} d\hat{\theta}'\hat{\chi}(\hat{\theta}')I_S \qquad (9)$$

where $I_s = I_c(\Lambda=0)$. For small values of its argument, $z = (a|\beta|)_{\Lambda=0} = \omega/\hat{\omega}_t|\hat{\theta}-\hat{\theta}'|$ the kernel I_s can be expanded

$$(2\pi i)^{-1}I_s = -\frac{3}{2}\gamma + (1+\frac{1}{2}\delta z^2)[i\pi/2 - \ell n(\delta^{\frac{1}{2}} z)] - i\pi^{\frac{1}{2}}\delta^{\frac{1}{2}}z - \delta(1-\frac{3}{4}\gamma)z^2 \qquad (10)$$

This approximation is accurate for localized modes. The exact I_s calculated from Eq.(7) is plotted below and compared with approximation (10) (dotted curve) to fifth order in z.
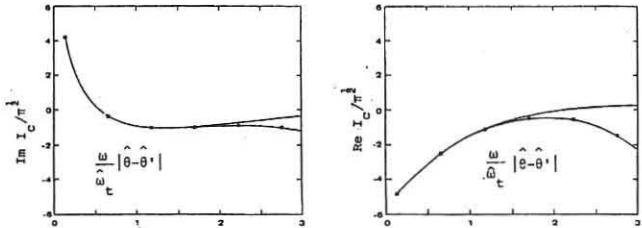
Next we turn to toroidal geometry and consider modes that are localized such that only the $m = \ell$ term has to be retained in Eq.(5) and have frequencies smaller than the mean bounce frequency of a deeply trapped particle. Then, $a|\beta|$ is small for all values of Λ and $\partial I_c/\partial\delta$ can be expanded

$$\partial I_c(\beta)/\partial\delta = f(a|\beta|) \approx -\frac{i\pi}{\delta} + \frac{\pi^{3/2}}{\delta^{1/2}}a|\beta| + \frac{i\pi a^2\beta^2}{2}[3-3\gamma+i\pi - 2\ell n(\delta^{\frac{1}{2}} a|\beta|)] \qquad (11)$$

The trapped particle response cannot be approximated either by the $p = 0$ term in Eq.(4) or by the $n = 0$ term in Eq.(8), as shown in the next figure where partial sums over p are plotted for circular cross sections with $\varepsilon_0 = 0.1$. In approximating $\partial I_T/\partial\delta$ we split the interval of integration in Eq.(8) into $(0,\pi^{\frac{1}{2}})$ and $(\pi^{\frac{1}{2}},\infty)$. In each of these intervals the sum of the integrals can be approximated and we obtain[3]

$$\frac{\partial I_T(\beta)}{\partial\delta} \approx f(a|\beta|) + \exp\left[\frac{ia\delta^{\frac{1}{2}}}{\pi^{\frac{1}{2}}}\right]\left\{\frac{\pi^{3/2}}{a\delta^{1/2}} - \left(\frac{a}{\delta^{\frac{1}{2}}\pi^{\frac{1}{2}}} - \frac{ia^2}{\pi}\right)\left(\pi^2\beta^2 + \frac{\pi^2}{6} - \frac{\pi}{2}\right) + \frac{ia^2}{6}\right.$$
$$\left. - \frac{ia^2}{2}\frac{1}{\pi}\sum_{p=0}^\infty \frac{\cos 2\pi p\beta}{p^3} - \frac{i\pi a^2\beta^2}{2}\{3-3\gamma+ i\pi - 2\ell n(\delta^{\frac{1}{2}}a|\beta|)\}\right\} \qquad (12)$$

$$\frac{\partial I_T(\beta+\frac{1}{2})}{\partial\delta} \approx \exp\left[\frac{ia\delta^{\frac{1}{2}}}{\pi^{\frac{1}{2}}}\right]\left[\frac{\pi^{3/2}}{a\delta^{3/2}} - \frac{i\pi}{\delta} - \frac{a\pi^{\frac{1}{2}}}{2\delta^{\frac{1}{2}}} + \frac{ia^2}{6} - \left(\frac{a}{\delta^{\frac{1}{2}}\pi^{\frac{1}{2}}} - \frac{ia^2}{\pi}\right)\left(\pi^2\beta^2 - \frac{\pi^2}{12}\right) - \right.$$
$$\left. \frac{ia^2}{2\pi}\sum_{p=1}^\infty \frac{\cos 2\pi p(\beta+\frac{1}{2})}{p^3}\right] \qquad (13)$$

In the last figure, $\partial I_T/\partial\delta$ from Eq.(12) is given as a function of Λ together with the exact expression from Eq.(8). The expressions (11), (12) and (13) represent the particle responses surprisingly well, even if $a = 2\pi/\bar{\omega}_b$ is not small for the chosen value $\omega/\bar{\omega}_b(\Lambda=1.1) = 0.2(1.8)^{\frac{1}{2}}$. The responses are continuous and have a sharp variation in an extremely small interval of Λ. This behaviour would be smoothed out if a small collisionality were included in the theory. The contribution of circulating particles is mainly imaginary, whereas that of trapped particles is mainly real. The integration over pitch angle leads to a logarithmic singularity[3] $\ell n||\theta|-|\theta'|$ in the kernel of the trapped particle response (3). Similarly to the plane slab case, this singularity is related to particles with vanishing parallel velocity, and, in toroidal geometry, is due to trapped particles near their turning points.
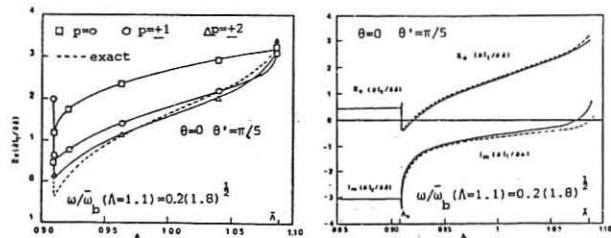
1 F.Pegoraro, and T.J.Schep, in Plasma Physics and Controlled Nuclear Fusion, Innsbruck 1978 (IAEA, Vienna, 1978), Vol.1, p.507
2 F. Pegoraro, T.J.Schep, Phys.Fluids 24, 470 (1981).
3 T.J.Schep, B.Braams, F.Pegoraro, Rijnhuizen Report RR81-132 (1981).

[*]Scuola Normale Superiore 56100 Pisa, Italy

CONVECTIVE RIPPLE TRANSPORT OF IONS AND ELECTRONS IN A TOKAMAK

A.V.Gurevich, Ya.S.Dimant, Yu.N.Dnestrovskij,
D.P.Kostomarov, A.P.Smirnov

Kurchatov Institute of Atomic Energy, USSR

Due to the rippled structure of the magnetic field in real tokamaks, the effective mechanism of particle transport arises. This transport is due to the drift of a special group of localized particles trapped in magnetic ripples [1]. Owing to the strong dependence on the energy, this transport through the Coulomb collisions leads to the distortion of the distribution functions of all the particles. The ripple transport may become important for energy and particle balances in tokamaks. In up-to-date tokamaks the electron ripple transport gets the global convective type for energies $W \gtrsim W_d$, where W_d [2] is ~ 10÷20 keV. The same quantity for ions is $(m_i/m_e)^{1/5} \approx 5$ times less than that for electrons. For tokamaks with today's temperatures, and especially with thermonuclear ones, this transport may play a very significant role. The theory of the convective ripple transport has been developed in papers [2-4]. Simplified kinetic equations for the distribution functions of passing, trapped and localized particles have been obtained there taking into account the drift of the latter across the magnetic surfaces. The most general and complete consideration of the problem has been made in [4].

In this paper we present the results of the numerical calculation of the distribution functions of ions and electrons which is based on the equations [2] where the radial electric field and the variation of the relative ripple depth δ along the drift trajectory are not taken into account. In future, the authors plan to generalize these results.

The results obtained here agree, in the main, with the experimental ones both for electrons [5] and for ions [6]. The parameters of the tokamak T-10 have been used. Note that the winding nature of the magnetic force line leads to an effective decrease in the depth and even to local disappearance of the magnetic ripple wells. In T-10 the ripple distribution is of such a type that the inner part of the torus is practically free of ripple wells. First, we consider the results for deuterium ions. Fig.1 shows the distribution functions of trapped particles in the symmetric case (a) and in the absence of the transport in the inner part (b) versus the energy for different values of an adiabatically-invariant variable $S=(1+\frac{\varrho}{R}\cos\theta)\sin^2\chi$ [2], where $\varrho \leqslant a$ is the minor radius of the given magnetic surface, R is the major radius of the torus, θ is the poloidal angle, and χ is the pitch-angle of the particle. The dashed line represents the initial Maxwellian distribution. Here the rise of the distribution function tail with energy W for $W \gtrsim 3$ keV may be seen. In Fig.2 the quantities $\frac{f(S,W)}{f_{max}(w)}$ are plotted for the cases corresponding to those in Fig.1(a), (b) for different energies. There is a marked asymmetry in the second case. Fig.3 shows the ratio between the localized particle distribution functions above and under the equatorial plane of the torus (drift is upward) against S

in the case (b). These distribution functions are averaged over the permitted range of the magnetic moments inside the ripple.

For electrons we must not neglect the longitudinal electric field since it leads to a strong distortion of the distribution function. The computation of the distribution function for the cases of electric field without the ripple transport has been made in Ref.[7]. The electric field leads to the increase in the distribution function tail, even in the trapped region. When there is a transport in the ripples, the distribution function tail rise looks like that transferred from the centre to the periphery (see Fig.4).

References

1. Kadomtsev B.B., Pogutse O.P., Nucl.Fusion 11 (1971) 67.
2. Gurevich A.V., Dimant Ya.S., Nucl.Fusion 18 (1978) 629; Gurevich A.V., Dimant Ya.S., Dnestrovskij Yu.N., Dokl. Akad.Nauk 244 (1979) 71.
3. Dnestrovskij Yu.N., Smirnov A.P., in "Matematicheskoe modelirovanie kineticheskikh i MGD-processov v plazme", Moscow State University, Moscow (1979) p.17.
4. Gurevich A.V., Dimant Ya.S., Nucl.Fusion 21 (1981) 159.
5. Gurevich A.V., Dimant Ya.S., Dnestrovskij Yu.N., Razumova K.A. Pis'ma Zh.Eksp.Teor.Fiz., 26 (1977) 733.
6. Petrov M.P. in Plasma Phys. and Contr. Nucl. Fus. Res. (Proc. 5th Int. Conf. Tokyo, 1974) vol.1, Vienna (1975) 43; Berezovskij E.L., Efremov S.L., Izvozchikov A.B., Petrov M.P., Petrov S.Ya., this conference.
7. Gurevich A.V., Dimant Ya.S., Dnestrovskij Yu.N., Smirnov A.P., Fiz. Plazmy 5 (1979) 777.

Fig.1a Fig.1b Fig.2a Fig.2b Fig.3 Fig.4

$n_0 = 2.5 \cdot 10^{13}$ cm^{-3}

$B = 1.5$ T

$T_{io} = 0.5$ keV, $T_{eo} = 1$ keV

B-14
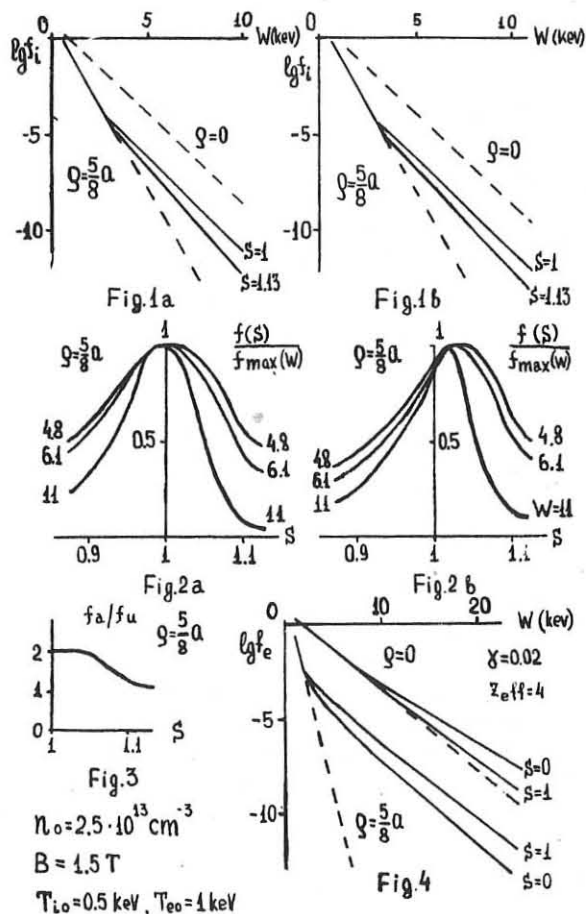
COMPUTATION OF PLASMA EQUILIBRIUM IN TOKAMAK WITH IRON CORE.

Yu.N.Dnestrovskij, S.V.Tsaun

I.V.Kurchatov Institute of Atomic Energy,

D.P.Kostomarov, A.M.Popov

Moscow State University

Moscow, USSR.

The numerical computations of the plasma equilibrium in tokamak with the iron core transformer for different discharge stages are described [1,2]. The equilibrium state is determined by the conductors position, its currents, β_J-value, and plasma current distribution. The currents in the toroidal conductors creating the poloidal fields are investigated for different moments of discharge in T-15 device. Let z, φ, Z be the cylindrical coordinates with Z-axis along the main axis of torus. S_p is the plasma cross-section region, S_μ is the iron volume cross-section by the median plane, Γ is the external and γ is the internal boundaries of S_μ. S_v is the vacuum region, I_p is the total plasma current, $I^{(n)}$ are the stationary currents.

The system of equations for equilibrium has the form:

$$\Delta_\mu^* \psi \equiv z \frac{\partial}{\partial z}\left(\frac{\frac{1}{z}\frac{\partial \psi_\mu}{\partial z}}{z \mu(B)}\right) + \frac{\partial}{\partial Z}\left(\frac{1}{\mu(B)} \frac{\partial \psi_\mu}{\partial Z}\right) = 0, \quad (S_\mu)$$

$$\Delta^* \psi = -\lambda \begin{cases} z^2 \frac{dP}{d\psi} + \frac{1}{2}\frac{dI^2}{d\psi} & , \psi > \psi_p \quad (S_p) \\ z \sum_n I^{(n)} \delta(z - z_n, Z - Z_n), \psi < \psi_p \quad (S_v) \end{cases}$$

$$\psi|_\Gamma = 0.$$

where ψ is the poloidal flux function, $\mu(B)$ is the iron magnetic permeability.

The equilibrium is numerically integrated by the "matching" method, which includes the following iteration process. Two first boundary problems inside the plasma-vacuum region and S_μ region with the boundary condition $\psi_\gamma^{(n)}$ are solved for every iteration step (m is the number of iteration). Function is determined from "finite conductivity" condition on γ vacuum-iron boundary:

$$\frac{\psi_\gamma^{(m+1)} - \psi_\gamma^{(m)}}{z_{m+1}} = \frac{1}{\mu(B^{(m)})}\frac{\partial \psi_\mu^{(m)}}{\partial n} - \frac{\partial \psi^{(m)}}{\partial n}.$$

Every problem is solved by finite difference methods. In T-15 device there are 62 current windings packed in 4 section pairs (Fig.1). The first section with a total current I_1 form the main dipole component of the vertical maintaining field. The second and the third ones, with the currents I_2, I_3, basically form quadrupole component of the poloidal field, which defines plasma cross-section form and decay index $\eta = -\frac{z}{B_z}\frac{\partial B_z}{\partial z}$, needed for the axisymmetrical stability. The fourth section with the current I_4 is an inductor. In quasi-static simulation of the discharge, we suppose the functions $I_p(t)$, $I^{(n)}$, $\beta_J(t)$, corresponding to experiment scenario. Fig.1 presents equilibrium level lines ψ = const in the initial part of the discharge, when the plasma current has not reached the flat top. In this stage, the inductor current and the plasma current have the same directions. In this case, $I_p = 0.56$; $I_1 = -0.148$; $I_{2,3} = -0.3$; $I_4 = 0.402$; $\beta_J = 0.12$. In this calculations

we suppose the quasi-parabolic plasma current distribution: $j_\varphi \sim \psi$. The iron transformer core is saturated $\mu \sim 3$. The external part of iron is unsaturated $\mu \sim 1400$ in this case. In Fig.2 the equilibrium level lines ψ =const are shown when $I_p = 1.4$; $I_1 = -0.8$; $I_2 = -0.3$; $I_3 = -0.3$; $I_4 = -0.342$; $\beta_J = 0.3$. This calculation corresponds to the moment when plasma current has the stationary value. The following figures present the different parameter dependences. In Fig.3 the magnetic axis position R of equilibrium plasma is shown depending on the currents I_1 when $I_2 = -0.05$ value is fixed (curve I), $I_2 = -0.2$ (curve II), and the currents I_2 when $I_1 = -0.675$ (curve III), $I_1 = -0.8$ (curve IV). The calculation corresponds to the discharge moment, presented in Fig.2. In Fig.4 the plasma ellipticity dependences in equilibrium are shown on current values in (I) section (curve I) and (II) section (curve II). The equilibrium corresponds to the steady state plasma current value presented in Fig.2. The calculations allow us to determine the time dependence of control currents needed for equilibrium for given tokamak discharge scenario.

References

1. R.Aymar, C.Leloup, M.Pariente – Report UER-CEA-FC-821, 1977.

2. E.N.Bondarchuk, N.I.Doynikov, B.S.Mingalev, Zh.tekh.Fiz., 47, p.521-526, 1977.
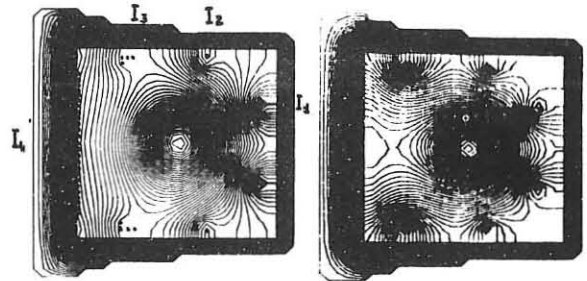
Fig.1   Fig.2
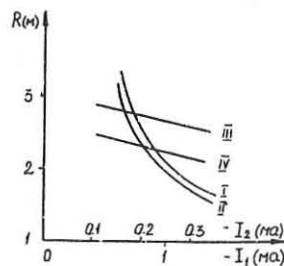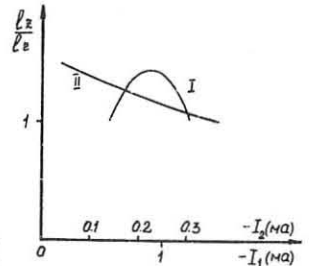
Fig.3   Fig.4

PARTICLE DIFFUSION AND ENERGY BALANCE SIMULATION IN A TOKAMAK

Yu.N.Dnestrovkij, S.E.Lysenko, S.V.Neudatchin, G.V.Pereverzev

I.V.Kurchatov Institute of Atomic Energy,
Moscow, USSR

D.P.Kostomarov

M.V.Lomonosov Moscow State University,
Moscow, USSR

·It is known that in tokamaks the particle confinement time is considerably shorter than that one could expect from the neoclassical theory /1/. This fact shows an anomalous character of the particle diffusion process. The experiments at ALCATOR /2/ show the anomalous pinch-effect also, though the experiments at other devices do not support this conclusion /3/. Until recently, there were no sufficient amount of experimental data for a reliable determination of the transport coefficients. The difficulty of the problem is in the fact that several processes are responsible for the formation of the particle density profile and the main source of particles is extremely skinned. The equation of particle balance has the form

$$\frac{\partial n}{\partial t} = \frac{1}{z}\frac{\partial}{\partial z}\left[z\left(D\frac{\partial n}{\partial z} - n v_P\right)\right] + P + P_{mix} \quad (1)$$

where n is the electron density, D is the diffusion coefficient, v_P is the pinch velocity, P is the influx of electrons due to ionization of neutrals and impurities, P_{mix} describes the effect of MHD-mixing.

It is too hard to determine the values of separate terms in (1) from the steady-state measurements. It can be done more precisely in some nonstationary processes such as pulsed gas puffing /4/ or MHD-mixing. For describing MHD-mixing in T-10 device we used the model /5/ with the transport coefficients given in /4,6/:

$$D = 4.10^{16}/n \quad (cm^2/s) , \quad v_P = v_P^{neo} \quad (2)$$

where v_P^{neo} is the neoclassical pinch velocity. Some radial profiles of particle fluxes $\Gamma_D = -D\frac{\partial n}{\partial z}$, $\Gamma_P = n v_P$ are given in Fig.1 ($n(o)=2.10^{13}cm^{-3}$). One can see that near the axis $|\Gamma_D| \ll |\Gamma_P|$ so the saw-tooth density oscillations are mainly determined by a drift flux Γ_P. The source P term is small near by the center. Comparison of the calculations made with the experiments shows that model (2) describes the regime under study fairly well.

Simulation of a discharge in T-11 based on the ideas presented with the heating of plasma by a fast neutral beam (0.6 MW) and with a simultaneous rise in density due to gas puffing /7/ was done. The behaviour of averaged plasma concentration in time and plasma density profiles are given in Fig.2 and 3. One can see that at a time t=45 ms the experimental and computed profiles are quite similar. An average density continues to rise in the experiment but it reaches saturation in the computations. This fact can be explained by an increasing role of the pinch-effect. It could be also that,in this regime, v_P is slightly larger than v_P^{neo}.

The preceeding results are related to the experiments with moderate electron concentration ($\bar{n} < 10^{14}cm^{-3}$). The situation is changed,if we use the greater values of density. The experiments with the pulsed gas puffing at a high density have been carried out at the FT device in the regime with parameters: $B_z=60$ kg, I=400 kA, a=20 cm. Some experimental dependences of an average density $\bar{n}$ (t) and the radial density profiles for the shots 3335, 3337, 3338 are given in Figs 4 a,b. Simulation of this process results in the necessity of increasing the modelling transport coefficients

in comparison with the values (2). The best results which are also given in Fig. 4 a,b have been obtained for a model

$$D = \frac{\chi_e}{5} , \quad v_P = v_P^{neo}\left(1 + \frac{\bar{n}}{n_o}\right) \quad (3)$$

where $n_o= 3.5 . 10^{13}cm^{-3}$. These formulae are applicable for the description of a deuterium plasma diffusion in the density range $2.10^{13} < \bar{n} < 2.10^{14}cm^{-3}$.

References

1. Mukhovatov V.S. In "Itogi nauki i tekhniki, Fisika plasmi", vol.1, part 1, page 6, M., 1980.
2. Antonsen T., Coppi B., Englade R., Nuclear Fusion, 19, N 5, 641-658, 1979.
3. Hughes M.H. Hugill J. in Plasma Phys. and Contr. Nuclear Fusion Res., 1, IAEA, Vienna, 457, 1979.
4. Berlizov A.B. et al., 8th Int.Conf.Plasma Phys. and Contr. Nucl.Fusion Res., Brussels, 1980, IAEA-CN-38/A-2.
5. Dnestrovkij Yu.N. et al., ibid, IAEA-CN-38/Y-1.
6. Hinton F.L., Hazeltine R.D., Rev.Mod.Phys., 48, N 2, part 1, p.239, 1976.
7. Mukhovatov V.S. 2.Joint Varenna-Grenoble Symposium on Heating in Toroidal Plasma, Como, Italy, 1980.
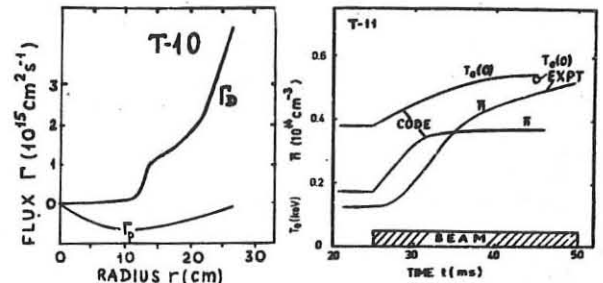
FIG. 1
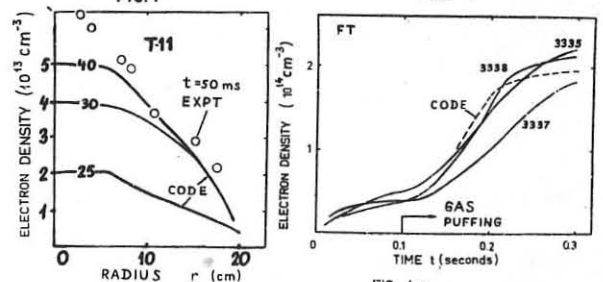
FIG. 2
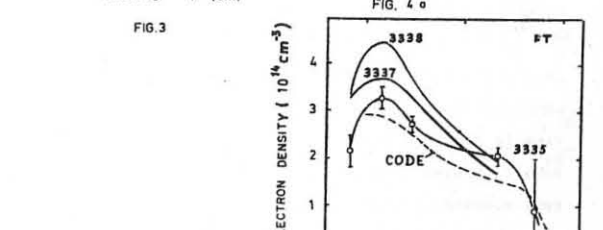
FIG. 3
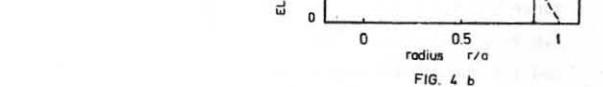
FIG. 4 a

FIG. 4 b

NUMERICAL SIMULATION OF THE PLASMA COLUMN BEHAVIOUR
AT THE EQUILIBRIUM CONTROL SYSTEM OPERATION IN
A TOKAMAK WITH A HIGH FIELD AND ADIABATIC
COMPRESSION

Yu.V.Gribov, V.A.Chuyanov

I.V.Kurchatov Institute of Atomic Energy,
Moscow, USSR

Yu.V.Mitrishkin, L.N.Fitsner

Institute of Control Sciences, Moscow, USSR

Abstract. A numerical model is proposed which allows
to check up the quality of the tokamak plasma equilibri-
um control system. The operation of the relay control sys-
tem in the tokamak with high field and adiabatic compres-
sion is considered. The possibility to simplify the mathe-
matical structure of the model describing the plasma column
behaviour is studied.

The paper aims at checking up the control system qua-
lity and optimizing the algorithm of the plasma equilibrium
control /1-2/ using the mathematical model of the object
allowing for the real tokamak winding and vacuum chamber
design. The vacuum chamber of the tokamak with high field
and adiabatic compression has no insulating meridional
joints and the varying poloidal magnetic field generate
in it toroidal currents. To calculate these currents the
chamber has been devided into 32 ring elements symmetric
in regard to the Z=0 plane. The currents in an inductor,
compression winding, control winding, chamber elements and
plasma column have been found by solving the set of equa-
tions of the following form:

$$I_i R_i + \frac{d}{dt}\left(\sum_{j=1}^{N} L_{ij} I_j\right) = E_i(t) \quad (1)$$

where I_i is the current in the i-th circuit, R_i and E_i
are the corresponding electric resistance and applied
E.M.F., respectively, $\|L_{ij}\|$ is the inductance ma-
trix, N is the number of circuits. Eq.(1) should be sup-
plemented with an equilibrium equation determining the
plasma column position. The equilibrium equation is
written in the limit of a circular, thin column /3/
and has been solved simultaneously with Eq.(1). When cal-
culating the mutual inductance for the plasma column and
the rest of the toroidal currents and also the vertical
magnetic field controlling the plasma column equilibrium,
the real plasma column dimensions and the poloidal mag-
netic field distribution on the plasma boundary have been
taken into account.

In the paper the results of simulation of the plasma
position control system operation before the major radius
compression are presented. Since a high-power output de-
vice is required for the device in question, a relay
control system is supposed to be used. The assumed con-
trol winding parameters were as follows: electric resis-
tance R ≈ 1.8×10^{-2} Ohm, inductance L = 4.9×10^{-4} H,
E.M.F. E_0 = ± 2.4 kV. The calculations have been perfor-
med for the 480 kA plasma current. In the relay system
operation studies the control signal of the output device
has been chosen in the form $Z = S + k\frac{dS}{dt}$, where
S is the plasma column displacement from equilibrium,
k is the numerical factor. From the point of view of the
reduction of the plasma column oscillation amplitude, the

optimal value of the K term appeared to be approximately
equal to the time of the current dipole component dam-
ping in the chamber.

The consideration performed has shown that the chosen
relay system allows the effective control of the plasma
column position at any expected slow variations of the
plasma parameters (with the characteristic times larger
than 10 ms) and at fast disruptive instabilities with
the β_J values varying less than by 0.5. In this
case the amplitude of the plasma column displacement was
less than 5% of the column major radius value.

In order to synthesize and analyse the optimal equi-
librium control system and to reduce the time spent on
the control numerical simulation the possibility has been
studied to simplify mathematical structure of the model
describing the plasma column behaviour. To realize this
the E.M.F. jumps have been applied to the control win-
ding as follows:

$$E = \begin{cases} +E_0, & 0 \le t \le t_0 \\ -E_0, & t > t_0 \end{cases} \quad \text{and} \quad E = \begin{cases} -E_0, & 0 \le t \le t_0 \\ +E_0, & t > t_0 \end{cases}$$

whish differed by the switch instant to. At t= 0
the chamber current was equal to zero. The calcula-
tions have shown that the resulting phase trajectories
in the (s, J) plane (S is the plasma column displace-
ment, J the control winding current) do not inter-
sect at the input signals of the same sign. The situa-
tion is adequate to the behaviour of the phase trajec-
tories of a set of two first-order linear differential
equations. So, to determine S and J one may substitute
20 nonlinear differetial equations of set (1) by a set
of two first-order linear differential equations, the coef-
ficients of which are matched according to the condition
of coincidence between its phase trajectories of model
of controlled object. Typical phase trajectories are
shown in Fig.1 (the asterisk labels trajectories obtain-
ed using a complete numerical model).

The coefficients in the approximating set of diffe-
rential equations depend on the β_J and l_i plas-
ma parameters and vary within the range 20 to 30%.

References

1. E.A.Azizov, Yu.A.Alekseev, N.N.Brevnov et al.,
   Paper V-3, VIIIth Intern.Conf.on Plasma Phys. and
   Contr. Nucl.Fus.Res., Brussels, 1980.

2. V.F.Demichev, V.A.Chuyanov, Preprint 3222, I.V.Kur-
   chatov Inst. of Atomic Energy, 1979.

3. В.Д.Шафранов, В сб. "Вопросы теории плазмы",
   под ред.М.А.Леонтовича, Госатомиздат, М.,
   1963, вып.2, с.92.
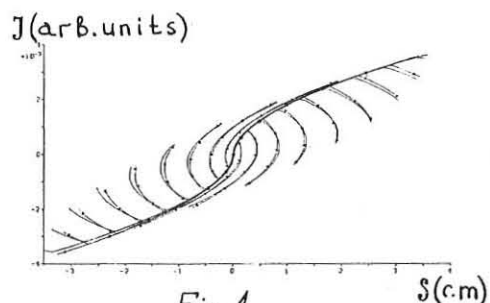
Fig.1

TRANSPORT CALCULATION IN A TOKAMAK WITH ADIABATIC COMPRESSION

O.P.Pogutse, N.V.Chudin, V.A.Chuyanov

I.V.Kurchatov Institute of Atomic Energy,
Moscow, USSR

Abstract. A one-dimensional model which is used for the transport simulation in a tokamak with adiabatic compression is described in this paper. This model allows to follow the evolution of a plasma discharge, including the breakdown, initial stage and the compression along the major and minor radii. The results of numerical calculations have shown an essential increase in the energy confinement time with compression along the minor radius.

The following set of equations is adopted for the transport calculation in a tokamak with adiabatic compression

$$\frac{dn}{dt} = (\gamma - \frac{\dot{R}}{R})n + \frac{1}{r}\frac{\partial}{\partial r}rD\frac{\partial n}{\partial r} + snn_a - R_\kappa n^2 \tag{1}$$

$$\frac{dn_a}{dt} = \frac{1}{r}\frac{\partial}{\partial r}rD_a\frac{\partial n_a}{\partial r} - snn_a + R_\kappa n^2 \tag{2}$$

$$\frac{3}{2}\frac{dP_e}{dt} = \frac{5}{2}(\gamma - \frac{\dot{R}}{R})P_e + \frac{1}{r}\frac{\partial}{\partial r}r[K_e\frac{\partial T_e}{\partial r} + \frac{3}{2}T_eD\frac{\partial n}{\partial r}] + \frac{j^2}{\sigma} - Q_{ie} - W \tag{3}$$

$$\frac{3}{2}\frac{dP_i}{dt} = \frac{5}{2}(\gamma - \frac{\dot{R}}{R})P_i + \frac{1}{r}\frac{\partial}{\partial r}r[K_i\frac{\partial T_i}{\partial r} + \frac{3}{2}T_iD\frac{\partial n}{\partial r}] + Q_{ie} - Q_{cx} +$$
$$+ \frac{3}{2}snn_aT_a - \frac{3}{2}R_\kappa n^2T_i \tag{4}$$

$$\frac{3}{2}\frac{dP_a}{dt} = \frac{1}{r}\frac{\partial}{\partial r}r[K_a\frac{\partial T_a}{\partial r} + \frac{3}{2}T_aD_a\frac{\partial n_a}{\partial r}] + Q_{cx} -$$
$$- \frac{3}{2}snn_aT_a + \frac{3}{2}R_\kappa n^2T_i \tag{5}$$

$$\frac{d\dot{\psi}}{dt} = (\gamma - \frac{\dot{R}}{R})\dot{\psi} + \frac{c^2}{4\pi}\frac{1}{r}\frac{\partial}{\partial r}r\frac{\partial}{\partial r}\frac{\dot{\psi}}{\sigma} \tag{6}$$

where $\frac{d}{dt} = \frac{\partial}{\partial t} + v_r\frac{\partial}{\partial r}$, $v_r = -\gamma\frac{r}{2}$, $\gamma = \frac{\partial \ln B_z}{\partial t}$, Q_{ie} describes the electron-ion energy exchange, Q_{cx} and W denote losses due to charge exchange, ionization and radiation. The other notations are generally accepted.

This set of equations is the generalization of one suggested in Ref./1/ and used for calculating the particle and energy balance in tokamaks /2/. The neoclassical coefficients are employed in the set of equations (1)-(6) for the ion thermal conductivity, and the anomalous coefficients corresponding to the Alcator scaling are used for diffusion and the electron thermal conductivity. It has been adopted that the transport coefficients can't be greater than the Bohm's values. The diffusion approximation is used for the neutral atoms. Boundary conditions are fixed for n, T_e, T_i and T_a. The neutral atom density is found from the condition of equality between the plasma flux and the neutral influx. The current density is determined from the external circuit equation

$$2\pi R\frac{\dot{\psi}}{\sigma} + \frac{1}{c}\frac{d}{dt}[\Psi_{ext} + \frac{LI}{c}] = 0 \tag{7}$$

The changes in the toroidal magnetic field and the major plasma radius with time are given to describe the compression. An effect of the system geometry is taken into account by a change in the minor radius of the chamber. The details of the model can be found in Ref./3/.

The calculations have been carried out for a plasma with the average density $\bar{n}=2.5 \times 10^{13}$cm^{-3}. During the initial stage the plasma current rises up to I≈400kA. After ohmic heating the toroidal magnetic field is increased from 2 T to 5 T within 10 ms. Then the plasma is compressed within 10 ms by the poloidal field along the major radius to R=42 cm.

The main results are represented in Figs.1-4, where the computed electron and ion temperature profiles and those of electron density are shown. The curve 1 illustrates the profiles before compression, the curves 2,3 - after the compression along the minor and major radii. The computed plasma parameters for the central region are in a good agreement with those which follow from the adiabatic compression law. A rise in the energy confinement time is a self-consistent effect of the profiles which cannot be taken into account in the zero-dimensional model /4/. Figure 4 shows an evolution of the energy confinement time with different compression velocities along the minor radius. Curves 1-3 correspond to the compression times τ_c =10,20,40 ms. The energy confinement time rise occurs due to plasma compression and a simultaneous expansion of the region in which the electron thermal conductivity is limited by Bohm's value. Therefore, a partial closing of the electron channel of losses (the main one) takes place.

References

1. Б.Б.Кадомцев, О.П.Погуце, В сб."Вопросы теории плазмы", Вып.5, М., Атомиздат, 1967, с.209.

2. Ю.Н.Днестровский, Д.П.Костомаров, В кн."Вычислительные методы в физике плазмы", М., "Мир", 1974, с.483.

3. В.В.Вихрев, О.П.Погуце, Н.В.Чудин, Э.И.Юрченко, Препринт ИАЭ-3321/8, М., 1980.

4. В.Л.Демичев, В.А.Чуянов. Препринт ИАЭ-3???, М., 1979.
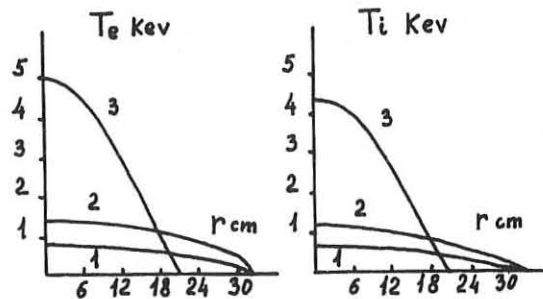
Fig.1

Fig.2
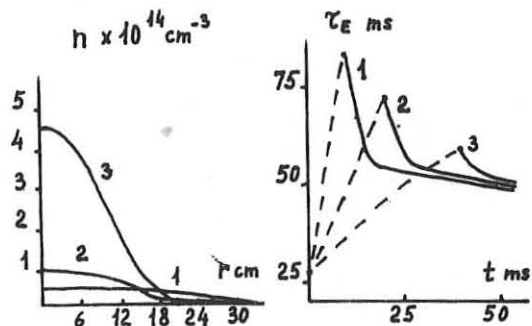
Fig.3

Fig.4

THE USE OF NEUTRON YIELD MEASUREMENTS TO STUDY THE SLOWING DOWN
OF MeV RANGE CHARGED PARTICLES IN JET

P.R. Thomas and W. Core

JET Joint Undertaking
Abingdon, Oxfordshire OX14 3 DB
United Kingdom.

In order that a d-t plasma should ignite, it is necessary that the 3.5 MeV α-particles produced in the fusion reaction deposit their kinetic energy in the plasma. When the slowing down is classical the power deposition is by coulomb collisions. The plasma is then heated by the fusion reactions, and ignition can occur when the energy confinement time is large enough. On the other hand, if the α-particle energy is converted into plasma waves and lost or the α-particles are created in loss orbits then there may be insufficient fusion power to balance the plasma losses. It is known from experiments with neutral beam injection that the slowing down of particles in the tens of keV energy range is classical, and that the power deposition is that expected [1].

The 1 MeV tritons produced in the reaction d(d,p)t have a poloidal Larmor radius which is 93% of that of d-t α-particles so that their orbits in the tokamak magnetic field are very similar. Tritons produced by thermal d-d reactions have a birth profile that is little different from that of d-t α-particles so that their trapping should be identical. Furthermore, their slowing down has a built in "stopwatch" since the tritons are produced at the same rate as the 2.5 MeV neutrons from d(d,n)^{3}He and their passage through 240 keV is marked by the peak in the t(d,n)^{4}He cross-section. It is proposed that the 2.5 and 14 MeV neutron rates from deuterium plasmas should be measured, in order to study the trapping and slowing down of these tritons.

The slowing down of 1 MeV tritons in plasmas with temperatures in the keV range is almost entirely due to the interaction with the electrons. Effects such as pitch-angle scattering and energy diffusion can be neglected so that the Fokker-Planck equation can be solved analytically. By folding the triton distribution function with the t(d,^{4}He) n cross-section, an expression for the ratio of 14 MeV to 2.5 MeV neutron production can be obtained.

$$R = \frac{K}{V_{te}} \frac{nd}{} \sqrt{\frac{2}{m_t}} \int_0^{1 \, MeV} \frac{dE \, E \, \sigma_{td}(E)}{(E^{\frac{1}{2}} + E_{cr}^{\frac{3}{2}})} \quad [1]$$

Here K is the trapping fraction multiplied by the branching ratio for the d-d fusion reactions, V_{te} is the collision frequency between tritons and electrons, n_d is the deuteron density and E_{cr} the critical energy. The dependence of R on density disappears because V_{te} is proportional to the electron density. R is plotted as a function of electron temperature in figure 1. At low temperatures it increases as $T_e^{\frac{3}{2}}$ because of the behaviour of the collision frequency. Measurement of the ratio of 14 MeV to 2.5 MeV neutron yields, will test the model for trapping and slowing down. This has already been done on PLT [2] where the measured ratio was consistent with equation 1. However, the plasma current in PLT is too low to trap all the 1 MeV tritons so that the measurement there was most sensitive to the trapped fraction. In contrast, JET will run with plasma currents of up to 5MA so that the 1 MeV tritons will nearly all be trapped. Therefore the same measurement on JET will be most sensitive to the slowing down time of the tritons. The drawback with this method is that the absolute measurement of the relative yields of different neutron groups from fusion devices is difficult because it is necessary to use separate detectors for each neutron energy.

The probability that a slowing down particle will undergo a fusion is proportional to σ (v)v. The σv's for the production of 2.5 MeV neutrons by 160 keV deuterons and 14 MeV neutrons by 1 MeV tritons is shown in figure 2 as a function of time. Time has been scaled by the time (t_s) it takes the triton to come to rest. t_s is tabulated in figure 2. It can be seen that there is a time delay of order the slowing down time between the peak production of 2.5 and 14 MeV neutrons. This time delay will be visible during rapid changes in the plasma reactivity. An example of the expected behaviour is shown in figure 3. Initially, 10 MW of 160 keV deuterons are injected into a JET plasma with a mean density of $3 \times 10^{19} m^{-3}$. The energy confinement time is assumed to be given by:

$$\tau_E = 5 \times 10^{-21} \, \bar{n} \, \bar{a}^2 \quad [2]$$

The injected power is stepped up by 20% for 1 second starting at t = 2 seconds. The effect of the time delay between 14 MeV and 2.5 MeV neutron production can clearly be seen. A similar effect will be observed with hydrogen injection or any other form of additional heating. Deuterium injection has the advantages though, that the count rate is high and the change in 2.5 MeV neutron production is very rapid. The advantage of the method is that the slowing down time is measured directly. The absolute measurements can be used to check that the d-d fusion rate is as expected, and that the triton trapping fraction is one. The processes of thermonuclear production, trapping and slowing down of MeV range charged particles with similar properties to d-t α-particles can therefore be measured in a single experiment.

It will be possible to perform this experiment with the additional heating and neutron diagnostics that will be installed on JET. 160 keV deuterium neutral injection will allow experiments of the kind illustrated in figure 3 to be performed. In addition, up to 15MW of ICRF will permit copious thermal production of tritons at elevated temperatures, so that birth profiles typical of d-t plasmas can be studied. The major difference between the populations of 1 MeV tritons and 3.5 MeV α-produced instabilities and the α contribution to β will have to await the use of d-t mixtures in JET. However, the basic processes will have been tested in the experiment proposed here In particular, the estimation of the triton slowing down time will be made using a method that does not depend on absolute measurements of neutron yields.

References

[1] Eubank et al: Proceedings of the Innsbruck Conference on Plasma Physics and Controlled Fusion Research (IAEA Vienna 1979), Paper IAEA-CN37-C-3, and references 1 to 5 cited therein.

[2] P. Colestock, J.D. Strachan, M. Ulrickson and R. Chrier; Physical Review Letters 43 (1979), p. 768.

Figure Captions
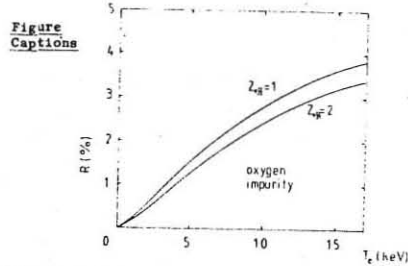
Figure 1) The ratio of 14 and 2.5 MeV neutron production in a deuterium plasma vs. electron temperature.
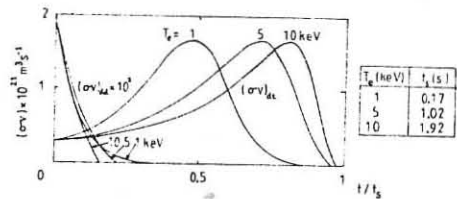
Figure 2) σV plotted against time for fusion reactions of 1 MeV tritons and 160 keV deuterons in a deuterium plasma at different electron temperatures.
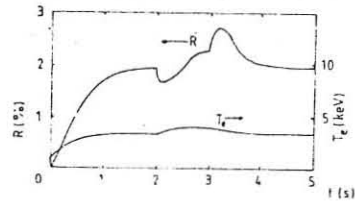
Figure 3) The ratio of 14 and 2.5 MeV neutron production as a function of time for 10 MW of 160 keV deuterons incident on a deuterium plasma. The injected power is increased by 20% between 2 and 3 seconds. Also shown is the electron temperature.

LOCAL MEASUREMETS OF ELECTRON DISTRIBUTION FUNCTION AND CURRENT IN TOKAMAK DEVISE.

CHULKOV G.N., SKOVORODA A.A.

I.V.Kurchatov Institute of Atomic Energy, Moscow, USSR.

The spatial distribution of the electron temperature T_e and the current is the impotant characteristic of the tokamak plasma. There is a possibility of the local measurement of these parameters by the determination of the microwave beam absorption profile near the maximum of the electron cyclotron frequency. The scheme of such measurements and the coordinate system used in the calculations are shown on Fig.1. The absorption of electromagnetic wave when $\omega \approx n\omega_{eo}$ is determined by the resonance region near the magnetic field maximum along the beam direction. The dimensions of this region are:

along the axis $OZ \sim \frac{a}{\sin\theta}$, $OY \sim a$, $OX \sim \frac{a}{\cos\theta}$. Because of the small dimension of this region it is possible to use the local magnetudes of plasma parameters(dencity, temperature et.a) and to approximate the magnetic field dependence on coordinates by means of following expression $B(y,z) = B_0\left(1 - \frac{y}{R} - \frac{z^2}{2R^2}\right)$. In this page for calculation of absorption coefficient we used the method of successive approximation[1]. The spatial dependence of the wave electric field amplitude is the following $\tilde{E} \sim E \exp\left[-\frac{y^2}{2a^2} - \frac{(x\cos\theta + z\sin\theta)^2}{2a^2}\right]$ where a -the beam width. The absorption coefficient η is determined by the expressionà

$$\eta = \frac{1}{2P} \int_{-\infty}^{\infty} dz \int_{-\infty}^{\infty} dy \int_{-\infty}^{\infty} dx \exp\left(-\frac{y^2}{a^2} - \frac{x^2\cos^2\theta}{a^2}\right) Re(\vec{E}^* \vec{j}) \quad (1)$$

where $\vec{j}$ current density exited by the wave, * complex conjugation, Re-real part, P -the stream of electromagnetic energy. Using the method described in[1] we obtain η on n-harmonic for maxvellian distribution:

$$\eta_n = \frac{\omega_p^2(\alpha_z)^2}{2\sqrt{2}\,a\,cN G}\left(\frac{m}{2\pi T}\right)^{1/2}\int_{-\infty}^{\infty} dv_{\parallel} e^{-\frac{mv_{\parallel}^2}{2T}}\left[nA^2 I_{n-1}(\eta) + \frac{2k_z}{\omega_e}v_{\parallel}A I_{n-1}(\eta)+\right.$$
$$\left.+2v_{\parallel}^2 I_n(\eta)\right]\int dz \int dy \exp\left(-\frac{y^2}{a^2}\right)\int d\tilde{v} \exp\left[i\,\Phi(z,y,v_{\parallel},\tilde{v})\right] \quad (2)$$

where $G = (1+\alpha_x)^2\cos\theta - \alpha_x\alpha_z\sin\theta$, $\Phi(z,y,v_{\parallel},\tilde{v}) = (\omega - n\omega_e(\ell_1)\times$ $\times\left(1 - \frac{v_{\parallel}^2}{2c^2} + i\nu\right)\tilde{v} - k_z(z_1 - z)$; $z_1 = z\cos\left(\frac{v_{\parallel}\tilde{v}}{\ell_1}\right) + (R+y)\sin\left(\frac{v_{\parallel}\tilde{v}}{\ell_1}\right)$; $\ell_1 = \sqrt{z^2 + (R+y)^2}$; $A = \frac{\alpha_x - 1}{\alpha_z}$; $\eta = \frac{\mu}{1 - i\frac{v_{\parallel}^2 n\omega_{eo}}{2c^2}\tilde{v}}$; $\mu = \frac{k_z^2 \rho_e^2}{2}$;

$\rho_e = \frac{v_T}{\omega_e}$, $v_T = \sqrt{\frac{2T}{m}}$;

$\alpha_{x,z} = \frac{E_{x,z}}{E_y}$ the components of the polarization vector(see, for example[2]; ν-collision frequency; $v_{\parallel}$ - the projection of electron velocity on magnetic field direction. Using the expression (2) it is possible to analyse the influence of Doppler effect, magnetic field line curvature, relativistic effect and beam width on the absorption. The expression similar to (2) was analised in detail in[1]. For the tokamak plasma diagnostic aim we can simplify(2) considerably. The absorption coefficient η at the tokamak conditions and $\theta < \frac{\pi}{2}$ ($k_z v_T \gg \left(\frac{v_T}{c}\right)^2 v$); $k_z^{5/3}\rho_e R^{2/3} \gg 1$) is determined mainly by the Doppler effect. In this case the expression (2) has the following form

$$\eta_n(\Delta\Omega_n) = \frac{\pi\omega_p^2 R(\alpha_z)^2 2^{1/4} e^{-\frac{W^2}{4}}}{2\omega_{eo} NCG(\alpha_z^2 + \frac{a^2}{R^2})^{1/4}}\left\{I_{n-1}(\mu)\left[A^2 U(0,-w)+\right.\right. \quad (3)$$
$$+ \frac{2^{1/2}\alpha_z\alpha_{\perp}A}{(\alpha_z^2 + \frac{a^2}{R^2})^{1/2}} U(-1,-w) + \frac{\alpha_z^2\alpha_{\perp}^2}{2(\alpha_z^2 + \frac{a^2}{R^2})} U(-2,-w)\right] + \frac{2}{n}I_n(\mu) U(0,-w)\right\}$$

where $\alpha_{z,\perp} = \frac{k_{z,\perp}\rho_e}{\eta}$; $W = \frac{2^{1/2}\Delta\Omega_n}{(\alpha_z^2 + \frac{a^2}{R^2})^{1/2}}$; $U(\ell,-w)$-parabolic cylinder function[3], $\Delta\Omega_n = \frac{n\omega_{eo}-\omega}{n\omega_{eo}}$. Using inequality $|A| \gg \alpha_{\perp}$, which is just for extraordinary wave(the absorption coefficient for this wave is much more then η for the ordinary wave),

we obtain:

if $W < -1$
$$\eta_n(\Delta\Omega_n) \simeq \frac{\tilde{\eta}_n(\Delta\Omega_n)}{2\sqrt{2}}\exp\left[-\frac{(\Delta\Omega_n)^2}{\alpha_z^2 + \frac{a^2}{R^2}}\right]\left[A + \frac{|\Delta\Omega_n|}{(1 + \frac{a^2}{\alpha_z^2 R^2})}tg\theta\right]^2 \quad (4)$$

if $W \approx 0$
$$\eta_n(\Delta\Omega_n) \simeq \tilde{\eta}_n\left((\alpha_z^2 + \frac{a^2}{R^2})^{1/2}\right)A^2\sqrt{\frac{\pi}{2}}\frac{1}{\Gamma(\frac{3}{4})}\left[1 - \frac{2\Gamma(\frac{3}{4})\Delta\Omega_n}{\Gamma(\frac{1}{4})(\alpha_z^2 + \frac{a^2}{R^2})^{1/2}}\right] \quad (5)$$

if $W > 1$
$$\eta_n(\Delta\Omega_n) \simeq \tilde{\eta}_n(\Delta\Omega_n)A^2 \quad (6)$$

$$\tilde{\eta}_n(\varepsilon) = \frac{\pi}{2\sqrt{2}}\frac{\omega_p^2 R(\alpha_z)^2}{\omega_{eo} NC\varepsilon^{1/2}G}; \qquad \Gamma \text{ -gamma function.}$$

The dependence of the absorption coefficient $\eta = \eta(\Delta\Omega_n)$ is showen on Fig.2. The maximum value of absorption coefficient is equal $\eta_{n,max} = 1,2\,\tilde{\eta}_n\left((\alpha_z^2 + \frac{a^2}{R^2})^{1/2}\right)A^2$ when $W \approx \frac{\pi}{4}$.

If $\alpha_z > \frac{a}{R}$ the measurements of the absorption line profile give us the opportunity to receive the local magnitude of electron temperature and longitidinal energy distribution function from (4). When plasma has a systematic velocity V_z (becose of the current, for example) it is necessary to replace in the expression (2) $\Delta\Omega_n$ on $\Delta\Omega_n + \frac{k_z V_z}{n\omega_{eo}}$. One can determine V_z by carring out the simultaneous measurements of absorption coefficients in two opposite directions K_z and $-K_z$. For this purpose it is necessary to use the "tail" and the maximum of absorption line (a).

It should be noted that the runaway electrons can be investigated by the same method. In the experiment the harmonic number and the angle θ depends on the necessary locality, magnetic field and plasma density. Using the linearly polarizate waves, which contain both extraordinary and ordinary components, it is necessary to take in to account that the absorption of ordinary wave is much smaller. It should be noted that the reflection from resonant region is small in comparison with the absorption.
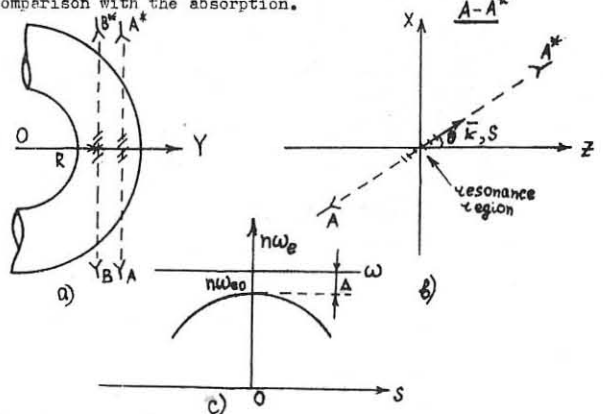
Fig.1 a,b -scheme of measurements and coordinate system, A, A*, B, B* -microwave horns, O-axis of tokamak
c -chage of n-harmonic of electron cyclotron frequency ω_e along the microwave(frequency ω) beam, $\Delta\Omega_n = \frac{\Delta}{n\omega_{eo}}$.
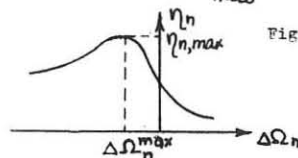
Fig.2 Dependence of absorption coefficient η_n on $\Delta\Omega_n$.

REFERENCES
1. Skovoroda A.A.Chulkov G.N.Preprint IAE-3335,1980(be publ.Nuc.F.)
2. Electrodinamika plasmi, Ahieser A.I.Nauka,1974.
3. Spravochnik po spetzialnim funkzijam, M. Abramovitz M. Nauka, 1979.

HEAT CONDUCTIVITY OF TRAPPED IONS IN
A TOKAMAK

P.H.Yushmanov

I.V.Kurchatov Institute of Atomic Energy,
Moscow, USSR

The thermal conductivity of ions trapped in a space among the longitudinal field coils is inversely proportional to the Coulomb collisions $\chi_i \sim \delta^{3/2} v_d^2 / v_i$, where $v_d \sim v_T^2 / \omega_\theta R$ is the toroidal drift velocity, δ is the ripple depth /1,2/. Such dependence remains until the distance, at which the trapped ion drifts for the effective confinement time in a local trap $\tau_{eff} \sim \delta / v_i$, does not exceed the characteristic size of the system non-uniformity. Evaluating the non-uniformity size as a (minor radius of the torus), Stringer has come to the conclusion that the thermal conductivity type $\chi_i \sim v_i^{-1}$ is true down to the considerably lower v_i than those obtained in fusion facilities /1/.

In many tokamaks the minimal non-uniformity size for the trapped particles is not a but Z_0 - width of a zone in which the local magnetic traps do exist.

The local traps are produced only in the range (see Fig.1)

$$|Z| < Z_0 = \delta(R, Z_0) N q R, \qquad (1)$$

where N is the number of the longitudinal field coils, q is the safety factor, R is the major radius of the torus. Substituting, for example, the parameters of INTOR R=5,2 m, q=1, N=12, δ=0,3% one will obtain $Z_0 \approx 20$ cm $\ll a$. Therefore, the condition for applicating the thermal conductivity type $\chi_i \sim v_i^{-1}$ is considered to be $v_d \tau_{eff} \ll Z_0$ or

$$v_i \gg v^0 = v_T^2 / \omega_\theta R^2 q N. \qquad (2)$$
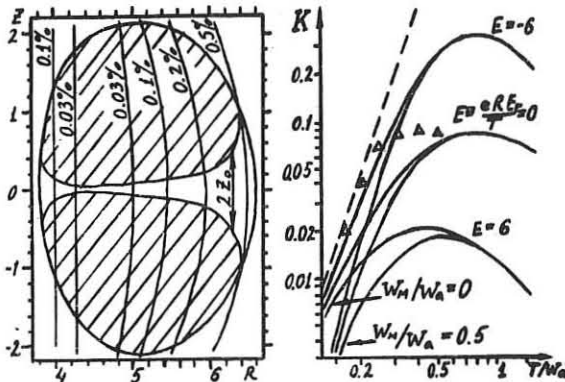
In the opposite limit case of very low collision frequency $v_i \ll v^0$, the trapped ions drift along the vertical without collisions. They do not leave the vessel, but having passed the distance $\sim Z_0$, they enter the region without any magnetic traps. Returning along the line of force, they move along the closed trajectories shifted at $\Delta r \sim Z_0^2 / r$ from the magnetic surface. Taking into account weak collisions, one evaluates the thermal conductivity $\chi_i \sim f \wedge r^2 / \tau_{eff} \sim v_i Z_0^5 / r^3 \delta^{1/2}$, where $f \sim \delta^{1/2} Z_0 / r$ is the fraction of locally trapped particles /3/.

In the range of low collision frequencies, a radial electric field E_1 impacts on the heat transfer in difference from the case $v_i \gg v^0$. Due to electric drift the trajectories of trapped particles are not vertical lines but arcs of a circle. Therefore, the displacement of particles becomes less: $\Delta r \sim (Z_0^2 / r) v_d / (v_E + v_d)$, where $v_E = E_r / B$ is the electric drift velocity. The thermal conductivity decreases correspondingly by a factor $v_d^2 / (v_d + v_E)^2 \sim R^2 / a^2$ /3/.

To find the thermal conductivity for arbitrary collision frequency, a kinetic equation for locally trapped ions have been solved for a magnetic field model with parabolic wells

$$B = B_0 [1 - 2 \delta \theta (1 - Z^2 / Z_0^2 - N^2 \varphi^2 / 4)], \qquad (3)$$

where $\theta(x) = 0$ if $x < 0$, $\theta(x) = 1$ if $x > 0$, φ - toroidal angle. The thermal conductivity obtained can be represented as (it is assumed that $r \gg Z_0$)

$$\chi_i = 0.034 \frac{Z_0^4 \delta^{1/2} n W_a}{r^3 m R \omega_\theta} \cdot K \left(\frac{T_i}{W_a}, \frac{e R E_r}{T_i}, \frac{W_M}{W_a} \right), \qquad (4)$$

where $W_a = (T^{3/2} v_i(T) m \omega_\theta R^2 N q \delta(R, Z_0) / 2 \delta)^{2/5}$ is the energy of particles for which $v_d \tau_{eff} = Z_0$ or $v_i = v^0$, $\delta = \delta(R, 0)$, W_M is the minimal energy of the locally trapped ions determined from the condition $v_i(W_M) = \delta^{3/2} v(W_M) N / R$. Dependence of K on T_i / W_a at different values of the parameters $e R E_r / T_i$ and W_M / W_a are given in Fig.2.

At $W_M \ll T \ll W_a$ the heat conduction of trapped ions (4) can be presented in the more simple way

$$\chi_i \approx \frac{\delta^{3/2}}{v_i} \cdot \frac{Z_0^3}{r^3} \cdot \left(\frac{T_i}{m \omega_\theta R} \right)^2. \qquad (5)$$

Function $K(T/W_a) \sim (T/W_a)^{7/2}$ corresponding to this thermal conductivity is shown in Fig.2 by a dashed line. The formula (5) coinsides with the result obtained by Counor /2/ within the accuracy range determined by a factor ~ 1.1.

The results of numerical calculations of heat conduction /4/, where transition from the dependence $\chi_i \sim v_i^{-1}$ to $\chi_i \sim v_i$ has also been obtained, are designated in Fig.2 as Δ. One can see the ratio of heat conductions obtained from a numerical calculations /4/ and from the formula (4) with $E_r = 0$ - what was likely to be used in simulation /4/ - does not exceed 2.

Determine the value W_a. Assuming approximately $\delta(R, Z_0) \approx \delta$, one has $W_a \approx (2 \cdot 10^{-7} n B R^2 N q)^{2/5}$, where n, B, R are measured in cm^{-3}, T, m respectively. Using the parameters of the INTOR $n = 2.10^{14}$cm^{-3}, $B = 5.5$ T, R=5.2 m, N=12, q=1 one obtains $W_a \approx 22$ keV. So, the operating range of temperatures for the INTOR is $T \sim 0.3 - 0.6 W_a$. In this range, the dependence of χ_i on T_i is found to be sufficiently weak as $T^{0.5 \div 2}$ for different radial electric fields. Therefore, it is unlikely to expect an effective plasma temperature control due to the dependence $\chi_i(T_i)$. On the contrary, the heat conduction dependence (4) on a ripple value δ is very strong. As W_a does not depend on δ and $Z_0 \sim \delta$, the heat conduction (4) is proportional to $\delta^{9/2}$.

References

1. T.E.Stringer. Nuclear Fusion, 12, 689 (1972).
2. J.W.Connor, R.J.Hastie. Nuclear Fusion, 13, 22 (1973).
3. P.N.Yushmanov. Pis'ma Zh.Ehksp.Teor.Fiz. 33, 97 (1981).
4. K.Tani, H.Kishimoto, S.Tamura. 8th Int.Conf. on Plasma Phys. and Cont. Nucl. Fus. Res. Brussel 1-10 July 1980, IAEA-CN-38/W-2-2.

ANOMALOUS ELECTRON VISCOSITY AND BALLOONING MODES

O.P.Pogutse, E.I.Yurchenko

I.V.Kurchatov Institute of Atomic Energy,
Moscow, USSR

A linear ideal ballooning mode theory has been recently developed /1-3/. In tokamaks these modes must be driven at pressure gradients exceeding the critical value of $\alpha > \alpha_c$ /3,4/ ($\alpha = -8\pi P' R q^2 / B_o^2$, R is the torus major radius, q the safety factor, B_o the toroidal field) and develop at a growth rate of the order of an inverse Alfven time $\gamma_o \sim 1/\tau_\theta$ ($\tau_\theta = a/C_\theta$, $C_\theta = B_J/\sqrt{4\pi\rho}$, B_J is the current field). In modern tokamaks with an auxiliary heating the pressure gradient is of the order of α_c due to the neutral injection, but one cannot be sure that the ideal threshold is surpassed.

Since the linear ideal ballooning mode theory is sufficiently well developed, the research is now concentrating on the problems connected with the presence of dissipation /5,6/. In the resistive model the pressure gradient threshold is shown to vanish and the instability must develop at a growth rate $\gamma_\sigma \sim 1/\tau_S (\tau_S/\tau_\theta)^{2/3} \ll \gamma_o$ ($\tau_S = 4\pi\sigma a^2/c^2$). Though this growth rate is much higher than the reverse skin time τ_S since $\tau_S/\tau_\theta \gg 1$, the estimates for transport coefficients associated with these modes show that $\mathcal{D} \sim \gamma/K_\perp^2 \sim a^2/\tau_S$, i.e. of the order of pseudoclassical. Such coefficients are known to be lower than experimental ones.

In the paper we attract attention to the fact that the inclusion of anomality associated with an electron channel, can enhance essentially the transport coefficients compared with pseudoclassical ones. The enhanced electron heat transport is a well-known feature of an electron anomality.

This effect can be related to an anomalous viscosity in an electron fluid. In order to explain experimentally the observed Alcator scaling $\tau_E \sim na^2$, one should introduce into an electron component the transverse viscosity term of the order $\mu \Delta \vec{V}_e = -\frac{\mu}{en}\Delta \vec{J}$ where $\mu \sim mna^2/\tau_E$. Then the Ohm law will read:

$$\vec{J}/\sigma = \vec{E} + \frac{1}{c}[\vec{V}\vec{B}] + \frac{\mu}{e^2 n^2}\Delta\vec{J} \qquad (1)$$

Using the procedure of Ref./6/ one can obtain a differential equation valid for higher-number ballooning modes ($m \simeq nq \gg 1$) in a tokamak with circular flux surfaces:

$$\frac{d}{dy}\frac{(1+S^2y^2)}{(1+\mu)}\frac{d\varphi}{dy} + \left\{\left(\frac{\alpha^2}{2} + \frac{S\alpha^2}{1+S^2y^2}\right)\frac{(1+\mu+1/\gamma^2\tilde{\tau}_c^2)}{(1+1/\gamma^2\tilde{\tau}_c^2)} - \right. $$
$$\left. - \alpha U - \gamma^2\tilde{\tau}_\theta^2(1+S^2y^2)\right\}\varphi = 0 \qquad (2)$$

Here $\mu = n^2q^2(1+S^2y^2)/\gamma\tilde{\tau}_S + S^2n^4q^4(1+S^2y^2)^2/a^2\gamma\tilde{\tau}_{P\mu}$, $S = q'z/q$ is the shear, $\delta = c/\omega_p$ is the collisionless skin-layer thickness ($\omega_p^2 = 4\pi n e^2/m$), $\tilde{\tau}_c = Rq/C_S$, $C_S^2 = \gamma_o P/\rho$ is the sound velocity, $\tilde{\tau}_{P\mu} = mna^2/\mu$ is the viscosity electron time; $U = \alpha/2 + z/R(1-q^{-2})$ is the magnetic well.

Below we confine ourselves to the most interesting case when the viscosity dominates $\tilde{\tau}_{P\mu} \ll \delta^2 n^2 q^2 \tilde{\tau}_S/a^2$ and perturbations are potential, and so the pressure gradient $\alpha < \alpha_c$ and ideal ballooning modes do not develop. In this case the plasma pressure is also sufficiently low and acoustic oscillations have no enough time for smoothing of ballooning perturbations along the field lines $\gamma\tilde{\tau}_c \gg 1$. In this case Eq.(2) reduces to a simpler one:

$$\frac{d}{dy}\left[\frac{a^2}{\delta^2}\frac{\gamma\tilde{\tau}_{P\mu}}{n^4q^4}\frac{1}{(1+S^2y^2)}\right]\frac{d\varphi}{dy} - \left\{\alpha U + \gamma^2\tilde{\tau}_\theta^2(1+S^2y^2) - \right.$$
$$\left. - \left(\frac{\alpha^2}{2} + \frac{S\alpha^2}{1+S^2y^2}\right)\frac{\delta^2}{a^2}\frac{n^4q^4}{\gamma\tilde{\tau}_{P\mu}}(1+S^2y^2)^2\right\}\varphi = 0 \qquad (3)$$

The analysis of this equation shows that the ballooning mode growth rate is weakly dependent on the anomalous electron viscosity value and increases with the mode number:

$$\gamma_\mu \sim \frac{\alpha^{3/5}S^{4/5}}{\tau_{P\mu}^{1/5}\tau_\theta^{4/5}}\left(\frac{\delta}{a}\right)^{2/5}(nq)^{4/5} \qquad (4)$$

The localisation region of these modes in the Fourier-space decreases with both the viscosity and mode number increase:

$$y^2 \sim \frac{1}{\alpha^{4/5}S^{7/5}}\left(\frac{a}{\delta}\right)^{4/5}\left(\frac{\tau_{P\mu}}{\tau_\theta}\right)^{2/5}\frac{1}{(nq)^{8/5}} \qquad (5)$$

With formulas (4) and (5) it is possible to estimate the diffusion coefficients associated with the ballooning mode development in the presence of the anomalous electron viscosity. Since $K_\perp^2 = n^2q^2(1+S^2y^2)/a^2$ the maximal (in nq) plasma diffusion coefficient exists:

$$\mathcal{D} \sim \frac{\alpha^{3/4}}{S^{1/4}}\frac{\delta a}{\sqrt{\tau_{P\mu}\tau_\theta}} \qquad (6)$$

This coefficient is higher that the pseudoclassical one when viscosity electron time $\tilde{\tau}_{P\mu} \lesssim \tilde{\tau}_S(\delta/a)^2 \tau_S/\tau_\theta$. Assuming the viscosity time to be of the order of the energy one $\tilde{\tau}_{P\mu} \sim \tilde{\tau}_E$ one can readily see that in the experiments this inequality is satisfied. The ohmic heating diffusion time $\tilde{\tau}_{\mathcal{D}}$ determined by coefficient (6) depends on the plasma parameters in the following way:

$$\tilde{\tau}_{\mathcal{D}} \sim (nT)^{1/2}a^2 \qquad (7)$$

and agrees in the order of magnitude with the experimentally observed one.

References

1. A.M.M.Todd et al. Phys.Rev. Lett., 38, 826 1977.

2. J.W.Conner, R.J.Hastie, J.B.Taylor Phys.Rev. Lett. 40, 396, 1978.

3. О.П.Погуце, Э.И.Юрченко, Письма в ЖЭТФ, 28, 344, 1978.

4. О.П.Погуце, Н.В.Чудин, Э.И.Юрченко, Физика плазмы 6, 621, 1980.

5. C.Bateman, O.B.Nelson. Phys. Rev. Lett, 41, 1804, 1978.

6. О.П.Погуце, Э.И.Юрченко, Письма в ЖЭТФ, 31, 479, 1980г.

C

OPEN-END SYSTEMS
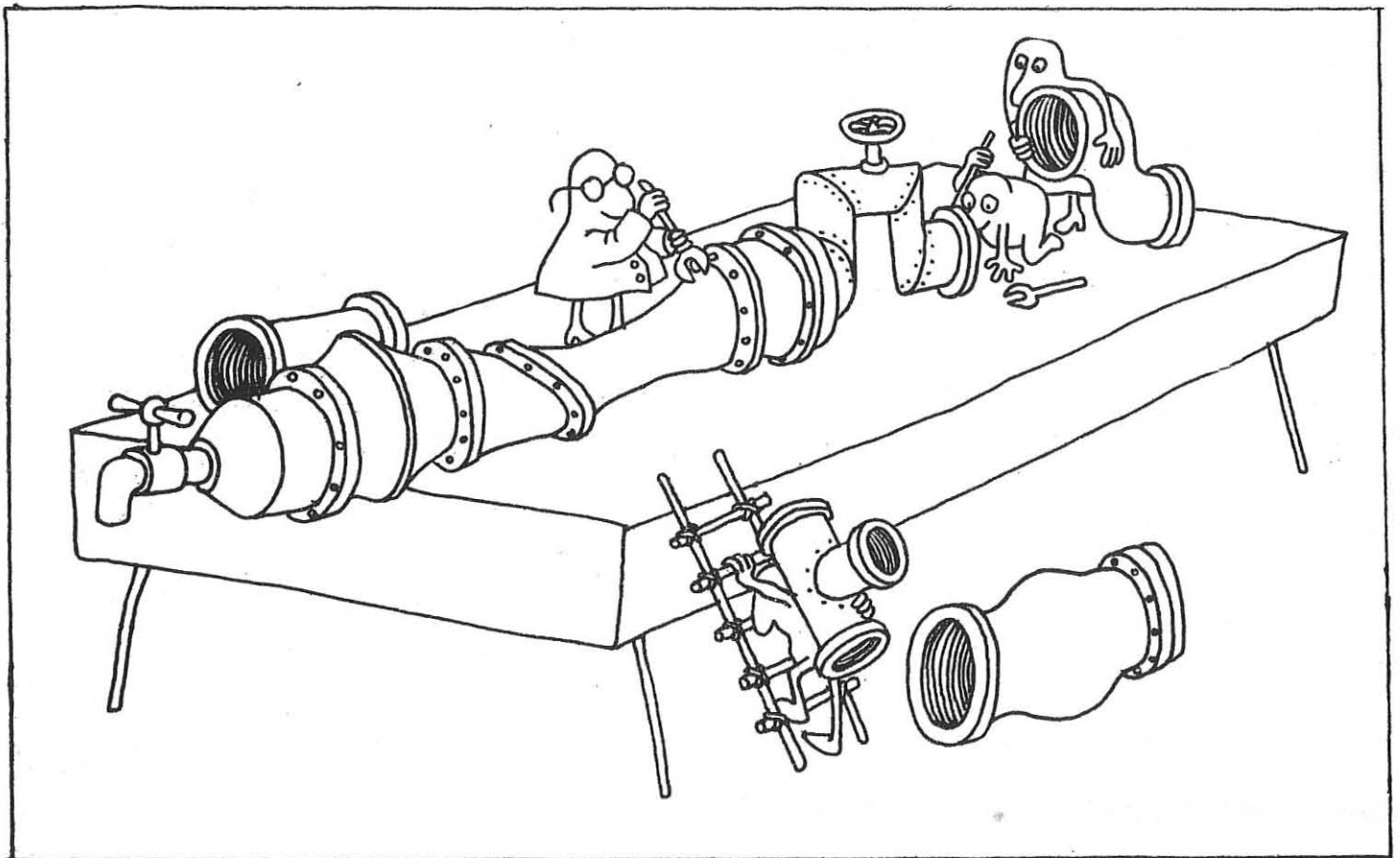
RADIAL TRANSPORT OF PLASMAS IN CENTRAL CELL OF
GAMMA-6 TANDEM MIRROR

T. Kawabe, K. Ishii, A. Itakura, Y. Kimura, S. Miyoshi
Y. Shinagawa, S. Suzuki, M. Tomishima and K. Yatsu

Institute of Physics and Plasma Research Center
The University of Tsukuba
Ibaraki, 305 JAPAN

Tandem mirror (ambipolar mirror)[1][2] is one of the attractive approaches to nuclear fusion reactor, and experiments have been carried out by use of GAMMA-6, TMX, PHAEDRUS and AMBAL-1. Expected confinement time of ions in the central cell of the tandem mirror has been suggested by Pastukhov[3], and it was verified by GAMMA-6 experiment[4]. At present, one of the essencial problems of this confinement scheme is the radial transport of the plasma at the central cell due to non-axisymmetric magnetic field configuration, which has been suggested by Ryutov and Stupakov[5]. In this paper, experimental results on the effects of radial electric field upon the radial ion transport in GAMMA-6 are described, and they are compared with the calculations of the drift surfaces of the ions in the central cell.

The GAMMA-6 magnetic field is formed by the following coils; (Fig.1).
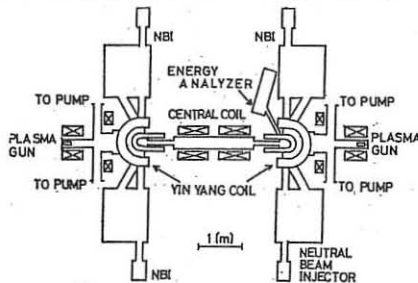
Fig. 1 Schematic diagram of GAMMA-6

The plugs are two pairs of Yin Yang coils to form minimum B configulation, while the central cell consists of two solenoidal coils. The magnetic-flux tubes in the minimum B plugs entering the solenoid are oriented to face one another. The field strength are 1.5 kgauss at the midplane of the plugs with mirror ratio of 2.4, and 500 gauss at the central cell under the typical experimental condition.

Plasmas are produced and injected by two pairs of titanium occluded washer guns from both ends on the axis. The typical plasma densities at the plugs and at the central cell are about $5 \times 10^{13}/cm^3$ and $10^{13}/cm^3$, respectively. The electron temperature is about 10 eV, while the ion temperature is about 30 eV. The cross sections of the plasma are elliptical of 4 cm x 6 cm in diameter at the midplane of the plugs and that of 3 cm x 40 cm at the central cell. Radial distribution of the plasma potential was measured by Langmuir probes and it showed that there was a dip on the axis during the discharge of the plasma guns to form a radial electric field of several 10 V/cm and that it was rather flat after the discharge.

The radial flux of the plasma ions was measured by a flux detector of Faraday cap type, which was located at the midplane of the central cell, and the radial position on the extention of the short axis of the elliptical cross section was scanned. The detector consists of a mesh grid which is biased negatively to repel the electrons and a collector to collect the ion flux.

Typical results of the temporal variation of the ion current to the collector of the flux detector is shown in Fig. 2, as well as the current (I_g) and Voltage (V_g) of the plasma gun discharge, radial potential difference (ΔV), and ion saturation current of the probe in the central cell plasma (I_{isc}). As is seen in Fig. 2, when the location of the detector was close to the plasma (r = 3 cm), the ion flux consists of two peaks, the one has similar shape with the temporal variation of the plasma density, while the

second peak comes just after the discharge of the plasma gun. When the location is far from the plasma (r = 10 cm) then the flux at the end of the gun discharge becomes dominant in the radial flux. This latter type of burst of the plasma reaches as far as r = 20 cm.

The coincidence of the starting time of the burst of the radial ion flux with the time of the end of the discharge of the plasma gun was veryfied by changing the duration of the discharge of the plasma gun in a range from 300 μsec to 700 μsec, and it was found that the coincidence was good within less than ±100 μsec. The expansion of the plasma seems to be quite fast in the radial direction.

This enhanced radial transport has been considered, and it seems to attribute to either the effects of the radial electric field on the ion drift motion or some instabilities which occur when the radial electric field becomes small.

To check the first model, calculations of the drift surfaces of the ions in the central cell of of the GAMMA-6 with the experimental conditions has been carried out based on the guiding center approximation with and without radial electric field. One of the example is shown in Fig. 3. As is seen in the figure, the drift surface of the ions is within the cross section of the plasma when there is radial electric field, while the drift surface would expand

Fig. 2 Temporal variation of the current(I_g) and Voltage (V_g) of the plasma guns, Potential difference (ΔV) Ion saturation current (I_{isc}) at the midplane of the central cell, and ion flux current (I_f) at r = 3 cm and r = 10 cm.
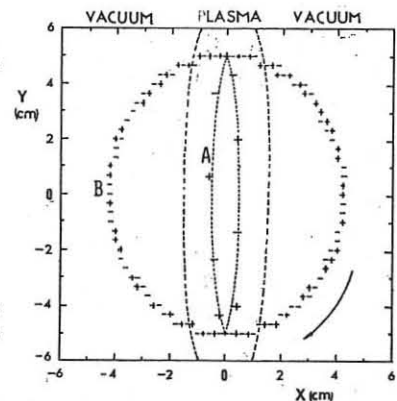
Fig. 3 Examples of the drift surface of the ions in the cross section of plasma column of the central cell with (A) and without (B) radial electric field.

beyond the plasma surface when there is no radial electric field. This is because the E x B term becomes dominant in the force acting on the ions.

So far, an enhanced fluctuations have not been observed in the plasma in the central cell when the gun discharge finished. Those facts suggest that the radial electric field plays an important role in radial transport.

REFERENCES

1) G.I.Dimov, et al.,Fizika Plasmy, 2, 597 (1976).
2) T.K.Fowler and G.B.Logan, Comments Plasma Phys. 2, 167 (1977).
3) V.P.Pastukhov, Nuclear Fusion 14 3, (1974).
4) S.Miyoshi, et al., IAEA Brussel Meeting paper CN38/F2-2.
5) D.D.Ryutov and G.V.Stupakov, Fiziki Plasmy 4, 501 (1978)

PLASMA HEATING BY R E B IN A LONG SOLENOID

V.S.Burmasov, A.D.Khilchenko, V.A.Kornilov, E.P.Kruglyakov,
V.N.Lukyanov, A.A.Podyminogin, Yu.A.Tsidulko, L.N.Vyacheslavov

Institute of Nuclear Physics, Novosibirsk 630090, USSR

New results in the study of the beam-plasma interaction at the CO1-1 device /1/ are reported. The main experimental parameters of the device were the following: the solenoid length L=7,5m, the homogeneous magnetic field strength B_0=13,5kOe. Plasma was produced by four oscillating discharges when supplying voltages to four discharge gaps located along a dielectric chamber. The hydrogen was filled in the chamber with the aid of five pulsed electrodynamic valves. This method made it possible to produce a fairly homogeneous plasma of 7.5m long and 9cm in diameter with the density n_e =(3-5)·10^{14}cm^{-3}. The plasma parameters were checked by the Thomson scattering method and with three Michelson interferometers /2/. Injection of the REB into the plasma was performed through a magnetic mirror (B_m=25kOe); in the diode region the magnetic field was close to its maximum (23,5kOe). At the exit of the system there is located a mirror with 31 kOe field (the mirror ratio R=2.3). The exit mirror can be removed, if necessary, and the exit collector-calorimeter turns out to be in a field close to the homogeneous one (B=12kOe).

In the most of experiments the plasma density at the system axis was n_e =3·10^{14}cm^{-3} and the radial gradient was small enough ($\frac{dn_e}{dR}$ =1.5·10^{13}cm^{-4}). The beam current density was held constant: j_b =1.5±0.2 kA/cm^2. Despite the quite large angular spread of the beam ($\sqrt{\overline{\theta_c^2}}$ =23° just behind the anode foil and $\sqrt{\overline{\theta^2}}$ =18° in a homogeneous magnetic field), the initial distribution of diamagnetism along the device is inhomogeneous, fig. 1. Such a distribution of diamagnetism is a strong argument in favour of the energy release mechanism based on the two-stream instability /3/. As it has been previously pointed out (see, e.g. /4/), the dismatch between the energy content calculated on the basis of the Thomson scattering measurements and the energy content found from diamagnetic measurements is accounted for by the appearance of "tails" in the energy distribution function. The plasma energy contents measured by the two methods differ by 30 times. The large length of the device allows the main parameters of the electrons in the "tails", i.e. density of "hot" electrons and their mean energy to be estimated in a sufficiently reliable manner. The simplest estimation for minimum energy was made with the help of a pulsed target from the neon plasma (the target length is about 100 cm, the density is about 3·10^{14}cm^{-3}) formed near the output of the chamber. In the case when a Coulomb mean free path of "hot" electrons proves to be of the order of a target length, these electrons will be effectively back-scattered whether or not there is a mirror at the output side. Fig. 2a presents two signals of the soft X-ray radiation. The signal plotted as a solid line corresponds to a magnetic configuration of the mirror type. The dotted signal corresponds to the case of an open end. The comparison of the two signals makes it possible to draw the conclusion that the target is transparent for a considerable portion of the "tail" electrons. This fact
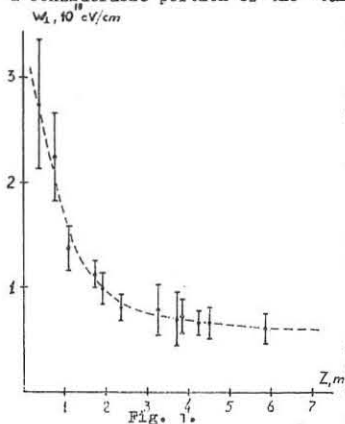
means that the effective temperature of "hot" electrons is T_e^* > 1 keV. Fig. 2b shows the diamagnetic signals detected in two configurations of the magnetic system: the mirror trap (solid lines) and the open end system (dotted lines).

For various estimations it is convenient to introduce the decay time of a diamagnetic signal. This time is shown in Fig. 3 for different

Fig. 1.

positions along the device both in the case of a mirror trap (dark circles) and in the case of an open end (light circles). It is seen that the common decay times can be introduced for the both configurations. In the case of the mirror trap the averaging over 164 signals resulted in $\tau^{(1/2)}$ =470±90ns. In the system with the open end the averaging over 88 signals yielded $\tau^{(1/2)}$ =230±50ns. It follows from the later estimate that the plasma diamagnetism is determined only by a group of energetic electrons leaving the system with a typical longitudinal velocity, estimated as $V_e \simeq \frac{L}{\tau^{(1/2)}}$=3·$10^9$cm/s. Further, since the time history of

Fig. 2a.

Fig. 2b.

diamagnetism depends on the boundary conditions ($\tau^{(1/2)}$ becomes nearly 2 times larger upon transition to the mirrortype configuration), one can assume that the hot electrons distribution is close to the isotropic one. In any case, a significant portion of these electrons have a momentum outside the loss cone. Assuming that the isotropy takes place, we find that the effective temperature of hot electrons is $T_e^{eff} \approx$ 10 keV. With a typical value of diamagnetism per unit length of the plasma column, $nT_\perp$ S = 10^{18} $\frac{eV}{cm}$ and S=30cm^2 the density of the "tail" electrons is estimated as follows: $n_e^{eff} \approx$ 3·10^{12}cm^{-3}, that accounts for 1% of the plasma density. Of course, this method gives the order of magnitude values of "temperature" and density.

Note that for the plasma and beam parameters indicated above a quite high efficiency of the REB-plasma interaction has been achieved. The energy input to the plasma is above 30% of the REB energy. It is interesting that the beam-plasma interaction can be suppressed considerably due to the radial density gradients. That is important for long distances beam transport. In comparison with described above results the experiments made with plasma gradient $|dn_e/dR|$ =8·10^{13}cm^{-4} have shown that interaction efficiency is decreased by more than 3 times.

Fig. 3.

References

1. A.V.Arzhannikov et al. "Plasma Physics and Controlled Nuclear Fusion Research 1978", v. II, pp 623-637, IAEA, Vienna, 1979.

2. V.S.Burmasov, E.P.Kruglyakov, A.A.Podyminogin. Fizika Plazmi, 4, No 1, 140 (1978).

3. B.N.Breizman, D.D.Ryutov. Nucl. Fusion, 14, 874 (1974).

4. A.V.Arzhannikov et al. "Plasma Physics and Controlled Nuclear Fusion Research 1974", v. III, pp 257-268, IAEA, Vienna, 1975.

EXPERIMENTS ON THE ATOLL DEVICE

M.S.Ioffe, B.I.Kanaev, V.P.Pastukhov,
V.V.Pitersky and E.E.Yushmanov

I.V.Kurchatov Institute of Atomic Energy,
Moscow, USSR

Abstract. The Atoll device is a ring-shaped magneto-electrostatic trap with a cusped magnetic field (MET) /1/. The described experiments aimed at: i)clarifying the conditions for plasma production in such a trap by energetic electron injection and determining the resulting plasma parameters, ii) studying the effect of gap electrostatic plugging on plasma confinement.

Fig.1 shows the machine lay-out. The field is generated by four pairs of coils (1) shaping 2-mm-wide gaps. The radii of the outer and inner gaps are 64 cm and 32 cm, respectively; the fields within the gaps are 8 and 16 kOe, respectively. The plugging electrods - "reflectors" (2) with suppressing rings are located behind the gaps, the rings being used when it is necessary to suppress the secondary electron emission from the reflectors. The latters are at a negative potential. A heated electron emitter (3) is placed on a small area of one of the reflectors, opposite to the middle of the gap. The electrons emitted are accelerated through the gap into the central part of the trap and initiate a Penning-type discharge at a low gas pressure. Secondary electrons due to ion bombardment of th reflectors play the main part in maintaining discharge. By means of the discharge the trap was being filled with plasma; the latter occupying a volume of about 50 l.
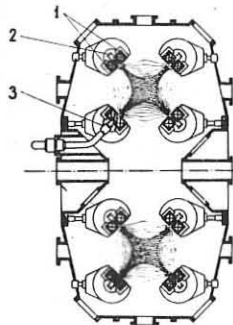
In the experiments the hydrogen pressure was $(2-6) \times 10^{-6}$ Torr, the reflectors potential $-(1.5-2.5)$ kV, the outer gap field $6.5.-8$ kOe. Under these conditions a plasma accumulation stage continues 2-3 ms, followed by an almost quasi-stationary plateau. Application of the negative potential to the suppressing rings stops the reflector electron flux,and hence, ceases the discharge, which results in a plasma free decay stage. Fig.2 shows radiointerferometer signal oscillograms illustrating temporal plasma density variation in all the above stages.
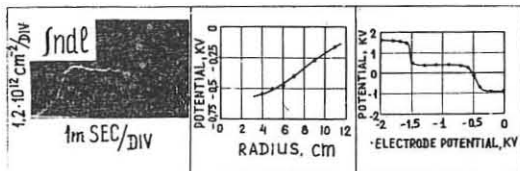
Fig.2   Fig.3   Fig.4

Main plasma parameters. In typical regimes the mean plasma density measured by an interferometer was $(1.5-3.0) \times 10^{11}$ cm^{-3}. The density distribution obtained from a miniature Langmuir probe measurements shows that the density in the centre may reach about 10^{12} cm^{-3}.

The negative plasma potential measured by the probe is $-$ (400 to 900)V, its magnitude being strongly dependent on the magnetic field. The potential is found to change considerably in the radial direction (Fig.3).The volt-ampere characteristic of the electrode(Fig.3)located behind the reflector hole gives data on the potential in the gap middle. The plasma and gap potentials appeared to be close one to another.

The electron temperature measured from the probe volt-ampere characteristic was about 30 eV. The ion energy is likely to be of the order of 50 eV, since the transverse electric field existing within the plasma is sufficiently high for new-born ions to reach the well bottom acquiring the above energy. Thus, in fact the ion motion is unmagnetized. With the above plasma parameters the magnetic field configuration remains vacuum one, since the value (the plasma pressure in the centre/the field minimal pressure on the boundary force line) is only a few %.

Measurements with the electrode located behind the reflector have shown that the part of the secondary electron inflow goes backward to the reflectors and the other part is trapped in the machine. The trapped electrons heat the plasma, a number ionization events falling at each trapped electron. The resultant electrons diffuse from the trap across the magnetic field, while the ions go out to the reflectors through the gaps. Since the gap middle potential (which is obviously equal to the confined plasma potential)is negative and exceeds essentially the ion "temperature", the ions cannot escape through the whole gap width, but only through a narrow passage (about one-fifth of the total gap width) in the gap middle. The higher the negative plasma potential, the smaller is the passage width. The former reaches automatically such a level that ion and electron losses are in equilibrium.

The transverse electron losses are particularly important. At a quasi-steady-state the confinement and ionization times seems to be equal, being a few hundred . Should the transverse electron diffusion be classical, the confinement time would be about 10 ms (N is the number of Larmor electron radii across the gap half width). Thus, in Atoll the electron transverse transport is much higher than the classical one. This conclusion is also confirmed by the fact that the radial density distribution does not stop abruptly at the boundary field line, as is the case with a classical transport, but continues far beyond it (the boundary field lines are those which touch the gap edges and pass at the distance of 6 cm from the centre). Ion-acoustic wave instability /2/ developing when electron gradient drift velocity exceeds the sound velocity, may be responsible for the anomalous electron transport.

Conclusions.

1) The fact that the Atoll plasma acquires a negative potential means that the method of magneto-electrostatic confinement works in principle. The gap effective width for ions is essentially less than the material gap, or than the ion Larmor radius.

2) The rate of the transverse losses from the trap exceeds considerably the classical one.

References
/1/ O.A.Lavrent'ev, "The Magnetic Traps", vol.3, "Naukova Dumka", Kiev (1968).

/2/ V.P.Pastukhov, Fizica Plazmy, 6, 1003 (1980).

ENERGY BALANCE IN RFC-XX

S. Okamura, K. Adati, T. Aoki, K. Hattori, S. Hidekuma
S. Hiroe, M. Ichimura, T. Kawamoto, R. Kumazawa, Y. Okubo
T. Okada, T. Sato, M. Sugawara and T. Watari
Institute of Plasma Physics, Nagoya University
Chikusa-ku, Nagoya, 464 Japan

Abstract: Energy flux out of an open end of the RFC-XX was measured by a thermal method. The rf plugging effect was confirmed with it. The energy balance in RFC-XX was investigated with ICRH plasma.

The characteristic of energy confinement or the energy flow analysis is one of the most important features for all confinement devices in the fusion research. From this point of view, we investigated various quantities of the plasma in RFC-XX in relation to the energy flow.

The RFC-XX is a confinement systems of the double cusp field configuration with a 2 meters solenoidal central section ($B_c = 1T$). It has six rf systems; four systems for the plugging of all cusp ends ($\omega \sim \omega_{ci}$) and two systems for the ICRH in the central section. The diagnostics are shown in Fig. 1. We used the diamagnetic loop signal to get the total energy contents in RFC-XX. A limiter-like obstacle with the thermister is set slightly inside the limiter to measure the perpendicular energy loss caused by the diffusion. A pyroelectric detector located at the central section detects charge exchange neutral energy flux from the plasma column. End loss flux is measured by both the multigrid energy analyzer and the pyroelectric detector at each open end except one for the plasma injection.

So far, the effect of the rf plugging has been studied in various cases. But in most of them the end losses were measured by some kinds of ion collector. It is commonly noted that in open ended confinement devices the electron heat conduction through the open end is very important. The energy flux measured by the pyroelectric detector gives an answer to this problem. The pyroelectric detector has the sufficient time resolution for our experiment ($\tau_{res} \sim$ 100 μsec), and with a small orifice it gives also the good space resolution. Fig. 2 (open circles) shows the energy flux profile escaping through the line cusp. The width of the left peak is the order of the ion Larmor radius and the right hump is related to the plasma in the central section. When we applied the rf plugging, the energy loss was suppressed as shown in Fig. 2. The dependence of the plugging effect on the rf voltage was also obtained and it shows the similar dependence as that obtained with the multigrid energy analyzer.

To investigate the rf plugging effect on the energy confinement, it is necessary to get the whole picture of the energy flow in RFC-XX. We studied it applying the ICRH power to the base plasma. The obtained power balance is the basic characteristic of RFC-XX without rf plugging. The candidates for the major energy loss channels are the particle end loss, the electron heat conduction, the charge exchange loss and the diffusion loss to the limiter. The radiation loss may be quite small as the electron tempera-

ture is very low ($\sim$ 14 eV from the Thomson scattering). If any, it is included in the measurement of the charge exchange loss. We first measured the diffusion loss with the limiter calorimeter in Fig. 1 and found that it is the order of 1 % of the input power. Then we plot the time history of the energy balance during the ICRH in RFC-XX as Fig. 3. Each data was derived as following: n_c is the density in the central section obtained from the microwave interferometer. Its increase after 500 μsec is due to the increase of neutral particles which is consistent with the charge exchange loss. $T_{i\perp}$ is the ion perpendicular temperature derived from the diamagnetic signal and the density, which agrees with the charge exchange neutral particle measurement. The closed circles show the decay time of the diamagnetic signal when the ICRH is turned off at that time, which is the overall confinement time τ_E of the device. τ_t corresponds to the particle end loss which is related to $T_{i\perp}$ as $\tau_t = \alpha T_{i\perp}^{-\frac{1}{2}}$. This is obtained in the series of experiments where $T_{i\perp}$ is varied. τ_{ie} reflects the energy transfer rate from ions to electrons calculated from n_c and T_e (T_e is almost constant during the ICRH). τ_x means the charge exchange loss deduced from the relative change of the pyroelectric detector signal and its absolute value is determined at the latest data in Fig. 3. Crosses for τ_E are the calculated values for overall confinement time from these three energy loss channels and they show good agreement with the measured values (closed circles) of τ_E.
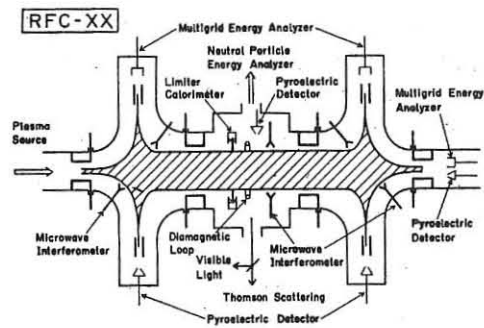
Fig. 1. Energy diagnostics of RFC-XX. It shows also parallel ring plates for line cusp plugging, Nagoya Type-III coils for point cusp plugging and Type-III coils for ICRH in central section.
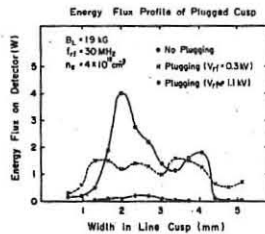
Fig. 2. Line cusp energy flux measured by pyroelectric detector.
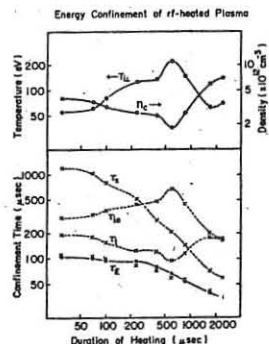
Fig. 3. Energy balance in RFC-XX with ICRH.

LONGITUDINAL CONFINEMENT AND PLASMA STABILITY IN A CENTRIFUGAL TRAP

A.A.Bekhtenev, M.S.Pekker, V.I.Volosov

Institute of Nuclear Physics, Novosibirsk 630090, USSR

A centrifugal trap (CT) is the modified trap with a rotating plasma wherein, unlike a conventional rotating plasma trap (RPT) with crossed E and H fields, magnetic mirrors can be absent, while the plasma is confined solely by a centrifugal potential U_i /1/.

In this system the maximum electric and magnetic field intensities are in the region (in the centre of the trap) in which the plasma density is maximum, too. The electric field intensity on the electrodes of this trap E_κ can be much lower than that in a conventional RPT.

In addition to the engineering advantages, we shall show that the main physical characteristics of this trap, i.e. the longitudinal confinement and stability of the plasma, may be better than those in a conventional RPT.

The plasma confinement boundary in the phase space for a similar trap is determined by two dimensionless parameters: the magnetic $R_H = H_\kappa / H_o$ and centrifugal $R_\tau = \tau_o^2 / \tau_\kappa^2$ mirror ratios, where the subscripts κ and o denote the edge and the centre of the trap, respectively; and τ is the plasma radius:

$$\mathcal{U}_\parallel^2 = \mathcal{U}_\perp^2 (R_H - 1) + V_E^2 (1 - 1/R_\tau) - 2e\varphi/M_i .$$

Here V_E is the drift velocity of the plasma in the centre of the trap, φ is the ambipolar potential between the end electrodes and the plasma. Figure 1 illustrates the plasma confinement boundaries in the phase space for a conventional rotating plasma trap ($R_H = R_\tau$) and for a centrifugal trap ($R_H \leqslant 1, R_\tau > 1$); S is the point of injection ($I - R_H = 1.0$; $II - R_H = 0.5$; $III - R_H = R_\tau \simeq 2.0$). The basic distinction between the plasma confinement times for these two traps is due that the confinement boundary is close to the injection region in the CT. That leads to a relative increase of the losses of fast ions in a centrifugal trap and, correspondingly, to a decrease in the equilibrium ion temperature, as well as to an increase of the magnitude of U_i/T_i at a given energy of the ion injection.

The magnitudes of $n\tau$ for these two traps are compared in Fig. 2 (here $R = R_\tau$, $M_i = 2.47$, i.e. DT plasma, the dotted line indicates the RPT, the solid line - the CT: I at $R_H = 1.0$; II at $R_H = 0.9$; III at $R_H = 0.85$). At $U_i/T_i < 1$ (i.e. at $R_\tau = 2-3$; $R_H \simeq 1$) the confinement in the CT is worse than in the RPT, since, in practice, the centrifugal barrier does not affect the plasma confinement and the latter is determined only by Coulomb scattering. The plasma confinement in the CT becomes better compared to the RPT if the magnitude of U_i/T_i becomes larger than unity with increasing R_τ ($R_\tau = 4 \div 6$) and decreasing R_H ($R_H \simeq 0.7 \div 0.8$).

These effects can improve also the factor Q in the CT at fairly high injection energies, $W_{EH} > 100-150$ keV. Figure 3 demonstrates the dependence of Q on the injection energy for a centrifugal trap (solid curve) and a rotating plasma trap (dotted line), the charge exchange processes inside the plasma and the energy processes at the end electrodes being taken into account (the factor $\Delta/2\varrho_i = 0.5$ /1/, DT plasma, the injection energy for deuterium is $W_{ED} = 2W_{EH}$, the injection energy for tritium is $3W_{EH}$).

The stabilisation of flute plasma oscillations in any RPT may be realised by two effects: the inhomogeneous radial profile of the velocity of rotation of the plasma (electric shear) and the stabilizing action of the electron longitudinal current to the conducting end electrodes. The latter condition can be written as /3/:

$$\frac{1}{\tau T_{ef}} > 5 \left(\frac{\varrho_i}{\alpha}\right)^2 \frac{V_E}{\tau} \cdot \frac{1}{T_i} \qquad (1)$$

Here τ is the mean radius and α is the radial dimension of the plasma layer, ϱ_i, T_i are the Larmor radius and the temperature of ions, τ is the longitudinal confinement time of the particles, T_{ef} is the mean longitudinal energy of electrons at the end electrodes. Below we shall compare the stabilisation conditions for the CT and RPT in a case when the geometrical dimensions τ and α and the injection energies W_{EH} and β are fixed, and the maximum values of H_o and n_o are determined by permissible values of E_κ .

In the CT the magnitude of E_o (and of H_o also) can be higher than in the RPT since $E_o = E_\kappa \sqrt{R_\tau}/R_H$, $R_H \leqslant 1$, $R_\tau > 3-5$, and the maximum field E_κ in the mirrors is limited severely by the breakdown voltage on the electrodes.

If the plasma density n_o and the field H_o (at $\beta =$ const) are restricted by E_o , then the condition (1) for the CT is improved proportionally $(H_{oCT}/H_{oRPT})^3 = (E_{oCT}/E_{oRPT})^3$ in comparison with a simple RPT.

Thus, with the parameters close to the reactor ones the longitudinal confinement and stability of the plasma in the CT can be better than those in a conventional trap with a rotating plasma.

References

1. A.A.Bekhtenev, V.I.Volosov, V.E.Pal'chikov, Nucl. Fus. 20, N 5, 579 (1980).

2. V.I.Volosov, M.S.Pekker. Preprint INP 80-168 Novosibirsk (1980).

3. A.A.Bekhtenev, V.I.Volosov. J.T.P. 47, 1450 (1977).
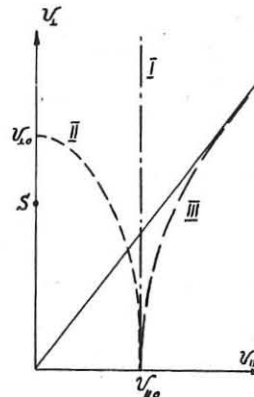
Fig. 1.
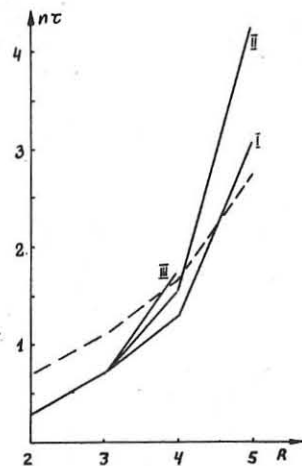
Fig. 2.
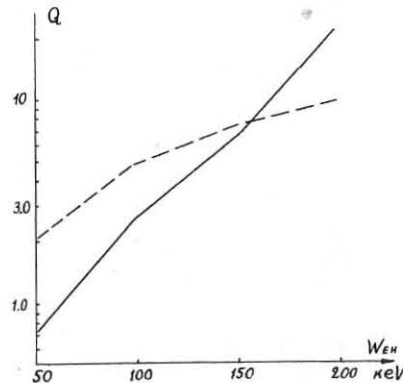
Fig. 3.

PLASMA CONFINEMENT OPTIMIZATION IN A
MULTIPLE-MIRROR MAGNETIC TRAP

P.Z.Chebotaev, B.A.Knyazev,
V.V.Mirnov, G.E.Vekstein

Institute of Nuclear Physics, Novosibirsk, USSR

Herein we consider linear thermonuclear devices with dense plasma, so that the ions mean free path λ is small compared to the plasmoid length L. The longitudinal plasma confinement in such a system may be realized by a corrugated magnetic field [1,2], and the transverse by the rigid reactor wall [3]. One of the most important characteristic of the pulsed thermonuclear reactor is the total plasma energy needed for breakeven. Using the well-known estimations for the longitudinal confinement time [1] $\tau_{\|} \approx L^2/v_{Ti}\lambda$ and the radial cooling time $\tau_{\perp 0} = R^2/\chi_\perp$ ($\chi_\perp$- classical temperature conductivity) it follows from the Lowson criteria ($\tau_{\|} = \tau_\perp \omega \bar{n}^{-1}$) that $L \omega \bar{n}^{-1}, R^2 \omega H^2$ and the plasma energy $W = 3nT \cdot L \cdot \pi R^2 \omega H^2$ doesn't depend on the density (the plasma temperature is fixed: $T \approx 10 \text{keV}$). So it is advantageous to use a high density plasma, because it reduces the length of the system (the upperlimit $n_{max} \approx 10^{18} \text{cm}^{-3}$, is determined by the tensile strength of device). That is why $n \sim 10^{18} \text{cm}^{-3}$ (the magnetic field $H \sim 10T$, $\beta \sim 10^2$) was chosen in the first reactor study [4]. In subsequent papers [5] it was shown that in the high-β plasma the energy confinement time is much less than the classical one, so it needs to use rather moderate plasma density $n \sim 10^{17} \text{cm}^{-3}$($\beta \sim 5 \div 10$). In this case the length of the system increases up to 200 m, and we examine in details reduction of the plasma length by a small amount of heavy ions with $Z \gg 1$ [6].

Unlike [6] where the impurities space distribution was considered to be constant during the relatively fast expansion of the hydrogen component, in this paper we take into account the diffusion flow of all the components. Their motion is determined by pressure gradients, electric field and friction forces between the particles and the multiple-mirror magnetic field. The balance of the forces takes the form:

$$-n_H m_H v_{TH}\left(\frac{\alpha}{\lambda_{Hz}} + \frac{\beta}{\lambda_{HH}}\right)u_H - \frac{n_H m_H v_{TH}\gamma}{\lambda_{Hz}}(u_H - u_z) + \quad (1)$$
$$+ eEn_H - \partial P_H/\partial x = 0$$

$$-\frac{n_H m_H v_{TH}\gamma}{\lambda_{Hz}}(u_z - u_H) - \frac{n_z m_z v_{Tz}}{\ell} \cdot \frac{u_z}{\left(\delta\frac{\ell}{\lambda_{zz}} + \frac{1}{\beta}\frac{\lambda_{zz}}{\ell}\right)} + \quad (2)$$
$$+ eZn_z E - \partial P_z/\partial x = 0.$$

Here $u_H, u_z, n_H, n_z, P_H, P_z$ are the bulk velocity, density and pressure of the components, and $v_{TH}, v_{Tz}, \lambda_{HH}, \lambda_{Hz}, \lambda_{zz}$ are the corresponding thermal velocities and mean free paths, which we define as follows:

$$\lambda_{HH} = T^2/n_H e^4 \Lambda, \quad \lambda_{Hz} = \lambda_{HH} n_H/n_z Z^2, \quad \lambda_{zz} = \lambda_{HH} n_H/n_z Z^4,$$
$$v_{TH} = (T/m_H)^{1/2}, \quad v_{Tz} = v_{TH}(m_H/m_z)^{1/2}.$$

The numerical factors $\alpha, \beta, \gamma, \delta$ depend on the mirror ratio K and are equal to [2]:

$$\alpha = (2\pi)^{3/2} K^2/6, \quad \beta = K^2/0.45; \quad \gamma = (2\pi)^{3/2}/6, \quad \delta = (4.8 K \ln K)^{-1}.$$

From eq. (1,2) we can find hydrogen and impurity velocities u_H, u_z and, taking into account that $n_e = n_H + Zn_z$, $n_e eE = -\partial P_e/\partial x$, we get the closed system of equations for $n_H(x,t)$ and $n_z(x,t)$. The boundary conditions at the end of the tube is that the diffusion velocities of the species are equal to the thermal ones. The procedure of the longitudinal confinement optimization is described in [7]. The variable parameters are the plasma temperature T, its energy W, the total number of impurities and their initial distribution $n_z(x,0)$. The effect is that in the presence of impurities the thermonuclear energy

output increases considerably. The maximum values of $Q = W_t/W$ are attained at the initial impurities distribution $n_z(x,0)$ with the sharp maximum in the region of the plasma density slope (see Fig. 1). In this case we have efficient slowing-down of the hydrogen plasma and rather moderate bremsstrahlung losses. For the heavy ions located near the point $x = 1.4 L$ with $\Delta x = 0.06 L$ the fusion energy output may be increased by a factor of 2 for $Z = 7$ and by a factor of 5 for $Z = 13$ (see Fig. 2). The energy $W \approx 4$ MJ/cm^2 is required for breakeven (Q = 1).

The improved transverse confinement may be attained by the profiling of the plasma density radial distribution [8]. In this case we get numerically the following formula for the radial cooling time: $\tau_\perp \approx 7.2 \cdot 10^{-2} \beta^{45} \tau_{\perp 0}$. So at the plasma density $n \approx 10^{17} \text{cm}^{-3}$ and magnetic field $H \approx 10$ T it needs that $R \approx 4.2$ cm for Q = 1. The total plasma energy for breakeven is of the order of 300÷500 MJ.

It is necessary to solve the complex two-dimensional problem to calculate self-consistently the radial and longitudinal losses. So we use the simplified approach in which the longitudinal plasma expansion is taken into account as the particle and energy sink in the radial plasma transport equations. The corresponding power is obtained from the computer calculations of the plasma flow in the multiple-mirror magnetic field [7].

References

1 G.I.Budker, V.V.Mirnov, D.D.Ryutov, Pis'ma JETP, 14, 320, 1971.
2 V.V.Mirnov, D.D.Ryutov, Nuclear Fusion, 12, No 6, 1972.
3 G.I.Budker, Proc. VI Europ. Conf. Plasma Physics, 2, 136, 1973.
4 G.I.Budker, E.P.Kruglyakov, V.V.Mirnov, D.D.Ryutov, Izvestia Academii Nauk, Energetica i transport, 6, 35, 1975.
5 G.E.Vekstein, Doklady Academii Nauk, 237, 295, 1977.
6 V.V.Mirnov, D.D.Ryutov, Proc. VII Europ. Conf. Plasma Phys. 1, 142, 1975.
7 B.A.Knyazev, P.Z.Chebotaev, Preprint INP, Novosibirsk, 80-145, 1980.
8 G.E.Vekstein, P.Z.Chebotaev, Preprint INP, Novosibirsk, 80-42, 1980.
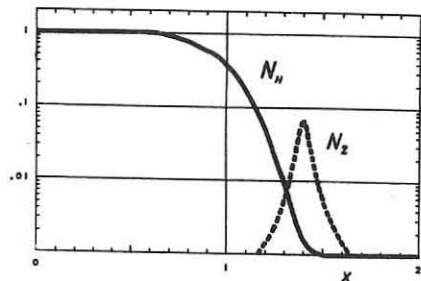
Fig. 1. The longitudinal distribution of the hydrogen component $n_H = n_H(x,0)/n_H(0,0)$ and the optimum one for the impurities $n_z = n_z(x,0)/n_H(0,0)$.
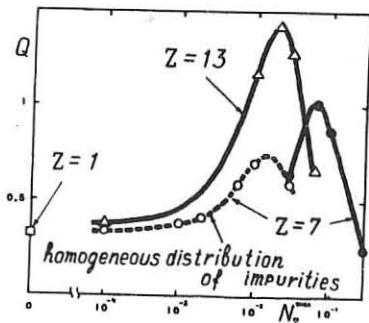
Fig. 2. The energy gain Q of the multiple-mirror reactor as a function of the impurities density and Z for the homogeneous and the optimum one longitudinal distributions

($T_0 = 6 keV$, $W = 5$ MJ/cm^2, K = 2).

DIRECT SIMULATION OF PLASMA TRANSPORTS IN AMBIPOLAR TRAP "AMBAL"

P.B.Lysyansky, M.A.Tiunov, B.M.Fomel'

Institute of Nuclear Physics, Novosibirsk 630090, USSR

Ambipolar plasma traps [1] allow the plasma end losses to be reduced as compared with usual open traps. In this case the influence of the radial losses on the plasma lifetime increases, the theory is given in [2]. The estimates of the radial transport [2-5] indicate a possibility of the unacceptable plasma losses and its close dependence on the trap's device.

A method of the direct plasma simulation by the ensemble of test particles is proposed to study and calculate the plasma transport in the real traps. Each particle is characterized by the co-ordinates (X, y) and the velocity $\vec{V}$ in the trap's midplane, which change due to the drift motion and collisions. The collisions are simulated by the chance changes of the test particles' velocities, in accordance with their scattering on the background plasma. The test particles, reaching the plasma radius or scattering into the loss cone, are considered as lost ones and replaced by particles whose co-ordinates and velocities correspond to the neutral injections. An iteration process is applied in computations for self-consistency between the background plasma and the ensemble of test particles. A method of mapping was developed to calculate the drift motion in the real magnetic field [5]. This method describes the transverse motion of a charged particle without calculating its longitudinal motion. If a particle, while moving through the trap, is insignificantly deviated from a magnetic force line, the displacement of the point where the trap's midplane is crossed by the guiding center of the particle can be found from the mapping [6]:

$$\Delta X = \rho \frac{\partial I}{\partial y} \quad ; \quad \Delta y = -\rho \frac{\partial I}{\partial X} \quad (1)$$

where ρ is the Larmor radius, and X, y are the co-ordinates of the particle in the midplane; the function $I(X, y, \theta)$ is determined by integration along the force line from the point (X, y) in the midplane to the point of reflection of a particle with the pitch-angle θ [5]: $I(X, Y, \theta) = \int \sqrt{1 - B(\ell)/B(0) \cdot \sin^2\theta} \, d\ell$, where $B(\ell)$ is the magnetic field on the force line, $B(0)$ is the magnetic field on the midplane.

The neoclassical radial transport of ions arises due to the distortion of the drift surfaces' form [2]. Fig. 1 shows the intersections of the drift surfaces by the midplane in the central cell of the AMBAL trap according to the fall of the particles' pitch-angle. The scattering of the test particle of the kind α on the background particles of the kind β characterized by the Maxwellian distribution is described by the functions [7]:

$$\langle \Delta V_{\parallel} \rangle^{\alpha/\beta} = -2 \left(\frac{m_\beta}{m_\alpha}\right)\left(\frac{T_\alpha}{T_\beta}\right)\left(1 + \frac{m_\alpha}{m_\beta}\right) G(x_\beta) \frac{V_{T\alpha}}{\tau_0^{\alpha/\beta}}$$

$$\langle (\Delta V_{\parallel})^2 \rangle^{\alpha/\beta} = 2 \left(\frac{m_\beta}{m_\alpha}\right)^{1/2}\left(\frac{T_\alpha}{T_\beta}\right)^{1/2} \frac{G(x_\beta)}{x_\beta} \frac{V_{T\alpha}^2}{\tau_0^{\alpha/\beta}}$$

$$\langle (\Delta V_{\perp})^2 \rangle^{\alpha/\beta} = 2 \left(\frac{m_\beta}{m_\alpha}\right)^{1/2}\left(\frac{T_\alpha}{T_\beta}\right)^{1/2} \frac{erf(x_\beta) - G(x_\beta)}{x_\beta} \frac{V_{T\alpha}^2}{\tau_0^{\alpha/\beta}}$$

$$X_\beta = V_\alpha / V_{T\beta}$$

Here V_α is the velocity of the test particle, $V_{T\beta} = (2T_\beta/m_\beta)^{1/2}$ is the thermal velocity of the background particles, m_α and m_β are the masses of the particles, $\tau_0^{\alpha/\beta} = m_\alpha^{1/2} T_\alpha^{3/2}/(\pi\sqrt{2}e_\alpha^2 e_\beta^2 n_\beta \Lambda)$ is the characteristic time of collisions and $G(x)$ is the Chandrasekhar function.

The changes of the test particle velocity during the time $\Delta t \ll \tau_0^{\alpha/\beta}$ in the local co-ordinate system (x, y, z), the axis of which is directed along the particle velocity before scattering, are described by:

$$\Delta V_z^{\alpha/\beta} = \langle \Delta V_{\parallel} \rangle^{\alpha/\beta} \cdot \Delta t + \xi_1 \cdot \sqrt{\langle (\Delta V_{\parallel})^2 \rangle^{\alpha/\beta} \cdot \Delta t}$$

$$\Delta V_{x,y}^{\alpha/\beta} = \xi_{2,3} \cdot \sqrt{\langle (\Delta V_{\perp})^2 \rangle^{\alpha/\beta} \cdot \Delta t / 2}$$

where $\xi_{1,2,3}$ are the random numbers with the mean value, $\langle \xi_i \rangle = 0$, and the dispersion $\langle \xi_i^2 \rangle = 1$. Using the scattering additivity, one may determine the change over time of the test particle velocity in the multispecies plasma.

In our modelling of the central cell plasma of the AMBAL trap the test particles are the H^+ ions. The background plasma consists from the H^+ ions and electrons. Computations were carried out at several values of the electrons' temperature: $0.3 \leq T_e \leq 1$ KeV. The plasma density, averaged over radius, was taken within the interval $3 \cdot 10^{12} \leq \langle n \rangle \leq 3 \cdot 10^{13} cm^{-3}$.

The outcomes of computations are the values of the ions' temperature, values and energy characteristics of the radial flux and end losses, radial profiles of the plasma density. Fig. 2 shows the dependences of the plasma confinement parameters from T_e and $\langle n \rangle$. The radial losses are everywhere less but comparable with the end losses. The ions' temperature T_i does not almost depend on $\langle n \rangle$ and depends linearly on T_e in the examined area of parameters.

The developed method and code allow the variants of the plasma traps' magnet devices to be evaluated from the point of view of the radial transport. Besides, the different characteristics of the plasma and fluxes may be determined with the help of the model, that is necessary when the experimental results are interpreted.

References

1. G.I.Dimov et al., Fiz. Plazmy, 2(1976), 597.
2. D.D.Ryutov, G.V.Stupakov, Fiz. Plazmy, 4 (1978), 501.
3. B.V.Chirikov, Fiz. Plazmy, 5(1979), 880.
4. R.H.Cohen, Nucl. Fusion, 19 (1979), 1579.
5. P.B.Lysyansky M.A.Tiunov, B.M.Fomel, Preprint 79-64, Institute of uclear Physics, Novosibirsk, 1979.
6. A.I.Morozov, L.S.Solovyev. Voprosy teor.plazm.,Vip.2,1963.
7. L.Spitzer, Physics of Fully Ionized Gases, N.Y. (1962).

Fig. I.
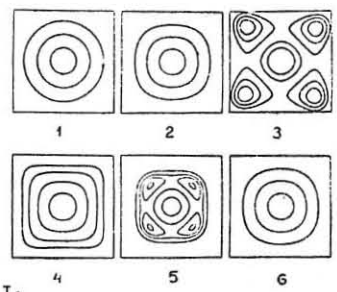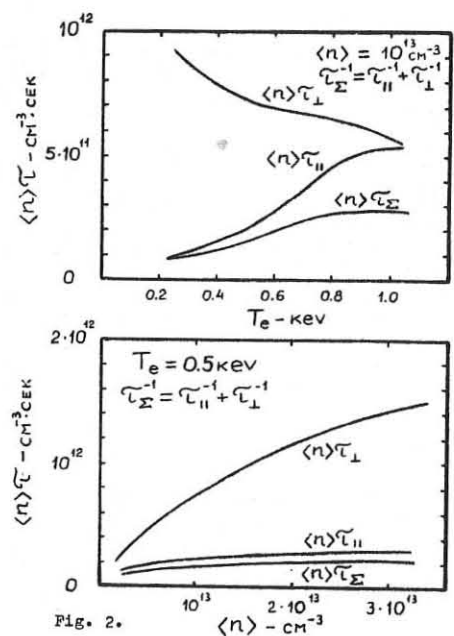
Fig. 2.

TRANSVERSE ION LOSSES FROM PLUGS OF AN AMBIPOLAR TRAP

L.S.Pekker, G.V.Stupakov

Institute of Nuclear Physics, Novosibirsk 630090, USSR

In the present paper we are concerned with central cell ion losses from the plugs of an ambipolar trap[1,2]. This effect was pointed out in Ref.[3] for the first time. It consists in that the central cell ions having a magnetic moment a little less than a critical value μ_0, $\mu_0 = \varepsilon/B_{max}$ (ε is the particle kinetic energy, B_{max} is the maximum magnetic field strength on a given field line), can be trapped into the plug while traversing the latter. The drift surface of a trapped ion oscillating between the ambipolar potential peak and the inner mirror of the plug can stick the wall (limiter) of the vacuum chamber, so that the trapped ion drifts out onto the wall for the drift time τ_d. As an illustration, Fig. 1 shows possible positions of a drift surface and a line where $B_{max} = const$, which are calculated in the paraxial approximation for different magnetic field configurations (for details see[4]). Fig. 1a corresponds to the situation when an ion trapped in point 1 does not strike the wall and comes back to the central cell in point 2. If the picture in Fig. 2 occurs then the trapped ion leaves immediately the plug. We assume that the last case takes place and calculate the loss rate due to the loss mechanism considered.

As a result of nonaxisymmetry of the trap, the maximum magnetic field strength B_{max} on a given drift surface depends on the asimuthal angle ψ (see Fig. 2). This means that an untrapped ion[*], when drifting in the plug, can arrive at a field line where B_{max} is larger, than at initial field line and so this ion is trapped. Such a mechanism of trapping we call collisionless in contrast to collisional trapping, due to Coulomb scattering in the plug. To find a condition when collisionless trapping is predominant, let us consider untrapped ions in the plug having magnetic moment μ within an interval $\varepsilon/B_1 < \mu < \varepsilon/B_2$, where B_1 and B_2 are defined in Fig. 2. The drift motion converts these particles into the trapped ones during the time scale τ_d, whereas collisional trapping requires scattering by the angle $\sim \Delta\mu/\mu_0$, where $\Delta\mu = (\varepsilon/B_2) - (\varepsilon/B_1)$. If the following unequality holds

$$\nu\tau_d < \left(\frac{\Delta\mu}{\mu_0}\right)^2, \qquad (1)$$

where ν is the collision frequency of "central" ions, collisional trapping can be neglected. We assume below that the unequality (1) does hold; the opposite case is studied in[4].

To make the estimate of the loss rate we suppose that every trapped ion leaves the trap. Condition (1) allows us to neglect the change of magnetic moment during the time τ_d. To find the trapped particles density n_{tr} we note that at a given point of the plug different drift surfaces pass which correspond to the trapped ions with magnetic moment from the interval $\Delta\mu$, so that $n_{tr} \sim n\,\Delta\mu/\mu_0$, here n stands for the plasma density in the central cell[**]. The number of the "central" ions trapped in the plugs is of the order of $n_{tr}V_p$, where V_p is the plasma volume in the plug, and the flux of these ions to the wall can be estimated as follows:

$$q \sim \frac{n_{tr}V_p}{\tau_d}. \qquad (2)$$

Let us now define the confinement time τ_c of the plasma in an ambipolar trap due to the considered loss mechanism:

$$\tau_c \equiv \frac{nV_s}{q} \sim \tau_d\,\frac{V_s}{V_p}\,\frac{\mu_0}{\Delta\mu}, \qquad (3)$$

where V_s is the plasma volume in the central cell. In the formula (3) we have taken into account that $V_s \gg V_p$. This formula can be used for estimations of the confinement time if it gives values of τ_c which are much higher than ν^{-1}, i.e. when

$$\nu\tau_d\,\frac{V_s}{V_p}\,\frac{\mu_0}{\Delta\mu} \gtrsim 1. \qquad (4)$$

If the opposite unequality holds, the confinement time becomes comparable with the ion-ion collision time.

The formula (3) can be transformed into a more practical form

$$\tau_c \sim \tau_d R\,\frac{L_s r^2}{L_p^3}\,\frac{1}{\ln(L_p^2/r^2)}, \qquad (5)$$

if one uses expressions $V_s = L_s r^2 R$ and $V_p = L_p r^2$, where r is the plasma radius in the plug, R is the mirror ratio in the central cell, L_s and L_p are the lengths of the central cell and the plug, respectively. The origin of the last multiplier is connected with that in the paraxial approximation $\Delta\mu/\mu_0 \sim r^2/L_p^2 \ln(L_p^2/r^2)$ (see details in[4]).

In conclusion we emphasise that our estimates are based upon the assumption that every trapped ion comes to the wall. In this case as the result of the paper shows, collisionless losses from the plug may lead to a decrease of the confinement time to the values comparable with the ion-ion collision time. To exclude these losses one must design the magnetic field so that the drift surfaces of trapped ions would not leave plasma volume.

The authors thank Prof. D.D.Ryutov for useful discussions.

[*] By untrapped we call the ions with $\varepsilon > \mu B_{max}$.

[**] Here we have taken into account that the mirror ratio for the plugs is not large.

References

1. G.I.Dimov, V.V.Zakajdakov, M.E.Kishinevskij. Fiz. Plazmy 2, 597 (1976).
2. T.K.Fowler, B.G.Logan. Comments on Plasma Phys. and Cont. Fusion, 2, 167 (1977).
3. D.D.Ryutov. Proc. of the 1979 Varenna School on Plasma Physics, v. 1, p. 80 (1980).
4. L.S.Pekker. Preprint 81-45, Institute of Nuclear Physics, Novosibirsk, 1981.
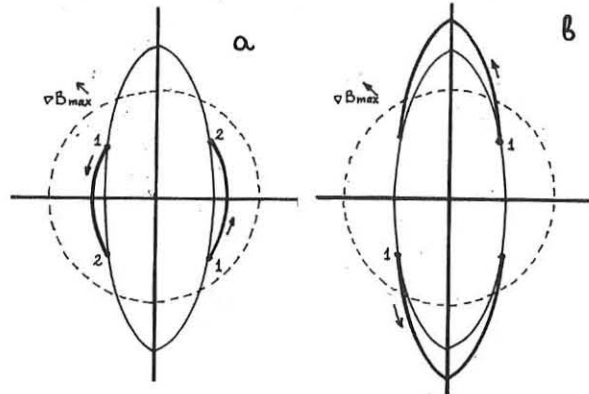
Fig. 1. The drift surface of a trapped ion (heavy line) and line $B_{max} = const$ (thin line) mapped along the field lines in the midplane of the plug. Dash line shows the wall of the chamber.
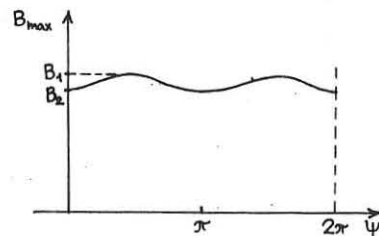
Fig. 2. Plot of B_{max} as a function of ψ on a given drift surface.

DISRUPTION OF MIRROR PLASMA INDUCED BY RESISTIVE DRIFT INSTABILITY

Shinji Hiroe, Toshiju Kunibe and Hidenori Akiyama

Institute of Plasma Physics,

Nagoya University,

Nagoya 464, Japan

ABSTRACT   We observe the disruption when high density plasma ($n_e \sim 10^{14}$ cm^{-3}, $\beta \sim 10$ %) is injected into symmetric mirror. This disruption has been observed only when resistive instability grows near the edge of plasma. The azimuthal mode numbers are $m = 0$ in the case of disruption and $m = 1,2,3,4$ in the case of resistive instability. The parallel wave length of resistive mode is much smaller than machine length.

Resistive instability plays an important effect on the confinement of Tokamak, RFP and Mirror. It is the purpose of this experiment to show that the growth of the resistive drift instability results in the disruption of plasma. The experimental set up is shown in Fig. 1. The field strength in the central section is almost constant as shown with the dotted line. To modify the constant field strength, iron rings are set inside the vacuum. As a result, the magnetic field strength is deformed as shown in Fig. 1 with solid line. At $z = \pm 31$ cm, there are another small humps due to the separation of iron rings where double probes, microwave horn and so on are placed. The high density plasma is injected along the magnetic field lines of forces with MPD arc jet.[1]

The density fluctuation is picked up with current probe connected to the double probe which are located at $z = -70$ cm, -31 cm, 0 cm, 31 cm and 164 cm. To measure the azimuthal phase, three probes are set at $z = -31$ cm. In order to measure the parallel wavelength, two probes are placed along the almost same magnetic lines of forces and the separation is 2.15 cm.

The typical plasma parameters are listed as follows: electron density (n_e) is 10^{14} cm^{-3}, the electron and ion temperatures (T_e and T_i) are 5 eV respectively, fuel gas is helium and β value is 0.1.

The photographs of density fluctuation are shown in Fig. 2. At the plasma center the density increases gradually, then abruptly decreases (we call this as disruption). The important phenomena is it that just before disruption the high frequency oscillation can be observed to grow rapidly (Fig. 2b). At $r = 4.0$ cm where the probe is far away from plasma, only a burst is observed (Fig. 2c). As shown in Fig. 2d another interesting result is the plasma dynamics along the field line. The density increases at the end of the vacuum vessel after the plasma inside the mirror abruptly disrupts.

As shown in Fig. 3, the average density profile just before the disruption is drawn with solid line. The density gradient is determined from this plots and the scale length of gradient is 1.5 cm. (The magnetic field curvature ranges from 5 to 20 cm.) The density profile just after the disruption is plotted with dotted line. Comparing these two profiles, the density profile just after the disruption becomes flat.

In order to measure the fluctuation level, the current probe are connected to data processer and data memory. The fluctuation level of disruption ($\tilde{n}_D$) and high frequency component ($\tilde{n}_H$) are plotted with open and closed circle, respectively. The fluctuation level ($\tilde{n}_D$) is large at the center and outside the plasma. The peak outside the plasma corresponds to the burst escaped accross the magnetic field lines of force (Fig. 2c). The high frequency component ($\tilde{n}_H$) is large near the edge of the plasma.

The another interesting result is the phase relation of the disruption which is picked up with the two probes (45°-probe and 0°-probe). Here 45°-probe is fixed and 0°-probe moves radially. The positive phase means that the phase of 0°-probe is faster than that of 45°-probe. We find that near the center of the plasma it is almost the same phase, but the phase changes abruptly to the inverse phase when 45°-probe moves beyond 2 cm. This tendency is same when we measure the phase defference between 0°-probe and 180°-probe and so on. This suggests that the azimuthal mode number of the disruption is $m = 0$, that is, the disruption does not go round.

However the high frequency instability goes round azimuthally and we have observed the instability of $m = 1,2,3$ and 4. It is one of the distinctive phenomena that the parallel wave length ($\lambda_{||}$) of the high frequency mode is about 26 cm and much smaller than the machine length.

We have surveyed the experimental results. The characteristics of the high frequency oscillations are itemized as follows.

1) The real frequency is in the range of the drift frequency due to the density gradient and almost 100 kHz. (Fig. 2)

2) The growth rate (γ) to real frequency ratio is near 0.3. (Fig. 2)

3) The azimuthal mode is $m = 1, 2, 3$ and 4.

4) The instability goes around in the direction of the electron diamagnetic drift.

5) The parallel wave length is $\lambda_{||} \simeq 26$ cm and is much shorter than the machine length.

6) The instability is excited at the edge of the plasma. (Fig. 3)

We identify this high frequency instability as the resistive drift instability. Following Mikhailovskii[2], the real frequency of this instability is the same as the electron drift frequency caused by the density gradient (ω_{ne}). We can calculate the growth rate to real frequency ratio with experimental parameters. The value of $\gamma/\mathrm{Re}\omega$ is $m^3/26$. At $m = 2$, $\gamma/\mathrm{Re}\omega = 0.3$ and 1 at $m = 3$. These values are the same order as the experimental value. At higher mode, $\gamma/\mathrm{Re}\omega$ is larger than 1 but in this case the transverse collisional viscosity of the ion becomes efficient and decreases the growth rate.

The characteristics of the disruption are itemized as follows;

1) When the disruption occurs, the plasma escapes abruptly along and across the magnetic field. (Fig. 2c and d)

2) The azimuthal mode number is $m = 0$. (Fig. 3)

3) When we stabilize the resistive drift mode by the line tying, disruption can't be observed.

4) The escape speed along the magnetic lines of forces is 10^7 cm/sec (Fig. 2d) and is almost equal to the Alfven speed of $n_e \sim 2 \times 10^{14}$ cm^{-3} and B $\sim$ 2kG.

For explaining this disruption with the mirror instability, the perpendicular to the parallel ion temperature ratio should be larger than 6. Such a large anisotropy is impossible in collisional plasma. The growth rate of the resistive flute mode is few tens microsecond which is 10 times larger than the time of the disruption. Moreover the value of $k_{||} v_A$ is larger than the growth rate where v_A is the Alfven speed. Moreover when we explain this strong instability as the flute mode, the result of $m = 0$ is impossible to be explained.

From the above discussion, this disruption can't be explained with the instability. We suggest that the equilibrium is possible to be destroyed due to the growth of the resistive drift instabilities.
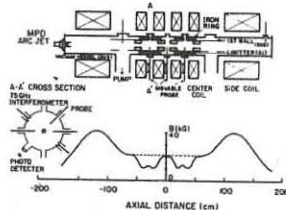
Fig. 1.   Schematic view of ASMIC-I device.
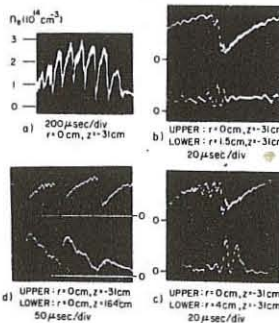
Fig. 2.   The typical photographs of the instabilities. The traces show the ion saturation current.
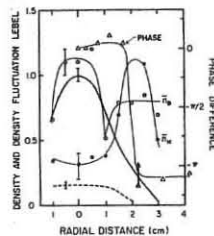
Fig. 3.   The average densities (ion saturation current) just before and just after the disruption are drawn with the solid and dotted line respectively. The density fluctuation levels of disruption ($\tilde{n}_D$) and the high frequency instability ($\tilde{n}_H$) are plotted by the open circle and the closed circle, respectively. The triangle shows the radial phase difference of the disruption.

REFERENCES

1) M. Inutake: Annual Review (1975 ~ 1980), Institute of Plasma Physics, Nagoya Univ.

2) A.B. Mikhailovskii: "Theory of Plasma Instabilities" Vol. 2, p97, Consultants Bureau, New York - London.

SUPPRESSION OF DRIFT-CONE INSTABILITY
IN PLASMA WITH A FINITE PRESSURE
BY A GROUP OF HOT ELECTRONS

V.V. Arsénin

I.V. Kurchatov Institute of Atomic Energy,
Moscow, USSR

Abstract. Drift-cone oscillations with a small incre-
ment in a mirror machine with the finite $\beta \lesssim 1$ can be sup-
pressed when a small group of high energy electrons with
the magnetic drift velocity close to the wave phase velo-
city is present there.

In a mirror machine with finite β , where the magne-
tic field rises from the axis, the directions of a wave
propagation as a drift-cone mode and a magnetic drift of
electrons are the same. Electrons with the magnetic drift
velocity, close to the wave phase velocity, exchange the
energy with the wave and the wave damping on resonance par-
ticles, at the sufficient amount of them, can become stron-
ger than the drive by non-equilibrium ions. If the elec-
tron distribution is a Maxwellian one the amount of re-
sonance electrons will be exponentially small and insuf-
ficient for stabilization in the most interesting case in
practice when $\beta_i = 8\pi n E_i/\beta^2 \lesssim 1$, $\beta_e \ll \beta_i$ (E_i -
average energy of ions). (But at $\beta_i \gg 1$ stabilization by
the Maxwellian "tail" is possible / [1] /). In this paper
we show that stabilization of plasma with such parameters
will be possible if electron distribution is not a Max-
wellian one, i.e. besides the population of cold electrons
there is a group of hot ones with a temperature of the or-
der of resonance energy, see Fig.1 (high energy "tails"
are obtained, e.g., at the electron cyclotron heating). The
case is considered when the oscillation drive by non-equi-
librium ions is weak (kinetic one) so that the increment
is considerably less than the frequency. The very oscilla-
tions were observed in the experiments at 2XIIB / [2] /. The
non-potentiality effect at the finite β (see, e.g.
/ [3] /), sensitivity of the increment to the ion distribution
shape, magnetic field inhomogenity effect / [4] / can result
in the increment smallness.

For the oscillations of interest with $K_{\parallel}=0$, $\kappa_\perp \rho_i \gg 1$,
$|\omega/\omega_{ce}| \ll 1$ (ρ_i - ion Larmor radius, ω_{ce} - elec-
tron cyclotron frequency) the dispersion equation obtain-
ed in an ordinary procedure with the finite β taken into
account (see, e.g. / [3] /) is expressed as:

$$1+\frac{\omega_{pe}^2}{\omega_{ce}^2}+\frac{\varpi K_y \omega_{pe}^2}{\omega \omega_{ce} \kappa_\perp^2}+\frac{\omega_{pe}^4}{\omega_{ce}^2(\kappa_\perp c)^2} = -i\left(\Im\varepsilon_e+\Im\varepsilon_i\right). \quad (1)$$

Here

$$\Im\varepsilon_e=-\frac{\pi\omega_{pe}^2\omega_{ce}\omega}{\kappa_\perp^2|K_y|\varpi_B}\left(1-\frac{\omega_{pe}^2}{\omega_{ce}^2}\frac{v_\perp^2}{2c^2}\right)\left[\frac{\partial F_e}{\partial(v_\perp^2/2)}+\frac{\varpi K_y}{\omega_{ce}\omega}F_e\right], \quad (2)$$

ω_{pe} - plasma frequency. $\varpi = \frac{d\ln n}{dx}(\varpi<0)$, $\varpi_B=$
$=\frac{d\ln B}{dx}$, $F_e\left(\frac{v_\perp^2}{2}, x+\frac{v_y}{\omega_{ce}}\right)$ - electron distribution
function. A flat model is used, X - axis is directed
towards the inhomogeneity Z - along the magnetic
field, the wave travels along y . We don't need the
expression for a small value $\Im\varepsilon_i$, which describes
the interaction of the wave with ions.

Let $E_i \ll m_e c^2$ and $\frac{\omega_{pe}^2}{\omega_{ce}^2}=\frac{m_e c^2}{2 E_i}\beta_i \gg 1$ then unity
in the left-hand side of eq.(1) can be omitted. Neglecting

the small right hand side of (1) one obtains

$$\omega = \frac{\varpi \rho_i \, K_y \rho_i}{\beta_i + \frac{m_e}{m_i}(K_\perp \rho_i)^2}\,\omega_{ci}, \quad (3)$$

so that ω will reach the ion cyclotron frequency ω_{ci}
(at which the drive of a wave by ions is possible)
if $|\varpi \rho_i| > 2\sqrt{\frac{\beta_i m_e}{m_i}}$; at $|\varpi\rho_i| \gg 2\sqrt{\frac{\beta_i m_e}{m_i}}$
one has

$$\omega = \frac{\varpi\rho_i \, K_y\rho_i}{\beta_i}\omega_{ci}. \quad (4)$$

Let us take into account the imaginary terms in
the right-hand side of eq.(1). Interaction with ions resu-
lts in an instability ($\Im\varepsilon_i <0$), and that with the re-
sonance electrons ($\Im\varepsilon_e >0$) results in a damping. The
stability criterion is as follows:

$$\Im\varepsilon_e > |\Im\varepsilon_i|. \quad (5)$$

Damping will be possible if the amount of resonance elec-
trons with the energy $\frac{m_e v_\perp^2}{2} = \frac{m_e \omega_{ce}\omega}{K_y \varpi_B}$ is sffici-
ently large. Using eq.(4) and the equilibrium equation
$\varpi_B \approx -\frac{\beta_i}{2}\varpi$ the value of energy can be written
as:

$$\frac{m_e v_\perp^2}{2} = \frac{4 E_i}{\beta_i^2}. \quad (6)$$

Take the energy distribution for the high energy
electron component as

$$\delta F_e = \frac{\delta n}{n}\frac{1}{E_e}\exp\left(-\frac{E}{E_e}\right), \quad (7)$$

where E_e is of the resonance energy order (6). Put (7),
(6) into (2) and express $\Im\varepsilon_i$ in terms of the incre-
ment Γ in the absence of stabilization ($\Im\varepsilon_e=0$): $\Im\varepsilon_i=$
$=-\frac{\Gamma}{\omega}\frac{\omega_{pe}^4}{\omega_{ce}^2(K_\perp c)^2}$, then the share of hot electrons
necessary for stability is obtained from eq.(5):

$$\frac{\delta n}{n} \gtrsim \beta_i^2 \frac{\Gamma}{\omega}. \quad (8)$$

Attention should be paid to the fact, that at $\beta_i < 1$
absorption of the wave mainly depends on the plasma inho-
mogeneity: in a sum $\left[\frac{\partial F_e}{\partial(v_\perp^2/2)} + \frac{K_y \varpi}{\omega_{ce}\omega}F_e\right]$ in eq.(2) the se-
cond term is $\sim \beta_i^{-1}$ times greater than the first one
describing the ordinary Landau absorption.

If the real increment Γ is sufficiently small in
comparison with a frequency ω so that the necessary
amount of hot electrons is also small, the energy den-
sity of these electrons $\delta n\cdot E_e$ can be much less than $n\cdot E_i$.
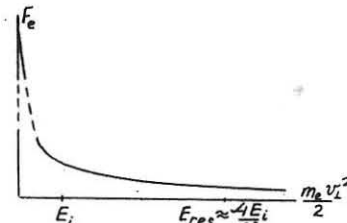
Fig.1. Electron
distribution
function

References

1. A.B. Michailovskii. Fizika plazmy (Sov.), 6, 55
   (1980).

2. W.C. Turner. Journal de Physique, 38, c 6-121
   (1977).

3. A.B. Michailovskii. Teoria plazmennich neustoichi-
   vostey, v.II, ch.15. M., Atomisdat, 1977.

4. G.N. Chulkov, A.V. Timofeev. Nucl. Fusion, 20,
   9 (1980).

Q-ENHANCEMENT IN NON-AXISYMMETRIC TANDEM MIRROR PLASMA*

T. KAMMASH
D. L. GALBRAITH
UNIVERSITY OF MICHIGAN
ANN ARBOR, MI 48109 USA

Abstract. The potential of Tandem Mirrors as fusion reactors depends to some extent on a satisfactory resolution of two critical issues. The question of ballooning stability and achievable betas on the one hand, and the attainment of large Q (ratio of fusion power to injected power) values in the presence of thermal alphas on the other. In this paper we find that a standard non-axisymmetric tandem (without thermal barriers) mirror has a particularly interesting transport properties that could lead to enhanced diffusion of thermal alpha particles across magnetic fields and a corresponding enhancement in the Q-value. This, of course, is to be reconciled with the ballooning instabilities that are associated with such configurations; but if high beta values based on finite Larmor radius stabilization can indeed be obtained, as indicated by some recent kinetic calculations, then the non-axisymmetric tandem can be viewed as a truly attractive fusion reactor.

The Tandem Mirror Concept[1,2] has been receiving increasing attention in recent years due to the fact that significantly larger Q-values can be obtained in this configuration than those obtained in the standard mirror. For MHD stability the plugs of a tandem device are generally chosen to have a minimum-B magnetic configuration. The resulting magnetic geometry, however, suffers from lack of axisymmetry which has been shown[3,4] to result in a considerable enhancement of particle losses across magnetic surfaces. This effect is attributed to the fact that in a non-axisymmetric magnetic field the amplitude of particle excursions with respect to these surfaces can substantially exceed the particles' Larmor radii. The collisions between particles can then lead to diffusion coefficients much in excess of their classical values as in the case of neoclassical diffusion in toroidal devices. The question immediately arises as to what impact will these enhanced particles losses have on the tandem as a power reactor. More specifically what effect will they have on its Q-value. We will show in this paper that inspite of the excessive losses of D-T ions, the enhanced cross-field losses of thermalized alpha particles relative to their axial losses is sufficiently large to result in a significant enhancement of the Q-value of the system.

To demonstrate this, we consider a nonaxisymmetric tandem mirror in which a mixture of equal amounts of D-T is assumed to undergo fusion reactions in the central cell only, and where the resulting alpha particles are assumed not to interact with the electrons and ions of the plugs. Ion losses due to charge exchange with the fuel provided by neutral injection is also included. Unlike most reactor studies of such a system we allow for different electron temperatures in the plugs and central cell so that the confining potential in the central cell can be written as[5]

$$e \Delta \varphi \simeq T_{pe} \ln \left[\frac{n_p}{n_e} \left(\frac{T_{ce}}{T_{pe}} \right)^{\nu} \right] ; \quad \nu \simeq 1/2 \quad (1)$$

where T_{pe} and T_{ce} are the electron temperatures in the plug and central cell respectively, and n_p and n_e are the corresponding values of the electron density in these regions. The particle and energy balance equations for the ions, electrons, and thermal alphas are given elsewhere[6] and will not be repeated here due to space limitations. It should be pointed out, however, that among other things these equations allow for physical exchange of electrons in the central cell and plugs as well as for energy deposition in the plugs by "transiting" electrons that pass from the central cell to the plugs and then reflected back into the central cell[7]. This is in sharp contrast to the usual approach in which no distinction is made between T_{ce} and T_{pe}. Under these circumstances it has been shown[8] that for reactor grade plasma in an axisymmetric tandem, a modest value of Q (< 2) is obtained due to the accumulation of thermal alpha particles in the system. Even in the presence of classical cross field diffusion a small Q-value is generated due to the fact that about 2.5 ions are displaced on the average for every thermal alpha particle that remains. As a result an enhanced Q-value can only be obtained if a mechanism for selective removal of thermal alphas can be found. The neoclassical diffusion in a non-axisymmetric tandem appears to provide such a mechanism.

As pointed out in references 3 and 4, the particles in the central cell of a tandem mirror undergo "neoclassical" transport across the magnetic field when their azimuthal drift frequency is much smaller than their bounce frequency. The diffusion becomes "resonant" when the drift and bounce frequencies are nearly equal, and becomes "stochastic" when the drift frequency far exceeds the bounce frequency. We have incorporated these diffusion coefficients in the system balance equations and have found that the dominant mechanism is that of the resonant diffusion in the plateau regime. The confinement time for such diffusion is given by[4]

$$\tau_{res} = \tau_{\|} \, L_{tr}^2 / \rho_c^2 \quad (2)$$

where $\tau_{\|} = L_c / U_{\|}$ is the axial bounce time, L_c is the length of the central cell, L_{tr} is the length of the transition region and ρ_c is the Larmor radius in the solenoidal field.

In addition to the above cross field diffusion the fusion

*Work supported by U.S. DOE

ions and alphas escape axially. This confinement time is given by the standard Pastukhov[9] formula which when extended to multispecies system can be written as[10]

$$\frac{1}{\tau_j} = \frac{4 \left\{ \frac{1}{x_j^2} e^{-x_j^2} + \frac{\sqrt{\pi}}{2 x_j^3} \left[1 - \Phi(x_j) \right] \right\}}{\sqrt{\pi} \, c_j^2 \tau_{\omega j} \sqrt{1 + c_j^2 / R_p} \, \ln \left(\frac{4 R_p}{c_j^2} + 2 \right)} \quad (3)$$

where

$$x_j = \left(\frac{z_j e \varphi}{T_j} \right) \quad (4)$$

and φ is the electrostatic confining potential, z_j is the charge number of the confined ions, and T_j is their temperature. The quantity $\Phi(x)$ is the standard error function, R_p is the plasma mirror ratio seen by the escaping ions, the constant c_j is given in terms of densities and masses of all the ion species in the system and $\tau_{\omega j}$ is the familiar 90% scattering time. For small alpha densities the constant c_j takes on the values 1, 2, and ~ 4 for electrons, ions, and alpha particles respectively.

In a steady state reactor whose plug plasma is heated by neutral injection E_{in}, and whose plug electrons are additionally heated by auxiliary means (Feaux) such as radiative heating, a measure of Q-enhancement due to non axisymmetry is shown in Fig. (1). The Q-value displayed has been maximized with respect to E_{in}, the injection energy, Feaux, and T_e, the fuel ion temperature in the central cell. We note that as the transition length L_{tr} becomes larger i.e., as we move in the direction of axisymmetry, the Q-value drops and asymptatically reaches the value it has when purely classical diffusion (uniform field) takes place. The primary reason for the Q-enhancement in the non-axisymmetric configuration is the bigger bite which "resonant" radial diffusion makes in the thermal alpha population than that which it makes in the ion population. The results indicate that the radial and axial confinements for the ions in the central cell are comparable while for the alphas the axial confinement is about 40 times longer than that in the radial direction. Thermal alphas are very well confined axially becuase of the higher potential they see due to their double charge.

Finally it may be argued that the Q-enhancement brought about by nonaxisymmetry may be offset by the severe ballooning instabilities which such geometry gives rise to. Although MHD studies[11] of such modes in tandems have placed serious limitations on achievable betas, recent kinetic studies of these modes[12] have indicated that high betas are indeed possible due to finite Larmor radius stabilization which seem to scale quite favorably with the length ratio (L_c / L_{tr}).

References

1. G. I. Dimov, V. V. Zakajdakov, M. E. Kishinevsky, Plasma Physics and Controlled Nuclear Fusion Research 3, 177 (1977) IAEA, Vienna
2. T. K. Fowler, B. G. Logan, Comments on Plasma Physics 2, 167 (1977)
3. D. D. Ryutov, G. V. Stupakov, Fiz. Plasmy 4, 501 (1978)
4. D. D. Ryutov, Varenna School on Plasma Physics, August 27-Spet. 8 (1979)
5. R. H. Cohen, I. B. Bernstein, J. J. Dorning, G. Rowlands, Nuclear Fusion 20, 1421 (1980)
6. T. Kammash, D. L. Galbraith, Proc. Int. Symp. Phys.Open Ended Fusion Systems, Tsukuba, April 15-18 (1980) p. 407
7. D. L. Galbraith, T. Kammash, Workshop on Ambipolar Potential Formation and Control in Bumpy Tori and Mirrors, Oak Ridge, May 11-12 (1981)
8. T. Kammash and D. L. Galbraith, Fusion Technology 2, 141 (1978) Pergamon Press
9. V. P. Pastukhov, Nuclear Fusion 14, 3 (1974)
10. D. L. Galbraith, T. Kammash, Plasma Physics 20, 959 (1978)
11. D. E. Baldwin, Bull. Am. Phys. Soc., 24, 966 (1979)
12. W. M. Tang, Bull. Am. Phys. Soc., 25, 893 (1980)

Q_{Max} vs R_{Ltr}

$\beta_c = 0.70 \quad \beta_p = 1.00$
$R_c = 7.49 \quad R_p = 1.07$
$B_{Max} = 17.655$
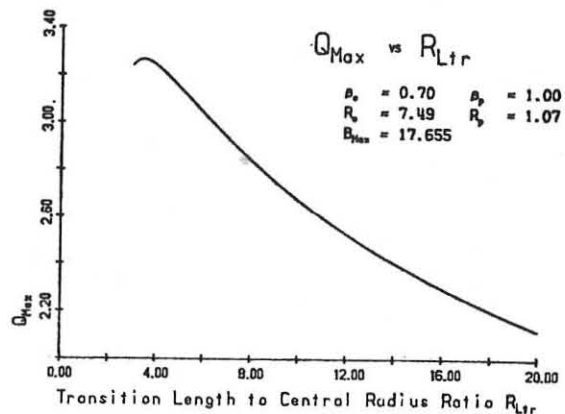
FIGURE 1

REB ENERGY DEPOSITION IN AN INHOMOGENEOUS PLASMA

P.Šunka, V.Babický, M.Člupek, K.Jungwirth, K.Koláček,
I.Kováč, G.O.Meskhi[x], V.Piffl, M.Řípa, J.Ullschmied
Institute of Plasma Physics, Prague, Czechoslovakia
[x])Lebedev Physical Institute, Moscow, USSR

Experimental results on heating of an inhomogeneous magnetized plasma by an intense REB ($W_b=0,1-1,2kJ$) are reported. The maximum heating efficiency $W_\perp/W_b=0,2$ was found. In the reflexing beam (virtual cathode) mode of operation, the energy of transverse motion of plasma particles reaches the value 400 Jm^{-1}, the kinetic pressure exceeding several times that of the external magnetic field ($\beta_i=4-6$). A theoretical model describing the dynamics of the overheated plasma was developed for correct interpretation of diamagnetic loop signals.

Measurements have been performed on the modified REBEX machine /1/ operated now at $U_b=500kV$, $I_b=60kA$, $t_b=100ns$, $W_b=1,7kJ$, $r_b=25mm$. The beam is injected into a (vacuum) chamber ($L_c=2$ m, R=75 mm) immersed in a mirror magnetic field ($B_o=0,5$ T, $B_m/B_o=1,5$) with a time delay t_d with respect to the firing of a plasma gun. The plasma gun located at $z=200$ mm generates a plasma cluster expanding along the magnetic field with a front velocity $2.10^4 ms^{-1}$. The average density of the short plasma column ($t_d=40$ μs) reaches the value of $3-4.10^{15} cm^{-3}$, while that of the nearly homogeneous plasma filling the whole interaction chamber at $t_d=150$ μs is $1-2.10^{13} cm^{-3}$ only. Local measurements of the plasma density and temperature by Thomson scattering were made at z=35 cm. The maximum density of $1-2.10^{15} cm^{-3}$ was found at $t_d=60$ μs. The scattered laser signal becomes negligible for $t_d<40$ μs the plasma being rather hollow in early stages of the plasma injection. The initial plasma temperature evaluated from scattering data lies within the range 1-3 eV, in a good agreement with the values deduced from the plasma diamagnetism and expansion velocity.

Since the h.v. diode is placed in a low magnetic field now ($B_d=0,2B_o\ll B_{\Phi b}$), a beam with a large angular spread is generated. The maximum beam energy injected through the plasma gun is $W_b=1,2$ kJ only. Due to the lowered injection efficiency also the reflexing beam phenomena are less pronounced if compared with the REBEX 1 experiment /2/.

The set of diamagnetic loops remained the basic diagnostic tool for evaluation of the plasma energy content /2/. A broad variety of diamagnetic signal waveforms reflects to a limited extent the complex nature of nonlinear processes of beam energy deposition and redistribution within the plasma region. Usually, signals with almost regular damped oscillations ($\omega<\omega_{ci}$) are observed. These oscillations were identified as magnetoacoustic configurational ones of the whole plasma column with the frequency $\omega_{ac}=g\frac{B}{R}\sqrt{\frac{2}{m(t)}}$, where $m(t)$ is the plasma mass per unit length and $g\to1$ for $R/r_b\gg 1$. They are effectively excited only if $\omega_{ac}t_b\lesssim \pi$. Aperiodic single pulses occur less frequently.

There are several possible channels for deposition of a part ΔW_b of the beam energy within the plasma region during the beam injection. In addition to the two-stream instability and return current dissipation representing sources of thermal energy predominantly for (some of) the plasma electrons, some beam electrons can be trapped inside the plasma. Finally, a part of energy can be acquired by expansion of the short-living hot component (rotating or oscillating beam). A part of ΔW_b is exchanged between the thermal and the mechanical energy of the oscillating column and the additional energy ΔW_B of the magnetic field frozen into the plasma. Both the energy losses e.g. by a longitudinal expansion $l=l(t)$, the energy dissipation $\frac{dQ}{dt}=\alpha \Delta W_B$ accompanying the magnetic field diffusion into a finite-conductivity plasma and the resonant ion heating ($\omega_{ac}\approx\omega_i$) result in damping of the oscillations.

The above mentioned processes are included in the thermodynamical model yielding a fairly general relation for the decrease $\Delta\Phi(t)$ of the magnetic flux through a diamagnetic loop encircling the plasma column ($t\gtrsim t_b$)

$$\Delta\Phi(t)\frac{B_o}{8\pi} = G \frac{l(t_b)}{l(t)}\left[\frac{q_b}{2} - K \exp\left(-\frac{\alpha}{4}t\right)\cdot\cos\left(\varphi + \int_{t_b}^{t}\omega_{ac}(t)dt\right)\right]$$

Fortunately, the efficiency $\Delta W_b/W_b$ can be determined from the diamagnetic data independently of the way of the beam energy deposition ($\Delta W_b=\int^{l(t)}q_b dz$, $G\to1$ for $R/r_b\gg 1$). The model accounts also for the possibility of depositing the beam energy only inside the central part of the plasma column. Measurements of the position of a hot plasma core boundary by a miniature movable magnetic probe and preliminary results of soft X-ray analysis support the reliability of interpretation of the diamagnetic signals. The existence of a short-living hot component is manifested by abruptly vanishing single pulses detected by the diamagnetic loops placed at the end of the plasma column.

Fig.1 shows radial profiles of the magnetic field at the instant of maximum expansion of the plasma column ($t=100ns$). The maximum hot core radius is then roughly twice that of the beam (for $t_d=40$ μs), the magnetic field being almost displaced at the axis. The total energy stored in a plasma (Fig.2) reaches 320 J at $t_d=50$ μs and it decreases to 160 J at $t_d=150$ μs. The maximum plasma diamagnetism was found at z=70 cm, $t_d=30$ μs, the corresponding energy deposited per unit length being as high as 420 Jm^{-1}. Although the energy transfer efficiency $\Delta W_b/W_b$ remains almost constant (20 per cent) at varying t_d, the deposited energy density w_b is maximum for short plasma columns in the present experimental setup. For a fixed regime (propagating or oscillating beam) the deposited energy scales linearly with W_b in the region of $W_b=0,1 - 1,2$ kJ.
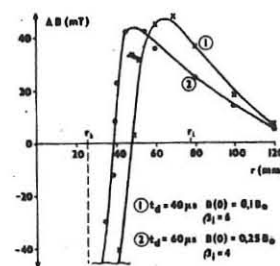
Fig.1
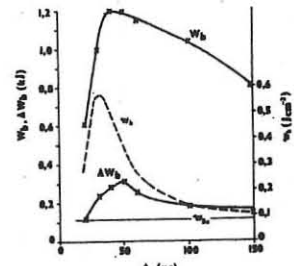
Fig.2

/1/ Annual Progress Report 1979-80, IPP CZ-239

/2/ Proc. 3rd Topical Conf. on Electron and Ion Beam Res. and Technology, Novosibirsk 1979, Vol. I, p. 103

PROPAGATION OF A RELATIVISTIC ELECTRON BEAM THROUGH GAS AND PLASMA

G.C.A.M. Janssen, P.H. de Haan, H.J. Hopman,
E.H.A. Granneman, A.G. Shkvarunets[*]
FOM-Institute for Atomic and Molecular Physics,
Amsterdam, The Netherlands
Association Euratom-FOM

ABSTRACT. Studies have been performed on the transport of a relativistic electron beam (REB) through gas (190 Pa=1.5 Torr, H_2) and through plasma ($n_e \sim 10^{20}$ m^{-3}). Stable propagation was observed in both cases and beam energy losses amounted to ~2.5% per meter. In case the beam is injected into gas a cold weakly ionized plasma ($n_e \sim 2 \times 10^{20}$ m^{-3}) is formed with a temperature $kT_i \sim 2$ eV, limited by line radiation losses. But when the beam is injected into plasma the temperature, $kT_e \sim 100$ eV, is limited by axial electron heat conduction losses. In both cases a stationary state is reached in which the beam energy transfer equals the plasma losses. Experimental data are compared to a computational model.

EXPERIMENT. A REB (850 keV, 6 kA, 3.5 cm fwhm diam. 50-400 ns pulse-length) is injected into a drift tube, 2.5 m long and 0.12 m diam. A 0.21 T magnetic field B_o with short mirrors of 0.3 T is applied. The driftchamber is either filled with hydrogen gas of 190 Pa pressure, or with plasma created by a discharge in 0.2 Pa hydrogen gas between the wall and two ring shaped electrodes, situated near the magnetic field mirrors. In the latter case the REB is injected into the afterglow, for which the plasma density $n_e < 10^{20}$ m^{-3}.

Available diagnostics provide a time resolved measurement of the width of spectral lines (H_α, H_β) and of the beam energy distribution. Plasma density is determined from the attenuation of an H^o beam. In addition there are Rogowski coils and diamagnetic loops.

The beam energy distribution can be measured with two devices. A magnetic energy analyzer accepts electrons with the angle between particle velocity and magnetic field $0 < \theta < 2^o$ [1]. A second analyzer accepts electrons with $10^o < \theta < 60^o$. This is a new type of analyzer. It consists of a slit, a hole and a collector plane [2]. When placed in a magnetic field, the combination selects the helical particle orbits in such a way that there is a one to one correspondence between points in the collector plane and (γ, θ), where γ is the electron energy, $\gamma = 1 + eV_b/mc^2$.

MEASUREMENTS. *INJECTION INTO PLASMA*. Optimum plasma heating is observed at $n_e \sim 10^{20}$ m^{-3}. Initially the return current fully compensates the beam current. However, the first 60 ns the return current decays rapidly due to turbulent friction, $\nu_{eff} \sim 6 \times 10^9$ s^{-1}. For later times the net current is almost constant in time and $\nu_{eff} \lesssim 5 \times 10^8$ s^{-1}. The first 150 to 200 ns the diamagnetic signal rises roughly linearly in time. The maximum value obtained suggests $nkT_i = 2.6$ kJ m^{-3}. For later times $nkT_\perp$ is proportional to the beam power P_b, which is decreasing in time. After the beam has been switched off, the diamagnetic signals decay proportional to $t^{-2/5}$, which is indicative of electron heat conduction as the main source of plasma energy loss. The time constant is ~200 ns.

INJECTION INTO GAS. Plasma formation takes place during the 20 ns rise of the beam current. The plasma density saturates at 2×10^{20} m^{-3}, as measured from H_β line widths. The H_α line width yields an atom temperature $kT_o=2$ eV, essentially constant in time. Initially there is a full current compensation. The return current decays monotonically at a rate corresponding to a characteristic collision frequency $\nu_{eff} = 8 \times 10^9$ s^{-1} which is predominantly explained by electron-neutral collisions (p=190 Pa). Beam energy loss starts at a high 12%, decreasing monotonically during the pulse. The time averaged loss is 6% over the 2.5 m length of the drift tube.

COMPUTATIONAL MODEL. The model we use is a substantial extension of the work of Hammer et al. [3]. It combines four atomic rate equations, to calculate the densities of the plasma components (e^-, H^o, H^+, H_2^+, H_3^+ and H_2), with four energy equations, to determine the temperatures of e^-, H^o, H^+ and the weighted sum of $H_2^+ + H_3^+$. The latter equations describe the energy transfer from the beam to the plasma and the energy exchange between the plasma components. The induced plasma return current is calculated self consistently and thus the strong coupling between beam and plasma current is included in the model.

Beam energy input into the plasma is caused by the decay of the return current and by the dissipation of high frequency waves excited in the interaction between beam and plasma electrons. The energy transfer through high-frequency waves, denoted by P_{wv}, see Fig. 1, is calculated by assuming that all beam electrons loose the amount of energy required to maintain the amplitude of the waves at the saturation level, as estimated by Thode [4] in the hydrodynamic limit. Ohmic dissipation of the return current is due to classical collisions, P_{c1}, and anomalous

resistivity associated with ion acoustic turbulence, P_{ia}, and with the presence of the high frequency waves, P_{ee}. The saturation level of the ion acoustic turbulence is determined by non-linear Landau damping. Plasma losses include bremsstrahlung, line radiation, P_{line}, and the dissociation and ionization of the neutral components H^o and H_2, P_{ion}. This zero-dimensional, time dependent model is well suited to describe the evolution of the beam-plasma system at low degrees of ionization. With decrease in gas density, the electron temperature rises and temperature gradients start to play a role. The largest profile dependent loss term is the electron heat conduction along the applied magnetic field. The model is presently being adapted to include this term.

RESULTS. *INJECTION INTO GAS*. Calculations show that the system reaches a stationary state at $t \sim 100$ ns. Then $kT_e \sim 2$ eV, $kT_i = kT_o = 1.5$ eV and $n_e \sim 2 \times 10^{20}$ m^{-3}, in agreement with measurements. The most abundant ion is H_3^+. Atom density is ~50 n_e. Moreover the model predicts correctly the time dependent behaviour of ν_{eff}, or the plasma return current, and beam energy loss. Fig. 1 presents the calculated power balance of the electrons. Beam pulse length in this case is 150 ns. It is seen that ion acoustic turbulence P_{ia} is turned off rapidly when plasma drift velocity approaches the ion acoustic velocity for $t > 25$ ns. Energy transfer is carried by classical resistivity P_{c1}, and hf wave dissipation, P_{wv}. Plasma losses are due to radiation (65%) and ionization plus dissociation (30%). Fig. 2 presents the energy input E to the plasma electrons as function of pressure p; $E=\int Pdt$; integrated over a 500 ns time interval. E_Ω represents the ohmic dissipation due to classical and anomalous resistivity. Computed and measured values follow the same trend as function of pressure. E_{tot} is the sum of E_Ω and E_{wv}, where E_{wv} is the electron energy gain from the hf wave dissipation. Comparison of measured beam energy loss (17.4 kJ m^{-3} at 190 Pa) with total computed energy input (20.2 kJ m^{-3}) indicates that the hf wave excitation is of hydrodynamic type and not kinetic.

INJECTION INTO PLASMA. The application of the model to this case is restricted because of the lack of loss terms. Conclusions can only be presented for short beampulses, such that kT_e remains smaller than ~100 eV. The ion acoustic instability is turned off after ~40 ns. This might explain the sudden change in ν_{eff} at t=60 ns, observed in the experiment. The dominant energy transfer mechanism is the dissipation of the hf waves. Because P_{line} is negligibly small all energy remains in the plasma. Therefore the calculations give a linear increase in nkT with time, in agreement with the measurement.

REFERENCES

[1] Jurgens B., de Haan P.H., Hopman H.J., de Jagher P.C., Phys. Rev. Lett. 39 (1977) 936.
[2] Shkvarunets A.G., to be published.
[3] Hammer D.A., Gerber K.A., Ali A.W., IEEE Trans. Plasma Sci. 7 (1979) 83.
[4] Thode L.E., Phys. of Fluids 19 (1976) 831.
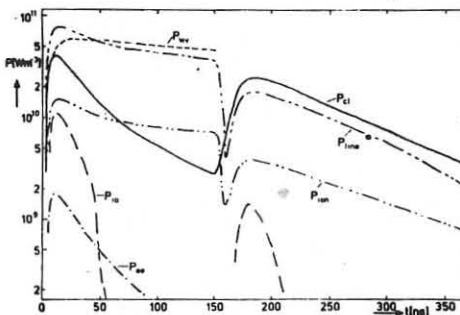
Fig. 1
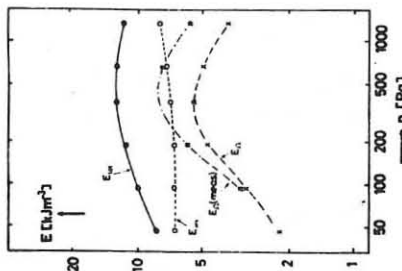
Fig. 2

PRINCIPAL RESULTS OF THEORETICAL AND EXPERIMENTAL STUDIES
OF ELECTROMAGNETIC TRAPS

Yu.S. Azovskij, V.I. Karpukhin, A.D. Komarov, O.A. Lavrent'ev, V.A. Maslov, M.G. Nozdrachev, N.N. Sappa, and I.A. Stepanenko

Kharkov Institute of Physics & Technology, Ukr. Acad. Sci., Kharkov, USSR

One of the most important problems in controlled thermonuclear fusion is to provide sufficiently long confinement time of high-temperature plasma particles and energy in a certain volume. In electromagnetic traps [1,2] this task is solved using a combination of electric and magnetic fields. Plasma ions are trapped in the potential well produced by electron space charge. In this confinement ion losses are only determined by diffusion in velocity space and the ion lifetime in the potential well grows exponentially with the increasing ratio of the potential barrier height to the ion temperature. For thermonuclear plasma parameters $n_e = 10^{20} m^{-3}$, $T_i = 10$ kev, it amounts to several tens of seconds already at $\Phi_i/T_i \approx 8$ [3-6]. Plasma electrons in the electromagnetic trap are confined by the magnetic field in the form of a spindle cusp and externally applied electric potential plugging the cusps. The electron lifetime is determined by two processes: electron diffusion across the magnetic field and electron escape over the barrier along the magnetic lines of force.

Experimental studies of plasma accumulation and heating in the "Yupiter-1A" and "Yupiter-1M" machines [7,8] show that the main channel of ion losses is through the ring cusp; the ion losses through the point cusps being approximately an order of magnitude smaller. The time for ion escape through the ring cusp is inversely proportional to the plasma density in the trap and equals ≈ 2 ms which is indicative of collisional nature of these losses. The time of ion escape through the point cusp does not depend on the plasma density, but is determined by the "geometric" time of ion flowing out through the point cusp. The main channel of electron losses is represented by diffusion across the magnetic field. The electron diffusion in velocity space rapidly decreases with the increasing plugging potential and is negligibly small for the operating conditions under study. The electron lifetime limited by the transverse diffusion is $\lesssim 1$ ms with the plasma density being $2 \cdot 10^{12} cm^{-3}$ and electron temperature 0.1 kev.

Computer simulation of plasma accumulation and heating in the electromagnetic trap in the approximation of classical transfer coefficients yielded a satisfactory agreement with experiment [9]. The computer simulation was also used to calculate steady-state plasma parameters for the designed "Yupiter-2" trap [10,11].

One of the principal processes limiting the plasma density in the electromagnetic trap is electron accumulation in the cusps and the resulting decrease of the potential barrier for ions. The space charge potential sag ΔU in the ring cusp and in the point cusps of the trap was measured experimentally. The ΔU –dependence on the plasma accumulation time is shown in Fig.1 (1:in the ring cusp; 2:in the point cusp). Initially, before the plasma is generated, the potential sag due to electron circulation reaches its maximum value of 1.9 kv in the point cusp upon injection of 4 kev electrons. In the course of plasma accumulation the ΔU values fall off to 0.4 kv in the ring cusp and to 0.6 kv in the point cusp. Fig.2 shows the potential sag in the ring cusp (1) and in the point cusp (2) as a function of the electron injection current for different times : a) 3.9 ms, b) 4.1ms (after switching off the beam). With the increasing plasma density –dashed curve– the potential sag increases slower than the density. This experimental result is of principal importance in estimation of the plasma parameters expected for the next generation of electromagnetic traps.
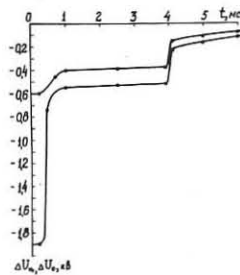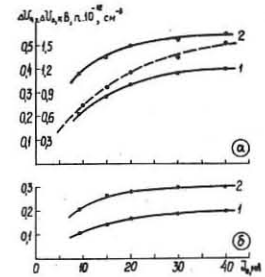
Fig. 1   Fig. 2

REFERENCES

1. Lavrent'ev O.A. Magnetic Traps. Kiev, 1968, issue 3, p.77-147.

2. Ware A.A., Faulkner J.E. Nuclear Fusion, 1969, 9, p.353-361.

3. Dolan T., Larsen J., Stansfield B.L. Can.Journ.Phys., 1975, v.53, p.2341-2347.

4. Sizonenko V.A., Stepanov K.N. Zh.Tekhn.Fiz., 1975, v.45, N 4, p.741-745.

5. Yushmanov E.E. Fizika Plazmy, 1978, v.4, issue 1, p.23-33.

6. Pastukhov V.P. Fizika Plazmy, 1978, v.4, issue 3, p.560-569.

7. Zalesskij Yu.G., Komarov A.D., Lavrent'ev O.A., Naboka V.A., Nazarov N.I., Potapenko V.A., Stepanenko I.A. Fizika Plazmy, 1979, v.5, issue 5, p.954-957.

8. Azovskij Yu.S. et al. Fizika Plazmy, 1980, v.6, issue 2, p.256-263.

9. Karpukhin V.I., Lavrent'ev O.A., Sappa N.N. Ukr. Fiz. Zh., 1978, v.23, N 8, p.1294-1300.

10. Lavrent'ev O.A. Ukr.Fiz.Zh., 1979, v.24, N 7, p.1019-1023.

11. Karpukhin V.I., Lavrent'ev O.A., Sappa N.N. Ukr. Fiz.Zh., 1980, v.25, N 7, p.1082-1088.

PLASMA LEAK WIDTH OF LINE- AND POINT-CUSP LIKE MAGNETIC FIELDS

Hideo KOZIMA, Shinji KAWAMOTO and Keiichiro YAMAGIWA

Department of Physics, Faculty of Science, Shizuoka University, Shizuoka 422, JAPAN

Abstract

Using permanent magnets, we formed arrays of magnets which generate line- and point-cusp like magnetic fields. Plasma parameters around those magnetic cusp fields were measured with a Langmuir probe in Ar and He plasmas. Leak width was defined by the half-value width of electron density peak at the cusp. The leak width of the line-cusp field was nearly equal to the hybrid gyrodiameter $2(m_e m_i T_e T_i)^{1/4}/eB$. Periodic variation of the magnetic field strength along the line-cusp induced modulation of the leak width along the cusp if the period was comparable or larger than the hybrid gyrodiameter. It is found for the first time that the leak width of the point-cusp field is qualitatively different from and is very large compared with that of the line-cusp field.

One of important problems of plasma confinement by cusped magnetic fields is the high loss rate of plasma along the magnetic field lines[1,2]. Electrostatic pluggings were investigated to reduce the loss by externally imposed[3] and self-consistent[4] potentials. At the present time, the leak width of the line-cusp field itself is in a controversy and proposed values for it spread from the electron gyrodiameter to the ion gyrodiameter through the hybrid gyrodiameter $2\rho_h = 2(m_e m_i T_e T_i)^{1/4}/eB$[4,6~8]. It is surprising to know that leak widths of the order of $2\rho_h$ are consistently explained by the concept of Rosenbluth sheath[9,1,2] by a simple model. In this work, we present new experimental data with permanent magnet arrays[7,10] to generate line- and point-cusp like fields. Preliminary result was published elsewhere[8].

Planer arrays of permanent magnets made of ferrite with hight 15 mm and diameter 20 mm were used. The field strength on the pole face was about 1500 G at the center. To generate line-cusp like fields, magnets in an array were placed with a separation d and the same polarity. The magnet arrays were arranged parallel each other with a separation of 20 mm between them as shown in Fig.1(a). Varying d, we could modulate the field strength along the cusp. For point-cusp like fields, magnets

Fig. 1

were placed equidistantly on a square lattice with a lattice constant D+d alternating polarity as shown in Fig.1(b).

Argon and Helium plsmas were produced in the left-hand part of the device as shown in Fig.2 using hot cathode discharge from thoriated tungsten filaments with a diameter

0.15 mm. Discharge voltages were 25 V for Ar and 45 V for He plasmas. The separation distance d was taken as 0, 10 and 15 mm for line- and 20 mm for point-cusp like fields.
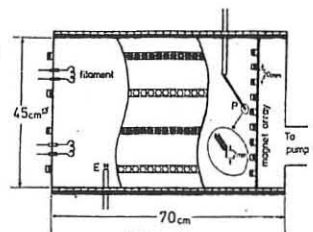
Fig. 2

Typical plasma parameters are as follows; $n_e = 10^8 cm^{-3}$, $T_e = 5$ eV and $T_i \fallingdotseq 0.5$ ev for Ar and $n_e = 10^8 cm^{-3}$, $T_e = 10$ eV and $T_i \sim 1$ eV for He plasmas. Data were taken with a cylindrical Langmuir probe (2×0.3 mm ϕ) parallel to the magnet face in the xy-plane at z = 10 mm above the face plane.

The half-value width of the density distribution peak at the cusp for a line-cusp like field with $d < 5$ mm is independent of the position and with d from 5 to 10 mm is
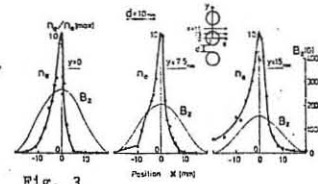
Fig. 3

given approximately by $2\rho_h$ at the position. Plots of density distribution and magnetic field strength around a line-cusp like field are shown in Fig.3 for a magnet array with d=10 mm. Half-value width of the distribution curves for y = 0, 7.5 and 15 mm are 4.5, 5.0 and 8.0 mm, respectively. On the other hand, the hybrid gyrodiameters at corresponding points are 4.3, 4.9 and 6.1 mm in good agreement with the half-value widths. Similar results were obtained for He plasmas.

In the case of $d \gtrsim 15$ mm the half-value width is very large compared with $2\rho_h$ at the corresponding position. Similar behavior was obtained for point-cusp like field as shown in Fig. 4.
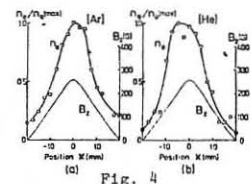
Fig. 4

Thus, experimental data given in this report show clearly the drastic change of the leak width of cusps if we go to point-cusp like field (and line-cusp like field with large modulation) from the line-cusp like field with small modulation.

References

1) I.Spalding, in "Advances in Plasma Physics" edited by A.Simon and W.B.Thompson (Wiley, N.Y., 1971) Vol.4. 2) M.G.Haines, Nucl.Fusion 17, 811(1977). 3)T.J.Dolan, B.L.Stansfield and J.M.Larsen, Phys.Fluids 18, 1383(1975). 4)N.Hershkowitz, J.R.Smith and H.Kozima, Phys. Fluids 22, 122(1979). 5)S.Kogoshi, K.N.Sato and T.Sekiguchi, J. Physics D11, 1057(1978). 6)K.N.Leung, N.Hershkowitz and K.R.MacKenzie Phys. Fluids 19, 1045(1976). 7)T.Fujita, T.Ohnuma and S.Adachi, Proc. Int. Conf. Plasma Phys.(Nagoya) 1, 168(1980). 8)H.Kozima and S.Kawamoto, Rep. Fac. Science, Shizuoka Univ. 15, 7(1981). 9)M.N.Rosenbluth, in "Magnetohydrodynamics" edited by R.Landshoff (Stanford Univ. Press, 1975). 10)N.Hershkowitz, J.R.Dekock and C. Chen, Nucl. Fusion 20, 695(1980)
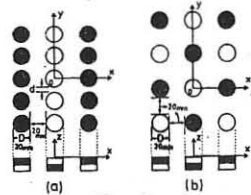
END LOSS LIMITATION IN A LINEAR THETA-PINCH
BY MEANS OF MAGNETIC MIRRORS

Zukakishvili G.G., Salukvadze R.G., Tikhanov E.K.,
Ryzhkov V.N., Chkuaseli Z.D.

Sukhumi Institute of Physics and Technology of the
State Committee on Utilization of Atomic Energy,
Sukhumi, USSR

I. INTRODUCTION. Several ways of end-loss limitation in gas-dynamical traps have been proposed and partially investigated during recent years. Among these methods are: mechanical plugs /I/, Ryutov multimirror systems with stationary fields /2/ and multimirror systems with dynamical fields using plasma electrodynamic stoppering /3/. A gas-dynamic flux can be successfully limited by means of mechanical plugs, however, energy losses due to longitudinal electron heat conduction couldn't be practically suppressed.

As a matter of fact, both channels of losses can be suppressed by means of magnetic mirrors. The theoretical conclusion has been experimentally verified by using Ryutov's multimirror system for alkaline and hydrogen plasmas with $n \leq 10^{15} cm^{-3}$. Experimental data concerning plasma electrodynamical stopping are unknown to the authors. In this respect, further experimental studies on end-loss suppression by means of magnetic mirrors for high density plasmas are of great interest.

2. The present paper deals with preliminary experimental results on MHD instability studies and mass and energy end-loss limitations using a single quasistationary plug. Dinamical and quasistationary multimirror systems are supposed to be investigated from now on.

Fig.I shows the device schematic. A theta-pinch is formed by a single-turn solenoid I6,5 cm in length and II cm in diameter (I). Field strengths have been varied within the range of I4 to 30 kG their halfcycle being from 7 to 9,5 μs. Plasma streaming out from the pinch ends spreads in a slightly corrugated quasistationary magnetic field with a halfcycle of 200μs and the strength H_T= 8 – –20 kG; the field is generated by three-turn solenoids (2). The theta-pinch is switched on close to the H_z field maximum. A small-power theta-pinch has been used to heat the plasma preliminarily. The same figure shows field distributions along the axis for H_T =20 kG, H_z = 30 kG(3); H_T =20 kG, H_z =20 kG(4); H_T=20 kG, H_z =I4 kG (5); H_T=20kG, H_z=0 (7) and H_T =7kG, H_z = 0(7). The quasistationary magnetic field, H_T, which propagates into the theta-pinch region and exerts a considerable influence upon plasma formation, is compensated by an initial reverse quasistationary field $-H_{zo}$. D_2 serves as an operating gas. Initial pressures are: P_o = 10^{-I} – 10^{-2} Torr. Pinch plasma densities amount to n=2 . 10^{16} – 10^{17} cm^{-3}.

Plasma dynamics have been investigated by means of magnetic, electrical and diamagnetic probes and streak-camera pictures as well. Electron temperatures have been measured by filtering soft x-rays.

3. Principal Results. 3.I. Plasma is stable only when the initial trapped magnetic flux is equal to zero or has a small negative value. A flute-type instability is developed in the plasma with a trapped positive flux while it (plasma) propagates through the mirror region. Fig.2 shows plasma end pictures for H_z=30kG, P_o=10^{-I}Torr and a zero trapped flux. Figs.2a and 2b correspond to H_T=8kG and 20 kG, respectively. Under these conditions, a mirror field configuration is realized only at the beginning and at the end of the H_z halfcycle. The plasma jet propagation velocity does not depend upon the H_T value and is equal to 7.10^6cm/s. (The moment of plasma outstream from the stopping coil ends and its contact with the wall are well seen in the tenth

frame pictures). However, the total number of the particles outstreaming from the ends is three times decreased on increasing the H_T field from 8 to 20 kG, according to diamagnetic measurements. The jet deceleration is observed only on increasing the mirror ratio up to the value of H_T/H_z=1,5.

3.2. Plasma electron temperature is essentially increased as a result of switching the mirror fields on. Thus, e.g., for H_z=30 kG, P_o=10^{-2}Torr in pure theta-pinch, T_e becomes 40-60 eV, while for H_T = 8-20 kG, T_e goes up to I50 eV, and has a slight dependence upon H_T. Fig.5 shows traces for H_z, D_β line, soft X-rays (X-ray) and the diamagnetic signal (D_m) measured at the end of the stopping coil. Rise in soft X-ray radiation duration and intensity is well seen with the H_T field turned on. The soft X-ray emission begins to fall down with the diamagnetic signal appearing and is connected with a longitudinal electron thermal conductivity established as a result of a plasma contact with the discharge chamber wall.

REFERENCES

I. Energy and Particle-Confinement Properties of an End-Plugged Linear Theta Pinch. R.J.Comisso, R.R. Bartsch, C.A. Ekdahl, K.F. McKenna and R.E. Siemon. Phys.Rev.Lett., 1979, v.43, No 6, p.442-445.
2. Theory and Calculations of Nonmagnetic Dense- Plasma Confinement. C.E. Vekshtein, V.V. Mirnov, D.D. Ryutov, P.Z. Chebotarev. 6th Conf. Proceedings. Berchtesgaden, 1976. IAEA-CN-35/E2I.
3. End Plugging of a Linear Theta Pinch by Pulsed Mirrors. Amiya K. Sen. Institute of Plasma Physics, Nagoya University, Japan. IPPY-346, July, 1978.
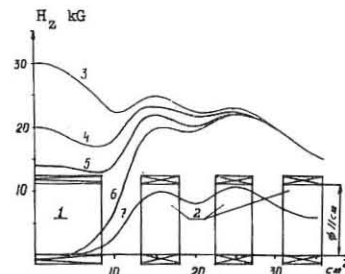
Fig.1. Device diagram and paraxial magnetic field distribution
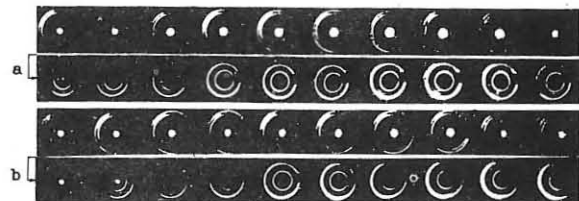
Fig.2. Pictures of the discharges P_o=10^{-I}Torr, H_z=30kG, a) H_t=8kG, b) H_t=20kG. Duration of the film exposure is 0,5 μs
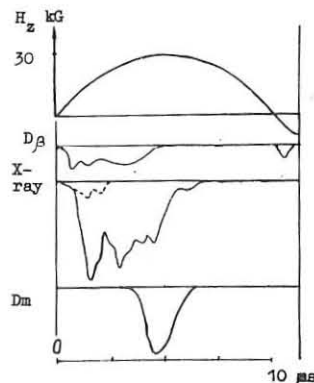
Fig.3. Theta-pinch discharge oscillograms for H_z=30kG, P_o=10^{-I}Torr. Low X-ray radiation curve for H_z=30kG, H_t=0 is dashed

PLASMA CONFINEMENT IN THE TANDEM MIRROR EXPERIMENT*

E. B. Hooper, Jr., S. L. Allen, T. A. Casper, J. F. Clauser,
P. Coakley,† F. H. Coensgen, D. L. Correll, W. F. Cummins,
J. C. Davis, R. P. Drake, J. H. Foote, A. H. Futch, R. K. Goodman,
D. P. Grubb, G. A. Hallock,** R. S. Hornady, A. L. Hunt,
C. V. Karmendy,†† A. W. Molvik, W. L. Pickles, G. D. Porter,
P. Poulsen, T. C. Simonen, B. W. Stallard, O. T. Strand†

Lawrence Livermore National Laboratory, Livermore, CA

ABSTRACT. Plasma confinement in the Tandem Mirror Experiment (TMX) is described. Axially confining potentials are shown to exist throughout the central 20-cm core of TMX. Axial electron-confinement time is up to 100 times that of single-cell mirror machines. Radial transport of ions is smaller than axial transport near the axis. It has two parts at large radii: nonambipolar, in rough agreement with predictions from resonant-neoclassical transport theory, and ambipolar, observed near the plasma edge under certain conditions, accompanied by a low-frequency, m = 1 instability or strong turbulence.

INTRODUCTION. The demonstration of successful enhancement of axial plasma confinement by ambipolar potentials in the TMX end cells[1,2,3] has led to a study of the total plasma confinement. Near the axis, plasma axial losses from the central cell exceed the radial losses; near the outer edge radial losses are comparable or dominant.

AXIAL ION CONFINEMENT. Here we demonstrate that confining potentials are generated throughout the cross section of TMX. The central-cell-to-ground potential, ϕ_e, was determined from the energy of secondaries caused by plasma ionization of a heavy-ion beam.[4] The plug-to-ground potential, ϕ_p, was determined from the minimum energy of ions which escape through the plugs to the end walls. The difference, ϕ_c, is in approximate agreement on axis with the potential predicted by the Boltzmann relation, $T_e \ln(n_p/n_c)$, where subscripts p and c refer to the plug and central-cell values. Good agreement is seen, out to a radius of 15 cm, in the radial potential profile shown in Fig. 1. Beyond 15 cm the comparison is poor, although the uncertainties are large. Central-cell ion confinement is found to be enhanced above that of magnetic mirrors by this potential, approximately as predicted by the Pastukov formulas applied to the tandem system.[5,6] Detailed calculation yields good agreement with measurement when the heating of ions by rf generated in the end plugs at the ion-cyclotron frequency is taken into account.[3]

AXIAL ELECTRON CONFINEMENT. The electron energy confinement time in TMX was a factor of up to 100 above that obtained in 2XIIB[7]— from 60 to 600 μs as compared to 3 to 7 μs. The confinement time was calculated as the ratio of stored electron energy to input power to the electrons; the input power arises from collisional drag with the energetic plug ions.

The body of the electrons in TMX was isolated from the end walls to ensure that secondary processes at the wall were small. This was achieved by decreasing the magnetic field at the wall by a factor of 300 from that at the plug mirrors, so that the electron density dropped from 1×10^{13} cm^{-3} in the plug midplane to 10^9 to 10^{10} cm^{-3} near the wall. In addition, the electron temperature dropped from 50 to 150 eV in the plug and central cell to 5 to 10 eV near the wall.

A comparison of the total energy reaching the end wall (measured by calorimeters) with the ion energy (measured by end-loss analyzers) showed that ions accounted for almost all of the energy reaching the end wall (Fig. 2), and thus that the energy flowing directly in electrons was small. The ion energy included $e\phi_p$ ($\approx 5T_e$) originating from the electrons; nevertheless, secondary electron processes (secondary emission, arcs) were of negligible importance. Secondary emission coefficients were measured by hot-wire probes near the wall; the ratio of secondary electrons to incident ions ranged from 0.3 to 0.9, in good agreement with predicted values. No evidence of unipolar arcs was found on the end walls.

The reflux of gas from the wall provides a source for cold-plasma generation. The measured density of this plasma, $\geq 10^9$ cm^{-3}, is in agreement with a model[8] that includes cold-gas recycling, secondary electron emission, and ionization. The cold ions are isolated from the main plasma by the electrostatic potential. As the rate of generation of electrons by ionization is much less than the loss rate from the tandem-confined plasma, the additional power drain on the confined plasma by end-wall processes is at most about 1 to $2T_e$ times the end-loss current: typically 10 to 30 kW. This compares to a typical input power to the central cell of 100 to 400 kW. Processes in the end regions and at the end walls of TMX were thus reduced to a minor role in the power balance.
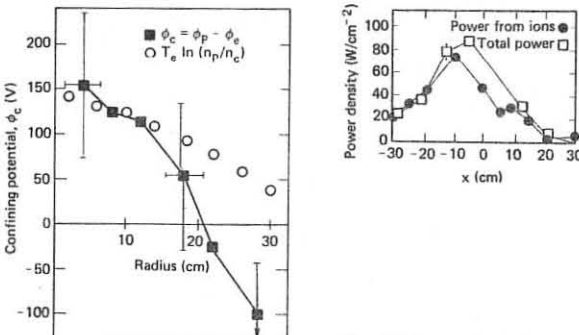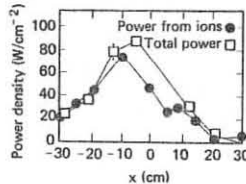
RADIAL TRANSPORT. Radial transport in the central cell of TMX is predicted to have a nonambipolar component arising from resonant-neoclassical transport due to the quadrupole fields in the transition regions.[9,10] Charge neutrality is maintained by a balancing electric current to the (metal) end walls. The net radial nonambipolar ion transport can then be related to the end-loss electron current by radial integration of the current-conservation equation.

The end-loss electron current density was determined from the difference between the net current density to the end wall (measured by collectors at the wall) and the ion current density (measured by Faraday cups). Azimuthal symmetry is assumed. Figure 3 compares measured ion transport with predictions based on theoretical diffusion coefficients.[9] Near the axis the measured electron current density includes that originating in the plugs from radial transport caused by charge exchange with the neutral beams. This current was calculated and subtracted from the measured value before integration. Its effect is large inside a 15-cm radius, but negligible outside that radius.

The errors in the predicted flux arise primarily from uncertainties in the radial electric field. The measured and predicted fluxes are comparable although large uncertainties exist in both. Resonant transport contributes substantially to, and may be the whole cause of, the radial nonambipolar ion transport.

Ambipolar processes were determined by comparing ion end-loss current density with ion sources predicted from gas-deposition codes. For low gas input into the central cell, the density is strongly peaked on axis and the measurement and prediction agree to within their uncertainty, indicating that radial ambipolar transport is weak compared with the nonambipolar transport.

As the gas input is raised, however, the calculated ion source and measured end losses differ by a factor of 3 or more at large radii (>20 cm in central-cell coordinates). This difference lies outside the estimated uncertainties in calculation and measurement, indicating an ambipolar flux comparable to the nonambipolar flux. The onset of this transport is accompanied by a low-frequency instability. At moderate gas inputs, an m = 1 mode is observed in the plasma with an azimuthal phase velocity approximately the same as the E × B velocity. The radial eigenfunction, Fig. 4, is largest in the region in which the large ambipolar transport is observed. At high gas inputs, the plasma edge becomes more turbulent. Although direct evidence is absent, it seems plausible that the observed ambipolar transport is due to this instability.

TMX UPGRADE. Because of the success of TMX, an improved tandem mirror, TMX Upgrade, is being constructed. TMX Upgrade is expected to yield improved axial and radial central-cell confinements. Axial confinement will be increased by using thermal barriers[11] to permit a difference in electron temperature between the plug region and the central cell. Radial confinement will be improved by a stronger magnetic field (0.3 T instead of the 0.1 T in TMX) and by a weak mirror within the axisymmetric part of the central cell; as a result the number of particles that undergo resonant transport will be reduced. The better confinement is predicted to yield increased central-cell temperatures ($T_e \approx 0.6$ keV, $T_i \approx 0.9$ keV).
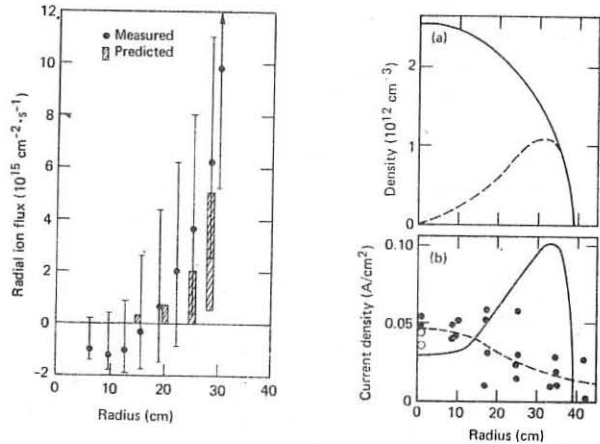
Fig. 3. Nonambipolar radial transport.
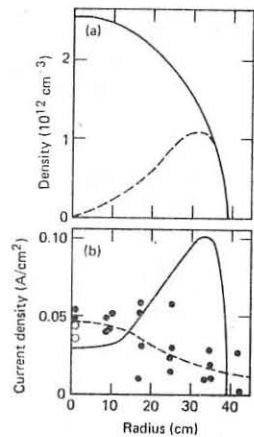
Fig. 4. Ambipolar radial transport: (a) average (solid line) and rms-oscillation densities, (b) ion end losses (data points and dashed line) and calculated ion source.

Fig. 1. Central-cell confining potential.

Fig. 2. Measured end-loss power referred to the central cell.

REFERENCES

1. F. H. Coensgen et al., Phys. Rev. Lett., 44, 1132 (1980).
2. T. C. Simonen et al., Proc. 8th Intern. Conf. Plasma Physics and Controlled Nuclear Fusion Research, to be published.
3. P. D. Drake et al., Nucl. Fusion 21 (1981).
4. G. Hallock, Ph.D. Thesis, Rensselaer Polytechnic Inst., in preparation.
5. V. P. Pastukov, Nucl. Fusion 14, 3 (1974).
6. R. H. Cohen, M. E. Rensink, T. A. Cutler, and A. A. Mirin, Nucl. Fusion 18, 1229 (1978).
7. T. C. Simonen, Lawrence Livermore National Lab. Rep. UCRL-85834, (1981).
8. G. D. Porter, Lawrence Livermore National Lab. Rep. UCRL-85847, (1981).
9. D. D. Ryutov and G. V. Stupakov, Pis'ma Zh. Ehksp. Teor. Fiz. 26, 186 (1977); JETP Lett. 26, 174 (1977).
10. R. H. Cohen, Nucl. Fusion 19, 1579 (1979).
11. D. E. Baldwin and B. G. Logan, Phys. Rev. Lett. 43, 1318 (1979).

INTERACTION OF A ROTATING INTENSE ELECTRON BEAM WITH A MIRROR CONFINED PLASMA

K. K. Jain, P. I. John, A. Sen and A. K. Sundaram
Physical Research Laboratory
Ahmedabad 380 009, India

We report here the results of an investigation of the magnetic response of a mirror confined hydrogen plasma to a pulsed (pulse length = 80 nanosecond), intense (Beam Current = 12 kiloamp) rotating (ratio of perpendicular to parallel velocity = 1.8) electron beam.

The experimental system is shown in figure 1 which also shows the equilibrium magnetic field configuration. The beam generator is a field emission gun energized by a waterline Marx generator combination. The beam is injected into the mirror through a nonadiabatic cusp and enters a magnetic mirror of peak magnetic field of $\sim$ 800 gauss and mirror ratio of 2.6. This region is filled by a 5 cm diameter column of hydrogen plasma of density 3×10^{12}/cc produced by a gas injected washer gun. The magnetic response in this region is measured using diamagnetic loops. Other diagnostics include Faraday Cups and damage plates.

The major experimental results are summarised below:

i) The primary electron beam is not retarded sufficiently to be trapped in the mirror region after interaction with the plasma. The beam duration is about 100 nanoseconds and we estimate the beam residence time in the mirror, as 15 nanoseconds.

ii) The magnetic perturbation rises to its peak in a time of 100 nanoseconds and then begins to decay.

iii) The diamagnetic response of the plasma within the mirror lasts for periods much longer than the beam duration or the beam
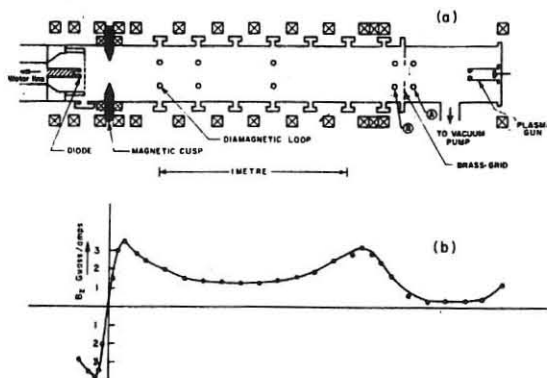
Fig. 1 Schematic diagram of the experiment.

residence time. The axial extent in which the diamagnetic signal persists for periods longer than the beam duration has a temporal variation. During the beam passage the entire plasma column shows

diamagnetic behaviour (see Fig. 2). After the beam passage the axial extent of the region begins to contract and at later times (more than about 300 nanoseconds) the region with finite ΔB is localized to about 60 cm within the mirror and symmetric about the mirror centre.

iv) The decay time is not significantly altered for heavier ion plasmas. However there is a weak dependence on the inverse of the ion mass.

The physical picture that emerges from the diamagnetic study based on diamagnetic perturbation is the following: The spiralling electron beam, during its exit from the mirror region, produces a persisting electron current in the same direction as the initial beam
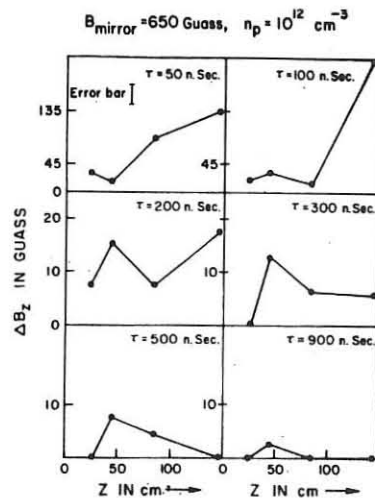
Fig. 2: Spatial variation of diamagnetic response within the mirror at different times.

current. This current is driven by the EXB drift of the plasma electron which are magnetized, with respect to the ions which are not. While the return current layer convects out of the region which have open field lines connected to the walls, the region inside the mirror traps the layer.

The weak dependence of the decay time with ion mass suggests that the mechanism proposed by Rostoker and Chu (1), ie. the ion acceleration across the magnetic field to short out the radial electric field and produce ion heating is not operative. For the present experiment, this should have produced kilovolt, non thermal ions, while experiments using neutral particle detectors failed to observe them. It may also be noted that in the decay phase, the ions would have been accelerated radially inwards. The decay time is also not in agreement with the classical conductivity of the plasma, if one assumes that the magnetic energy (7 Joules/meter) of the return current is dissipated within the plasma and is shared by the plasma particles; indicating the necessity of a new theoretical model.

References.

1. K. R. Chu and N. Rostoker; Physics of Fluids 17, 813 (1974).

D

PLASMA FOCUS DEVICES, Z- AND Θ-PINCHES
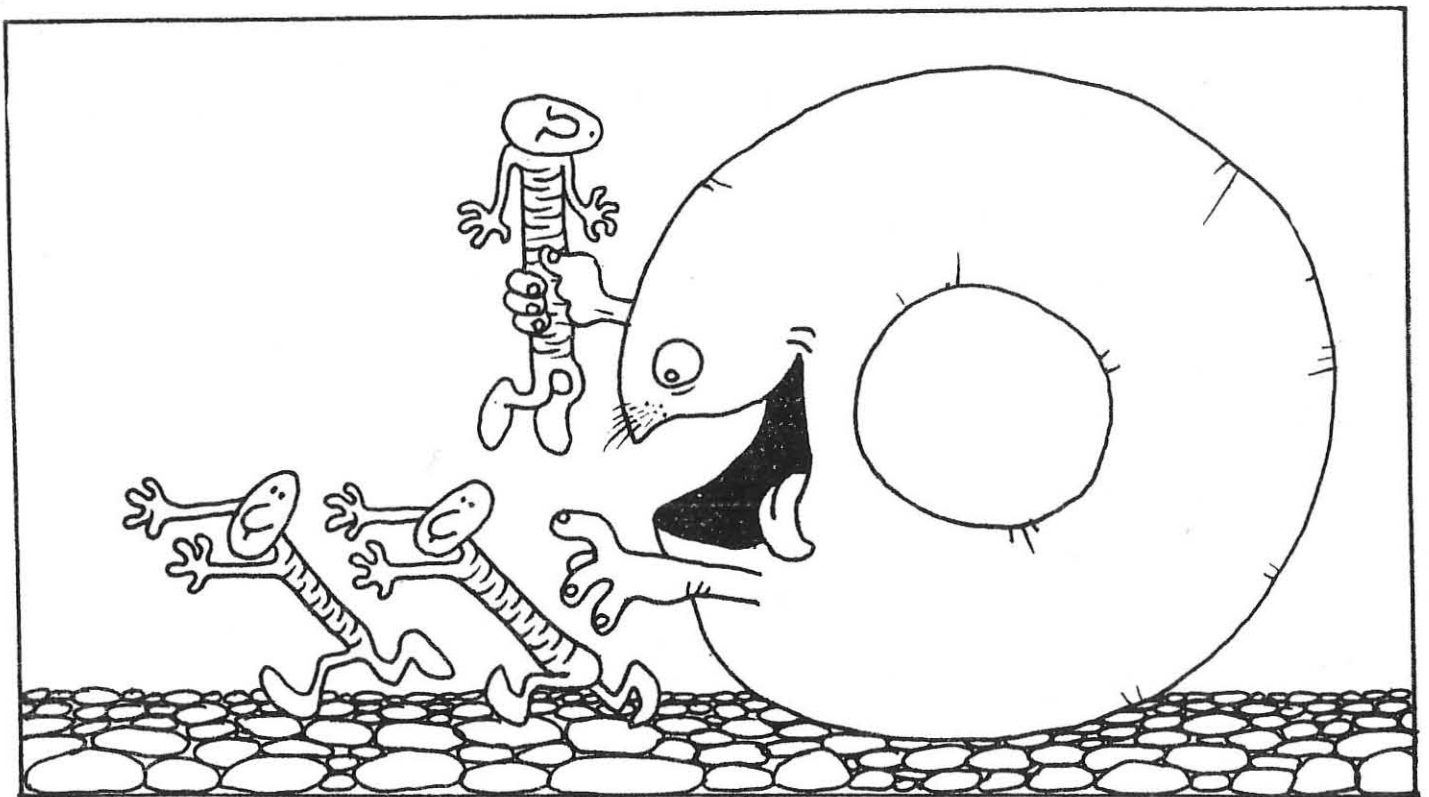
ION EMISSION CHARACTERISTICS OF PLASMA FOCUS DEVICES

L. Bertalot, R. Deutsch, H. Herold, U. Jäger, A. Mozer, M. Sadowski, H. Schmidt

Institut für Plasmaforschung, Universität Stuttgart, Federal Republic of Germany

Abstract: The angular distribution of ion emission has been studied experimentally with CN films and compared with model calculations. Thomson spectrograms revealed deuterons of maximum energy E_m up to 5 MeV and different impurities with E_m (1,8 to 14 MeV) being proportional to the ion charge. The ions are emitted mostly in single bursts (FWHM $\leqslant$ 8 ns) and sometimes in multispike pulses.

In previous experiments performed at the plasma focus devices Nessi (55 kJ, 19 kV) and DPF 78 (28 kJ, 60 kV) the ion source localization and the directional emission characteristics have been studied /1/. Side on ion pinhole measurements revealed that high energy deuterons are emitted from one or more small sources ($\leqslant$ 0.5 mm) located in the dense focus plasma. Experiments with cellulose nitrate (CN) films showed that the ion emission is strongly peaked in axial direction and modulated in space.

Further measurements with these detection methods have been performed at the same devices. Fig. 1 shows an example of the angular distribution of ions from a single discharge. Such distributions were obtained with CN films arranged in a half circle (see fig. 1) and covered with Al foil steps for a rough energy resolution. Ions with energies $0.1 \leqslant E \leqslant 5$ MeV were detected up to angles Θ of 85°. The distributions are anisotropic, exhibit a characteristic drop of the intensity at Θ between 40° and 80° and often show an asymmetry to the z axis.

Numerical model calculations of the ion trajectories have been performed for different plasma configurations with cylindrical symmetry and with a $m = 0$ constriction. Further assumptions were: B_φ (r, z) is produced by axial currents only and is constant in time during the ion emission; point sources with either isotropic or forward directed emission have been considered. Fig. 2 shows a calculated angular distribution for a single source upstream of a $m = 0$ constriction (fig. 3). The measured and calculated angular distributions were compared for different model source positions. The best fits were achieved for sources close to the anode tip either in, or upstream of a constriction (fig. 3). Obviously the angular modulation and the asymmetric emission can be explained by a "focusing" of the deuterons caused by the constriction, and by asymmetric positions of the sources, respectively.

Fusion reaction protons were detected too. In contrast to the deuteron emission their angular distribution is nearly isotropic. Pinhole pictures of the protons taken side on showed that the proton source is extended and matches approximately the pinched plasma region.

The energy distribution of fast deuterons and of impurity ions has been investigated with a Thomson analyzer adjusted in axial direction at the Nessi focus device. The instrument and its calibration using CN films as detector are described in /2/.

The deuteron energy distributions observed vary considerably from shot to shot, but generally decrease exponentially with energy. They range from 0.35 MeV (lower detection limit) to $\approx$ 1.5 MeV. Particularly at low filling pressures "high energy" spectra with $0.35 \leqslant E \leqslant 5$ MeV have been observed too. Impurity ions as O, N, C, Cu in different ionization stages and impurity protons have been identified. Their distribution functions are similar in character, as can be seen from fig. 4, which is taken from a single shot. The most remarkable fact is, that the maximum energy E_m of the different ion species is proportional to the charge number Z, but does not depend on the particle mass (e.g. for protons: $E_m \approx 1.8$ MeV; for O^{8+}: $E_m \approx 13$ MeV). The ratio of the total number of impurity ions accelerated to deuterons corresponds roughly to their fraction in the filling gas.

From these findings conclusions can be drawn on the acceleration processes: Obviously the impurities and possibly most of the deuterons are accelerated in a common process. The charge proportionality of E_m points to a linear acceleration of the high energy ions in electric fields. Taking into account the small size of the ion sources rather high E-fields of about 50 MV/cm should exist in the sources. The features of the deuteron acceleration (occurrence of "high energy" spectra) make it plausible that either more than one acceleration process exists or that tandem acceleration takes place.

In order to study the temporal evolution of the deuteron emission several small plastic scintillators (100 µm thick 4 mm and/or 0.5 mm in dia, covered with 0.35 µm Al) were placed along the deuteron parabola

track on the end plate of the analyzer. Deuterons of energies within the limits 0.3 to 2.5 MeV could be detected. Signals as obtained from distinct channels are presented in fig. 5a,b. The measurements have been performed with different ion extractor (skimmer) systems. With the small skimmer aperture (1 mm dia) usually single ion pulses have been detected (fig. 5a). Their minimum FWHM was $\leqslant$ 8 ns. The rise time of the detection system was $\leqslant$ 4 ns. Particularly with a larger skimmer aperture (3.5 mm dia) longer deuteron pulses with a complex structure have been observed (fig. 5b). They seem to be composed of a series of bursts with the individual FWHM also $\leqslant$ 8 ns. The time delays of the deuteron pulses in different channels in relation to the leading edges of the hard x ray signals are consistent with appropriate times of flight (jitter $\approx$ 5 ns). Hence it can be concluded that the deuterons of different energies are generated by a common process, presumably in time correlation with the fast electrons or hard x rays. The appearance of multistructured pulses may be explained by the existence of several ion sources distributed along and somewhat off the axis. Experiments with different pressures were carried out. No distinct difference in the shape of the pulses (except the amplitude) has been observed in the range of 2 - 4 mbar, D_2. No precise correlation could be established between the high energy ($\geqslant$ 0.35 MeV) deuteron intensity and the neutron yield.

References

/1/ L. Bertalot et al. 8th Int. Conf. on Plasma Phys. and Contr. Fus. Res., Brussels 1980, CN 38/G-1-2

/2/ H. Herold, A. Mozer, M. Sadowski, H. Schmidt Rev. Sc. Instr. 52, 24 (1981)
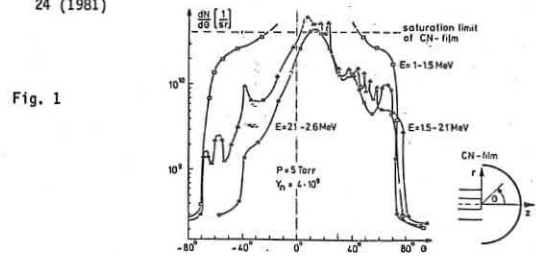
Fig. 1
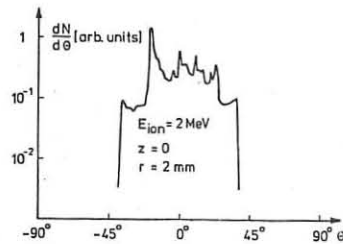
Fig. 2
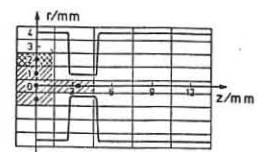
Fig. 3
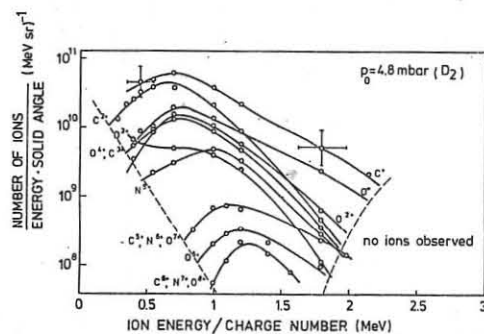
Fig. 4
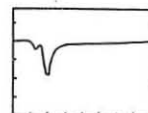
Fig. 5a
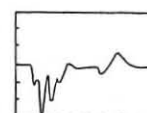
Fig. 5b

SPACE-RESOLVED INVESTIGATIONS ON THE PLASMA FOCUS NEUTRON
EMISSION

K. Hübner, J.P. Rager[+], K. Steinmetz
Institut für Angewandte Physik, Universität Heidelberg, FRG
+ Associazione EURATOM-CNEN, Centro Frascati (Rome), Italy

Abstract: The spectral and spatial properties of the neu-
tron emission of the Frascati 1 MJ-plasma focus have been
investigated by means of a 4-channel radial neutron-colli-
mator system. Additionally neutron energy spectra of the
primary source as well as their dependence on the observa-
tion angle were measured. The results demonstrate the exi-
stence of local azimuthal ion streamings and of an axial
stream-target interaction within the primary neutron source
of bulk ion energies around E_d=100 keV, while radial local-
ly dependent neutron emission intensities were observed.

Introduction: In the past /1,2/ space and time-resolved in-
vestigations were performed on the neutron emission of the
Frascati plasma focus by means of nuclear emulsion plates,
neutron pinhole imaging, activation counters and time-of-
flight spectrometry. The experimental results reported in
/1,2/ show that the plasma focus neutron source is composed
of a primary (bulk) source located close to the inner elec-
trode (z=0 to 5 cm) and emitting up to 80% of the total
yield, while a secondary (corona) source at z=8 to 10 cm
delivers the remaining part of the yield. The end-on ener-
gy spectrum of the bulk source (see Fig. 4 in /1/) is
clearly different from the fully space-integrated ones, be-
cause it has two peaks, one at E_n=2.85 MeV and an additio-
nal maximum at E_n=2.45 MeV, while the side-on spectrum is
centered around 2.45 MeV. Though the energy spectra are an-
isotropic, the intensity of the neutron emission is spa-
tially uniform, i.e. A=1. These features render difficult
an interpretation based on beam-target production, despite
the existence of the 2.85 MeV line in the end-on neutron
spectrum.
In order to find a consistent explanation of the spectral
and spatial properties of the bulk source emission, radial-
ly space-resolved and angle-resolved measurements of neu-
tron intensities and energy spectra now have been carried
out.

Experiments and Interpretation: A 4-channel neutron colli-
mation system with a space-resolution of 2 cm (Fig.1) was
used to measure space-resolved neutron fluences and energy
spectra at single discharges (Mather system, 400 kJ, 5 Torr
D_2). The observation fields were r=0.1 to 2.1 cm (channels
1 and 3), r=-2.1 to -0.1 cm (channels 2 and 4), z=0.8 to
3.2 cm (all channels). The observation angle-dependent
energy spectra were detected by a quarter circle set-up
with nuclear emulsion plates fixed at 0°, 20°, 40°, 90°
with respect to the device axis.
Fig. 2 gives two examples of space-resolved energy spectra
of the bulk source, taken at a single shot at 90° by chan-
nel 1 and 2. Compared to space-integrated side-on spectra
/1/ the spectral structures are changed, because the spec-
trum of channel 2 (Fig. 2b) shows a line maximum which is
shifted to E_n=2.05 MeV. In the left-hand side spectrum
(Fig. 2a) no shift of the main line is observed, though
there is a small bump at E_n=2.85 MeV. Also the local neu-
tron intensities are strongly different: the intensity of
the left half part of the bulk source is higher by a fac-
tor 1.7 compared to the right one. The observation of spa-
tially dependent neutron spectra and intensities can be
interpreted by a local azimuthal stream-target production,
in which the ions stream with E_d=100 keV into or through
a deuterium plasma. Note that the neutron energy spectra
are time integrated, i.e. such streams can exist on a long
time scale in the order of the neutron production time
($\simeq$ 200 ns). Furthermore, Fig. 2a indicates that within the
left half part of the source at least two local streaming
ion components with antiparallel directions were existent,

which is in agreement with the increased neutron intensity
observed there. Also the fact, that the fluence-weighted
sum-spectrum of both space-resolving channels practically
is identical with the full side-on spectrum of the bulk
source (Fig. 4a in /1/), explains the typical large broa-
dening of the space-integrated side-on spectra by local
azimuthal ion streams.
The angle-resolved neutron spectra show an energy shift of
the main line from 2.85 MeV with increasing observation
angle (0° to 40°), which can be explained reasonably by an
axial stream-target interaction of E_d=100 keV. The most
interesting feature is the occurence of a second line in
the 40°-spectrum at 2.45 MeV, also observed in the end-on
spectrum of the bulk source /1/. For a consistent picture
of these properties a neutron production mechanism has to
be considered, eventually composed of local azimuthal ion
streams of E_d=100 keV and an axial beam-target component
(E_d=100 keV) which can even occur in a certain time sequen-
ce.

Conclusions: The results from space-resolved neutron energy
spectra demonstrate local azimuthal ion streams within the
neutron bulk source, which provoke locally dependent neu-
tron emission intensities and energy spectra. The azimuthal
energy component of the streaming ions responsible for a
large part of the neutron production has been determined
to E_d=100 keV. The spectral features of the spectra at 90°
and 40° and a total fluence anisotropy value of A=1 require
an additional axially streaming ion component of E_d=100 keV.

References:
/1/ J.P. Rager et al., 8th Conf. on Plasma Phys. and Contr.
    Nucl.Fus.Res.IAEA, Brussels, 1980
/2/ K. Hübner et al., 7th Int.Conf. on Plasma Science,
    IEEE, Madison, 1980

Fig.1: 4-channel neutron
collimation system

Neutron Energy Spectra of a Single
Shot vs Observation Angle ⊕.

Fig.2

a)

b)
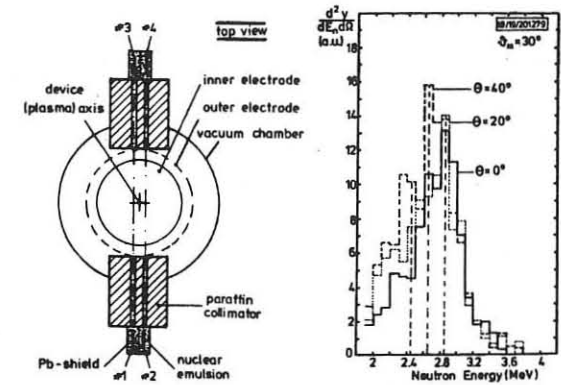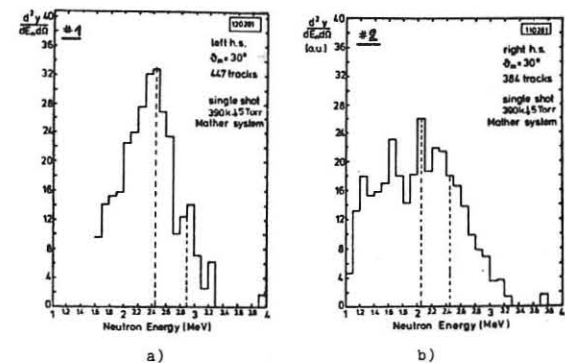
Fig. 3: Space-resolved neutron energy spectra of a single
discharge (shot No. 5194)

LIGHT SCATTERING IN A PLASMA FOCUS,
MEASUREMENT OF k- AND ω-SPECTRA

J. Ehrhardt, P. Kirchesch, R. Bätzner, K. Behler,
G. Böckle, H. Bruhns, K. Hübner, K. Steinmetz, N. Wenzel
Institut für Angewandte Physik, Universität Heidelberg, FRG

Abstract: Thomson scattering measurements have been carried out at the Heidelberg plasma focus (12 kJ, 0.5 MA). The angular distribution of the spectral integrated ($\Delta\lambda=15\text{Å}$) light $S(k)$ was observed as well as the spectral resolved $S(\omega)$ at $45°$. The results show the existence of two different regions of the plasma, one close to the anode and the other more far away in which the plasma parameters are different. In the lower part turbulent effects have been found.

Principle of measurement: In the optical arrangement for the primary ruby laser light (25ns, 8 J) we used a pinhole for spatial filtering and a baffle system in order to reduce the stray light. The diagnostic system for simultaneous observation at different scattering angles ($12.5°$ to $135°$, $k \perp$ to the focus axis) was mounted inside the vacuum chamber, the signals were fed through the vessel by fibre optics. With this setup we achieved good flexibility in the alignement without influencing the focus discharge. For the spectral-resolved measurement one channel was mounted outside the vessel at an angle of $45°$.

We carried out $S(k)$-measurements at seven different points of the discharge (fig. 1). In order to give an impression of the plasma dimensions the dotted line shows the plasma structures at the onset of the m=0 instability observed by shadowgraphy.

We got three different types of $S(k)$-spectra (fig. 2). Curve A shows a spectrum which coincides very well with a theoretical one calculated following the theory of Salpeter for which Maxwellian velocity distribution of the plasma particles is assumed (dashed lines in fig. 2). Curve B shows a strong increase at small angles but it is possible to fit it for larger ones, while curve C cannot be fitted with any thermal scattering spectrum. Type B and C indicate light scattered by plasma turbulences. By comparing the theoretical and the experimental spectra we are able to deduce the electron density and temperature. In order to get an impression about the error in the determination of the temperature we made simultaneous measurements of $S(k)$ and $S(\omega)$. We found that the difference between the two obtained values is not more than a factor of two.

Results: In the region near the anode we measured all three types of the spectra but on the axis and very near to it (points 3,4) we could not see any turbulence. Type C existed only during the imploding phase in front of the luminous plasma sheet. There the plasma was very thin and cold, consequently we did not observe scattered light at $45°$ in this situation. Type B was measured outside the axis (points 5,6,7) mostly before the neutron production started and also up to 150 ns later.

For this type the scattering was enhanced above the thermal level by a factor ranging from 3 up to 10. The spectra indicate an onset of the turbulence at $\alpha \approx 2$ and a frequency of the order of the ion plasma frequency. Scattered light with higher frequencies was suppressed by interferential filters. We observed lifetimes of the turbulence between 10 and 18 ns.

The temperature and density values depend on observation point as well as on observation time. The maximum temperature we found was $T_i = 1$ keV at point 5 and the density peaked at $3\cdot10^{18}$ cm^{-3} during maximum compression decreasing down to 100...400 eV and 4...$6\cdot10^{17}$ cm^{-3} during the neutron production.

The $S(\omega)$-measurements were carried out at point 3. One spectrum is shown in fig. 3. From these spectra we obtained the ion temperature and the ratio between electron and ion temperature. These values were in the range 100 eV < T_i < 800 eV respectively 0.25 < T_e/T_i < 0.9.

In the upper part of the focus discharge (points 1,2) we never observed any turbulence. In this region the plasma parameter ranged between 20...400 eV and 1...$10\cdot10^{17}$ cm^{-3}. It was a quiescent widespread plasma with reproducible time development of temperature and density (fig. 4).

Neutron production: We will discuss the results of light scattering in connection with the neutron production. In our focus the source of neutrons ranges from the anode up to 25 cm in z-direction. The axial dependence of the number of neutrons is given in fig. 5. We can distinguish three regions in the neutron source. The first one near the anode approximately is the region where previously the pinch compression occured. The second one is determined by the quiescent plasma observed in points 1 and 2. The third region up to 25 cm is located in the filling gas.

For the first two regions we measure a line density of about $5\cdot10^7$ neutrons/cm and approximately 1/3 of the total neutron production. In the third region the mean line density is 10^7 neutrons/cm. From the plasma parameters as determined by light scattering for the first two regions one estimates a thermal production in the order of 10^3 neutrons/cm. Together with measurement of the anisotropy of the neutron emission (A = 1.1 for the first two regions, A = 1.6 total) and of the neutron energy spectra we are led to the conclusion that fast deuterons ($\approx$ 100keV) are responsible for the neutron production, while the observed plasma acts as a target.

These fast deuterons must be produced in the lowest region of the neutron source and in this connection it is interesting to note that only in this region and mainly during the start of the neutron production we observe plasma turbulence. But as yet we are not able to verify a correlation between neutron production and turbulence. This problem suffers essentially from the fact that light scattering is a local measurement, whereas the neutron production takes place in an extended region.
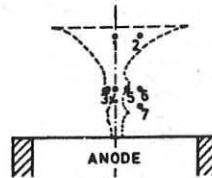
Fig.1: Observation points

1:	z = 25 mm	r = 0 mm
2:	z = 25 mm	r = 6 mm
3:	z = 12 mm	r = 2 mm
4:	z = 12 mm	r = 0 mm
5:	z = 12 mm	r = 3 mm
6:	z = 12 mm	r = 6 mm
7:	z = 8 mm	r = 6 mm
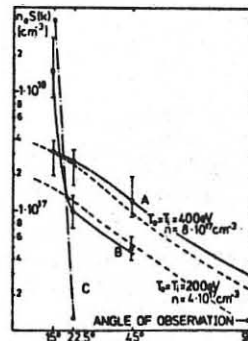
Fig.2: S(k)-spectra
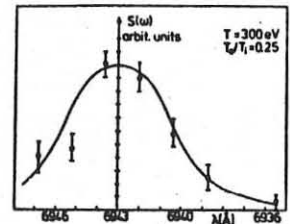
Fig.3: S(ω)-spectrum
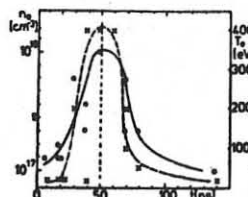
Fig.4: Electron density (o) and temperature (x) at points 1 and 2 during neutron production (start: t=0, maximum: t=50ns)
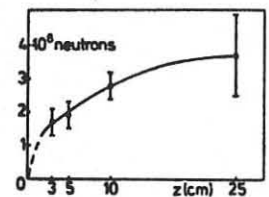
Fig.5: Axial dependence of neutron production

STUDY OF MEDIUM ENERGY IONS IN A PLASMA FOCUS DEVICE

A.Bocancea, T.Chera, N.Mandache, A.Pantea, V.Zoiţa
CENTRAL INSTITUTE OF PHYSICS
P.O.Box MG-7, BUCHAREST, ROMANIA

Abstract : The ions emitted along the plasma focus device axis were studied in the energy range (10-600)keV. It was found that the energy spectrum was modulated within this energy range.

1. Experimental setup

The measurements were performed on the IPF-2/20 plasma focus device /1/ working at 16 kV, 10 kJ with a hollow central electrode. A combined time of flight and electrostatic deflection method was used for ion energy analysis /1/. In order to reduce the interaction with the analyser probe, the external electrode was partialy closed, leaving only a 2 cm diameter aperture, on the axis (Fig.1). This modification of the Mather configuration does not affect the performance of the device : the neutron production per pulse ($2x10^8$) remained unchanged.

A flight base of 135 cm (200 ns time of flight for a 230 keV proton) was ensured in a two-stage differentially pumped drift tube (10^{-4} torr for a working gas pressure of 1,3 torr). By analysing the composition of the energetic particles (protons and H atoms) entering the analysing system it was concluded that the steady-state equilibrium fraction was approximatelly attained.

2. Experimental results

Using the analyzer system in the monoenergetic mode ($\Delta E/E=0,05$) the duration and time of emission (time of maximum amplitude) for ions of various energies in the range (10-400)keV were determined. The monoenergetic ions are emitted in pulses of 15-40 ns (FWHM). The times of emission are distributed over an interval of 20-30 ns.

With the analyzer working in the multienergetic mode (large aperture in front of the detector) the proton spectrum was determined. Fig.2 and 3 show two typical oscillograms, the energy ranges of the analyzer being (60-600)keV and (30-300)keV respectivelly. These results indicate the existance of a strong modulation in the energy spectrum.

In most of the discharges one can identify the existence of a group of higher energy ions (200-250)keV with the rest of the ions having energies below (100-120)keV. Still higher energy ions (400 keV), of smaller intensity were detected in some discharges (Fig.2).

The modulation in the energy spectrum is found also at lower energies (Fig.4).

From the oscillogram presented in Fig.3, taking into account, among others, the values of the equilibrium fractions, the energy distributions of the energetic particles (protons and H atoms) was determined (Fig.5). For a deuteron energy distribution similar to that of Fig.5, the product Nσ, where σ is the cross section for the d-d reaction, was calculated and plotted on the same figure. The broad peak around the 230 keV deuteron energy represents a confirmation of the results obtained on the same device, in experiments using a tritium target /2/. It should be noticed that the major contribution to the neutron production is due to lower energy deuterons (40-120)keV.

3. Conclusions

The energy spectrum of the ions emitted axially from the plasma focus in the energy range (10-400)keV is strongly modulated. Such modulation effect has been reported at even higher energies in /3,4,5/.

References
/1/ Cebanu,A. et al., VIII Conf. on Pl.Phys.and Controlled Nucl.Fus.Research,Bruxelles,(1980)
/2/ Tsois,N.,Ionescu,G.,Mandache,N., IEEE Int.Conf.on Pl. Science,Santa-Fé, 18-20 May, (1981)
/3/ Filippov,N.V., et al., 8th Europ.Conf.and Controlled Fus.and Pl.Phys.,Prague 1977, vol.1, p.63
/4/ Krompholz,H. et al., Phys.Lett., vol.76A,nr.3,4 (1980)
/5/ Belyaeva,I.F., Nucl.Fus.,vol.20,No.8 (1980),p.1037.
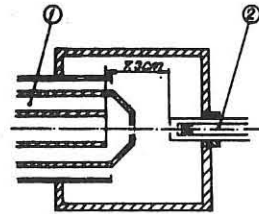
Fig.1. Electrode configuration (1) of the IPF-2/20 device and position of the analysing system probe (2)
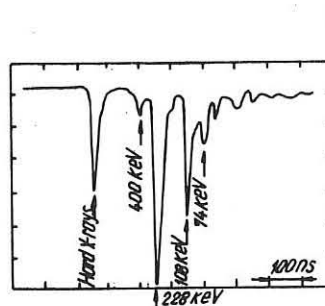
Fig.2. Analyzer output signal for energy range (60-600) keV
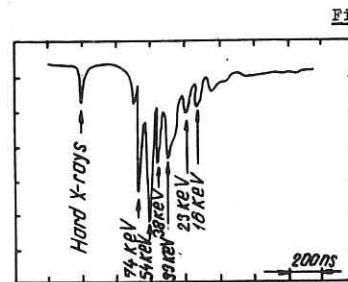
Fig.4. Analyzer output signal for energy range (10-100) keV
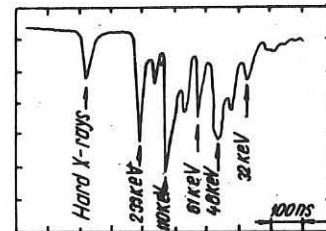
Fig.3. Analyzer output signal for energy range (30-300) keV
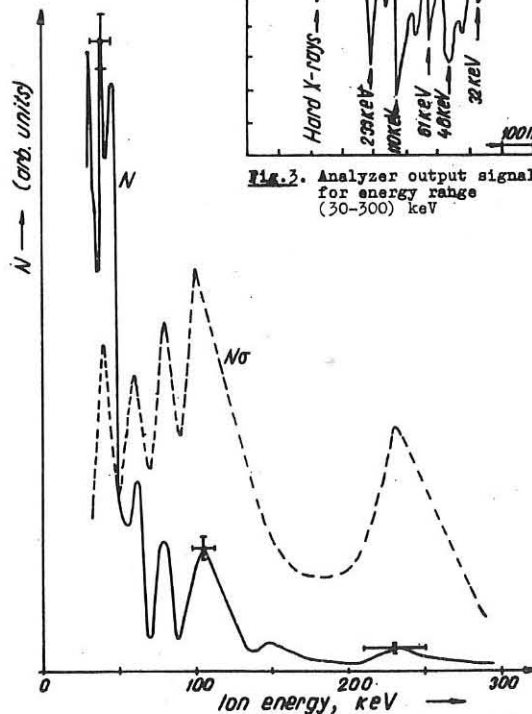
Fig.5. Energy distribution of energetic particles emitted axially by the plasma focus and the product Nσ (dashed curve).

ANALYSIS OF ENERGETIC PARTICLES
IN DENSE PLASMA FOCUS

M. YOKOYAMA, Y. KITAGAWA, Y. YAMADA and C. YAMANAKA

Institute of Laser Engineering, Osaka University,

Suita, Osaka, 565, JAPAN

The plasma focus is not only one of the complementary fusion device between low-β Tokamak and high compression inertial fusion, but very suitable for detailed studies of non-classical processes in the absorption of intense laser light. Recently, there has been considerable interest in generation of intense high energy electron and ion beams in plasma focus devices in relation to the inertial confinement fusion.

High energy deuterons and protons in a Mather type plasma focus device were measured by nuclear activation techniques. Radioactivity induced in graphite, aluminum and cupper targets provided the deuteron intensity, energy spectrum and angular dependence. As well high energy protons were measured by cellulose nitrate particle track detectors.

The experimental set-up and target parameters are shown in Fig. 1. The plasma focus device was operated at 30 kV for a stored energy of 18 kJ at 1.5 Torr D_2 (low pressure mode), and 5 Torr D_2 (high pressure mode), respectively.[1] A γ-ray spectroscopy system consisting of a NaI(Tℓ) detector and 2048-channel computor pulse height analyzer was used to count the γ-ray from targets after focus discharge. Nuclear activation reactions by deuteron are given by Table I. The evolution of plasma was measured by a ruby laser holography.

Fig. 1.

Target species	size	z (cm)	
Al,C	45mm⌀, 5mm	32.5	
Al (stack)	20mm⌀, 17μm	33	
	45mm⌀, 17μm	50	
Cu	25mm⌀, 3.5mm	20	

High energy deuteron produce 3.4×10^6 atoms of ^{13}N in an 8 cm² graphite target placed 32.5 cm above the anode and 2.2×10^4 atoms of $^{28}Aℓ$ in an aluminum target of the same diameter at the same location. The yield ratio of ^{13}N and $^{28}Aℓ$ provided the mean deuteron energy of 1.55 MeV under low pressure mode and 1.44 MeV under high pressure mode, respectively. The mean fluence of 7×10^{11} deuteron per steradian was estimated. Stacks of 10 aluminum foils were used to measure the deuteron energy spectrum. Fig. 2 and Fig. 3 show deuteron and proton energy spectrums, respectively. Under low pressure mode of D_2, the main energy component was up to 2 MeV and the high energy tail was from 2 MeV to greater than 3 MeV. The energy spectrum of proton measured by CN film technique had also shown to consist of two exponentially decaying components.[2,3] The main component was under 1 MeV and the maximum of the high energy tail was greater than 2 MeV. The experimental equations for proton energy spectrums are expressed as follows,[4]

$$\frac{dn}{dE_p} = 10^9 \exp(-8.8 \, E_p) \qquad (E_p \leq 1 \text{ MeV})$$

and

$$\frac{dn}{dE_p} = 3 \times 10^5 \exp(-0.9 \, E_p) \qquad (E_p \geq 1 \text{ MeV}).$$

The mean proton energy was smaller than 1 MeV.

The angular distribution of deutron was measured by placing 7 graphite targets above the anode at various angles from 10° to 90°, respectively. The intensity of high energy deuterons fell by a factor of two for a 20° displacement from the axis. The angular distribution of deuteron beam ($E_d > 330$ keV) was ≲ 30° under low pressure mode. Under high pressure mode, distribution showed multi-structure, and two

Reaction	Threshold (MeV)	Half-life	Energy of delayed γ-ray (MeV)
$^{13}C(d,n)^{13}N$	0.33	9.97min	0.511
$^{27}Al(d,p)^{28}Al$	0	2.24min	1.780
$^{63}Cu(d,2n)^{63}Zn$	6.58	38.5min	0.511(79.3%) 0.669(11.2%)
$^{65}Cu(d,2n)^{65}Zn$	4.49	243.7days	1.115(50.6%)

Table 1

peaks were observed at ≲ 20° and ∿ 60°, respectively. The results of angular distributions of deuteron under low (1.5 Torr D_2) and high
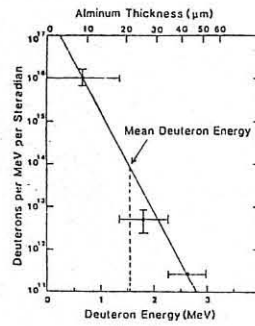
Fig. 2.
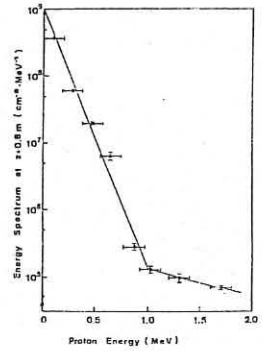
Fig. 3.

(5 Torr D_2) pressure modes were shown in Fig. 4. The angular distribution of proton was also measured by CN films with Aℓ foils. The protons above 770 keV was directed in the angle of 10° from the axis. The total yield of high energy protons was estimated as 3×10^{14} for 30 kV at 4.2 Torr H_2. The proton peak current was 4.6 kA and 0.7 % of the total focus current.

The high energy electron beam was also observed by detecting the hard x-ray due to electron bombardment of inner electrode of the plasma focus device. By Si PIN detector with 1 mm thickness of Pb, high energy (> 300 keV) electron beam was observed under 30 kV, 4.0 Torr H_2
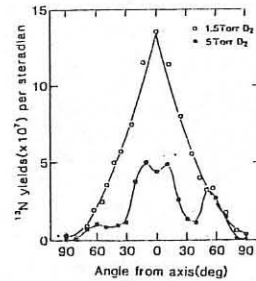
Fig. 4.
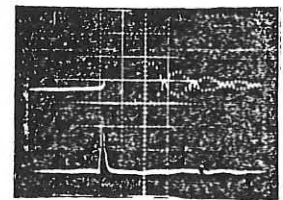
Fig. 5.

operation. The pulse width was 10 ns. The upper trace of Fig. 5 shows focus current and the lower trace shows Si PIN detector signal.

To see the spatial and temporal location of the generation of high energy ions on and off axis of the inner electrode of plasma focus device, a 3 channels ruby laser holographic interferometry (2 ns exposure time) was used. From the preliminary results, it was found that high energy protons generate in a few ns at the end of the cylindrically convergent collapse phase, when a hemispherical plasma of 1 mm diameter was observed at the center of the anode tip surface under low pressure mode operation. While at the plasma focus discharge without high energy ion generation, even under the low pressure mode operation, the hemi-spherical plasma could not observe.

In conclusions, experimental results showed that energy spectrums of deuteron and proton had two components and mean deuteron energy of 1.55 MeV under low pressure mode and 1.44 MeV under high pressure mode, respecively. The angular distribution of deuteron beam was ≲ 30° under low pressure mode. Under high pressure mode, distribution showed multi-structure, and two peaks were observed at ≲ 20° and ∿ 60° respectively.

References

1) M. Yokoyama, Y. Kitagawa, Y. Yamada, C. Yamanaka and K. Hirano 8th IAEA Int.conf. on Plasma Phys. Cont Nucl. Fus. Res. IAEA-CN-38/G-1-3, Brussels, (1980)

2) Y. Kitagawa, Y. Yamada, A. Ishizaki, M. Naito, M. Yokoyama and C. Yamanaka, IEEE Int. Conf. Plasma Science 3£4, Wisconsin (1980) P. 74

3) Y. Kitagawa, Y. Yamada, H. Saibara, M. Yokoyama and C. Yamanaka IEEE Int. Conf. Plasma Science, Santa Fe (1981)

4) Y. Yamada, Y. Kitagawa, M. Yokoyama and C. Yamanaka, Phys. Letters A. (to be published in 1981)

CONTRACTION OF PLASMA IN A VACUUM SPARK AS A RESULT OF
RADIATION LOSSES

V.V.Vikhrev, V.V.Ivanov

I.V.Kurchatov Institute of Atomic Energy,
Moscow, USSR

K.N.Koshelev, Y.V.Sidelnikov

Institute for Spectroscopy, Academy of Sciences,
Troitsk, Moscow District, USSR

Abstract. The formation of the X-ray sources,"hot-
spots" in the vacuum spark are explained as a result of
plasma pinching due to radiation losses and plasma out-
flow. The temperature of the X-ray sources found to in-
crease with the atomic number of the anode material. In
the case of the iron anode the temperature is achieved
~ 1 keV with the plasma confinement parameter $n_e \tau$
$\sim 10^{14} cm^{-3} \cdot s$.

The micropinch region in a vacuum spark usually con-
siste of several X-ray sources with the radius of about
$2-10 \mu m$ and the axial length $20-40 \mu m$. The electron tem-
perature of the X-ray sources is about 1-10 keV and there
are observed spectra of the atoms with up to 40 electrons
removed /1,2,3/.

The vacuum spark plasma is formed from the anode ma-
terial and has the high radiation cooling rate. Radia-
tion losses became essential in the energy balance of
the spark if the plasma current exceeds 100 kA/3/. The
plasma pinching due to radiation losses and the plasma
outflow results in an essential increase of $n_e \tau$ /4/.
This determines an increased interest to the plasma pin-
ching due to radiation losses in the Z-pinch devices.

The development of the discharge in the vacuum spark
may be represented as follows /5/. After the expansion
of the anode plasma to the cathode the arc is formed. The
number of particles in any cross-section of the arc is
not constant along the axis but a quasiequilibrium in
the radial direction between the plasma pressure and
the magnetic field is established. The plasma column
is compressed or expanded due to the disbalance bet-
ween energy losses and the heating.

If the arc current is less than ~ 100 kA the plas-
ma column is not subject to a sausage-type instability
and can't pinch to the radii less than ~ 0.1 cm. After
increase of the current higher than ~ 100 kA the plasma
column becomes unstable and necks with radii $\sim 10^{-2} \div$
$\div 10^{-4}$ cm can be formed somewhere in the column. The deve-
lopment of the plasma column neck with the radius $\sim 10^{-3}$ cm
was observed by means of a laser shadow techniques /6/.

A computation of the neck evolution for current
$I=150$ kA was carried out by using non-stationary model
described in /5/. The neck radius R (cm), the electron
density n_e (cm^{-3}), the current I (kA), the temperature
T (eV) and the mean ionic charge z are shown in the figure
as functions of time. The time scale to the right of
dot-and-dash line is of 1/200 of that to the left. The
electron density is equal $\sim 3.10^{20} cm^{-3}$ in the first
minimum of the neck radius ($\sim 2,5.10^{-2}$ cm), the plasma
temperature ~ 50 eV. The neck radius is nearly constant
during the next 20 ns but the number of particles in
the neck cross section is decreased due to the plasma
outflow and the plasma temperature is increased. The in-
crease of radiation losses due to ionization of L-shell
of the iron atoms result in the second compression of
the plasma column and the following plasma parameters
are reached: $n_e \sim 10^{24} cm^{-3}$, $R \sim 1.6 \mu m$, $T \sim 1$ keV
and $n_e \tau \sim 10^{14} s \cdot cm^{-3}$. After the second compression,
the plasma column neck expands due to an appearance
of the anomalous Ohmic heating. The radiation emission

from the ions with $Z > 23$ begins after the neck expan-
sion to the radius 5.10^{-4} cm. The electron density is
3.10^{23} then and the temperature 2 keV. These results
correspond to experimental data for the He -like lines
of FeXXV /7,8/.

The computations show that the plasma temperature in
the vacuum spark to the moment of the maximum compres-
sion and the value of $n_e \tau$ may be represented as fol-
lows:

$$T (eV) = (1 \div 2) Z_n^2 \qquad (1)$$
$$n_e \tau (s \cdot cm^{-3}) = 10^{14} Z_n^{0.2} I \qquad (2)$$

where Z_n - the atomic number; I is taken in MA.

As it follows from (1) and (2), the plasma tempera-
ture and $n_e \tau$ are increased with Z_n. For two-compo-
nents plasma with very different atomic numbers the
plasma temperature and $n_e \tau$ depend mainly on the ele-
ment with higher Z_n.

This conclusion was checked up in the experiments
with pure iron and equicomponent Fe-Mo alloy anodes.
The plasma temperature had been estimated from relative
intensities of the dielectronic satellites Fe XXIV and
the resonance line Fe XXV, as usually /7,8/. The experi-
mentally observed
~ 3.5 times redu-
ction of the rela-
tive dielectronic
satellites inten-
sities in the case
of two component
plasma corresponds
to the temperature
increase from 1300
eV to 2200 eV.

The results
presented in this
work predict a
possibility of cre-
ating the plasma
with $n_e \tau \sim 10^{14}$ and
with $T \sim 10$ keV
(in the plasma of
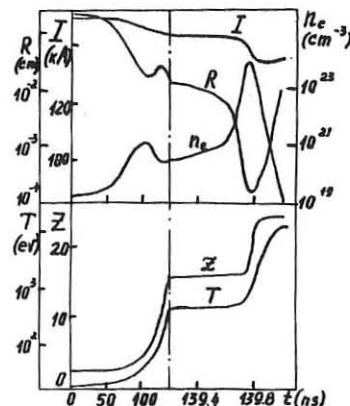
tungsten and deuterium, for example) in a Z - pinch of
a small power. The presence of an impurity with a high
atomic number in the Z - pinch plasma is favorable be-
cause it leads to the plasma pinch due to radiation los-
ses, creating increased value of the plasma confinement
parameter $n_e \tau$.

References

1. Cohen L. et al. J.Opt.Soc.Am., 1968, v.58, p.843-
846.
2. Cilliers W.A., Dalta R.U., Griem H.R.-Phys.Rev.,
1975, v.A 12, p.1408-1418.
3. Negus C.R., Peacock N.J. - J.Phys., 1979, v.D12,
p.91-111.
4. Vikhrev V.V. - "Pis'ma-v-ZETF", 1978, v.27, N 2,
p.104-107.
5. Vikhrev V.V., Ivanov V.V., Koshelev K.N. Plasma
Dynamics in Micropinch. Preprint IAE-3359/6, 1980
(in Rus.).
6. Gribkov V.A. et al. Investigation of vacuum spark
with laser shadow techniques. Preprint Lebedev's
Institute N 178, 1979 (in Rus.).
7. Kononov E.Y., Koshelev K.N., Sidelnikov Y.V. -
"Fisika Plasmy", 1977, v.3, p.663-673 (in Rus.).
8. Kononov E.Y. et al. - "Pis'ma-v-ZETF", 1980, v.31,
N 12, pp.720-723 (in Rus.).

MEASUREMENTS OF RADIAL DENSITY DISTRIBUTIONS IN THE PPA INTERELECTRODE GAP BY CO$_2$-LASER INTERFEROMETRY

A.G. Belikov, V.P. Goncharenko, D.K. Goncharenko,

N.T. Derepovskij, I.K. Nikolskij

Institute of Physics & Technology, the Ukrainian Academy
of Sciences, Kharkov, USSR

The plasma flow at the muzzle of the accelerator is
strongly nonuniform in its velocity and density and is,
to a great extent, determined by the processes occurring
in the interelectrode gap. Therefore, the study of the
plasma motion in the gap represents an actual problem.

Here we report the experimental results of CO$_2$-laser
interferometric measurements of plasma density and the
results of numerical calculations. The plasma dynamics was
investigated in the coaxial pulsed plasma accelerator
(PPA) with the main parameters: electrode length – 24 cm,
diameters of central and external electrodes – 3cm and
14 cm, respectively. The amplitude of the discharge cur-
rent was $\sim 10^5$A, the first halfperiod duration was 12μsec,
the operating gas was hydrogen. Large gas load and a ra-
ther low voltage applied to the electrodes (5kV) determi-
ned a slow working regime of the accelerator.

A CO$_2$-laser interferometer was assembled by the Mi-
chelson scheme (Fig.1), the interference signal was regi-
stered with the Ge:Au photoresistor at 78°K. Time resolu-
tion of the interferometer (0.2μsec) was determined by
the frequency band of the amplifier. Plasma probing by
chords was used in the experiment in order to obtain ra-
dial density distributions. For this purpose, longitudi-
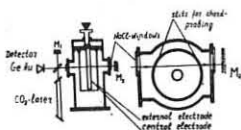
Fig.1

The setup of the experiment

nal slots, 3mm high, were cut in the external electrode,
ranging from r = 1.8cm to r = 6.0cm with a 0.6cm step.
The probing was performed in seven planes starting from
the gas inlet plane (z=0) up to the accelerator muzzle
(z = 24cm) with a 4cm spacing. At each position, 5 mea-
surements were taken. The inverse Abel transformation
was realized by using the Pearce coefficient technique
[1]. Figs.2 and 3 show the electron density distributions
for z=0 and z= 24cm planes.
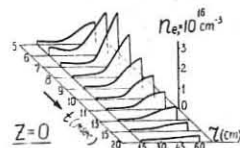
Fig.2

Radial plasma density di-
stributions for the gas in-
let plane (z=0).

For the numerical calculations, we used a nonstationary
two-dimensional MHD-model of a coaxial PPA [2]. The set
of equations for the plasma was solved together with
equations for the external electric circuit. Here the
plasma was considered as a complex load. A more detailed
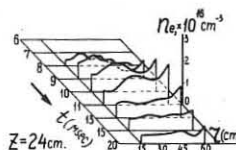
Fig.3

Radial plasma density dis-
tribution for the PPA muz-
zle plane (Z = 24cm).

information about the typical quantities of the problem
is given in [3]. The equations contain six dimensionless
parameters. Among them the most important parameters are
$\beta = P_o/m_o H_o^2$, $\eta = 1/m v_o \sigma \ell_o$, $\xi = M^{1/2}/e\ell_o (m n_o)^{1/2}$. Here ℓ_o
is the accelerator length, v_o is the typical plasma ve-
locity and H_o is the magnetic field strength. The pa-
rameters η and ξ for the present accelerator system
were estimated to be $\eta = 10^{-2}$ and $\xi = 5 \cdot 10^{-2}$, however
in calculations these parameters varied in a wide range.
The characteristic property of the obtained radial den-
sity distributions that were measured by the CO$_2$- laser
interferometer lies in the essential nonuniformity in
the gap cross section. In the region of the central ele-
ctrode within a distance of 1.5-2.0 cm the plasma densi-
ty decreases typically by 3-5 times in comparison with
the maximum density value. The calculations also show
a nonuniform character of radial plasma density distri-
butions. When the central electrode has a positive po-
tential ($\xi > 0$), the plasma is pressed to the external
electrode, whereas at $\xi < 0$ the contrary situation is
observed. This plasma compression is caused by longitu-
dinal Hall currents.

Fig.4 shows the results of numerical calculations.
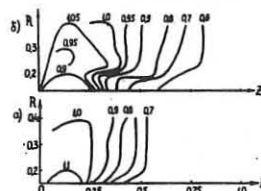
Fig.4

Equal plasma density lines.
$\xi = +0.08$, $\eta = 0.1$ $\beta = 2$ for
$\tau = 0.3$(a) and $\tau = 0.4$ (b)

Unfortunately, in the calculations we failed to obtain
such a strong displacement of the plasma from the region
adjacent to the anode that was observed in the experiment.
This disagreement of data can be explained by some diffe-
rences existing between the calculation parameters and
experimental conditions. To approach the experimental
conditions, the value of β should be taken to be several
times smaller; however in this case, when the contributi-
on of the Hall currents is essential, it is impossible
to perform the calculations with such values of ξ. Ne-
vertheless, the results of the numerical calculations
correctly show the tendency in the plasma behaviour. It
means that the PPA-model used permits one to estimate the
effect of different plasma parameters on plasma accele-
ration processes and the plasma formation behind the ac-
celerator muzzle.

1. W.D.Pearce. In col.: Production and studies of high
   temperature plasma.Tr.from. Eng.,ed V.A.Fabrikant,M,
   IIL publ,1962, p.221.

2. K.V.Brushlinskij, A.I.Morozov. In:Voprosy teorii plas-
   my,M., Atomizdat,1974, N 8, p.88-163.

3. A.G.Belikov et al.VANT,Kharkov,1977,Is.1(6),p.11-18.

A SHORT Z-PINCH

A.I.Zemskov, V.V.Matveev, V.V.Prut, A.M.Udalov

I.V.Kurchatov Institute of Atomic Energy,
Moscow, USSR

The purpose of a given work was an experimental che-
cking of the optimal matching conditions described previ-
ously by measuring the discharge characteristics and the
parameters of hard X-ray radiation. The study was perfor-
med at the experimental facility with a short Z-pinch dis-
charge chamber into which a ring-shaped plasma sheath
was injected.

The experimental facility includes a capacitor bank
($C = 60 \mu F$, $U_o = 20kV$), discharge chamber, plasma
injector, control and diagnostic equipment. The discharge
chamber consists of two stainless steel electrodes sepa-
rated by the plexiglass insulator with an inner diameter
50 cm and 8 cm high /Fig.1/.

To protect the insulator from the ultraviolet radia-
tion and to prevent the secondary breakdown, the anode is
profiled and an additional steel screen is installed inside
the chamber. The distance between the electrodes in the
flat central part is 4 cm.

Plasma from the injector enters the discharge chamber
through the ring-like channel formed with two cones: an
average radius of the puffed-in plasma sheath is 10 cm.
Inside the injector chamber, a plasma is generated as a
result of the chamber wall ablation. Therefore, the plasma
chemical composition corresponds to the material of the
chamber walls. The injector chamber is 8 cm long with
the diameter 2 cm. Injector is connected with the capa-
citor bank $C=280 \mu F$, $U_o = 4kV$. The amount of injected
particles is regulated by the applied voltage and time
delay (50÷100 μS) between the signals initiating the in-
jector and the main bank. In addition, the mass of acce-
lerated plasma depends on average atomic weight of plasma
components. To obtain proper matching of the accelerated
plasma, sheath and electrical circuit parameters (in the
18÷20 kV main bank voltage range), a sulphur was used as the
injector chamber wall material /1/.

The quality of the sheath has been studied with the
triggering probes which have showed that the sheath is
relatively thick. The parameters measured are: current,
inductive and resistive components of the voltage (the lat-
-ter was measured with the cable connected to the cen-
ters of the electrodes). The main discharge ($J_o \lesssim 1$ MA)
starts symmetrically along the inlet holes. An analysis
has shown that the mass of the accelerated plasma sheath
is 50 micrograms and the final velocity $\simeq 2.7 \times 10^7$ cm/s.
The accuracy of hitting the centre is 2÷3 mm. At the
collapse of the sheath, the current falls steeply to the
$\simeq 30\%$ of its value and a resistive component of the vol-
tage demonstrates a sharp peak. The collapse is accom-
panied by an X-ray emission. Some temporal (with an orga-
nic scientillator and a photomultiplier) and spatial
(with a pinhole camera) measurements have shown that the
X-ray radiation lasts for $\tau \approx 100$ ns and it is locali-
zed at the centre of the anode.

X-ray radiation dose has been registered with the do-
simeters located inside the insulator. The dose depends
on voltage as $D \sim U_o^3$ in the range of 10÷20 kV.
Use of the dosimeters with foils (Cu, Ag, Pb) has allowed
to estimate the energy spectrum. For this purpose, the
spectral function has been approximated by an analytical
dependence with indefinite coefficients. A set of Fred-
holm equations of the first kind have been reduced to
a minimization of a net square functional by these coef-
ficients. The control measurements have been carried out
by a relative blackening of the X-ray films with filters,

12 films have been displaced in one cassette of lead, The
spectrum is close to the bremsstrahlung one of an X-ray
tube with the upper energy $E_m \approx 100$ keV.

Measurements of the total X-rays energy Q carried out
with a lead calorimeter have shown that the value of Q is
equal to: $Q \approx 2$ J when the energy of a capacitor bank is
equal to 10 kJ. These measurements allow to calculate
an effective electron current J_e as $Q = 10^{-9} \tilde{z} J_e E_m^2 \tau$,
$J_e \approx 50$ kA. Though J_e is strongly dependent on E_m
determined with low accuracy, it is evident that at a
final stage a considerable fraction of the discharge cur-
rent is transferred by fast electrons. An increase in the
electric field, in which these electrons are accelerated,
occurs due to a sharp decrease in the cross-section (focu-
ssing) of the plasma sheath near the axis, so that the
ohmic voltage $U_R = \ell J / \pi z^2 \sigma$ will reach ~ 100 kV
at $\tau \sim 1$ mm, if one assumes that $\sigma = 30$ $T_{eV}^{3/2}$ (Cou-
lomb conductivity), $\ell \sim 1$cm, $J \sim 300$ kA. Some estima-
tions show that $U > C_s$ (U is the electron current
velocity, C_s is the sound velocity). In this
case, some instabilities arise, the nonlinear effects
prevent their development limiting the directed veloci-
ty of electrons and, thus, decreasing σ . Then, the
measured U_R and, correspondingly, the regime of run-
away electrons is reached near the axis.

In conclusion, one should particularly emphasize a
fairly good reproducibility of the current waveforms
and the X-ray doses. This fact will allow
to hope on a stable fusion yield if a corresponding
working medium in the injector is used.

References

1. A.I.Zemskov, V.V.Prut, V.A.Khrabrov - J.Tech.Physics,
1972, v.42, N 2, p.358.
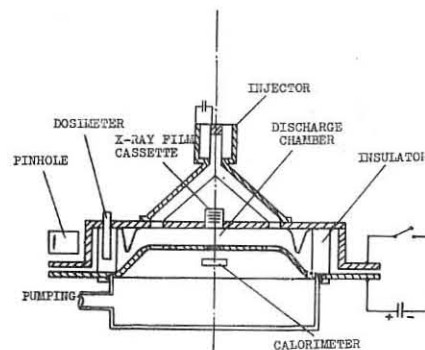
Fig.1 Diagram of the experimental facility
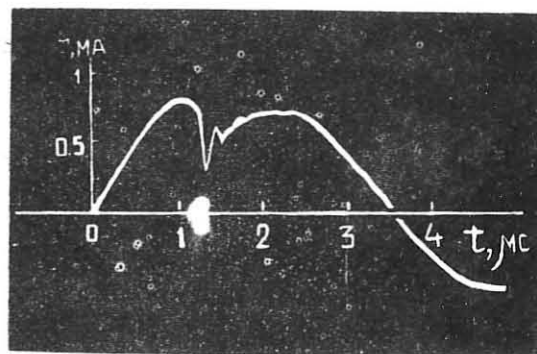
Fig.2 Current oscillogram

SHAPING OF LOCAL HIGH-TEMPERATURE PLASMA FORMATION
IN A POWERFUL PINCHING DISCHARGE

U.A.Bykovsky and V.B.Lagoda

Moscow Engineering Physics Institute, Moscow, USSR

Specific properties of high-temperature plasma formations (PF) observed in powerful pinch discharges /1/ are the highest (for present-day plasma instruments) values of electron temperature and electron density. A PF observation in investigations carried out by various devices testifies to the common features in the physical processes taking place in plasma at the initial (including pinch) discharge stage. Here arises an essential question if it is possible to consider the pinch current-carrier plasma to be locally homogeneous or consisting of separate current channels each of which, has its own self-congruent system of magnetic fields /2/. The latter provides the conductivity of high currents without developing any instability such as "sausage" and "kink". The paper presents the results of the investigation of PF formed in a high-current discharge with the electrode geometry (fig.2) close to that for the Mather coaxial accelerator (MCA) and with initiation by plasma generated at the buttend of the inner electrode (IE) by means of a focussed radiation of the impulse laser. The low-inductive discharge similar to the one reported in /3/ had the total capacitive storage energy as high as 2 KJ while the maximum current was 200 KA. The diagnostic apparatus included transmitters of X-ray radiation and of microwave radiation, an image converter camera, X-ray pinhole camera, a time-of-flight mass-spectrometer connected with the magnetic one and a Faraday cup. T_e value was measured by a filter method. Time resolution of the equipment was about 7 ns. Distribution of the current density in the inter-electrode gap was restor-
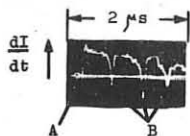
Fig.1. Typical waveform of dI/dt.
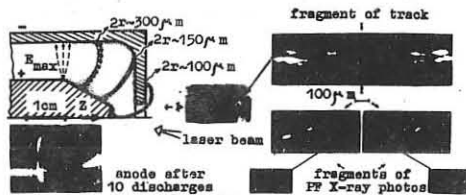
Fig.2. Schematic cross-section of coaxial accelerator. Comparison of diametrical dimensions of striations with those of plasma formations.

ed according to the pattern of the tracks arising after the discharge on the electrodes surface when special coatings were deposited onto it /4/.

In 60÷100 ns after the breakdown initiation by the laser plasma the first pinch-effect was observed (A,fig.1). The following plasma column decay gave rise to the secondary current sheath (CS) which in its turn accelerated towards the axis and collapsed (B,fig.1). Such a process followed by the heating of the electrodes lasted up to the flaming of arc at the raise of plasma column voltage at the moment of the next pinching in turn. High spatial resolution of the track method /4/ (~20 μm) allowed to detect the effect of CS breaking into self-contained striations. The latter were grouped in pairs and maintained up to the stage of collapse. As the CS advanced to the axis the diametrical dimension of an individual track decreased. The comparison of the tracks at the ultimate phase of CS motion with the PF image recorded by the pinhole-camera (fig.2) makes possible to find the proximity of their diametrical dimensions. Insertion to IE of the sharply angular convexity which produced a region of an increased electrical field strength enabled us to regulate the process of CS shaping. A hollow on the IE buttend provided the CS "roll off" regime at the moment of pinch by analogy with the case of MCA with a hollow anode. Location of the CS
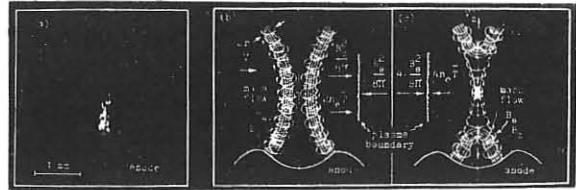
Fig.3. a: X-ray pinhole (10 μm diameter) photo (30-shots time integrated); b,c: scheme of Bostick's vortex filaments collapse (left-handed and right-handed).

primary junction resulted in the space stabilization of the PF formation (fig.3a). T_e of PF was as high as 7 KeV.

Let's consider (fig.3b) the CS collapse scheme assuming that the obtained striations have the structure analogous to the well studied Bostick's vortex filaments /2/. Let's assume that the CS consists of two filaments containing inside axial magnetic fields B_z equal in values and opposite in directions, and moving towards the discharge axis from the opposite sides with the velocity V_k. The pressure balance at the surface of an individual filament before the junction will correspond to the equation: $(N_1 T_1 + N_e T_e) + r^2 B_z^2/2 = J^2/2c^2$ (1), where T_i, N_i, N_e, r, J, c are the ion temperature, ion and electron linear densities, radius and current of filament, speed of light correspondingly. The junction of filaments (fig.3c) will lead to the rearrangement of B_z-lines and their receding at the rate of V_z along the discharge axis. This will be followed by ranishing of the last addend in the left part (1) by a break of the previously existed pressure balance and by a compression of the current channel. According to the equation: $J = \frac{2Z}{\alpha} e N_e c_s$ /1/, where Z, α, e, c_s — mean value of the ion charge, ratio of current channel radius to ion Larmor radius in the azimuthal magnetic field B_θ, an electron charge, sound speed in plasma correspondingly. As the value of $2Z/\alpha$ approaches unity, the electron drift velocity will draw near the c_s and a transition to the ion-acoustic turbulence condition will take place. That condition will be accompanied by a rapid energy input to the plasma. Buneman instability is likely to become at an intermediate stage leading to $T_e \gg T_i$. During the experiment at the stage of compression we recorded about ten pairs of striations. This reasoning can be easily transferred to this case if we assume that the sum of B_z taken at all collapsing filaments is equal to zero. The existence of turbulent processes in the PF region was proved by the presence of microwave radiation at the friquency $\sim 10^{10}$ Hz. The signal had a form of pulse train with the summary duration 20÷80 ns and with periodicity between separate spikes ~ 20 ns (fig.4). The train amplitude and duration correlated with the value of discharge current at the moment of collapse.

The ion flux recorded after the PF decay in the axial direction through a hole of the outer electrode consisted of a series of clots. The major part of the flux was concentrated in the aperture angle 10°. The collector measurements allowed to estimate the total number of flowing ions with the value of $\sim 10^{17}$. We registered ions of $Fe^{+15}, Cu^{+19}, Mo^{+20}, W^{+25}, Pb^{+26}$. The energy of flowing ions was as high as 1 MeV. The fact that the results of measurements proved to be independent of the electrode polarity was rather assential. The recorded pattern may arise from the acceleration of ions appearing during the turbulence heating by means of ion-acoustic waves.
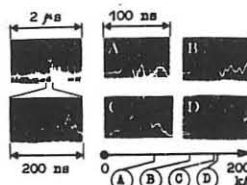
Fig.4. Microwave signals.

/1/. U.A.Bykovsky et al —JETP Lett., 31, N5, p.265, 1980.

/2/. W.H.Bostick et al—Annals of the N.Y.Ac.Sc.,251,2,1975.

/3/. U.A.Bykovsky et al —JETP Lett., 30, N8, p.489, 1979.

/4/. G.Herziger et al — Phys. Lett., 69A, N4, p.273, 1978.

THE REXIMPLO SPHERICAL PINCH: IMPROVED NEUTRON PRODUCTION AND 3-D COMPUTATIONAL ANALYSIS

E. Panarella and R.P. Gupta

National Research Council, Ottawa, Canada, K1A 0R6

Abstract: Work on the REXIMPLO experiment has progressed along two lines:

1) experimentally, a factor of ∼10 increase in neutron production has been obtained by a proper synchronization of the spark channel generation relative to the launching of the implosive shocks and by stepping up the energy of the condenser bank by ∼50 percent;

2) a 3-D computational analysis has offered a clear insight into the magnetic pressure (B^2) distribution inside the spherical arrangement, which allows redesign of the pinch in order to achieve better plasma confinement.

As a continuation of the work reported at the 9th European Conference on Controlled Fusion and Plasma Physics in Oxford [1], we have recently increased the neutron production in our spherical pinch device by properly timing the initiation of the spark channel formation relative to the implosion phase, and by increasing the implosion bank energy by ∼50 percent.

The experimental arrangement is essentially that described in [2] (Fig. 1). A linear spark in deuterium at 1 Torr initial pressure is created by discharging a small condenser bank (2μF-21KV-441J) between two electrodes aligned along a diameter of a spherical vessel (∼8 cm radius) and the spark channel is consequently compressed by implosive quasi-spherical shocks created by discharging a much larger condenser bank (67μF-21KV-14.8KJ) in the spherical pinch. When the spark channel is created close to the time of collapse of the imploding shock, the neutron output increases by about an order of magnitude, goin from 4.41×10^5 to 3.42×10^6 neutrons per shot, on average.

To see more clearly the time history of the neutron emission and to relate it to the compression of the spark channel, let us refer to Fig. 2 which shows a streak record of the plasma luminosity within the channel and a simultaneous oscilloscope record of the neutron signals. One notices that the imploding shocks generated at the periphery of the discharge vessel are strong to the extent that no radiation in the visible range is emitted. Only when the shocks collide with the spark channel, the concomitant phenomena of channel compression and refraction of the shocks within the channel increase the channel luminosity in the visible range. Neutrons appear as burst of ∼1 μsec duration of decreasing intensity, occurring roughly at the times when the refracted shocks collapse at the center of the vessel and when maximum channel compression takes place.

In order to understand the details of plasma confinement, we have recently started to work on a 3-D computational analysis of the magnetic pressure (B^2) contour lines inside the spherical pinch (Fig. 3-4). Because of the greatly varying magnetic field distribution and other plasma parameters in the domain of interest, the finite element method, rather than the finite difference scheme, was used. The problem is irreducible to lower spatial dimensions, although it does have reflections and inversion symmetries. Because of these symmetries, only an octant of the sphere is needed to be considered in all the computation. Therefore, the portion of shell in the first octant is divided on each side into 36 triangles by joining 26 nodes, as shown in Fig. 3. The nodes are the intersections of lines radiating from the centre. The sections of these lines between the two surfaces of the shell and the triangles constitute triangular prism elements which are split into three tetrahedra such that the adjoining prisms have matching edges. The current density stream function is then calculated on the surface and the Laplace equation for the magnetic scalar potential is solved in order to deduce the magnetic field inside the sphere. The plots shown in Fig. 4 are contours of the magnetic pressure B^2 in three perpendicular planes of the sphere (see Fig. 1), assuming that the plasma is a perfectly conducting rigid ball. The most unfavourable situation exists in the x-y plane, where the magnetic pressure decreases along any direction radiating from the plasma ball, which means that the plasma is not contained in that plane. The situation improves in the y-z plane, where the magnetic pressure increases in the z-direction and therefore the plasma is confined in that direction. Finally, the most favourable situation exists in the x-z plane, where the magnetic pressure increases in all directions as one moves away from the plasma ball, and therefore the plasma is perfectly confined in this plane.

Work is underway in order to: a) prove experimentally that the neutrons emitted are of thermonuclear origin. To this end, we are setting up around the plasma a 6-channel neutron detection system capable of assessing the symmetry of neutron emission, and b) redesign the pinch to approach the ideal situation whereby the magnetic pressure B^2 increases in every direction radiating from the plasma ball.

[1] E. Panarella and R.P. Gupta, Proc. 9th European Conference on Controlled Fusion and Plasma Physics, Oxford, England, September 1979, p. 52.

[2] E. Panarella, Canad. Journ. Phys. 58, 983 (1980).
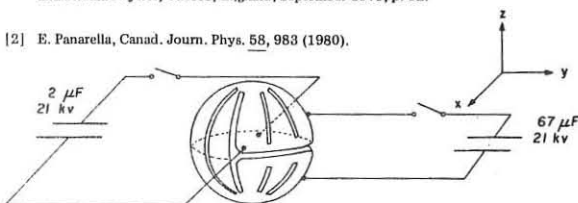
FIG. 1 — SPHERICAL PINCH ARRANGEMENT
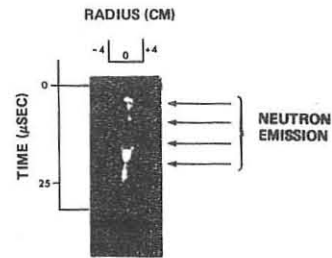
GAS: DEUTERIUM
PRESSURE: 1 TORR

NEUTRON SIGNALS

TIME (μSEC)

FIG. 2 — THE UPPER PHOTOGRAPH IS A STREAK RECORD OF THE PLASMA LUMINOSITY WHICH SHOWS THE INITIAL SPARK AND THE SUBSEQUENT COMPRESSIONS OF THE SPARK CHANNEL BY THE IMPLOSIVE SHOCK. THE LOWER PHOTOGRAPH IS AN OSCILLOSCOPE RECORD OF THE TIME HISTORY OF NEUTRON EMISSION.

ψ → CURRENT STREAM FUNCTION
Ω → MAGNETIC SCALAR POTENTIAL
1, 2, 3 ... GLOBAL NODE NUMBERING
a, b, c ... LOCAL NODE DESIGNATION
①, ②, ... TRIANGULAR ELEMENT NUMBERING
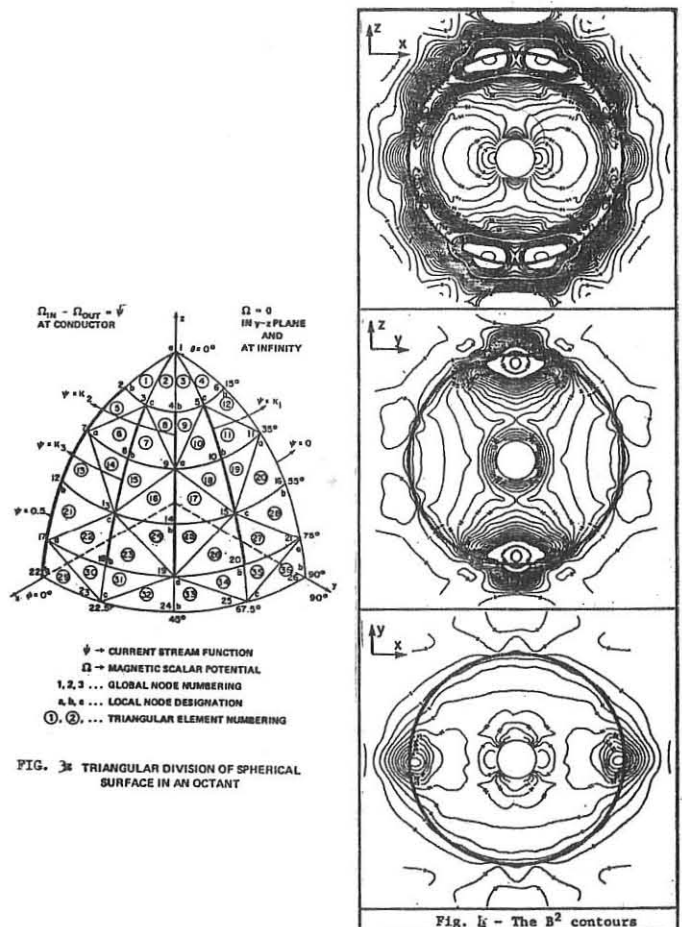
FIG. 3 — TRIANGULAR DIVISION OF SPHERICAL SURFACE IN AN OCTANT

Fig. 4 — The B^2 contours

ANOMALOUS THERMAL LOSSES IN A HIGH-β PLASMA

G. E. Vekstein

Institute of Nuclear Physics, Novosibirsk, USSR

An interest to high-β plasma properties was initiated by a few suggestions to use such a plasma in a controlled fusion research [1,2,3]. In this case the role of magnetic field is only to suppress thermal conductivity, so the magnetic field strength may be rather moderate. Furthermore a lot of microinstabilities peculiar to a low pressure plasma are absent when $\beta \gg 1$.

However, the process of high-β plasma cooling possesses some distinctive features, resulting in enhanced thermal losses and a considerable decrease of the energy confinement time [4]. The reason is that in noninertial systems (plasma confinement time is greater than sound propagation time) high-β plasma must be in contact with the cold walls of an installation. This report considers the cooling of a hot, strongly magnetized high-β plasma which is brought into sudden contact with a cold wall.

Initially a homogeneous hot plasma with temperature T_0 and density n_0 is located at a half-space $x > 0$ and at $x = 0$ is bounded by a rigid wall with zero temperature. The magnetic field is parallel to the wall plane, and its strength H_0 is so that the plasma is strongly magnetized: $(\omega_{Hi}\tau_i)_0 \equiv \delta_0 \gg 1$ but $\beta_0 \equiv 8\pi n_0 T_0/H_0^2 \gg 1$. From the mechanical equilibrium condition

$$nT = const = n_0 T_0 \tag{1}$$

it follows that in the near-wall layer with low temperature plasma density increases in time, so the plasma flow to the wall appears. The heat conductivity equation

$$\frac{3}{2}\frac{\partial(nT)}{\partial t} = \frac{\partial}{\partial x}\left(\varkappa\frac{\partial T}{\partial x} + \frac{5}{2}nT\upsilon\right) \tag{2}$$

shows that the total heat flux is constant in space:

$$\varkappa\frac{\partial T}{\partial x} + \frac{5}{2}nT\upsilon = \frac{5}{2}n_0 T_0 \upsilon_0 \tag{3}$$

where $\upsilon_0(t)$ is the hot plasma velocity at $x \to +\infty$. In the near-wall layer the plasma velocity decreases rapidly ($\upsilon \approx \upsilon_0 T/T_0$), so the convective heat flux is important only in a hot plasma with $T \sim T_0$, and at $T \ll T_0$ the thermal conductivity plays the main role:

$$\varkappa\frac{\partial T}{\partial x} = \frac{5}{2}n_0 T_0 \upsilon_0 \tag{4}$$

Since $\varkappa$ depends on the magnetic field, eq. (4) must be solved together with the magnetic field evolution equation, because in high-β plasma the magnetic field may be strongly destroyed by the plasma motion and thermoelectric effects (Nernst effect) [5]:

$$\frac{\partial H}{\partial t} = \frac{\partial}{\partial x}\left(\frac{c^2}{4\pi\sigma_\perp}\frac{\partial H}{\partial x} + \upsilon H + \frac{c}{e}\beta_\wedge\frac{\partial T}{\partial x}\right) \tag{5}$$

It is seen from (5) that Nernst effect results in an additional drift of the magnetic field to the wall. The corresponding velocity $V_H = \frac{c}{eH}\beta_\wedge\frac{\partial T}{\partial x}$ is connected with the heat diffusion velocity $V_T \sim \frac{\varkappa}{nT}\frac{\partial T}{\partial x}$ [5]:

$$V_H \sim \begin{cases} (m_e/m_i)^{1/2}V_T, & \omega_{Hi}\tau_i > 1 \\ V_T/(\omega_{He}\tau_e), & (m_e/m_i)^{1/2} < \omega_{Hi}\tau_i < 1 \\ V_T, & \omega_{He}\tau_e < 1 \end{cases} \tag{6}$$

Because $V_T \sim \upsilon_0$ (see eq. (4)), it may be concluded, that in a hot region the magnetic field is carried to the wall by plasma motion, and in a cold near-wall layer the main role is played by the Nernst term. The magnetic field profile depends strongly on the wall boundary condition for eq. (5). We consider two extreme cases: nonconducting and perfectly conducting walls. At first we note, that there is no any length scale in our problem, so the solution is of the self-similar nature. The corresponding variable is connected with temperature conductivity of a hot plasma χ_0:

$$\xi = x/(\chi_0 t)^{1/2}, \quad T(x,t) = T_0 T(\xi), \quad n = n_0 n(\xi), \quad H = H_0 H(\xi), \quad \upsilon = \left(\frac{\chi_0}{t}\right)^{1/2}\upsilon(\xi) \tag{7}$$

where $T(\xi), n(\xi), H(\xi), \upsilon(\xi)$ are dimensionless functions. In these notations the heat losses enhancement is revealed in that $\upsilon(\xi \to +\infty) \approx \upsilon_0 \gg 1$. From (5) we have now

$$-\frac{\xi}{2}\frac{dH}{d\xi} = \frac{d}{d\xi}\left\{\frac{(m_e/m_i)^{1/2}}{\beta_0 T^{3/2}}\frac{dH}{d\xi} + (\upsilon + V_H)H\right\} \tag{8}$$

A detailed analysis of eq. (8) will be presented elsewhere, and here we give only the final results. If a wall is nonconducting, the boundary condition is: $H(\xi = 0) = 1$. In this case the left-hand part of (8) may be neglected, so the magnetic field drift is constant. Besides, if $\beta_0 > m_i/m_e$ the magnetic viscosity is not important, and magnetic field may be obtained from a very simple condition:

$$(\upsilon + V_H)H = \upsilon_0 \tag{9}$$

Using (6) we get now that at $T > (m_e/m_i)^{1/2}$ the magnetic field is frozen into a plasma, so $H = n = T^{-1}$. Then, at $T < (m_e/m_i)^{1/2}$ the Nernst effect is important, and H is of the order of $(m_i/m_e)^{1/2}$ up to $T = T_1 \sim (m_e/m_i)^{1/5}\delta_0^{-2/5}$, where the ions become unmagnetized: $(\omega_{Hi}\tau_i)_1 \sim 1$. Then the magnetic field decreases rapidly and is of the order of unity up to $T = 0$, i.e. to the wall. The magnetic field profile in this case is shown in Fig. 1. After that we can solve eq. (4) and find the temperature profile $T(\xi)$, where υ_0 is still an unknown parameter. To find υ_0 one should use the continuity equation for a plasma, which in the self similar variables is as follows:

$$-\frac{\xi}{2}\frac{dn}{d\xi} = \frac{d}{d\xi}(n\upsilon) \tag{10}$$

Taking into account that $n = T^{-1}$, for the plasma flux we get: $n\upsilon = \int \xi(T)dT/2T^2$, so $\upsilon_0 = \int \xi(T)dT/2T^2$. The main contribution comes from the region with temperature $T \sim T_1$, and $\upsilon_0 \sim \delta_0^{1/5} \gg 1$. The plasma, which flows from the hot region, is accumulated at temperature $T \sim T_1$. So at $T > T_1$ plasma flux $n\upsilon \approx const$ and $\upsilon \approx \upsilon_0 T$. At $T < T_1$ the flux decreases rapidly and vanishes at the wall. Returning now to usual notations, the total heat flux to the wall is

$$q \sim (\omega_{Hi}\tau_i)_0^{1/5} n_0 T_0 (\chi_0/t)^{1/2} \tag{11}$$

and the effective thermal conductivity, $\varkappa_{ef} \sim \varkappa_0 (\omega_{Hi}\tau_i)_0^{1/5} \sim n_0 cT_0/eH_0$, is of the order of the Bohm one. This result proves to be valid up to $\beta_0 \sim 1$.

In the opposite case of a perfectly conducting wall the total magnetic flux remains constant. So in the near-wall layer the magnetic field drift due to Nernst effect must be balanced by the magnetic diffusion drift in the opposite direction. As a result, the buffer magnetic layer is formed with $\beta < 1$ and $H = H_0 \beta_0^{1/2}$. Then the magnetic field smoothly decreases up to $H = H_0$ in a hot plasma (see Fig. 2). The effective thermal conductivity depends now on the relation between large parameters β_0 and δ_0. If $\beta_0 > \delta_0^{4/3}$ the buffer field layer is rather thin and $\varkappa_{ef} \sim \varkappa_0 \delta_0^{1/3}$. At $\beta_0 < \delta_0^{4/3}$ the effective thermal conductivity is $\varkappa_{ef} \sim \varkappa_0 \beta_0^{1/4}$.

References

1. E.P.Velikhov. Comments on Plasma Physics, 1, 171, 1972.
2. G.I.Budker. In Proc. VI Europ. Conf. on Plasma Physics, 2, 136, 1973.
3. Gerwin R.A., Malone R.C., Nuclear Fusion, 19, 155, 1979.
4. G.E.Vekstein. Doklady Academy Nauk, 237, 295, 1977. Pisma JETP, 30, 596, 1979.
5. Braginsky S.I. In Reviews of Plasma Physics, 1, 205, 1965.

Fig. 1.

Fig. 2.
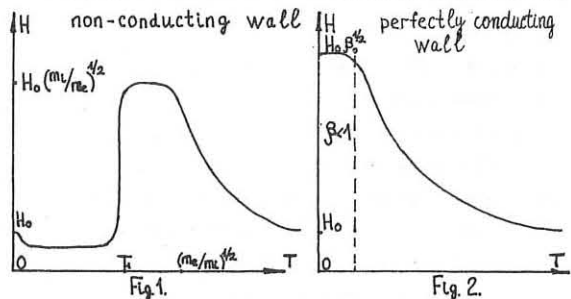
STUDY OF THE HEATING OF A DENSE PLASMA
IN LINEAR THETA-PINCH SYSTEMS

V.A.Burtsev, A.A.Bardinov, A.B.Berezin, A.P.Zhukov,
V.A.Kubasov, B.V.Ljublin, V.N.Litunovski,
V.M.Kozhevin, V.A.Ovsjannikov, A.N.Popitaev,
V.G.Smirnov, V.A.Titov, Yu.I.Sholokhov

D.V.Efremov Scientific Research Institute of
Electrophysical Apparatus, Leningrad, USSR

Abstract. The paper presents the status report on the heating of a dense plasma in the linear theta-pinch UTRO with fast-rising magnetic field. The plausible ways aiming to rise the efficiency of the heating are discussed the basic results of numerical simulation and physical processes optimisation in the similar devices are described.

I. Experimental conditions. The method of inductance-capacity energy storage ($W_o \lesssim 0.6$ MJ) has been used for production of magnetic fields up to $B_z \lesssim 60$ kG with the rise time $\tau_p \lesssim 0.5 \mu s$. The opportunity to form at these conditions the dense ($n_e \simeq 2 \cdot 10^{17}$ cm^{-3}) and sufficiently hot ($T_e + T_i \sim 0.5$ keV) plasma column with small radial compression [1] is shown.

II. Experimental results. The main attention has been drawn to the elucidation of the suprothermal particles generation mechanism ($\bar{W}_e \gtrsim 20$ keV; $\bar{W}_i \gtrsim 1.5$ keV) at high initial filling pressures ($P_o > 0.2$ Torr). Experimental study of magnetic field diffusion and the comparison with the results of numerical simulation shows that the most probable mechanism of the anomalous plasma conductivity in the phase of radial compression is the development of the low-hybrid drift instability. The microfluctuations of plasma density accompanying this process are proposed to be among the main reasons of experimentally observed significant broadering of probing ruby laser radiation line (from $\Delta\lambda_D = 3 \cdot 10^{-5}$ nm up to $\Delta\lambda \simeq 8 \cdot 10^{-3}$ nm). Strongly modulated oscillation of the internal magnetic field with reversal of both of measured components were observed during compression stage (fig.1). Basing on the X-ray emission analysis data obtained using filters, the radial distribution of mean suprothermal electrons energy has been plotted (fig.2). The preliminary value of electron temperature, corresponding to this time interval does'nt exceed $T_e \sim 100$ eV. The maximal neutron yield ($N \sim 10^7$ per shot) and its dependence on deuterium pressure (fig.3) differs substantially from the respective data by numerical simulation under assumption of the thermal origin of the neutrons. The set of the date obtained does'nt contradict with the alternative hypothesis that the hard X-ray emission and the neutron yield could be attributed to the deceleration of the charged particles, primarily accelerated in the regions of magnetic field zero lines on the plasma target. The similar conditions could be realized at noncontrollable reconnection of magnetic force lines during dense plasma compression in the complex magnetic field structure. The evolution of the mean electron energy made within the framework of the model described in ref.[2] is in the reasonable agreement with experimental data.

III. Numerical simulation of the linear theta-pinch with inductance-capacity energy storage. The self-consistent model has been used based upon "snow-plow" approximation and taking into account both the variations of the entropy, caused by the processes of the joule and shock heating and the magnetic field diffusion at the electron scattering on the electric field fluctuations. The work of magnetic field as proposed, could be increased by means of plasma delay in the near to the wall region. This proposal can be realized, par example, by freezing of some deuterium on the chamber wall or by the spraying of the mass using for instance, the laser induced target explosion in the axial zone. In the case of reconstructed UTRO-M device (solenoid length is 3 m) with concave initial plasma density profile the temperature rises up to factor 2.5.

The temperature growth and the enhancement of the neutron yield could be achieved also by providing the dynamic interaction of encountering radial shock waves. Fig.4 shows optimized dependences of the temperature and the neutron yield on the operational parameters of UTRO-M. Evaporation explosion energy used in calculation is 750 J.

IV. Application of pulsed CO_2-lasers. The following subjects have been considered at the simulation study of laser radiation ($W_L = 1 \div 10$ kJ, $\tau_L = 1 \div 3 \mu s$) with the theta-pinch UTRO-M plasma: heating by axial beam in the quasistationary magnetic field; stability of the laser beam propogation in the plasma column; combined laser heating with adiabatic plasma compression. The optimal conditions for the range of incidence angles at laser radiation, plasma density profile and beam profile have been obtained. Preliminary laser heating of a plasma would allow to increase ten fold the efficiency of the consecutive heating by adiabatic compression. The plasma energy content, as estimated, can reach $W_{pl} \sim 100$ kJ ($T \sim 0.5$ keV; $n \sim 3 \cdot 10^{18}$ cm^{-3}; $B_{zm} \sim 300$ kG).

References

1. V.A.Burtsev, A.B.Berezin, et al., in Plasma Phys. and Contr.Nucl.Fus.Res.1978, IAEA, Vienna, 1979, v.II, p.205.

2. S.V.Bulanov, P.V.Sasorov, Izv.AN SSSR, Phys., v.39, No.2, 1975, p.375.

Fig.1

Fig.2

Fig.3

Fig.4
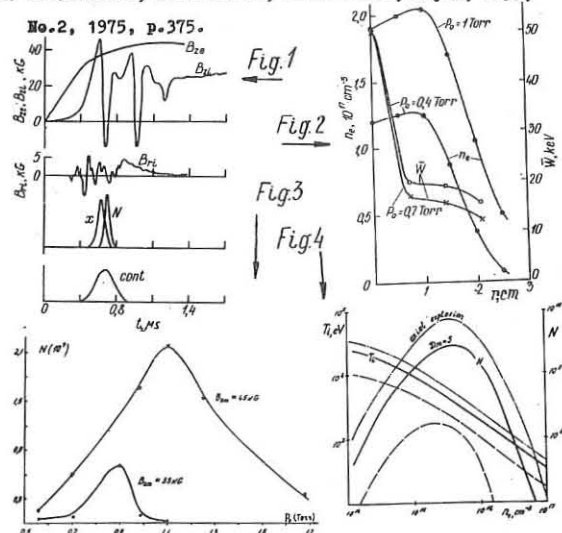
EFFECTS DUE TO VIOLATION OF THE SECOND ADIABATIC INVARIANT

B. Lehnert

Royal Institute of Technology, S-10044 Stockholm 70, Sweden

Abstract. When the curvature of the longitudinal invariant surfaces varies in space, the constancy of the second adiabatic invariant of charged particle motion can become violated. This non-adiabatic effect applies in the first place to ions, thereby producing charge separation and electric currents in a quasi-neutral plasma. An example is given where these currents have a stabilizing effect on plane kink disturbances.

1. Introduction

In closed-field line and mirror type magnetic geometries, ions and electrons drift from field line to field line at the same time as they perform nearly periodic orbits along the field lines at full thermal speed. For small Larmor radii this transverse drift takes place in steps which closely follow the longitudinal invariant surfaces determined by the constancy of the first and second adiabatic invariants of charged particle motion [1,2].

However, on account of their larger mass and lower thermal speed in a plasma of nearly isotropic temperature $T_i = T_e \equiv T$, ions will be subject to more limited restrictions with respect to the constancy of the second adiabatic invariant than electrons [3]. After completing one period of longitudinal motion along the magnetic field $\underline{B}$, the ions have at the same time drifted a certain distance $\Delta L_{\perp i}$ across $\underline{B}$. Thus, when $\Delta L_{\perp i}$ becomes comparable to the scale of the spatial variation of the invariant surfaces, the constancy of the second adiabatic invariant is expected to become violated, and the ions to "slip" across these surfaces. The resulting plasma dynamical effects will be outlined here in the special case of plane kink disturbances, but such effects are also expected to become important to a manifold of other situations.

2. Non-Adiabatic Particle Motion in a Z-pinch

As an illustration we consider a Z-pinch having its axis along z in an unperturbed state where there is an axial current density $j = j_o \left[1 - (r/a)^\nu \right]$ determined by the radial coordinate r and the pinch radius a. The corresponding axial guiding centre drift velocities u_{io} and u_{eo} of ions and electrons are given by

$$u_{io} = -u_{eo} = 2M\nu(r/a)^{\nu-1}/ea(\nu+2)\left[1 - (r/a)^\nu/(1 + \tfrac{1}{2}\nu)\right] \equiv 2Mf_\nu/ea > 0 \qquad (1)$$

Here W denotes the velocity of gyration, $M = mW^2/2B = \text{const.}$, $u_{\shortparallel} = (8kT/\pi m_i)^{1/2}$ is the particle velocity along $\underline{B}$, and particles with $2u_{\shortparallel}^2 = W^2$ are considered, being equivalent to the bulk of an isotropic thermal distribution with $W^2 = 2kT/m_i$.

A small kink perturbation $\underline{\xi} = (\xi_o\sin\gamma z,0,0)$ in the zx-plane of Fig.1 is introduced, having the wave length $\lambda = 2\pi/\gamma \gg \xi_o$. The magnetic field is assumed to be strong enough for the average electron drift motion to be adiabatic and to have the form $\underline{U}_e = u_{eo}(\xi_o\gamma\cos\gamma z,0,1)$ in the frame xyz. The longitudinal invariant surfaces then become nearly "concentric" with the perturbed plasma surface of Fig.1.

For ions we define the adiabaticity parameter θ_i where

$$\theta_i \equiv 4\Delta L_{\perp i}/\lambda = 16\pi M f_\nu/eu_{\shortparallel}\lambda = 8\sqrt{2}\pi f_\nu(a_i/a)(a/\lambda); \quad \Delta L_{\perp i} = 2\sqrt{2}\pi f_\nu a_i \quad (2)$$

and $a_i = 2M/eW$ stands for the ion Larmor radius. When $\theta_i \ll 1$ the ion motion thus remains adiabatic. For θ_i-values of order unity the ions become slightly non-adiabatic, in the sense that there is a certain "slip" between the ion motion and the invariant surfaces. This regime will be further discussed here. The extreme non-adiabatic case $\theta_i \gg 1$ is out of the scope of this report.

According to the exact equation of particle motion, the surfaces traced by the transverse drifts of magnetically confined ions and electrons become concentric in axisymmetric geometries of constant spatial curvature. Consequently, the ion drift is expected to have a component directed across the invariant surfaces only when the curvature of the invariant surfaces varies in space, such as in Fig.1. Further, this velocity component should only become important in cases where θ_i cannot be neglected as compared to unity.

A detailed deduction of this non-adiabatic behaviour cannot be given here. Only a tentative argumentation is presented which has to be tested by later more rigorous deductions. We consider the paths traced by the average guiding centre drifts, in the plane $y = 0$ of Fig.1 which passes through the axis of the plasma column. Assuming

Fig.1. Plane short-wave kink perturbation of a plasma column. The non-adiabatic ion motion produces a current pattern $\underline{j}^x$ outlined by the dashed contour. The $\underline{j}^x \times \underline{B}$ force tends to stabilize the perturbation.
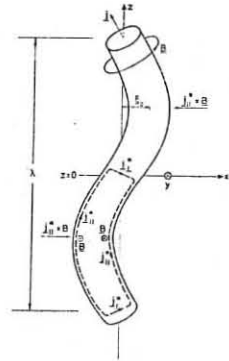
first that both ions and electrons are adiabatic and drift at the antiparallel average velocities $\underline{U}_i$ and $\underline{U}_e$ along the same path $x = x(z)$, a Taylor expansion yields

$$\underline{U}_i(z) - \underline{U}_e(z) \simeq \left[\underline{U}_i(z + \Delta z) - \underline{U}_e(z + \Delta z)\right] -$$

$$- \left[\underline{U}_i'(z) - \underline{U}_e'(z)\right]\Delta z - \tfrac{1}{2}\left[\underline{U}_i''(z) - \underline{U}_e''(z)\right](\Delta z)^2 \qquad (3)$$

for arbitrary but small values of Δz. In this case the corresponding current density $en(\underline{U}_i - \underline{U}_e)$ becomes directed along the invariant surfaces both at z and $z + \Delta z$. Next we consider a case where the drift surface curvature is constant at $z + \Delta z$, but changes rapidly enough for the adiabaticity condition of ions to be violated at z for $\Delta L_{\perp i} = |\Delta z|$. In this case $\underline{U}_i(z + \Delta z) - \underline{U}_e(z + \Delta z)$ of eq. (3) still becomes directed along the invariant surfaces. On the other hand, the average ion drift then results from a meanvalue formation over a relatively large step length $\Delta L_{\perp i}$ which contains contributions of rapidly changing curvature. In a first approximation this implies that $|\underline{U}_i''(z)| \ll |\underline{U}_e''(z)|$ in eq. (3), i.e. the rapid spatial changes of the drift orbit are "smeared out" in a meanvalue formation for ions, but not for electrons. In its turn, this results in an "uncompensated" remainder of the last term in eq. (3), leading to a "slip" of the ions across the adiabatic drift surfaces. Thus, there arises a corresponding current density

$$\underline{j}_\perp^x \simeq \tfrac{1}{2} en \, \underline{U}_e''(z)(\Delta z)^2 = 32\pi^5 f_\nu^3(\xi_o/a)enW(a_i/\lambda)^3(1,0,0)\cos(2\pi z/\lambda) \qquad (4)$$

in the xyz frame of Fig.1, as obtained from eqs. (1)-(3) when neglecting $\underline{U}_i''(z)$. This current density has maximum strength at the inflexion points of the kink perturbation, i.e. where the change in curvature has its maximum.

3. Non-Adiabatic Effects on Plasma Dynamics

The current of eq. (4) only forms a segment of a pattern which has to be set up to neutralize the corresponding electric space charges in a quasi-neutral plasma. In a first approximation this pattern is therefore suggested to be closed as outlined by the dashed loop in Fig.1. The loop includes a component $\underline{j}_{\shortparallel}^x$ having the modulus $|\underline{j}_{\shortparallel}^x| = (\lambda/2\pi a)|\underline{j}_\perp^x|$ and running parallel to the pinch surface.

The resulting $\underline{j}_{\shortparallel}^x \times \underline{B}$ force is transverse to the plasma column and performs an average work $\langle w^x \rangle = \langle \underline{j}_{\shortparallel}^x \times \underline{B} \cdot \underline{\xi} \rangle/2$ per unit volume, as obtained from integration over one wave length. Assuming a current distribution with $\nu = 2$ and putting $2nkT = j_o Ba$, we obtain a stabilizing contribution $\langle w^x \rangle = \mu_0 4 j_o^2(a_i/\lambda)2/4 > 0$. The work of the kink force is destabilizing and can be approximated by $\langle w_k^x \rangle = -31\pi^2\mu_0 j_o^2(a/\lambda)^2/2048$ [3]. Consequently, the ratio between these two energy contributions becomes

$$\theta^x \equiv -\langle w^x \rangle/\langle w_k \rangle = c^x(a_i/a)^2; \quad c^x = 512\pi^2/31 \qquad (5)$$

and increases linearly with the plasma temperature T. As an example a hydrogen plasma is chosen with a pinch current of 10^4A and a temperature $T \approx 3 \times 10^5$ K. Wave lengths $\lambda \lesssim 10a$ then become non-adiabatic. In this range eq. (5) yields $\theta^x \approx 20$. Consequently, the plane kinks considered here are expected to become stabilized at wave lengths of the order of and smaller than the pinch radius.

[1] Kadomtsev, B.B., Plasma Physics and the Problem of Controlled Thermonuclear Fusion (Ed. by M.A. Leontovich), Akad. Nauk USSR, 1958, Vol. III, p. 285.

[2] Northrop, T.G. and Teller, E., Phys.Rev.117(1960)215.

[3] Lehnert, B., Royal Institute of Technology, Stockholm, TRITA-PFU-80-11(1980).

DETERMINATION AND EVALUATION OF THE PARAMETERS
OF A D P F USING AN ALTERNATIVE METHOD

S. SINMAN

Middle East Technical University, Electrical Engineering
Department, Plasma Engineering Laboratory, Ankara-Turkey

A. SINMAN

Ankara Nuclear Research and Training Center, Electron Physics
Laboratory, Ankara-Turkey

Abstract: In this study, for the data processing in our Dense
Plasma Focus (DPF) system, a multiparameter numerical hierarchy
obtained from the fundamental equations based on the snowplows
model and its conclusions have been developed. Evaluating the
data along the transients of the total plasma current, the
anode current and the focus voltage recorded by on oscilloscope,
they have been possible to determine the time domain plasma par-
ameters such as the shock thickness, the sheat temperature, ve-
locity and electron density, the pressure at the focus phase
and the plasma temperature. Besides, the dissipated energy
through the focus notch or in other words, the plasma temperature
has also been calculated by means of the numerical integration.
In the text, a performance chart together with some other cor-
relation curves for the optimization of the DPF systems are sub-
mitted and discussed.

System: The plasma focus (Mather type) is consisting of 1.5 kJ
condenser bank, a controlled spark-gap switch, a co-axial ac-
celerator (internal and external electrode radii are 2.0 cm and
4.0 - 6.0 cm respectively and accelerating tunnel is 10.0 -
12.5 cm) and needed electronic control and measuring systems.

Preliminaries: It is known the fact that the plasma focus develop-
ment in a dense plasma system depends upon the breakdown, ac-
celeration and collapse phases respectively. For the plasma fo-
cus discharges which contain all these three phases, a modified
electrical circuit model is seen in Fig. 1.

Note: $L_{of} < \bar{L}_d(t)$, $Z_{of} > \bar{Z}_d(t)$
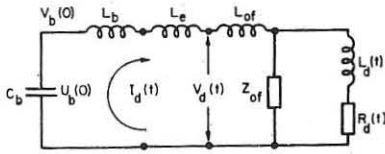
Fig. 1. Equivalent electrical circuit for DPF.

In the Figure; C_b is the bank capacitance, $V_b(o)$ the bank voltage
(fully charged), $U_b(o)$ the initial storage energy, L_b the induc-
tance of the capacitor bank, L_e the external inductances, L_{of}
the inductance of the focus electrode system, Z_{of} the character-
istic impedance of the electrode system and $L_d(t)$ and $R_d(t)$
are the inductance and the resistance of the discharge respec-
tively. The discharge voltage signals which can be recorded on
the oscilloscope, may approximately be written as,

$$V_d(t) = (d/dt)[L_d(t)I_d(t)] + I_d(t)R_d(t) \qquad (1)$$

On the other side an improved time varying discharge resistance
can be given to be,

$$R_d(t) = (2\pi C_b)^{-1} T_d Ln[V_1(o)/V_2(T_d)\gamma] \qquad (2)$$

where T_d is discharge period, $V_1(o)$ and $V_2(T_d)$ are the onset and
the one period after amplitudes of the discharge, the correction
coefficient $\gamma = V_b(o)/V_b(T_d/2)$, here $V_b(T_d/2) = [2U_b(t)/C_b]^{1/2}$
and $U_b(o)-U_f(T_p/2) = U_b(t)$. $U_b(o) = 0.5C_b V_b^2(o)$ numerically but
$U_f(T_p/2)$ by the numerical integration method can be found. By
the reason of the numerical hierarchy other fundamental equa-
tion of plasma focus /1/ are:
- Spitzer's resistivity relation; $\varrho = 3.3 \times 10^{-6}/T^{3/2}$ ohm-cm (3)
- The velocity of current sheat with respect to Snowplows;

$$v_s = (c^2 E^2/4\pi \varrho_0)^{1/4} \text{ cm/sec} \qquad (4)$$

- The shock thickness $T_s = (2w_{pe})^{-1} c a^{-1/2}$ cm $\qquad (5)$
where $a^{-1/2} = 2.9 \times 10^{-3} n_e^{1/2}/B$
- Magnetic pressure $B^2/8\pi = \bar{n}_e k(T_e + T_i)$ dyne/cm^2 (6)
- Minimum compression radius /2/ $r_m = c^2/4\pi q_s v_s$ cm (7)
where the turbulent electrical conductivity $q_t = w_{pe}^2/4\pi f_c$
$f_c = 4.3 \times 10^{-5} \bar{n}_e (kT_e)_{eV}$ cycle/sec.

Numerical Hierarchy: The fundamental focus parameters can be
calculated by the help of the following equations:
- The shock thickness from Eq. (5); $T_s(t) = Const/I_d(t)$ cm (8)
- The plasma resistivity using Eq. (8);

$$\varrho(t) = V_d(t)\pi T_s^2(t)/I_d(t)\ell_f \text{ ohm-cm} \qquad (9)$$

- The electron temperature by means of Eqs. (3) and (9);

$$T_e(t) = [3.3 \times 10^{-6} \varrho^{-1}(t)]^{2/3} \text{ keV} \qquad (10)$$

- The electron density from Eq. (4);

$$\bar{n}_e(t) = [V_d^2(t)/d_{ac}^2]Const[\ell_f/t]^{-4} \qquad (11)$$

where d_{ac} is the gap between the anode and cathode, ℓ_f is the
length of the electrodes.

Results: As is seen in the electrical equivalent circuit of the
focus system (Fig.1), the geometric inductances L_b, L_e and L_{of}
are being more effective on the discharge period. Although the
plasma impedance, $\bar{Z}_p(t) = [L_d^2(t)w^2 + R_d^2(t)]^{1/2}$ has a non-linear

property (e.g., in the focus phase it is 185 mohms) depending on
the pressure and using gas (H, D or He), the half period ($T_d/2 =
3.5$ µsec typically) has approximately shown a maximum increase
of 45 o/o. The inductances per conventional power capacitor
group ($C_b = 4 \mu F$, $V_b(o) = 10 - 15 kV$, $U_b(o) = 200 - 450 J$) have
been found as $L_b = 82.9$ nH, $L_e = 70$ nH and the inductance of focus
accelerator as 16 nH. Using a versatile bank system; at the 0.2,
0.4 and 0.6 kJ energy levels, experiments have been done and
extrapolating for the energy thresholds of the 1.1, 1.8, 3.5 kJ
they have been arrived to those expecting results. As it has
mentioned in the numerical hierarchy, during evaluation too,
current and voltage oscillograms and the physical parameters of
the DPF system have been accepted to be basic data. Besides, the
oscillograms taken from the studies done by the others /3-4/,
have also been evaluated by this method and it has been noticed
that the numerical results obtained is very close to orginal ones.
As it is known, the first half period contains of breakdown,
acceleration and collapse phases. The different input energy
levels being as a parameter, the functional relation between
the plasma temperature and the efficiency is seen in Fig. 2. The
efficiency has been calculated from the value of energy used in
first half period. In Fig. 3 a performance chart is presented.
In the chart, the gases to be used (H, D and He), the gap be-
tween focus electrodes (1.25, 1.75, 2.0 and 2.25) and the input
energy levels have been selected as the parameters and the cor-
relation between the electron density n_e and the electron tem-
perature (for the most probable distribution) has been shown.
Thus, it has been possible to define a DPF system together with
the physical and electrical parameters depending on the speci-
fications of discharge medium.

Conclusion: A 'Mather' type versatile DPF system has been re-
alized. Controlling in a wide operational range of the input
energy with a constant bank voltage but with a variable bank
capacitor (T_d constant) and using various electrode geomet-
ries, the properties of the different plasma media (H, D and
He at the pressure range 1.0 - 10.0 Torr) has been determined
by a simple and alternative method. This can also be converted
into fully automatic digital data processing system. On the
other hand, it can be possible to investigate and optimize the
system arrangement of DPF by means of a simpler way, for the
different employments. The preliminary comparision have exhi-
bited the accurary of the method.

References: /1/ Grim,H.R., and Lovberg,R.H.; Plasma Physics,
New-York, Academic Press., Part A, Ch., 6.; Part B, Chs., 11
and 15, (1971). /2/ Kaeppeler,H.J., Plasma Phys. Cont. Nucl.
Fusion Res. Proc. Conf., 6th, Berchtesgaden, Vol.III, p. 437,
(1977). /3/ Bottoms,P.J. et al., Plasma Phys. Cont. Nucl.
Fusion Res. Proc. Conf., 3rd, Novosibirsk, Vol.II, p.67(1968).
/4/ Hirano,K., et al., Jap. J. App. Phys. 17 No.19 (1978)1619.
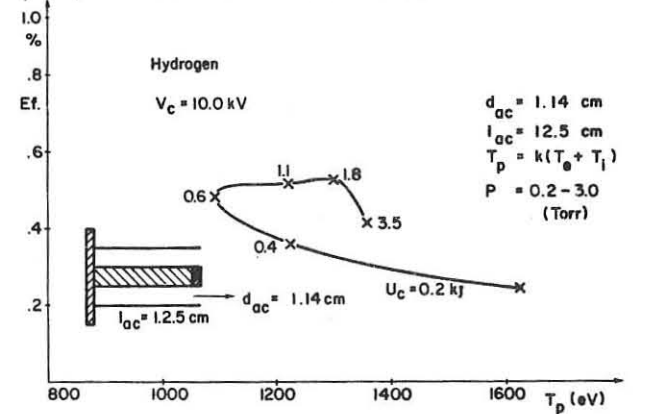
Fig. 2. Efficiency of DPF system.
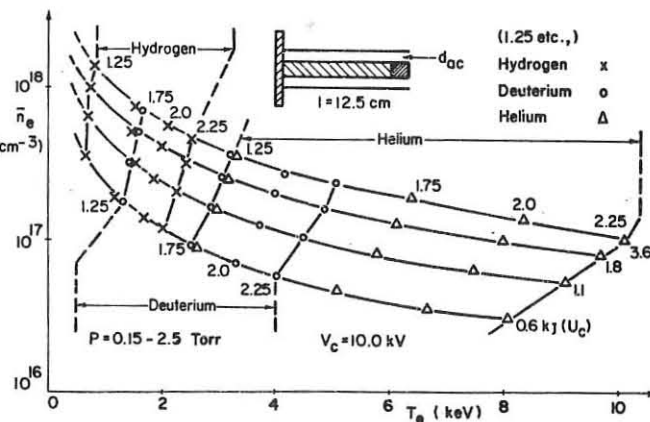
Fig. 3. Performance chart of DPF system.

INVESTIGATION OF THE BREAKDOWN AND RUN-DOWN PHASES
OF THE DPF DISCHARGE

S. Czekaj, S. Denus, W.Koziarkiewicz, W.Nawrot,
W.Skrzeczanowski, R.Socha, K.Tomaszewski, M.Zadrożny

S.Kaliski Institute of Plasma Physics and Laser Microfusion
p.o. box 49, 00-908 Warsaw 49, POLAND

The preliminary experimental investigations of the plasma focus initial phases are presented in this paper. The formation of the current sheath /CS/ and acceleration phase were investigated by means of time-resolved photographs and time-resolved magnetic field measurements. Spectral measurements were used for investigations of the plasma produced in the area between electrodes near the insulator.

The electrical data of the plasma focus device were: capacitance $C=21\mu F$, Inductance $L_o=100nH$, charging voltage $U=34kV$. The electrodes of Mather type had a length of 14.5cm and diameters of center and outer electrodes of 5 and 10cm, respectively. The center electrode /CE/ was insulated by alumina tube /I/ with an outer diameter of 6cm. The discharge vessel was filled with deuterium at pressure of 0.6, 1.5 and 3 Torr.

Photographs of the discharge were taken by means of an image converter camera /exposure time 20ns/. Fig.1 shows end-on and side-on pictures of the initial phenomena of the breakdown phase. At the zero time one can observe two types of breakdown: the gliding and the radial one [1] . About 300ns later CS expands radially and axially. The structure of the CS at the end of electrodes is determined by plasma layer being created in the limited area at the insulator end-face. This layer has a filament structure and expands axially and radially reaching the outer electrode after 1μs.
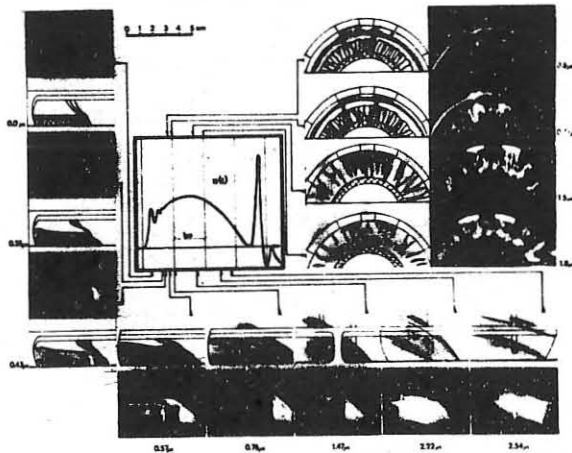
Fig. 1

Since this time the plasma layer has a parabolic shape. The insulator thickness is probably the main parameter which determines the creation of this layer.

The plasma behind the sheath front in the area between electrodes was studied by means of a spectral method. Measurements were made in the wavelength range of 4100-6700Å. The ISP51 prism spectrograph and the SPM2 grating monochromator were used. The optical set-up allowed to observe the area of 70μm width at 1cm from the insulator edge.

Carbon impurity spectral lines were found in the time -integrated spectrum. It is interpretated as the result of the oil particle penetration from the diffusion pump into

the vessel. The absence of the Al, O and Si lines gives evidence for the weak plasma interaction with the insulator material.

The time-dependence of D_α , CII and CIII line intensity is shown in Fig.2. The pulse maxima are lower for smaller
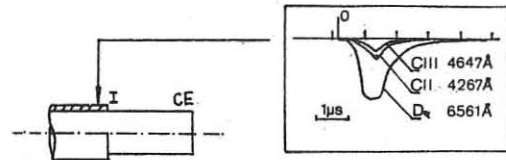
Fig. 2

pressures. The electron temperature calculated from the ratio of CIII and CII lines at the pulse maximum /1.4μs after breakdown/ amounted to 0.85eV. Plateau in the D_α trace is caused by self-absorption. The electron density amounted to $10^{16}cm^{-3}$, as was calculated from the Stark broadening of the time-integrated D_β line.

Magnetic field measurements were performed by means of two probes positioned first at $z_1=-11mm$, $z_2=-40mm$, then shifted to $z_1=-36mm$, $z_2=-65mm$ and $z_1=-81mm$, $z_2=-111mm$ /z=0 corresponds to the end of the electrodes/. The radial position of the probes was 35mm in all cases.

From the time delay between $\frac{dB}{dt}$ signals an average velocity of the CS near the end of the CE was calculated. The results are shown in Fig.3.
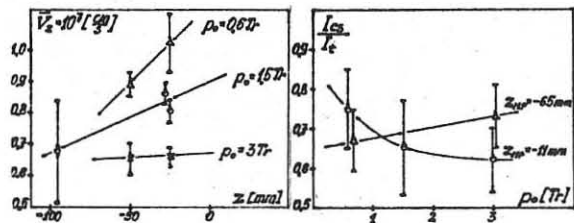
Fig.3   Fig.4

The CS velocity is not constant [2] but slighly increases in time [3] and depends on the initial gas pressure according to the simple snow-plow model [4].

By numerical integrating of $\frac{dB}{dt}$ signals the current carried by the current sheath /I_{CS}/ has been determined. This current was compared with the total current /I_t/ measured by the Rogowski coil. Fig.4 shows the I_{CS}/I_t ratio as a function of filling pressure for different axial positions of the magnetic probe. It is found that only some fraction of the total current flows through the CS [3] and [5-8]. Other evidence pointing to this conclusion is obtained from image converter photographs and spectral diagnostics.

References

[1]. H.Krompholz et al, Phys. Letters, 77A, 4, 246 /1980/
[2]. D.E.Potter, Phys. Fluids 14, 9, 1911 /1971/
[3]. S.P.Chow et al, J.Plasma Physics 8, 1, 21 /1972/
[4]. T.D.Butler et al, Phys. Fluids 12, 1904 /1969/
[5]. T.Oppenlander et al, Plasma Phys., 19, 1075 /1977/
[6]. A.Bernard et al, in Pl. Phys. and Contr. Nucl. Fus. Res.,
     IAEA Vienna 1977, Berchtesgaden 1976, CN-35/E 18-4
[7]. C.Gourlan et al, 8th Europ. Conf. on Contr. Fus. and
     Pl. Phys. Prague 1977, vol. II, p. 247
[8]. S.Czekaj et al, IPPLM Report No 17/80

INFLUENCE OF EXTERNAL B_z MAGNETIC FIELD UPON THE PROCESS

OF CREATION AND DISINTEGRATION OF PLASMA COLUMN

IN PLASMA-FOCUS DEVICE

S.Czekaj, S.Denus, A.Kasperczuk, R.Miklaszewski, M.Paduch,
S.Śledziński, J.Wolski, M.Zadrożny

S.Kaliski Institute of Plasma Physics and Laser Microfusion
00-908 Warsaw 49, POLAND

The experiment was carried out on the PF-150 system of the following parameters: E_o=50kJ, U_o=30kJ, I_{max}=600kA, r_{ce}=2.5cm, r_{oe}=5cm. The aim of the investigation was to identify the instabilities which are generated in the pinch and the post-pinch phase. The coil system applied enabled to obtain initial B_{zo} field within 0 ÷ 2kGs range. A detailed description of the experimental system as well as wider discussion of the obtained results are presented in ref./1/. A particular attention was paid to investigation of plasma dynamics in collapse phase and plasma column creation and disintegration phases.

The presence of field B_z involves important changes in plasma sheath behaviour in collapse phase:

- plasma sheath velocity decreases particularly in the final stage of the collapse Fig.1
- widening of plasma sheath from $\triangle r$=0.15cm for B_{zo}=0 up to $\triangle r$=0.7cm for B_{zo}=2kGs appears at the distance of 0.7 - 0.8cm from the axis, which testifies to free penetration of the field B_z across the shock wave front Fig.2

Fig.1. Plasma sheath velocity vs. radius.

- plasma sheath curvature radius increases which involves reduction of plasma axial outflow.
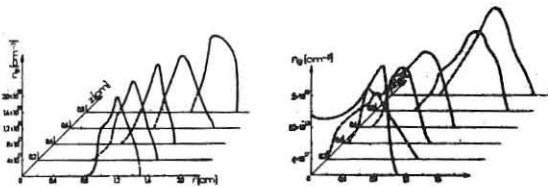
Fig.2. Profiles of the plasma sheath concentration for B_{zo}=2kGs, Δt=32ns.

By means of a magnetic probe positioned on the axis of the system it was found that the field B_z had been compressed to the value B_z =65kGs. This testifies to the fact that the plasma sheath completely sweeps the field.

In the phase of plasma column creation the magnetic B_z changes plasma characteristics as follows:
- minimum radius of the column at maximum compression grows
- decompression phase duration as well as maximum radius of the column reached at the end of this phase increase Fig.3.
- distribution of plasma concentration in the column is virtually different. The column is here of characteristic hollow structure with deep minimum of concentration at the axis Fig.4.

The presence of the compressed field B_z in the plasma column changes the mechanism of its disintegration. Without the B_z field, after 10-30ns from the end of decompression phase there follows disintegration of plasma column by MHD type instabilities /usually 2 neckings along the column length/. For B_{zo}=0.5kGs the mechanism of disintegration is similar but the number of neckings increases up to 5 ÷ 6, however, for $B_z \gtrless$ 1kGs the increment of the instability growth is too small to cause disintegration of the column. So disintegration of the column follows through diffusion of the field B_z into the axis of the system.

Simultaneously a slow development of m=0 and m=1 types instabilities is observed.
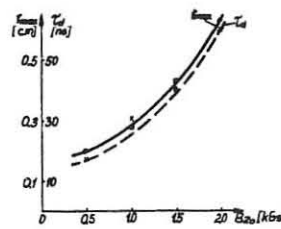
Fig.3. Decompression time and maximum radius vs.B_{zo}.
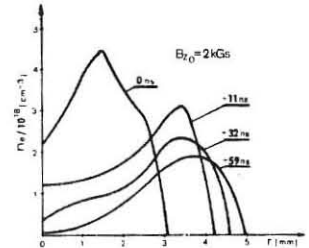
Fig.4. Plasma column concentration profiles.

Fig.5 presents a dependence of an average life-time of the column upon the initial B_{zo} field intensity.
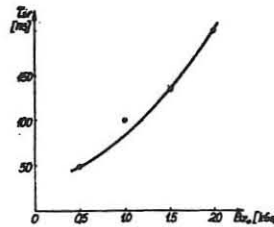
Fig.5. Average life-time of the column vs.B_{zo}.
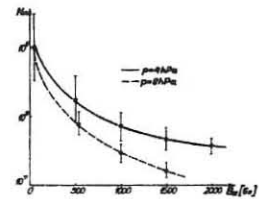
Fig.6. Total neutron yield vs. B_{zo}.

This parameters is defined to be a time interval between maximum compression and disappearance of the column, independently of the mechanism of its disintegration. The presence of the field B_z causes reduction of total neutron yield /Fig.6/ as well as X radiation emission, particularly from the near-electrode region, which is in consistence with results obtained elsewhere /2, 3, 4, 5/.

Experiments are actually performed in which the influence of B_z external magnetic field on the electron and ion beam intensities are investigated and macroinstabilities are identifield in a more detail.

REFERENCES

/1/ S.Czekaj et al, IPPLM Report No 4/81

/2/ J.W. Mather et al, Phys. Fluids 12, 11, 2343 /1969/.

/3/ M.J. Berstin et al, Phys. Fluids 14, 5, 1010 /1971/.

/4/ C.H. Maisonnier et al, 5-th Europ. Conf. on Contr. Fusion and Plasma Physics Grenoble Vol. II,pp. 183 /1973/.

/5/ W.M. Bostick et al, J. Plasma Phys. 8, 1, 7 /1972/.

INVESTIGATIONS OF A Z-PINCH PLASMA-FOCUS SYSTEM WITH PULSED GAS FILLING

N.G. RESHETNYAK, R.D. MELADZE, K.V. SULADZE

Sukhumi Institute of Physics and Technology of the State Committee on Unilization of Atomic Energy, Sukhumi, USSR

ABSTRACT

The paper deals with experimental investigations of a plasma focus system with depressed secondary break-downs. It is shown that with secondary break-downs removed from the discharge gap, neutron and hard X-ray radiations are of relaxation type. In optimal discharges total durations of these radiations are I,5 and 5 s. respectively.

The main results have been obtained in a device (Fig.I)
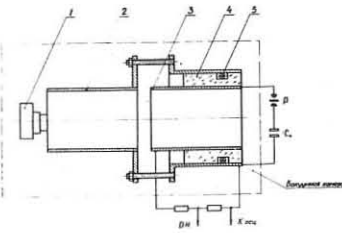
Fig.I Experimental device diagram: I-vacuum valve; 2,3-Z-pinch electrodes; 4-insulator; 5-Rogowsky belt.

having the following parameters:~0,5 MA of discharge current, 20 kV of the condenser bank voltage, 38 kJ of stored energy. The discharge was initiated between tubular electrodes 2 3 placed 3 cm apart (hollow copper electrodes are I4cm in diameter and 20cm in length). The electrodes were situated inside the large-volume vacuum chamber. The chamber was pumped to 10^{-6} Torr. The discharge gap was filled with deuterium by means of a pulse valve (I) via the cathode (2).

The optimal operation mode of the system characterized by the peak output of hard X-rays has been found as a function of neutral gas density distribution over the interelectrode gap (Fig.2c). The most interesting type of plasma dynamics is developed after the first compression stage of the current sheath. An essential feature of the plasma

Fig.2. Traces of hard X-ray pulses for various pressures: (a) 8Torr; (b) 3Torr; (c) I Torr.

sheath dynamics is the cumulative jet ejections along the discharge axis aided by the geometry of a converging plasma layer.

Figs.3 a,b show typical current-voltage curves evidencing that the current sheath radial compressin to the axis is accompanied by a sharp rise in voltage up to 40÷50kV and the discharge current drop. The first specific feature appears in the current and voltage curves. Later on, the specific features recur, therefore, the current and the voltage attain a relaxation character at this stage. Current drops and voltage rises are each time accompanied by synchronous pulses of neutron and X-ray emissions (Fig.3 c,d), this being a characteristic feature for the discharge operation studied. [I]. The total period duration for the neutron emission is nearly ~I,5 s, while the hard X-rays last for ~5 s.

The results of magnetic probe and spectroscopy measurements indicate

Fig.3 Total discharge current traces (a); (b) voltage at the electrodes; (c) neutron dN_1/dt; (d) X-ray dN_2/dt pulses.

that there are no secondary break-downs in the system after the peak compression stage for a few microseconds. The observation is confirmed by high-speed photoes of the discharge showing "a dark pause"[2] existence which is evidenced by the D_β line behaviour (Fig.4b). Comparing high-speed
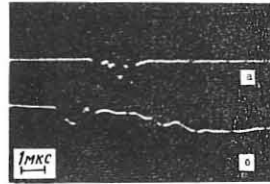
Fig.4 Traces for:(a)neutron pulses; (b) D_β line.

photoes with oscillograph traces (Fig.4b) it is seen that D_β line intensity is sharply decreased at the moment of the maximum plasma compression. This fact witnesses that the plasma is fully ionized for~2 s. At this stage of the discharge there appears a neutron emission (Fig;4a).

The pinch photo in hard X-rays (Fig.5) has
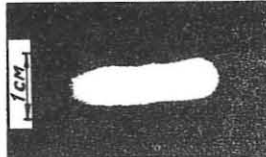
Fig.5 Soft X-ray picture of the pinch.

an image of a filament stretched along the axis,~0,6 cm in diameter and~3 cm in length. The plasma electron temperature varies over the range of 0,8÷1,2 keV.

Collector measurements showed that ion and electron beams are formed at the moment of a specific feature appearing at the discharge current curve in the axial direction. The ion beam energy spectrum analyzed using Thomson mass-analyzer indicated that the accelerated deuteron energy lies within the range of 20÷150 keV.

One of the principal factors indicating the type of processes in the system investigated is a spatial distribution of neutron fluxes. The experiments showed that for the regimes studied, neutron fluxes in the axial direction ($\phi_{0°}$) are 1,2-1,4 times exceeding the ones in the normal direction. The anisotropy coefficient is K= $\phi_{180°}/\phi_{90°}$ ~0,6. The spatial anisotropy grows with the increase in neutron output, which amounts to $4 \cdot 10^9$ neutrons per discharge. Apparently, a certain part of neutrons is due to the high-temperature plasma while another part results from accelerated deutrons interacting with the gaseous target.

The experimental data analysis allows us to suggest that current and voltage functions, generation of beams and hard radiations observed for a well-developed discharge stage are due to plasma column disruptions [3]. Such a state in a discharge occurs several times being specific (characteristic, typical) for the given plasma focus system.

REFERENCES

I. N.G. Reshetnyak, R.D. Meladze in: 3d All Union Conference on Plasma Accelerators. Abstracts of the Papers. Minsk, 1976, p.IIO.

2. Toepfer A.J., Smith D.R., Beckner E.H. Phys.Fluids,1971, v.I4, p.52.

3. V.A. Gribkov, O.N. Krokhin, G.V. Sklizkov, N.V. Filippov, T.I. Filippova in:"Powerful lasers and Laser Plasma" (Collection of Articles), "Nauka" Publishers, 1976, v.85, p.I93.

MECHANISM FOR GENERATION OF NONEQUILIBRIUM PARTICLES IN DYNAMICAL Z-PINCHES.

Yu.V.Matveev, R.G.Salukvadze

Sukhumi Institute of Physics and Technology,
Sukhumi, USSR.

ABSTRACT. Neutron emission in a Z-pinch has been investigated in the region of the second singularity in the discharge current. It is found that filament formation process exerts a positive effect upon deuteron acceleration in an electric field generated by a switching off breakdown. Neutron output is increased 10-30 times by a reverse trapped field H_φ.

There is no consistent treatment for radiation generating regimes in Z-pinches up to now. The features observed /1/, determining radiation generation in the first regime, i.e., in the region of the first "singularity" in the current (small neutron outputs, neutron and X-ray pulses of various durations) are satisfactorily explained /2/ by the type of switch-off breakdown-generated e.m.f. pulses. Cross-sections of D-D reactions versus deuteron energious and various permeabilities of radiations are also taken into consideration. It is supposed that for the following "singularities", radiations are predominantly generated with the particles accelerated while the pinch is partitioned into current filaments /3/.

We have studied radiations generated in the second regime, i.e., at the second "singularity" in the discharge current (a trained-up porcelain chamber, i.e., with metallized walls, 28cm in diameter and 50cm in length; $W_c \approx 15kJ$, $V_o=24kV$, $\dot{I}_o \approx 3 \cdot 10^{11}A/s$, $I_{max} \approx 3,5 \cdot 10^5 A$, T/2 $\approx 9\mu s$, $p_o \lesssim 2.5 \cdot 10^2 Torr$ D_2). Such discharges show diffuse distributions of the compressed current, gas captured by the second luminous sheath and plasma decay into filaments after it becomes expanded past the first "singularity".

It has been established that the filament-formation process is the property peculiar to the trained-up chamber discharges with the initial pumping-out less than 10^{-5}Torr. Plasma decay into current filaments is much reduced by adding some heavy gas (e.g., 0,5% of Argon) to D_2.

Fig.2 gives the data showing (a) plasma availability at the chamber wall, (b) current characteristics in the supply circuit, and (c) neutron burst. The figure also shows magnetic probe data (the probes being placed at various distances from the chamber axis) and (d) $6 - v$ the probe data concerning plasma compression at the axis. The neutron burst could not be explained by a coaxially laminating /4/ equilibrium pinch plasma decay into filaments (H_φ sign is reversed). At the same time filament formation preceding the radiation is an important component the particle acceleration mechanism. This is evidenced by the same influence of impurities upon the filament formation and neutron outputs.

Neutrons appear when the pinch is turned off by the wall-side secondary breakdown (Fig.2) shifted from the halfcycle end towards the second "singularity" region by decreasing p_o. Thus, turning-off breakdowns are common to the processes providing particle acceleration in various regimes.

While generating the radiations, the e.m.f. directed along the central current amounts to 50 - 70 kV. It is 1,5 - 2 times the e.m.f. excited in the first regime /2/ and provides an explanation for the energy of majority of accelerated particles /5/. Such an e.m.f. is realized by the L - R circuit resistance equal to 0,2 - 0,4 Ohm.

Additional electrodes nearly 2 skin-layers in thickness introduced into the chamber made clear that the length of lines with $H \approx 0$ between the filaments and the diameter of the region with an electric field providing neutrons are ~24cm and ~10cm, respectively. There is no evidence of electrode-side processes positively influencing hard radiations (electrodes were made of materials with various

melting points; the electrode surfaces had been iced by NH_3.

On applying the H_φ field opposite to the discharge current field, in front of the plasma sheath, 10 - 30 rise in neutron emission has been observed /6/ (Fig.3). This rise in Y_n is due to increasing the e.m.f. up to $\simeq$ 100 kV and possible elongation of current filaments.

Neutron outputs increase towards the cathode (i) in a chamber without plate electrodes, (ii) in the chamber compartment 24 cm in length, and (iii) on imposing the H_φ field. This is due to filaments of various lengths.

CONCLUSIONS. Acceleration of charged particles along the Z-pinch in the regime with radiations generated in the region of the second "singularity", is realized by the E_z field formed at the switching-off breakdown; acceleration of particles is promoted by expanding pinch-plasma decay into current filaments prior to the breakdown; a reversed trapped H_φ field enhances the neutron output 10 - 30 times; there is no necessity in using a m=0 mode instability in order to explain accelerated particles in cylindrical Z-pinches.

It is a pleasure to thank I.Ya.Butov, V.I.Baryshev and L.P.Stoopnitskaya for their help.

REFERENCES

1. A.M.Andrianov et al; Plasma Physics and CTR, 1958, Moscow, v.4, p.182.
2. I.Ph.Kvartskhava et al; Pisma v Zhetf, v.15, p.619, 1972.
3. I.G.Persiantsev et al; Pisma v Zhetf, v.16, p.68, 1972.
4. I.Ph.Kvartskhava, Yu.V.Matveev et al; Plasma Phys. and Contr. Nucl. Fus. Res., v.3, p.149, 1974, IAEA, Vienna, 1975.
5. V.F.Demichev et al; Plasma Physics and CTR, v.4, p.81, 1958.
6. Yu.V.Matveev, I.Ph.Kvartskhava; Eight Europ. Conf. on Contr. Fusion and Plasma Phys. (Conf. Proc., Prague, 1977), 1, 87, 1977.

Fig.1

Fig.3   Fig.2

Fig.1   Filament-formation probability in % (1) for the first current half-cycle; time interval (II) from the first "singularity" up to the onset of filament formation process; (III) - time interval between the first and second "singularities". Neutrons are recorded at $P_o \lesssim 2,5 \cdot 10^{-2}$ Torr D_2.
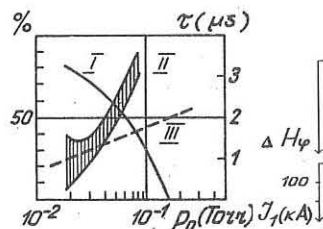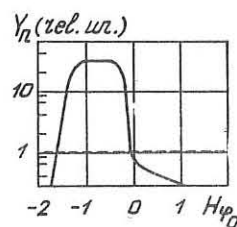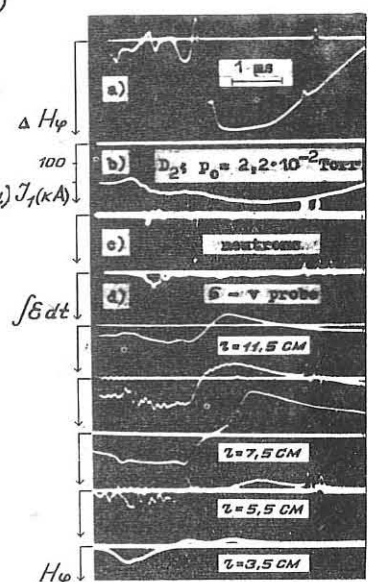
Fig.2   Probe signals referring to a single discharge.

Fig.3   The peak neutron output versus H_φ (r=13cm) with the rod 0,8cm in diameter. Dotted line shows the peak emission in rodless experiments.

KINETIC STABILITY OF BENNETT PINCH

A. S. Sharma, U. Krishnamurty, A. Sen and A. K. Sundaram

Physical Research Laboratory
Ahmedabad 380 009, India.

An equilibrium of a cylindrical plasma is the well known Bennett pinch. The plasma in this configuration carries a current along its axis, producing an azimuthal magnetic field which in turn confines the plasma. At equilibrium the plasma is charge neutral and hence has no electric field. An exponential distribution function for this equilibrium is constructed from the constants of motion: the energy

$H_0 = \frac{1}{2} m V^2$ and the axial momentum

$p_z = m V_z + q A_z(\tau)/c$, where $A_z(\tau)$ is the equilibrium vector potential. The self-consistent equilibrium density and azimuthal magnetic field $B_\theta(\tau)$ profiles are obtained from $A_z(\tau)$:

$$A_z(\tau) = -\left(\frac{2 B_0}{K}\right) \ln(1 + (1/4)K^2 \tau^2)$$

$$n(\tau) = \frac{n_0}{(1 + (1/4)K^2 \tau^2)^2} \quad \text{and} \quad B_\theta(\tau) = \frac{B_0 K \tau}{(1 + (1/4)K^2 \tau^2)}$$

where K is the scale-length.

To investigate the stability of the Bennett pinch, the distribution function in the presence of the perturbation may be divided into the adiabatic and non-adiabatic parts[1]. The adiabatic part maintains the form of the equilibrium distribution function, while the non-adiabatic part consists of the resonant contributions, etc. The non-adiabatic part of the distribution function is obtained by integrating over the unperturbed particle orbits. For the Bennett equilibrium the majority of the particles are in the vicinity of the axis and in this region B_θ is linear in the radial distance τ. Consequently the majority of the particles execute betatron orbits, which has large excursions across the azimuthal field lines. This demands a different approach to the radial eigenmode analysis compared to the case of small excursion Larmor orbits. In the procedure adopted in this study the eigenfunctions are expressed in terms of Bessel functions, which are the vacuum eigenfunctions of the cylindrical system under consideration. With this representation a proper description of the stability problem when the dominant particle orbits are betatron orbits is achieved. The eigenvalues then are the roots of a matrix dispersion relation[2]. In general this dispersion relation cannot be solved analytically and the eigenvalues are computed numerically. In the case of electrostatic perturbations[3] of the type

$$\phi_1 \sim \exp\left\{ i(kz + \mu\theta - \omega t) \right\},$$

the radial eigenmode equation is a second order ordinary differential equation. Among the eigenvalues computed from the matrix dispersion relation for this case at low frequencies an unstable eigenvalue has nearly zero frequency and another eigenvalue has finite frequency but is heavily damped. For $\omega \sim kV$, where V is the average velocity of the ions, an analytic expression for the eigenvalue is obtained. This mode with given k and μ is helical in structure and can resonate with the particles which also have a helical trajectory. The resonance drives the mode unstable[3]. In the case of electromagnetic perturbations, four coupled second-order ordinary differential equations in ($\phi_1, \vec{A}_1$) constitute the radial eigenmode equation. The perturbed current density in the axial direction is found to be dominant and the above set of four equations can be reduced to two coupled equations in ϕ_1 and A_{1z}. The eigenvalues of the electromagnetic modes are computed numerically from the resulting matrix dispersion relation. At low frequencies the magnetohydrodynamic modes are expected to be significantly modified due to the large excursion betatron orbits of the particles. Also other electromagnetic modes such as the Alfven, magnetosonic and high frequency modes are being investigated.

References

1. D. Pfirsch, Z. Naturforsch. 17A, 861 (1962)
2. R. C. Davidson, Phys. Fluids 19, 1189 (1976)
3. A. S. Sharma, Plasma Physics (communicated).

THE REPRODUCIBILITY OF NEUTRON YIELD AND DISCHARGE SYMMETRY
OF THE PF DEVICE

A.Jerzykiewicz, A.Jonca, J.Nowikowski, C.Pochrybniak,
J.Waliszewski

Institute of Nuclear Research, Świerk, Poland

Abstract: The paper presents the result of investigations
concerning the influence of electrodes system geometry in PF
Mather-type device on the reproducibility of neutron yields
and spacial positioning of the pinch. The work was done on
the apparatus PF-20 /21 µF, 33 kV/.

The reproducibility of both neutron yields /Y/ and the
spacial positioning of the pinch are of high importance in
Plasma Focus-laser /1/ experiments. The presented in the pa-
per systematic investigation of the problem was undertaken
after preliminary results /2/ that proved the spread of
neutron yields to be much greater than the one given in the
publications /3/. At the same time, it turned out that fre-
quently a pinch was shifted in relation to the electrode sym-
metry axis.

The investigation was made on the PF-20 apparatus /C=
= 21µF, V = 33kV/. The inner electrode shape, namely the
front cavity, simulated the arrangement of diaphragms and a
lens introducing the laser beam into the pinch region. The
used electrode systems are shown in the fig.1. The changes
comprised the insulating system and the outer electrode. The
former one consisted in proving two alumina insulator ver-
sions - pulled over and inserted in the electrode /fig.1a,
1b/. For each version the variation of the distance d bet-
ween the ring-like outer electrode protrusion and the cylin-
drical insulator surface was effectuated, d = 0.5, 2.5,
6.5 mm being applied. The latter consisted in replacement of
a solid electrode by a perforated one /fig.1c/, 61% of the
surface removed. Two versions, with wall thickness of 5 or
2 mm were applied. That electrode was in turn exchanged by
a rod type /fig.1d/. With the electrodes 1c, 1d only the
distance d = 0.5 mm was used.

The neutron yield was measured with a silver counter.
The photographs of the pinch were made with ø = 0.2 mm pin-
hole camera Al filter 2.5 µm. The pure D₂ was used. In one
case /electrodes 1b, d = 6.5mm/ the effect of N₂ admixture
/0.5%, 2%, 4% of D₂ pressure/ was investigated.

The presented results of neutron yield for a given
electrode arrangement and gas conditions contain the values
picked up in a sequence of a few series, usually performed
within a few days period. Each series comprised about 10
discharges made with one gas filling. Series done on a gi-
ven day were preceded with training discharges. Seldom a
whole sequence was done in one day. On the ground of long
sequences /n≥150/ performed with electrode arrangement
fig.1a we stated that the majority of cases gave Poisson
distribution for neutron yields /fig.2/.

The estimation of reproducibility of Y was done by
calculating the variance for a particular sequence:

$$S_n^2 Y = \frac{1}{n-1} \sum_{i=1}^{n} \left(\bar{Y} - Y_i \right)^2$$

Y_i - neutron yield
$\bar{Y}$ - the mean value for a sequence possessing n results

The denoted by P% ratio of neutron yield variances to the
mean neutron yield for pure D₂ is given in table 1, for D₂ -
N₂ mixture in table 2. The shaded areas show P% which corre-
spond to the optimum mean neutron yields, given in the
last column. The figure 3 shows exemplary plots. The curves of
neutron yields versus pressure for some cases are given in
fig.4.5. Exemplary histograms are shown in the fig.6. The
notation in the drawings is the same as in the tables 1, 2.
We stated that values of P% for a given series are substan-
tially smaller than for a whole sequence of series. It seems
that P% diminishes with the increase of $\bar{Y}$. The smallest va-
lues - about 20% were obtained for electrode system 1b and
1d.

We considered a discharge as symmetric when, in the
image, the displacement of its axis in relation to electrode
system axis was smaller than a half of the pinch diameter.
The analysis of photographs exhibited a considerable dif-
ference in the fraction of symmetric discharges for diverse
electrode arrangement - from a dozen or so to almost 100%
/table 3/. The greatest fraction was obtained at d = 0.5mm,
the poorest at 6.5mm. The nitrogen admixture substantially
elevated the percentage of symmetrical discharges /table 3/.
It may be well to add that, contrary to the previous notions
e.g. /3/, even at quite nonsymmetric discharges the neutron
yields close to maximum were noted.

References:

1 Kaliski S. et al - VII European Conf. on CFPP Lausanne,
  /1975/, Vol.II, p.188.
2 Nowikowski J. - Rep. INR 1505/XXIV/PP/B, /1974/
3 Mather J.W. - Methods of Exp. Physics, Vol.9, part B,
  p.187, Acad.Press, New York /1971/

TABLE 1

version a.

p[Torr]	0.5	0.75	1.0	1.25	1.5	1.75	2.0	2.25	2.5			$\bar{Y}_n \times 10^8$
1	d = 0.5	49	—	68	—	50	—	47	—	49			5.5
2	d = 2.5	55	37	50	41	48	53	70	71	—			5.9
3	d = 6.5	50	—	40	—	33	—	48	—	54			7.5

version b.

p[Torr]	1.0	1.25	1.5	1.75	2.0	2.25	2.5	2.75	3.0	3.25	3.5	$\bar{Y}_n \times 10^8$
1	d = 0.5	30	—	26	—	21	—	49	—	54	—	59	18.0
2	d = 2.5	37	—	33	—	33	39	41	—	90	—	—	14.6
3	d = 6.5	35	—	54	40	32	37	64	51	—	—	—	15.7

version c.

p[Torr]	0.75	1.0	1.25	1.5	1.75	2.0	2.25	2.50	2.75	$\bar{Y}_n \times 10^8$
1	a = 5.0	43	33	—	29	65	35	52	63	—	14.1
2	a = 2.0	—	23	29	28	33	46	33	52	51	12.2

version d.

p[Torr]	1.0	1.25	1.5	1.75	2.0	2.25	2.50	3.0	3.5	$\bar{Y}_n \times 10^8$
1	d = 0.5	25	27	29	21	24	23	56	44	69	18.2

TABLE 3

N_2%	0								0.5	2.0	4.0
version	1a			1b			1c	1d	1b		
d	0.5	2.5	6.5	0.5	2.5	6.5	0.5	0.5	6.5	6.5	6.5
symmetry %	35	16	11	91	88	32	52	78	77	91	85

TABLE 2

P[Torr] / N_2%	1.0	1.75	2.5	3.0	3.5	$\bar{Y}_n \times 10^8$
0.5 %	29	27	22	30	40	22.3
2.0 %	39	31	21	23	—	18.4
4.0 %	36	21	21	44	63	14.4
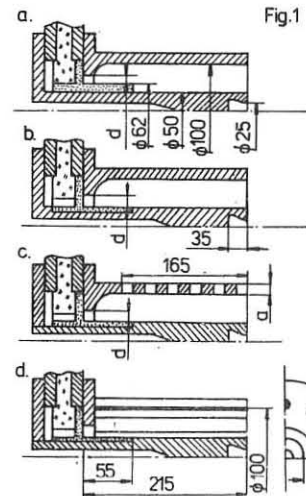
Fig.3

Fig.1
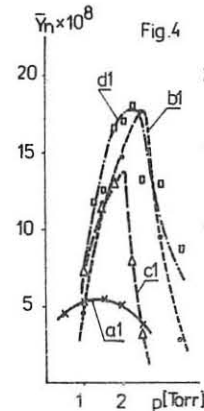
Fig.2

Fig.4

Fig.5
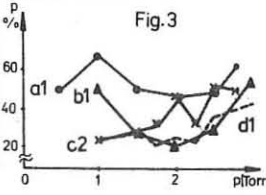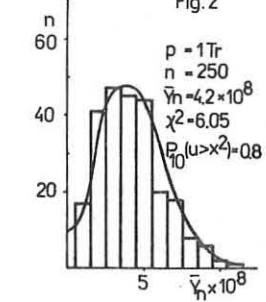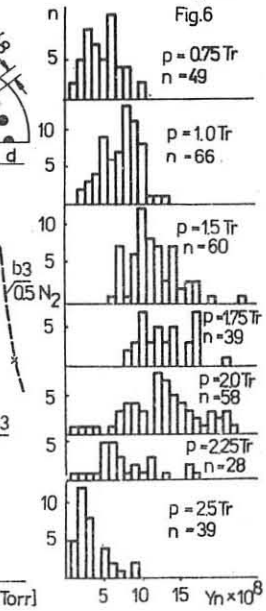
Fig.6

COMPUTATIONAL OPTIMIZATION OF THERMONUCLEAR REACTION INTENSITY FOR MATHER'S TYPE PLASMA-FOCUS DEVICES.

Z.Jankowicz, A.Masłowski[x], A.Jerzykiewicz, M.Rabiński,
Z.Bartosiewicz[x], J.Kałat[x].

Institute of Nuclear Research, 05-400 Swierk, Poland.
[x]Technical University of Białystok, 15-351 Białystok, Poland.

Abstract: This paper presents the results of the thermonuclear reaction intensity optimization for the Mather's type plasma-focus /PF/ devices. The calculations were caried out on the basis of 1½ dimensional MHD model for the radial phase. The optimization problem, that is maximization of the integral value of the thermonuclear neutron yield, was solved using Davidon-Fletcher-Powell method.

Introduction: The optimization of PF device in /1/ was worked out on the basis of 2D snow-plow model. However, it was only electrical model which did not take into account the plasma compression and heating in the radial phase. Such an analysis is possible using the MHD model. Unfortunately, because the 2D MHD model involve long time computations, the optimization of PF parameters is very difficult. To omit this problem in /1/ the autors took into consideration /in phenomenological manner/ the α_i Imshennik's parameter /adopted to Mather's type PF device/ introducing the limits to available initial gas density ρ_o and the inner electrode radius R_o. The optimization aim was then to reach, at the pinch moment, maximum of current I_p because the total neutron yield is $N \sim I_p^{max(3+4)}$. Simultaneously the value I_p should fulfil the conditions imposed on α_i /1/.

Optimization problem: The aim of the presented paper is optimal, from maximum neutron production point of view, choice of initial parameters such as ρ_o, R_o, L_o, I_o where ρ_o, R_o are defined as before and I_o, L_o are current and inductance at the beginning of the radial phase respectively. Simultaneously, we proof the validity of the concept of introducing the α_i parameter in /1/.

We choise as quality index of optimization the integral value of the thermonuclear neutron yield, defined as:

$$N = \int_0^{t_k} \int_0^R r \frac{C n^2}{T_i^{2/3}} \exp(-\beta/T_i^{1/3}) dr dt \qquad (1)$$

where: $t_k(\underline{x})$ - maximum time validity of MHD model,
$R(t,\underline{x})$ - radius of plasma,
$n(t,\underline{x})$ - plasma concentration,
$T_i(t,\underline{x})$ - ion temperature,
$\underline{x} = \{x_i\} = (\rho_o, R_o, L_o, I_o)$ the set of parameters,
C, β - physical constants /2/.

As it is know, the total neutron yield in PF discharges is caused by not yet explained in detail phenomena, so relation (1) cannot describe the real values of N at length. Nevertheless, on the scope of MHD approximation, the thermonuclear model of neutron generation is the most reasonable to applied in determination of N. It is also possible to optimize the final values of $n(t_k, r)$ and $T_i(t_k, r)$ at the moment of pinch formation, what is the one of the main plasma analysis purposes in general.

Model: The $R(t,\underline{x})$, $T_i(t, \underline{x})$, $n(t,\underline{x})$ functions, occuring in (1), are obtained by solving the 1½ D mathematical model of radial compression /3/. This model under consideration is the system of six MHD equations describing changes of concentration n, radial velocity v_r, magnetic field $H\varphi$, ion temperature T_i, electron temperature T_e and the averaged axial velocity v_z, with additional equation of total electric circuit for finding the instantenous value of current I(t). Conserning the calculations of I(t) values of L(t) and $R_a(t)$, that is the inductance and ohmic resistance of plasma and external circuit, are known from MHD equations. In considered MHD model, variable length of the pinch resulted from the plasma axial velocity during the plasma outflow from the dense pinch region. The selfconsistent outflow calculations cause the applied model is not a typical 1D one, but include the principal effect of phenomenon two-dimensionality. The model is solved using the implicit finite difference method in the Lagrangean mesh. The calculations were interrupted at the moment t_k, when the MHD approximation reached the limit of physical application.

Optimization method /4/: The optimization problem, that is maximization of functional (1), was solved using Davidon-Fletcher-Powell method /5/, based on variable metric technique. This algo-

rithm was augmented by projection method /6/, which solved constraints problem. The sequent points are generated according to the relation:

$$\underline{x}_{k+1} = \underline{x}_k + \rho_k \underline{b}_k \qquad (2)$$

were $\underline{b}_k$ is a search direction in k-th iteration, ρ_k is step length. The direction $\underline{b}_k$ is calculated according to the formula:

$$\underline{b}_k = H_k \underline{g}_k \qquad (3)$$

where $\underline{g}_k = DF(\underline{x}_k)$ is gradient at the point $\underline{x}_k$, H_k is possitive defined matrix

$$H_{k+1} = H_k + \frac{\rho_k \underline{b}_k \underline{b}_k^T}{\underline{b}_k^T \underline{y}_k} - \frac{H_k \underline{y}_k (H_k \underline{y}_k)^T}{\underline{y}_k^T H_k \underline{y}_k} \qquad (4)$$

$$\underline{y}_k = \underline{g}_{k+1} - \underline{g}_k \qquad (5)$$

and the step length is determined as the maximum of the function $t \to F(\underline{x}_k + t \underline{b}_k)$. During the gradient evaluation the partial derivatives of $\tilde{n}$, T_i, R upon the $\underline{x}$ are approximated by finite differences as follows:

$$D_j n(\underline{x},t,r) = \frac{n(\underline{x}+\Delta x_j e_j, t, r) - n(\underline{x},t,r)}{x_j} \qquad (6)$$

and likewise for T_i and R. In order to evaluate (6) it was necessary to calculate the model in five points - the first defined by optimization algorithm and next additional four points obtained by perturbation of $\underline{x}$ parameters $(\underline{x} + \Delta x_j e_j; j = 1,2,3,4)$. The value of the optimum perturbation was found to be 10^{-5}.

Computational difficulties: The main difficulty connected with the computer program realization was a long time of MHD model calculations, as well as the proper choise of criterion parameters which end the maximum seeking in search direction.

Conclusions: Up to this time some numerical results are obtained, especially conserning the choise of the optimal accurancy parameters which caused the algorithm can be computationally more efficient. The calculations were carried out for several a priori selected points. Some of those appeared almost stationary ones, with a small influence of $\underline{x}$ on N.

Starting from the guess point: $\rho_o = 1.135 \cdot 10^{-6}$ g/cm³, $R_o = 5$ cm, $L_o = 30$ nH, $I_o = 3 \cdot 10^6$ A, the obtained results are as follows:

A. At the beginning of the optimization process the R_o radius decreased up to the 3.9 cm, while the other parameters were practically constant. This fact caused decreasing of the depth of the current singularity at compression moment by reducing the inductance increment ΔL_R in the radial phase. At the moment of the end of the pinch the current I_p rises when $\Delta L_R/L_o$ decreases. It leads to the plasma concentration increase.

B. During next iterations, when the influence of R_o radius changes on value of functional (1) fell, the inductivity L_o increased up to its maximum value 80 nH, which achived on its upper constraint. Physical interpretation of this fact is just the same as in A.

C. When L_o approached its upper available value, then R_o radius increased from 4 cm up to approximately 7.5 cm with tendency to grow up. I_o and ρ_o practically did not change. It means that the number of plasma particles grow because of $n \sim \rho_o R_o^2$. It caused the neutron yield increase.

During optimization process the integral neutron yield N increased about 20 times in comparison with initial value. Computations are carried out.

References:

/1/ Z.Jankowicz at al., Optimization of the Mather's Type PF Devices Based on 2D Snow-Plow Numerical Code and Analytical Considerations, Proc. 9th European Conf. on Controlled Fusion and Plasma Physics, Oxford 1979, DP11, p.107.

/2/ L.A.Artzymovich, Controlled Thermonuclear Reactions /in Russian/, Moscow 1963.

/3/ Z.Jankowicz, INR report /in print/.

/4/ A.Masłowski at al., Computer Optimization of Intensity of Reaction in Thermonuclear Devices /in Polish/, Proc. 3rd Conf. on Automatization in Design, Białystok /Poland/ 1980, p.229.

/5/ P.E.Gill W.Murray, Numerical Methods for Constrained Optimization, Academic Press, 1974.

/6/ J.B.Rosen, The Gradient Projection Method for Nonlinear Programming, J.Soc. Ind.Appl. Part I: 8 /1960/ p.181, Part II: 9 /1961/ p.514.

ION BEAM MEASUREMENTS IN CYLINDRICAL
ION IMPLOSION FUSION FACILITIES

M.Gryziński,J.Baranowski,E.Górski,A.Horodeński,L.Jakubowski,
J.Langner,M.Sadowski,E.Składnik-Sadowska,K.Zdanowski.

Institute of Nuclear Research, Świerk, Poland.

Abstract. Thomson analyzer and D_2O ice target have been used
for deuteron beam measurements in the RPI-5,RPI-15 and SOWA-
-150 facilities. Deuteron beams of mean energy of several
tenth of keV and currents of the order of 100 kA have been
detected. The total energy of the ion pulse produced by the
15 kJ RPI-15 facility was found to be of the order of 1 kJ.

Introduction

Generation of powerfull highly convergent ion beam is a
key point of the ion beam fusion. Generation of low energy
ion beams of the order of several tenth of keV, in contrary
to the ion beam-pellet fusion operating with MeV ion beams,
is a characteristic feature of the ion implosion approach[1].
The rod plasma injector /RPI/ operating on the basis of the
magnetic insulation concept invented in our laboratory[2-3],
seems to solve the problem of the production of high current
beams at a low acceleration voltage. In the last few years
the efficiency of the ion acceleration in RPI devices has
been increased appreciably by proper designing of electrodes
and proper formation of the gas cloud [4]. We present here
the results of the ion beam measurements performed with se-
veral our implosion facilities /RPI-5,RPI-15 and SOWA-150/.

Methods of measurements of ion beams

In order to determine an ion beam intensity two different
methods were applied: a direct method based on measurements
of an ion flux by means of a calibrated Thomson analyzer and
an indirect method based on d-d nuclear reactions induced on
an additional diagnostic deuteron target.

To get additional informations on the ion beams, some
measurements with Cd-paraffine collimators have been carried
out with a scintillator counter. The neutron time measurements
enabled the ion beam intensity versus time to be estimated.
The basic scheme of experimental system is shown in Fig.1.
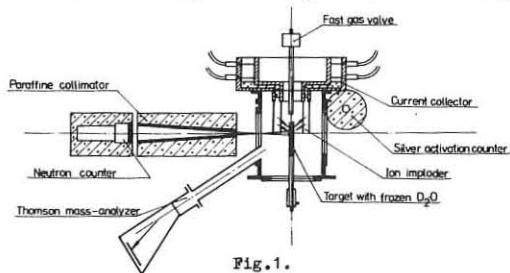
Fig.1.

Results of measurements

Mass-energy analysis enabled energy spectra of emitted
deuterons to be determined. The typical spectra for the
three, differing only in the supplying system, facilities
RPI-5, RPI-15 and SOWA-150 /working as a RPI device/ are
shown in Fig.2. It is worthy to note that the mean energy
of the ion beam increases with an increase of energy of
the supplying system. The detailed calibration measurements
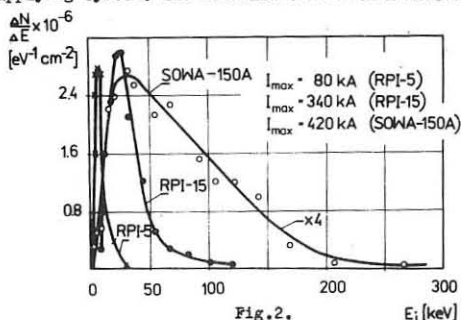
Fig.2.

made possible the determination of an absolute value of the
ion flux and the total energy of the ion beam pulse.

Neutron measurements with the D_2O target /Fig.3/ enabled
to determine an ion pulse shape and /in combination with
mass-energy measurements/
also the absolute value of
the ion flux. Time measu-
rements of neutron gene-
rated in the D_2O target
have shown a strong cor-
relation between the vol-
tage generated between the
electrodes of the imploder
and the neutron yield.
Under specific conditions
neutron emission exactly
follows the voltage chan-
ges. The duration time of
the ion beam pulse has
been found to be of the
order of 200 ns. Calcula-
tions of neutron yield,
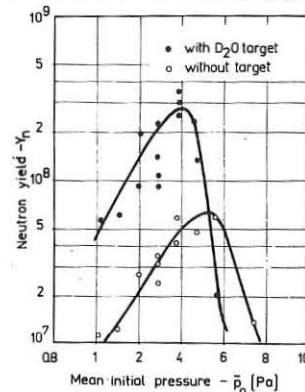
Fig.3.

as carried out on the basis of the detected energy spectrum
/Fig.4/, have shown that the mean number of ions in the
pulse is of the order of 1.8×10^{17}.
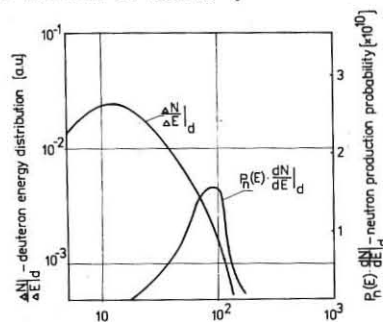
Fig.4.

The obtained value is in a good agreement with the data
obtained from analysis of Thomson parabola tracks. Total
energy of the ion beam pulse for RPI-15 facility was found
to be $\sim$ 1 kJ. For the same facility the mean ion beam cur-
rent was of the order of 60 kA /the momentary values exceed
100 kA/.

Neutron measurements performed with a paraffine collima-
tor, have shown that the ion beam is in average inclined to
the axis of the device at $\sim$ 30 degrees.

Conclusions

The estimated values: 10% energetic efficiency of the
ion beam generation, 1 kA/cm² initial ion beam density, and
few tenth keV mean ion energy, show that one of the impor-
tant problems of ion implosion fusion has been solved. The
other problem which must be now properly solved is forma-
tion of an appriopriately convergent ion beam. At the mo-
ment the beam is focused in cylindrical volume of few mili-
meters in diameter and 1 - 2 centimeters in length. This
shows that ion beam density reaches the level of 100 kA/cm²
in the focal region.

References

1. M.Gryziński et all. Plasma Physics and Controlled Nuclear
   Fusion Research, Innsbruck, 1978,vol.III, 225.
2. M.Gryziński,J.Nowikowski,M.Sadowski,E.Składnik-Sadowska,
   S.Suckewer. Proc. 2nd Europ.Conf.,Stockholm, 1967.
   /Plasma Phys., 10 /1968/ 450/.
3. M.Gryziński, Institute of Nuclear Research Rap. INR 711/
   XVIII/PP, Warsaw, 1966 /in Polish/; Nukleonika 14 /1969/
   679.
4. M.Gryziński,J.Nowikowski,L.Jakubowski. Nukleonika 21
   /1976/ 1225.
5. E.Składnik-Sadowska et all. /to be published/.

ABSORPTION OF MAGNETOACOUSTIC WAVES IN HIGH-β PLASMAS

F. Moser, E. Räuchle and P.G. Schüller

Institut für Plasmaforschung der Universität Stuttgart

D-7000 Stuttgart 80, Fed. Rep. of Germany

Abstract: The oscillations of a radially inhomogeneous high-β plasma column are investigated experimentally and theoretically. The high-β plasma is produced by a theta pinch discharge. The waves are launched during the post implosion phase in the frequency range of about 1 MHz. The spatial distribution of the wave fields is determined and a high absorption is observed.

The absorption of magnetoacoustic waves is an efficient mechanism to heat a plasma. It was investigated under various conditions in the past /1/. In this paper we present theoretical and experimental investigations in the transition region from the collision dominated to the collisionless regime. In the theoretical treatment the linearised MHD-equations are used where viscous and resistive effects are included. In the equation of motion

$$\rho_o \cdot \ddot{\vec{\jmath}} = -\nabla \tilde{p} + (\tilde{\jmath} \times \vec{z}) + (\tilde{\jmath} \times \vec{z}_o) - \nabla \tilde{\Pi} \qquad (1)$$

we use the classical Braginskii form for the stress tensor $\tilde{\Pi}$ /2/. In addition the generalised Ohm's law, Maxwell's equations, the adiabatic pressure equation and the equation of continuity are used. At high temperatures ($T_i > 50$ eV) the stress tensor is determined by kinetic processes. We approximate it by introducing an effective viscosity coefficient in the classical form to agree with experimental results. At these temperatures viscosity is the dominant dissipation process. It can be shown that in this approximation axial ion Landau damping effects can be included /3/. The investigations are applied to conditions of a high-β plasma with strong radial inhomogeneities as realised in the post implosion phase of a theta pinch. The measured quasi-stationary profiles of density and magnetic field are given in fig. 1 for two different times t_1 and t_2 after crowbar of the theta pinch (t_1: no magnetic field on the axis, t_2: small magnetic field at r=0). A usual assumption here is that the temperature is only weakly dependent on the radius r. For oscillations of a cylindrical plasma of the form $S = S_o(r)e^{i(k_z z - \omega t)}$ a coupled system of 3 ordinary differential equations of second order for the radial and axial displacements $\tilde{\jmath}_r$, $\tilde{\jmath}_z$ and the radial component $\tilde{B}_r$ of the oscillating magnetic field is derived:

$$a_{i1}\frac{d^2 \tilde{\jmath}_r}{dr^2} + a_{i2}\frac{d\tilde{\jmath}_r}{dr} + a_{i3}\cdot\tilde{\jmath}_r + (\cdots\tilde{\jmath}_z\cdots) + (\cdots\tilde{B}_r\cdots) = 0 \qquad (2)_{(i=1,2,3)}$$

The coefficients a_{ik} are functions of the inhomogeneous plasma parameters, the axial wavelength k_z and the frequency ω. Here, in the post implosion phase, the zero order magnetic field is related to the pressure distribution by the equilibrium condition $\nabla\left(p_o + \frac{z_o^2}{2\mu_o}\right) = 0$

To investigate the spectrum of the free oscillations and the radial dependence of the wave fields (eigenvalues, eigenfunctions) we solved the differential equations with homogeneous boundary conditions.

For applications to experiments with defined magnetic field amplitudes at the boundary the mathematical inhomogeneous problem was treated numerically. For long wavelengths ($k_z \cdot R \ll 1$) the excited fields are only weakly dependent on k_z. Theoretical and experimental results of such a case are shown in fig. 2, it resembles with the case for $k_z = 0$ investigated earlier /4/, /5/. Here no magnetic field oscillations are observed on the axis. The propagation of the magnetic field to the center (r=0) is possible for an equilibrium distribution as in case 2 in fig. 1. This is shown theoretically and experimentally in fig. 3.

In the theoretical investigation of the equations (2) the local resonances of the cusp continuum are strongly reduced by viscosity (fig. 4). Resonance curves are given in fig. 5 for different values of k_z. An enhancement of the amplitude can be obtained in a broad frequency band. Maximal amplitudes are obtained for axial wavelengths of the order of the plasma diameter.

The experimental set-up is shown in fig. 6: plasmalength 3 m, plasma diameter 0.15 m, coil length 2 m, coil diameter 0.4 m, magnetic field 1 kG, antenna coils divided in four segments, hydrogen filling pressure 2-5 mTorr, modulating magnetic field 0.2 kG. The magnetic field was measured by multiple magnetic probes, the density distribution by axial interferometry (CO_2 and He-Ne), electron temperature by $90°$-laser Thomson scattering (40 eV), ion temperature (100 eV, diamagnetic loop). These measurements correspond to the time of the launching of the waves (post implosion phase, 4 μsec after main field crowbar). The waves were excited by a wave launching circuit as pulses in the frequency range of 0.8 to 1.5 MHz. The radial and axial magnetic wave field distribution were meas-

ured by multiple magnetic probes. The probe signals were Fourier analysed in time for a comparison with the theoretical Fourier solution (figs. 2 and 3). For a direct comparison of real time signals the equations were also solved numerically in a real time formalism. The measured and calculated time dependent $\tilde{B}_z(t)$ at the radial position r = 7.5 cm is given in fig. 7. In both types of results (figs. 2, 3 and 7) there is a good agreement between theory and experiment, i.e. MHD-equations are capable to describe magnetoacoustic wave propagation in the investigated parameter range. The necessary choice of the macroscopic viscosity coefficient of 0.1 of the classical value indicates however that kinetic effects are significant. Related to those effects the influence of axial ion Landau damping was considered by Turner /3/, whereby the introduction of an effective viscosity is formally justified. In our case this mechanism is of importance for short wavelengths only ($k_z \cdot R \gg 1$). We attribute the strong damping occuring also for long wavelengths to the effect of radial ion Landau damping. This damping mechanism leads to a total absorption rate of 35 MW in agreement with the experimental results.

References:

/1/ A.R. Jacobson, C.J. Buchenauer, J.N. Downing and S.K. Thomas, Phys. Rev. Lett. 37, 897 (1976)

/2/ S.J. Braginskii, Review of Plasma Physics, Vol. 1, p. 213, New York, 1965

/3/ L. Turner, Phys. Fluids 23, 1415 (1980)

/4/ E. Holzhauer, G. Janzen, F. Moser, G. Müller, E. Räuchle, E. Schneider and P.G. Schüller, part of paper IAEA-CN-37 / Q-3, Innsbruck 1978

/5/ F. Moser, E. Räuchle, E. Schneider und P.G. Schüller, Z. Naturforschung 34a, 1190 (1979)
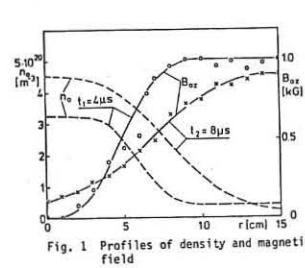
Fig. 1 Profiles of density and magnetic field
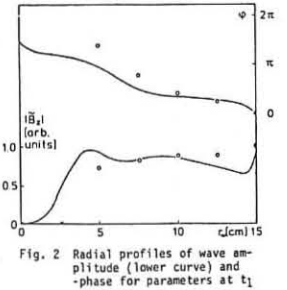
Fig. 2 Radial profiles of wave amplitude (lower curve) and -phase for parameters at t_1
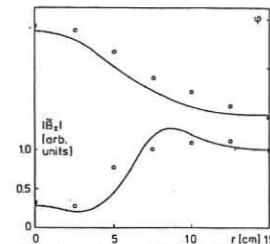
Fig. 3 Radial profiles of wave amplitude (lower curve) and -phase for parameters at t_2
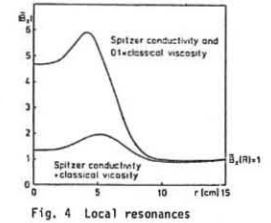
Fig. 4 Local resonances
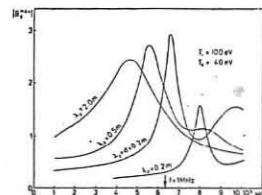
Fig. 5 Resonance curves for different values of k_z
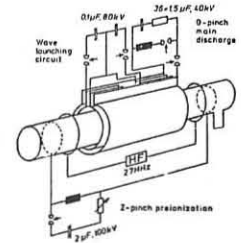
Fig. 6 Experimental set-up
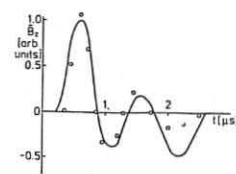
Fig. 7 Time dependence of the axial wave magnetic field

E

STELLARATORS AND BUMPY-TORUS
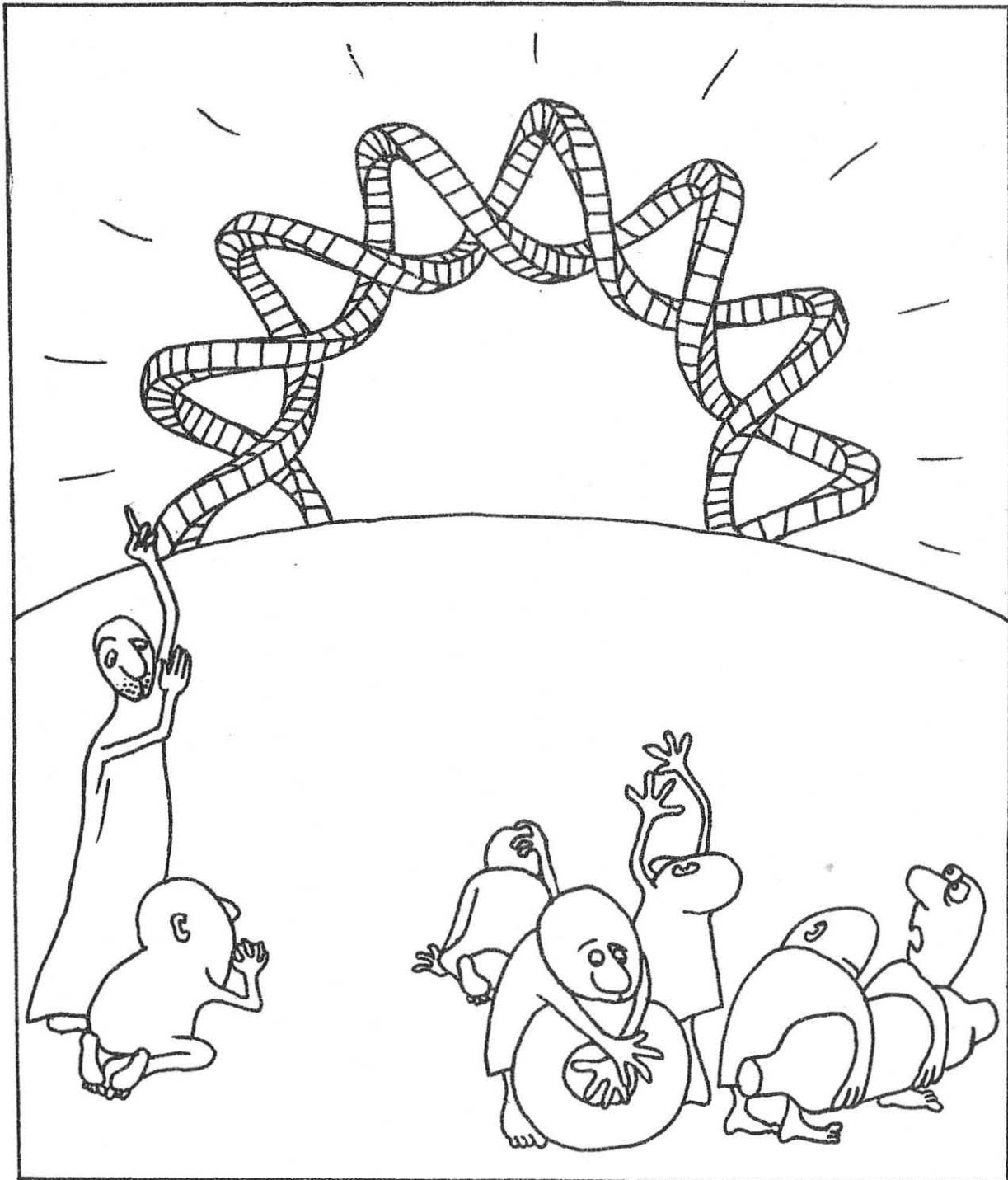
RECENT EXPERIMENTAL RESULTS IN HELIOTRON E

K. Uo, A. Iiyoshi, T. Obiki, S. Morimoto, O. Motojima
A. Sasaki, K. Kondo, M. Sato, T. Mutoh, H. Zushi
H. Kaneko, S. Besshou, F. Sano, T. Mizuuchi
S. Sudo, Y. Nakashima, N. Nishino

Plasma Physics Laboratory
Kyoto University
Gokasho, Uji, Japan

The Heliotron E [1] is an asymmetric toroidal system with large rotational transform and shear. The major radius and average plasma minor radius are 2.2 m and 0.2 m respectively. The helical coil (l = 2, m = 19) produces a magnetic field of 20 kG. The first phase experiment is to study the confinement properties of the ohmically heated plasma and an ECH plasma. The full power operation was started in October, 1980. The following results have been obtained.

I. Ohmic Heating Experiments

We have got two regimes of plasma parameters.

CASE A (low I_{OH} and large $\bar{N}_e \tau_{E_e}$ plasma)		CASE B (high T_e and low $\bar{N}_e$ plasma)	
$T_e(0)$	100 ~ 250 eV	$T_e(0)$	800 ~ 1000 eV
$T_i(0)$	100 ~ 250 eV	$T_i(0)$	100 ~ 200 eV
$\bar{N}_e$	2 ~ 8.5 × 10^{13} cm^{-3}	$\bar{N}_e$	0.5 ~ 1.0 × 10^{13} cm^{-3}
I_{OH}	10 ~ 30 kA	I_{OH}	80 ~ 100 kA
τ_{E_e}	30 ~ 50 msec	τ_{E_e}	1 ~ 2.0 msec
$\bar{N}_e \tau_{E_e}$	(0.6 ~ 2.0) × 10^{12} cm^{-3} sec	B	20 kG
B	10 ~ 20 kG		

A typical confinement scaling of ohmically heated plasma is that the energy confinement time of the electron, τ_{E_e} is inversely propotional to the drift parameter of the plasma current, $\xi = V_D/V_{T_e}$, where V_D is the drift velocity of the plasma current and V_{T_e} is the electron thermal velocity (see Fig. 1). A fairly long confinement time (20 ~ 50 msec) has been obtained in a low current regime (CASE A, Fig. 2). To get a high electron temperature ($T_e(0) \approx 1$ keV), the ohmic input power must be increased and ξ increases due to the increase of the plasma current. Therefore, the confinement time becomes short and the high temperature plasma is produced only in a low density case at present (CASE B). On the other hand, high density is obtained in a low current regime (Fig. 3). This is closely related to the disruption free property of heliotron by the stabilizing effect of the helical field. The disruption of the plasma current which is one of the severe problems in tokamaks has not been observed in Heliotron E. In low magnetic field (B ≈ 10 kG) and high ohmic current experiments, the central toroidal beta of the electron reaches up to 1 %. The obtained safety factor at the boundary (q_{OH}) is 0.98 without major disruption.

II. ECRH (Electron Cyclotron Resonance Heating) Experiment

A 28 GHz, 200 kW Gyrotron for the electron cyclotron resonance heating was applied on the neutral gas without using the ohmic discharge. The resonance field was 10 kG. A currentless plasma of $T_e(0) \sim 500$ eV, $T_i \sim 100$ eV and $\bar{N}_e \sim 4 \times 10^{12}$ cm^{-3} was obtained as shown in Fig. 4. The observed electron energy decay time in the afterglow stage was 40 ± 8 msec, and the par-ticle confinement time was more than 70 msec. Since the electron energy decay was dominated by the equipartition with the ions, we solve a transport code to estimate the energy losses of the ions and electrons considering the neoclassical theory. The results agrees with the observed ones within the experimental errors.

III. NBI Experiments (Near Future Program)

The neutral beam injection heating experiment in the currentless regime is expected to demonstrate the intrinsic plasma confinement characteristics of the heliotron in contrast with tokamaks. The neutral beam injectors with the total neutral beam power of 2.5 MW and the pulse duration of 200 msec are ready for operation. Injection angle of one beam line is just perpendicular to the toroidal direction and other two at 28° from perpendicular direction. We expect good trapping efficiency in these injection angles by Monte Calro simulation [1].

REFERENCES:

(1) K. Uo et al., in the Seventh International Conference on Plasma Physics and Controlled Nuclear Fusion Research, Brussels (1980) CN-38/H-4
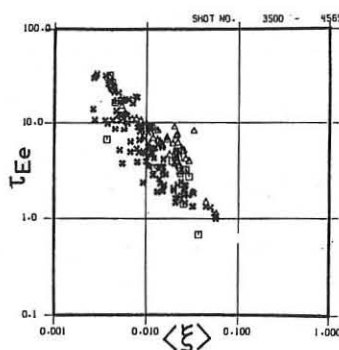
Fig. 1 Electron global confinement time (τ_{E_e}) versus mean drift parameter ($<\xi>$)
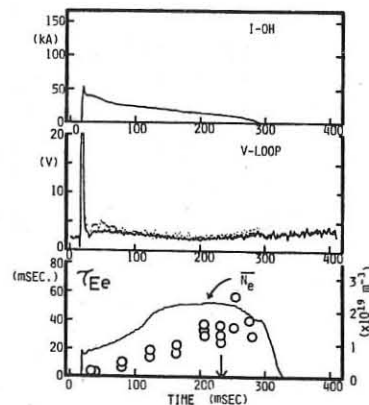
Fig. 2 Temporal evolution of Plasma Current I-OH, one turn voltage V_L, mean electron density $\bar{N}_e$ and global electron confinement time τ_{E_e}.
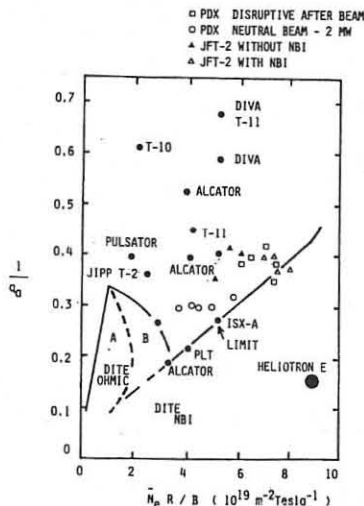
Fig. 3 Obtained critical density of the torii. q_a is the safety factor of Ohmic current at the boundary.
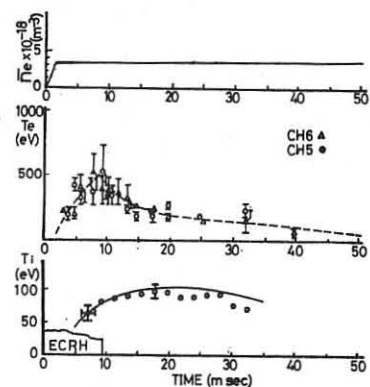
Fig. 4 ECRH Experiment: Temporal evolution of mean electron density $\bar{N}_e$, central electron temperature T_e and ion temperature T_i.

RADIATION LOSSES IN L-2 STELLARATOR WITH OHMIC HEATING

E.D. Andryukhina, M.A. Blokh, G.S. Voronov, E.F. Gippius,
K.S. Dyabilin, V.N. Kolesnikov, N.F. Larionova, N.V. Lunin,
O.I. Fedyanin, A.V. Paramonov, I.S. Shpigel'

Lebedev Physical Institute, Moscow, USSR

1. INTRODUCTION

Investigation of plasma energy loss channels plays an important role in plasma energy balance studies. Energy losses connected with impurities radiation are one of the main loss channels.

In this report experimental results on radial profiles of radiative loss power and spectral line intensity distributions (iron and oxygen beeing the dominating impurities) on L-2 stellarator are presented.

On investigation of L-2 plasma energy balance [1] two ranges of energy confinement time versus plasma current dependence were found to take place: if $I/B < 1.2-1.4$ (plasma current over magnetic field strength kA/kOe) grows, if $I/B > 1.4$ falls. Measurements of radiative losses and impurities observation have been made for these regimes.

Fig.1

2. EXPERIMENTAL CONDITIONS

L-2 stellarator has the following parameters: magnetic field B=20kOe, major radius R=100cm, plasma radius a=11.5 cm, helical windings l=2, rotational transform $\iota(0)=.185, \iota(a)=.785$. Deuterium plasma is generated with ohmical discharge, current 15 - 23 kA lasts 25-30 ms. The discharge time history for two values of plasma current ("A", $I_1=16kA$ and "B", $I_2=22-23kA$) are plotted in Fig. 1. Average electron density $\bar{n}_e=1.1 \times 10^{13} cm^{-3}$, electron temperature Te (0)=400eV, ion temperature Ti=70 eV, Zeff=3-4, ohmic power P1=40-45 kW, P2=75-80 kW, radiation power W1=16-18kW, W2=30-40 kW.

3. RESULTS

3.1 ELECTRON TEMPERATURE PROFILES

were measured by Thomson scattering at $r/a < 0.6$ and at $r/a > 0.6$ from positioning of maximal line intensities of light impurities (OII, OV, CIII, CV). Electron temperature in the point of localization of ion specimen was taken to be $0.5 \times (1+0.2)$ of proper ionization potential. Profiles (Fig.2) look as having high
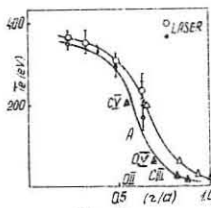
Fig.2
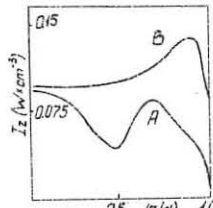
Fig.3
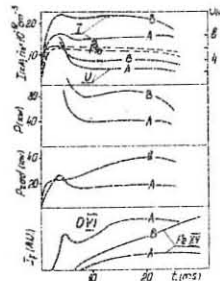
slope region at 6 to 8 cm and low temperature plateau in periphery. General view of Te(r) is unaffected with plasma current variation, Te(r) is constant, high temperature region slightly expands.

3.2 RADIATIVE LOSS PROFILES

Radiation power was measured with pyroelectric detectors. Both absolute radiation power and its temporal behavior essentially depend on plasma current. If plasma current equals to I1 relative loss power is 30% of total ohmic power, in the I2 case it changes from 20 to 50% during the discharge.

Profiles evaluation was carried out by conventional Abell procedure, elliptical shape of magnetic surfaces being taken into account assuming intensities homogeniously distributed in a surface.
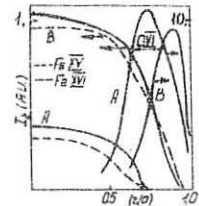
Fig.4

The profile (Fig.3) essentially deforms when plasma current varies. In "A" regime emission is peaked at $r/a \approx 0.7$, this peak shifts to periphery in "B" regime, also total emission flux grows. Impurity ion concentration is the most probable cause of profile evolution.

3.3 LINE RADIATION MEASUREMENTS

Measured profiles of FeXV ($\lambda=284\text{Å}$), FeXVI ($\lambda=335\text{Å}$) and OVI($\lambda=1032\text{Å}$) line intensities are plotted in Fig. 4.

Time dependencies of iron and oxygen lines differ (see Fig.1) though ionization potentials of proper ions are rather close (iron lines starts 5 ms later). In quasistationary phase of the discharge oxygen lines are localised near the edge and move out with current increase. The observed iron ions (FeXV and FeXVI) are concentrated in central region, their concentrations gorw and existance domain expands with plasma current.

Comparison of O and Fe lines intensities and their profiles implies to absence of coronal equilibrium. In this condition correct calculation of ion concentration and line emission power seems to be impossible.

On the other hand Fe ions line emission growth with current does not contradict with loss power increase.

4. CONCLUSION

1. Space resolved measurements of radiative loss power and FeXV, FeXVI and OVI line intensities were carried out.

2. Radiation losses in the plasma core are shown to amount to 20% of ohmic power. They are higher than ohmic power at the edge.

3. Loss power profiles and their dependence on plasma current qualitatively agree with spectroscopic data.

4. Electron temperature profiles changes slightly, plasma resistanse is practically constant for different current regimes. This behaviour of plasma resistanse may be connected with either changes in n_i profiles or light to heavy impurities submission.

5. It seems now that falling of energy confinement time with the plasma current increasing cannot be explained by radiation losses.

REFERENCE 1
E.D. Andryukhina et al. "FIZIKA PLAZMY" 4, n5, 1022, (1978)

EQUILIBRIUM AND STABILITY OF A CURRENT CARRYING PLASMA WITH THREE-DIMENSIONAL MAGNETIC AXIS (ASPERATOR NP-4)

Y.Funato, I.Sakamoto, T.Takahashi, S.Kitajima, Y.Ikeda, M.Nakazawa,
H.Watanabe, S.Nagao and Asperator group*

Faculty of Engineering, Tohoku University, Sendai,980, JAPAN

ABSTRACT   Results of ohmic heating in Asperator NP-4, which is a
toroidal device with a three-dimensional and multi-period magnetic axis
, are described. A toroidal plasma with a longitudinal current can be
maintained in equilibrium with the spatial axis close to the vacuum
field axis beyond the skin time of the conductive shell. MHD stabili-
ties of the plasma against m=0, m=1 and m=2 modes are examined. It is
confirmed experimentally that the plasma current in this system is lim-
ited by the onset of the helical instability with m=1 poloidal mode.

INTRODUCTION   It has been pointed out by V.D.Shafranov that the mag-
netic configuration formed in a closed solenoid with a spatial (three-
dimensional) axis was the simplest stellarator configuration with a
circular cross-section of enclosed magnetic surfaces (1). Asperator
NP-4 is the multi-period system (8 period) among many stellarators with
spatial axis. The results of the design study on this toroidal system
and of the preliminary experiment on a toroidal device Asperator NP-3
were reported previously (2)(3). Theoretical problems of MHD proper-
ties of a plasma with a spatial magnetic axis have been investigated
for a long time (4)(5). For the sake of its high rotational transform
angle with shear and well, these field configurations are useful to
confine a high beta plasma. Asperator NP-4 is an upgrade of NP-3 and
has the pitch angle of about 45° and the period number of 8 of the helix
of the magnetic axis. The important differences between NP-4 and NP-3
are in such point that the minor radius of the toroidal chamber is 13
cm, which is much larger than that of NP-3(3.5 cm) and the period number
n=8, that of NP-3 is 16. In this report, the discharge characteristics
in the ohmic heating and conditions of plasma equilibrium and stability
in such a system are studied experimentally.

DEVICE   The device parameters of Asperator NP-4 are listed in Table-
I. The stainless steel vacuum chamber has a helical axis and was fabri-
cated by connecting six elbow tubes per one period. The skin time of
the chamber is es-
timated to be about
0.3 msec. It has
two insulating gaps
to allow for ohmic
heating. The base
pressure of 9×10
Torr in this cham-
ber is obtained by
TMP and Ti-getter
pump. The longi-
tudinal magnetic
field is produced
by 96 circular
solenoids with the
helical axis.

Average major radius	(R)	152.4	cm
Minor radius of chamber	(a)	13.3	cm
Bore radius of limiter	(a_p)	9.5	cm
Axial length	(L)	13.54	m
Period number	(n)	8	
Radius of axial helix	(r_a)	19.05	cm
Curvature of axis	(k)	2.627	m⁻¹
Torsion of axis	(κ)	2.627	m⁻¹
Longitudinal field	(Bs)	3.0	kG
Half period of Bs	(T/2)	60	msec
Ohmic heating flux	(Φ)	0.25	Vsec
Period of ohmic heating	(Tj)	2-3	msec

Table I. Main device parameters of Asperator NP-4

The plasma is preionized by 2.45 GHz micro wave power and the density
is measured by 6 mm micro-wave interferometer.

VACUUM FIELD CONFIGURATION

One of the most characteristic
point in the three-dimensional
magnetic system is that the nest-
ed magnetic surfaces are formed
only by the solenoidal fields
without the longitudinal plasma
current and also without the
helical winding fields. It has
been shown that the vacuum mag-
netic surfaces were exist exper-
imentally without helical wind-
ing in the figure-eight system
(6). The magnetic surfaces
calculated numelically of NP-4
device are shown in Fig.1.
The magnetic quantities in this
system are written by using
Mercier's intrinsic coordinate

Fig.1 Estimated magnetic surfaces
and measured rotational transform
angle θ in Asperator NP-4.

system(ρ,ω,s). Properties of lines of force of the device were measur-
ed with a electron beam method. The results are shown in Fig.1 togeth-
er. In Asperator NP-L, which is a counterpart of NP-3 and NP-4, the
method for measuring lines of force was tested previously (7). The
quantity θ in Fig.1 shows the mean rotational transform angle existing
between s=0 and s=2.75λ, where λ is the pitch length of the axis. Then
the average rotational transform angle of 254°± 5° (ᵻ=0.706± 0.014)
per one period is obtained, which is good agreement with the theory.
The measured magnetic axis is shifted from the geometric axis of the
longitudinal field coils towards the curvature center by 16 mm which
is confirmed by the numerical calculation.

EQUILIBRIUM   As shown in Fig.1, the magnetic axis of the vacuum field
with circular surfaces is displaced toward the principal normal of the
axis . This displacement is equivalent to the existing of a magnetic
hill. Therefore, a plasma current is necessary to produce the well (8).
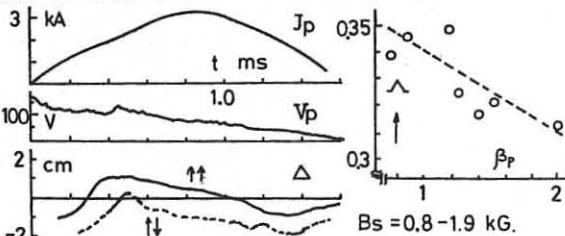
Fig.2 Plasma current Jp (1 kA/div.),one
turn voltage Vp(50 V/div.) and column
shift Δ (1 cm/div.) v.s. time (0.2 ms/div.)
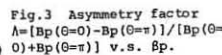
Fig.3 Asymmetry factor
$\Lambda=[Bp(\theta=0)-Bp(\theta=\pi)]/[Bp(\theta=0)+Bp(\theta=\pi)]$ v.s. β_p.

* T.Terasawa, Y.Miura, K.Kobayashi, N.Sasaki and
K.Harafuji.

In Fig.2, the time variations of the plasma current Jp, the one turn
voltage of the discharge and the horizontal shift of the current column
are shown. The column shift directed to the principal normal to the
system were obtained by Mirnov's method. Without the application of the
externally controlled field, a stable discharge was obtained during
about 2 msec. It is seen from the figure that the column staies within
several centimeters around the chamber axis over the discharge period ,
in which only the solenoidal field is applied externally. The skin
time of the stainless steal vacuum chamber is estimated to be about 0.3
msec and the value is much shorter than that of current duration. Then
we consider quantitatively the equilibrium of a current carrying plasma
whose axis is a spatial with curvature k and torsion κ (k=κ in our case)
(9)(10). Fig.3 shows the asymmetry factor of the poloidal field Bp due
to the plasma current versus poloidal beta β . The factor Λ is defined
by the equation: $\Lambda=[Bp(\theta=0)-Bp(\theta=\pi)]/[Bp(\theta=0)+Bp(\theta=\pi)]$. It is seen
from Fig.3 that the current column shifts toward the weaker field region
(θ=π) as the poloidal beta increases. If the poloidal beta values are
not so large, the results obtained in our device are confirmed by the
theory (9)(10).

STABILITY   MHD fluctuations of Bp due to the plasma current were in-
vestigated using 24 magnetic probes arranged arround the limiter and the
real time Fourier analyzer. Fig.4 shows the time history of the m=0, m=1,
and m=2 fluctuations in Bp due to the current. In this figure the plas
ma current Jp and the total rotational transform angle $\mu=\mu(\kappa)+\mu(Jp)$ on
the current axis are also shown, where $\mu(\kappa)$ and $\mu(Jp)$ are the rotational
transform angle per period due to the torsion and the current, respec-
tively. It is remarkable in the figure that at fixed values for Jp the
m=1 mode appears drastically. In the case of Fig.4, the plasma current
is anti-parallel to the axial magnetic field Bs and so the rotational
transform by the current is additive to that of vacuum field by the
torsion of the axis. If the current distribution is assumed to be para-
bolic, a magnetic surface with q(0)=1 is generated near the axis in con-
ditions of the plasma radius a=9.5 cm, Jp=3.1 kA and Bs=1.5 kG. That
is, the total rotational transform angle is found to be equal $\mu=1$, which
can result in the development
of the helical instabilities
with low m mode . In many
stellarators, the m=1 mode
oscillation seems to play the
dominant role in major current
disruption. In NP-4 device,
however, the critical plasma
current Jc is given by the
onset of the m=1 oscillation.
Fig. 6 shows the experimental
Jc as function of the axial
magnetic field Bs. The growth
rate of the m=1 oscillation
are measured with magnetic
probes and results are shown
in Fig.7. In order to confirm
the shear due to the current,
moreover, the poloidal field
distribution was measured di-
rectly by inserting the magne-
tic probes under a low current
operation. The result of measurement of Bp distribution is shown in
Fig.5. It is seen from the figure that the current profile is almost
nearly the parabolic form. The shear of the external rotational form
produced by solenoids with spatial axis is negligible. Therefore, the
radial profiles of the current density and the safety factor are similar
to those of tokamak. And we confirmed experimentally the critical
current Jc for the m=1 helical stability of a current carrying plasma
in a system with spatial magnetic axis and
with the multi field period;

$$Jc=\frac{2\pi a^2 Bs}{\mu_o L}\cdot(2\pi n-\kappa L) \quad (1)$$

where n is the integer (n=1 in Asperator
NP-4 experiment), L is the pitch length of
the helix and κ the torsion of the axis.

In three-dimensional torus, the major
toroidal curvature 1/R and the local cur-
vature k of the axis are exist together.
When the safety factor q(k) for the radius
of curvature k is about 1, the factor q(R)
for the major radius R is o.125 in NP-4
device.

In conclusion, it was confirmed that the
stability in the system with spatial axis
and multi period is determined mainly by
the local curvature effect.

Fig.4 Mode, rotational transform vs. t.
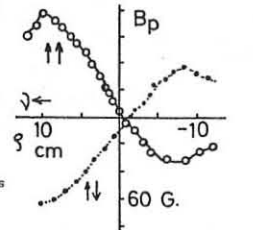
Fig.5 Distribution of poloi
-dal field Bp due to plasma
current. Bs=1.6 kG,Jp=2.5 kA
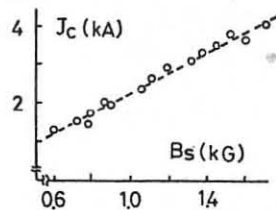
Fig.6 Critical plasma current Jc
v.s. longitudinal field Bs for m=1
mode. $P_a=2 \times 10^{-4}$ Torr.
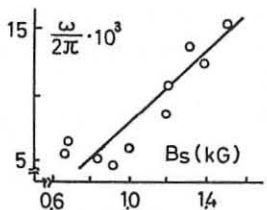
Fig.7 Growth rate of m=1 mode
V.S. Bs.

REFERENCES   (1) V.D.Shafranov: Nuclear Fusion, Vol.20, No.9(1980)1075.
(2) S.Nagao and Asperator group: 7th. Symp. on Eng. Problem Fusion
Research, Knoxvill, 1 (1977) 841. (3) Y.Goto and Asperator group: Proc.
9th Europ. Conf. Controlled Fusion & Plasma Phys. BP19, Culham (1979)73.
(4) V.D.Shafranov: Nuclear Fusion, 8 (1968) 253. (5) C.Mercier: Nuclear
Fusion, 4 (1964) 213. (6) M.M.Dremin, A.M.Solntsev and A.M.Stefanovskij
: Proc. 6th Conf. on Plasma Phys. & Controlled Nuclear Fusion Research,
Berchesgaden (1976) Vol.2, 155. (7) Y.Funato, I.Sakamoto, T.Asaishi,
T.Saito and S.Nagao: Plasma Physics, Vol.22 (1980) 545. (8) S.Nagao,
et. al.: Int. Workshop on Stellarators, Schloss Ringberg, F.R.Germany,
14-16, July (1980) B-3-6. (9) L.S.Solovev and V.D.Shafranov: Rev. of
Plasma Phys. (Consultants Bureau, New York, 1970) Vol.5, p.1. (10) H.
Watanabe et.al.: J. Phys. Soc. Japan, Vol.49 (1980) 1542.

OPTIMIZING THE MAXIMUM TRANSFORM FOR ℓ=3 STELLARATORS BY PITCH ANGLE WINDING MODULATION

L.E.Sharp, J.W.Blamey and S.K.Tin

Plasma Research Laboratory
The Australian National University

It has been shown[1] that by spatially modulating the pitch angle of the helical conductors of an ℓ=3 stellarator according to the law

$$\theta = m\phi + \alpha\sin\theta + O(\beta\sin 2\theta)$$

the efficiency of the windings in producing the rotational transform can be improved. Further, by using a different modulation parameter for the forward and return conductors an effective vertical field periodic in phase with the winding can be introduced to control the position of the magnetic surfaces.

Using a modified version of the Culham code MAGBAT[2] we have computed the magnetic surfaces and average rotational transform t (taken here as the ratio of the number of complete revolutions of $\underline{B}$ in θ for not less than ten rotations in ϕ). The helical conductors are approximated by 3 filamentary currents poloidally spaced 10° apart at $\phi=0$, and a wide range of aspect ratios ($A \equiv R_o/r_w$) and helical field parameters $X=I_h/r_w B_\phi$ where r_w, R_o are the minor/major winding radii in conventional coordinates, and I_h is the winding current. The parameters A, x and α determine both the shape and position of the surfaces.

Since (i) t for an outer surface is very sensitive to its distance from the separatrix and (ii) allowance must be made for space to accommodate both finite conductor size and vacuum hardware, we have chosen to restrict our calculations to cases where the separatrix radius is fixed at $r_s=0.8\ r_w$ and to present transforms calculated for $r=0.9\ r_s = 0.72\ r_w$, the radius of a surface r being defined as that of its circumscribing circle.

To produce a self-consistent model for the optimum transforms for different parameters we have adopted the following iterative procedure:

1. For a given A, x, α the computation is started for a field line at the separatrix at $\phi=0$, $r=0.8\ r_w$.
2. The modulation difference parameter $\delta \equiv [\alpha(+)-\alpha(-)]\ /2$ (where $\alpha(\pm)$ are the modulation coefficients for forward and return helical conductors) is adjusted to centre the surface at $r=0.9\ r_s$ on the geometric (minor) axis.
3. Since this affects r_s, the current I_h is adjusted to restore $r_s=0.8\ r_w$.
4. δ is again adjusted to centre the surfaces.
The iteration is continued until a consistent solution is obtained, twice usually being sufficient.

The required transform t at $r=0.8\ r_s$ is then obtained. Fig. 1 shows how the optimized transform computed in this way depends on mean modulation parameter $\bar{\alpha}$ for various values of m and aspect ratios of 4 and 9.

The normalized current required to achieve the condition $r_s=0.8\ r_w$ can be found from Fig. 2.

The results show that the maximum transform per field period t/m at large aspect ratios and small m (m/A < 1) occurs when $\bar{\alpha}A \approx 1$. It is interesting to note that $\bar{\alpha}A \approx 1$ corresponds closely to the condition that the windings are helically symmetric in <u>true toroidal</u> coordinates[3] following the law:

$$\Theta = m\phi$$

where Θ is the appropriate poloidal coordinate. Under these conditions the mean rate of poloidal rotation of a field line is almost uniform (as in a straight stellarator) i.e. the toroidal effects have been minimized.

For large winding angles (mA ≥ 1) the monotonic increase in t with $\bar{\alpha}$ (Fig. 1) is a consequence of our specification of a surface only by its maximum radius, ignoring its shape, thus allowing for progressive distortion of the surfaces with increasing $\bar{\alpha}$. In practice, this apparent improvement requires disproportionately large helical currents.

REFERENCES

(1) L.E.SHARP, L.F.PETERSON and J.W.BLAMEY, 9th European Conference on Controlled Fusion and Plasma Physics, Oxford,]7-2] September, 1979.
(2) MARTIN, T., Culham Laboratory, UKAEA, Private Communication.
(3) W.N.C. SY, J. Phys. A. (1981) to be published.
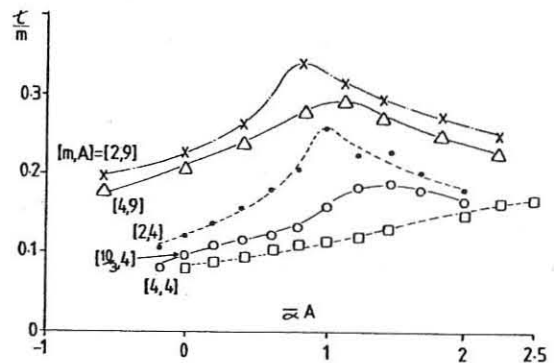
Fig.1. Rotational transform t/m for a centred magnetic surface, $r=0.72\ r_w$ as a function of $\bar{\alpha}A$ for A = 4, 9.
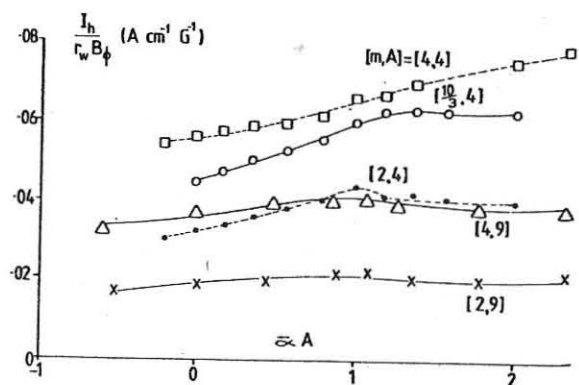
Fig.2. The helical conductor current ($I_h/r_w B$) corresponding to the cases shown in Fig. 1.

EFFECT OF WINDING MODULATIONS
ON THE DISPLACED AXIS OF TORSATRONS

W. N-C. SY
Research School of Physical Sciences,
The Australian National University,
Canberra, Australia

1. Introduction

Among non-axisymmetric toroidal plasma containment devices, the ultimate torsatron[1] requires the least number of external current windings to produce nested magnetic surfaces. Modulations of the helical windings can compensate toroidal effects and centralize the displaced axis[2], whose otherwise large departure from the geometric toroidal axis can lead to the formation[3] of interior island structures and a resultant decrease in useful confinement volume. In this paper, analytic results are presented on the effect of winding modulations on the displaced axis of a torsatron.

2. A Distribution of Modulated Windings

In quasi-toroidal coordinates (ρ, θ, ϕ), consider a modulated winding law defined by

$$\nu(\phi - \phi_0) = \theta + \sum_{n=1}^{\infty} \beta_n \sin n\theta , \qquad (1)$$

where $\beta_n \equiv 2(-1)^n J_n(\gamma n)/n$, γ is a numerical constant (zero in the absence of modulation), and ϕ_0 is a constant specifying a particular position of the helix. If an angle χ is introduced by $\theta \equiv \chi + \gamma \sin \chi$, then (1) can be written equivalently as

$$\nu\phi = \chi - \chi_0 , \qquad (2)$$

where χ_0 is a poloidal angle and ν is usually a rational number. A distribution I of thin helical current filaments which produces an ultimate torsatron configuration of polarity ℓ can be defined by

$$\frac{dI}{d\chi_0} = \frac{I_0}{2\pi}(1 + \cos\ell\chi_0) , \qquad (3)$$

where I_0 is the total current through any given meridonal plane.

3. Magnetic Field of the Central Region

The nett toroidal current in the helical windings, evident from (3), gives rise to components of the magnetic field which are independent of the toroidal angle. These components can be investigated by the use of the Biot-Savart law, which ensures the boundary conditions are satisfied explicitly. The displaced axis can be defined as the circle at which the "secular" terms of the magnetic field perpendicular to the meridonal plane, vanish. Since this usually happens near the geometric axis, the nature of the displaced axis can be examined by an expansion about the geometric axis.

Consider a vacuum chamber of major and minor radius, R_0 and a respectively. Then the region of interest is $r \sim \varepsilon \ln \varepsilon$, where $r \equiv \rho/a$ and $\varepsilon = a/R_0$. Calculations from the Biot-Savart law[4] show that the "secular" components of the magnetic field $\langle B_\alpha \rangle$, accurate to $O(\varepsilon^3)$ read (SI units),

$$\langle B_\alpha \rangle = \frac{\mu_0 I_0}{4\pi a} \frac{b_\alpha}{(1+\varepsilon r\cos\theta)^{3/2}} , \qquad (4)$$

where

$$b_R = 2\Theta r\sin\theta , \qquad b_Z = \Lambda - 2\Theta r\cos\theta ,$$

$$b_\phi = 2\varepsilon\nu(1+r^2+\frac{9\varepsilon^2}{8}) , \qquad (5)$$

with

$$\Theta \equiv 1 + r^2 - \frac{\varepsilon\alpha}{4} - \frac{3\varepsilon^2}{8}(\ln\frac{8}{\varepsilon}-\frac{3}{2}) + r\cos\theta(\frac{\varepsilon}{2}-\alpha) ,$$

$$\Lambda \equiv \varepsilon\{\ln\frac{8}{\varepsilon}-\frac{1}{2}+\frac{\varepsilon^2}{8}(\ln\frac{8}{\varepsilon}-\frac{15}{4})\} - \alpha\{1-\frac{\varepsilon^2}{4}(\ln\frac{8}{\varepsilon}-\frac{9}{2})\} , \qquad (6)$$

$$\alpha \equiv J_1(\gamma) .$$

For brevity, the cylindrical components (R, Z, ϕ) of the magnetic field have been given. It can be observed that modulation has no effect on the toroidal component of the magnetic field.

4. The Displaced Axis

From (5), it can be seen that the shift ρ_A of the displaced axis from the geometric axis is given by

$$\delta \equiv \rho_A/R_0 = \Lambda/2\Theta \approx \frac{\varepsilon}{2}(\alpha_0 - \alpha) , \qquad (7)$$

where $\alpha_0 \equiv \varepsilon\{\ln(8/\varepsilon)-\frac{1}{2}\}$. Evidently, the displaced axis moves along the equatorial plane toward the principal toroidal axis as the magnitude of modulation α increases, according to an approximately linear relationship (7).

The average rotational transform on the displaced axis can be estimated by

$$\ell_A = 2\Theta(1+\delta)/\varepsilon^2\nu(1+\delta^2+9\varepsilon^2/8) . \qquad (8)$$

The results of (7) and (8) are displayed in Figure 1. The decrease in average rotational transform on the displaced axis with increase in winding modulation arises from (a) an increase in the toroidal component of the magnetic field due to inward shifts of the displaced axis and (b) a decrease in the poloidal component also. These results are in qualitative agreement with those found from numerical simulation[5], where a different helical current distribution is used.
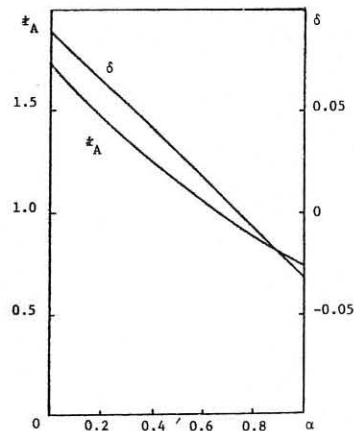
Fig. 1 Average rotational transform on the displaced axis ℓ_A and its displacement from the geometric axis δ as functions of the modulation parameter α for the case $\varepsilon = 1/4$ and $\nu = 12$.

REFERENCES

(1) Hubert, P. EUR-CEA-7C-533 (1970).
   Gourdon, C., Hubert, P., Marty, D., C.R. Hebd. Séances Acad. Sci. 271 (1970) 843.

(2) Hamberger, S.M., Sharp, L.E., Malein, A., Bradley, J., McKay, W., in Plasma Physics and Controlled Nuclear Fusion Research (Proc. 5th Int. Conf. Tokyo, 1974) Vol. 2, IAEA, Vienna (1975) 21.

(3) Gourdon, C., Marty, D., Maschke, E.K., Dumont, J.P., in Plasma Physics and Controlled Nuclear Fusion Research (Proc. 3rd Int. Conf. Novosibirsk, 1968) IAEA, Vienna (1969) 847.

(4) Sy, W.N-C., J. Phys. A (1981) to appear.

(5) Kruckewitt, T.W., Shohet, J.L., Nucl. Fusion 20 (1980) 1375.

Confinement of Stellarator Plasma in JIPP T-II Device

J. Fujita, K. Kawahata, Y. Kawasumi, O. Kaneko, T. Kuroda,

K. Matsuoka, K. Matsuura, K. Miyamoto,* N. Noda, Y. Oka,

K. Ohkubo, K. Sakurai, M. Sato, S. Tanahashi

Institute of Plasma Physics, Nagoya University, Nagoya 464, Japan
*Department of Physics, Faculty of Science,
University of Tokyo, Tokyo 113, Japan

Abstract

The plasma confinement of ohmically heated stellarator plasmas has been studied. Major disruptions which appear in tokamak configuration are suppressed with the helical field of $\iota_h/2\pi \gtrsim 0.14$, and the total rotational transform angle $\iota_\Sigma/2\pi$ at the plasma surface becomes larger than 0.5, that is $q_\Sigma(a) < 2$. The strong MHD oscillations of $m = 2$, $n = 2$ and $m = 1$, $n = 1$, and the hollow structures of the electron temperature profiles are observed in the case of $q_\Sigma(a) < 2$. The energy confinement time τ_E as long as 14 ms is obtained with a control of the plasma current waveform, and inversely proportional to the electron drift parameter.

Introduction and Experimental Arrangements

JIPP T-II is a hybrid device of stellarator and tokamak, which has $\ell = 2$ helical windings with 4 periods.[1] Main parameters are as follows: major radius R = 91 cm, limiter radius a_L = 17 cm, the maximum toroidal field B_t = 30 kG and the rotational transform angle due to helical field $\iota_h/2\pi = 0.25$ at B_t = 25 kG. The results on auxiliary heatings by injections of neutral beams and lower hybrid wave into stellarator plasmas were previously reported.[1] Here, we describe the results on the confinement of ohmically heated stellarator plasmas. The high density and/or low current plasmas are produced with a control of the plasma current waveform (I_p control).[2] Parameters of the ohmically heated plasma with B_t = 22.4 kG and $\iota_h/2\pi$ = 0.14 are followings: $I_p \leq 130$ kA, $T_e \leq 1.2$, $T_i \leq 400$ eV, $\overline{n_e} \leq 4 \times 10^{13}$ cm^{-3}, $\tau_E \leq 14$ ms and the effective plasma radius a_{eff} = 14 cm (geometric means of radii of ellipse).

Experimental Results

Major disruption is one of the most dangerous instabilities of tokamak plasmas, which prevents the safety factor q-value at the plasma surface from decreasing less than two. When the helical field of $\iota_h/2\pi > 0.14$ is introduced, the plasma becomes free from major disruption, and the minimum $q_\Sigma(a)$ value becomes less than two.

Figure 1 shows typical experimental results for $q_\Sigma(a) < 2$. The plasma current I_p is 93 kA at the peak, where the total q-value $q_\Sigma(a)$ is 1.9. When the plasma current rises and $q_\Sigma(a)$ reaches the value of 2 (the time t_1 in Fig.1), the intensity of electron cyclotron emission (ECE) at the second harmonic decreases rapidly, and loop voltage (V_{loop}) increases slightly. No appreciable MHD oscillations are seen on the magnetic probe signals ($\dot{B}_\theta$) at this time. In the discharge of $q_\Sigma(a)$ lower than 1.9, the strong MHD oscillations[3] of $m = 2$, $n = 2$ and $m = 1$, $n = 1$ are observed, therefore, these phenomena imply that an anomalous energy loss occurs in the region of $q_\Sigma(a) < 2$.

Time evolutions of the electron temperature profile in the case of $q_\Sigma(a) < 2$ are examined by the use of the rapid scanning Fourier-transform spectrometer. The electron temperature profiles are maintained in bell shape until $q_\Sigma(a)$ decreases to about 2 as is shown in Fig.2. When the plasma current increases and the safety factor $q_\Sigma(a)$ lowers than 2, the electron temperature profile becomes a hollow structure. When $q_\Sigma(a)$ becomes again larger than 2 at the decreasing phase of I_p, the profile returns to the bell shape. Figure 3 shows the dependence of the central

electron temperature $T_e(0)$ and the intensity of FeXVI line on ι_Σ. $T_e(0)$ increases with ι_Σ for $\iota_\Sigma/2\pi < 0.5$, while in the case of $\iota_\Sigma/2\pi > 0.5$, $T_e(0)$ decreases and FeXVI line steeply increases. The active plasma-wall interaction is also observed for $q_\Sigma(a) < 2$ by a TV camera system which views the plasma column tangentially. The strong light emission is localized near the apexies of the elliptic magnetic surface. This indicates the occurrence of the arcing between plasma and wall. It is considered that the hollow electron temperature profile is due to the radiation losses of the heavy impurities resulting from the active plasma-wall interaction.

Next, we describe the experimental results with the I_p control system. With an operation of the constant plasma current I_p = 25 kA ($q_\Sigma(a)$ = 4) the highest density $\overline{n_e}$ produced stably is 3×10^{13} cm^{-3} with $T_e(0) \approx 550$ eV and $T_i(0) \approx 250$ eV. In this case the total energy confinement time τ_E is 14 ms which is about 2 times larger than that of Alcator scaling. The dependences of τ_E and τ_{Ee} ($= \frac{3}{2}\langle n T_e\rangle 2$ $a_{eff}^2 R/IV$) on the electron drift parameters $\xi = v_d/v_{th,e}$, where $v_d = I_p/e\pi a_{eff}^2 \overline{n_e}$ and $v_{th,e}$ is electron thermal velocity, are plotted in Fig.4. The lower points of ξ are obtained by applying I_p control system. The both of τ_E and τ_{Ee} are inversely proportional to ξ, of which dependence has been also observed in other stellarator experiments.[4]

References

1) J. Fujita, S. Itoh, K. Kadota, K. Kawahata, Y. Kawasumi, O. Kaneko, T. Kuroda, K. Matsuoka, K. Matsuura, K. Miyamoto, N. Noda, Y. Oka, K. Ohkubo, K. Sakurai, K. Sato, M. Sato, S. Tanahashi, Y. Terashima, K. Toi: Plasma Physics and Controlled Nuclear Fusion Research (Proc. 8th Int. Conf. Brussels, 1980) CN-38/H-3-2, IAEA, Vienna.
2) S. Tanahashi, K. Matsuura, J. Fujita, A. Miyahara and JIPP T-II Group: 11th Symposium on Fusion Technology, Oxford (1980) CP.1-6.
3) JIPP T-II Group: Proc. Int. Conf. on Plasma Physics 1 (Nagoya, 1980) 5.
4) G. S. Voronov and M. S. Rabinovich: 9th Europ. Conf. on Controlled Fusion and Plasma Physics, Oxford (1979) 223.
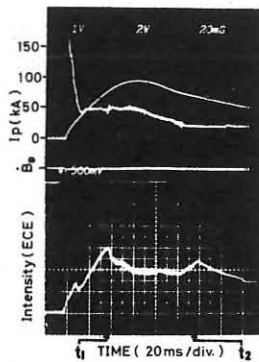
Fig.1 Time behaviors of plasma current (I_p), loop voltage (V_{loop}), fluctuations of the poloidal magnetic field ($\dot{B}_\theta$) and electron cyclotron emission (ECE) at the second harmonic. Times t_1 and t_2 correspond to $q_\Sigma(a)$ = 2.

Fig.3 Dependence of the central electron temperature $T_e(0)$ and the line intensity of FeXVI on $\iota_\Sigma(a)$.

Fig.2 Radial electron temperature profile determined from the second harmonic electron cyclotron emission as a function of time. Arrows indicate the points of $q_\Sigma(a)$ = 2.
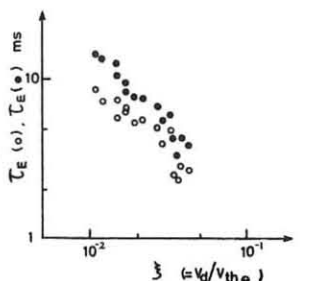
Fig.4 Dependence of τ_E and τ_{Ee} on the electron drift parameter ξ ($\xi = v_d/v_{th,e}$).

PLASMA CONFINEMENT IN NAGOYA BUMPY TORUS

H.Iguchi, M.Fujiwara, M.Hosokawa, H.Ikegami, K.Kadota, K.Matsunaga,
H.Sanuki, T.Shoji, K.Takasugi, M.Tanaka, F.Tsuboi, H.Tsuchidate,
A.Tsushima, F.M.Bieniosek*, R.Parosa**

Institute of Plasma Physics, Nagoya University, Nagoya Japan.
*Rensselaer Polytechnic Institute, Troy, New York, USA.
**Institute of Telecommunication and Acoustic Techical University
of Wraclaw, Wraclaw, Poland.

1. INTRODUCTION

Nagoya Bumpy Torus (NBT) is a plasma confinement device with 24 linked magnetic mirrors. Plasmas are produced and heated by high power microwaves at a frequency of 8.5 GHz and stabilized by high β hot electron anuli formed at the midplane of each mirror section. Typical parameters of NBT are listed elsewhere[1]. Experiments have been performed in two different modes, namely, SR-mode and FR-mode, which respectively have second ECH resonance and fundamental resonance near the anuli. It has been observed in FR-mode that a higher β-value of the hot electron anuli is obtained and that the core plasma density is approaching cutoff of the input microwaves. Ion cyclotron heating has been applied to the plasma in the bumpy torus magnetic field configuration and ion heating has been observed, accompanied by a change in plasma space potential.

2. FR-MODE OPERATION

FR-mode operation has two advantages compared to SR-mode. First, in order to confine high density and high temperature plasmas in future devices, higher β-value of the hot electron anuli is required[2], which can be achieved more effectively in FR-mode for a fixed microwave frequency. Second, microwaves can be used only to form hot electron anuli and plasma heating can be trusted to other methodes such as ICH, NBI and etc. From experience, we know that bumpy torus plasmas are better confined in higher magnetic fields, and at FR-mode we can considerably ease the requirements on high power millimeter wave sources. The temperature, radial position, and β of hot electrons have been studied in detail and compared in both modes (FR- and SR-modes). Figure 1 shows the energy spectrum of hard X-rays emitted from the hot electron anuli. Hot electron temperature T_h in FR-mode is almost twice as high as that at SR-mode and reaches 160 keV with input power of 45 kW. It is confirmed that the β-value is also higher in FR-mode by a factor of two from the measured value of $n_h T_h$. Figure 2 shows the radial position of the hot electron anuli measured with an ionization probe as a function of the magnetic field strength at the midplane. It is found that the anulus positions are shifted outward from the resonance zone in FR-mode, and the anulus diameter at 3.2 kG (FR) is almost the same as that at 1.8 kG (SR).

Figure 3 shows the line integral density $\langle n_e l \rangle$
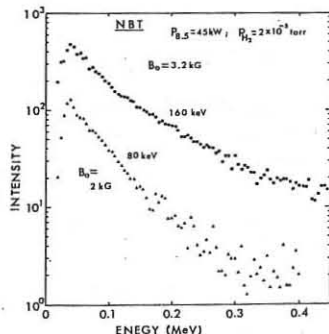
Fig. 1 Energy spectrum of hard X-rays emitted from hot electron anuli.
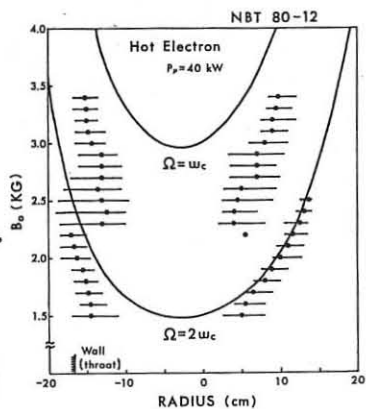
Fig. 2 Radial position of the anuli.
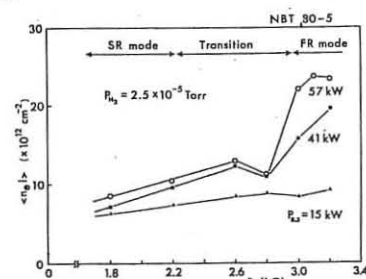
Fig. 3 Line integral density of electrons as a function of the magnetic field.

of electrons as a function of the magnetic field strength at different input microwave powers. In FR-mode, a remarkable increase in $\langle n_e l \rangle$ at high input power is observed. In this case, plasmas are well confined inside of the anuli as shown in Fig. 4, which shows the radial profile of $n_e f(T_e)$ measured with a lithum neutral beam probe[3]. In C-mode operation, in which the ambient neutral gas pressure is high enough to prevent formation of the hot electron anuli, plasmas are observed to spread to the wall. In the case of FR-mode operation with only 8.5 GHz microwaves, no ECH resonance zone exists in the core plasma region and the plasma remains cold (10~20 eV). Electron heating by microwaves at 10.5 GHz and 18 GHz, and ion heating by ICH are now being studied.

Fig. 4 Radial profile of $n_e f(T_e)$ at FR-mode operation.

3. ION CYCLOTRON HEATING

Several conjectures have been discussed associated with the ion heating in bumpy torus plasmas, namely enhancement of diffusion, destruction of ambipolar potential well, cooling of electrons due to ejected impurities, etc. Ion cyclotron heating has been carried out on NBT. Taking account of the plasma density in NBT ($n_e \lesssim 10^{12}$ cm^{-3}) and nonuniformity of the toroidal magnetic field, the slow wave mode is expected to be effective for heating ions. The slow wave can propagate at frequencies below the local ion cyclotron frequency and be absorbed at the magnetic beach where the wave frequency equals the local ion cyclotron frequency. In order to excite the slow wave from the high magnetic field side, a half-turn antenna was installed. The wave is observed to penetrate into the plasma and propagate along the field line with decreasing amplitude. At the same time, ion heating of core plasma is detected from the Doppler broadening of impurity line (OII) and hydrogen line (H_α) radiation. An increase in the body temperature of 25 eV is measured when introducing ICH power of 11 kW at 5.5 MHz, and an increase in the temperature of impurity oxygen ions proportional to the input RF power is observed (Fig. 5). Because of neutral hydrogen atomic density of the order of 10^{11} cm^{-3} in the plasma, ion energy is dominantly determined by the charge exchange. ICH causes not only an increase in ion temperature, but also a change in the profile of the ambipolar potential. In typical T-mode operation, it is observed that the potential is increased by ICH injection, as measured by both a heavy ion beam probe and a Langmuir probe (Fig. 6). A possible explanation for this effect may be based on the reduction of the ion-ion collision frequency as the ions are heated. The resulting enhancement of ion confinement with respect to the electron confinement then naturally results in an increase in the ambipolar core potential.
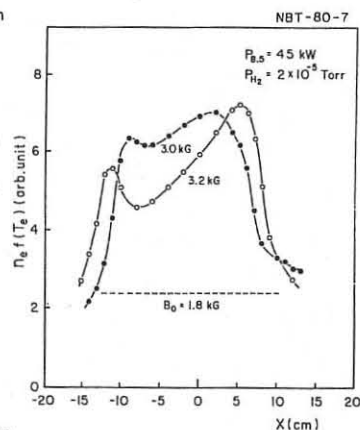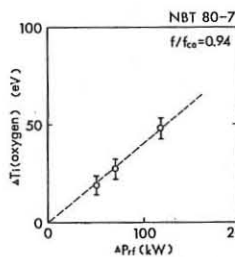
Fig. 5 Increase in ion temperature as a function of input RF power.
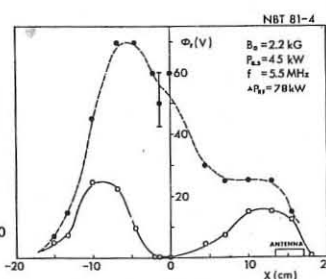
Fig. 6 Potential change accompanied by ion cyclotron heating.

REFERENCES
1) NBT Group and EBT Group, Proc. 8th IAEA Conf. on Plasma Phys. and Contr. Nucl. Fus. Research, Brussel, 1980, IAEA-CN38/BB-4.
2) H. Sanuki, et. al., EBT Ring Physics (Proc. of Workshop, N.A.Uckan ed.) Oak Ridge National Labolatory, Conf-791228 (1980) p. 453.
3) K.Kadota, et. al., Plasma Physics, Vol. 20 (1978) p.1011.

CURRENT PROFILE AND PLASMA TRANSPORT CONTROL

UNDER ALFVEN WAVE ABSORPTION.

R.A.Demirkhanov, A.G.Kirov, L.F.Ruchko, A.V.Sukachov.

Sukhumi Institute of Physics and Technology,
Sukhumi, USSR.

ABSTRACT

Experimental investigations carried out in the R-0 stellarator are given showing the possibility to excite high local quasistationary dragging currents ($j \simeq 40A$ cm^{-2}) and to control the ohmic current profile with $\omega < \omega_{Bi}$ Alfven waves absorbed. The transport process can be influenced as well:with helical HF wave propagated in the direction of electron diamagnetic drift particle and plasma energy transports along the smaller radius are considerably decreased.

Radio-wave of low-frequency Alfven range $\omega < \omega_{Bi}$ used for generating a stationary current in toroidal systems appear to have a number of physical and technological advantages [I,2]. In earlier experiments [4,5] we have shown radially localized excitation of Alfven waves and their efficient absorption by a plasma. Papers [6,7] gave the first demonstration of stationary dragging currents generation under Alfven heating and the wave propagation direction influence upon plasma density profiles has been studied. The present experiments deal with measurements of dragging current radial structures and studies of HF field propagation direction influence upon the plasma energy confinement time and diffusion.

The experiments have been carried out in the $l = 3$ R-0 stellarator with ohmic heating R=50 cm, b is the quartz chamber radius (5cm), a is the separatrix radius (3,5-4cm), hydrogen or helium are operating gases with initial pressures of $10^{-4} \sim 10^{-3}$ torr, in main modes T_e =I0-20 eV and n_e =(0,5-2) 10^{14}cm^{-3}. A helical HF circuit generated helical standing or travelling waves in a plasma which propagated simultaneously in toroidal and poloidal directions with the phase velocity of $\vec{v}_{ph} = \vec{v}_{\varphi} + \vec{v}_z = \pm(\omega a/m \cdot \vec{B}_{\varphi}/B_{\theta} - \omega R/n \cdot \vec{B}_{\theta}/B_{\varphi})$, m=2 and n=2 being poloidal and toroidal wave numbers, respectively. The signs "plus" and "minus" correspond to a "diamagnetic" wave (wave rotation in the direction of electron diamagnetic drift and to a "paramagnetic" one, respectively. The HF field is 800 kHz in frequency, its pulse length being $\tilde{\tau} \le 2,5$ ms, plasma HF inputs varied from 0,I to I,0 MW in power $\tilde{P}$, B_o = I ÷ 7 kGs. The high power input into the plasma allowed to obtain high plasma specific energies ($\beta \simeq 10^{-2}$) enabling us to operate without any ohmic heating current and to observe the rf-driven current in its "pure" form.

Fig.I shows typical traces for dragging currents, plasma specific energies, absorbed HF powers and corresponding distributions of current densities over the minor radius. The ohmic current transformer being turned off, the distributions have been measured by means of magnetic probes.

The r f driven current persists as long as the HF power input proceeds. Assymetry in curve I indicates that there exists a notable dipolar current component (Curve 3) which may be identified with the toroidal equilibrium current. At given <nT> and B_o, i_o, this current has a fairly coincidence with its calculated value. Curve 2 shows the distribution for rf-driven current itself. The current density maximum is localized in the region where an intense Alfven wave is excited. The peak current density has a good coincidence with the calculated one according to the following relation: $j = \sigma_{\parallel}/\sigma_{\perp} \cdot e/m_e v_e \cdot \tilde{P}/V \cdot k_{\parallel \omega}$ [3].

The HF field imposed on the ohmic discharge led to increasing or decreasing in the total current (as function of the HF wave direction) and to rebuilding its profile. The profile rebuilding degree had been a function of the ohmic heating power ratio to the HF one fed into plasma. For a standing wave (Curve I), the current density distribution is close to $j = j_o [1 - (r_o/a)^5]$. For a "paramagnetic" wave when the r f driven current is directed opposite the ohmic one at $r_p/a \simeq 0,7$, the current profile undergoes sharpening and narrowing. With the "diamagnetic" direction

of propagation, the rf-driven current makes a sum with the ohmic one, resulting in increasing for the current density at $r_p/a \simeq 0,7$ and its distribution flattehning. On increasing the absorbed HF power-to-ohmic heating power ratio, more exotic distributions can be obtained with the current sign changed at the plasma column boundary (a "paramagnetic" wave), or there may be some hollow distributions (a "diamagnetic" wave).

Effects of travelling Alfven waves on the transport have been determined according to the change in plasma radial profiles (measured with a double electrical probe) and variations in the total energy life time as a function of the HF wave rotation direction. The experiments on plasma density profile measurements show that during the "diamagnetic" rotation, plasma particles undergo a decrease in their speed while being transported along the minor radius at the plasma column periphery, whereas the "paramagnetic" rotation is accompanied by the increase in this speed. Fig.3 shows the energy life time versus the magnetic field for various directions of the HF field. It is seen that for the "diamagnetic" case, the thermoisolation is better; the difference in the energy life times for "diamagnetic" and "paramagnetic" rotations grows with the magnetic field decrease. Indeed, the comparison with the theory [2,3] reveals that under experimental conditions, the rotating HF field influence upon the plasma transport along the minor radius should be noticeable, growing with the magnetic field decrease, since the radial velocity value derived from the relation $v_{r} = k_{\varphi}/\omega e n_e B_o \cdot \tilde{P}/V$ [3] is comparable with that of the diffusion v_{r2}, estimated after the plasma density decay time, τ_n, from the moment of the HF field fast switch-off ($\tau_{off} \ll \tau_n$) and after the inhomogenuity characteristic dimension Δ, $v_{r2} \sim \Delta / \tau_n$.

REFERENCES

I. N.J.Fisch, C.F.F.Karney, Phys.Fluids, 24, I, 27, I98I.
2. S.Inoue, K.Itoh.Preprint HIFT-26, Hiroshima, I980.
3. V.V.Nemov. Fizika plazmi, 4, I280, I978.
4. A.G.Kirov et al. 9th Europ.Conf.on Contr.Fus. and Plasma Phys., Oxford, I979, I, p.I8.
5. A.G.Kirov et al.2nd Int.Symp.on Heat.of Tor.Pl.,Como,I980.
6. R.A.Demirkhanov et al.Preprint SFTI-I2,Sukhumi, I98I.
7. R.A.Demirkhanov et al. Pisma v ZhETF, 33, 3I, I98I.

Fig.2. Radial distribution of the symmetric current density component in the Ohmic discharge;t_o = 0,2, H_2 :I-st.wave,B_o=4,7 kGs, j= $j(r_p =0)$=4IA·cm^{-2}; 2,4-"para" wave,B_o=6,2 kGs(2-j_o=40A·cm^{-2}, 4-J_o=I2 A·cm^{-2});3,5-"dia"wave, B_o=6,2kGs(3-j_o=29A·cm^{-2},5-j_o=I8A·cm^2.
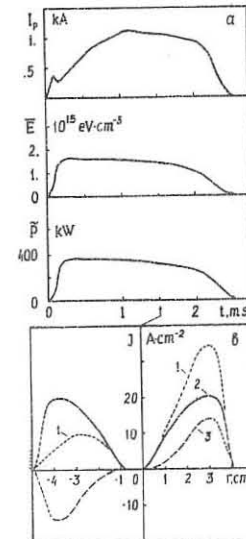
Fig.I.a)Plasma current, specific energy, absorbed HF power;b)radial distribution of the current density:I-total current density,2-symmetric current component,3-dipolar current component. B_o=5,4kGs,t_o=0,2,p=I,5·10^{-3} torr, H_2, "dia" wave,U_{loop}=0.
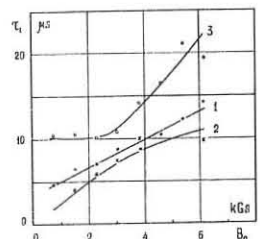
Fig.3. Energy confinement time vs toroidal magnetic field: I-st.wave;2-"para"wave,3-"dia" wave; t_o=0,2, H_2, U_{loop}=0.

CLOSED MAGNETIC TRAP WITH RECTILINEAR SECTIONS

V.M.Glagolev, B.B.Kadomtsev, V.D.Shafranov, B.A.Trubnikov

I.V.Kurchatov Institute of Atomic Energy. Moscow, USSR

Abstract: We discuss here the possibility of a long stright sections in a plasma magnetic trap closed into a topological torus by means of special connectors, the linear sections being unperturbed by charge separation currents.

Introduction. Studies in the fusion reactor concepts based on the magnetic confinement have shown advantages and disadvantages of the open (mirror) and closed (toroidal) magnetic traps. It is natural to ask whether it is possible to design a system which combine the best features of both, i.e. that which includes long stright sections with high β (the main operating section of the reactor) and curvilinear connectors, eliminating the problems assosiated with the mirror loss cones but having no effect on equilibrium and transport in the stright sections. We shall call such systems "dracon" (Russian abbreviation of the "long equilibrium configuration"). If the magnetic field strengts in the connectors is considerably greater than that in the linear sections, one can expect $\beta = 5 \div 6$ % for the connectors and $\beta = 20 \div 25$ % for the linear sections at the same time.

Equilibrium connector. Feasibility of the "dracon" is assosiated with an idea of a special connector of the rectilinear elements (CREL). CREL realises φ-angle turn transform of the stright magnetic field lines in the presence of plasma (Fig.1). An equilibrium plasma pressure in "dracon" depends only on the CREL design no matter what the linear section length is. The condition for this is an equality of the integral $\int dl/B$ for all field lines at a given magnetic surface. This one is reduced to a requirement [2,3]:

$$\int_{-\ell/2}^{\ell/2} [\text{ch}\frac{\zeta}{2}\cos(\delta - v) - \text{sh}\frac{\zeta}{2}\cos(\delta + v)]kB^{-3/2}ds = 0 \qquad (1)$$

in a paraxial approximation. Here s is the axis arc length accounted off from the CREL middle, $B(s)$ is the axial magnetic field strength, $v = \int^s [(\delta' - \varkappa)/\text{ch}\frac{\zeta}{2}]ds$; $k(s), \varkappa(s)$ are the curvature and torsion of the axis; $\exp\zeta(s)$ is the ratio of magnetic surface crossection semiaxes, $\delta(s)$ is an angle between the principal normal and small semiaxes. The functions $B(s), k(s), \zeta(s), \varkappa(s)$ are considered to be even while $\delta(s), v(s)$ are odd ones.

Let's consider a simple case of the near circular magnetic surface cross-sections, $\zeta \ll 1$; $\text{ch}\zeta/2 \approx 1$, $\text{sh}\zeta/2 \approx 0$. In this case, eq.(1) is reduced to

$$\int_{-\ell/2}^{\ell/2} kB^{-3/2}\cos\iota(s)ds = 0 \qquad (2)$$

where, $\iota(s) = \delta(s) - v(s)$ is a rotational transform. Consider three types of the CREL.

A planar axis CREL with nonuniform field. The axis of this CREL, shown in Fig.2, consists of three arcs with curvatures $k_1 = 1/R_1$, $k_2 = -1/R_2$. The angle openings (see Fig.2) are $\theta_1 = (2\theta_c + \varphi)/4$, $\theta_2 = (2\theta_c - \varphi)/4$; $\theta_c = \theta_1 + \theta_2$. Neglecting the transition regions, the magnetic fields B_1, B_2 can be related as follows:

$$B_2/B_1 = [(2\theta_c - \varphi)/(2\theta_c + \varphi)]^{2/3} \qquad (3)$$

For example, at $\theta_c = \varphi(\theta_1 = 3\varphi/4, \theta_2 = \varphi/4)$ we have $B_1/B_2 = 2.1$. Such CREL is feasible at a small or even at a zero rotation transform. It can be considered, as a separate unit of the Spitzers scallops [4] or of the bumpy torus [1].

A planar axis CREL with uniform field is shown in Fig. 3. The curvature of its axis changes sign as above. The greater the sag of the CREL middle part the less the rotational transform providing necessary equilibrium properties of the CREL. The Table 1 shows the parameters of the 180° CREL with $\iota_c \equiv 2(\iota_1 + \iota_2) \equiv \iota(\frac{\ell}{2}) - \iota(-\frac{\ell}{2}) = 3$.

Table 1

ι_1	1	0,9	0,8	0,75
ι_2	0,5	0,6	0,7	0,75
$2\theta_1/\varphi$	0,61	0,72	0,82	0,86
R_1/R_2	5,26	3,57	2,54	2,16

Ratio of the arc radii providing constant pitch of a helical winding is shown in the 4-th line of the Table.

A CREL with a spatial (nonplanar) axis, having an uniform field, should satisfy the condition

$$\int_{-\ell/2}^{\ell/2} k \cos\alpha \, ds = 0 \qquad (4)$$

where, $\alpha(s) = \int^s \varkappa ds$ is the turn angle of the principal normal counted off from a strip $\omega = \text{Const}$ passing through the axis perpendicular to its normal cross-sections. The curvature of a nonplanar curve is considered to be positive. For the CREL composed of three toroidal sectors with angle openings θ_0, $\theta_1 = \theta_{-1}$ (negative index corresponds to $S < 0$), it follows from (4)

$$\frac{1}{2}\theta_0 + \theta_1 \cos\alpha_0 = 0 \qquad (5)$$

In case of the 180° CREL composed of three semitori ($\theta_0 = \theta_1 = \pi$), the angle α_0 between the semitori planes is appeared to be equal to 120°. The "dracon" design based on this CREL as well function $\alpha(s)$ are shown in Figs 4,5.

Equilibrium in a CREL with spatial axis. The displacement of the plasma column boundary satifies the equation [5]:

$$\frac{d^2\xi}{ds^2} = -\frac{1}{2}\beta(1-\frac{a^2}{b^2})k \cos[\omega - \alpha(s)] \qquad (6)$$

Along the rectilinear sections, $k(s) = 0$, $d\xi/ds = \text{Const}$, the value of this constant being dependent on the integral $\int k \cos\alpha \, ds$. Thus, the displasement does not depend on the stright section length L, if the condition (4) is satisfied. In this case the maximal displacement (in stright sections) is

$$\xi_{max} = \frac{\beta}{2}(1 - \frac{a^2}{b^2})\frac{\cos\theta}{\sin\alpha/2}\int_0^{\ell/2} sk(s)\sin\alpha(s)\,ds \qquad (7)$$

Here, θ is counted off from the principal normal, ℓ is the CREL length. To estimate β_{eq}, we put $\xi_{max} = b - a$, $a \approx b$. Then

$$\beta_{eq} = b\sin\frac{\alpha_c}{2}/\int_0^{\ell/2} sk \sin\alpha \, ds \qquad (8)$$

The values of β_{eq} for the slightly different CREL designs with $k(s) = \text{Const}$, $b = 1/2k$ are given in Table 2.

Table 2

Type of a CREL	l	α_c	β_{eq} %
Three semitori	$3\pi/k$	202°	5,75
Helix semi-pitch with toroidal sectors at the ends	$2,7\pi/k$	208°	6,7
Helix pitch with toroidal quarters at the ends	$2,5\pi/k$	192°	7,6

Conclusion. Feasibility of a closed trap with an arbitrary length of linear sections having rather high β is shown. Actually, finite β and some other effects can limit stright section length. The problem of stabilizing sections of fan type used in mirror devices as well as the problem of superbanana particles inside CREL remine to be solved.

References

1. B.B.Kadomtsev,"Plasma Physics and the Problem of Controlled Thermonuclear Reacions",(in Russian), USSR Academy of Sciences,M,vol.3,1958,p.285 (or Pergamon Press, London,1960).
2. V.D.Shafranov, Atomnaya Energiya, 22(1967)356.
3. D.Lortz,J.Nührenberg,Nucl.Fusion,18(1978)807.
4. A.S.Bishop, Project Sherwood,Addison-Wesley Publishing Company,Inc.,1958 ,p.46.
5. V.D.Shafranov, Nucl.Fusion,3(1963)183; 4(1964)232.
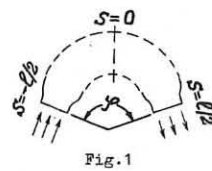
Fig.1
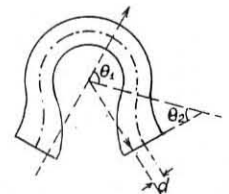
Fig.2
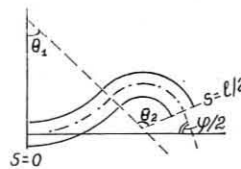
Fig.3
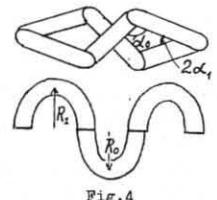
Fig.4
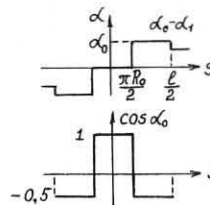
Fig.5

DESCRIPTION OF THE PLASMA EQUILIBRIUM FOR A HIGH-β
STELLARATOR

M.I.Mikhailov
"Energiya" Scientific-Manufacturing Association,
Moscow, USSR

V.D.Shafranov
I.V.Kurchatov Institute of Atomic Energy,
Moscow, USSR

Abstract. Recent results concerning β -limit in stellarators are discussed. Then we describe a method for a more accurate computation of equilibria in a stellarator. Threedimesional nonlinear plasma equilibrium equations are shown to be reduced to a twodimensional form.

Until recently the studies of the stellarator plasma equilibrium and stability have been performed as a rule using the approximation in which the equilibrium equations are linear with respect to the plasma column displacement. The dependence of the plasma pressure limit on various stellarator parameters has been studied by this approach. The existence of the optimal stellarator parameters at which equilibrium and stability limited β has a maximum has been confirmed. The argumentation for this is as follows. A very large aspect ratio stellarator has usually a high magnetic hill and, hence, a small stability limited plasma pressure associated with the localized modes. For example, $\beta_{st} \lesssim$ 1% for a straight l=2 stellarator /1/. A small aspect ratio stellarator can have only moderate magnetic hill and even an averaged magnetic well is possible here, when the magnetic axis is shifted in the direction of the toroidal field decrease. Thus, there is no essential restrictions on β_{st} /2/. As to β_{eq} this becomes lower because the total rotational transform decreases together with R/a. The intersection of the curves $\beta_{eq}(R/a)$ and $\beta_{st}(R/a)$ defines the optimal aspect ratio and the maximum attainable $\beta_{max} = \beta_{eq} = \beta_{st}$. For an l=2 stellarator of a moderate stellarator parameters ε_2, ma/R, Δ/a the following simple estimate can be given for β_{max}:

$$\beta_{max} = 4\left(\frac{\Delta}{a}\right)^2 \left(\frac{ma}{R}\right)^2 \varepsilon_2^2 . \qquad (1)$$

This value of the plasma pressure is attained at $(R/a)_{opt} = 8|\Delta|/\varepsilon_2^2 a$. Here Δ is the magnetic axis displacement, a is the plasma column radius, ε_2 and m characterize the outer helical magnetic field described by the potential (l=2):

$$\varphi_\ell^0 = \varepsilon_\ell \frac{R}{m} B_o I_\ell \left(\frac{\ell m \ell}{R}\right) \sin \ell(w - m \varsigma). \qquad (2)$$

The parameters ε_2 and ma/R in (1) are not independent since ε_2 and the separatrix radius a_s are closely related /3/. With the fixed ratio a/a_s β_{max} can be represented as a function of ε_2 (or ma/R) only. It can be shown that β_{max} as a function of these parameters has a maximum too. For example, for $a = 2a_s/3$ and $\Delta/a = 1/2$ we find that $\beta_{max} \approx 6\%$ can be attained at $R/a \approx 16$, $\varepsilon_2 \approx 0.5$, ma/R ≈ 0.5.

As one can see from the above expressions $(R/a)_{opt}$ and particularly β_{max} are strongly dependent on a permissible value of Δ. In linear approximation, however, we cannot know the Δ-value with a sufficient accuracy. Thus, the mentioned above β_{max} and $(R/a)_{opt}$ should be considered as estimates only. The importance of a more exact calculation of these parameters requires the development of a nonlinear (in Δ) approach to the stellarator equilibrium problem.

In general the problem of the plasma equilibrium in a stellarator is essentially threedimensional. Here we show, however, that this problem can be reduced to a twodimensional one.

We base on the equilibrium equations formulated in the flux coordinates ρ, θ, ς with "straight" magnetic field lines /4/:

$$4\pi^2 p' \sqrt{g} = \left(I' - \frac{\partial \nu}{\partial \varsigma}\right)\Phi' - \left(J' + \frac{\partial \nu}{\partial \theta}\right)\chi'$$

$$-\nu + \frac{\partial \mathcal{Y}}{\partial \rho} = \frac{g_{13}}{\sqrt{g}}\chi' + \frac{g_{13}}{\sqrt{g}}\Phi'$$

$$J + \frac{\partial \mathcal{Y}}{\partial \theta} = \frac{g_{22}}{\sqrt{g}}\chi' + \frac{g_{23}}{\sqrt{g}}\Phi'$$

$$-I + \frac{\partial \mathcal{Y}}{\partial \varsigma} = \frac{g_{23}}{\sqrt{g}}\chi' + \frac{g_{33}}{\sqrt{g}}\Phi'. \qquad (3)$$

Here g_{ik} are the metrical coefficients, χ, I; Φ, J are the poloidal and toroidal magnetic fluxes and currents, respectively; the periodic functions $\nu(\theta,\varsigma)$, $\mathcal{Y}(\theta,\varsigma)$ characterize the charge separation current and the magnetic field potential.

Set (3) has been used earlier to study a stellarator behaviour in two slightly different cases: a) a small ma/R but arbitrary ε and b) a small ε, arbitrary ma/R Here we consider the second of these cases which corresponds to the "ordinary" stellarator ordering:

$$\varepsilon_\ell^2 \sim \frac{1}{m} \sim \frac{a}{R} \ll 1$$

In this ordering $g_{12}/\sqrt{g}$, $g_{22}/\sqrt{g}$ do not depend on ς, meanwhile the nontrivial metric coefficients of the vacuum flux coordinate systems have the following form:

$$(g_{13})_v = \frac{R}{B_o}\frac{\partial \varphi_\ell^0}{\partial \rho_v}; \quad (g_{23})_v = \frac{R}{B_o}\frac{\partial \varphi_\ell^0}{\partial \theta_v};$$
$$(g_{33})_v = R^2; \quad (\sqrt{g})_v = \rho_v R \left(1 - \frac{1}{RB_o}\frac{\partial \varphi_\ell^0}{\partial \varsigma}\right). \qquad (4)$$

The main point of our consideration is now to show that the plasma flux coordinate system is connected with the vacuum one by a twodimensional transformation:

$$\rho_v = \rho_v(\rho,\theta); \quad \theta_v = \theta_v(\rho,\theta). \qquad (5)$$

Indeed, using (5) we find readily

$$g_{13} = (g_{13})_v \rho_v' + (g_{23})_v \theta_v'; \; g_{23} = (g_{13})_v \dot{\rho}_v + (g_{23})_v \dot{\theta}_v;$$
$$g_{33} = (g_{33})_v; \quad \sqrt{g} = (\sqrt{g})_v (\rho_v' \dot{\theta}_v - \dot{\rho}_v \theta_v'). \qquad (6)$$

Here $\rho_v' \equiv \partial \rho_v/\partial \rho$, $\dot{\rho}_v \equiv \partial \rho_v/\partial \theta$. It follows from (5), (6), and the last equation of set (3) that

$$\sqrt{g} = \rho R \left(1 - \frac{1}{RB_o}\frac{\partial \varphi_\ell^0}{\partial \varsigma}\right). \qquad (7)$$

Hence

$$\frac{g_{13}}{\sqrt{g}} = \left\langle\frac{g_{13}}{\sqrt{g}}\right\rangle_\varsigma + \frac{1}{B_o\rho}\left[\frac{\partial \varphi_\ell^0}{\partial \rho_v}\rho_v' + \frac{\partial \varphi_\ell^0}{\partial \theta_v}\theta_v'\right],$$
$$\frac{g_{23}}{\sqrt{g}} = \left\langle\frac{g_{23}}{\sqrt{g}}\right\rangle_\varsigma + \frac{1}{B_o\rho}\left[\frac{\partial \varphi_\ell^0}{\partial \rho_v}\dot{\rho}_v + \frac{\partial \varphi_\ell^0}{\partial \theta_v}\dot{\theta}_v\right],$$
$$\frac{g_{33}}{\sqrt{g}} = \left\langle\frac{g_{33}}{\sqrt{g}}\right\rangle_\varsigma + \frac{1}{B_o\rho}\frac{\partial \varphi_\ell^0}{\partial \varsigma}.$$

Here $\langle \; \rangle_\varsigma$ denote an averaging over ς. It is the "gradient" form of $(g_{13})_v$, $(g_{23})_v$ in (4) which allowed us to reduce the expressions in the square brackets to the component of $\nabla \varphi_\ell^0$. Now the ς depending terms in Set(3) are excluded by setting $\mathcal{Y} = 2\pi \varphi_\ell^0 + \langle \mathcal{Y}\rangle_\varsigma$,

$$\nabla \mathcal{Y} = \langle \nabla \mathcal{Y}\rangle_\varsigma + 2\pi \nabla \varphi_\ell^0$$

Thus, twodimensional transformation (5) does satisfy equilibrium equations in the ordering considered and we obtain twodimensional nonlinear equilibrium equations. This agrees with the results of papers /5/, /6/ obtained by an explicit averaging.

We can further reduce our twodimensional equations to a onedimensional form. To do this one should prescribe a definite θ -dependence of ρ_v, θ_v (5) and introduce the parameters such as the diplacement, ellipticity, triangularity etc. of the average magnetic surfaces. In this way we obtain a chain of onedimensional nonlinear differential equations for the introduced parameters. These equations can be used for more accurate numerical studies of the problem of the β limit in stellarators.

References

1. Danilkin I.S. Fiz. Plazmy 1978, 4, 1033.
2. Shafranov V.D., Yurchenko E.I. Nuclear Fusion, 1968, 8, 329.
3. Morozov A.I., Solov'ev L.S. in Voprosy teorii plazmy, 2, Moscow, 1963, p.3.
4. Shafranov V.D. Nuclear Fusion 1968, 8, 253.
5. Strauss H.R. Plasma Physics 1980, 22, 733.
6. Kovrizhnykh L.M., Shchepetov S.V. Fiz. Plasmy, 1980, 6, 976.

Equilibrium in a Stellarator. The pressure Limit.

I.S.Danilkin, L.M.Kovriznykh, S.V.Shchepetov.

Lebedev Physical Institute of the USSR Academy of Science
Moscow, U S S R

Let us consider some conclusions from recent theoretical MHD equilibrium and stability investigations for stellarator with strong magnetic shear[1-4] These theoretical analyses were undertaken in connection with paradoxically low estimations of the β limit ($\beta = 2P/B^2$) for stellarators[5-6] and the necessity to verify β limitations due to the so called "magnetic hill" found earlier in other works[7,8]

Detailed analisis has shown[2-4] that the above mentioned low estimations of β are associated with particular cases of unsuitable magnetic configurations, and thorough investigations of magnetic hill problems indicate[4] that the results earlier obtained are a consequence of exceeding of accuracy. In the framework of an adequate approach, including all necessary orders of expansion parameters, the magnetic hill effect does not produce significant β limitations.

Let us recall that the plasma self-stabilization effect in stellarators with strong magnetic shear removes β limitations associated with plasma stability (more fully described in our report to this conference entitled "Does the MHD stability determine maximal plasma pressure in a stellarator?").

Thus the upper limit of attainable β in considered systems depends on the permissible perturbation level of the magnetic configuration (i.e. the value of β_e). One can further see that for even a rough field correction this limit of β can easily reach approximately 10 %.

In fact, for toroidal systems with non zero rotational transformation angle, the main finite β effect reduces to appearance a slightly non-uniform, vertical field component $B_\perp^{(\beta)}$. This component displaces the cross-section centres of magnetic surfaces (labeled by mean radius r) outwards along the major radius R_o of the torus. The displacement-function $\xi(r)$ is described in the above mentioned papers[7,8] by linear (in ξ, β) equation

$$(r^3 \xi^2 \xi')' + \xi[(\xi^{*'} r^3)\xi - p'\langle\nabla\Phi\rangle^2 R_o r^3/B_o^4] = 2p'R_o r^3/B_o^2, \quad (1)$$

where $\xi = \xi^* + \xi^I$, ξ^* is the contribution of the vacuum magnetic field, ξ^I is the ohmic heating current contribution, $\langle\nabla\Phi\rangle^2$ represents the mean square (for one period of the system) of the vacuum magnetic field module described by the scalar magnetic potential function Φ , and primes denote differentiation with respect to r.

According to papers[2,7,8] there is some $p = p_{cr}$ when $\xi \to \infty$ as $p \to p_{cr}$ (see Fig.1), but far from $p = p_{cr}$, ξ is of the order of β and small, since $\beta \ll 1$. Hence, a posteriori, the second term in the square brackets in eq.(1) responsible for the growth of $\xi(r)$ is of the order of β^2 , representing an exceeding of accuracy.

Therefore in the paper[4] all the necessary orders in ξ, β are kept. One must also include an additional response of the second order the appearance of mean magnetic surface ellipticity. This ellipticity is described by the coefficient $\alpha(r)$ which is amplitude of the second poloidal harmonic. For this case, functions $\xi(r)$ and $\alpha(r)$ are described by simultaneous equations

$$(r^3 \xi^2 \xi')' + (r^3 \xi^{*'})'\xi = 2rR_o p/B^2 (1 + 5\alpha/2r + 5\alpha/2 - 9\xi'^2/4) + \langle\nabla\Phi\rangle^2 R_o \xi/2B_o^2 r) -$$
$$- r^2 \xi/R_o (4 - \xi'^2/2) + 2r^2[(\xi^* \xi' r^2)/r]' + \xi \xi' r^3 \xi'(-3\alpha' + 15\xi'^2/4) + \quad (2)$$
$$+ \xi^2 r^2 \xi(-3\alpha' + 3\alpha/r + 9\xi'^2/2) - 2r^2 \xi[3(\alpha\xi r)' - 9r\xi'^2 \xi/2](L_2 A) - 2r^2 \xi(3r^2 \xi \xi' +$$
$$+ 2r^2 \xi \alpha + 2\xi^2 r)(L_3 A) - 2r^5 \xi^3 (L_4 A),$$
$$(r^3 \xi^2 \alpha')' - 3r\xi^2 \alpha + 4r^3 \xi \alpha (L_2 A) = 3r(r^2 \xi^2 \xi'^2)/4 - 2r^4 \xi \xi^2 (L_3 A),$$

where $L = [\xi^2 \xi^2 r^2]^{-m} A = \xi^2 r^2$, and $\xi(r)$ is the function for displaced magnetic surfaces

$$\xi = (\xi^R + \xi^I)(1 - \xi'^{R}/2) + \xi^2 (L_2 A),$$

(as $\xi^* \to 0$, eqs.(2) are transformed to those for tokamaks[9]). Analyses of (2) give smooth solutions for ξ, α only, without any singularities contained in eq.(1) (see Fig.1). By means of (2) one can obtain a value of $\beta_e \simeq 7.5$ % using the displacement of the magnetic surface with $r = \xi/2$ to the edge of the plasma column $a = r + \xi$ which corresponds to the lossed approximately 3/4 of usefull aperture for the L-2 stellarator parameters ($a/R_o = 0.115; \xi^* \simeq 0.2; \xi^* = \xi_a^* - \xi_o^* \simeq 0.7; \xi_o^* \simeq 0$) and "conducting wall" boundary condition at $r = a$.

This value is less than $\sim 25\%$ below that obtained by using the formula of the work[1] where β_e was evaluated to a first order in β , but without the magnetic hill term which exceeds the accuracy in this case.

Thus, the performed analyses[1-4] confirm that it is possible to use as a rough upper limit of β in stellarator the estimation[1]

$$\beta \lesssim \beta_e \sim (a/R_o) \xi_a^2,$$

which together with the MHD stability condition $\xi \lesssim \frac{1}{N}\frac{R}{a}$ (see the above mentioned report to this conference) in the interval $0 \leq \beta \leq \beta_e$ (or $\beta_{cr} \gtrsim \beta_e$) reduce to

$$\beta_{e\,max} \sim \xi_a/N$$

But this estimation too will be exceeded by using a feedback control system for proper compensation of the main finite effect which is the vertical field component $B_\perp^{(\beta)}$. For instance, if we make use of the approximation $\xi^* \simeq \xi_o^* + \frac{\xi_a^* - \xi_o^*}{a r^2} r^2$ then we obtain[1]

$$B_\perp^{(\beta)}(o)/B_\perp^{(\beta)}(a) \approx \frac{\ell_n \xi_a^*/\xi_o^*}{1 - \xi_o^*/\Delta\xi^* \ell_n \xi_a^*/\xi_o^*} \sim 2,$$

(free boundary condition). It is evident from this relation that by rough compensation of $B_\perp^{(\beta)}(a)$ one can obtain almost twice the value of β_e , maintaining the strong self-stabilization effect (magnetic wall) arising due to finite β . For the L-2 stellarator case this could signify the possibility to attain $\beta_e \sim 10$ % or more.
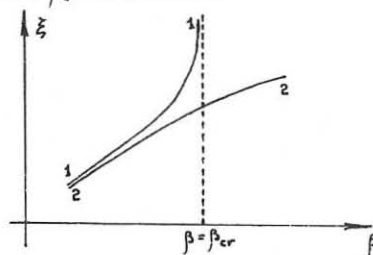
Fig.1. Magnetic surfaces displacement function $\xi(r)$ versus β . The curve (1-1) follows from eq.(1), the second (2-2) from eqs.(2).

References:

1. I.S.Danilkin, Fizika Plazmy, 4, 1033 (1978)
2. L.M.Kovriznykh, S.V.Shchepetov, Fizika Plazmy, 6, 976 (1980)
3. L.M.Kovriznykh, S.V.Shchepetov, Preprint FIAN N 146 (1979)
4. L.M.Kovriznykh, S.V.Shchepetov, Preprint FIAN N 1 (1981)
5. Project Matterhorn, The proposed model C-stellarator facility, NYO-7899, Princeton, 1957
6. D.Lortz, J.Nührenberg, IAEA-CN-37/H-5, 7th Conf. on Pl.Phys and CTR, Insbruck,23-30 aug.1978; Zeitschr.f.Naturf.31a, 1277 (1976)
7. J.M.Green, J.L.Johnson, K.E.Weimar, Pl.Phys., 8, 145 (1966)
8. M.I.Mikhailov, Fizika Plazmy, 6, 45 (1980)
9. V.D.Shafranov, E.I.Jurchenko, In proc. of Conf. on Pl.Phys. and CTR, v.2, IAEA,Vienna, 1971, p.512.

DOES THE MHD STABILITY DETERMINE MAXIMAL PLASMA PRESSURE IN A STELLARATOR?

L.M.Kovriznykh, S.V.Shchepetov.

P.N.Lebedev Physical Institute. The Academy of Sciences of the USSR.

Moscow, USSR.

The opinion is widespread, that one of the deficiencies of a stellarator[1] is the small value of $\beta = \frac{8\pi p}{B^2}$ (p-is plasma pressure, B-magnetic field), limited by the MHD-stability condition of plasma.

Really, if one takes into consideration the criterion of stability for interchange modes [1], which was derived neglecting all effects of toroidality, then maximal pressure is determined by the value of shear and appears to be rather small. For example, for the L-2 (USSR), with $t^* = 0.2 + 0.7 \frac{z^2}{a_o^2}$ $N/n_o = 7$ (where t^* - is rotational transform created by external helical field, N - number of periods of helical field, n_o - helical multipolarity) $\beta_{max} < 1\%$.

However, according to the paper [2], in stellarators with planar circular magnetic axis and large magnetic shear, toroidality leads to improvement of stability conditions for interchange modes, while β increases. The mechanism of such a self-stabilisation can be clearified by following: displacement of the magnetic surfaces under the action of magnetic fields, created by diamagnetic currents, occurs in the direction of increasing of major radius of torus. If $t^{\prime\prime}/t>0$, then line of magnetic force passes quick the region of unfavorable curvature (on the external part of torus) and is delated on the internal part of torus.

For example, it can be shown, that for systems without ohmic heating current and with large magnetic shear (for simplicity we suppose, that helical field is described by the scalar potencial, depending on poloidal azimuth ϑ and toroidal azimuth s for the combination $n_o\vartheta$ - Ns) the stability criterion, derived in the paper [2], is satisfied under any β, if:

$$6 N \Delta t^* / n_o + 2\Delta t^{*2} \leqslant 4 \frac{R_o}{a_o}(1 + 2\varepsilon_\perp R_o/a_o\Delta t^*) + 13 \quad (1)$$

where: $\varepsilon_\perp = B_\perp/B_o$, R_o - is major radius, $B_\perp$ - correcting component of vertical field, B_o - toroidal field at the axis, and we substitute $t^* = \Delta t^* z^2/a_o^2$, $P = P(0)(1 - z^2/a_o^2)$.

For systems without shear the criterion of the interchange mode stability does not limit maximal pressure if:

$$4 N t^*/n_o + 2t^{*2} \leqslant 13 \quad (2)$$

i.e. for stability it is necessary to creat the vacuum magnetic well.

But the criterion in the paper [2] was derived in a first approximation to ξ/a_o, i.e. it was assumed that averaged over s magnetic surfaces are the system of nonconcentric tores (ξ represents displacement of magnetic surfaces). So this approximation is valid at $\beta << t^2\delta$, $\delta = a_o/R_o$.

For more strict solution of the problem of determining maximal plasma pressure it is necessary to use the higher order terms of ξ/a_o, including the ellipticity of avereged magnetic surfaces, described by the parameter $\alpha \sim \xi^{\prime 2}$. After this the stability criterion takes form [3]:

$$S = (t^\prime)^2/4 + (\beta^\prime/2)[Q_1 + W_1] > 0 \quad (3)$$

$$Q_1 = <(\nabla\Phi)^2> R_o^2/2zB_o^2 - \xi R_o(z^3 t^*)^\prime/2z^3 t \quad (4)$$
$$+ R_o[(\xi^* t^* z^2)^\prime/2]^\prime + t^2 - (2t - t^*)/2t$$

$$W_1 = \frac{R_o}{2z}\{\xi^\prime(-3\alpha^\prime + 3\alpha/z + 3\xi^{\prime 2}/2) - \quad (5)$$
$$- \frac{2}{t}[3(\xi\alpha z)^\prime - 3\xi\xi^{\prime 2}z/4](L_2 A) -$$
$$- \frac{2}{t}[2z\varphi^3 + 2\varphi\alpha z^2 + 3z^2\varphi^2\xi^\prime/2]\times(L_3 A) - \frac{2}{t}z^3\xi^3(L_4 A) +$$
$$+ \frac{R_o^2}{2z}\{<\frac{(\nabla\Phi)^2}{B_o^2}>^\prime[\frac{3}{2}\xi^{\prime 2} - \xi\xi^\prime t^\prime/t - 2\xi^2(L_2 A)/t] +$$
$$+ [\frac{<(\nabla\Phi)^2>}{zB_o^2}]^\prime(3\xi^2/4 + z\xi\xi^\prime) + [\frac{<(\nabla\Phi)^2>}{4zB_o^2}]^{\prime\prime}\xi^2 z\}$$

where: ξ is displacement of centers of magnetic surfaces in vacuum, Φ - is potencial of helical magnetic field, $L_m \equiv [\frac{1}{z}\frac{\partial}{\partial z}]^m$, $A = t^* z^2$, t - is total rotational transform on displaced magnetic surfaces $t = (t^* + t^c)(1 - \xi^\prime z/2) + \beta^2(L_2 A)$ t^c - describes contribution of ohmic heating current, $<...>$ means avareging over period of system. While $W_1 = 0$ (i.e. nonlinear terms are vanished) (3) becomes equal to criterion derived in the paper [2]. The detail analusis (3)-(5) is possible only by computer methods. However, one can make sufficiently simple estimations. For example, while $t^c = 0$, $t^*(z) = t^*(0) + \Delta t^* z^2/a_o^2$, $\Delta t^* >> t^*(0)$ one can show that the nonlinear terms lead to additional stabilisation, in particular, at the plasma column edge, where destabilasing term $\sim <(\nabla\Phi)^2>$ is maximal.

So it is possible to conclude that while $\beta \lesssim t^2\delta$ the nonlinear terms don't practically change the stability condition (1).

As the stability criterion with respect to ballooning modes in a stellarator without ohmic heating [3,4] unlike a tokamak is less stringent [5,6] than the criterion (3) ($t^\prime/t \geqslant 0$!) then for not very long systems (as the transform angle increases almost proportionally to R_o) the maximal pressure, within the model considered, is not limited by ideal MHD stability condition (see formula (1) and (2)).

Consequently for stellarator systems with planar axis and large shear, the maximal pressure is determined by it's maximal value due to condition of equilibrium [7], which (while condition (1) is satisfied) can be equal to $t^*(a_o)/N$ for the systems under consideration (see details in the paper by I.S.Danilkin, L.M.Kovriznykh, S.V. Shchepetov " Equilibrium in a stellarator. The pressure limit " presented to this conference).

References:

1. J.L.Johnson,C.R.Oberman,R.M.Kulsrud, E.A.Frieman. Phys.Fluids,1,281 (1958)
2. L.M.Kovriznukh,S.V.Shchepetov.Fizika Plasmy,6,976 (1980), (in Russian); Preprints FIAN N°N° 36,146 (1979), (in Russian)
3. L.M.Kovriznukh,S.V.Shchepetov.Preprint FIAN N°1 (1981)
4. L.E.Zakharov, M.I.Mikhilov,V.I.Pistunovich et al.Proc. of 8 IAEA Conf. on Plasma Phys. and Contr. Nucl. Fus. Res,, Brussels,1980, IAEA-CN-38/K-2.
5. J.W.Connor,R.J.Hastie,J.B.Tailor.Phys.Rev.Lett.,40, 396 (1978)
6. O.P.Pogutse,E.I.Yurchenko.Pis'ma v JETP,28,344 (1978), (in Russian).
7. I.S.Danilkin.Fizika Plasmy,4,1033 (1978),(in Russian).

[1] Below we shall mean under a stellarator the installation with planar circular geometric axis, where the rotational transform is created by the set of helical harmonics, appeared due to external conductors (including so-called torsatrons).

THE DISTINGUISHING FEATURE OF PLASMA HEATING BY HIGH TURBULENT CURRENT IN "URAGAN-2" STELLARATOR

N.F.Perepelkin, V.A.Suprunenko, M.P.Vasil'ev, A.S.Slavny,
A.V.Arsen'ev, A.G.Dikij, V.G.Konovalov, V.D.Kotsubanov,
A.E.Kulaga, A.P.Litvinov (Kharkov Inst.of Phys.& Technol.,
Ukr.Acad.Sci.,Kharkov,USSR)

ABSTRACT. In the stellarator the plasma turbulent heating
has been performed by a short powerful current pulse with-
out violation of plasma column equilibrium.The conditions
of heating and its efficiency have been investigated.

In the stellarator "Uragan-2" the turbulent heating of a plasma has been performed by a powerful current pulse of 20 kA, 200 V, 0.5 ms in the field H_z =20 kG.Two-component ion-hot plasma has been obtained where the temperature for 90% of particles is T_i ≈0.3 keV and for 10% T_i' ≈ 0.75 keV.A calculated value of ion temperature which could be obtained in an ohmic discharge at Coulomb collisions is T_i ≈0.13 keV.The angle of rotational transform at plasma boundary reached $0.7_c+1.0_A=1.7$. Catastrophic violations of plasma column equilibrium were not observed. The threshold nature of ion heating from electric and magnetic fields and complicated dynamics of microprocesses in the turbulent plasma for $\omega_{ce} > \omega_{pe}$ are likely to be associated with the nonlinear stage of ion-sound instability [1].The ion heating is shown not to be associated with the effect of quasi-stationary run-away of electrons and excitation of "fan" instability.A high level of stationary noises near ion plasma harmonics ω_{pi} and $2\omega_{pi}$ resulted in trapping of fast electrons by microfields.

The plots of ion heating and run-away electron hampering versus the electric field for constant density of $6 \cdot 10^{12}$ cm^{-3} is given in fig.1. The energy of accelerated

Fig.1

electrons $\mathcal{E}_e^{max}$ is seen not to depend on the electric field, while the ion temperature T_i' grows linearly with field E beginning from the threshold E_{DP} =0.05 V/cm (crosses:with pre-ionization, circles:without pre-ionization of a gas). A regime of free acceleration in the stellarator develops in a slightly ionized plasma at low electric fields $E < E_{DP}$. In a high field $E > E_{DP}$ the electron run-away is suppressed. The energy spectra of ions are characterized by two-temperature distributions (fig.2). The number of particles and their energy grow strongly with the magnetic field $T_i' \sim H_z^2 \sim I \cdot H_z$.
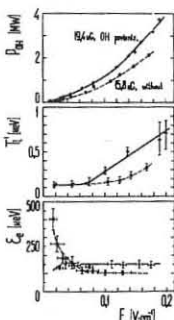
The electron distribution function for such discharges is non-Maxwellian. Due to hot electron trapping by microfields it is observed the combinative spectrum of the cy-

Fig.2

clotron harmonic radiation $2\omega_{ce}$, and in plasma resonance conditions $2\omega_{pe} = \omega_{ce}$, $\Delta\omega$ =0 there appears the modulation of hot electron flux into a target in plasma P_γ ($\mathcal{E}_e \sim$ 10-20 keV under magnetic field change (fig.3). The hot electrons temperature obtained from Doppler broadening of cyclotron radiation line $2\omega_{ce}$ is T_e' ~5-6 keV in fig.3 the shaded region is the
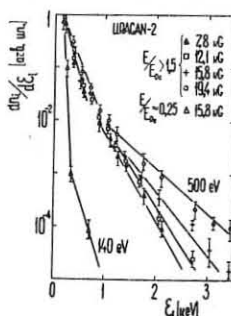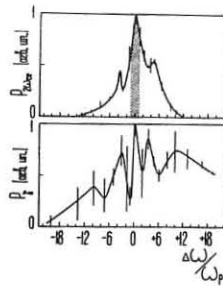
Fig.3

broadening of 1.5% due to magnetic field inhomogeneity in the race-track). For the bulk of electrons there is a great disagreement between laser and microwave data. In particular, radiation intensity $P_{2\omega_{ce}}$ gives T_e ≈250 eV, according to laser measurements $T_e \approx$ 90 eV. However, because of above-mentioned anomalies due to the great disturbance of electron distribution function and particle trapping, it is rather difficult to evaluate the errors without a detailed investigation of distribution function itself by other methods.

At the plasma edge strong magnetic perturbations have been observed by means of an open single-turn probe. The characteristic of these signals is shown in fig.4. The integration constant for the signals is as follows: 3- 400; 4- 100 μs, the dashed lines indicate magnetic signals of a current field beyond plasma. In experiments either "diamagnetic" (shaded) or "paramagnetic" perturbations in a plasma were observed which appeared at an instant of high density depression and depended on tuning of a helical magnetic field and probe position.

Fig.4

In the high current regime (15 kA, 15.8 kG, in fig.4 the density depression moment is indicated by the arrow) the appearance of a "diamagnetic" signal $-\Delta\vec{H}_z$ depended on tuning by a helical field to resonance $\ell_z = \ell_c + \ell_h = 1.5$. For low currents (2 kA,7.2 kG) only a "diamagnetic" signal appeared which, as shown in
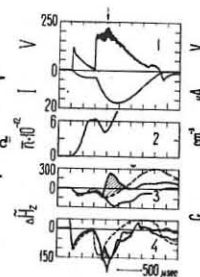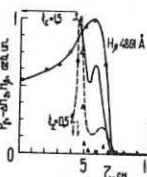
Fig.5

fig.5 (broken line),was also (as well as X-radiation signal from the target P_γ^Δ) highly localized on a radius at tuning to resonance $\ell_z = 0.5$. The dependences of "diamagnetic" amplitude on the summation angle ℓ_z at tuning by the helical field are given in fig.6 for two various conditions ω_{ce}/ω_{pe} =1 and 2.
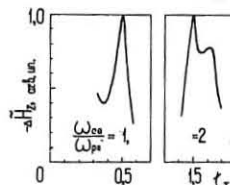
Fig.6

Thus along with the ion heating and density perturbations,in the turbulent plasma magnetic perturbations on rational magnetic surfaces have been detected which correlate with X-ray signals of hot electrons bombarding a target in plasma resonance area.The analysis shows the energy lifetime of hot ions to be 5-6 times lower than the value estimated from neoclassical theory and to be ~ 40 μs.

REFERENCE

1. N.Perepelkin et al. 9th Europ.Conf.Contr.Fusion. 85, Oxford 1979.

MHD STABILITY OBSERVATION OF HIGH BETA PLASMA
IN MODIFIED BUMPY FIELD

A.Sekine, S.Shiina, Y.Ogura, K.Saito, Y.Osanai,
Y.Nogi, H.Yoshimura, J.Todoroki, S.Hamada

Atomic Energy Research Institute, College of
Science and Technology, Nihon University, Tokyo,
Japan

1. Introduction

Modified Bumpy Torus had been proposed to confine a
high beta plasma in the closed magnetic line system con-
taining equal amplitude ℓ and $-\ell$ magnetic fields and rela-
tively large $\ell = \pm 1$ field component(1). So far the sector
experiment in MBT had shown that the confined plasma was
in a stable equilibrium during the observed period limited
by a ion transit time from the midplane to sector ends(2).
Recent theory on the basis of a diffuse plasma boundary,
finite surface distortion to match the observed plasma
shows the existence of equilibrium in large $\ell = \pm 1$ system
and the improvement of the stability over that predicted
by a sharp boundary, small surface distortion theory(3),
due to magnetic-well stabilization effect(4). Here, the
long wavelength m=1 mhd instability in the magnetic config-
ration with $\ell = 0$ and $\ell = \pm 2$ fields and without $\ell = \pm 1$ fields
is experimentally studied with the aim of confirming indi-
rectly the magnetic-well effect through comparison with
the observed stability in sector experiment.

2. Experimental device

The linear theta pinch machine is operated with the use
of the same condensor bank as in sector experiment. The
averaged magnetic field is 10kG in the rise time of 2μsec
and decays with the time constant of 40μsec. The coil
length and innerdiameter are ~2m and 8cm respectively, which
are the same dimension as sector coil. As shown in Fig.1,
the magnetic configuration composed of $\ell = 0$ and $\ell = \pm 2$ fields
is generated by modifying the initially applied bumpy field
with two symmetrical conducting shells. In this figure, θ_1 ,
$\theta_2 (= \pi - \theta_1)$ are the angle of each shell and r_s is shell radi-
us. The magnetic scalor potential, ϕ_i , in this system is
given by following expression,

$$\phi_i = B_\circ z + \frac{B_h}{h}\left\{ I_\circ(hr) + \frac{1}{2}(hr_s)^2\sum_{\ell=1}^{\ell}\alpha_\ell(\frac{r}{2r_s})^\ell\cos\ell\theta\right\}\sin(hz), \quad (1)$$

$$B_h = B_h^\circ / \{ 1 - (hr_s)^2 \log|\cos\theta_1| \}$$

$$\alpha_2 = \cos^2\theta_1 - 1, \text{ etc.}, \quad \alpha_1 = \alpha_3 = \cdots = 0,$$

where B_h gives the modulation amplitude of the longitudi-
nal vacuum magnetic field on axis, $B_z(0) = B_\circ + B_h\cos(hz)$, B_h°
the modulation amplitude of initially applied bumpy field,
α_ℓ the coefficient of $\pm\ell$ -th field component, and $I_\circ$ the
modified Bessel function of order zero. Then the magnetic
configuration generated is composed of $\ell = 0, \pm 2$, etc. and
does not include $\ell = \pm 1, \pm 3$, etc. fields. Since $\theta_1 = 35°$, h=
0.285/cm, $r_s = 6.3$cm and the mirror ratio on axis of initial
bumpy field, $R_m^\circ = 1.85$, in the present experiment, $B_h/B_\circ = 0.182$
, $\alpha_2 = 0.341$. The predicted value of $B_h/B_\circ$ is found to be
nearly equal the observed value.

3. Experiment results

The plasma stability is measured from axial direction
by means of high speed camera and Ruby laser light Mach-
Zehnder interferometer. Vacuum balanced loop-magnetic probes
rolled around discharge tube are used to measure the mag-
netic flux excluded by the plasma. The excluded flux in
conjunction with the plasma radius as determined by the
Mach-Zehnder interferometer allows the determination of β
value. The initial filling pressure of hydrogen gases is
fixed to 10mtorr. Experiment is carried out in three types
of magnetic configuration, that is, the $\ell = 0 + \ell = \pm 2$ field,
the pure bumpy field(no conducting shell), and the straight
field. In the $\ell = 0 + \ell = \pm 2$ configuration, the plasma begins
to move toward nearly vertical(y-axis) direction in the
time of ~4μsec after discharge starts. In this time the
plasma cross section is vertically elongated with the
ellipticity of 1.6 defined as the radius ratio in x- axis
and y-axis, the averaged radius is 1.5cm, and the averaged
β value is 0.7. After then, the plasma displaces to tube
wall with the drift time of 2~3 sec, elongating the shape.
In the pure bumpy field with $B_h/B_\circ$~0.3, the plasma moves

toward horizontal(x-axis) direction with the drift time of
~1.5μsec, which is somewhat fast compared with that in the
$\ell = 0 + \ell = \pm 2$ field. The shape of plasma cross section is
nearly circular, the averaged plasma radius and β value
are the same as in the $\ell = 0 + \ell = \pm 2$ field. The excluded flux
decays faster in both field configurations mentioned above
than in straight field. In straight field, the plasma drift
is not observed during the period of ~10μsec, after then,
the plasma shape is deformed rotating around the axis, just
likely m=2 rotating instability.

4. Comparison with MHD theory

In this section, the observed plasma drift is compared
with the long wavelength m=1 mode predicted by MHD theory
assumed a sharp boundary plasma with an arbitrary, but
nearly cylindrical shape. When the plasma surface is ex-
pressed in the form $r = a(1 + \sum_\ell \delta_\ell\cos(\ell\theta - kz))$, the distortion
amplitude normalized to mean plasma radius a, δ_ℓ ,is given
by

$$\delta_\circ = -b_\circ/2(1-\beta), \quad \delta_\ell = 2b_\ell/ha(2-\beta) \quad (\ell \neq 0, \, ha \ll 1), \quad (2)$$

according to a sharp boundary model. The coefficient $b_\circ$
is the modulation of the longitudinal vacuum magnetic field
on axis and b_ℓ is determined by Fourier analysis of the
radial vacuum magnetic field on r=a, $B_r(a)/B_\circ = -2\sum_\ell b_\ell \cdot$
$\cos(\ell\theta)\sin(hz)$. In the present experiment, $b_\circ = B_h/B_\circ = 0.182$
and $b_2 (= b_{-2}) = -b_\circ(ha)\alpha_2/8 = 0.003$ using the measured value of
a=1.5cm. From eq.(2), $\delta_\circ = -0.30 \sim 0.11$, $\delta_2 (= \delta_{-2}) = 0.012 \sim 0.009$
, at $\beta = 0.7 \sim 0.2$. On the base of a sharp boundary, small δ_ℓ
model, the growth time of long wavelength m=1 mode is pre-
dicted to be $2.6 \sim 7.2$sec in horizontal direction and 2.1
$\sim 5.8\mu$sec in vertical direction, at $\beta = 0.7 \sim 0.2$, neglecting
the smaller surface distortion of δ_ℓ for $|\ell| \geq 4$ and using
Alfven speed of $v_A = 1 \times 10^7$ cm/sec. These predicted growth
times agree well with the experiment results, in the points
of the plasma drift time, the direction of plasma drift,
and the configuration dependence of drift time.

5. Conclusion and discussion

On contrary to the linear plasma, the sector plasma
does not show the plasma drift during the confined time
of ~15μsec, although the straight forward application of
a sharp boundary, small δ_ℓ model to sector plasma leads to
nearly same growth time as that in linear plasma. The com-
parison of the observed stability in linear and sector ex-
periments gives the indirect evidence on the existence of
the stabilization effect due to self-magnetic well for-
mation in the sector plasma with finite $\ell = \pm 1$ surface dis-
totion , which is predicted by the recent theory based on
a diffuse boundary, finite $\ell = \pm 1$ distortion. Then the self-
magnetic well effect will give the most likely explanation
of the observed plasma stability in sector experiment and
enhance the confinement time of high beta plasma in MBT.

It is pointed out that any system which the dominant
fields are $\pm\ell$ fields has a Z independent force of the form
$\cos(2\ell\theta)$, which causes a long wavelength m=2 mode, then
does not produce the well-confined equilibria(5). This
force is not clear in both linear and sector experiments.
The diffuse boundary theory mentioned above predicts that
the self-magnetic well has the stabilizing effect also
on long wavelength m=2 mode as well as the m=1 mode.
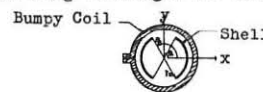
Fig.1 Scheme of linear Device

Fig.2 Mach-Zehnder inter-
ferometer photograph
: (1) is taken in
straight field, (2)
pumpy field, (3)$\ell = 0$
$+ \ell = \pm 2$ fields, at t=
4 sec.
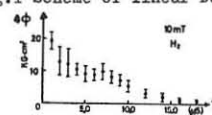
Fig.3 Excluded flux in straight
field

References
(1) J.Todoroki, et.al: Plasma Physics and Contr. Nucl.
    Fusion Research 1976(LAEA),Vienna, 1977) 2, p.215
(2) H.Gesso, et.al: Proc. of Inter. Conf. on Plasma
    Physics 1980 1, 7P-ii-11
(3) G.Miller: Physics of Fluids, 20, No.6, 1977, p.928
(4) J.Todoroki: To be prepared for publication
(5) J.P.Freidberg, R.A.Gerwin: Nuclear Fusion, 17, 1977,
    p.443

BASIC STUDY OF AN OPEN ENDED NON-PLANAR MAGNETIC AXIS PLASMA CONFINEMENT SYSTEM (ASPERATOR NP-01)

Yukihiro Goto, Shin-ichi Tsuchiya and Shigeo Nagao

Faculty of Engineering, Tohoku University, Sendai, JAPAN

ABSTRACT. Basic study of Asperator NP-01, which is an open ended mirror system with a helical magnetic axis, are descrived. The magnetic configuration of Asperator NP-01 has been calculated by an electronic computer and investigated with electron beam. Experiments of plasma injection into that magnetic configuration have been made to clear plasma behaviour in the helical magnetic field.

INTRODUCTION   A magnetic field system with a non-planar axis is a desirable field configuration for plasma confinement, because it has a set of nested magnetic surfaces without plasma current. Theoretical problem of MHD equilibrium and stability of plasma in the system with non-planar helical magnetic axis have been investigated in detail for a long time [1] [2]. However that devices of such system are fairly complex in the structure and plasma confinement investigations are very difficult [3] [4].

In this paper, the basic study of Asperator NP-01 is described. This device is an open ended mirror system with a helical magnetic axis and has a good helical symmetry. So the field analysis is more simple than toroidal system. A toroidal system with a closed magnetic axis differs basically from this system with an exactly helical symmetry. It is interesting to point out that the basic properties of an open ended system is not very much disturbed by the introduction of toroidal curvature when the curvature k of the helical magnetic axis is larger than the toroidal curvature $1/R$ [5].

The term of magnetic surface will be used here although that a large number of force lines with a rotational transform in the open ended system forms a configuration similar to the magnetic surface formed by a single force line in a closed system.

DEVICE   The helical region of the vacuum chamber has been made by connecting six $10''\phi$ stainless steel elbow tubes with $45°$ central angle per one pitch. The vacuum chamber is shown in Fig.1 and device parameters are shown in Table 1. The insulated wires have been wound 47 turns per one elbow directly on the vacuum chamber as the main field coil. Moreover
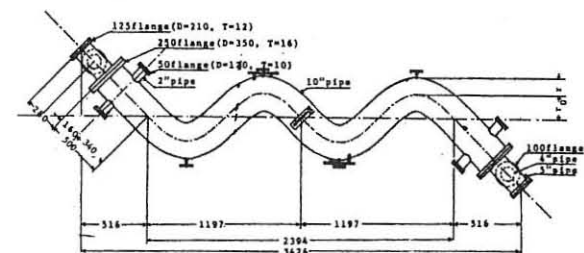
Fig.1 Helical vacuum chamber of Asperator NP-01

the helical stabilizing windings of $\ell=1$, $\ell=2$ and $\ell=3$ have been wound on the main field coil. All coils are excited by condenser discharge currents. For the plasma injection, co-axial gun has been used.

VACUUM FIELD CONFIGU-RATION   The value of

Table 1 Device parameters of Asperator NP-01

Radius of vacuum chamber	r_{in}	0.130 m
	r_{out}	0.134 m
Number of helical pitch	N	2
Radius of axial helix	r_0	0.191 m
Curvature of axial helix	k	2.625 m^{-1}
Torsion of axial helix	κ	2.625 m^{-1}
Length of axial helix	L_s	3.38 m
Mirror position length	$2L_m$	1.00 m
Longitudinal field	B_s	1.05 kG
Half period of B_s	$T/2$	6.00 msec

main field B_s has been calculated by means of superposing the magnetic field produced by a current loop of each turn coil. The field produced by the helical stabilizing winding currents I_1, I_2 and I_3 have been calculated by Biot-Savart's equation. The magnetic field of this device is described by the sum of the fields produced by the main field coil and the helical windings. The main field distribution of cross-section at the helical region was measured by a magnetic probe. The measured value was about 9% smaller than the calculated one. That difference is caused by the skin effect of the conductive vacuum chamber wall.

The lines of magnetic force are obtained by solving the differential equation (1) with Runge-Kutta method.

$$dx/B_x = dy/B_y = dz/B_z \qquad (1)$$

These results were calculated by an electronic computer.

The trajectories of the magnetic lines of force to $\nu-\beta$ plane are

(a) $I_2 = I_3 = 0$ (b) $I_2 = I_3 = 4$ kA
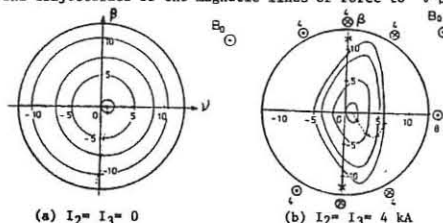
Fig.2 Magnetic surface profiles ($B_s = 1.05$ kG, $I_1 = 0$)

shown in Fig.2. From this results, the rotational transform angle without helical winding fields is determined to about $270°$ per one pitch.

It was recognized that $\ell=1$ helical field displaced the location of the surfaces without the distorsion of its sharp at the direction ν. The difference between the helical axis of the device and the helical magnetic axis is only 1 cm. So $\ell=1$ helical field was not used in this study.

The other hand, an electron gun with crossed filaments was used to determine the rotational transform angle and the shear of the field lines experimentaly. The electron gun was placed at one side linear region in the vacuum chamber. Displacement of electron beam was observed by means of fluorescent screen which was fixed at the another end of helix.

Some experimental results are shown in Fig.3. The measured rotational transform angle per one pitch without helical winding field is between $270°$ and $280°$ and there is little shear. This result corresponds to the calculated one. As can be seen from Fig.3, there is a finite shear on the magnetic surfaces and the shear increases with the helical winding field.
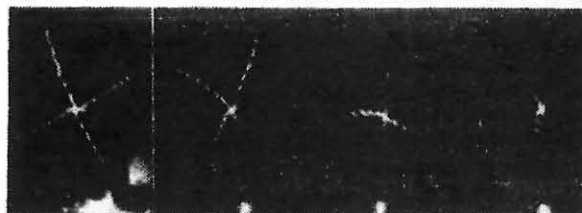
(a)$I_1=I_2=I_3=0$ (b)$I_2=I_3=2$ kA   (c)$I_2=I_3=3$ kA   (d)$I_2=I_3=4$ kA
Fig.3 Displacement of electron beam on the fluorescent screen

Moreover, specific volume $U(\nu)$ were calculated for many cases without and with helical winding fields. Average welldepth profile without helical field has a magnetic hill. Though the profile with appropriate helical field has a well. The welldepth for the case of Fig.2(b) is about 2%.

PLASMA INJECTION EXPERIMENT   The experiments of plasma injection into Asperator NP-01 have been made to clear plasma behaviour in the helical magnetic field. Used plasma source was a co-axial plasma gun which was mounted on an end of the device. The radial distributions of plasma density at many position of helix($\lambda/4$, $3\lambda/4$, $5\lambda/4$ and $7\lambda/4$) were measured with floating double probes. The current signals of double probe have been converted to light signals with photo-diode and transmitted by light cable and inverted electrical signals with photo-multiplier. So oscilloscope has been decoupled electrically from the double probe.

Injected plasma into the magnetic field with non-planar magnetic axis were expected to progress along magnetic line of force as a result of short circuit effect of the conductive end plate of the device. It was made sure that a part of injected plasma from one end of the device arrived at the another one. But the plasma was reduced markedly and it was difficult to full the plasma in the chamber uniformly. Maybe, that reduction of plasma was due to drift across the magnetic field by collision of plasma particles and neutral particles which came from the plasma gun. So it was not yet to clear the effect of helical winding fields.

CONCLUSION   The properties of magnetic field with open ended non-planar axis have been investigated in detail with the numerical calculation and with the experiment by electron beam. It was recognized that the rotational transform angle of this device without helical field was about $270°$ per one pitch and there was little shear. Superposing appropriate helical field, the profile of specific volume has a well and there is shear. Moreover, it was sure that a part of plasma injected from one end of the device progressed along the magnetic lines of force and arrived at the another one.

There is a schedule that the plasma source will be inproved to clear the plasma behaviour in the helical magnetic field.

REFERENCES   1) C.Mercier: Nucl. Fusion, 4, (1964) 213.
2) V.D.Shafranov: Nucl. Fusion, 8, (1968) 253.
3) S.Nagao et al.: 7th Symp. on Eng. Problem Fusion Research,1(1977)841.
4) Y.Goto et al. : 9th Europ. Conf.Controlled Fusion & Plasma Phys.1(1979)
5) Y.Funato et al.: Plasma Phys. 22 (1980)545.

F

INERTIAL CONFINEMENT
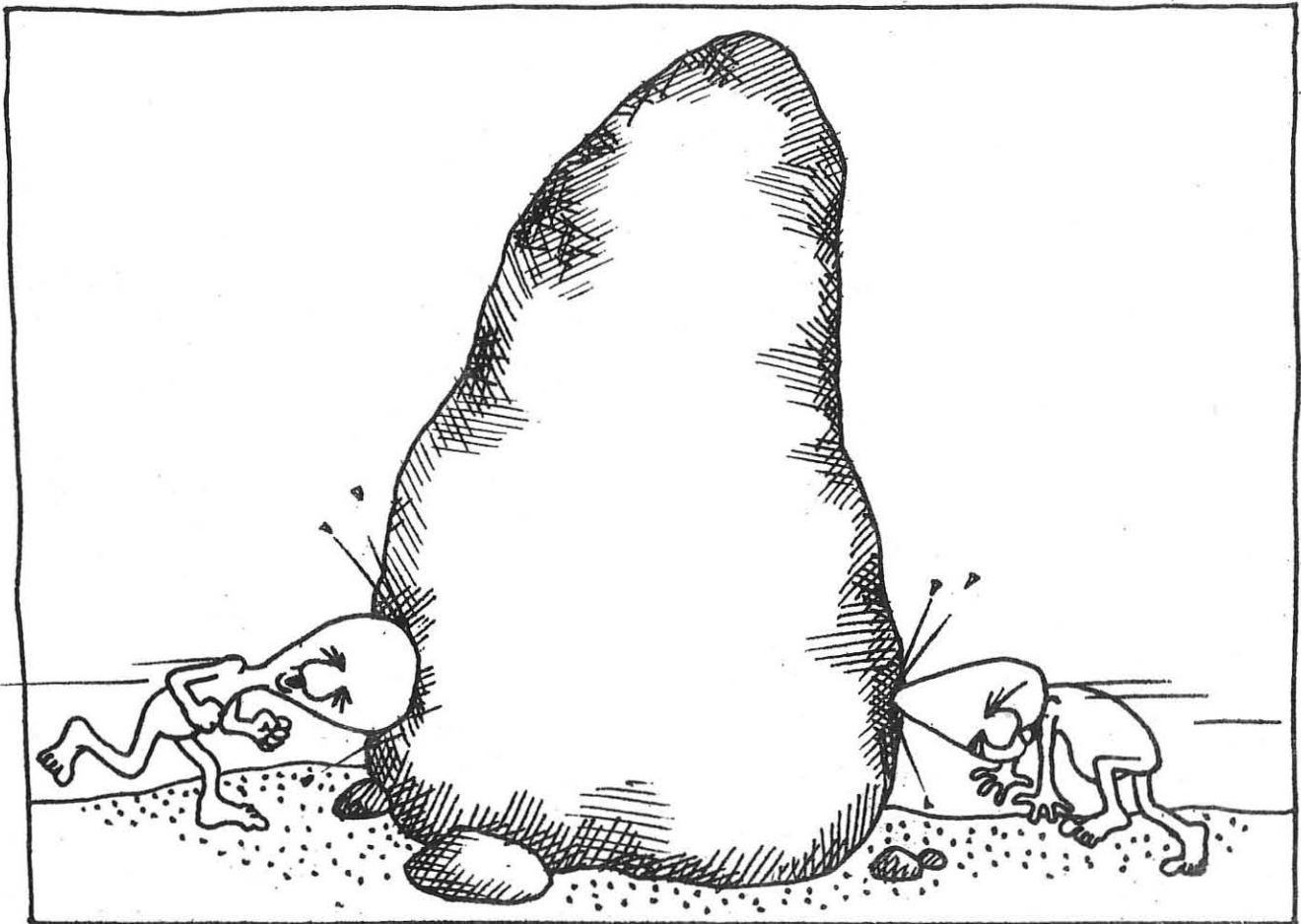
ANOMALIES OF LASER BEAM PENETRATION AND ABSORPTION IN THE NONUNIFORM PLASMA ABOVE ITS CRITICAL VALUE

N.S. Erokhin, S.S. Moiseev[*], V.V. Mukhin, V.E. Novikov,
R.Z. Sagdeev[*]

Institute of Physics & Technology, the Ukrainian Academy
of Sciences, Kharkov 310108, USSR

There are three competing processes responsible for the energy absorption of a laser beam in the target's plasma corona: Coulomb collisions, linear transformation of the obliquely incident plane-polarized electromagnetic wave into the longitudinal one, and parametric mechanisms [1]. Unfortunately, it is impossible to interpret main experimental data unambiguously, since with the parameters attainable at present (laser power, collision frequency, etc.) these data lie within the applicability region of the three above-mentioned processes. Therefore the investigation of the energy absorption in the transition region presents a great interest. We show in this report that the consideration of transverse dimensions of the wave beam, viz., diffraction and nonlinear refraction due to plasma displacement out of the axis region, changes qualitatively the picture of a laser beam propagation in the inhomogeneous plasma and the correlation between the competing processes. It is found that a significant increase of the collisional absorption may take place at moderately high laser powers.

Let us consider a normal incidence of the axisymmetric TM-wave bunch of radius a on the plane-laminar plasma with the density $n_e = n_0(z)$[**]. Here, to simplify the calculations, we assume the beam to be of a Gaussian type. This assumption does not effect the obtained results significantly. Taking into account that the transverse ponderomotive force exceeds the longitudinal one in the region of interest and that the striction effect has some time to become sufficiently large for achieving plasma transparence, we obtain in a standard way the following equations for the longitudinal refraction factor $N_z = cK_z/\omega$ and for the dimensionless beam width $f(z)$:

$$N_z^2 = \mathcal{E}_o(z) + \frac{\Delta^2 N_z}{f^2|\mathcal{E}|} - \frac{\alpha^2}{f^2} ; \quad \mathcal{E}_o(z) = 1 - \frac{n_0(z)}{n_c(\omega)} \quad (1)$$

$$\left(a N_z \frac{d}{dz} \right)^2 f = \frac{\alpha^2}{f^3} - 2\frac{\Delta^2 N_z}{f^3|\mathcal{E}|} ; \quad n_c = \frac{m_e \omega^2}{4\pi e^2}$$

where $\alpha = 2c/a\omega$ is the diffraction parameter; $\mathcal{E} = \mathcal{E}_1 + i\mathcal{E}_2$ is the nonlinear dielectric function of the plasma; $\Delta^2 = W_\infty/n_cT$ is the nonlinear parameter; W_∞ the energy density at the beam axis. It is important to note that according to [2], the nonlinear term was taken into account in the expression for the longitudinal refraction factor. This term is responsible for the existence of the conditions for laser beam propagation beyond the linear reflection point. The analysis of equations (1) shows, before all, that for the laser beam of finite radius, the roots of the equation for the refraction factor N_z never cross at the real axis. Consequently, there will be no jump of plasma density

[*]Institute of Space Research, the USSR Acad. of Sciences.
[**]See p.1. Propagation and self-focusing of the wave TE bunch without absorption was considered in [2].

in the region of the laser beam propagation, which is in contradiction with [3].

The energy absorption of the laser beam along the propagation way is described by the equation $d\mathcal{S}_z/dz = \mathcal{R}(z)\mathcal{S}_z$. The damping decrement value is determined by the group deceleration $\mathcal{R} = \omega\mathcal{E}_2/v_g$, $v_g = cN_z$. Hence, the rate of collisional absorption increases considerably in the plasma region where the group deceleration (c/v_g) is maximum. The total absorption depends naturally on the dimensions of this region. According to the linear theory [4], the collisional absorption concentrates mainly in the vicinity of the reflection point and approaches $Q = 1 - \exp\left(-\frac{2L\mathcal{E}_2}{\lambda}\right)$, where $\lambda = \frac{c}{\omega}$, $L = |dz/d\mathcal{E}_o|$ is the typical scale of the plasma density variation. In the case of a self-focusing laser beam, the region of the large group deceleration can extend beyond the linear reflection point. The optimal irradiation regime is observed with not very high energy flows $\mathcal{S}_z \gtrsim \left(\frac{\lambda}{L}\right) c n_c T$ and the beam radii $a \sim L$, $\alpha^2 \ll \Delta^2$.

The laser beam under the regime considered goes beyond the linear reflection point without narrowing and then it gets focused. The diameter of the focal spot may be found if one takes into account the diffraction and nonlinear saturation. So the laser-beam energy absorption equals Q before the linear reflection point, and it is determined as $\exp(-2L\mathcal{E}_2\mu/\lambda)$ in the supercritical plasma. Here we take $\mu = 0.5(a/L)^{0.8} \cdot (L/\lambda)^{0.2}$. We obtain, for example, $\mu = 2.24$ for $a = L$ and the third harmonic of a neodymium laser $L/\lambda = 1.8 \cdot 10^3$. Thus, under the optimal regime, the role of the collisional absorption increases as the laser beam wavelength decreases $\partial \sim \omega^2$, $\mathcal{E}_2 \sim \omega$ (mainly due to the contribution from the region beyond the linear reflection point of plasma). At the same time, the role of parametric mechanisms and resonance absorption will decrease due to the reduction of W/n_cT and λ/L[*].

Note that, in addition to the collisional absorption with a laser beam going beyond the linear reflection point, the resonance absorption will contribute to the beam energy dissipation both at the front of the beam [5] and at its lateral surface. The collisional absorption will be lesser for more intense laser beam levels, but in this case one may expect the formation of focuses before the linear reflection point, which, according to [6,7], increases the role of parametric mechanisms.

References

1. " Lasers and thermonuclear problems", Atomizdat.M, 1973.
2. N.S.Erokhin, S.S.Moiseev, V.V.Mukhin, V.E.Novikov,A.Tur Soviet-French Seminar on RF Plasma Heating. Proceedings, Nauka publ., Leningrad, 1974, p.20; N.S.Erokhin, S.S. Moiseev, V.E.Novikov, ZhŢF 48 (1978) 1769.
3. V.B.Gildenburg, ZhETF 46 (1964) 2156.
4. A.M.Prokhorov et al, Uspekhi Fiz.Nauk 119 (1976) 401.
5. R.Z.Sagdeev, V.D.Shapiro, ZhETF 66 (1974) 1651.
6. V.E.Lugovoj, A.M.Prokhorov, Usp.Fiz.Nauk 111 (1973) 203.
7. N.S.Erokhin,S.S.Moiseev, V.V.Mukhin, ZhETF 68(1975) 536.

[*]It should be pointed out that if L/λ increases, the role of convectional decays becomes considerable in view of a quasihomogeneous character of the supercritical region.

INTERACTION OF THE INTENSE FOCUSED REB WITH DENCE PLASMA

R.V.Chickin, Yu.M.Gorbulin, Yu.G.Kalinin, Yu.A.Markov,

A.Yu.Shashkov, V.A.Skoryupin, D.M.Zlotnikov.

Kurchatov Atomic Energy Institute, Moskow, USSR

The experimental results of focusing of intense REB and heating of the thin foils are presented in this paper. The experiments have been carried out on "Mirage" accelerator [1]. The cathode which have been applied in "Angara 1" [2] was used. The following parameters were obtained in the focusing regime: the focal spot current density $j \sim$ 10 MA/cm^2, energy dissipated in diode E ~ 8 kJ, power ~ 1.5×10^{11}W with the rate of increase ~ 10^{19}W/s and power density ~ 10^{13}W/cm^2. Typical oscillograms treated by digital calculator are presented in Fig.1.

One must note that the absence of the delay between the current and the voltage front as well as a greater rate of increase of the current as compared to "Angara 1" take place. Apparently it is due to the existence of the short but sufficiently greate voltage prepulse as well as to the greater steepness of the voltage front.

With the help of X-ray pinhole camera with space-resolution 300μm the time integral measurements of the beam focal spot size were carried out (Fig.2). The plasma radiation along the diode axis was detected by light streak camera (Fig.4), which consisted of the time-delay analyzer cascade and microcanal plate (MCP) brightness amplifier. The time resolution was 2 ns, the number of resolved elements was about 40.

The vacuum ultraviolet (VUV) image of the focal spot was formed by the pinhole camera and detected by the streak camera, MCP served as the photocathode of the latter. The absolute intensity was measured by vacuum diode (VD) [2].

The impulse (τ = 10 ns) YAG:Nd^{3+} laser with frequency multiplicators (λ_ω = 1064 nm, $\lambda_{2\omega}$ = 532 nm, $\lambda_{4\omega}$ = 266 nm) was used to sound the diode gap and the space behind the anode foil. The gap image was rormed by lens L3 (Fig.2). The system operated in the single exposure regime. The simultaneous three-wavelength shadow-graphs were obtained.

Numerical estimations and experimental data enable one to consider that the shadows on the photographs were due to the absorption of the laser light. One can define the plasma temperature knowing the space distribution of the absorptence $K_{2\omega}(x)$ for wavelength 532 nm and the absolute intensity of the radiation $B_{2\omega}(x)$ at the same wavelength:

$$B_{2\omega}(x) / K_{2\omega}(x) = I_{2\omega P}(T(x)),$$

where $I_{2\omega}(T(x))$ is the spectral brightness of the blackbody radiation at the frequence 2ω. It is essential that this equation is independent of the absorption mechanism. In $K_{2\omega}(x) < 1$ region some space averaged temperature along the incident beam is calculated. If $K_{2\omega}(x) = 1$, then the surface temperature will be obtained. Apparently thus determined value must correlate with the temperature measured by VD. If the temperature exceeds the quantum energy of the laser light, the absorption has mainly the inverse

bremsstrahlung nature [3]. Using the corona-model equilibrium of the plasma ionization states [4] for the ion concentration in $K_{2\omega}(x) \sim 0.5$ region one can obtain

$$N_i = 3.43 \times 10^{18} \times \sqrt{\ln(1/(1-K))/LT},$$

where L is the effective plasma size along the incident beam. The typical value of N_i is ~ 10^{18} - 10^{19}1/cm^3.

The VUV intensity distribution in the focal spot is plotted in Fig.3, the curve corresponding to the time of signal maximum. This curve and the signal from absolute calibrated VD allow to define the maximum radiation temperature more accurately then before. It reached 30 eV and that approximately corresponds to the energy value E_{foil} (Fig.1) deposited in anode foil taking into account the "magnetic stopping" theory [2].

Analysis of the shadowgraphs shows the unsymmetrical character of the anode plasma expansion (Fig.3). This fact can be explained either by pressure of the magnetic field of the focal spot current or by pressure of the low dence hot plasma in diode gap which is transparent for laser light. Knowing the concentration and expansion rate of plasma one can estimate that this pressure is ~ 10^9 - 10^{10} din/cm^2. This pressure is corresponding to the magnetic field $H \sim (2 - 8) \times 10^5 \theta$ or to the pressure of the low dence hot plasma with $nT \sim 10^{21}$ - 10^{22} eV/cm^3.

1. Ю.М.Горбулин и др. Вопросы атомной науки и техники. Серия "Термоядерный синтез", в.2, с.84-90, 1979.
2. M.V.Babykin et al. Proc.III-rd Int.Top.Conf. on High Power Electron and Ion Beam Research and Techn. v.II, p. 499, Novosibirsk, 1979.
3. Я.Б.Зельдович, Д.П.Райзер. Физика ударных волн и высокотемпературных гидродинамических явлений, М, 1963, с.213.
4. D.Mosher. Phys.Rev., A, v.10, p.6, 1974.
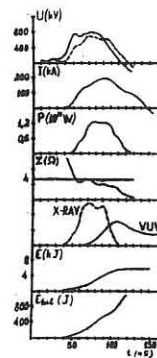
Fig. 1
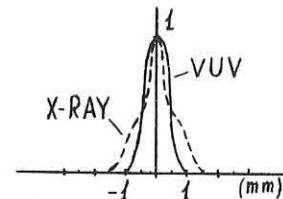
Fig. 3
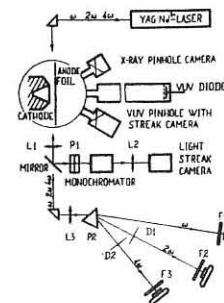
Fig. 2
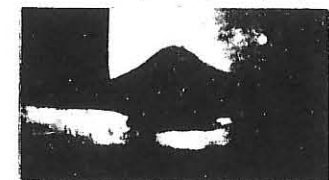
Fig. 4

ELECTRON CHERENKOV HEATING UNDER PARAMETRIC
INSTABILITY IN SPATIALLY INHOMOGENEOUS PLASMAS

V.P.SILIN, V.T.TIKHONCHUK

P.N.Lebedev Physical Institute, USSR

The plasma heating under the powerful electromagnetic radiation action is connected, in particular, with the excitation of parametric instabilities. The detailed estimation of the parametric absorption rate exists now in a very idealized model of a spatially homogeneous plasma. In the present paper estimations of absorption rate and electron heating are obtained in realistic conditions of spatially inhomogeneous weakly collisional plasmas, when the mean free path of electrons is large enough compared with the scale length of a density inhomogeneity.

The problem of interest consists of several physically different but mutually connected subproblems. The first - is the level of the nonlinear saturation of parametrically induced longitudinal Langmuir waves. Amplitudes of these Langmuir waves are determined by the waves convection and nonlinear decay interaction. The intensity of Langmuir waves in the instability region determines the part of the pump wave flux transformed into Langmuir waves flux. This problem was considered in detail, see, for ex., ref./1-3/.

The next problem is the redistribution of the absorbed energy and formation of Langmuir turbulence quasistationary spectrum. The existence of the quasistationary spectrum implies the place, where an energy runs off. Previously discussed possible mechanisms of the energy run off are electron-ion collisions /1/ and the aperiodic parametric instability of Langmuir waves /2,3/, resulting in the wave capture and collapse /4/. We shall not take into account these possibilities because the high electron temperature and the density inhomogeneity lead to a high enough threshold of the aperiodic instability /5/. The physical reason of the threshold presence is because of the growth rate must be larger then the inverse time of the Langmuir wave passing through the instability region. For real scale lengths $L/r_D < (M/m)^{3/2} \sim 10^5$ (r_D - is the Debye radii; M,m - are ion, electron masses) the inhibition of the aperiodic instability takes place if the primary instability spatial growth rate $\mathfrak{F}_o$ is small enough

$$\mathfrak{F}_o < (M/m)^{1/2}/L. \qquad (1)$$

We shall consider below the case in which the condition (1) is fulfilled. So in our consideration the energy running off mechanism is the convection of Langmuir waves from amplification region into underdense plasma layers and the following Landau damping. Using the balance condition between absorbed from the pump field and transfered from Langmuir waves to electrons energy fluxes one can obtain the estimation of the Langmuir turbulence spectrum width

$$\delta\omega \simeq \Delta\omega_o \mathfrak{F}_o L, \qquad (2)$$

where $\Delta\omega_o$ - is the spectral width of a parametric instability region.

The third problem is connected with the determination of the electron energy distribution function which arises under the Langmuir waves Cherenkov absorption. We can use the quasilinear approximation /6/ to solve this problem. (The possibility to separate problems of the Langmuir waves turbulence spectrum deriving and the electron Cherenkov heating is connected with the negligibly small Landau damping in the parametric instability region.)

Langmuir waves energy flux is directed in the underdense side. Therefore the Cherenkov interaction leads to the electron acceleration in the same direction. Provided that the electron distribution function in an overdense plasma $f_o(\varepsilon)$ is Maxwellian with the temperature T_e, we obtain the formulae for the accelerated electrons energy distribution function $f_h(\varepsilon)$ in an underdense side

$$f_h(\varepsilon) \simeq f_o(\varepsilon)\frac{T_e}{T_e + \delta\varepsilon} \exp{-\frac{\delta\varepsilon}{T_e}} , \qquad (3)$$

here $\delta\varepsilon \doteq (\delta\omega/\omega_{Le})\varepsilon^2/T_e$ - is the width of the quasilinear diffusion region for the electron with the energy ε, ω_{Le} - is the electron plasma frequency. The function (3) takes place in the interval ($\varepsilon_1, \varepsilon_2$) of electron energies. Electrons having an energy $\varepsilon > \varepsilon_2 = T_e(\omega_{Le}/\mathfrak{F}_o v_s)^{1/4}$ pass the resonance region very quickly and have no time for a considerable diffusion (v_s - is the acoustic velocity). The lower value $\varepsilon_1 = T_e\ln[(\omega_{Le}/\mathfrak{F}_o v_s)(m/M)] > T_e$ arises due to Langmuir waves damping. According to the energy conservation law, accelerated electrons carry the energy flux q_e exactly equal to q_{abs} - the parametrically absorbed part of the pump wave flux. When the condition (1) is fulfilled and $\mathfrak{F}_o r_D \ll 1$, we have

$$q_e = q_{abs} = n_o T_e v_s (M/m)(\Delta\omega_o/\omega_{Le})\mathfrak{F}_o^2 L r_D, \qquad (4)$$

where n_o - is the average electron density in the parametric resonance region.

The mechanism of the electron heating discussed in our paper has Cherenkov nature and therefore results in the electron acceleration. However due to a finite spatial extent of a wave-particle resonance region, the maximum electron energy ε_2 exceeds T_e not more than 20 - 30 times. This result qualitativly differs the wave convection regime in nonuniform plasmas from the regime of the Langmuir collapse in spatially homogeneous plasmas, where the electron acceleration to a very high energies takes place /7/.

Refereces.

1. V.Yu. Bychenkov, V.P.Silin, V.T.Tikhonchuk. Pis'ma Zh. Eksp. Teor. Fiz., 26, 309, 1977; V.P.Silin, V.T.Tikhonchuk. Phys. Lett., 78 A, 246, 1980.

2. A.A.Galeev, R.Z.Sagdeev, V.D.Shapiro, V.I.Shevchenko. Zh. Eksp. Teor. Fiz., 73, 1352, 1977.

3. S.L.Musher, A.M.Rubenchik. Fiz. Plazmy, 1, 982, 1975.

4. V.E.Zakharov. Zh. Eksp. Teor. Fiz., 62, 1745, 1972.

5. T.A.Davydova, K.P.Shamray. Preprint of the Inst. of the Theor. Phys. of the Ukr. Ac. Sci., ITF-77-140P, Kiev, USSR, 1978; V.T.Tikhonchuk, A.A.Chernikov. Fiz. Plazmy, 7, No 3, 1981.

6. A.A.Vedenov, E.P.Velikhov, R.Z.Sagdeev. Nuclear Fusion, 1, 82, 1961.

7. V.V.Gorev, A.S.Kingsep, V.V.Yan'kov. Zh. Eksp. Teor. Fis., 70, 921, 1976.

ANOMALOUS ABSORPTION AND FAST PARTICLES
GENERATION IN LASER)- PLASMA INTERACTION
EXPERIMENTS AT WAVELENGTH OF 0,53 um and 1,06 um.

V. V. Aleksandrov, M. V. Brenner, V. D. Vikharev, N. G. Kovalskij,
M. I. Pergament, A. A. Chernov, V. N. Yufa

I. V. Kurchatov Institute of Atomic Energy

S. I. Anisimov, M. F. Ivanov, L. N. Shchur

L. D. Landau Institute of Theoretical Physics

A. M. Rubenchik

Institute Of Automatics and Electrometry,
SOAN USSR

USSR

Spectral and time resolved measurements of plasma radiation at the laser harmonic frequencies 2ω and $3/2\omega$ and X-ray spectra were carried out in experiments on solid flat targets irradiation by the high-power pulses of Nd-glass laser. Analysis of data obtained at different conditions (wavelength, power density and angle of incidence were varied) and comparison with results of the numerical computations allow to draw certain conclusions about mechanisms of absorption and fast superthermal electrons generation in a plasma corona. All experiments were carried out on the "Mishen 1" facility [1] . The flat massive targets made of aluminium, copper and polyethylene were irradiated in the vacuum chamber. Frequency doubling of the output laser radiation was accomplished by a KDP crystal. The main measurements were carried out in the range of the power densities $10^{13} \div 10^{14}$ W/cm^2 at a pulse halfwidth 3,5ns and a 100 um-dia focal spot. The detailed investigations [2] made it possible to establish that for the relatively large focal spot dimensions plasma expansion may be considered to be one-dimensional up to the regions of plasma corona with densities near a quarter of the critical value. The one-dimensional hydrodynamic model takes into account the classical and anomalous absorption, the radiation losses, the electron-ion energy exchange, the harmonics generation and the electron thermal conductivity with the free streaming limit. The $3/2\omega$ harmonic intensity versus time, obtained in these computations, is given in Fig 1. The laser pulse and $3/2\omega$ radiation pulse recorded by the streak camera with image converter [3] are shown in Fig 2. The same parameters of the laser pulses were used in the computations and in the experiments. The good agreement is seen providing the evidence of the correct assumptions to be used in the theoretical model. The $3/2\omega$ pulse time delay can be accounted for as follows. The threshold power density for the two-plasmon decay instability exitation is determined in our case by collisions and, hence, its value falls with temperature rise. So, if the effective absorption takes pla-

Fig 1. Numerical simulation of $3/2\omega$ emission. Laser pulse(solid line) and $3/2\omega$ emission (dash line)
--- $I_\omega = 10^{14}$ W/cm^2
—— $I_\omega = 10^{13}$ W/cm^2

ce near the $^nc/4$ surface, "the threshold of disappearance" of the $3/2\omega$ -harmonic turns out to be essentially lower than the threshold of its appearance. The strong dependence of the $3/2\omega$ -harmonic intensity of the power density (Fig 3) can be also explained by the plasma heating at the $^nc/4$ surface. The dependence of the $3/2\omega$ -harmonic intensity on temperature is strong enough:

Fig 2. Laser pulse and time resolved $3/2\omega$ emission Al-target , $I_\omega = 10^{14}$ W/cm^2

$$\frac{I_{3/2\omega}}{I_\omega} \sim \left(\frac{v}{c}\right)^5 \left(\frac{m}{M}\right)^{1/6}\left(\frac{\omega_p L}{c}\right)\left(\frac{I_o}{mnc^3}\right) [4]$$

If the heat flow is supposed to be proportional to the temperature T, we shall obtain the $I_{3/2\omega} \sim I_\omega^{7/3}$ dependence that is close to the observed one. The method was proposed to investigate the processes, which are responsible for fast electrons generation, based on the study of correlation between $3/2\omega$-harmonic intensity and presence of the "hard" X-ray component in plasma radiation spectrum for different incidence angles of the laser beam [5]. The lack of the hard X-ray component at angles of incidence exceeding

Fig 3. $3/2\omega$ emission intensity via laser intensity Al-target

$50\div60°$ (Fig 4) leads to the superthermal electrons observed at relatively small angles due to the exitation of the two-plasmon decay instability. An important information can be obtained when 2ω -harmonic is used as a heating radiation. The threshold power densities for the parametric instabilities exitation at n_c and $^nc/4$ surfaces vary as ω^3 and ω^4 correspondingly. Thus it is possible to overcome the threshold value for the parametric instability exitation at n_c surface but remaining power density still below the two-plasmon instability threshold (we are interested to investigate laser-plasma interaction in the range of power densities $10^{13} \div 10^{14}$ W/cm^2). In experiments on irradiation of the targets by the laser pulses a wavelengths of 0,53 um at a power density of $5\cdot10^{13}$ W/cm^2 the second harmonic radiation was recorded, but $3/2\omega$ -harmonic radiation was not observed. In these conditions experiments with small angles of the flat targets inclination relative to the incident beam seems to be very important.

Fig 4. X-ray spectra from a laser irradiated polyethylene target for different incident angles $I_\omega = 8\cdot10^{13}$ W/cm^2

References

1. V.V.Aleksandrov et.al. Zh.E.T.F.,v.71,p.1826,1976.
2. V.V.Aleksandrov et.al. Preprint IAE-3196,Moscow,1979.
3. V.V.Aleksandrov et.al. Preprint IAE-2852,Moscow,1977.
4. A.M.Rubenchik."Power laser radiation absorption and garmonic generation",XIII International Conference on phenomena in ionized gases,Berlin,1977.
5. V.V.Aleksandrov,N.G.Kovalskij,V.P.Silin. Zh.E.T.F., v.79,p.850,1980.

THE INTERACTION EFFICIENCY OF THE LASER RADIATION WITH THE FLYING AWAY PLASMA CORONA

N.E.Andreev, V.L.Artsimovich, Yu.S.Kas'yanov, V.V.Korobkin, V.P.Silin, P.V.Silin, G.L.Stenchikov, A.S.Shirokov

P.N.Lebedev Physical Institute, Moscow, USSR

The investigations of the powerful laser radiation interaction with plasmas have created quite a number of the new physical ideas among them the idea about the sufficient influence of the plasma flow velocity onto the nonlinear laser plasma interaction takes the especial place. The previous theoretical papers have demonstrated for p-polarized radiation of Nd-glass laser that the transition from subsonic to supersonic flow near the critical density layer led to the diminishing of absorption and to growing up of the radiation reflection /1/, led to the fast electron generation suppression /2/, and to the suppression of the second harmonics emission correlated in time with the suppression of the radiation absorption /3/.

In this talk we should report 1) the theoretical results of the fourth harmonics of Nd-laser radiation interaction with plasmas, 2) the theoretical results of the third Nd-laser radiation harmonics emission from the flying plasmas, 3) the theoretical results about the field selfrestriction phenomenon, 4) the experimental results of spectral-temporal investigation of the scattered radiation which demonstrate the dependence of the laser-plasma interaction efficiency as a function of the plasma motion.

Our theory of the laser-plasma interaction dynamics is based on the LAST-code /3/ which describes the nonlinear electrodynamics and hydrodynamics that take into account the Miller's force and the electron redistribution connected with Cherenkov wave-electron interaction. Fig.1 gives the simulation results of the radiation ($\lambda_0 = 0.265$ μm, $v_E/c = 0.0068$) interaction with the plasmas ($v_{ei}/\omega_0 = 0.01$ and 10 $c/\omega_0 = \ell$ —
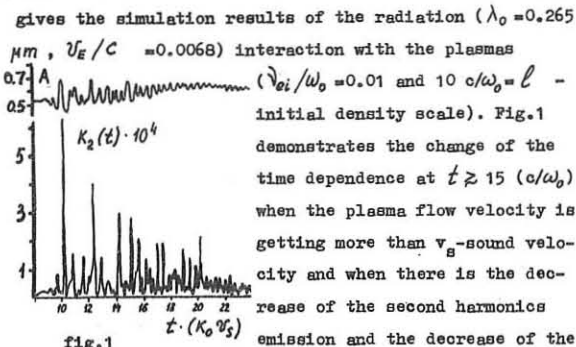
fig.1

initial density scale). Fig.1 demonstrates the change of the time dependence at $t \gtrsim 15$ (c/ω_0) when the plasma flow velocity is getting more than v_s-sound velocity and when there is the decrease of the second harmonics emission and the decrease of the absorption oscillations. Such time-dependence corresponds to the suppression of cavitons and the suppression of fast electrons creation because of the transition to the supersonic motion. In comparison with the results of laser plasma interaction simulation in the case of the main frequency of the Nd-laser radiation our fig.1 demonstrates growing role ($\sim 90\%$) of the collision dissipation. On the contrary for $\lambda_0 = 1.06$ μm in the subsonic plasma flow ($v_{Te}/c = 0.050$, $v_s/c = 0.015$, $v_{ei}/\omega_0 = 5 \cdot 10^{-3}$) only a half of absorbed energy produces the main body

electron heating and other part produces the fast electrons /3/. The peaks of the 2-d and 3-d harmonics correlate with the absorbtion peaks that are connected with the creation of the strong internal plasma fields.

The transition from subsonic to supersonic regime suppresses simultaneously the fast electrons and 2-d and 3-d harmonics.

In the case of supersonic stationary flow the Miller's force produces the defocusing plasma features /4/ that is the reason of the wave field selfrestriction /5,6/ . If N is density and V is velocity of plasma in such layers where the electric field is equal to zero then in the case $N \leqslant n_c$ we have $E^2 \leqslant 16\pi n_c Z \varkappa T_e \left(n_c/N - 1 \right) \left[(V/v_s)^2 - 1 \right]$. The illustration of the self-restriction effects is fig.2 where the space structure of s-polarized electric field is obtained by LAST simulation.

The experimental spectral-temporal investigation of scattered radiation /5,7/ found the second harmonics peaks correlation with the absorption peaks that is demonstrated on fig.3 where a) — is time dependence of Nd-laser radiation, b) — is backscattered light, c) — is second harmonics intensity, d) — is red and e)— is blue

fig.2

part of the main frequency spectra intensity. The sharp decrease of second harmonics emission (3c) correlates in time with the increase of reflection (3b) and with the increase of the blue part intensity (3c), that shows the transition from subsonic to supersonic regime. The whole complex of these experimental results demonstrates the decrease of the electric field in plasma that leads to decreasing of absorption and second harmonics emission at supersonic regime.
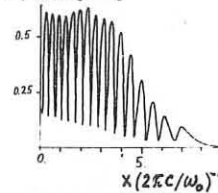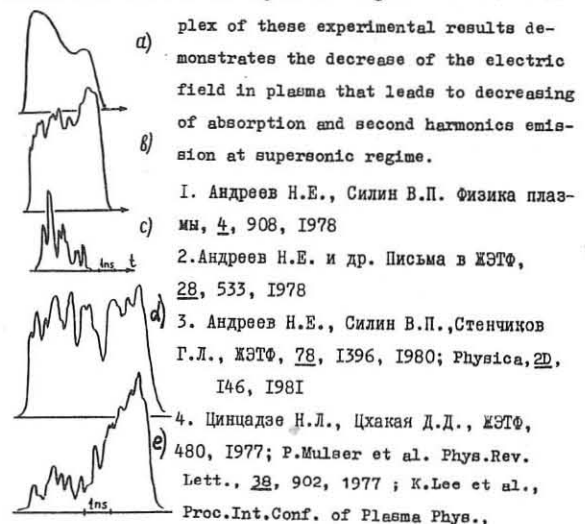
fig.3

1. Андреев Н.Е., Силин В.П. Физика плазмы, 4, 908, 1978

2. Андреев Н.Е. и др. Письма в ЖЭТФ, 28, 533, 1978

3. Андреев Н.Е., Силин В.П.,Стенчиков Г.Л., ЖЭТФ, 78, 1396, 1980; Physica, 2D, 146, 1981

4. Цинцадзе Н.Л., Цхакая Д.Д., ЖЭТФ, 480, 1977; P.Mulser et al. Phys.Rev. Lett., 38, 902, 1977 ; K.Lee et al., Proc.Int.Conf. of Plasma Phys., 1980, v.1, p. 393, Nagoya, Japan.

5. Андреев Н.Е. и др. Письма в ЖЭТФ, 31, 639, 1980

6. Андреев Н.Е., Силин В.П., Силин П.В., ЖЭТФ, 79, 1293, 1980

7. Andreev N.E. et al., Phys.Lett., 82A, 177, 1981.

THE THEORY OF THE HALF-INTEGER HARMONICS GENERATION
IN THE INHOMOGENEOUS LASER-PRODUCED PLASMAS

V.YU.BYCHENKOV,A.A.ZOZULJA,V.P.SILIN,V.T.TIKHONCHUK

P.N.Lebedev Physical Institute,USSR

Half-integer harmonics radiation from the laser-produced plasma can be used for diagnostic purposes/1-3/. This paper aim is to study half-integer harmonics generation dependence on the plasma inhomogeneity and the polarisation of the pump-wave,obliquely incident onto a plasma.Harmonics generation in the inhomogeneous plasmas was dealt with in /4,5/,supposing normal incidence of the pump-wave.It will be shown below that harmonics generation under the obliquely incident pump-wave difers substantially from that under the normally-incident pump.For S-polarised pump the satellites intensity ratio in the two-component harmonic spectrum depends on the irradiation and scattering angles.For P-polarised pump the considerable harmonics spectrum broadening arises.

Half-integer harmonics generation in laser-produced plasma is connected with the two-plasmon instability in the quarter-critical density region.Near the instability threshold nonlinear interaction of Langmuir waves is negligibly small,therefore Langmuir waves energy flux $W(\omega,\vec{K_\perp})$ ($\omega \approx \omega_0/2$ is Langmuir wave frequency, $\vec{K_\perp}$ its wave-vector component,perpendicular to the density inhomogeneity direction)is simply connected with the convective amplification coefficient $\mathscr{X}(\omega,\vec{K_\perp})$ /6/:

$$W(\omega,\vec{K_\perp}) = T_e \exp\left(2\mathscr{X}(\omega,\vec{K_\perp})\right)$$

$$\mathscr{X}(\omega,\vec{K_\perp}) = \frac{\pi L}{6 K_{ox} V_{Te}^2} \frac{(\vec{K}\vec{V_E})^2 (\vec{K}\vec{K_o} - K_o^2/2)^2}{K^2 (\vec{K}-\vec{K_o})^2} \tag{1}$$

Here T_e is electron temperature, V_{Te} is their thermal velocity, L is plasma inhomogeneity scale length, $\vec{V_E}$ is electron oscillational velocity amplitude in the pump field, $\vec{K_o}=(K_{ox},\vec{K_{o\perp}})$ is the pump-wave wave-vector near $n_c/4$, $\vec{K}=(K_x,\vec{K_\perp})$,where

$$K_x = \frac{(\omega - \omega_0/2)\omega_0}{3 K_{ox} V_{Te}^2} - \frac{\vec{K_\perp}\vec{K_{o\perp}}}{K_{ox}} + \frac{1}{2}\frac{K_o^2}{K_{ox}} \tag{2}$$

Harmonics intensities are proportional to the Langmuir waves energy flux $W(\omega,\vec{K_\perp})$, and,consequently,harmonics spectrum is determined by $\mathscr{X}$ dependence on ω and $\vec{K_\perp}$.

Under the S-polarised pump $(3/2)\omega_0$ harmonic spectrum has two components with the frequency shift between them $\Delta\omega_{3/2} \sim (V_{Te}/c)^2 \omega_0$(c is the speed of light).But these components relative intensity depends on the scattering angle. This situation is shown schematically in Fig.1(pump-wave incidence angle $\theta_0 < 45°$).The boundary between the regions with different shading corresponds to the components equal intensity. Over this boundary the "blue" component is more intensive than the "red" one,and under boundary "red" component is more
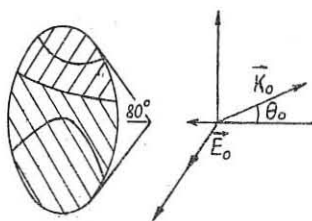
Fig.1

intensive.Solid lines within the shaded regions represent "red" and "blue" components maximum intensity emission directions.It is seen from Fig.1 that the "red" component dominance region is more,then that of the "blue"component

The transformation coefficient into $(3/2)\omega_0$ harmonic for S-polarised pump is given by the expression:

$$K_{3/2}^{(s)} \simeq 10 \frac{m\omega_0^3}{q_o}\left(\frac{V_{TE}}{c}\right)^6 \exp\left[\frac{\pi}{12}\left(\frac{V_E}{V_{Te}}\right)^2 \kappa_o L\right]\sqrt{1-\frac{4}{3}\sin^2\theta_o} \tag{3}$$

The qualitatively different situation takes place under the P-polarised pump.In this case for $\omega-\frac{\omega_0}{2}>\left(\frac{V_{Te}}{c}\right)^2\omega_0$ amplification coefficient(1) tends to constant value:

$$\mathscr{X}_P = \frac{\pi}{6}\frac{V_{EX}^2}{V_{Te}^2}\kappa_{ox}L \tag{4}$$

In this case isotropic harmonic angular distribution and substantial harmonic spectrum broadening up to the maximum value

$$\Delta\omega_{3/2\ max} \sim \frac{1}{3}\omega_0 \frac{V_{Te}}{c}\sqrt{\frac{3}{4}-\sin^2\theta_o} \tag{5}$$

which is determined by the Landau damping,are arising.

The transformation coefficient for P-polarised pump is equal to

$$K_{3/2}^{(P)} \simeq \frac{e^2\omega_0^2}{mc^4}L\left(\frac{V_{Te}}{c}\right)^3 \exp(2\mathscr{X}_P) \tag{6}$$

More weak $K_{3/2}^{(P)}$ dependence on the electron temperature, compared with $K_{3/2}^{(s)}$,should be noted.

Emission on the frequency $\omega \sim \frac{\omega_0}{2}$ also can be connected with the pump-wave combination scattering on the plasmons/3,5/.But this process probability is small compared with the Langmuir waves conversion into the electromagnetic radiation.According to conversion features/8/ $\omega_0/2$ harmonic radiation should be P-polarised and contained within the relatively narrow angle cone $\theta' \sim (\kappa_o L)^{-1/3}$.

Transformation coefficient into the $\omega_0/2$ harmonic

$$K_{1/2}^{(P)} = 10^{-3}\frac{m\omega_0^3}{q_o}\left(\frac{V_{Te}}{c}\right)^3 (\kappa_o L)^{-2/3}\exp(2\mathscr{X}_P)$$

is comparable with(6).In the S-polarised pump case transformation coefficient $K_{1/2}^{(s)}$ value should be at least two orders of magnitude less than $K_{1/2}^{(P)}$.The one-half harmonic emission spectrum for P-polarised pump should have "blue"-shifted part with the frequency shift value,given by(5),analogous to the $\frac{3}{2}\omega_0$ spectrum.

I.Ю.В.Афанасьев и др.,"Взаимодействие мощного лазерного излучения с плазмой",ВИНИТИ,"Радиотехника",17,М.,1978.
2.А.И.Авров и др.,Письма в ЖЭТФ 24,293,1976;ЖЭТФ,72, 970,1977.
3.В.Ю.Быченков и др.,Физика плазмы,3,1314,1977.
4.А.З.Гусаков,Письма в ЖТФ,3, 1219,1977.
5.А.Н.Стародуб,М.В.Филиппов,Физика плазмы,5,№5,1979.
6.А.А.Зозуля,В.П.Силин,Краткие сообщения по физике ФИАН. №1,49,1981.
7.В.П.Силин,Краткие сообщения по физике ФИАН,№10,35,1979.
8.В.В.Железняков,Е.Я.Злотник,Изв.ВУЗов,"Радиофизика", 5,664,1962.

ION ACCELERATION UNDER LASER PLASMA
EXPANSION.

A.V.Gurevich, A.P.Mescherkin
Physical Institute Academy of Sciences of the USSR
Moscow, USSR

Fast ions observed in an expanding laser plasma can carry away a considerable part of laser pulse energy. X-ray investigations show that at a sufficiently high laser pulse intensity electrons have a non-Maxwellian velocity distribution with a considerably pronounced "tail" of fast particles [1]. Since ions are accelerated due to interaction with electrons, the presence of "tails" has an essential effect upon the energy spectrum of accelerated ions. Therefore, the investigation of the spectrum of ions with different charge Z_k and mass M_k may serve an effective method of laser plasma diagnostics [2].

The possibility of collective ion acceleration in an expanding rarified plasma was pointed out in [3]. The present paper is aimed at a detailed theoretical investigation of the above-mentioned ion acceleration process and a comparison of theoretical results with those of laser experiments [4].

1. An arbitrary non-Maxwellian electron distribution function is analysed. The presence of non-Maxwellian "tails" in distribution functions containing a comparatively small number of fast electrons (of order of 1% or even less) changes essentially the amount of accelerated ions, and the ion front velocity.

2. Ions moving in a rarification wave in plasma are shown to have a sharp front. Ion concentration on the front has a jump discontinuity. The discontinuity appears in the process of expansion both at a sharp and at a smeared initial plasma boundary. This makes an essential difference between hydrodynamic plasma flow and analogous flows in ordinary hydrodynamics where the rarification wave is always restricted to contact discontinuities. The front velocity increases logarithmically with time.

3. Expansion of multicomponent plasma containing ions of different mass M_k and charge Z_k is considered. Ion acceleration is shown to increase as the charge Z_k increases. The energy spectra of accelerated ions at a identical ratio Z_k/M_k are identical functions E/Z_k (E is the ion energy).

4. Development of perturbations in an unsteady flux of a freely expanding plasma is analysed. Perturbations propagating in the direction opposite to the flux direction are shown to increase. Such waves do not change greatly the self-similar nature of the motion. They are referred to as quasi-self-similar waves. As a result of quasi-self-similar wave excitation the energy spectrum of accelerated ions becomes of oscillating character.

5. Non-one-dimensional plasma motion is considered. It is shown that under plasma cylinder expansion the character of ion acceleration is sufficiently close to the one-dimensional case (although somewhat weaker). In the case of spherical expansion the picture changes radically: the accelerated ion energy is limited to the value $E_m \approx 2Z T_{eff} \left\{ ln \left[R_0/2D_0 \sqrt{Z} ln(R_0/D_0) \right] \right\}^2$ where R_0 is the characteristic initial dimension, D_0 is the Debye radius in the initial plasma. At $\frac{E_m}{ln(R_0/D_0)} \leq E \leq E_m$ the energy spectrum of accelerated ions keeps all the above-mentioned specific features of the one-dimensional spectrum.

6. Plasma expansion in the presence of a standing wave which forms an electromagnetic barrier hampering a free plasma motion is discussed. Part of plasma is shown to penetrate through the barrier forming a flux of accelerated ions. In the presence of a non-Maxwellian "tail" of fast electrons this penetration essentially increases. In this case there exists a laminar shock ion-sound wave which propagates in the direction of dense plasma. This wave is induced by reflection from the barrier.

7. Fig.1 presents comparison of theory with the results of experiments [5]. Fig.1a illustrates observed energy spectra of accelerated ions D^+ and C^{+6} which have the same ratio Z_k/M_k. In the chosen scale the spectra of these ions are similar, which is in full agreement with theory (item 3). The electron temperature in the tail of the distribution function $T_{eff} \sim 18$ kev, it agrees with the results of X-ray measurements [5]. Fig.1b presents the energy spectra of ions H^+ and C^{+6} which have different ratios Z_k/M_k. The spectrum oscillation period in Fig.1 increases proportionally to $\sqrt{E}$ (since in the variables $\sqrt{E/Z}$ it is approximately constant). This coincides with theory (item 4). The limiting energy of accelerated ions is also in agreement with theory (items 2,5). Note that the jet acceleration of ions observed in [6] under spherical laser radiation of a target can also be explained by an plasma break through the electromagnetic barrier by local anomalous absorption (item 6).

References

[1] N.G.Basov, V.Volovsky, E.Voryna, S.Denus, Yu.A.Zacharenkov, S.Kalisky, G.V.Sklizkov, U.Farny, A.S.Shikanov, Preprint FIAN N 494, 1978; P.M.Campbell, R.R.Johnson, F.J.Mayer, L.V.Powers, D.C.Slater Phys. Rev. Lett. 39, 274, 1977. K.Eastabrook, W.L.Kruer Phys. Rev. Lettr. 40, 42, 1978.

[2] A.Gurevich, D.Anderson, H.Wilhelmsson Phys. Rev. Lettr. 42, 769, 1979

[3] A.V.Gurevich, L.V.Pariiskaya, L.P.Pitaevskii ZETF 49, 647, 1965 (Sov. Phys.- JETP 22, 449, 1966).

[4] A.V.Gurevich, A.P.Mescherkin ZETF 80, 1810, 1981; Kratkie soobscheniya po fizike, Sbornik FIAN SSSR, N 4, 27, 1981.

[5] R.Decoste, B.M.Ripin Phys. Rev.Lettr.40,34,1978; R.Decoste NRL Report 3774, Washington 1978

[6] Yu.A.Zacharenkov, O.N.Krochin, G.V.Sklizkov, A.S.Shikanov Pis'ma ZETF 25, 415, 1977.

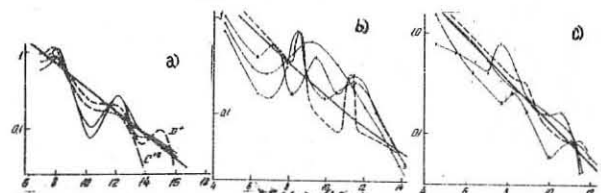Fig.1. Energy spectra of $d(N/N_0)/d(E/Z)$ versus $\sqrt{E/Z}$ of accelerated ions C^{+6} and D^+ for the targets CD_2(a) and H^+(b), C^{+6}(c) for the targets CH_2 at different concrete realization [5]. Solid curves stand for the theory in the self-similar approximation, dashed lines in Figs.b,c represent the theory taking into account excitation of quasi-self-similar waves. E-in kev.

PULSE SHAPING STUDIES IN GAS-FILLED RELATIVISTIC ELECTRON BEAM DIODE

K.C. Mittal, A.S. Paithankar, S.K. Iyyengar and V.K. Rohatgi
Plasma Physics Section, Bhabha Atomic Research Centre,
Trombay, Bombay 400 085, INDIA

Introduction

In the recent years, intense high power relativistic electron beams (REB) have found applications[1] in many branches of fusion research. For instance, plasma heating[2] by REB in magnetically confined devices and development of high power CO_2 laser require beam pulses of very long duration ($\sim \mu s$), while inertial confinement fusion scheme, flash X-ray radiography, studies of fusion materials etc., require pulses of a few nanosecond durations. Hence pulse shaping studies of REB are of great relevance. The pulse duration of the beam, for a given REB-vacuum diode is dependent on the design parameters of pulse source and associated pulse forming network. However, it is of great interest if for a given pulse source and diode system, one is able to control the beam pulse by manupulating the diode parameters only. Studies of electron beam generation in plasma filled diode[3] and gas filled diode[4] have been reported. In this paper we report the effect of variation of the gas pressure in REB diode on the current and voltage pulse shaping of the beam.

Experimental System

The experimental studies on gas-filled diode were performed on REB-75 system described elsewhere[5],[6]. The schematic of the system is shown in Fig. 1. The system consists of a field emission diode having planar cathode of graphite 6 mm diameter and thin foil of titanium (thickness 0.0125 mm) as anode. The cathode is mounted on an epoxy casting so as to provide insulation between ground and cathode. The anode-cathode gap is maintained at 8 mm as dictated by diode design considerations[5]. The diode is connected to a Marx-type pulse power source capable of giving a maximum of 75 Joules, 375 kV, and 2.5 kA electron beam pulse. The diagnostics employed consist of a fast response (rise time < 3 ns) copper sulphate voltage divider for beam voltage, Rogowski coil for diode current, Faraday cup for measuring transmitted electron beam current and dosimeter film to monitor the beam uniformity. For the measurement of transmitted beam current, thin titanium foil of 2.5 cm diameter was used as window for Faraday-cup. This foil was isolated from the graphite collector of the Faraday-cup, so as to discriminate the discharge current and measure only the transmitted beam current. For measuring the diode current at anode the Faraday-cup was replaced by a thick aluminium collector (not shown in Fig. 1) touching the anode foil window and current was measured by the Rogowski coil. Thus Rogowski coil measures both the beam current and discharge current when the diode gas pressure is high. The gas (air) pressure in the gap was varied from 10^{-5} Torr to 2×10^{-1} Torr and corresponding voltage and current waveforms were recorded on the Tektronics 7834 storage oscilloscopes having 400 MHz bandwidth. The oscilloscopes were kept in Faraday-cage and triaxial cables were employed for carrying the signals to the oscilloscopes so as to minimise any unwanted electromagnetic pick-ups.

Results and Discussions

Fig. 2 (a-e) shows the oscilloscope traces of transmitted beam voltage and current pulses for various pressures. It is seen that compared to vacuum case ($\sim 10^{-5}$ Torr), the voltage and current pulse duration is reduced as diode gas pressure (air) is increased. Fig. 2 (f-h) shows the typical traces of voltage and current pulses measured at the anode as a function of gas pressure. Fig. 3 shows the plot of normalised transmitted beam current (a), diode voltage (b) and diode current at anode (c) as a function of gas pressure. The peak current and voltage have been normalised with respect to their corresponding peak values for the vacuum case. The peak diode voltage remains constant throughout the pressure range, indicating that the diode gap is able to sustain the full voltage till the peak is reached at all the pressures, while the diode current at anode and transmitted beam current increase with pressure. Fig. 4 shows the variation of pulse full width at half maximum (FWHM) of transmitted beam current (a), the diode voltage (b) and diode current at the anode (c). Both the transmitted beam current and voltage pulse widths decrease with increasing pressure, while the pulse width of the diode current at anode is nearly constant. Physically the results indicated in Figs. 2-4 can be explained as follows : In case of vacuum diode the voltage and current pulse durations are governed by time varying impedance of the diode. This impedance is a function of cathode and anode plasmas and their movement

across the gap. This movement of the plasma and consequent gap closure cause the voltage collapse and limit the maximum pulse duration. The most important feature in this experiment is that even at 10^{-1} Torr pressure (see Fig. 3) the gap is able to sustain the same peak voltage ~ 250 kV as in the case of vacuum diode. This means that during the first ~ 10 ns when the voltage pulse reaches the peak, diode impedance is large enough and gap is able to sustain full voltage. The main processes[4] which will determine the shape of current and voltage curves in a gas-filled diode are the volume ionisation of the gap by the fast electrons from the cathode and charge exchange between the charged particles and neutrals. The additional plasma formed by the gas ionisation reduces the diode impedance. Depending upon the plasma density (which in turn depends on gas pressure) desired pulse duration can be obtained as seen in Fig. 4. Thus when the plasma density is sufficiently high ($10^{12} - 10^{14}$ cm^{-3}) the voltage across the gap collapses leading to the short duration pulse. A similar effect was observed by Miller et al[3] during their studies in plasma filled diode. The increase in the transmitted beam current (Fig. 3) as pressure is increased can again be explained as due to the decrease in the diode impedance caused by plasma formed by the ionisation of the gas. The dosimeter film placed after the anode foil shows uniform beam current and radial spike-like structure, observed earlier[7], is not seen in the transmitted beam.

Thus by adjusting the pressure in the gas-filled diode, one can have desired voltage and current pulse duration as shown in Fig. 4. Though this pulse shaping is at the expense of total energy of the beam, it is of great interest when pulse duration is of primary concern.

References

1) H.H. Fleischmann, Phys. Today, 28 (5), 35, 1975.

2) A.S. Paithankar, V.K. Rohatgi, BARC Report No. 1031, 1979.

3) P.A. Miller et al, Phy.Rev.Lett. 35(14), 940, 1975.

4) V.V. Glebov et al, 3rd Intl.Conf. on High Power Electron and Ion Beams, Novosibirsk, Vol.II, 585, 1979.

5) S.K. Iyyengar et al, BARC Report No. 960, 1977.

6) V.K. Rohatgi et al, submitted to Radiation Effects.

7) V.K. Rohatgi et al, INIS-mf - 4833, 1978.
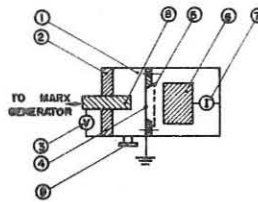
Fig.1 Schematic of Experimental System.
1-Vacuum Chamber, 2-Epoxy insulator, 3-Resistance voltage divider, 4-Anode foil, 5-Dosimeter film, 6-Graphite collector of Faraday cup, 7-Current shunt 8-Graphite cathode and 9-To Gas leak valve and vacuum pumps.
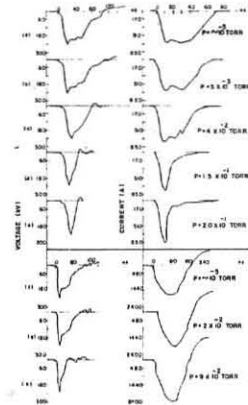
Fig.2 Voltage and Current waveforms at various pressures. (a) to (e) - Transmitted beam voltage and current. (f) to (h) - Diode voltage and current at anode.
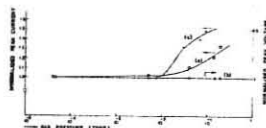
Fig.3 Variation of normalised voltage and current as a function of pressure.
a) Transmitted beam current
b) Diode voltage
c) Diode current at anode
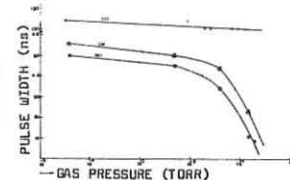
Fig.4 Variation of Pulse width (FWHM) as a function of pressure.
a) Transmitted beam current
b) Diode voltage
c) Diode current at anode

INVESTIGATIONS OF SPHERICAL LASER COMPRESSION OF PLASMA

M.Borowiecki, S.Denus, J.Farny, H.Fiedorowicz, J.Godzik,
S.Nagraba, W.Pawłowicz, L.Sulwiński, W.Szypuła, A.Wilczyński,
J.Wołowski, E.Woryna.

S.Kaliski Institute of Plasma Physics and Laser Microfusion
00-908 Warsaw 49, Poland

Experiments are currently under way at IPP&LM in which D_2-gass-filled microspheres are being irradiated in a tetrahedral geometry with four beams of up to 20J/beam from a Nd: glass-laser. Laser pulse duration was 3 ns and pulse rise time 1 ns: A lens-mirror illumination system ensuring more uniform illumination of microtarget surface /glass or ablator covered microsphere/ with laser radiation was used in the last experiment.

The following diagnostics were used to study physical processes occuring in the generated plasma: X-ray /microphotography, temporal and spectral measurements of emitted radiation/, optical /streak shadowgraphy, investigation of radiation reflected from plasma/, ionic /ion emission flux measurements/ and the neutron one. Fig.1 presents a scheme of the experimental system.
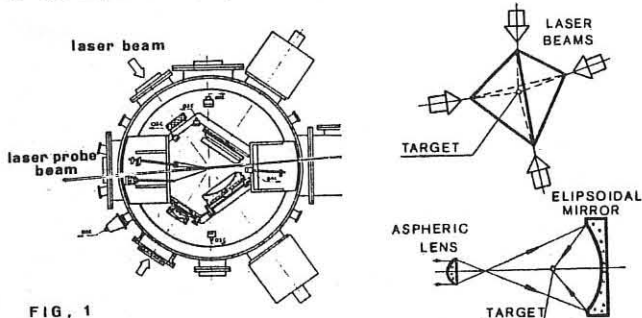
FIG. 1

X-ray microphotographs /see Fig.2/ were made by means of pin-hole camera.

A majority of the obtained photographs were of nonsymmetrical and heterogenous shape, which could be related to the nonsy-mmetrical illumination of the microsphere with laser radiation.

In some microphotographs characterized by the best symmetry one can distinguish illuminating area in the central part of the microsphere which is interpreted to be X-ray radiation emission from plasma generated in results of microsphere implosion. The fact that fast X-ray radiation detector /1GHz/ records two pulses distant by approximately 1.5 ns which would correspond to implosion velocity of some $10^7 cm$/s, speaks for such an interpretation.

100 μm
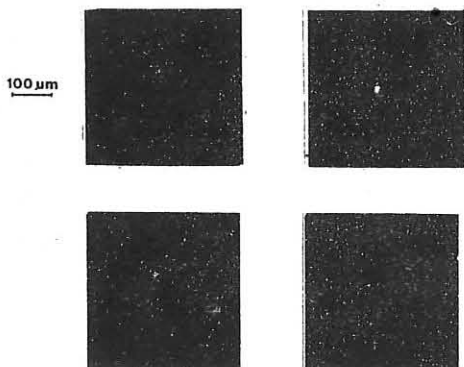
FIG.2 X-ray microphotographs of plasma

Spectral measurements of X-ray radiation were carried out by means of a semiconductor detector matrix shielded with 20,50 and 140μm Be filters. The electron temperature determined on their base varied within 150-400eV.

Streak shadowgraphs of expanding plasma were made by means of an arrangement shown in Fig.3. A fast streak camera with 50 ps temporal resolution and 10 μm spatial one were used.
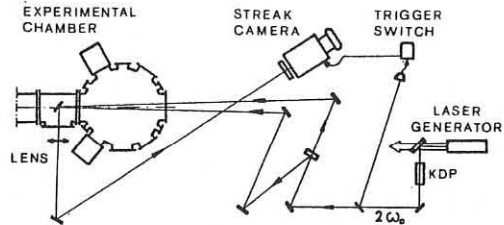
FIG. 3

An examples of a streak shadowgraph in a temporal developments are shown in Fig.4.

In the period corresponding to the laser pulse rise time incident on the target / 1ns/, a fast expansion of shade with /2 ÷ 5/ × $10^7 cm$/s velocity was observed, then, after 1 ns, there followed a relative stabilization of position /at approximately 400 μm dimension/.

200 μm

1 ns
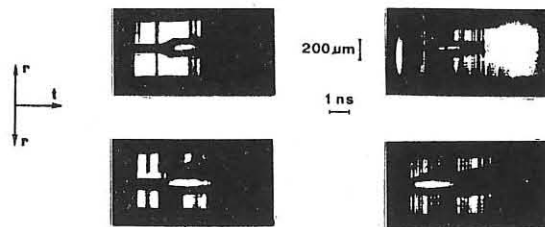
FIG.3. Streak shadowgraphs of plasma

Ion emission measurements were conducted by means of four ion collectors. On the base of the obtained results we defined plasma corona parameters as well as, in the inderect way, implosion parameters /Fig.5/
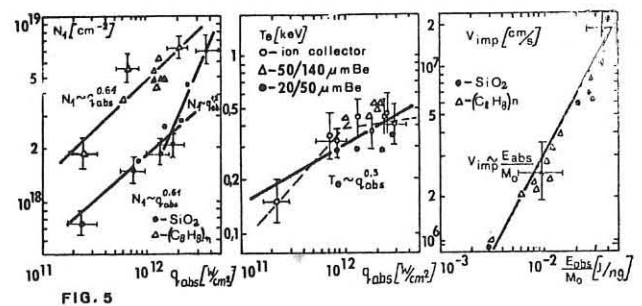
FIG. 5

Estimated values of the electron temperature approximate the values abtained from x-ray measurements. From the estimations it appears that implosion velocity is proportional to the absorbed energy divided on to the initial microsphere mass. Measured plasma expansion symmetry is shown in Fig.6.
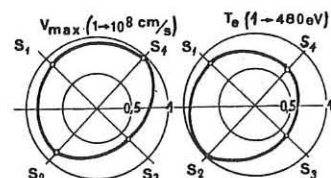
FIG. 6

Neutron measurements accomplished with use of a scintillation probe proved that no neutron flux emission appeared above the value of 300 neutrons /4Π.

AN ANALYSIS OF POSSIBLE CURRENT INSTABILITIES
ACCOMPANYING LIGHT ION BEAM TRANSPORT TO THE
TARGET.

A.V.Gordeev, A.S.Kingsep, L.I.Rudakov, K.V.Tchukbar

I.V.Kurchatov Institute of Atomic Energy, Moscow 123182,
USSR

1. In a program of light ion beam fusion they are going to transport the beam with a total current $I \sim 30$-$50MA$ on the target of diameter $a \sim 1$ cm. The beam energy $\mathcal{E} == e U \sim 2$ - 3 MeV and pulse duration $\tau \sim 1$ - $2 \cdot 10^{-8}$s. For the proton beam these parameters correspond to the density $n \sim 2$ - $3 \cdot 10^{16} cm^{-3}$ and the velocity $V_\delta \sim 2$ - $3 \cdot 10^9$ cm/s. In the NRL and SANDIA concepts the beams are transported through the long ($L \sim 5$ m) channels with a plasma density n up to 10^{18} cm^{-3} /1/. The important requirement to the beams is the small angular width. While transportation in a dense plasma the instabilities of the current can break this condition. First of all, the instabilities in a plasma channel /2,3/ result in the local separation of both beam and plasma currents. As a result the beam angular width is growing. On the other hand, the potential instability in a plasma corona where the beam current density is especially high leads to the damping of the return current. As $I \geq I_{Ai} = M c^2 V_\delta /2e$ the beam can miss the target, as a result. Besides, the plasma turbulent heating in a corona is also dangerous. As the estimates show the Bremsstrahlung of the hot electrons may break the dynamics of the target shell collapse.

We consider the situation when the beam current exceeds essentially the net current

$$\vec{j} = \vec{j_\delta} + \vec{j_P} = \frac{c}{4\pi} curl \vec{H} \ll \vec{j_\delta} \tag{1}$$

and the frequency scale $\omega \gg \omega_{Hi}$. Plasma may be described by the equations

$$M_i \frac{d\vec{v}}{dt} = e \vec{E} \qquad \text{for the ions} \tag{2}$$

$$\vec{E} + \frac{1}{c}[\vec{v}\vec{H}] + \frac{ne\vec{v}}{\sigma} = - \frac{\nabla P_e}{ne} \qquad \text{for the electrons} \tag{3}$$

and there is the MHD-equation for the beam

$$n_\delta M \frac{d\vec{V_\delta}}{dt} = n_\delta e \vec{E} + \frac{1}{c}[\vec{j_\delta}\vec{H}] - T_\delta \nabla n_\delta \tag{4}$$

which is valid in the case of more than one oscillations of the beam ions in a channel.

Under the condition (1) the generation of the magnetic field is described by the equation

$$H = c \int_0^t \frac{d}{d\tau} \frac{j_P}{\sigma(\tau,t)} dt \tag{5}$$

2. Return current in a plasma channel products the force pushing the beam ions out of the beam. This force results in instability if the plasma density decreases with a radius. The helical mode of this instability is described by the following dispersion equation /2,4/:

$$\frac{\tilde{\omega}'\tilde{\omega}''}{\kappa_\varphi^2}\left(\frac{4\pi ne}{cH}\right)^2 + \frac{4\pi ne}{cH}\frac{\partial V_z}{\partial \tau} - \kappa^2\left(1 + \frac{\omega_{pi}^2}{c^2} \times \right. \tag{6}$$

$$\left. \times \frac{V_z^2}{\omega^2 - \kappa^2 c_s^2} + \frac{\omega_{p\delta}^2}{c^2}\frac{V_\delta^2}{(\omega - \kappa_z V_\delta)^2 - \kappa^2 V_{T\delta}^2}\right) = 0$$

where Z axis is along the beam, $V^2_{T\ell} = T_\delta /M$,
$\omega_{p\delta}^2 = \frac{4\pi n_\delta e^2}{M}$; $\omega_{pi}^2 = \frac{4\pi ne^2}{M_i}$; $\tilde{\omega} = \omega - \kappa_z V_z$;
$\tilde{\omega}' = \tilde{\omega} + i\frac{\kappa^2 c^2}{4\pi\sigma}$; $\tilde{\omega}'' = \tilde{\omega} + i\frac{\kappa^2 c^2}{4\pi\sigma}\left[1 + \frac{\omega_{p\delta}^2}{c^2}\frac{V_\delta^2}{(\omega - \kappa_z V_\delta)^2 - \kappa^2 V_{T\delta}^2}\right]$;
$\kappa^2 = \kappa_z^2 + \kappa_\varphi^2$; $V_z = -\frac{j_\delta}{ne}$.

Maximum growth rate by the condition $V_z > C_s$ corresponds to the intersection of the helical and acoustic modes

$$\gamma = \frac{1}{2}\left(\frac{Zm}{AM}\right)^{1/2}\frac{V_z}{C_s}\omega_{He}\left(\frac{\kappa C_s}{\omega_{He}}\right)^{1/2}. \tag{7}$$

By the conditions $\gamma > \frac{\kappa^2 c^2}{4\pi\sigma}$, $\omega_{He} > \nu_{ei}$ when the formula (7) is still valid, the upper limit of the growth rate equals to

$$\gamma \approx 10^{-3}\omega_{He}\frac{V_z}{C_s} \approx 10^8 s^{-1}, \quad \omega_{He} = 3 \cdot 10^{10} s^{-1},$$

for the parameters $n = 10^{18} cm^{-3}$; $C_s = 3 \cdot 10^6 cm/s$; $j_\delta = 10^6 A/cm^2$

3. The magnetic field generation in a corona is described by Eq.(4). The beam-turn in the self-generated field occurs by the condition

$$V_\delta \leq \frac{e}{Mc}\int H dz \sim \frac{c}{a}\int dt \frac{j_\delta \ell(t)}{\sigma(t)} \tag{8}$$

where $l(t) \sim c_s t$ is the characteristic scale in the blowing-off corona. The estimates show that Coulomb conductivity turns out to be more than the critical one by one order. But if $V_z \gg C_s$ in a corona anomalous resistance due to ion-acoustic instability plays the main role. By the level of turbulence $E^2_\sim /nTe$ high enough the effective collision frequency for the electrons may turn out to be of the order of ω_{pe}. Then from Eq.(8) with $\sigma = ne^2/m\nu_{eff}$ we can see that beam-turn is allowed in this case. The second effect is the plasma turbulent heating. One can obtain that Te reaches during the pulse 50 - 60 keV, as a minimum, which corresponds to 2 - 3 % of the beam total energy input. The electrons of this energy radiate while interaction with a dense plasma the share of their energy $\frac{Z e^2}{\hbar c}\frac{Te}{mc^2} \sim$ 6 % as a result of collisions with the nuclei with Z $\sim$ 80. The free path length of the protons with $\hbar\omega \sim 50$ keV is comparable with that for the protons with $eU \sim$ 3 MeV. Resulting preheating of the pellet shell may complicate the implosion of the DT fuel. Thus in the light ion beam fusion concept the effects of the magnetic field generation are to be taken into account.

References

1. Cooperstein J., Goldstein Shyke A. et al. V Workshop on "Laser interaction and related plasma phenomena", New York, Nov.5-9, 1979.
   Yonas G. Proceedings of the 3rd Int.Top.Conf. on High Power Electron and Ion Beam. Novosibirsk, 1979, v.II, p.390.

2. Gordeev A.V., Rudakov L.I. JETP, 1968, No.54, p.2310.

3. Lee E.P., Yu S.S. et al. Phys.Fluids, 1980, v.23, No.10, p.2095.

4. Ivanov A.A. et al. Fizika i Tekhnika Poluprovodnikov, 1968, No.2.

"Theoretical Understanding of CO_2 Interaction Experiments"* by
J. M. Kindel, B. Bezzerides, D. W. Forslund, R. S. Goldman,
R. D. Jones, E. K. Stover, and D. C. Wilson
Los Alamos National Laboratory, University of California,
Los Alamos, New Mexico 87545 USA

We summarize our recent theoretical modeling and understanding of Los Alamos high intensity CO_2 interaction experiments with particular emphasis on thin tungsten and gold microballoon experiments. Two features of these experiments are super hot electron generation and multi-harmonic CO_2 light generation. Two dimensional particle simulations and analytical models are used to describe the latter phenomena. For super-hot electron generation we discuss the role of filamentation or self-focussing, stimulated Raman scattering and Raman bubble formation.

For the case of thin microballoons i.e., whose thickness is the order of a hot electron range, we expect a fairly uniform energy deposition around the pellet because of the additional symmetrizing effect of the hot electrons passing through the thin shell. On the laser side of the pellet at intensities where the laser oscillatory velocity exceeds the electron thermal velocity i.e., $v_o/v_e \gg 1$, the hot electron density exceeds the critical density with a lower density shelf at a tenth critical density. On both the inside and outside of the thin tungsten or gold shell we expect substantial fast ion loss -- as high as 50% of the absorbed laser energy for some experimental thicknesses. Correspondingly with the significant loss of hot electron energy to ions, we observe in the modeling a reduction in hard x-ray yield. This corroborates what has been observed experimentally. For some thicknesses of gold, one observes a large fraction of the absorbed laser energy in internal kinetic energy even in the presence of fast ions. Our modeling of the experiments were those performed by Day, Hauer, Houkaday, Priedhorsky, and Rocket at Los Alamos.

In the experiments modeled above and others carried out over the past year at Los Alamos, there has been an increase in the apparent hot electron temperature. This has been elucidated by the hard x-ray measurements of Priedhorsky, but in addition has been corroborated by Thomson Parabola data of Begay. Two suggestions for the presence of a superhot component to the electron distribution have been self-focussisng or filamentation and stimulated Raman scattering with an accompanying bubble formation. Two dimensional plasma simulations suggest that warm ions are required for filamentation to develop and at this point we have only observed whole beam self-focussing in the simulations.

Because the underdense shelf is somewhat less than quarter critical density, oblique stimulated Raman scattering dominates. Because the scattered light waves have a turning point, albeit in a highly underdense plasma, Raman bubbles develop. A typical two dimensional simulation result is as follows: A focussing laser at 3×10^{15} W/cm^2 is incident on a 160 μm uniform plasma at a tenth critical density with a background underdense plasma temperature of 30 keV -- which is produced by resonant absorption. We observe due to the Raman instability a superhot electron distribution at "200 keV" with electrons out to 2 MeV at a density at least two orders of magnitude less than critical density.

Lastly, we discuss our current understanding of multi-harmonic emission of CO_2 light. Previously we have reported plasma simulation results of high harmonic emission of intense laser light. The simulations were carried out at a laser intensity where profile modification produced density jumps of 10-70 times critical density. We observed a flat power emission spectrum at the higher harmonics. These results were qualitatively consistent with the experimental results of Carman which have shown a flat harmonic spectrum out to very high harmonics.[1]

A simple physical model is presented to explain the salient features of these simulations and the above experiments. It is shown that the experimentally observed result of constant harmonic production efficiency out to a cutoff at the harmonic where the upper density shelf is underdense is a direct consequence of the almost impulsive force on the plasma located in the density jump region. This force is due to the self-consistent restoring force of the neighboring super-critical density plasma. Thus the high harmonic emission is an indication of the strongly nonlinear response of the region near the critical density.

To elucidate the proposed mechanism we will present a highly simplified model that identifies its basic features. Consider a very steeply rising density profile i.e., one in which a flat subcritical profile rises sharply to a flat highly supercritical profile with plasma frequencies ω_{pu} and ω_{pl} ($\omega_{pu} \gg \omega \gg \omega_{pl}$), corresponding to the upper and lower density shelves, respectively. Such structures are expected when $v_o/v_e \gg 1$, where $v_o = eE_{driver}/m_e\omega$, with E_{driver} the driver intensity, and v_e is the electron thermal speed. Under the influence of the incident field, a fluid element will oscillate in and out of the density jump about its equilibrium position. This fluid element will experience a restoring force and therefore corresponding acceleration, $F_{res} = -\omega_p^2\delta$ where δ is the displacement from the fluid's equilibrium position. Energy conservation, $1/2\, m_e v_o^2 = 1/2\, m_e \omega_{pu}^2 (\delta)_u^2$, sets the maximum excursion in the overdense region, $(\delta)_u \approx v_o/\omega_{pu}$, whereas the maximum excursion in the underdense region is $(\delta)_l \approx v_o/\omega$, since as compared with the overdense region the restoring force is small compared with that due to E_{driver}. If we furthermore demand that the overall motion of the fluid element driven by E_{driver} be periodic with the driver period $2\pi/\omega$, we are led to a schematic representation of δ and $\ddot{\delta}$ as shown in Fig. 1, where from the above discussion

$$(\delta)_u \approx \frac{\omega}{\omega_{pu}}(\delta)_1 = \left(\frac{n_c}{n_u}\right)^{1/2}\frac{v_o}{\omega} \text{ and } (\ddot{\delta})_u \approx \frac{\omega_{pu}}{\omega}(\ddot{\delta})_1 = \left(\frac{n_u}{n_c}\right)^{1/2}\omega v_o \quad .(1)$$

As shown in Fig. 1 the time in which the fluid element experiences strong acceleration is $\Delta T \sim \pi/\omega_{pu}$ since the motion is approximately that of a harmonic oscillator of period $2\pi/\omega_{pu}$ in the overdense region. This strong, impulse-like acceleration will cause high harmonic emission from the step region.

To estimate the emission rate into the nth spectral line $\omega_n = n\omega$, we Fourier analyze $\ddot{\delta}^2$. It can be shown utilizing Fourier transforms and the well-known Larmor formula that the intensity of emission in the nth harmonic is given by

$$I_n = \frac{2}{3}\frac{e^2}{c^3}\omega_{pu}\omega v_o^2\, C \int dx_o n_o(x_o) \quad , \quad \frac{n\omega}{\omega_{pu}} < 1$$

$$I_n \to 0 \quad , \quad \frac{n\omega}{\omega_{pu}} \gg 1 \quad , \tag{2}$$

where the integral in Eq. (2) is over the depth of radiating plasma, and C measures the enhancement above single-particle emission (C = 1) due to coherency effects. This result confirms the principal experimental observation of a flat spectrum for high harmonics with a well-defined cutoff and predicts a roll-off for the spectrum at $n_{max}^2 = n_u/n_c$. Thus, as suggested by a recent simulation study of high harmonic emission,[1] one can directly measure the upper density given the cutoff harmonic number. It should be noted that Eq. (2) predicts both even and odd harmonic emission, consistent with the observations, a direct consequence of the strongly asymmetric force as shown in Fig. (1).

1. R. L. Carman, D. W. Forslund, and J. M. Kindel, Phys. Rev.-Lett., 46, 29 (1981).
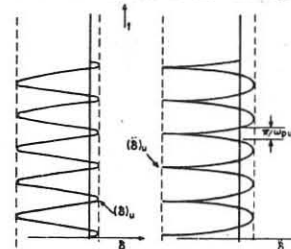
FIGURE 1. SCHEMATIC REPRESENTATION OF THE DISPLACEMENT δ AND ACCELERATION $\ddot{\delta}$ OF A FLUID ELEMENT AS IT OSCILLATES IN AND OUT OF THE DENSITY JUMP.

ONE DIMENSIONAL MAGNETOHYDRODYNAMIC CALCULATIONS
OF A HYDROGEN GAS PUFF

S. Maxon and P. D. Nielsen
Lawrence Livermore National Laboratory
Livermore, California 94550   U.S.A.

ABSTRACT

A one-dimensional Lagrangian calculation of the implosion of a hydrogen gas puff is presented. At maximum compression, 60% of the mass is located in a density spike .5 mm off the axis with a half width of 40 μm. The temperature on axis reaches 200 eV.

1. METHOD OF CALCULATION AND INITIAL CONDITIONS

Using the full magnetohydrodynamic (MHD) equations[1] coupled with the circuit equation, we numerically solve for the discharge of a capacitor bank into a cylindrical shell of hydrogen gas. The Lagrangian code LASNEX[2] is used. Artificial viscosity is added to the ion viscosity to calculate stable supersonic shock waves. The transport coefficients in the presence of a magnetic field are taken from Braginskii and neutral resistivity is included.

The energy and pressure of the gas are taken from a hydrogen equation of state. The MHD equations are differenced and solved in one dimension, assuming dependence on radius, velocity, and time.

The capacitor bank has the parameters V_o = 16 kV, L = 14.5 nH, and C = 21.6 μF for a total energy of 2.765 kJ and a quarter cycle rise time of .9 μs. The length of the pinch is 1 cm.

The initial density and pressure profiles for the gas are plotted in Fig. 1. The initial pressure results from setting the temperature at 2 eV in the region 2.16 ≤ r ≤ 2.2 cm to simulate breakdown and formation of a thin current sheath along the outside surface of the gas. The current returns at a radius of 3 cm. We
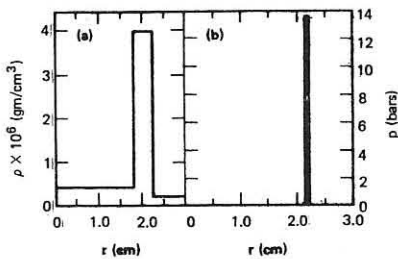
FIGURE 1. Initial density and pressure

use a density dependent switch for the resistivity so that material with density less than ρ_c is given insulating properties.

2. NUMERICAL RESULTS

Initially, the pressure spike shown in Fig. 1 spreads out, causing both an inward and an outward going shock wave. The outward going shock raises the density above ρ_c so that there is an outward going current sheath as well as the current sheath at 2.2 cm, which is the initial breakdown path. As the problem evolves further current sheaths are "created" in the outer region and subsequently propagate inward due to the $\vec{J} \times \vec{B}$ force, to join the main current sheath.

The early time solution at t = .1 μs consists of a density spike corresponding to a compression of 7.5 and a half-width of .14 mm. located at r = 2.04 cm.[3] The radial velocity of the density peak, as a function of time is plotted in Fig. 2. The first outgoing shock reaches the fixed insulator at .2 μs and dissipates. At this time, the density in the outer region drops below ρ_c everywhere, so that the entire region (r > 2.2 cm) becomes insulating. Therefore, the entire current flows on the outer surface of the gas and the implosion begins.
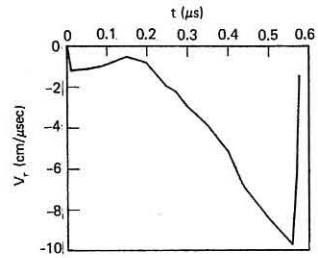
FIGURE 2. Radial velocity of density maximum

Notice the decrease in acceleration at .45 μs. Once again, this is due to the appearance of another current sheath in the outer
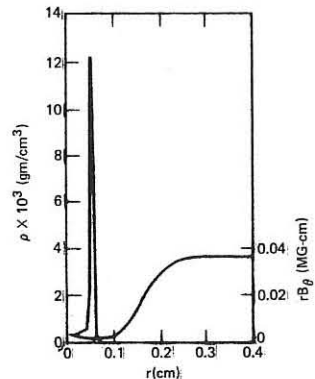
FIGURE 3. Density and rB_θ at maximum compression

region. The density and rB profiles at maximum compression, t = .577 μs, are plotted in Fig. 3. The temperature on axis is 165 eV while the temperature in the spike is 3 eV. The density spike contains 60% of the mass and has a half width of 40 μm. The quantity rB_θ takes the value .083 MG-cm in the insulating region (r ≥ 1 cm) but drops to the value shown in Fig. 3 because of a current sheath located between .5-1.0 cm. The current rises to .43 MA at t = .54 μs and drops to .4 MA at t = .585 μs.

These results are preliminary because we have not finished investigating their dependence on zone size. Two dimensional calculations will be made to see how axial flow changes the nature of the solution. We are also running this problem without the use of the density dependent resistivity.

REFERENCES

1. See, for example, S. Maxon and J. Eddleman, Phys. Fluid 21, 1856 (1978).

2. G. B. Zimmerman, Lawrence Livermore National Laboratory Report UCRL-74811 (1973); and P. D. Nielsen and G. B. Zimmerman, Lawrence Livermore National Laboratory Report UCRL-53123 (1981).

3. S. Maxon and P. D. Nielsen, Lawrence Livermore National Laboratory Report UCRL-85804 (1981) (submitted for publication).

NEW MATHEMATICAL METHODS OF INVESTIGATION
OF SOME NONLINEAR EFFECTS IN PLASMA

A.A.Samarskii, V.A.Galaktionov, S.P.Kurdjumov,

A.P.Mikhailov

Keldysh Institute of Applied Mathematics of the

USSR Academy of Sciences, USSR

In this paper we formulate some new mathematical methods of investigation of nonlinear stage of overheating unstability and in particular the aggravation regims in continuous media. We restrict our attention to Caushy problem for quasilinear parabolic equation describing the processes of heat conduction and combustion in one dimension

$$T_t = (k(T)T_x)_x + Q(T) , \quad t > 0 , \quad x \in \mathbb{R}^1 , \tag{1}$$

$$T(0,x) = T_0(x) \geqslant 0 , \quad x \in \mathbb{R}^1 ; T_0(x) \not\equiv 0 . \tag{2}$$

Here t is the time, x – space variable, $T(t,x)$ – temperature, $k(T) \geqslant 0$ – heat conduction's coefficient, $Q(T) \geqslant 0$ – power of heat sources.

1. The resonant excitement's conditions. The initial function $T_0(x)$ in (2) is called resonant (critical) if the temperature T doesn't decrease with time in whole space, that is

$$T_t(t,x) \geqslant 0 , \quad t > 0 , \quad x \in \mathbb{R}^1 . \tag{3}$$

Theorem 1 ([1,2]). The inequality

$$(k(T_0(x)) T_0'(x))' + Q(T_0(x)) \geqslant 0 , \quad x \in \mathbb{R}^1 \tag{4}$$

is the necessary and sufficient condition foe the resonant excitation of combustion in the sence of (3).

The inequality (4) permits one to determine the geometrical size of resonant initial indignation $T_0(x)$ and it's evolution in time.

2. Approximate similarity solutions (a. s. s.). The effective method of investigation of nonlinear diffusion and combustion consists in construction and analysis of similarity solutions of eq. (1). For example in the case $k(T) = T^6, 6 > 0, Q(T) = T^\beta, \beta > 1$ similarity solutions of eq. (1) showing for $\beta \geqslant 6+1$ the property of localization of diffusion process construct in [4,5] where their asymptitic stability is also established.

However a little number of eqs. (1) has the similarity solutions [6]. It is shown [7-9] that so-called approximate similarity solution can be constructed for some eqs. (1). This solution don't satisfy the eq. (1), but the solution of the considered Caushy problem asymptotic converges to it. For example it is shown [8] that in the case $k(T) \equiv 1, Q(T) = (1+T)\ln^\beta(1+T), \beta > 1$ the a.s.s. satisfies the first order Hamilton – Jacobi equation

$$\tilde{T}_t = (\tilde{T}_x)^2/(1+\tilde{T}) + (1+\tilde{T})\ln^\beta(1+\tilde{T}) , \quad t > 0 , \quad x \in \mathbb{R}^1$$

and $\| T - \tilde{T} \|_C \to 0$ as $\max_x T(t,x) \to +\infty$ (notes that in this case eq. (1) has no any proper similarity solution [6]).

3. Generalized comparison theorems. It is well Known that the solutions of parabolic equations have the continuous and monotone dependence from the initial – boundary data of considered problems. Because of that the similarity solutions of fixed equation are the specific bounds between classes of nonsimilarity solutions with different properties. However as mentioned above the similarity solutions of eq. (1) exists in very rare cases.

Let us formulate the new approach to comparison of solutions of Caushy problems for different parabolic equations (ν = 1,2)

$$T_t^{(\nu)} = (k^{(\nu)}(T^{(\nu)})T_x^{(\nu)})_x + Q^{(\nu)}(T^{(\nu)}) , \quad t > 0 , \quad x \in \mathbb{R}^1 , \tag{5}$$

$$T^{(\nu)}(0,x) = T_0^{(\nu)}(x) \geqslant 0 , \quad x \in \mathbb{R}^1 . \tag{6}$$

One of these equations may be of sufficiently simple type and has the solution with known properties.

Theorem 2([1,2]). Let $T_0^{(2)}(x) \geqslant T_0^{(1)}(x)$ in $\mathbb{R}^1$ and functions $k^{(\nu)}$, $Q^{(\nu)}$ satisfy the inequalities

$$k^{(2)}(s) \geqslant k^{(1)}(s) , \quad [k^{(2)}(s)/k^{(1)}(s)]' \geqslant 0 ,$$

$$k^{(1)}(s) Q^{(1)}(s) \geqslant k^{(2)}(s) Q^{(1)}(s) , \quad s > 0 .$$

Let, in addition, $T_t^{(2)}(t,x) \geqslant 0$ for all $t > 0$, $x \in \mathbb{R}^1$ (see theorem 1). Then $T^{(2)} \geqslant T^{(1)}$ for all $t > 0$, $x \in \mathbb{R}^1$.

Similar theorem can be proved in the cases of arbitrary (including nonquasilinear) parabolic equations [1] and can also be formulated for the comparison not of the solutions itself but of some nonlinear functions of its [10].

4. The methods described above give the possibility of theoretical investigation of various nonlinear effects in continuous media (for example T – layer's effect), which have been studed earlier in the numerical and physical experiments and also by some analytic and qualitative methods [4,5,11,12].

REFERENCES

1. V.A.Galaktionov, S.P.Kurdjumov, A.P.Mikhailov, A.A.Samarskii.- Zh. Vychisl. Mat. i Mat. Fis., 1979, v. 19, no. 6.

2. V.A.Galaktionov, S.P.Kurdjumov, A.P.Mikhailov,A.A.Samarskii.- Dokl. Akad. Nauk SSSr, 1979, v. 248, no. 3.

3. V.A.Galaktionov.- Preprint no. 16, Inst. Appl. Math. USSR Acad. Sci., 1981.

4. A.A.Samarskii, N.V.Zmitrenco, S.P.Kurdjumov, A.P.Mikhailov.- Dokl. Acad. Nauk SSSR, 1976, v. 227, no. 2.

5. A.A.Samarskii, G.G.Elenin, N.V.Zmitrenco, S.P.Kurdjumov, A.P.Mikhailov.- Dokl. Acad. Nauk SSSR, v. 237, no. 6.

6. V.A.Dorodnitsin.- Preprint no. 57, Inst. Appl. Math. USSR Acad. Sci., 1979.

7. A.A.Samarskii, V.A.Galaktionov, S.P.Kurdjumov, A.P.Mikhailov.- Dokl. Acad. Nauk SSSR, v. 247, no. 2.

8. V.A.Galaktionov, S.P.Kurdjumov, A.P.Mikhailov, A.A.Samarskii.- Preprint no. 161, Inst. Appl. Math. USSR Acad. Sci., 1979.

9. V.A.Galaktionov.- Differentsialn. Uravn., 1980, v. 16, no. 9.

10.V.A.Galaktionov.- Dokl. Acad. Nauk. SSSR, 1980, v. 251, no. 4.

11.N.V.Zmitrenco, S.P.Kurdjumov.- Prikl. Meh. i Tehn. Fis., 1977, no. 1.

12.N.V.Zmitrenco, S.P.Kurdjumov, A.P.Mikhailov, A.A.Samarskii. - Pisma v Zh. Eksper. i Tehn.Fis., 1977, v. 26, no. 9.

PLASMA FINITE MASS COMPRESSION AND RAREFACTION REGIMES
PERMITTING A TIME-REVERSE IN A DISSIPATIVE MEDIUM

N.V.Zmitrenko, S.P.Kurdyumov

Keldysh Institute of Applied Mathematics,

Academy of Sciences, Moscow, USSR

1. It is known that in a general case revers of time is impossible in a macroscopic dissipative medium. However there are examples when a rarefaction (a "direct" motion) and compression symmetrically inverted with respect to this rarefaction (an "inverse" motion) can be feasible from the physical point of view. In this case the space profiles of all the values (except for the velocity profile signs) in the both processes coincide. Their change with time in the compressed mass repeats all the states of the system, which occured in the case of mass scattering, but in a reverse order. For example the compression without any shock waves [1] considered within a self-similar problem [2,3] is such a process. The same self-similar problem with a heat conductivity and a heat source gives another example of an open dissipative system where mutually-symmetrical motions have a real physical sense.

2. Let us briefly describe the results of investigation of the self-similar problem [2,3]. We consider one-dimensional motions of a finite mass M_0 accomplished under the action of a spherical, cylindrical or plane piston for a set of gas dynamics equations written in lagrangian variables (mass x and time t) and involving heat conductivity and a heat source in power dependence of temperature T and density ρ. The total mass $M_t = (2\pi N + (1-N)(1-N/2))M_0$, where N =0,1,2 for the cases of plane, cylindrical and spherical symmetry. A self-similar solution corresponds to the separation of variables x and t and the time dependence has a power form determined by a law of the piston motion $r_{\ast} \sim t^n$. The parameter n is fixed by a form of the dependence of the heat conductivity coefficient and the heat source upon T and . Such variable separation describes both the rarefaction (then $0 < t < \infty$, $t \to \infty$) and the compression (then $-\infty < t < 0$, $t \to 0$). The value profiles are determined by a set of ordinary differential equations (a "self-similar" system). These equations are the same for both a rarefaction problem and a compression problem, differing only in the sign of the expressions for the heat conductivity and the heat source. The sign is negative for the compression problem.

3. The mutual-symmetrical motions (i.e. solutions with the same value profiles for the compression and rarefaction) correspond to the same solutions of the "self-similar" system. An investigation shows that if a "direct" motion has a parameter $n = n^{(1)}$ and an adiabatic exponent γ_1 then the "inverse" motion has to have the parameters $n^{(2)}$ and γ_2 such that

$$n^{(2)} = n^{(1)} = n, \quad n_{\gamma}^{(2)} = -n_{\gamma}^{(1)} \qquad (1)$$

for the execution of time reverse processes in the system.

Here

$$n_{\gamma}^{(\alpha)} = \frac{2(\frac{n}{n_{\ast}^{(\alpha)}} - 1)}{\gamma_{\alpha} - 1}, \quad n_{\ast}^{(\alpha)} = \frac{2}{2 + (\gamma_{\alpha} - 1)(N+1)}$$

4. Formula (1) leads to the following relation-ship between γ_1 and γ_2 :

$$\gamma_2 = 1 + (\frac{1}{y} - \frac{1}{\gamma_1 - 1})^{-1}, \quad y = \frac{1 - n}{n(N+1)} . \qquad (2)$$

This dependence is represented in Fig.1 for the specific magnitudes of n and N. It follows that the mutual-symmetrical motions are possible only at $n \leq 1$ ($y \geq 0$), since it is naturally to demand $1 \leq \gamma_{\alpha} < \infty$. The physical unreal branch of hyperbola (2) is shown in Fig.1 by a dashed line. On this branch either $\gamma_1 < 1$, or $\gamma_2 < 1$.

5. The change of the entropy S_t is given by [2,3]:

$$\frac{dS_t}{dt} = 2M_t \cdot c_v (\frac{n}{n_{\ast}} - 1)t^{-1}, \qquad (3)$$

where c_v is a specific heat. The case of the equality $\gamma_1 = \gamma_2$ (the point C in Fig.1) corresponds to the motions with a conservation of the entropy (in this case it follows from (2) that $n = n_{\ast}$) and the "direct" and "inverse" motions are feasible for the same medium with the same adiabatic exponent γ. An analitic solution [1-3] was obtained for this case. The γ_1 and γ_2 values are different in a general case, when the dissipative effects in the medium fix the exponent $n \neq n_{\ast}$. From (2) it follows that if $n_{\ast}^{(1)} > n$, then $n_{\ast}^{(2)} < n$ and vice versa, i.e. the sign dS_t/dt in the "direct" and "inverse" motions is the same according to (3). It has to be like this in problems with the same profiles of a dimensionless temperature, i.e. the same signs of a heat flux through the piston. Thus, by choosing medium parameters (γ) and under the specific boundary regimes and initial data it is possible to implement the processes going in the opposite time directions in two open dissipative macroscopic systems, as if they are reversed in time.

References

1. Kidder R. - Nuclear Fusion, 1974, V.14, N.1, p.53-60.

2. Zmitrenko N.V., Kurdyumov S.P. - In: Problemy lazernogo termoyadernogo sinteza, Moscow, Atomizdat, 1976, p.279-294.

3. Zmitrenko N.V., Kurdyumov S.P. - Zhurnal prikladnoy mekhaniki i tekhnicheskoy fiziki, 1977, N.1, p.3-22.

FIG. 1
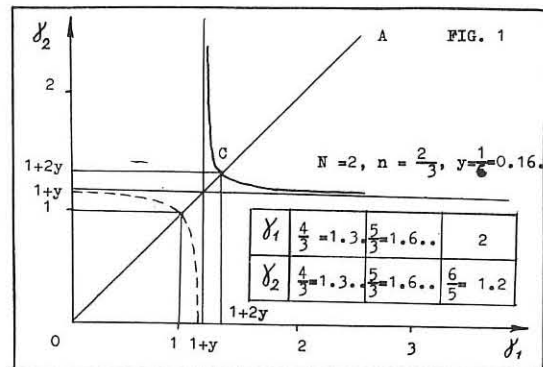
THE MOTION OF THE PLASMA HEATED BY POWERFUL PROTON BEAMS

A.V.Dobkin, T.B.Malyavina, I.V.Nemchinov

Institute of Physics of the Earth of the USSR Academy of

Sciences, Moscow, USSR

Recently, much attention has been given to the use of intense ion beams for inertial confinement fusion. Target proton beam irradiation may be also interesting for the other scientifical and technological purposes. At the high temperatures target ablation layers which often consists of the high or middle atomic number element are highly, but not completely, ionized. Under such conditions the plasma thermal radiation effects are able to play consideribIe role.

We have considered plasma corona dynamic of the proton beam which power density is in the range $q_0 = 10^{10}-10^{14}$ w/cm², the proton energy is in the range $\varepsilon_o \sim 0.1-10$ MeV, impulse time is of the order of $\tau \sim 0.1-1$ mks and plasma temperatures $T \sim 10-100$ eV. Plasma dynamic will be onedimensional (plane), unless the thickness of the plasma layer x is small in comparison with the target radius r_o and with the beam radius R. In this case, onedimensional gasdynamic computer program has been used. The program involves the solution of the radiation-transfer equations[1], energy deposition due to the proton collisions with bound and free electrons [2], target ablation. When the time is increasing, the heat radiation fluxes are growing and can reach the order of the beam energy fluxes. Temperature growth stops. Large part of the heat radiation energy about 20-50% of the beam energy leaves plasma for vacuum, which is accordance with the estimations [3]. The flux radiation from the high temperature corona incidents on the target results in its additional ablation. If the target is sufficiently thin, the plasma cloud will expand and irradiate in both directions: either forward or backward. For example, at the fig.1 computer results are presented for the interaction of the proton beam ($\varepsilon_o = 1$ MEV, $q_o = 10$ GW/cm²) with the aluminium foil, which initial thickness ($m_o = 4$ mg/cm²) is equal to the proton range in the cold material. Plasma parameters: T – temperature, P – pressure, u – velocity, q_p – proton power density, q_r – heat radiation power density, m – plasma mass – are presented at the irradiation time t = 0.25 mks, when x ≈ 1 cm.
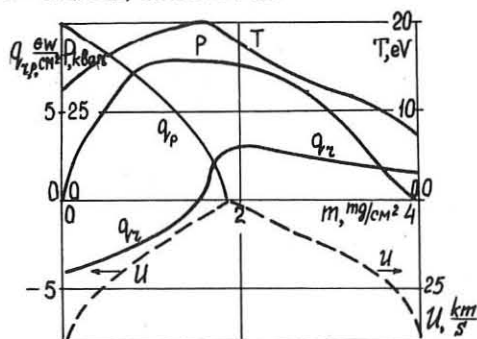
Fig. 1

When x of the order of r_o or R, the plasma density is decreasing faster then in the plane case. External layers becomes transparent for the particles. Quasi-stationary regime of the plasma motion and heating occurs, as well as in the case of laser irradiation [4,5]. Let us consider uniform irradiation of the spherical target of the radius r_o by the powerfull proton beam. Quasy-stationary spherically simmetrycal plasma dynamics is described by the method [4,5]. At the radius r_* where the velocity of sound is equal to the velocity of plasma, the relationship between the "differential" proton range $l = \varepsilon /(d\varepsilon/dr)$ and the radius r_* takes place: $r_* = \lambda l_*$, where λ is of the order of unity. The parameters in this critical point are described by the subscript (*). Computer results of the stationary corona are presented on the fig.2. The aluminium sphere of the $r_o = 1$ cm is irradiating by the proton beam with $\varepsilon_o = 1$ MeV, $q_o = 22$ GW/cm².
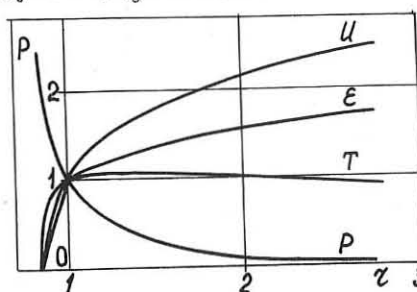
Fig. 2.

Plasma parameters are divided by their quantites at the critical point ($\varepsilon_* = 500$ KeV, $T_* = 20$ eV, $u_* = 23$ km/s, $P_* = 6$ kbar, $r_* = 1.2$ cm). Computer results of the stationary regime can be presented in this way:

$$P_o = 2.3\, q_o^{0.6}\, r_o^{-0.4}\, \varepsilon_o^{0.75}; \quad T_* = 5.6\, q_o^{0.4}\, r_o^{+0.4}\, \varepsilon_o^{-0.6}$$

where scale of the quantites are the following: P_o – kbar, q_o – GW/cm², r_o – cm, ε_o – MeV, T – eV. The electron conductivity may by sufficient for rather high T_*. For example at the $q_o = 5 \cdot 10^4$ GW/cm², $\varepsilon_o = 10$ MeV and $r_o = 0.4$ cm, when $T_* = 100$ eV, the fluxes of the electron conductivity are about 30% of the q_o, being the same order as the heat radiation flux. In this case the pressure at the target is $P_o = 10$ Mbar plasma density is $\rho_* = 0.1$ g/cm³. Thus when the target is irradiating by the powerfull proton beam, considerable part of the beam energy can be transfered into the plasma corona thermal flux energy.

Literature

[1] Nemchinov I.V., J.Prikl.Matem. i Mechan., v.34, №4, 1970, p.706-721.

[2] Gott Ju.V. Interaction of particles with matter in plasma investigations, Moscow, Atomizdat, 1978.

[3] Dobkin A.V., Kosarev I.B., Nemchinov I.V., J.Techn. Phis., v.49, № 7, 1979, p.1405-1407.

[4] Nemchinov I.V., J.Prikl. Matem. i Mechan., v.31, № 2, 1967, p.300-319.

[5] Malayvina T.B., Nemchinov I.V., J.Prikl.Mechan. i Tech.Phis., № 5, 1972, p.58-75.

STUDY OF TURBULENCE SPECTRUM OF INHOMOGENEOUS
PLASMA HEATED BY A POWERFUL LASER

N.G.Basov, M.V.Osipov, A.A.Rupasov, A.S.Shikanov,

G.V.Sklizkov

P.N.Lebedev Phys.Inst., USSR Acad.Sci., Moscow

Data on energy distribution of plasma waves along the spectrum makes it possible to estimate quantitative yield of each of anomalous mechanisms of laser plasma interaction into the laser energy absorption and fast particle generation. An effective method for plasma turbulence spectrum diagnostics is the method of combination scattering of the probing radiation /1,2/. In the present work this method is used for studying the n_c (plasma critical density region $n_c \simeq 10^{21} cm^{-3}$) and $n_c/4$ regions for Nd-laser heating radiation. The experiments have been performed with nine-beam Nd-laser "Kalmar" at P.N.Lebedev Physical Institute. Laser radiation of $\sim$200J of energy was focused onto a spherical target. Pulse duration was $\simeq$1ns. As the probing radiation we have used the second harmonic of heating light, obtained by doubling the frequency in KDR crystal (placed in one of the laser beams).The energy of the probing radiation was $\simeq$1J.The width of the heating and probing radiation spectra did not exceed $\simeq$5Å.The registration of plasma scattered radiation in various spectral regions has been performed in several directions by using transmitting optics and spectral devices which ensured space resolution of $\simeq$ 15 μm. In case the slit of the spectrograph crosses the target image in the probing region (as shown in Fig.1d),
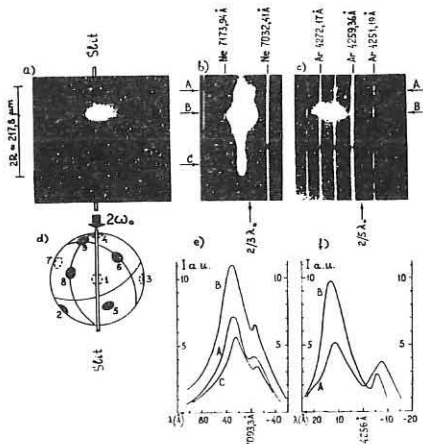
Fig. 1.

then the radiations near the frequencies $3/2\,\omega_o$ and $5/2\,\omega_o$ are observed (Fig.1b,c). Specificities of space localization of the observed radiations, their frequency shift by $\triangle\omega \simeq \omega_o/2$ with respect to the probing wave (equal to electron Langmuir frequency for $n_c/4$ region), and its two-component spectral structure (Fig.1b,c) give a possibility to associate the occurance of these radiations with the combination scattering of the probing wave ($t_2+1 \longrightarrow t_{3/2}, t_{5/2}$) on plasmons resulting from two-plasmon parametric instability ($t_o \longrightarrow 1 + 1$) within the $n_c/4$ region.Note that the radiation near $3/2\,\omega_o$ frequency was superimposed in spectrograms with the radiation of $3/2\omega_o$ harmonic, generated by plasma in the result of combination scattering (on the plasmons in $n_c/4$ region) of the heating radiation ($t_o + 1 \longrightarrow$

$\longrightarrow t_{3/2}$), and, thus, located along the whole plasma corona surface (Fig.1a,b). The intensity of the scattered radiation is determined by the energy spectral density of the plasma waves $W_\ell(K_\ell)$.Therefore simultaneous measuring of the intensity of the $3/2\omega_o$ and $5/2\omega_o$ lines of the combination scattering of the probing radiation and $3/2\,\omega_o$ harmonic allows one to find the dependence of W_ℓ on the wave number of plasma waves K_ℓ (Fig.2).

Fig.2.
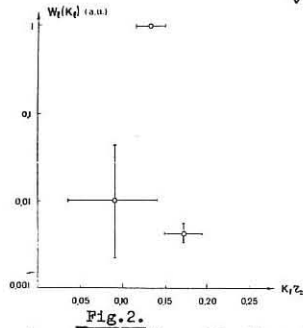
Plasmon wave number for each of the three radiations is determined from the law on pulse conservation at a scattering on the given angle. The estimations based on the performed measurements of the scattered radiation intensity show that within the $n_c/4$ region no more than 10% of the heating radiation is absorbed due to parametric instabilities .

In the scattered probing beam spectrum we have also found the radiation near $3\omega_o$ frequency (Fig.3) with a clearly seen two-component spectral structure /2/ (with respect to $\lambda_o/3$ both components are "red"shifted : 18Å and 2.5 Å, respectively). And at two-fold decrease in the heating radiation flux density the more shifted component disappeared, and only a weakly shifted and more narrow spectral component was observed. The

Fig. 3.
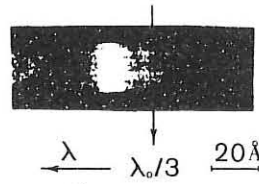
analysis of possible mechanisms of the formation of $3\omega_o$ radiation shows that it results from combination scattering of the probing wave on plasmons, excited by the heating radiation in $n_c(t_2+1 \rightarrow t_3)$ region. In this case the more shifted component near $3\omega_o$ occurs at scattering on parametrically excited plasma waves ($t_o \rightarrow 1+s$), and less shifted one on the plasmons linearly transformed from the heating radiation. The measurement of $\triangle\lambda_3$ (the shift of the narrow component due to Doppler effect with respect to $1/3\lambda_o$ allows one to estimate the rate of the motion u of the n_c region: $\triangle\lambda_3/\lambda_o = 5/9\,u/c$. For the value $\triangle\lambda_3 \simeq 2.5$ Å (Fig.3) $u \simeq 1.3 \cdot 10^7$ cm/sec. When using the given probing radiation with the frequency of $2\omega_o$ it turns to be impossible to obtain the dependence $W_\ell(K_\ell)$ for the n_c region, because of the coincidence of the other combination frequency (ω_o) of the probing wave scattering, and the heating radiation frequency. Thus, to obtain the turbulence spectrum in the n_c region one should slightly shift the probing wave frequency or measure the radiation intensity $3\omega_o$ for a number of scattering angles.

References

1. N.G.Basov,V.Yu.Bychenkov et al.Pis'ma v JETP, 30, 439, 1979; Phys.Lett., 77A, 163, 1980.
2. N.G.Basov, M.V.Osipov, A.A.Rupasov, G.V.Sklizkov, A.S.Shikanov. Pis'ma v JETP 33, 210, 1981 .

X-RAY EMISSION AND SPHERICAL TARGET IMAGE AT INHOMOGENEOUS RADIATION (THEORY AND EXPERIMENT)

N.G.Basov, N.N.Demchenko, A.P.Favorsky,[*] E.G.Gamaly,
A.A.Kologrivov, V.B.Rozanov, A.A.Samarsky,[*] A.S.Shikanov,
G.V.Sklizkov, V.F.Tishkin,[*] G.A.Vergunova

P.N.Lebedev Physical Inst., USSR Acad.Sci.,Moscow

* Appl.Math.Inst., USSR Acad.Sci., Moscow

The present paper is aimed at the analysis of the experiments on the target X-ray emission performed at "Kalmar" and other installations. "RIM-code (program) for the calculation of the target emission has been developed for this purpose.The stationary equation was solved at a given space-time density and temperature profiles.The ionization state, angular distribution and the outgoing radiation spectrum, the film illumination behind the pin-hole camera were determined in the program.

In the laser target the typical ionization times turn to be of the same order of magnitude as the time of heating andhydrodynamic expansion, and due to this fact the ionization process is non-stationary and non-equilibrium.Calculation takes into account the electron shock ionization, the three-body recombination and the photorecombination.

The effect of non-equilibrium and non-stationary ionization the radiation spectrum has been estimated by equation:

$$\varepsilon_{\omega\rho} = I_{\omega\rho} \left\{ \sum_{z,\gamma} k'_{z\gamma} \frac{1 - \bar{z}/\bar{z} \,\nu_{ion}}{1 + R_{z\gamma}} + \varkappa'_{b\omega} \right\},$$

where $I_{\omega\rho} = \frac{2\pi\hbar\omega^3}{c^2}\left(e^{\frac{\hbar\omega}{\kappa\tau}} - 1 \right)^{-1}$ is the spectral intensity of the equilibrium radiation; $k'_{z\gamma}$ and $\varkappa'_{b\omega}$, the coefficients of the ion photoabsorption with the ion charge z at γ level and bremsstrahlung absorption at frequency ω corrected by the stimulated emission;

$$R_{z\gamma} = \begin{cases} 0, & \hbar\omega < |E_\gamma|; \\ \nu_\omega/\nu_r, & \hbar\omega \gtrsim |E_\gamma|; \end{cases}$$

E_γ is the γ level energy; ν_{ion}, ν_r, ν_ω, the ionization rates at the electron shock, three-body recombination and photorecombination.

As the example we have calculated the radiation spectrum (the number of quanta in 4π ster.) of the glass shell target for the "Kalmar" experiments /1/. The target radius is R_0=70 μm; the wall thickness ΔR=2 μm; absorbed energy E_{ab}=20 J; laser pulse duration τ_ρ =2.5 ns (Fig.1). Under these conditions the K-shell state is defined from the ionization by the electron impact and photorecombination, the same processes determine the states of the inner electrons of L-shell, although for external L-electrons the three-body recombination turns to be the decisive one.
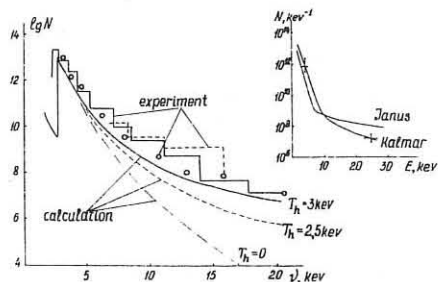
Fig. 1.

In this case the nonequilibrium has a strong effect on the emission of hard quanta $\hbar\omega \gtrsim 2.5$ keV, as for K-shell $R_{z\gamma} \simeq 300$, the role of non-stationarity here is not strong,

as $\bar{\dot{z}}/\bar{z}\cdot\nu_{ion} \simeq 0.1$. For $\hbar\omega \gtrsim 8$ keV the hot electrons' radiation becomes the main one. As follows from the experimental and theoretical data the total energy of the hot electrons amounts no more than 1% of the absorbed energy, and this corresponds to the resonance absorption contribution.

In the right corner of Fig. 1 are presented the spectra of the "compressed" shell ("Kalmar") and "exploding" shell ("Janus" /2/).

The analysis of the X-ray emission confirms the conclusion on the possibility of describing the "Kalmar" experiments within the frames of hydrodynamics and clas - sical transfer processes. To find the stability boundaries we have studied the experiment with a considerable inhomogeneity of the irradiation.
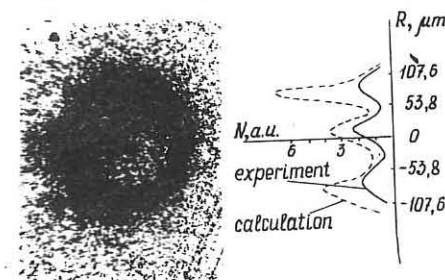
Fig. 2 .

Fig. 2 shows the pin-hole of a polysterene target under inhomogeneous irradiation. R_0 = 179 μm; ΔR=6.9 μm; E_{ab} = 17 J; τ_ρ =2.5 ns . The same figure presents the experimental and theoretical dependences of the photofilm (placed behind the pin-hole camera) illumination on the radius (in relative units).

The calculation of the absorbed energy distribution with account of refraction has been performed .
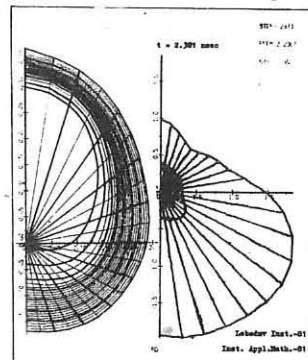
Fig. 3 .

Fig. 3 demonstrates a two-dimensional picture of the target motion at the moment t = 2.381 ns from the beginning of the laser pulse for the same experiment shown in Fig.2. Note the fact of a high symmetry of compression at a strong external non-symmetry of the radiation for moderate fluxes (low corona temperature).

References

1. N.G.Basov, A.A.Erokhin et al. Pis'ma v JETP, 1977, 26, 581-585 .

2. Laser Program Annual Report 1976, LLL,UCRL-50021-76 .

GENERATION OF SPONTANEOUS MAGNETIC FIELDS AT LASER
PLASMA COMPRESSION

E.G.Gamaly, I.G.Lebo, V.B.Rozanov

P.N.Lebedev Phys. Inst., USSR Acad. Sci., Moscow

Due to the violation of spherical symmetry in the laser target the occurance of thermocurrent sources and megagauss magnetic fields is possible. At laser plasma compression the fields are strengthened both due the compression $B \sim \rho/\rho_0$ and the development Reilegh-Taylor instability at the inner shell boundary. In [1] is presented the problem of the magnetic field generation in spherical targets at moderate radiation fluxes ($q \lesssim 10^{14}$ w/cm^2 for Nd -laser). At $\delta\rho/\rho \ll 1$; $X = \omega_B \tau_e \ll 1$ 2) $\partial/\partial\varphi = 0$, 3) the law of the instability development is known $(\delta\rho/\rho) \sim exp\{\int \tilde{\omega}_\ell dt\}$ 4) gas parameters change due to the adiabatic law we get the following system of equations:

$$\delta\rho/\rho = \sum_\ell (\delta\rho/\rho)_\ell P_\ell(\cos\vartheta); \quad B = \sum_\ell B_\ell P_\ell^{(1)}(\cos\vartheta)$$

$$\frac{dV}{dt} = \frac{C_s(1+\Phi(t))}{R^3} ; \quad \rho = \rho_0(R_0/R(t))^5 \quad (1)$$

$$C_1 = \frac{C^2}{4\pi\sigma_0}\frac{\ell(\ell+1)}{R_0^3} ; \quad C_2 = \frac{c}{e}\frac{2T_0}{\rho_0 R_0} ; \quad C_3 = \frac{4\pi R_0^5}{M_{sh}}\rho_0$$

$$\frac{d}{dt}\left(\frac{B}{\rho}\right) = -\left[C_1 R + \frac{C_4}{R^3}\right]\left(\frac{B}{\rho}\right) + C_2\left(\frac{\delta\rho}{\rho}\right)_\ell^0 exp\,\omega_\ell(t) \quad (2)$$

$$C_4 = \frac{2\partial_0''}{\partial_0 \delta_0 f_x}\frac{\tau_0 T_0 R_0^2}{m_e L_\rho} ; \quad \frac{dT}{dr} \sim \frac{2T}{R(t)} ; \quad \frac{d\ln\rho}{dr} \sim \frac{1}{L_\rho}$$

$\partial_0'', \partial_0 \delta_0$ — Braginsky coefficients;

$\Phi(t)$ - takes into account effect of the shell compression.

At the deceleration stage $\rho_g = \rho_{sh}$, if the gas and shell are compressed adiabatically, then $\rho_g = \rho_0\left(\frac{R_0}{R}\right)^5$

$$V = \frac{4\pi R^3}{3} ; \quad \left(\frac{\rho_{sh}}{\rho_{sh}^0}\right)^{\delta_{sh}} = \left(\frac{V^0}{V}\right)^{\frac{5}{3}} ; \quad \frac{d\rho_{sh}}{dt} = -\frac{5}{3f_{sh}}\frac{\rho_{sh}}{V} 4\pi R^2 \vartheta$$

The change of the shell inner energy $\frac{dE_{sh}}{dt} = M_{sh}\frac{\rho_{sh}}{\rho_{sh}^2}\frac{d\rho_{sh}}{dt}$, from this follows $M_{sh}\frac{dV}{dt} \sim -\frac{1}{\vartheta}\frac{dE_{sh}}{dt}$, and then

$$\Phi(t) = \frac{5}{3f_{sh}}\frac{M_{sh}}{\rho_{sh}^0 V^0}\left(\frac{V}{V^0}\right)^{\frac{5}{3f_{sh}}-1}$$

The solutions of (I)-(2) may be obtained in quadratures: $\frac{d}{dt} = -\vartheta\frac{d}{dr} ; \quad \vartheta_1 = \sqrt{V_0^2 - \frac{C_3}{R_0^2}} ; \quad R_m = \sqrt{C_3}/\vartheta_1$

$$\omega_\ell = \int\sqrt{-\frac{dV}{dt}\frac{(\ell(\ell+1))^{0.5}}{R(t)}}\,dt = (\ell(\ell+1))^{0.25}\,Arcsin\frac{R_m}{r}\Big|_{R_0}^{R(t)}$$

$$B_\ell = \left(\frac{\rho}{\rho_0}\right)\left[-\frac{C_2}{\vartheta_1 exp\,\omega_\ell(R_0)}\int\frac{r\,exp\,\omega_\ell(r)dr}{\sqrt{r^2-R_m^2}\,F(r)} \cdot F(R(t))\right]$$

$$F(r) = e^{\frac{C_1}{2\vartheta_1}\mu + \frac{C_4}{\vartheta_1 R_m^\ell}\gamma} \cdot \gamma^{\frac{C_1 R_m^\ell}{2\vartheta_1}} \quad (3)$$

$$\mu = r\sqrt{r^2-R_m^2} ; \quad \gamma = r - \sqrt{r^2-R_m^2} ; \quad \psi = \sqrt{r^2-R_m^2}/r$$

In the Eq.(2) the first term describes the diffusion, the second - the saturation owing to the appearance of a crossed term in the thermal flux; the third one describes the field generation due to the development of the Railey-Taylor instability. With the increase of magnetism the influence of the mechanism of field saturation,which is conditioned by a crossed term in heatconductivity,decreases and this may be effectively taken into account by the correction coefficient f_x in C_4 ($x \sim 1$, $f_x = 5$).

In the compressed plasma, even in the case the field source is suppressed $C_2 = 0$ the plasma magnetism grows due to compression $X \sim \frac{B}{\rho}T^{1.5}$; $\frac{B}{\rho} = const, T \sim R^{-2}$

Fig.1 presents the results of target calculation. Note, that in the calculation I the Larmor radius of α -particles at $B_m \simeq 20$ mGs is less than the free path and is comparable with the dimensions of the compressed region. The effective length of the α -particle in DT plasma increases, and, hence, the energy fraction transferred from α -particle to the fuel, also increases. $X = \omega_B\tau_e \sim 1,2$, and hence, the thermal flux reaching the wall will decrease and the mean full temperature will increase. Both effects may promote the better combustion conditions.

Fig.2 shows the calculation of the field for superposition of the harmonics $(\delta\rho/\rho) = \sum_\ell(\delta\rho/\rho)_\ell^0 exp\,\omega_\ell(t) \cdot P_\ell$

$R_0 = 200\mu, V_0 = -300$ km/s $(\delta\rho/\rho)_1 = .04; (\delta\rho/\rho)_2 = .0025$

$T_0 = .32$ keV, $\rho_0 = .42$ g/cm^3 $L_1 = 4, L_2 = 10$

$M_{sh} = 2\cdot10^{-4}$ g, $\alpha = \beta = 200$
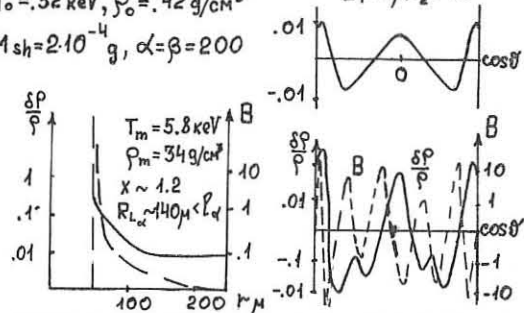
It is seen that the space and time distribution of the perturbations correlats to the field distribution (with the $\pi/2$ shift), and this may be used for the diagnostics of the instability.

For the observation of the magnetic fields in the compressed plasma three methods are proposed (Fig.3a,b,c).

a) by optical methods in a cone having the form of an "open book";

b) the measuring of the voltage drop and the currents on the walls of a conic shell target;

c) irradiation of the shell laser target by a 100 kev electron flux. Then at B $\sim$ 10 mGs, $R_{Le} \sim 1\mu$, the free path $\ell_e \gtrsim 10 \mu$ (for $\rho_{SiO_2} = 100$ g/cm^3).

Thus, one may observe the electron scattering at the magnetic fields. At 100 a current and the beam radius of 100 m and the life time of the compressed target 10^{-10} sec about $N_e \sim 10^6$ electrons should undergo scattering.

Faraday effect
$\Delta\varphi = V \cdot \ell \cdot B$
V - Verde coefficient
a)

$B = \frac{2I}{cr}$
$E_e \sim \frac{\nabla p_e}{N_e c}$
$V \sim 100V, T \sim 0.1$ keV; $\rho \lesssim 100 \frac{g}{cm^3}, \ell_e \gtrsim 10\mu$
b)

$I = 100A$
$B \sim 10$ mGs, $R \sim 1\mu$
c)

1. I.G.Lebo etc. Preprint FIAN N 68, Moscow, 1980
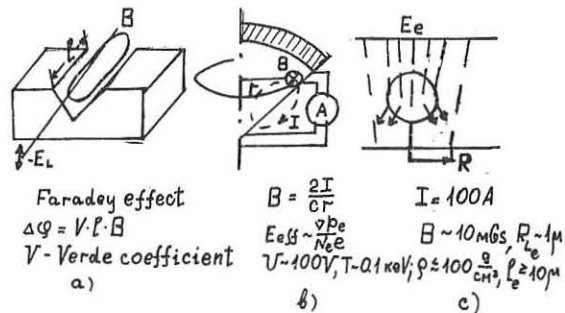
XUV RADIATION TRANSPORT IN LASER IRRADIATED
HIGH-Z METAL FOILS

J. Mizui, N. Yamaguchi and S. Takagi
Institute of Plasma Physics,
Nagoya University,
Nagoya 464, JAPAN
and
K. Nishihara
Institute of Laser Engineering,
Osaka University,
Suita 565, JAPAN

Abstract

Spatially resolved XUV spectra were measured from the rear side of gold foils irradiated with 1.05-μm wavelength, 100-ps pulses at intensities of 3×10^{14} W/cm^2. In the energy range of 0.1 to 1.0 keV the radiation intensity decayed exponentially with foil thickness up to 1 μm but remained almost constant over the range of 1 to 6μm. These results indicate that ablation by the radiation heat flux is occurring.

Emission and reabsorption of XUV radiation play an important role in high-Z plasma energy transport. Conversion efficiencies from laser energy to XUV radiation energy have been measured with multichannel x-ray diodes and range from 15 % to 2.3 % for laser intensities of 10^{14} to 10^{16} W/cm^2 and gold targets.[1,2] The spectrum has been shown to be Planckian with color temperatures ranging from 66 to 134 eV. Under the assumption that the radiation is black-body with a color temperature of the same order as the plasma temperature, and using a diffusion approximation with the Rosseland bound-free mean free path, we can estimate the ratio of radiation to thermal electron heat flux to be much greater than one. Under these conditions ablation of the plasma by the thermal radiation can occur.[3] We report on a direct measurement of the transport of XUV radiation through high-Z (gold) and low-Z (aluminum) foils.

The experiments were performed on the HALNA Nd: phosphate-glass laser system with an output energy of 7 to 15 J in a 100-ps full width at half maximum pulse. The laser output was focussed to a 200-μm diameter spot with an F/1.33 aspheric lens, giving an intensity of 3×10^{14} W/cm^2. Targets were 5-mm wide foils of gold or aluminum with thicknesses from 0.5 to 10 μm. The spectrum was measured using a grazing-incidence (88°) spectrograph with a 2-m radius gold coated concave grating.

The XUV radiation intensity from the rear surface is plotted as a function of foil thickness in Fig. 1. The intensities are measured at 52.4 Å (Al XI, $2p^2P - 3d^2D$) and 50.0 Å (continuum) for aluminum and at 47 Å (many closely spaced lines) for gold. For aluminum (a) the intensity decays exponentially with a scale length of 0.69 to 0.80 μm and goes to zero at 3 μm. For gold the intensity also decays exponentially initially with a scale length of 0.20 μm, but for thickness from 1 to 6 μm the intensity remains almost constant (b). The exponential decay scale lengths are several times larger than the absorption lengths for

the unionized target materials, but are consistent with the absorption lengths in highly ionized material. Suprathermal electron heating is also another candidate to explain the exponential part of the decay curves. However it is difficult to account for the gold target plateau by these mechanisms. This plateau is only observed in the gold target where the XUV radiation flux is expected to be greater than the thermal electron flux. From our estimates we can conclude that there is a plateau in the rear-side temperature of many tens of eV which is almost constant for Au foil thickness from 1 to 6 μm.

When the outward radiation flux is as large as observed for the Au targets[1,2] and the target is optically thick to the radiation, the inward radiation flux heats a plasma inside the target at tis front.[3] Ablation of the plasma can then occur. The ablation plays the role of a piston and drives a shock wave ahead of itself. In order for the high temperature of the rear-side plasma to be evaluated, the shock-heated front has to propagate to the rear surface within the emission time of the black-body radiation.

References

1. P.D. Rockett, W. Priedhorsky and D. Giovanielli; Report of Los Alamos Scientific Laboratory, LA-UR-80-2442 (submitted to Phys. Fluids).
2. M.D. Rosen, et al.; Phys. Fluids 22, 2020 (1979).
3. K. Nozaki and K. Nishihara; J. Phys. Soc. Japan 48, 993 (1980).
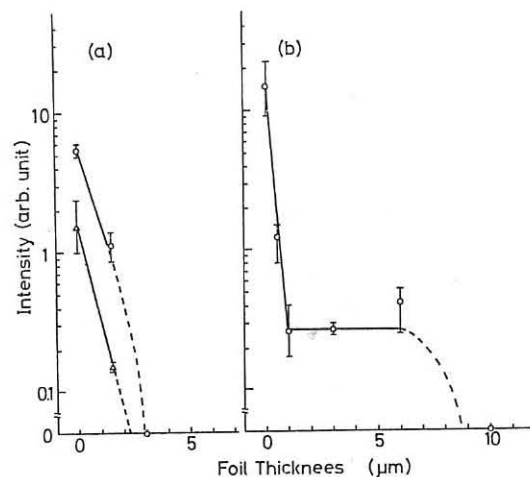
Fig. 1. Radiation intensities as functions of the foil thickness. In (a), open circles show the data for 52.4 Å (Al XI, $2p^2P - 3d^2D$) and open triangles the data for 50.0 Å (continuum) radiation from the aluminum. (b) shows the data for 47 Å radiation from the gold. The data for the 0 μm foil thickness are taken from the radiation of the laser-side plasma.

THE 2ω₀ SPECTRUM IN LASER PLASMA INTERACTION

E R WOODING, J ELAZAR[†], N A SAYED

ROYAL HOLLOWAY COLLEGE

UNIVERSITY OF LONDON, U K

[†]ON LEAVE FROM BELGRADE UNIVERSITY

The second harmonic spectrum has been studied when radiation from a neodymium laser has interacted with a solid target. The back-scattered radiation was collected by the lens which focussed the laser radiation on the target. By tilting the target, 2ω₀ radiation could be collected in the backwards direction and in the specular direction, as shown in Figure 1.

The laser was the Rutherford neodymium glass laser which produced pulses of 1.7 nanosec duration with energies up to 100 J and wavelength of 1.0525 μm. An f5 lens focussed the laser beam to a 100 μm diameter spot and also collected light scattered backwards. A paraboloid of focal length 63.5 mm collected light over an angle of 62°. It was coated with Al Mg F, but this coating deteriorated during the course of the experiment. The targets consisted of 1 mm steel pins with ends ground at various angles up to 45°. The ends were polished and coated with aluminium or gold. The radiation collected by the lens or paraboloid was steered by mirrors onto the slit of a grating spectrograph. It was necessary to attenuate the 2ω₀ radiation with neutral filters to prevent damage to the spectrograph slit and consequent production of intense plasma over the slit.

The spectra contained much fine structure. There was structure with a spacing of less than 1 Å, but irregularities in the paraboloid result in a coarse spatial structure.

The wavelength displacement of 2ω₀ is shown in Figure 2 to be between 10 and 12 Å towards the red for aluminium and 8 to 10 Å towards the red for gold, but there is no significant difference between the backscattered and reflected components. The displacement of the back-scattered radiation was measured at the centre of the image and that from the paraboloid at the specular angle.

Several explanations of the displacement have been presented[1] which depend on the interaction of a plasmon and a laser photon, the plasmons being generated by a linear process[2] or by parametric decay[3]. Cairns[4] argues that an ion acoustic wave propagating through the critical surface leads to coupling of the photon and plasmons whose frequency

differs from that of the incident light by integral multiples of the ion sound frequency ω_i. Using the ion acoustic dispersion relation:-

$$\omega_i = k_i c_s$$

where the wave number k_i is that given by Mannheimer and Klein[5]

$$k_i = \frac{2\pi}{L} \left(\frac{\omega_o}{\sqrt{3}} \frac{L}{v_e} \right)^{2/3}$$

with L the density scale length and v_e the electron thermal velocity. The wavelength displacement may then be calculated:-

$$\delta\lambda = \frac{\lambda_o}{4} \frac{\omega_i}{\omega_o}$$

Calculations of $\delta\lambda$ were carried out using values of density scale length, temperature and effective charge which corresponded to the irradiance and target material. Displacements of 3 to 7 Å were calculated. Cairns shows that as many as 20 components may occur with a spacing of ω_i, the first and second ones being of low amplitude. Hence the measured and calculated displacements are in agreement if the first or second components are lost in spectral noise.

Because the plasma parameters are related to the position of the turning point in the plasma, it was expected that there would be an appreciable angular dependence of the specular spectra. However, it is seen in Figure 3, that the displacement of the second harmonic from the precise value of 2ω₀ shows no obvious trend with angle of incidence.

The breadth of the 2ω₀ spectra depends on the ion wave number[4]. Experimental values of the measured breadth (FWHM) are plotted against irradiance in Figure 4. There is no significant variation of breadth with irradiance or atomic number of the target. The ion acoustic wave number is out of the range used in Cairns' computation so comparison with his result is not possible.

Acknowledgment

References

1. Basov N G, Bychenkov V Yu, Krokhin O N, Osipov M V, Rupasov A A, Silin V P, Sklizkov G V, Starodub A N, Tikhonchuk V T and Shikanov A S Sov J Quant Electron (1979) 9 1081-1102.

2. Piliya A D Sov Phys Tech Phys (1966) 11 609-614.

3. Perkins F W and Flick J Phys Fluids (1971) 14 2012-2018.

4. Cairns A J Plasma Phys (1979) 22 149-156.

5. Manheimer W M and Klein H H Phys Fluids (1975) 18 12 99-1307.
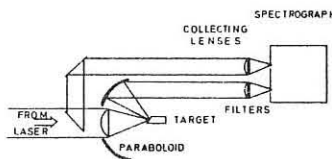
Figure 1. Optics for spectral analysis.
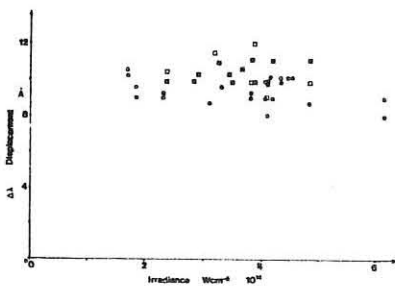
Figure 2. Displacement of 2ω₀ against irradiance.
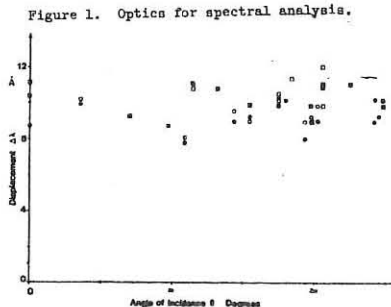
Figure 3. Displacement of 2ω₀ against angle of incidence.
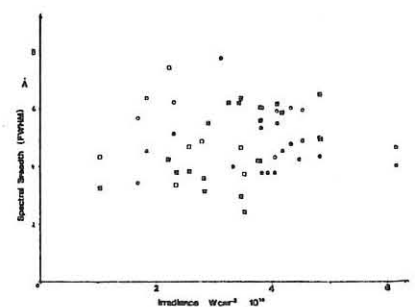
Figure 4. Breadth of 2ω₀ spectrum against irradiance.

G

REACTOR PROBLEMS
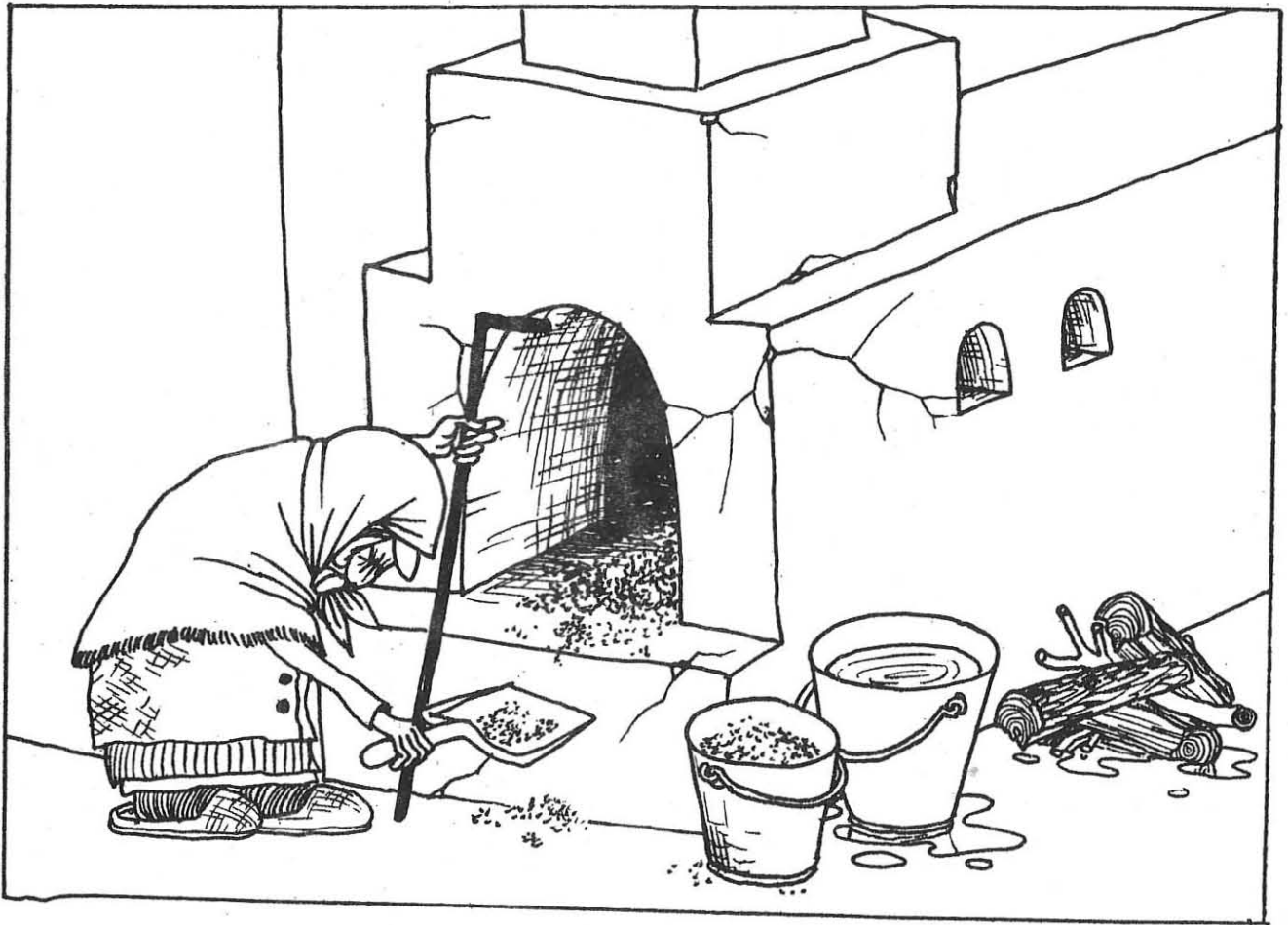
ALPHA - PARTICLES DYNAMICS IN A TOROIDAL PLASMA CLOSE TO

IGNITION

U.Carretta[+], S.Corti, G.Grosso, M.Lontano, R.Pozzoli
Istituto di Fisica del Plasma, CNR-Euratom Association
Mllan - Italy

[+]Centro di Studio per Ricerche sulla Propulsione e sulla
Energetica, CNR-Politecnico di Milano - Italy

Many aspects related to the role of alpha-particles in Tokamak devices have been widely investigated and reported in literature (see, e.g., the review paper /1/ and references therein).

However, a particular attention must be paid to the alpha-particles behaviour in Tokamaks near the ignition conditions, i.e., where the alpha-particles power released to the plasma balances both thermal and bremsstrahlung losses.

Here, we analyze the space-averaged energy evolution of alpha-particles produced during an ohmically-heated Tokamak discharge. We refer, in particular, to compact toroidal devices of the Ignitor type /2/.

The discharge is described by means of a zero-dimensional code which includes a thermal alpha population and an energy distribution function for energetic alpha particles.

Electrons, deuterons, tritons and neutrals are treated as fluid populations.

The dynamics of the discharge is coupled self-consistently with the primary of the transformer.

We note that the evolution of the alpha-particles energy distribution, correlated to the time behaviour of a Tokamak discharge, is not fully exploited in the literature.

As an illustration of the obtained results we report the evolution of the energy distribution of alpha-particles for a low and a high-density regime.
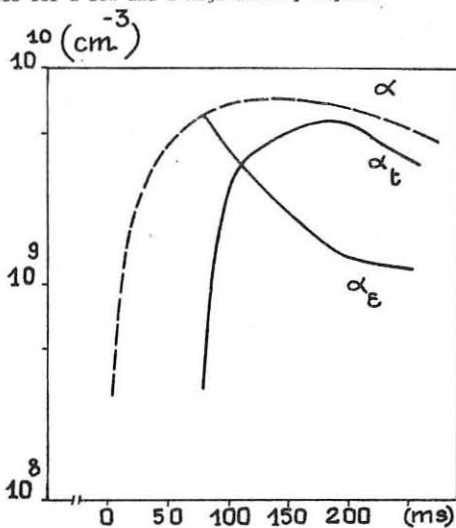
FIGURE 1 - Alpha-particles density vs. time for the low density case; α = total alpha-particles density; α_t = thermal alpha-particles density; α_{ε} = energetic alpha-particles density

The starting values of electron density and temperature in the two cases are: $n_e = 2 \cdot 10^{14} cm^{-3}$, $T_e = 4.8$ keV ; $n_e = 2 \cdot 10^{15} cm^{-3}$ and $T_e = 5.5$ keV , respectively. They represent the peak values obtained after using gas-puffing, ohmic heating and major radius compression.

The time behaviour of both thermal and energetic alpha particle densities for the first type of discharge is shown in Fig. 1 .

In this case ignition is not reached and the plasma temperature decreases continuously after the end of compression.
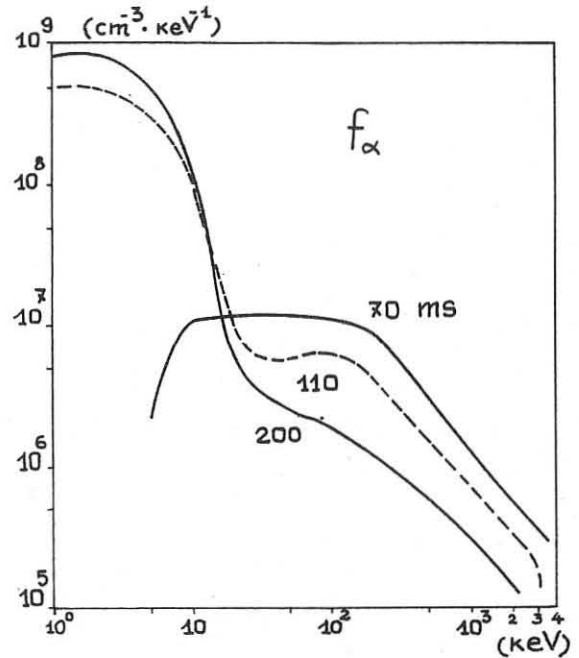
FIGURE 2 - Alpha-particles energy spectra at three times for the low-density discharge

The evolution of alpha-particles energy spectrum for the same low-density case is shown in Fig. 2 .

A quasi-stationary distribution is established in about 80 ms . The subsequent evolution leads to a complete thermalization due to the decrease of the alpha-particle source term. The high-energy behaviour of the distribution is of the type $f(\varepsilon) \propto 1/\varepsilon$, while at the intermediate range of energy the distribution can show a minimum as predicted
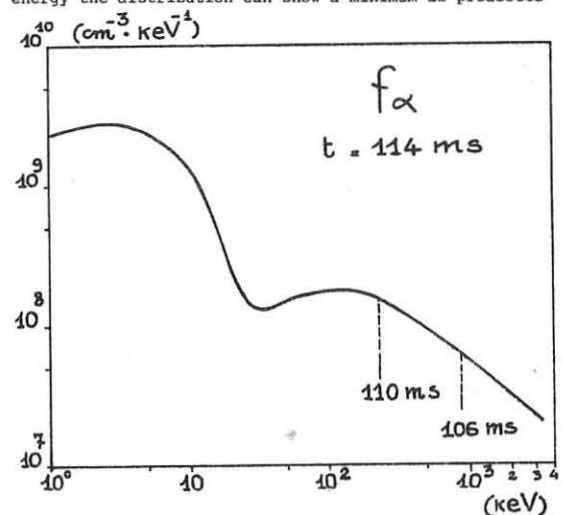
FIGURE 3 - Evolution of alpha-particles distribution for the high-density case

e.g. in ref. /3,4/.

The evolution of alpha-particles distribution in the second case is shown in Fig. 3 . In this case, the stationary state is reached in about 14 ms , the density of alpha particles is increasing in time leading the plasma to ignition.

REFERENCES

/1/ - Ya.I.Kolesnichenko, Nuclear Fusion, 20, 727 (1980)

/2/ - B.Coppi, Comments plasma phys. Controlled Fusion 3 Part E (1977) 47

/3/ - D.Pfirsch, Proc. Course on Phys. of plasmas close to thermonuclear conditions, Varenna (1979), CEC, Brussels, 1, 237

/4/ - Ya.I.Kolesnichenko, A.D.Fursa; Fiz.Plazmy 1, 806 (1975) Sov.J.Plasma Phys. 1, 442 (1975)

α- PARTICLE RIPPLE LOSSES DURING SLOWING DOWN IN A TOKAMAK REACTOR
By

D. Anderson, H. Hamnén, M. Lisak

Institute for Electromagnetic Field-Theory and
EURATOM-FUSION, Research (EUR-NE),
Chalmers University of Technology,
S-412 96 Göteborg, Sweden

1. Introduction

In a tokamak reactor, the ideal axisymmetry of the magnetic field configuration is destroyed by the finite number of toroidal field coils, which superimpose a small ripple component on the main toroidal field. Although the ripple is generally very small it may have significant effects on the confinement of very high energy particles, since these, if trapped in the ripple mirrors, will experience an uncompensated vertical drift which could carry them out of the plasma. For high energy fusion products, like α-particles, the drift time out of the plasma is generally much shorter than the characteristic time for collisional scattering out of the ripple mirrors. This leads to the appearance of a loss region in velocity space centered around $v_{\parallel} = 0$, [1].

The direct α-particle loss, i.e. the loss of particles "born" in the loss region, is usually negligible since the toroidal field ripple is very small. However, due to pitch angle scattering, particles tend to diffuse into the loss region during slowing down. The purpose of the present study is to determine the corresponding particle and energy losses.

2. Analysis

The dynamics of the α-particle slowing down process is assumed to be governed by the Fokker-Planck equation, [2]

$$\frac{\partial f}{\partial t} = \frac{1}{\tau_s v^2} \cdot \frac{\partial}{\partial v} [(v^3 + v_c^3) \cdot f] + \frac{\alpha v_c}{\tau_s v^3} \cdot \frac{\partial}{\partial \chi} [(1-\chi^2) \frac{\partial f}{\partial \chi}] + S \qquad (1)$$

where $\chi = v_{\parallel}/v$, $\alpha = Z_{eff}/(8 \cdot [Z])$, $[Z] = \sum_i Z_i^2 \cdot n_i \cdot \frac{m_p}{m_i} /n_e$ and

$$\frac{1}{\tau_s} = \frac{4\sqrt{2\pi}}{3} \cdot \frac{\sqrt{m_e}}{m_\alpha} \cdot \frac{e^4 \cdot n_e \ln\Lambda}{T_e^{3/2}} \qquad (2)$$

The critical velocity, v_c, at which electrons and ions contribute equally to the slowing down is given by

$$v_c^3 = \frac{3\sqrt{\pi}}{4} \cdot \frac{m_e}{m_p} \cdot [Z] \cdot v_e^3 \qquad (3)$$

The fusion processes can be assumed to generate monoenergetic particles with velocity v_f, isotropically in velocity space, implying that the source function $S(v,\chi)$ can be written

$$S(v,\chi) = S_0 \cdot \delta(v - v_f) \cdot K(\chi) \qquad (4)$$

where $K(\chi) = 1$ outside the loss region and $K(\chi) = 0$ inside.

It is convenient to divide the α-particle distribution function into two parts, f_{th} and f, where f_{th} describes the thermalized fraction and f the high energy tail, since f after some characteristic slowing down time becomes stationary, [3]. Our goal is then to solve for f the stationary form of (1), with the boundary condition $f(v, \chi = \pm\Delta) = 0$, where $\chi = \pm\Delta$ are the boundaries of the loss region, in the velocity interval extending down to $v = v_s$, where v_s is the velocity for which the drift time out of the plasma becomes equal to the scattering time out of the mirrors. It is assumed that no losses occur for $v < v_s$.

3. Results

By formally letting the width of the loss region approach zero, it is possible to obtain the exact solution to the problem, [4]

$$f(v,\chi) = \frac{S_0 v_f^2}{\tau_s} \cdot \frac{H(v_f - v)}{v^3 + v_c^3} \cdot \left| \sum_{n \text{ odd}} \frac{2n+1}{n+1} \cdot \left(\frac{1 + (\frac{v_c}{v_f})^3}{1 + (\frac{v_c}{v})^3} \right)^{\frac{Z_{eff} \cdot n(n+1)}{24 \cdot [Z]}} \cdot P_n(\chi) \cdot P_{n-1}(0) \right| \qquad (5)$$

where $H(z)$ is the Heaviside step function and $P_n(\chi)$ are the Legendre polynomials. The sum describes a step function in pitch angle that gradually smoothens out when we pass towards lower velocities, and the term in front of the sum is the solution we would get in the absence of the loss region. The particle loss fraction, defined as the ratio of the total number of particles passing the loss region boundaries per unit time to the number produced, is straightforward to calculate from the exact solution and we get

$$F_\ell = 1 - \frac{1}{4} \sum_{k=0}^{\infty} \frac{4k+3}{(k+1)^2} \left(\frac{1 + (\frac{v_c}{v_f})^3}{1 + (\frac{v_c}{v_s})^3} \right)^{\frac{Z_{eff}}{12 \cdot [Z]} \cdot (2k+1)(k+1)} \qquad (6)$$

The corresponding energy loss fraction, Q_ℓ, is defined analogously. However, eq. (5) is not very suitable for an analytic evaluation of Q_ℓ. The Fokker-Planck equation can also be solved using an approximate integral method, [5], which has the advantage of giving simple analytic expressions for particle and energy losses in good agreement with exact and/or numerical solutions. This yields for the energy loss fraction (for electron temperatures T_e less than 40 keV)

$$Q_\ell \approx 0.037 \, Z_{eff}^{1/2} \, T_e^{3/4} [1 - 0.26 \, T_e^{1/4}] \qquad (7)$$

where T_e is the electron temperature in keV.
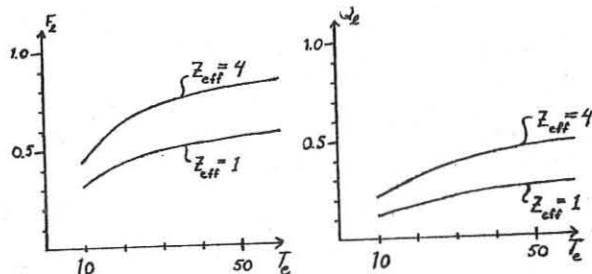
For typical Tokamak reactor parameters the particle and energy loss fractions amount to 40-60% and 15-30% respectively. The present analysis assumes the ripple to be homogeneous over the plasma cross section. If ripple inhomogeneities are taken into account, the losses may be effectively reduced, but on the other hand a spatial redistribution of the deposited α-particle power will occur, which may have significant effect on power deposition profiles, thermal equilibrium, and stability properties [4].

References

[1] V.S. Belikov, Ya. I. Kolesnichenko, V.A. Yavorskii, Sov. J. Plasma Phys., 3(3), May-June 1977, 273.

[2] J.G. Cordey, W.G.F. Core, Phys. Fluids 17, 8(1974), 1626.

[3] Ya. I. Kolesnichenko, Nucl. Fus. 20, 6(1980), 727.

[4] H. Hamnén, CTH-IEFT/PP-5.

[5] D. Anderson, H. Hamnén, M. Lisak, CTH-IEFT/PP-6.

ALPHA PARTICLE BOOTSTRAP CURRENT IN A TOKAMAK MAGNETIC AXIS REGION

V.Ya.Goloborodko, Ya.I.Kolesnichenko, V.A.Yavorskij.

Institute for Nuclear Research of the Ukrainian SSR
Academy of Sciences, Kiev, USSR.

Abstract: Alpha-particle bootstrap current generation has been shown to take place in a magnetic axis region of a tokamak-reactor. Due to this effect the theory of the stationary bootstrap tokamak has to be revised.

In Ref. [1] it has been shown that the α-particle drift losses in the tokamaks may result in the generation of the longitudinal plasma current. Apparently, this mechanism of the current generation may be used to create a steady-state tokamak-reactor with a small current, $I \sim 1$ MA. Under greater plasma currents the magnetic field confines the high energy α-particles produced in the central part of a plasma, and current caused by the α-particle loss is not generated near the magnetic axis. According to the neoclassical theory [2] the bootstrap current (J^b) is also canceled in the axis region because this current is proportional to the density and temperature gradient. That is why the steady state large current ($I \gg 1$ MA) tokamak reactor based on the use of the plasma processes only is considered to be impossible (i.e. the injectors or the HF-field generators are needed). In the present paper we show that actually there are no reasons for such pessimistic conclusion. Specifically, we show that because of the large radial excursions of the high energy α-particles the generation of the considerable plasma current in the magnetic axis region (including the axis) has to take place, this current being determined by the second (or more higher) radial derivatives of the plasma parameters.

Evidently, that the main part of the current is created by the α-particles with velocities greatly exceeded the thermal ion velocity (V_{Ti}). It enables us to consider only the α-particles with velocities $V > (m_i/m_e)^{1/6} V_{Ti}$, $m_{e,i}$ being the electron and ion masses. The distribution function of these particles (f_α) satisfies the following drift-kinetic equation:

$$(\vec{V}_d + \vec{V}_{\parallel}) \cdot \nabla f_\alpha = C_{\alpha e}\{f_\alpha, f_e\} + S_v \qquad (1)$$

Here $C_{\alpha e}$ is a collisional term describing the α-particle slowing down by the electrons, S_v describes the α-particle production, $\vec{V}_d$ is a particle toroidal drift velocity, $\vec{V}_{\parallel}$ particle velocity along the magnetic field. Taking into consideration that the particle bounce period is small compared with the characteristic slowing down time (τ_s) we get:

$$f_\alpha(V,W) = \int_V^\infty dv' v'^2 \langle \tau_s^{-1}\rangle^s \langle S_v \rangle \qquad (2)$$

where $\langle \ldots \rangle$ denote averaging over the particle drift trajectories; $W = W(J,v)$ is solution of the equation $dJ/dv = (J - \langle \Psi \tau_s^{-1}\rangle\langle \tau_s^{-1}\rangle^s)V^{-1}$, $J = V_{\parallel}/\omega_B + \Psi$, $\Psi = \Psi(r)$ being the flux surface function, $\omega_B = eB/(mc)$.

We use Eq.(2) to find the α-particle distribution function in the magnetic axis region: $r \ll \delta^{2/3} R$, where $\delta = 2 q(0) V_\alpha/(\omega_{B_\alpha} R)$, q is a tokamak safety factor, R a large torus radius, $V_\alpha = (2\mathcal{E}_\alpha/m_\alpha)^{1/2}$, $\mathcal{E}_\alpha = 3.5$ Mev. For this purpose we put $S_v = n^2 \langle \delta v\rangle \delta(v - V_\alpha)/(16\pi V_\alpha^2)$ assuming that all α-particles produced in the axis region are confined in a plasma, i.e. assuming

$$I > \frac{5.4}{\sqrt{A}} \quad (MA) \qquad (3)$$

where A is the torus aspect ratio. To carry out the averaging in Eq.(2) we use the near-axis particle trajectory analysis of Ref. [3]. Calculations yield the distribution function with the typical pitch angle ($\chi = V_{\parallel}/V$) dependence shown in Fig.1.

Now we can get the α-particle current in the magnetic axis region:

$$J_\alpha^b = -0.33 \frac{e_\alpha q^2(0) V_\alpha^3}{\omega_{B_\alpha}^2} \frac{d^2}{dr^2}(S\tau_s) \qquad (4)$$

where $S = n^2 \langle \delta v\rangle/4$. Eq.(4) has been obtained under the suppositions that the radial α-particle excursions do not exceed the characteristic width of the distribution $S(r)$ (i.e. $I \gtrsim 5$ MA). Otherwise J_α^b is determined by both the second and higher derivatives of $S(r)$. It follows from Eq.(4) that if $n(0) \sim 10^{15}$ cm^{-3}, $T(0) \sim 20$ Kev, $q(0) V_\alpha A/\omega_{B_\alpha} R \sim 10^{-1}$ and the radial distributions of the plasma temperature and density are parabolic then $J_\alpha^b \sim 100$ A cm^{-2}.

Note that Eq.(4) may be obtained up to O(1) factor by means of the qualitative analysis. For this purpose we have to take into account that $J_{\parallel} \sim -0.5 e|V_\parallel|(\Delta r)^2 d^2 n_\alpha^t/dr^2$ (n_α^t and Δr are the trapped particle density and the radial excursion) and $V_{\parallel} = V\delta^{1/3}$, $\Delta r = qV_\alpha/(\omega_B \delta^{1/3})$, $n_\alpha^t \sim \delta^{1/3} n_\alpha$, $n_\alpha \simeq S\tau_s$.

$\overline{J}_\alpha$ and the current before the thermonuclear reaction have the same direction. However the α-particle current gives rise to the oppositely directed electron current $\overline{J}_e = -2/Z_{eff}\overline{J}_\alpha$, Z_{eff} being the effective charge number. Hence, the alpha driven current $\overline{J}_{\alpha e} = \overline{J}_\alpha + \overline{J}_e$ can serve for a seed current in the steady-state tokamak if $Z_{eff} > 2$ only. Otherwise $\overline{J}_{\alpha e}$ has the opposite direction and may result in the unfavourable consequences.
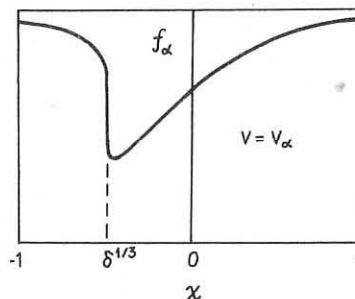
Fig.1.Alpha particle distribution function in the axis region versus the pitch-angle $\chi = V_{\parallel}/V$.

References.

1. Ya.I.Kolesnichenko, S.N.Reznik, V.A.Yavorskij. Eighth IAEA Conference on Plasma Physics and Controlled Nuclear Fusion Research, Brussel (1980), paper W-4.
2. A.A.Galeev, R.Z.Sagdeev, in Problems of Plasma Physics, 7, Consultants Bureau, N.Y. (1979) 1.
3. V.A.Yavorskij. Preprint KIYaI-77-4, Kiev, 1977.

INTOR POLOIDAL FIELD CONFIGURATION

Vabishchevich P.N., Degtyarev L.M., Drozdov V.V.

Keldysh Institute of Applied Mathematics,

Academy of Sciences, Moscow, USSR

Bespoludennov S.G., Zakharov L.E., Pistunovich V.I.

Kurchatov Institute of Atomic Energy,

Moscow, USSR

I. Introduction

The INTOR design raises the problem of creation and longtime maintenance of the equilibrium configuration by means of external coils. The necessity to obtain the high pressure configuration ($\beta \approx 6\%$) with the safety factor on the plasma surface q_p=2.I imposes strong restrictions on the plasma cross-section as well as on the pressure, toroidal current density and safety factor profiles. In the INTOR version with a single-null poloidal divertor the plasma cross-section is vertically asymmetric. Elongation and triangularity near the active null point of separatrix are larger then in the upper part of the plasma. The numerical computation of asymmetric MHD-equilibria, that includes estimation of the necessary EF (equilibrium field) coil currents at the different stages of discharge (through an increase in beta) is considered.

2. INTOR-Equilibrium

To obtain estimates on the EF coil currents we solved numerically the equation for the MHD-equilibrium with separatrix of the form

$$R = R_o + a\left(\cos\omega\left(\frac{1+\sin\omega}{D+\sin\omega}D\right)^\gamma - \frac{1}{2}\sin^2\omega(\delta_1+\delta_2+(\delta_1-\delta_2)\sin\omega)\right)$$
$$Z = Z_o + \frac{1}{2}a\sin\omega(k_1+k_2+(k_1-k_2)\sin\omega) \tag{I}$$

For the INTOR design configuration R_o=5.3 m , Z_o=0.6 m , a=1.2 m , the upper and lower triangularity δ_1=I.2 , δ_2=0.4, the upper and lower ellipticity K_1=I.5, K_2=I.7, the separatrix angle parameters D=I.3, γ=0.5.

The computations were made with the help of a code based on the transverse variable method [I] . In this paper we use nonorthogonal flux coordinates. The boundary of the current channel was assumed to be removed from separatrix, because on separatrix $q = \infty$. Within the current channel we use the following pressure and safety factor profiles:

$$p(\psi) = p_o\left(1 - \left(1 - \frac{\psi-\psi_p}{\psi_o-\psi_p}\right)\right)^2$$
$$q(\psi) = q_o + (q_p-q_o)\left(1 - \frac{\psi-\psi_p}{\psi_o-\psi_p}\right)^2 \tag{2}$$

Here ψ_o and ψ_p are values of the flux function ψ on the magnetic axis and on the current channel boundary, respectively, q_o=I, q_p=2.I.

We solve the self-coordinate task of the flux-conservation evolution. The value of the toroidal field B in the center of the camera (R=5.2m) was fixed (B_T=5.5T), and there was no surface current on the plasma boundary.

3. Results

We have demonstrated the possibility of creating the INTOR configuration with a single-null poloidal divertor by means of the external EF-coils. The field configuration with 9 coils is presented in Fig.I. We have investigated the influence of the plasma pressure on the separatrix shape. The results were used in the Soviet version of the INTOR project [2].

On the base of the above mentioned computations [2] we have solved the problem of optimization by the number and position of the EF coils in the case β_I=2.6. These coils are consistent with the space requirements and engineering restrictions.

The coil location together with the required ampere-turns are given in Table I.

Figure 2 shows the topology of the equilibrium field with the plasma parameters: β_I=2.6, β_ψ=2.2, β=5.7%, I_p=6.4MA. Here $\beta_I = \frac{2\int p dS}{\int dS}\left(\frac{\int d\ell}{\int B_p d\ell}\right)^2$, $\beta_\psi = \frac{8\pi\int p dS}{I_p^2}$, $\beta = \frac{2\int p dS}{\int B_T^2 dS}$. All the integrals are taken over the cross-section (S) and along the contour (ℓ) of separatrix.

From comparison of Fig.I and Fig.2 it is evident that the optimization of the coil positions allows to improve the geometry of separatrix without increasing the ampere-turns.

The computations were also made with the coil location that was proposed by the INTOR International Working Group (see Table 2, Fig.3).

The absence of coils in the inductor region ($R \simeq$ I.4m, $|Z| \lesssim$ 3m) may deflect down the inner diverter channel at the cost of increasing the ampere-turns.

Figure 4 (with $\sum_{i=1}^{12}|I_i| =$ II6.8 MAT) illustrates this possibility. The equilibrium configurations in all the figures were obtained with the above plasma parameters. Further moving the coils from the midplane of TC (toroidal coil) resulted in reducing the triangularity and expanding the inner divertor channel.

References

I Vabishchevich,P.N., Degtyarev,L.M., and Favorskiy,A.N., "Physika Plasmy" (Plasma Physics), 1978, 5,995.

2 INTOR /PHY/8I (March I98I), USSR.

Table I.

R(m)	I0,3	3,5	I,4	I,4	I,4	4,0	6,0	I0,3	I0,8	$\sum_{i}^{9}\|I_i\|$
Z(m)	5,4	6,9	3,6	−0,8	−4,2	−7,I	−7,I	−5,7	−5,0	
current MAT	−4,82	I2,22	I,2I	−I0,77	7,46	I6,97	20,35	−7,I7	−I4,46	95,53

Table 2

R(m)	Z(m)	current MAT
I2,5	5,4	−I,28
I2,5	6,0	−I,2I
4,7	7,I	I,23
3,8	7,0	I,63
2,5	6,6	I,59
I,35	4,95	I,46
I,35	4,I5	2,0I
I,35	3,35	2,28
I,35	2,55	I,45
I,35	I,80	−I,0I
I,35	I,05	−4,65
I,35	0,30	−7,48
I,35	−0,45	−7,42
I,35	−I,20	−4,55
I,35	−I,95	−0,95
I,35	−2,75	I,69
I,35	−3,55	2,64
I,35	−4,35	2,53
3,0	−6,9	3,72
4,7	−7,I	I5,83
7,2	−7,0	I0,24
I2,5	−5,5	−II,I6
I2,5	−4,9	−I2,22
$\sum\|I_i\|$		I00,26

Fig.1

Fig.2

Fig.3

Fig.4

D-T IGNITION IN THE TOKAMAK-REACTOR WITH DIVERTOR

Yu.L. Igitkhanov, A.S. Kukushkin, V.I. Pis-
tunovitch

I.V. Kurchatov Institute of Atomic Energy,
Moscow, USSR

Abstract. A self-consistent model for computing the balance of energy and particles in plasma for a tokamak-reactor with divertor has been developed. The D-T ignition feasibity in plasma with the INTOR parameters under the conditions of strong recycling and injection of a 75 MW neutral beam is shown.

The 1-D transport model for a core of the reactor is completed with the equations of transport through the serape-off layer. In this model, the plasma diffusion to the separatrix and the electron heat conductivity are described by the Alcator scaling and ion heat transport is taken to be the neoclassical one. Plasma heating is carried out by neutral beam injection, and fueling - with pellet injection and gas puffing. The 1-D model is chosen for simulating a scrape-off layer where plasma diffusion and heat transport across the layer are described by the hydrodynamic equations. The Bohm's coefficients for transversal diffusion and those for heat conduction are chosen. The heat and particles escape along the field lines in the divertor volume is taken into account as sink terms in the transversal transport equations. A kinetic integral equation for neutrals is solved together with the transport equations through the main plasma and the layer to determine the density and the temperature of hydrogen neutrals. The flux equal to the neutral backflow from the divertor volume is set as the neutral source at the wall. The possibility of a mirror and diffusive reflection of atoms from the wall is taken into account.

The solutions of the transport equations in the main plasma and in the scrape-off layer are brought to the agreement with boundary conditions at the separatrix. For the inside problem, the boundary values of temperatures and density (obtained from the solution of the problem in the scrape-off layer with incoming fluxes of energy and particles which are, in turn, determined by the inside problem solution) are set.

The D-T ignition problem for a tokamak with the INTOR parameters has been considered. Calculation results are presented in Figs. 1,2. 91% of fueling is provided by hydrogen neutrals from the wall and the rest 9% - by the pellet injection and with the neutral beam. The reactor heat power is 130 MW. Cyclotron radiation and bremsstrahlung power loss is 13 MW. About 30 MW are transferred to the wall by neutrals with mean energy of 280 eV. 50 MW power is captured into the divertor. The mean values of the plasma parameters in the main plasma region are: $T_i = T_e = 11$ keV; $\bar{n} = 1.2 \cdot 10^{14}$ cm^{-3}. The total ion flux through the separatrix $\phi_i^s \approx 9.7 \cdot 10^{22}$ s^{-1}. Densities of the heat fluxes from the main plasma at the separatrix are $q_i^s = 9.5$ W/cm^2; $q_e^s = 21$ W/cm^2. The total neutral flux from the wall $1.2 \cdot 10^{24}$ s^{-1} consists of the neutralized ion flow and of the wall-reflected neutrals (the reflection coefficient is equal to 1). The flux captured in the divertor $\phi_p = 3.7 \cdot 10^{23}$ s^{-1} about 40 times exceeds ϕ_i - flux originated from the pellet and beam injection. Such relation between fluxes will correspond to the recycling at the level $R_t \geq 97\%$, if one determines the recycling coefficient as $R_t = 1 - \phi_i/\phi_p$. The calculation shows that about 75% of the plasma recycling occurs in the scrape-off layer and the rest - in the region beyond the separatrix.

Dynamics of heating for the reactor with divertor in the strong recycling conditions with 75 MW neu-

tral beam power is shown in Fig. 3. At time instant t=6 s when the neutral beam is switched off, the plasma reaches the values close to the INTOR parameters. Reactor fueling with the neutral gas only, without pellet injection, turns out to be ineffective one because the main part of the gas becomes ionized in the scrape-off layer and escapes into the divertor volume.

The dependence of plasma parameters at the injection-switch-off instant (t-6 s) on the neutral density at the separatrix is given in Fig. 4. Feasibility of the ignition conditions, when the parameter $I = W^{\alpha}/W_{loss} \geq 1$ (here W^{α}, W_{loss} are power released in α-particles and total loss power, respectively), depends strongly on the neutral density at the separatrix and consequently on the pumping efficiency. To obtain stationary reactor operation one must have some burn control mechnism which is not considered in the present paper.

References

1. Kukushkin A.S. in: USSR contribution to INTOR Moscow, 1980, v.1.
2. Igitkhanov Yu.L., Kukushkin A.S., Pistunovich V.I., 8th Intern. Conf. on plasma phys. and contr. Nucl. Fus. Res., Brussels, 1980. IAEA CN-38-V-2-1.

Figure captions

Fig.1. Distribution of plasma n and neutral N_0 densities, ion T_i and electron T_e temperatures in the main plasma at t=6 s (the instant of injection switch-off, INTOR parameters).

Fig.2. The same across the scrape-off layer. T_0- the neutral temperature.

Fig.3 Heating dynamics of the reactor with divertor with 75MW NBI and INTOR parameters.

Fig.4 Dependence of parameter $I=W^{\alpha}/W_{loss}$ and mean values of density, temperature and β at t=6 s on the neutral density at the separatrix with constant pellet fueling rate.

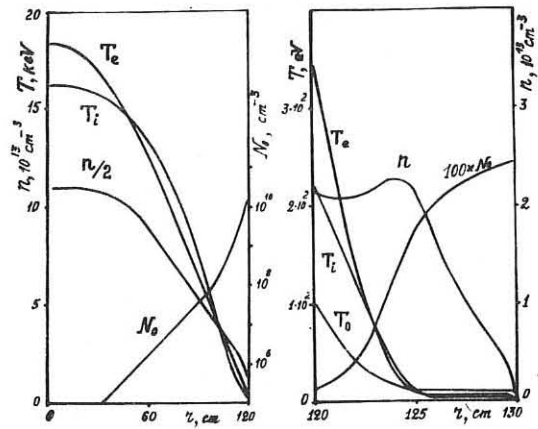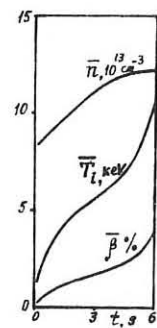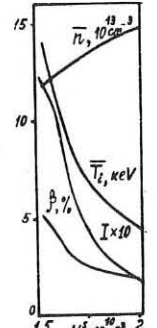Fig. 1.

Fig. 2.

Fig. 3.

Fig 4.

MODELLING OF START-UP IN THE INTOR

V.A.ABRAMOV, Yu.N.DNESTROVSKY, G.I.KROTOVA,
A.S.KUKUSHKIN, S.E.LYSENKO, G.V.PEREVERZEV,
O.P.POGUTSE, K.N.TARASYAN
I.V.Kurchatov Institute of Atomic Energy,
Moscow, USSR

The 1-D diffusion models are used for the considera-
tion of gas breakdown, ionization, current rise and addi-
tional heating phases. The dependence of minimum break-
down voltage from stray magnetic fields is discussed.

The start-up in the INTOR includes the phases: break-
down, ionization, current rise, additional heating to igni-
tion. Let us consider the gas breakdown. The experiments on
the present tokamaks show that breakdown occurs for $E/p \geqslant$
100 V/cm torr (E - induced electric field, p - gas pres-
sure). For this condition we may use the next expression
for electron value $\bar{\varepsilon}$: $\bar{\varepsilon}$ (eV)=0.2 E/p·exp (130 p/E).
The ionization frequency is given by $\nu_{ion} = 6E^2/\bar{\varepsilon}$. The
electron losses take place due to stray vertical magnetic
field $B_\perp$. For the condition $B_\perp \gg B_{min} = \frac{2 \cdot 10^{-2}}{R(cm)}$ ·
· $(\frac{E}{p} + 400)$ the losses due to toroidal drift may be neg-
lected (R - large radius). The loss frequency is given
by $\nu_{loss} = 3.5 \cdot 10^5 E/p \frac{B_\perp}{B_z a}$ (B_z - toroidal magnetic
field, a - chamber radius, cm). The electron losses due
to atomic processes and diffusion are negligible. For
these conditions breakdown criterion is given by $E > E_{min}$,
where

$$E_{min} = \frac{1.3 \cdot 10^4 p}{\ell n \left(\frac{530 p a B_z}{B_\perp} \right)} \qquad (1)$$

The dependence $E_{min} = f (p)$ for T-11 parameters (at
B = 14 G) is given in Fig.1. There is reasonable agree-
ment between theoretical predictions and experimental data.
It should be noted equation (1) gives E_{min} vs. $B_\perp$ more
weak then experiments show. The experimental data obtain-
ed at T-7, T-11, T-12 show that breakdown is influenced by
stray fields if $B_\perp \geqslant 10^{-3}B_z$. If the magnitude of stray field
in the INTOR is taken $B_\perp \sim 0.01$ T then we have $E_{min} = 0.48$ v/m
at $B_z = 5.5$ T and p=1.5 . 10^{-4} torr. Thus for the loop vol-
tage V = 100 V the breakdown criterion is fulfilled. The
desirable lowering of the breakdown voltage in the INTOR
may be realized. The T-7 experiments show that stable break-
down occurs at E = 1.5 v/m for proper conditions (for the
INTOR we have V = 50 V). The treatment of ionization and
current rise stages will be carried out in terms of 1-D
model taking into account heat and particles diffusion,
ionization losses and losses due to charge exchange, line
radiation of hydrogen and impurities. The neutral gas dis-
tribution is calculated from the kinetic equation. The cal-
culations showed that the ionization phase in the INTOR
differes from the similar phase in the T-10 device only in
some details. Large dimensions of the plasma column give
rise to a strong screening of the neutral flux and to an
increasing T_e in this region. As a result the profile $n_e(r)$
is nearly monotonous. By the end of the ionization phase
($\tau_i \sim 10$ ms) I $\sim$ 50 kA, T_e = 2 - 4 eV, $\beta_p \sim 0,2$. The
greater fraction of the Joule heating being spent for ra-
diation and charge exchange losses ($Q_{rad} \approx 70\%$, $Q_{cx} \approx 20\%$).
At $T_\sim \approx 2$ eV , $\tau_{sk} \sim 10$ ms and as a result profiles $n_e(r)$,

$T_e(r)$, $j(r)$ decrease monotonously at the radius. In this
phase the role of thermal conductivity and diffusion is
small, therefore, the uncertainty of the transport coef-
ficients used in the model is insignificant. Of great im-
portance is a correct account for radiation and ionization
losses mostly depending on the neutral distribution.

To prevent disruptions we must choice the current rise
rate $\dot{I}$ so that next condition have been fulfilled: $\dot{I} < I/\tau_{sk}$
In accordance with the condition the $\dot{I}$ is given by

$$\dot{I} = \begin{cases} 6 \cdot 10^6 \text{ A/s} & \text{at } I < 0.6 \text{ MA} \\ 1.2 \cdot 10^6 \text{ A/s} & \text{at } 0.6 < I < 6.4 \text{ MA} \end{cases} \qquad (2)$$

Two modes of the current rise are possible: 1) at first,
the current increases up to I = 6.4 MA and then the addi-
tional heating is switched on; 2) the current rise from
I = 4 MA up to I = 6.4 MA occurs during the additional
heating. The second mode of operation allows to save about
1 v.s. The additional heating at the lower current and, cor-
respondingly, at the greater value of q(a) results in the
extra ripple losses. The current rise stage simulation
is performed for the linear increasing of plasma density
(at t = 3 s n= 3.10^{13} cm^{-3}; this value is rather smaller
than the Murakami-limit). The calculations are carried
out for plasma with impurities ($n_{ox} = 2.10^{11}$ cm^{-3}, $n_{Fe}=$
= 5.10^{10} cm^{-3}) within the framework of corona model (non-
stationary effects are negligible). The impurities distri-
bution is uniform. The results show the basic ideas obtain-
ed in modelling of the T-10 type devices were also valid
in the current rise stage. The adopted impurities concen-
trations are sufficient for the reradiation of an energy
flux and a periphery cooling. The profiles $n_e(r)$, $j(r)$,
$T_e(r)$ are monotonous. During the ionization and current
rise phases the flux swing requirement is 92 V.s (77 V.s-
inductive component, 15 V.s - active component). Heating
to ignition is performed by the injection of neutral
atoms with the energy of the main component E_o =175 keV
and P_{total}=75 MW. The beams are injected at the angle 20°
to the normal. Dynamics of the reactor transition to the
steady-state operation at high initial density is given
in Fig.2. The time to plasma ignition is 5-6s and only
0,5% of the beam power is lost on the walls. The ripple
losses don't exceed 10%. Another scenario with density
rise during the heating phase suggests that 10-12% of
the beam power is directly deposited into the wall
during 2-3 s. The heating at the reduced initial densi-
ty does not accelerate the approach to the ignition. There-
fore the possible high plasma density is recommended by the
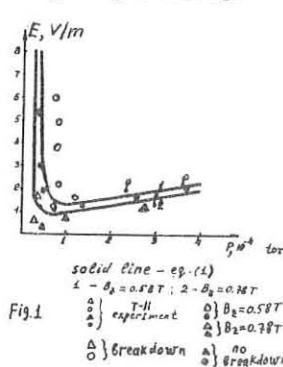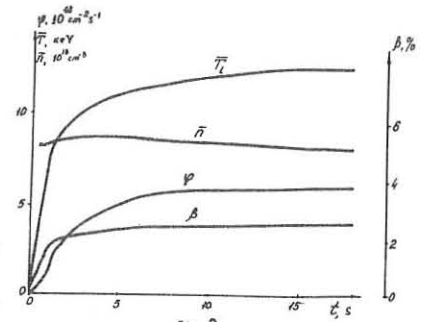beginning of heating.

Fig.1

solid line - eq.(1)
$1 - B_z = 0.58$ T ; $2 - B_z = 0.78$ T
T-11 experiment: $B_z = 0.58$ T, $B_z = 0.78$ T
breakdown, no breakdown

Fig. 2

ANALYTICAL STUDY OF THE SCRAPE-OFF LAYER AND THE PLASMA COLUMN PERIPHERY

T.F.Volkov, V.D.Kirillov

I.V.Kurchatov Institute of Atomic Energy,
Moscow, USSR

An abreviated version of /1/ is given this paper. The following problems are discussed: periphery of the plasma column - its boundary - scrape-off layer - the wall. The structure of a scrape-off layer includes a sink to the limiter along the field. Cooling by secondary electrons from a limiter plays a leading role in the energy sink (except its convective part), as a particle sink is determined by ions. Besides the discharge data $(R, \mathcal{L}, H)$ the scrape-off layer parameters depend on the position of the wall, transverse transport and, first of all, on the particle Γ_a and energy Q_{ia}, Q_{ea} fluxes across the plasma column boundary. These fluxes can considerably differ from those outcoming from the plasma bulk Γ_a, Q_{ia}, Q_{ea} due to the ionization and charge-exchange of neutrals, coming from the wall and from the limiter. The recycling value R_c can be determined as an average number of the particle returns into the plasma column till its absorption (evacuation) $R_c \cong \frac{\Gamma_a + \Gamma_{nc}}{\Gamma_0} - 1$. The neutral flux due to charge-exchange from the plasma column Γ_{nc} and other fluxes are determined from the balances in Fig.1 with simplifying assumption $T_e = T_i = T$:

$$\frac{\Gamma_{nc}}{\Gamma_0} \cong R_c = \frac{1 - S(1 - \hat{\Gamma}_w) - S_w \hat{\Gamma}_w}{S_w A + (1-A)[S(1 - \hat{\Gamma}_w) + S_w \hat{\Gamma}_w]}, \tag{1}$$

$$\Gamma_a / \Gamma_0 = 1 + (1-A) R_c, \tag{2}$$

$$\Gamma_{nc} / \Gamma_0 = A R_c, \tag{3}$$

$$Q_a / Q_0 = 2\mathcal{F}(1 - Q_R/Q_0)/(2\mathcal{F} + \Gamma_{nc}/\Gamma_a), \tag{4}$$

$$\frac{T_a}{T_0} \cong \frac{Q_a/Q_0}{\mathcal{F} \Gamma_a/\Gamma_0} = \frac{1 - Q_R/Q_0}{\mathcal{F}[(1-A)R_c + 1] + A R_c/2}, \quad T_0 \cong \frac{Q_0}{5\Gamma_0}, \tag{5}$$

$$\frac{Q_R}{Q_0} = \frac{\Gamma_0 R_c}{Q_0}[(1-A)\mathcal{E}_H + A \mathcal{E}_z], \tag{6}$$

where $\Gamma_{nc}/\Gamma_a \cong AR_c/[(1-A)R_c+1]$, and $\hat{\Gamma}_w = \Gamma_w/\Gamma_a$ is the particle flux fraction reaching the wall, S, S_w are the particle absorption and f reflection factors by the limiter and the wall, respectively, $\mathcal{E}_H$ and $\mathcal{E}_z$ is the energy necessary to ionize the atom of hydrogen and impurity ion. A formfactor $\mathcal{F}$ (Fig.2) does not depend on the outcoming fluxes Γ_0 Q_0 and it is determined by value $\hat{\Gamma}_w$, by the parameter α characterizing the relative secondary electron cooling, and by the presence of thermodiffusion. The minimal value of $\alpha = 1$ corresponds to the absence of heat conduction, as $\alpha \approx 15$ - to its maximal contribution. The plasma column albedo respective to neutrals $A \cong \Gamma_{nc}/\Gamma_a$ is a function of a ratio between the ionization and charge-exchange rates near the plasma column boundary. It can be considered equal to $A \approx 0.4$ in estimations, but in the more precise computations one should take into account its dependence on temperature which is of the order of that on the boundary T_a. The right-hand sides (1-5) do not practically depend on Γ_0 and Q_0, because one can neglect radiation Q_R, as its contribution does not exceed 20% /1/. For the precise estimations, one should take into account $Q_R[T_a, A(T_a)]$ in (5).

T_a/T_0 as a function at the wall position $\hat{\Gamma}_w$ is shown in Fig.3. The boundary temperature is determined, first of all by the recycling ($S=1$ correspond to an "ideal" divertor, $S=0$ - to the limiter). An electron cooling effect $\sim (\alpha - 1)$ thermodiffusion and effect of transport mechanism acception (in terms of $\mathcal{F}$) can be considered as corrections. In contrast to this, the boundary density n_a and scaling for a coordinate x_a (and hence, the scrape-off layer width $x_w = x_a \hat{x}(\hat{\Gamma}_w, \alpha, m, \ell)$) depend significantly on the values of transport coefficients:

$$n_a = \left[S^{-\ell} \frac{\sqrt{10 m_i}}{F_{m\ell}} \cdot \frac{\mathcal{L} \Gamma_a^{\ell + 5/2}}{Q_a^{\ell+1/2}} G \mathcal{F}^{\ell+1/2} \right]^{\frac{1}{m+2}}, \tag{7}$$

$$x_a = \left[S^{-\ell} (10 m_i)^{\frac{m+\ell}{2}} F_{m\ell} \frac{\mathcal{L}^{m+1} \Gamma_a^{\frac{3m+\ell}{2}}}{Q_a^{\frac{m+\ell}{2}-\ell}} G^{m+1} \mathcal{F}^{\frac{m+\ell}{2}-\ell} \right]^{\frac{1}{m+2}}, \tag{8}$$

where, the numbers m, ℓ and $F_{m\ell}(R, q, H)$ are the set by the power dependence of the diffusion factor on temperature and density $D = F_{m\ell} n^m T^\ell$. The second formfactor G is given in Fig.4.

Formulae (6), (7) and (8) are scaling laws which allow also to obtain the main parameters of the layer. The dependence n_a/n_0 for the Bohm transport ($m=0$, $\ell=1$, $F_{m\ell} = 3.9 \cdot 10^{13} H^{-1}$) at $A=0.4$, $S_w = 0.02$ is given in Fig.5. Scaling number n_0 will be equal n_a if recycling is absent ($\Gamma_w = 0$, $\Gamma_a = \Gamma_0$, $Q_a = Q_0$) and $\alpha = 1$. The position of the wall $\hat{\Gamma}_w$ and the property of a limiter S due to their effect on the recycling, can change the boundary density by more than the order of magitude.

An expression for a scrape-off layer width differs from x_a by dimensionless factor $\hat{x}_w$. Its precise value is given in /1/, but in estimations it can be taken equal 2-3, if $\alpha \approx 5$. Formulae (6-8) applied to T-10 or PLT type tokamak ($S=0$, $S_w = 0.02$, $\Gamma_0 = 10^{15} \text{sm}^{-2} \text{s}^{-1}$, $Q_0 = 2 W \text{sm}^{-2}$, $q=3$, $H = 35 \text{kOe}$, $R = 150 \text{sm}$, $\mathcal{E}_z = 500 \text{eV}$, $\mathcal{E}_i = 40 \text{eV}$, $f = 10^{-2}$) give values, dependent on the position of the wall.

$2 \text{sm} \leq x_w \leq 8 \text{sm}$, $45 \text{eV} \leq T_a \leq 10 \text{eV}$, $7 \cdot 10^{12} \text{sm}^{-3} \leq n_a \leq 10^{14} \text{sm}^{-3}$

One should note that analytical expressions for the temperature and density profiles for $T_e \not\approx T_i$ as well are given in /1/.

References

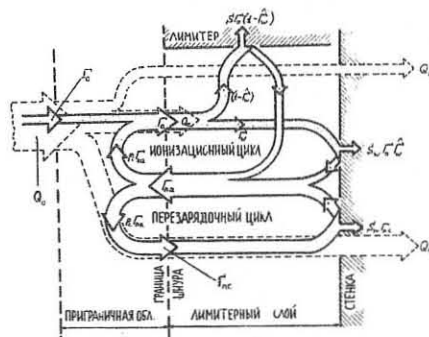1. T.F.Volkov, V.D.Kirillov. Model periferinykh sloev plasmy tokamaka. Preprint IAE-3358/8, 1980, Moskow.
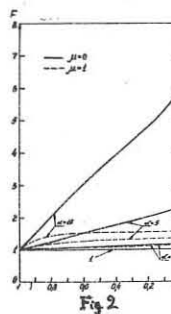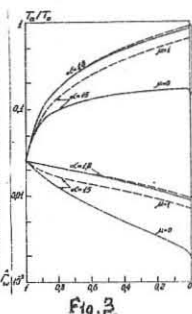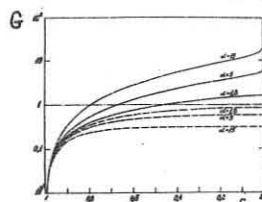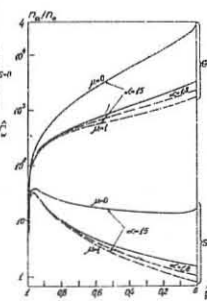
Fig.1

Fig.2

Fig.3

Fig.4

Fig.5

In Fig.2-5 Bohm transport with thermodiffusion ($\mu = 1$ ——), or without it ($\mu = 0$, ----) is given.

PLASMA EFFECT ON THE GAS CONDUCTANCE OF
A DIVERTOR CHANNEL

Yu.L.Igitkhanov, A.S.Kukushkin, A.Yu.Piga-
rov, V.I.Pistunovich

I.V.Kurchatov Institute of Atomic Energy,
Moscow, USSR

Abstract. The backflow of neutral atoms from the di-
vertor volume to the main chamber is shown to drop expo-
nentially with increase in plasma density and inflow mean
plasma velocity. The interpolation relationship for the
gas conductance of a cylindrical channel with plasma is
suggested.

Realization of the divertor operation with strong re-
cycling and pumping requirements depends significantly on
the real conductance of the divertor channel with respect
to the neutral backflow from a divertor volume to a main
plasma. Sputtering of the divertor throat with charge-
exchange neutrals depends on the level of "locking" the
backflow neutrals in a divertor volume.

It is well known that in a vacuum pipe or in the presence
of sufficiently rarefied plasma, when the neutral gas out-
flow can be considered as Knudsen one, the channel resis-
tance is connected with momentum loss due to collisions
of atoms with a wall. With the plasma density increase in
a channel, ionization and charge-exchange of neutrals have
a considerable effect on the conductance: ionization de-
creases the conductance of a channel, the effect of charge-
exchange being more complicated. On one hand, at the colli-
sions due to charge-exchange a gas momentum loss
decreasing the conductance occurs. On the other hand,
charge-exchange of slow atoms with ions in hot plasma
leads to the neutral mean free path increase and to a de-
crease in probability of ionization in the channel
thus increasing the conductance of a channel.

A quantitative calculation of these effects on the
channel conductance has been carried out numerically with the
Monte-Carlo method. The cylindrical channel of radius a
and length L was chosen as a model. The conductance of a
channel Σ was determined as a product of the apperture con-
ductance Σ_{app} and the neutral-pass-through-channel proba-
bility, $\Sigma = \Sigma_{app} \cdot C$, where $C = \varphi_{out}/\varphi_{in}$. C -
is the reduced conductance defined as the ratio between
directed outflow φ_{out} leaving the channel and in-
coming flux of atoms $\varphi_{in} = \frac{1}{4} n \bar{v}_T \pi a^2$. The ionization
was treated as an absorbtion, charge exchange - as inelas-
tic scattering of the neutral atom with a medium. Boundary
conditions allowed for the diffusive and mirror reflection
of atoms dependent on the angle and energy of an inci-
dent neutral /1/. The calculations has been made for atoms
of the D-T mixture. The temperature of the diffusively ref-
lected atoms was taken to be 3 eV (calculations had shown
a weak dependence on this temperature).

The reduced channel conductance C for various va-
lues of plasma temperature and density is given in Fig.1.
Distribution of the plasma parameters were taken to be con-
stant along the channel and parabolic one along the ra-
dius. The gas conductance of the vacuum pipe of the same
size calculated by the Dushman formula /2/ is plotted
there for the comparison. These results can be descri-
bed by the interpolation formula for the gas conductance
of a cylindrical channel

$$\Sigma = \Sigma_{app} \, exp(-L/L_D)/\left\{1 + \frac{3}{8}\left(\frac{L}{a} + \mu \frac{L}{L_D}\right)\right\} \quad (1)$$

where, $L_D = \sqrt{\frac{v_T^2 \tau_i}{v_{cx} + v_i + v_w}}$ is an effective diffusion
length connected with collisions both in plasma and with
the wall. Here, $v_T = \sqrt{\frac{2T}{M_i}}$ is the thermal velocity of plas-
ma ions; $v_i = n\langle\sigma v\rangle_i$; $v_{cx} = n\langle\sigma v\rangle_{cx}$ - ionization
and charge-exchange frequencies, respectively. The tem-
perature of neutral gas is supposed to be equal to that
of plasma. $v_w = \alpha \cdot v_T/a$ corresponds to the neutral-
-wall collision frequency. In the dense plasma limit $L_D \ll L$,
the channel conductance is determined by collisions with
plasma, and the neutral atom propagation becomes the dif-
fusional one /8/. It explains the appearance of the exponen-

tial dependence of the conductance on the plasma density. In
the opposite limiting case of rarefied plasmas $L/L_D \ll 1$,
the formula (1) converts to the Dushman formula. When $L \ll a$,
the conductance should depend weakly on the transversal
dimensions of the channel that is provided by an additio-
nal term in the denominator in formula (1). The coefficients
α and μ are chosen by the method of least squares and
they are found to be equal $\mu = 0.94$, $\alpha = 0.59$. For not ve-
ry long pipes, $L/a \lesssim 5$, and at plasma densities up to
10^{14} cm^{-3} the formula (1) describes the channel conductance
with an accuracy of 10÷15%.

The directed plasma flow effect upon the channel con-
ductance is illustrated in Fig.2. When plasma is dense
enough, neutrals can be locked in the divertor channel
due to the preferable backscattering during the charge-
exchange with ions of the incoming plasma.

Obtained in the case $\lambda \ll L$, the conductance depen-
dence, $exp(- M L/\lambda)$-like, on the parameter $M = v_0/v_{T_i}$
is in a good agreement with the values given in Fig.2.

References

1. JAERI-M8622, Jan.1980; Japan Contribution to the
   INTOR (1980).
2. Dushman S., Scientific foundations of vacuum
   technique, New York-London, 1949.
3. Igitkhanov Yu.L., Kukushkin A.S., Stakhanov I.P.,
   "Nuclear Fusion", 18, 1185 (1978).

Figure captions

Fig.1 Dependence of the reduced channel conductivity
C on the mean plasma density. Channel parameters:
lenght L=50 cm, radius a=20 cm. Mean plasma tempe-
rature T is equal to the temeprature of incoimng
neutrals T_o. Plasma rests.

Fig.2 Dependence of C on the plasma flow velocity V_0
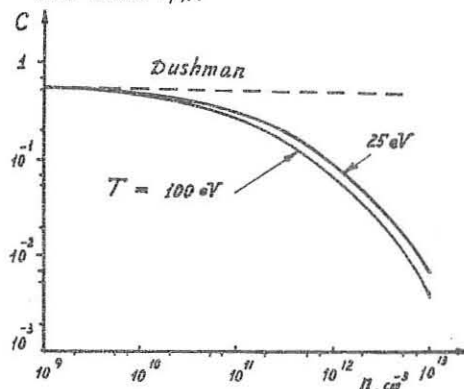(parameter $M = \frac{v_0}{v_T}$). Curves are plotted for diffe-
rent values L/λ.

Fig. 1
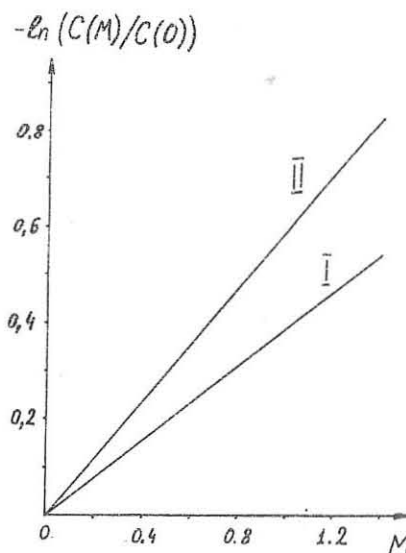
Fig. 2

A FEASIBILITY OF CURRENT PROFILE CONTROL IN
A TOKAMAK BY FUEL PELLET INJECTION

N.M.Vasil'ev, V.Eh.Lukash
Institute of High Temperatures
USSR Academy of Sciences

According to the results of conceptual design, the optimal plasma density value in a tokamak-reactor with moderate toroidal magnetic field equals 10^{14}cm^{-3}[1]. It is assumed usually that discharge creation as well as heating up to the ignition temperature are realised at the density value, which is lower by the order of magnitude that one mentioned above, afterwards plasma density being increased somehow up to nominal value. One can use gas puffing for this purpose. However it can result in a discharge disruption instability development due to current density profile picking caused by plasma cooling in the outer regions when the density exceeds certain critical value [2,3]. Fuel density increase in a tokamak chamber, after the discharge development is over, can be realised also by high-velocity injection of deuterium-tritium ice pellets. In this case it is possible to control somehow the space distribution of a cold fuel source by changing injection parameters, such as the pellet velocity, and injection frequency and its size. Thus it is also possible to influence electron temperature and current density distributions which are greatly responsible for the discharge disruption instability development.

This paper includes the simulation results of tokamak chamber fuel density increase after discharge creation stage by the injection of a single pellet. The objective of simulation is to estimate the dependence of plasma current density and electron temperature radial profiles on injection parameters.

The simulation was conducted by means of space-time dependent plasmaphysical model based on energy and material balance equations for charged and neutral particles with account for recycling of the latter near the wall [4] for a present generation tokamak with following performance:

- major radius, m 1
- minor radius, m 0,3
- toroidal magnetic field, T 2,0
- plasma current, MA 0,38

It was assumed that additional plasma heating was realised by a beam of fast deitons with 40 keV energy and 25 A current.

The following process scenarium was considered.

At the initial moment corresponding to the termination of plasma column creation the injector of neutrals is turned on. 30 msec later, the average temperature of ions reaching $T_i \simeq 1500$ eV, the pellet is injected into plasma. There were $4.5 \cdot 10^{19}$ particles in the chamber before "shot". This is corresponded to the averaged ion density of approximately $2 \cdot 10^{13}$cm^{-3}. Injection of pellets containing $1.7 \cdot 10^{20}$, $2.5 \cdot 10^{20}$ and $3.5 \cdot 10^{20}$ particles increased density up to 10^{14}, $1.4 \cdot 10^{14}$ and $1.8 \cdot 10^{14}$ cm^{-3} correspondingly.

Fig.1 shows $j(z)/j(0)$ and $T_e(z)/T_e(0)$ distributions along the chamber radius for the case of pellet injection with the velocity of 1000 m/sec corresponding to the moments t=40 msec and t=150 msec. One can see that in the case shown the region of maximum particle rate

is located at the central portion of plasma column - the pellet covers a distance of $(1,2 \div 1,4)$ column radius. Substantial distortion of plasma current density and electron temperature profiles is observed at t= 40 msec, distortion mentioned being increased with the size of injected pellet. However at t=150 msec j and T_e are distributed much more uniformly along the chamber radius.

The similar dependences for the case of pellet injection with the velocity of 200 m/sec are depicted on Fig.2. Here the region of maximum partical release is located at the column outside region, where plasma current and electron temperature distortions occur, so the distribution pattern is different in principle.

References

1. Vasil'iev N.M., Lukash V.Eh., Nedospasov A.V. e.a. Concept of tokamak-type reactor with high-temperature blanket. - In: Proc. of the 7th Int. Conf. on Plasma Physics and Contr. Nuclear Fusion Res., Innsbruck, 1978; Vienna, IAEA, 1979, v.3, p.379.
2. Equipe TFR, Nuclear Fusion, 1980, v.20, p.1227.
3. Mukhovatov V.S. Tokamaki. - V sb.: Itogi nauki i tekhniki. Fizika plazmy, t.1, tch.1, M., 1980, 6.
4. Vasil'iev N.M., Lukash V.Eh. Reprint IVTAN, N 7-50, 1979.

Figures

Fig.1. Radial distribution of j/j(0) and T_e/T_e(0) for injection rate of 1000 m/sec
(———— t=40 msec; - - - - t=150 msec)

Fig.2. Radial distribution of j/j(0) and T_e/T_e(0) for injection rate of 200 m/sec
(———— t=40 msec; - - - - t=150 msec)

RECYCLING EFFECT ON DIVERTOR PLASMA PARAMETERS
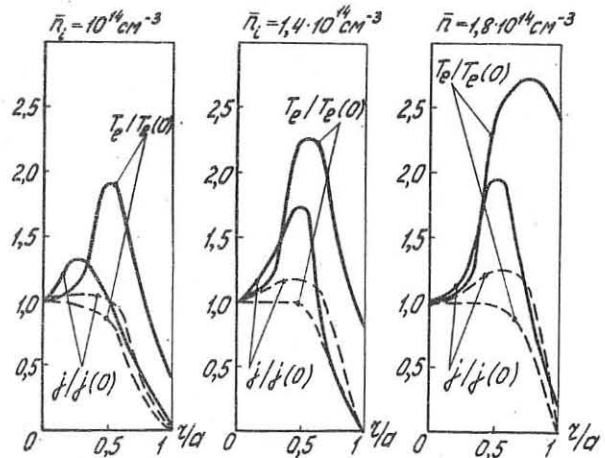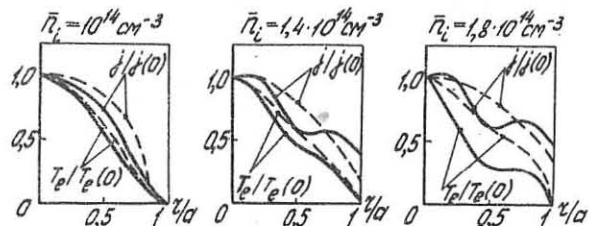
A.V. Nedospasov, M.Z. Tokar

Institute of High Temperatures of the USSR Academy of Sciences, Moscow, USSR

The main divertor functions will be plasma flow neutralization for the following exhaust of the unburnt fuel and helium and for the conformity of reactor plasma parameters with pumping system technical characteristics. In this work the plasma temperature and density in a divertor and conditions of such a conformity are determined on the base of the heat and particle balances with recycling on a collector plate.

Charged particles neutralization on the plate is a source of neutrals in the divertor layer. If there are no essential magnetic field lines divergence and plasma layer broadening owing to transverse diffusion in the divertor chamber, the equations of continuety and motion along the magnetic field are as follows:

$$\frac{d(nV_e)}{dl} = K_i n n_a , \quad \frac{d(nV_e^2)}{dl} = -V_s^2 \frac{dn}{dl} - K_{ex} n n_a V_e , \quad (1)$$

where 1 is the distance from the plate along the magnetic lines; n, n_a are the plasma and neutrals densities; k_{ex}, k_i are the charge-exchange and ionization constants; V_s is the sound velocity. Under the boundary condition $V_e(0) = -V_s$ Eqs.(1) have the solution

$$\left[\frac{nV_e}{\Gamma_e(0)}\right]^2 = (1+\beta)\left[\frac{n}{n(0)}\right]^{\frac{2\beta}{1-\beta}} - \beta\left[\frac{n}{n(0)}\right]^2 \quad (2)$$

where $\beta = \frac{K_i}{K_i + K_{ex}}$, $\Gamma_e = nV_e$.

The ratio $n_d/n(0)$ (n_d is the plasma density at the fully ionized region boundary) approaches to its maximum value $A = \left(\frac{1+\beta}{\beta}\right)^{\frac{1+\beta}{2}}$ in the strong recycling limit- $-n_d V_{ed} \ll -\Gamma_e(0)$. If recycling is absent ($n_d V_{ed} \approx \Gamma_e(0)$) $n(0) \approx n_d$. We assume $n_d = fn(0)$ ($1 < f < A$). The cold neutrals coming from the plate are ionized, charge-exchanged and some of them leave th plasma layer without collisions. The probabilities of ionization (w_1), charge-exchange (w_2), and leaving (w_3) are:

$$\omega_1 = \frac{\beta K n_d}{K d n_d + V_a} , \quad \omega_2 = (1-\beta)\frac{K d n_d}{K d n_d + V_a} , \quad \omega_3 = \frac{V_a}{K d n_d + V_a} \quad (3)$$

where V_a is the mean velocity of the cold atoms, $K = K_i + K_{ex}$.
For the charge-exchanged atoms the plasma layer is transparent. These atoms can hit the divertor plate and intersect separatrix with probabilities θ and ξ, respectively. Future of the atoms leaving the plasma layer depends on a pumping mode. We consider two different cases: A. The divertor chamber surface is gettered with titanium or is a cryopanel. Neutrals hiting it will be trapped. In this case one can obtain the following expressions for the plasma density and temperature in the divertor chamber based on the heat and particle balances:

$$T_d = \frac{q_o}{J_o}\frac{W}{\gamma + K} , \quad n_d = f\frac{J_o}{2n_o S_p \sin\alpha}\sqrt{\frac{J_o m_i}{2q_o}}\frac{(\gamma + K)^{1/2}}{W^{5/2}} \quad (4)$$

where $W = 1 - \eta\frac{\omega_1 + \xi\omega_2}{1-\eta\theta\omega_2}$, $K = \gamma_o \eta\frac{\omega_3 + \omega_2(1-\xi)}{1-\eta\theta\omega_2}$, S_p is the plate surface area being in contact with plasma. n_o is the number of nullpoints, q_o is the total heat flux into the divertor, J_o is the total particle flux across the separatrix; $\gamma \approx 8$, $\gamma_a \approx 2$ are heat transport rates for plasma and neutrals, respectively, [1]; $1-\eta$ is the trapping efficiency of the divertor plate; α is the pitch angle between the magnetic field and the plate plane. For example for PDX device [2] discharge parameters are $q = 230$ kW, $d \approx 5$ cm, $S_p\sin\alpha \approx 4a\pi d/q(a) \approx 0.06 \cdot m^2$, the particle outflux across the separatrix evaluated on the base of the particle life time $J_o \approx 1.5 \cdot 10^{21}s^{-1}$. The divertor layer is transparent for both the charge-exchanged neutrals and the atoms coming from the divertor plate ($\omega_1 \approx \omega_2 \approx 0$). According to Eq.(4) $n_d = 10^{11}$ cm^{-3}, $T_d \approx 180$ eV. B. The divertor chamber surface has the room temperature. Atoms hiting it are thermolized and come back into the chamber as moleculses with the mean velocity $V_m = 10^5$ cm s^{-1}. These molecules are exhausted by turbomolecular pumps with a volume rate V. Some molecules hit the plasma layer with S_e area and dissociat to Frank-Condon neutrals. These neutrals partici-

pate in the same processes as the atoms from the plate. In the case under consideration the plasma temperature and density are given by Eq.(4) but coefficients W and K have another form ($\xi = 0$ and the plate is saturated with fuel— $\eta = 1$):

$$W = \frac{\omega}{\omega_1 + \omega}\frac{1-\theta\omega_2-\omega_1}{1-\theta\omega_2} , \quad K = \gamma_a\frac{1-\theta\omega_2+\omega}{1-\theta\omega_2}\cdot\frac{\omega_2+\omega}{\omega_1+\omega} , \quad \omega = \frac{2V}{S_e V_m n_o} . \quad (5)$$

As an example we shall consider a tokamak reactor with parameters a=1.5 m, q(a)=3, q_o=80 MW, $J_o = 10^{22}s^{-1}$, d=20 cm and single null-point poloidal divertor. Fig.1, 2 show n_d, T_d dependences on V with some different S_p. If variation of the plate surface area is stipulated by α variation the value $S_p\sin\alpha$ is constant and equals $4\pi ad/q(a)$. With sufficiently small α $S_p \approx S_1$, $\theta \approx 0.5$. A decrease of T_d and specific heat loading is accompanied with divertor plasma density rise. Cold dense plasma can protect the reactor working volume from pollution by impurities arising in the divertor chamber. Choosing the divertor plate surface area one can obtain the plasma density n_d within the range $10^{12} - 10^{13}$ cm^{-3}.

In conclusion it will be noted the following. Beyond the recycling region the plasma mean velocity V_{ed} is given by the expression

$$V_{ed} = V_s\frac{J_o}{2n_o f\Gamma_e(0)S_p\sin\alpha} = V_s\frac{W}{f}$$

With sufficiently small pumping rate $W \sim 2V/n_o S_1 V_m \ll 1$. For example with $V = 5\cdot10^5$ ls^{-1} and S_p=30 m^2, $V_{ed} = 0.02$ V_s. This will lead to a divertor layer broadening and an increase of plasma-wall interaction [3]. In modern divertor devices $V_{ed} \approx 0.3V_s$ [1] that may be explained by high probabilities of particle trapping on the surfaces and neutrals leaving of the divertor layer across the separatrix.

1. Sengoku S., Ohtsuka H. J. Nucl. Mater. 93-94 (1980), 75.
2. Owens D.K., Amnasalam V., Barnes C., Bell M., Bol K. et al. J. Nucl. Mater. 93-94 (1980), 213.
3. Nedospasov A.V., Tokar M.Z. Nucl. Fusion, 21 (1981), 581.

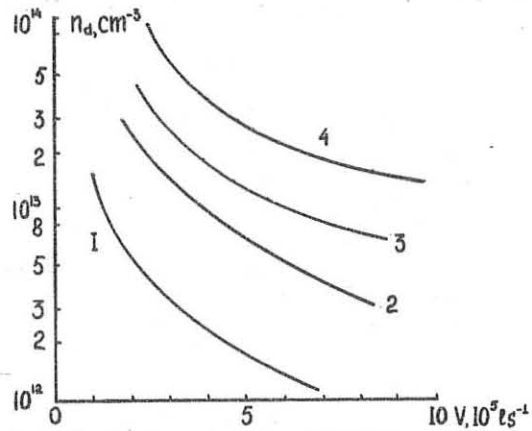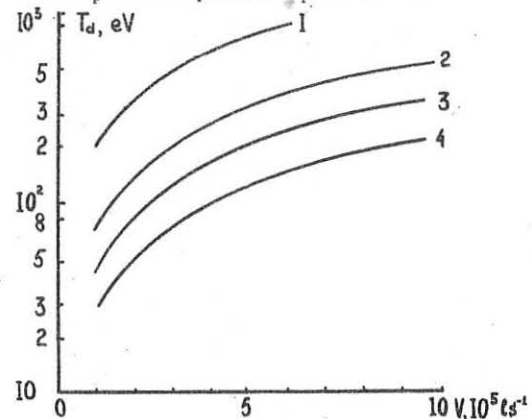Fig.1. Divertor plasma density vs pumping rate (1-S_p=10 m^2, 2-S_p=30 m^2, 3-S_p=50 m^2, 4-S_p=80 m^2).

Fig.2. Divertor plasma temperature vs pumping rate (1-S_p=10 m^2, 2-S_p=30 m^2, 3-S_p=50 m^2, 4-S_p=80 m^2).

MAGNETIC FLUCTUATIONS. THEIR ROLE IN THE CONFINEMENT OF HIGH ENERGY PARTICLES

F.Pegoraro and B.Coppi
Scuola Normale Superiore 56100 Pisa Italy

The confinement and the subsequent thermalization of high energy particles may provide an effective heating mechanism in a high temperature plasma. Thus an important question concerning the physics of a plasma approaching thermonuclear ignition is whether the charged fusion products induce oscillations, which in their turn spoil the confinement of the fusion products, and thus reduce the rate at which their kinetic energy is transferred to the thermal component of the plasma. In a magnetically confined axisymmetric plasma shear-Alfvén oscillations play a special role since they are able to resonate with the fusion products via their magnetic curvature drift motions. In addition these oscillations can couple to interchange modes (i.e. to Rayleigh-Taylor type instabilities) and thus give rise to the so-called ideal MHD ballooning instability [1]. This instability occurs when the pull of the expansion force in the equilibrium configuration, as described by the dimensionless variable $G \sim (L_c/2\pi)^2 (\beta/r_p R_c)$, is stronger than the restoring force due to the tension of the magnetic field lines which is roughly proportional to $(k_\| L_c)^2$. Here L_c and R_c are the connection length and the radius of curvature of the equilibrium configuration, β is the ratio between the kinetic and the magnetic pressures, $r_p^{-1} = -d\ln p/dr$, $k_\|$ is the effective parallel wave number and $k_\| L_c$ is a function of the dimensionless shear parameter $\hat{s}$ and of G itself. The latter dependence arises from the deformation of the magnetic surfaces in finite β equilibria. By referring to the $G-\hat{s}$ plane, it has been shown in [2] that three regions can be distinguished: a first and a second stability region for $G < G_1(\hat{s})$ and $G > G_2(\hat{s})$ respectively, and a ballooning unstable one for $G_1(\hat{s}) < G < G_2(\hat{s})$, with $G_1(\hat{s})$ and $G_2(\hat{s})$ as threshold values depending on the shear parameter $\hat{s}$. The oscillations in the two stability regions can be characterized as a mixture of shear-Alfvén and interchange modes. Their space and time evolution can be described by adopting the so-called "ballooning" representation [3] which is convenient in the case of oscillations with large toroidal wavenumbers and long parallel wavelengths. In these stable regions the resonant interaction between the fusion products and the oscillations could be expected, in principle, to enhance their fluctuation level at the expense of the free expansion energy [4] which is contained in the inhomogeneous distribution of the fusion products.

In this paper we present the conclusions reached through a series of investigations (Ref.[5] to [9]) in which we have examined how effective is the resonant interaction between shear-Alfvén-interchange oscillations and the charged fusion products in a realistic confinement configuration. In particular we have addressed ourselves to the question whether, in such a configuration, these oscillations do actually exist as normal modes [10] and whether they can cause a substantial deterioration of the confinement of the charged fusion products. We find that a severe deterioration is not likely to occur with the possible exception of those configurations where "opalescent" oscillations can take place, as might be the case in fusion reactors expected to operate at finite values of the parameter G.

First we consider shear-Alfvén-interchange oscillations in the absence of fusion products and find that, in the two stable regions, their spectrum is continuous and there are no regular eigenmodes. However, in the second stability region in a relatively wide domain bordering the ballooning unstable region, a "quasi-discrete" portion of the spectrum is identified, similar to that which is found in temporarily bound quantum mechanical systems that have a finite probability of disintegrating.

Then wave packets are considered, and their propagation is found to experience a transient amplification analogous to that described in Ref.

[11]. More importantly, in the region where the quasi-discrete spectrum occurs, wave packets also exhibit an "opalescent" amplification which is reminiscent of that which occurs at a phase transition. It is thus to be expected that the transition from a ballooning unstable configuration to a stable one, in the second stability region, is not precisely defined since relatively strong magnetic fluctuations may persist well inside the "stable" region.

When the fusion products are considered and their "resonant" interaction with the wave packets identified through a "memory-preserving" term in their evolution equation, it is found that the resonant amplification of the wave packets is generally small. This is due to the lack of coherence of the wave packets and to their transient behaviour which allows the resonant interaction to occur for a finite time interval only. The length of this interval increases in the case of opalescent fluctuations which can thus be further amplified by the resonant interaction. Then the quasi linear space diffusion flux of the fusion products is derived and found (contrary to the results of Ref. [12] where eigen-modes have been used) to be rather small, again with the possible exception of the opalescent region.

This analysis can be extended by explicitly including the source of magnetic noise in the plasma. An idealized model can be used in which the only source is given by the fluctuations of the discrete particle distribution. Then, consistent with the fluctuation-dissipation theorem, it is found that, under realistic conditions, the fusion products give the most important source of noise in the relevant frequency band and for perturbations with a polarization vector that suits the MHD constraints. The ensemble average of the square of the fluctuation amplitude can be expressed in terms of the correlation function of the discrete density of the fusion products. The latter is proportional to the averaged density of the fusion products divided by the relevant correlation volume which is roughly given by $L_c/k_\perp^2$. Here $k_\perp$ is the characteristic wavenumber in the direction perpendicular to the magnetic field lines. Thus, in view of the smallness of this source term and of the lack of coherent resonant amplification due to the absence of normal modes, the statistical level of fluctuation of shear-Alfvén-interchange oscillations can be expected to be rather small, which confirms the result obtained in terms of wave-packets. In addition it is shown that the transient amplification described in Ref.[11] ought not to play an important role since it occurs only under rather improbable initial conditions. More specifically the probability of the various initial conditions compensates exactly for the effect of the transient amplification.

1 B.Coppi, J.Filreis and F.Pegoraro, Ann.Physics 121, 1, 1979
2 B.Coppi, A.Ferreira and J.J.Ramos, Phys.Rev.Lett. 44, 990, 1980
3 F.Pegoraro and T.J.Schep, Physics of Fluids, 24, 478, 1981
4 A.B.Mikailovskii, Sov.Phys.JETP 41, 890, 1976
5 B.Coppi and F.Pegoraro, Comments on Plasma Physics and Controlled Fusion 5, 131, 1979
6 B.Coppi and F.Pegoraro, in Physics of Plasmas in Thermonuclear Regimes, proceedings of the 1979 Varenna Workshop. Eds. B.Coppi and Sadowski
7 F.Pegoraro, Massachusetts Institute of Technology R.L.E. Report PRR-80/9
8 B.Coppi and F.Pegoraro, Massachusetts Institute of Technology Report PTP 81/2 submitted for publication to Annals of Physics
9 F.Pegoraro, Massachusetts Institute of Technology Report PTP 81/8
10 A.V.Timofeev, Sov.J.Plasma Phys. 2, 280, 1976
11 Y.Y.Lau, Phys.Rev.Lett. 42, 779, 1979
12 M.Bornatici and F.Engelmann, in Physics of Plasmas in Thermonuclear Regimes, proceedings of the 1979 Varenna Workshop. Eds. B. Coppi and W.Sadowski.

PARAMETERS OPTIMIZATION OF ENERGY HYBRID TOKAMAK REACTOR

A.V.Komin, A.B.Mineev, E.V.Seko
D.V.Efremov Scientific Research Institute of Electrophysical
Apparatus
A.S.Kukushkin, D.K.Kurbatov, V.V.Orlov, V.I.Pistunovich
I.V.Kurchatov Institute of Atomic Energy
A.N.Karkhov, G.V.Levental
High Temperatures Institute of the USSR Academy of Sciences

U S S R

A simplified mathematical model has been used for parametric study of Energy Hybrid Tokamak Reactor of the type described in (1). In the model we took into account the approximate values of the expenditures on the blanket, magnet system, fast deuterons injection system and the group of systems which cost depends only on the power of Hybrid Fusion Power Plant (HFPP).

The following values were taken as independent variables: the main geometric values (plasma minor radius a, inverse aspect ratio A, ellipticity ε), the main plasma parameters (pressure p, temperature T, tritium abundance in plasma), some parameters of reactor system (axial magnetic field B, the energy and power of injection).

In the model we took into account the main constraints posed by plasma (energy balance, quasy-neutrality, maximum plasma pressure β_m, safety factor q), the limitations caused by material properties (maximum neutron flux U_m, maximum magnetic field B_m on a superconductor), and limitations due to maximum available thermal power P_m.

As an optimization criterion we have chosen the minimum of the relative redused expenditures per kW·hr at the energy delivered by the system F:

$$F = Z/Z_A = (Z_T/Z_A + n \cdot \eta_T/\eta_A)/(1 + n \cdot \eta_T/\eta_A)$$

where Z_T, Z_A, Z - the expenditures per kW·hr netto at HFPP, Nuclear Power Plant (NPP) and in the system without fuel component for NPP, n - netto thermal power ratio of NPP and HFPP accounting expenditures discontinuity η_A, η_T is NPP and HFPP efficiency. Fig. I shows F on Z/Z_A dependence for $n = 3.35$ that corresponds to the blanket parameters used in the work. At the contemporary level of NPP fuel component $\xi = 0.2 - 0.3$ the system considered is competitive at a ratio of specific capital cost not larger than 2.1 - 2.9.

The following limitation values were chosen for the basic reference variant: $P_m = 7.5$ GW, $\beta_m = 0.05$, $U_m = 1$ MW/m^2.

The weak dependence of F on fusion reactor parameters (Fig. 2) permits to choose the parameters according to physical and technical criteria. The smallest value of minor radius $a \sim 1.5$ m can be chosen as an additional criterion. Together with this the other parameters of fusion reactor will be: $A = 4.5$, $\varepsilon = 1.8$, $q = 2.6$, $B = 4.8$ T ($B_m = 9.3$ T), $T = 8.6$ keV, $p = 4.3$ MPa ($\tilde{n} \sim 1.6 \cdot 10^{20}$ m^{-3}).

Optimum for the accepted alcator scaling is an ignition type of a reactor. Ignition injection power is 140 MW at 350 - 400 keV beam energy.

Neutron flux on the wall is limited to the accepted value of $U_m = 1$ MW/m^2. Optimum thermal reactor power is 6.4 GW.

Optimum HFPP parameters are: electrical netto power is 1.8 GW; Pu production is 3.9 t/year; NPP total electric power is 7.8 GW. With estimated economical characteristics the system under consideration is competitive at NPP fuel component $\xi \sim 0.35$. The structure of investments to separate HFPP systems is the following: blanket and shield 12%, electromagnetic system 10%, fast deuterons injection system 6%, energy conversion system and automation 32%, other systems (including constructions) 30%, unforseen expenditures are taken to be 10% of the investments sum. The increasing either of chosen limiting values P_m, U_m, β_m practically does not affect the economical characteristics of the system, whether the decreasing of any of them spoils the system economy.

The sensitivity F for the change of economical parameters (in percent ratio of F to corresponding parameter change) is: for blanket - 0.08, for magnet system - 0.02, for injector 0.01.
The ambiguity and obscure character of the calculations allow to consider them as preliminary estimations only. Nevertheless, a number of definite conclusions can be made.

1. The system comprising hybrid fuel producing reactor and NPP is close to a competitive one. In connection with the growth of expenditures per fuel component the system will be competitive in near future.

2. The given specific expenditures for electric power produced by the system are to a large extent defined by the amount of expenditures on NPP. The uncertainty of economical evaluations of separate HFPP systems influences weakly the final economical characteristics of the system.

3. The economical characteristics of the optimum system are practically stable in the range 7 - 10 GW of fusion reactor thermal power. In the given power range the optimum fusion neutron flux on the wall is about 1MW/m^2. The magnetic field in the vicinity of superconducting coils does not exceed 10 T in optimum versions.

References

1. E.P.Velikhov, V.A.Glukhikh et al., Hybrid Fusion Tokamak Reactor for Fission Fuel and Electric Energy Production. Atomnaja Energija, v.45, issue I, 1978.
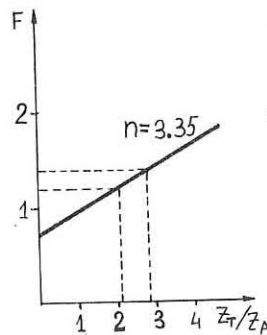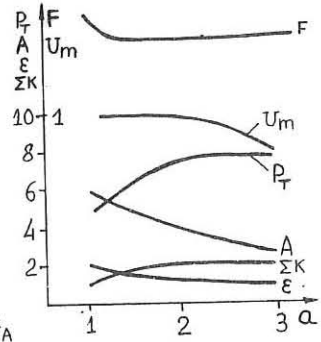
Fig. 1

Fig. 2

PARAMETRIC ANALYSIS OF POWER PLANT BASED ON LASER FUSION

Yu.K.Kalmikov, A.V.Komin, M.V.Krivosheev

D.V.Efremov Scientific Research Institute of
Electrophysical Apparatus

V.B.Rozanov

P.N.Lebedev Physical Institute
of the USSR Academy of Sciences

USSR

The paper describes the study of the electricity cost $\mathcal{Z}$ dependence on the parameters of laser fusion power plant. The simpliest model is used accounting the following main systems of the plant: laser, power supply, cavity, blanket, power conversion system.

The preliminary analysis has shown that, proceeding from the up-to-date knowledge, economically the most favourable plant would be the installation with CO_2 laser and liquid protection of the cavity walls, producing both electric energy and plutonium for Nuclear Power Plants (NPP). Accordingly henceforth we computed $\mathcal{Z}$ value for a complex comprising a hybrid power plant, a nuclear fuel processing plant and NPPs that utilize this fuel.

The dependence of pellet energy gain $Q = W_F/W_L$ on laser energy W_L (W_F - fusion energy) was approximated by the expression:
$$Q = Q_m \frac{x^2}{1+x^2}, \quad x = \frac{W_L}{1.6 \ (MJ)}$$
Cavity radius $R_{(M)} = 1.9 \sqrt{W_{F(MJ)}/\Delta T^\circ}$ /1/ where ΔT is fuel temperature rise per pulse limited by allowable stresses in fuel elements. Microexplosion repetition rate was considered proportional to the time of free fall of liquid protection material in the cavity /1/:

$$f \ (Hz) = k_f \cdot 1.6/\sqrt{R_{(M)}}, \quad k_f \sim 1.$$

Performing analysis we accepted as the basic the version with the following parameters: $Q_m = 100$, laser efficiency $\eta_L = 0.05$, laser lifetime (the number of pulses after which the laser system is to be replaced) $N_L = 10^8$, specific laser cost was taken minimum considering the estimations known /2/ $C_L = 100$ \$/J, $k_f = 1$, $\Delta T = 50^\circ$. The variation $\mathcal{Z}/\mathcal{Z}_A$ where $\mathcal{Z}_A$ is contemporary NPP electricity cost was studied by changing one of the parameters.

At the very large $Q_m \sim 1000$ the electricity cost comes close to NPP electricity cost (Fig. 1). Laser power plant is incompetitive if $Q_m \lesssim 100$. When $Q_m \approx 100$ the complex under consideration appears to be competitive only if there is not less than threefold price rise for natural uranium.

At $\eta_L \sim 0.05$ only a small fraction of energy produced by the complex is spent for laser supply. In connection with this the electricity cost dependence on laser efficiency appeares to be weak. The laser cost is about 30% from the total expenditures for the complex. That is why the double increase in laser cost will result in 30% increase of electricity cost. Laser lifetime does not influence

greatly $\mathcal{Z}$ value at $N_L > 10^8$ pulses when laser system operation time is not less than the standard time of expenditures justification.

It is possible to attain the competitivness of the complex at $Q_m \sim 100$ increasing microexplosion repetition rate by about an order (Fig. 2). This will result in considerable complication of the reactor design /1/.

To perform high fuel production rate the cavity radius should not be too large, and fuel elements at the same time undergo large thermal stresses. If to provide fuel elements lifetime (to be about 10^8 pulses) it is necessary to diminish ΔT, then electricity cost can grow considerably (Fig. 3).

Consequently, laser power plant that is in competitiveness close to NPP must simultaneously have high pellet energy gain ($\gtrsim 100$), high enough laser pulses repetition rate ($\gtrsim 1$ Hz), long laser and fuel elements lifetime ($\gtrsim 10^8$ pulses) and comparatively low laser system cost ($\lesssim 100$ \$/J).

References

1. Yu.K.Kalmikov, "The Questions of Atomic Science and Techniques", series "Fusion", M., 1980, issue 2(6), p.32.
2. J.H.Pendergrass, Trans.Amer.Nucl.Soc., 1980, v.35, p.141.

Fig.1

Fig.2

Fig.3
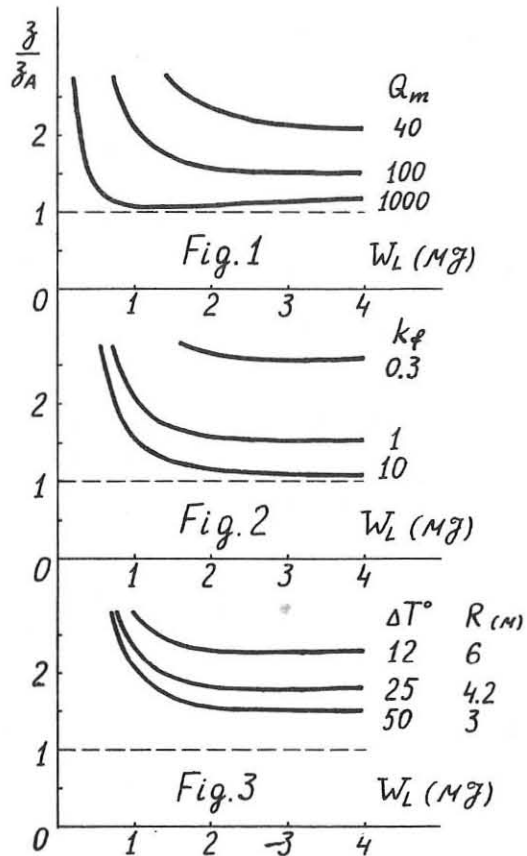
REACTOR ASPECT OF A STELLARATOR WITH A CLOSED HELICAL
MAGNETIC AXIS

N.Sasaki,K.Harafuji,Y.Funato,H.Watanabe and S.Nagao

Faculty of Engineering, Tohoku University
Aoba Aramaki, Sedai 980, Japan

It has been shown theoretiaclly by many authors [1]
that a stellarator with a helical magnetic axis is one of
the most promising devices to confine a high beta plasma
for nuclear fusion, since it is the only stationary torus
where the magnetic well configuration is compatible with
the shear of field lines.   While in these theories it has
been assumed that the field configuration connected with a
linear helical axis have a perfect helical symmetry, in the
toroidal system there are four methods to recover its sym-
metry, that is, a large period number n, the pitch angle
about 45 deg. of the axial helix, a small amplitude oscil-
lation of magnetic surfaces with respect to the principal
normal direction of the axis and a small modification of
the axis to the simplest closed one [2].   Thus it may be
worth while to examine the reactor aspect of such a stella-
rator with a helical magnetic axis and in the following it
will be shown that the drawback of the three dimensional
arrangement of the toroidal field coils is more than offset
by the potentiality of a stable and stationary confinement
of a high beta plasma by the profiled toroidal coils only
without special poloidal coils.

Firstly, the profile of the toroidal coils is given by,

$$\rho^2 + \varepsilon_b \rho^2 \cos 2\theta + (3/2)\varepsilon_b Q_b \cos + (1-\varepsilon_b/2)Q_b k\rho^3 \cos 3\theta + \ldots$$
$$= b^2 \cosh n, \tag{1}$$

where ρ, $\omega=\theta+\kappa s$ and s are the coordinates of Mercier's sys-
tem along the axial helix with the curvature k and the tor-
sion κ. ε_b and Q_b are the ellipticity and the triangular-
lity of the profile respectively with the average radius b.
η is given by $\varepsilon_b = \tanh \eta$.   As for Eq.(1) it should be noted
that this is a general expression, referring to the geomet-
ric centre of the profile and is independent of the magnet-
ic axis of the plasma column.   Therefore, by the circular-
izing transformation of the coordinate system, given by

$$\rho \cos\theta = e^{-\eta/2}\rho' \cos\theta' + \Delta, \quad \rho \sin\theta = e^{\eta/2}\rho' \sin\theta', \quad \cdot \tag{2}$$

the expression of the profile becomes as follows.

$$\rho'^2 + e^{-\eta/2}Q_b k\rho'^3 \cos 3\theta' + \ldots = b^2 \quad \text{and} \quad \Delta=0. \tag{3}$$

Now it is obvious from Eq.(3) that the average radius
of the profiled coils must be smaller than that of separat-
rix surface $b_s = (\sqrt{3\pi})^{-1/2}(e^{-\eta/2}kQ_b)^{-1}$.

Secondly in the following will be investigated the
positional equilibrium of the plasma column, where there is
a rather wide vacuum region between the plasma and the inner
surface of the toroidal coils as the boundary condition for
the equilibrium solution, to be used for the blanket of the
reactor.   Some examples of the solution of Shafranov's
equation for plasma column equilibrium insides and outsides
the column are shown in Fig.1 in the case where $\varepsilon_b=0.4$, $Q_b=$
1.0, ka=0.2, kb=0.4 and beta value=0 % and 15 % are given
and where the plasma limiter is adjusted to make ka being
equal to 0.2.   These results of computor calculations agree
very well with those obtained analytically, where $\varepsilon_a=0.18$,
$Q_a=1.2$ and $k\Delta=0.05$ on the periphery of the plasma column ka
=0.2 and $\varepsilon_o=0.24$, $Q_o=0.68$ and $k\Delta=0.08$ on the magnetic axis
for the example in Fig.1.

Next it is very interesting to show that the vacuum
field, which is characterized by ε_o, Q_o and $k\Delta$ on the axis
and is necessary to confine a high beta plasma, can be pro-
duced approximately by the currents on the profiled toroid-
al field coils given by Eq.(1).   In Fig.(2), the magnetic
surfaces nested by such 30 line current coils per period
with $\varepsilon_b=0.4$ and $Q_b=1.0$ are illustrated for comparison.   In
most examples so far calculated it was known by experience
that the vacuum field ε_o and Q_o by the profile coils are
nearly equal to the halves of ε_b and Q_b respectively.   And
if the discrepancy between these values is not negligible,
it may be necessary and sufficient to superpose a vertical
field produced by a single circular current near the genera-
trix circle of the helix or to make the toroidal field coil

on the boundary surface somewhat sinusoidal, as will be giv-
en by [3],

$$s = s_o + s_\ell \sin \ell\theta, \quad \ell=1,2,3\ldots . \tag{4}$$

where s_ℓ is a small amplitude of ℓ-mode component on the
boundary surface of Eq.(1).   Thus the modularity of the
toroidal system may not be injured so much here, since no
special poloidal field coils interlinked with the toroial
field coils are not employed in any way.

Lastly, in order to make the characteristic features
of a fusion reactor of a stellarator type with a closed he-
lical magnetic axis clear, the main parameters of the device
of Zero Phase INTOR class are listed in Table I.

Table I   Main Device Parameters of Asperator Reactor

Average major radius(Generatrix circle)	R=13 m
Average plasma radius*	a=1.04 m
Ellipticity of plasma column	ε_a=0.18
Triangularity of plasma column	Q_a=1.2
Volume of plasma column	V=392 m^3
Toroidal magnetic field	B_s=2.64 T
Average radius of torodal field coil	b=2.08 m
Ellipticity of toroidal field coil	ε_b=0.4
Triangularity of toroidal field coil	Q_b=1.0
Radius of axial helix	r_o=2.6 m
Curvature radius of axial helix*	k^{-1}=5.2 m
Period number	n=5
Plasma temperature	T=10 keV
Plasma density	n_p=1.3x$10^{20}m^{-3}$
Average beta value	β=15 %
Energy confinement time	τ_E=1.4 sec.
D-T thermal power	P_T=1000 MW

* Plasma radius and curvature radius are assumed here
to be nearly equal to those of Zero Phase INTOR.

[1] L.S.Solov'ev and V.D.Shafranov: Review of Plasma Phys.
vol. 5, Consultants Bureau, New York.

[2] S.Nagao and Asperator Group: Proc.7th Symp. on Engineer-
ing Problems on Fusion Research, Knoxville, Oct.,1977.

[3] S.Nagao: Research Report, IPPJ-26, 1964, Institute of
Plasma Physics, Nagoya University.

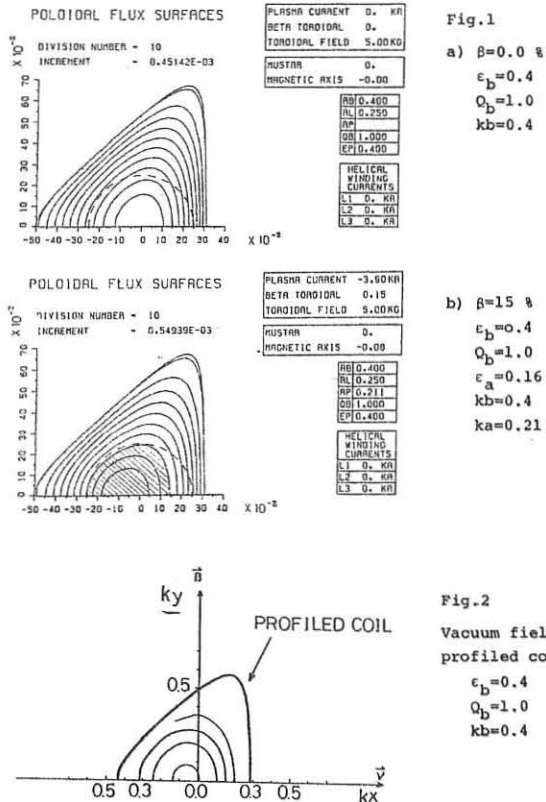Fig.1

a) β=0.0 %
ε_b=0.4
Q_b=1.0
kb=0.4

b) β=15 %
ε_b=0.4
Q_b=1.0
ε_a=0.16
kb=0.4
ka=0.21

Fig.2

Vacuum field by
profiled coils

ε_b=0.4
Q_b=1.0
kb=0.4

PROPOSED SCENARIO FOR BURN CONTROL IN TOKAMAK REACTORS

A. Sestero

Associazione EURATOM-CNEN sulla Fusione, Centro di Frascati, C.P. 65,
00044 - Frascati, Rome, Italy

INTRODUCTION

A combination burn control scenario for a tokamak fusion reactor is proposed, whereby the temperature of the burning plasma is feedback--stabilized around the lower (unstable) equilibrium point. Adjustments in the equilibrium temperature, it is suggested, could be obtained by feeding small amounts of high-Z impurities into the plasma. Small, random deviations from the equilibrium would be controlled via compression-expansion in major radius of the plasma, whereas larger perturbations - conceivably all of the cooling type - would be controlled via the additional heating. The feasibility of the proposal is investigated on a profile-corrected, zero-dimensional, linearized model, whereby separate energy balances are taken into account for electrons, ions and α-particles. The control-theory aspects of the problem are studied in terms of the conditions of *observability*, respectively *controllability*, of the system. The proposal appears to be viable if enough precision can be obtained from the diagnostics, and if the perturbations, for which the intervention of the additional heating is required, are not too frequent, nor too large.

MATHEMATICAL MODEL OF THE BURNING PLASMA

The power-balance equations for α-particles, electrons and ions are written, respectively, as follows:

$$\frac{dE_\alpha}{dt} = G - \bar{\nu}_{e\alpha} E_\alpha + W_\alpha,$$

$$\frac{dE_e}{dt} = \bar{\nu}_{e\alpha} \hat{E}_\alpha - \bar{\nu}_{ei}\left(E_e - E_i\right) - L + W_e + P_e, \qquad (1)$$

$$\frac{dE_i}{dt} = \bar{\nu}_{ei}\left(E_e - E_i\right) + W_i + P_i,$$

where t is the time; E_α, E_e, E_i are the total energy contents of the α-particle, electron, and ion species, respectively; G is the power source associated with the production of α-particles; L is the power loss from the electron species (assumed to be mostly due to radiation from impurities); $\bar{\nu}_{e\alpha}$ is the (volume averaged) energy equipartition rate between electrons and α-particles; $\bar{\nu}_{ei}$ is the (volume averaged) energy equipartition rate between electrons and ions; W_α, W_e, W_i are the variations of the energy content, respectively, of α-particle, electrons and ions, which result from the mechanical work associated with the compression or expansion of the plasma; and P_e, P_i are the fractions of additional heating power that go to the electrons and to the ions, respectively. Besides the approximations involved in the zero-dimensional treatment, a number of other approximations are implied in the writing of Eqs (1): the ohmic power input is neglected, compared with the α-particle power source; the direct power losses from the α-particle and ion species are neglected, compared with the electron losses; the direct energy transfer between α-particle and ions is neglected; in the coupling term between α-particles and electrons, the mean electron energy is neglected compared with the mean α-particle energy; and, finally, the electron and ion density profiles are assumed to be equal (thus neglecting the α-particle contribution to charge density), and the temperature profiles similar

(which allows to write the ion-electron coupling term as proportional directly to the difference between the total energies of ions and electrons). As the pressure profiles of α-particles, electrons and ions are assumed to remain always self-similar, the mechanical work terms W_α, W_e, W_i can be given the following expression:

$$W_{\alpha,e,i} = - \frac{4}{3} \frac{E_{\alpha,e,i}}{R} \frac{dR}{dt}, \qquad (2)$$

where R is the (variable) major radius of the plasma.

The steady-state (d/dt = 0) solution of Eqs (1) is found, corresponding to the unstable thermal equilibrium. Then the Eqs (1) are linearized around this equilibrium with respect to the *state variables* E_α, E_e, E_i. We point out that the dependence on the latter variables of the various terms on the right-hand side of Eqs (1) is both direct, and through the plasma temperature and density. In particular, dependence on density entails dependence on R, since, assuming the conservation of the total number of particles contained within a given flux surface, the plasma density is seen to be proportional to $1/R^2$. Hence, it becomes necessary to relate R to the state variables, which is done by investigating the conditions for the horizontal equilibrium of the plasma column. In terms already of the linearized quantities, one obtains:

$$(n - n_c) \frac{R_1}{R_0} = \frac{\beta_{po}}{\chi_0} \frac{E_1}{E_0} - b, \qquad (3)$$

where, as usual, the subscript 1 denotes the perturbations, and the subscript O the equilibrium quantities. In the latter equation one has introduced $E_1 = E_{\alpha 1} + E_{e1} + E_{i1}$, and $db/dt = (dB_v/dt)/B_{vo}$, where B_v is the value of the vertical equilibrium field taken at the distance R_0 from the symmetry axis. Furthermore, n is the decay index of the vertical field, n_e is its critical value for horizontal equilibrium, β_p is the poloidal *beta* of the plasma, and

$$\chi = \ln \frac{8R}{a} + \frac{\ell_i}{2} - \frac{3}{2} + \beta_p, \qquad (4)$$

where a is the minor radius of the plasma, and ℓ_i is the (energy-related) coefficient of internal inductance of the plasma column.

APPLICATION TO INTOR PARAMETERS

An application to INTOR parameters is carried out, with the following results. In a typical, representation case, a growth time of 1.37 s is found for the thermal instability. Within the framework of modern linear control theory, it is found that the system satisfies the conditions of good observability (with respect to a number of considered diagnostics) and good controllability (with respect to the *entries* represented by the variables db/dt, P_e, and P_i). Thus, in principle, such standard procedures as *asymptotic state estimation* and *mode synthesis* are applicable, allowing for an effective, flexible control. Finally, the following practical conclusions are tentatively drawn. Because of the engineering constraints on the radial shift, the compression-expansion method appears to be acceptable only if enough precision can be built in the feed-back system, so as to maintain the burning plasma within about 1% deviation from the equilibrium in the power balance. In this case the required temporal swing rate of the vertical field would be contained within the very modest amount of 0.01 - 0.02 tesla/second, and the radial shift would remain below 10 cm. Occasional, larger perturbations of the cooling type could be counteracted by the switching-on of the additional heating system. Since, for the control of a 10% unbalance in the plasma power equilibrium, from about 20 to 30 MW of additional heating power are to be fed into the plasma, it is hoped that perturbations of such magnitude can be kept infrequent during the plasma life, otherwise practical problems would be foreseen in the application of the present control scenario.

ACKNOWLEDGMENTS

THE INTERACTION OF NEUTRONS IN THE PLASMA OF FUSION REACTORS AND THE BALANCE OF NUCLEAR FUEL

B. Kühn

Zentralinstitut für Kernforschung Rossendorf der Akademie der Wissenschaften der DDR, DDR-8051 Dresden PF 19

In the development of energetics on the basis of the d+t-fusion reaction it is assumed, that it will be possible to reproduce the tritium in the blanket of the fusion reactor by means of the reaction $^6Li + n \rightarrow t + {}^4He$. The source of the neutrons is the fusion reaction itself. To reproduce the fuel for the given reactor, to replace unavoidable losses and to provide fuel for the start of new reactors the breeding factor has to be greater than unity.

In this paper the interaction of 14.1 MeV neutrons from the fusion reaction with the particles in the plasma is discussed with respect to the reproduction of tritium. Thereby it is realized, that the primary neutrons have to be multiplied by some (n,2n)-reactions which have all negative Q-values.

The interactions of neutrons possible in the plasma of fusion reactors are compiled in tab.1 together with the cross sections and some kinematic parameters of relevance for the present problem. From all reactions continuous

Tab.1 Neutron reactions in the fusion plasma

Reaction	Q (MeV)	Threshold (MeV)	E_n^{max} (MeV)	E_n^{min} (MeV)	Cross Section (barn)	
(1) d(n,n)d	0	0	14.1	1.57	0.64	/1/
(2) t(n,n)t	0	0	14.1	3.52	0.86	/2/
(3) d(n,2n)p	-2.225	3.338	11.83	0	0.175	/3/
(4) t(n,2n)d	-6.258	8.344	7.5	0	0.1 ± 0.05	/4/
(5) t(n,3n)p	-8.483	11.31	4.8	0	(10^{-3})	/4/

neutron spectra arise. The upper and lower limits of their energies E_n^{max} and E_n^{min} after the first interaction are indicated in tab.1.

The elastic scattering (1),(2) leads to a smaller mean energy and therefore to a decreased ability of the neutrons to multiply themselves. The deuteron break up results in additional neutron production and in a relatively soft (unknown) neutron spectrum.

The tritium break up (4),(5) causes losses of fuel, which have to be replaced by additional breeding in the blanket. As the Q-value of the break up is -6.258 MeV the spectrum of the secondary neutrons is soft (unknown). The cross section data are very poor. From contradictory information in literatur /4/ the values indicated in tab.1 were estimated.

A suitable measure of the neutron interaction in the plasma is the ratio N_i/N_n of the number of interactions N_i of type (i) to the number of produced neutrons N_n. Both numbers are defined in unit volume and time and are measured in $[cm^{-3}sec^{-1}]$. N_i follows from

$$N_i = \varrho \, \phi_n \, \sigma_i, \qquad (6)$$

where ϱ is the density of one of the fuel components $[cm^{-3}]$, ϕ_n the neutron flux $[cm^{-2}sec^{-1}]$ and σ_i the cross section of reaction (i) [barn].

The neutron flux is a function of the source density of neutrons N_n, of the size and the geometrical configuration of the space filled with plasma and of the position in the plasma. For the present discussion it is assumed, that the fusion takes place in a sphere of radius R with uniform source density N_n. In this case the element of the neutron flux in the centre (r = 0), which arose in a volume element $r^2dr\,d\varphi\,\sin\vartheta\,d\vartheta$ at radius r is equal to

$$d\phi_n(0) = \frac{1}{4\pi} N_n dr \, d\varphi \sin\vartheta \, d\vartheta .$$

By integration over the volume of the sphere one obtains

$$\phi_n(0) = N_n R.$$

The neutron flux at the surface of the sphere results from the full number of neutrons generated in the plasma $\frac{4}{3}\pi R^3 N_n$ divided by the surface $4\pi R^2$

$$\phi_n(R) = \frac{1}{3} N_n R.$$

For the further estimations a uniform average value of the neutron flux for the volume of the sphere of

$$\phi_n = 0.5 \, N_n R \qquad \text{was assumed.} \qquad (7)$$

By insertion of (7) into (6) the ratio searched for is obtained:

$$N_i/N_n = 0.5 \varrho \, R \sigma_i. \qquad (8)$$

This relation gives the probability of the interaction of a fusion neutron within the plasma volume. It depends on the cross sections, on the fuel density and on the radius of the plasma only. It do not depend on special conditions of the fusion like the temperature or the period of burning. In tab.2 the ratio N_i/N_n is shown for the conditions in different fusion reactors. In usual fusion machines with magnetic confinement the plasma is completely transparent for neutrons. In the case of inertial confinement it is assumed, that pellets with an initial radius of about 1 mm

Tab.2 The ratio N_i/N_n for the conditions in different fusion reactors

ϱ (d+t) (cm^{-3})	$2 \cdot 10^{14}$	$4.6 \cdot 10^{22}$	$4.6 \cdot 10^{25}$	$4.6 \cdot 10^{26}$
R (cm)	100	0.1	0.01	0.0046
ϱ R (cm^{-2})	$2 \cdot 10^{16}$	$4.6 \cdot 10^{21}$	$4.6 \cdot 10^{23}$	$2.1 \cdot 10^{24}$
	TOKAMAK	solid hydrogen	1000 x sol.hydr.	10 000 x sol.hydr.
Reaction	N_i/N_n			
d(n,n)d	$0.32 \; 10^{-8}$	$0.74 \; 10^{-3}$	0.074	0.34
t(n,n)t	$0.43 \; 10^{-8}$	$0.99 \; 10^{-3}$	0.099	0.46
d(n,2n)p	$0.09 \; 10^{-8}$	$0.20 \; 10^{-3}$	0.020	0.093
t(n,2n)d	$0.05 \; 10^{-8}$	$0.12 \; 10^{-3}$	0.012	0.053
t(n,3n)p	$0.5 \; 10^{-11}$	10^{-6}	10^{-4}	$5 \; 10^{-4}$

and a density of solid hydrogen shall be compressed by a factor of thousand or more to reach ignition. Under these conditions the interaction of the neutrons in the plasma already cannot be neglected. At about $\varrho R = 23 \; 10^{23} cm^{-2}$ the sum of the N_i/N_n reaches unity. That means, in the average each neutron interacts in the plasma. In these conditions the losses of tritium attain about 5 %. At greater ϱR multiple scattering leads to a further decrease of the mean neutron energy. The increasing cross sections of elastic scattering at smaller energies cause a faster increasing of N_i/N_n. On the other hand the neutrons become unable to perform break up reactions. Therefore at greater ϱR the ratios N_i/N_n for the break up reactions asymptotically approache constant values, which for the tritium break up amounts between 5 and 10 %. The ratio of the break up rates for deuterium and tritium is almost constant at all pellet sizes ϱR. At very great ϱR the neutrons will be thermalized. This effect helps to heat the plasma /5/, but the neutrons lose their ability to multiply themselves in the blanket. In this case the breeding factor attainable surely will be smaller than unity. Therefore the useful size of the pellets in principle is limited from the point of view of the balance and reproduction of tritium.

In the case of inertial confinement the interaction of the neutrons in the pellet will play a notable role with respect to the fuel balance and has to be taken into account in the design of such fusion reactors. More accurate cross section data especially for the tritium break up and measurements of break up neutron spectra are needed for more quantitative conclusions.

References:
1 J.D. Seagrave, Three body problem in nuclear and particle physics, eds. J.S.D. McKee, P.M. Rolph, Amsterdam 1970 p.66
2 J.D. Seagrave, Few body problems, light nuclei and nuclear interactions, eds. G. Paič, I. Slaus, New York 1968 p.822
3 B. Sundquist, Few body systems and nuclear forces II, Proc. Graz 1968, eds. H. Zingl, M. Haftel, H. Zankel, Berlin 1978 p.270
4 D.S. Mather, L.F. Pain, AWRE-Report No. 047/69 (1969) J.D. Seagrave ibid /1/ p.58, ibid /2/ p.822 S. Shirato et al., Nucl.Phys. A 267 (1976) 157
5 T.D. Beynon, G. Constantine, J.Phys. G (Nucl.Phys.) 3 (1977) 81

THE LOCAL HYBRID DIVERTOR FOR TOKAMAK

Bazaeva A.V.,Bykov V.E.,Georgievsky A.V.,Gorobets I.D.,
Nesterov S.A.,Kaminsky A.O.,Kuznetsov Y.K.,Pavlichenko O.S.
Peletminskaya V.G.,P yatov V.N.,Smirnov V.G.,Tolok V.T.

Physical Technical Institute of Ukrainian
Academy of Sciences,Kharkov, USSR

1. An analysis of reactor aspects of different divertors for tokamak showed that one of the most promissive concepts is the bundle divertor /1/. The bundle divertor,in its simplest form,has the drawbacks of a large field perturbation and high stresses.Further prospects of the bundle divertor will depend on optimization of its magnetic configuration and engineering design.

In this report we present the basic results of a study of the local hybrid divertor which were done in KhPTI in the frame-work of design of tokamak TB-O.A main peculiarity of this divertor is the usage of local poloidal multipole windings-to pick the diverted magnetic field lines up from the surface of torus-and solenoids with the special orientation of coils-to take the diverted bundle of flux away of toroidal field windings. The designed divertor has the advantages of a small perturbations of magnetic field in a plasma and comparatively low stresses which allow the tokamak operation at magnetic field up to 4 T.

2. The stagnation line location,which is characterized by its distance from the torus axis,R_{st}, is the parameter of the local toroidal divertor(e.g.the bundle divertor/2/) which defines the level of field perturbations and forces
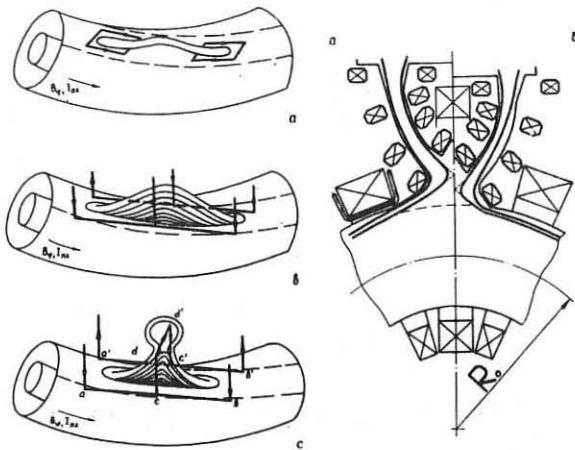

Fig. 1   Fig. 2

on windings of divertor as well. In conventional bundle divertor this distance can be varied in some extent by tilting of divertor coils. Further possibility to increase this distance is connected with an application of magnetic field $B_\perp$ perpendicular to the torus surface for additional lifting of diverted magnetic flux.

The field $B_\perp$ at the torus surface can be created in different ways.The simplest one is to put the elongated current loops (fig.1a) along the field lines on the torus surface. If the flux lifting is produced on a small part of torus,a sort of bundle divertor configuration with the strong perturbations of toroidal field is created. With current configuration of fig.1b type these perturbations are much smaller, but at this case magnetic field lines go up and

down,yet the diverted bundle of flux isn't pulled out. The field null region is necessary for a formation of diverted bundle of flux.Such region can be created with the help of current loops presented on fig.1c.In this case the field lines are pulled out as in the case 1b but a current dd' produces a toroidal field null region on some distance from the torus surface. A small solenoids with the tilted coils can be used for removal of diverted flux out of toroidal field coils /3/ and for increase of null action of current dd' as well.

3. The coil configuration of the hybrid divertor for tokamak TB-O is shown on fig.2a.In our preliminary design we have used local multipole windings on fig.3. These windings (1-diad and 2-triad) produce nulls of different order and different field perturbations as well. A space needed for installation of 4-coil solenoids was obtained by a change of one of 20 circular toroidal field coils with the special eye-glass shape coil. The important feature of multipole windings configuration was the arrangement of these windings on the torus surface according to the pitch angle of magnetic field lines.Such arrangement decreases excursions of magnetic field lines inside of the separatrix.At computer calculations of magnetic field configuration of divertor we took into account the poloidal field of plasma current ($q(a_L)=2.5$) and a vertical magnetic field for horizontal position control ($\rho_v=2$). These calculations showed that with both kinds of multipole windings the magnetic field configuration analogous to the bundle divertor configuration is created. The installation of poloidal multipole
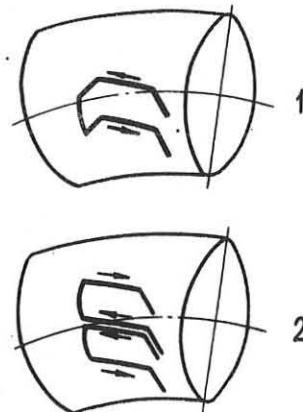
Fig. 3

windings has helped to increase the stagnation point distance R_{st} and the eye-glass coil to reduce the toroidal field at the stagnation point location.

A similar configuration can be created by means of 4-coil solenoids with strongly tilted first coils also(fig.2b). But in this case stagnation point distance R_{st} is smaller than for the hybrid divertor.The parameters of these divertors are presented in Table 1; for the comparison we now listed the parameters of DITE bundle divertor also.

References
/1/.INTOR,Zero Phase,IAEA,Vienna (1980).
/2/ .P.E.Stott,C.M.Wilson,A.Gibson,Nucl.Fus.,47,5(1977)
/3/. А.В.Георгиевский, О.В.Бирюков,А.Г.Дикий,Д.Е.Зисер,
В.Г.Пелетминская, Атомная энергия, 24, вып.I, 61 (1968).

Table 1.

	DITE divertor	TB-O divertor Fig.2a	TB-O divertor Fig.2b
Toroidal magnetic field,B_o,T	1,8	4,0	4,0
Major radius, R_o, m	1,2	1,1	1,1
Limiter radius, a_L, m	0,27	0,31	0,31
Separatrix radius,a_s, m	0,2 1	0,26	0,26
Normalized stagnation axis distance, $\frac{R_{st}}{}$,	1,28	1,47	1,38
Divertor acceptance angle,f_D,rad	1	0,5	0,5
Magnetic field p-erturbations at R_o, $\frac{\Delta B}{B_o}$ %	2	0,2	0,8

H

HEATING AND CURRENT DRIVE
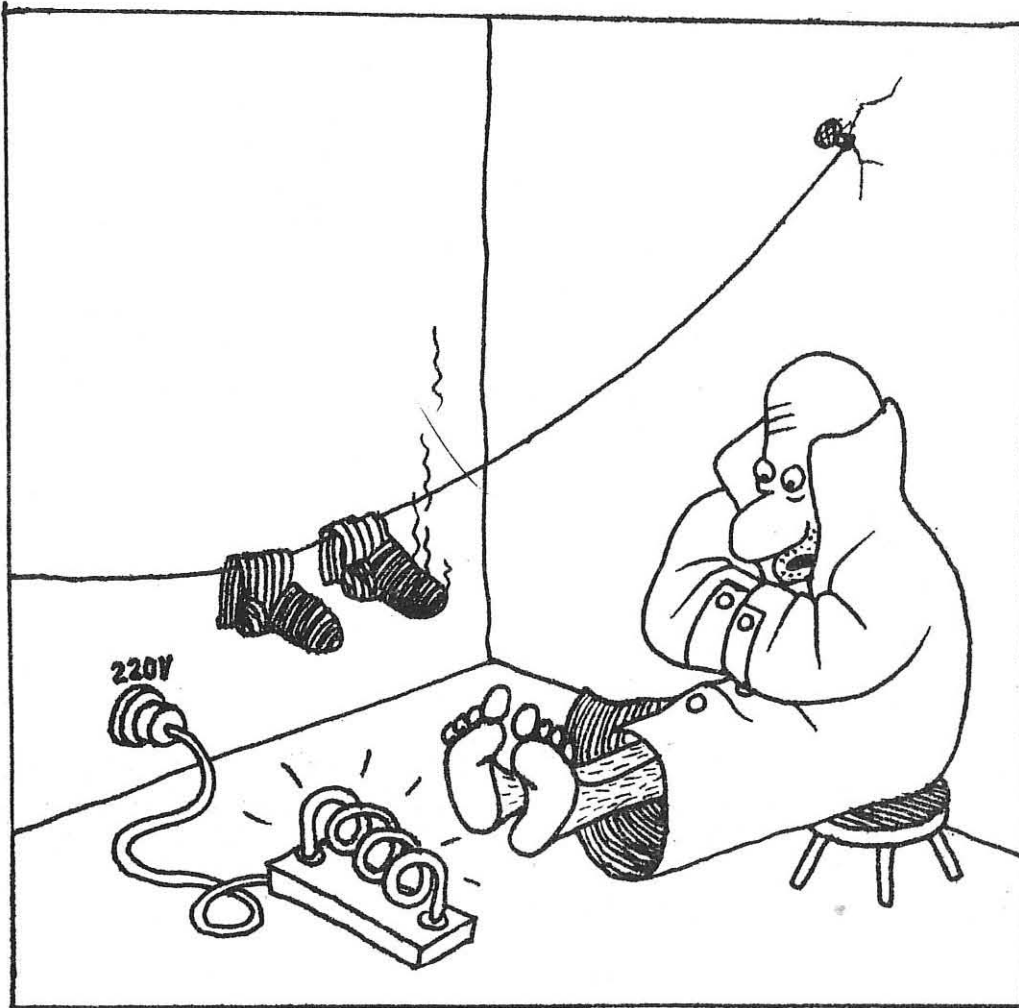
HIGH POWER ECRH AT THE SECOND HARMONIC IN TOSCA

M W Alcock, P A Gaisford*, B Lloyd**, A W Morris**, W A Morris,
R Peacock, D C Robinson, M A Protheroe* and Y Wen***

Culham Laboratory, Abingdon, Oxon, OX14 3DB, UK
(Euratom/UKAEA Fusion Association)
*Royal Holloway College, University of London
**University of Oxford, ***Peoples' Republic of China

ABSTRACT   ECRH experiments at 28GHz, power levels of
20÷150kW and at the second harmonic have been performed.
Theory predicts strong absorption and local heating and
both are observed. The loop voltage can be decreased by
50%, the plasma energy content increases and a current re-
distribution occurs.

INTRODUCTION   High power ECRH has been applied to plasmas
in the TOSCA device [1] with λ=1cm, a pulse length of up to
2ms and at a power level of up to 150kW from the low field
side of the torus using the circularly polarised TE'_{02} mode.
The objective of these experiments is to increase beta,
control the current distribution and investigate current
drive. The regions in which auxiliary heating has been in-
vestigated were 0.4T < B_ϕ < 0.6T, 6kA ≤ I ≤ 14kA, 2.5 x
$10^{18}m^{-3}$ ≤ $\bar{n}_e$ ≤ 1.5 x $10^{19}m^{-3}$. The plasma position was
controlled in some experiments with a fast feedback system
with a time constant of 40μs. The effectiveness of heating
at the second harmonic has been confirmed experimentally[2]
and local efficient heating for an optically thin plasma at
the second harmonic predicted[3]. The theoretical calculat-
ions which include wall reflections indicate that strong
local heating for the X-mode at small radii is favoured by
a geometrical effect of the flux-surface and resonance
configuration. Figure 1 shows the variation of the predicted
heating profile with increasing central density for the X-
mode. The profile moves outwards at higher densities due to
the presence of the low density X-mode cut-off.

EXPERIMENTAL RESULTS   Figure 2 shows a number of the
characteristics associated with the heating pulse, namely a
decrease in the loop voltage by up to 50% (e.g. 1.6V to
0.8V), an increase in the plasma current of typically 10%
(associated with a decrease in plasma inductance), no change
in the plasma density (in contrast to heating studies at the
fundamental), an outward
displacement of the
plasma column, an increase
in the local soft X-ray
emission (E~1keV) in the
resonant region and an
increase in the cyclotron
emission at 35 GHz. An
increase in the transverse
energy of the plasma is
also observed with a dia-
magnetic loop. No signifi-
cant increase in the
emission or impurity radia-

Fig. 1 Variation of heating
profile with density
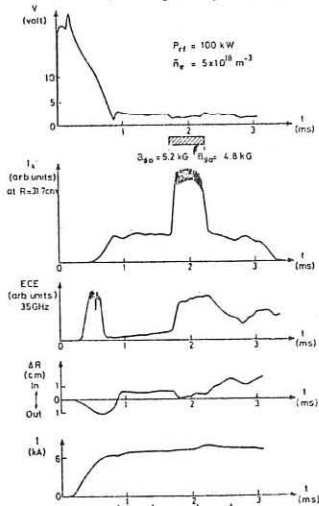
Fig.2 Discharge characteristics
associated with ECRH. (Arrows shown bank timings.)

tion at 4647Å (OII) is
observed. The cyclotron
emission is observed with
a super heterodyne det-
ector employing a local
oscillator tunable from
28-40GHz. The emission is
typically observed to
increase by a factor of 2
or 3 upon injection of a
100kW pulse from the gyro-
tron. The rise and fall
times are usually compar-
able to the bulk energy
confinement times. The
role of superthermal
electrons is not yet fully
established partly because
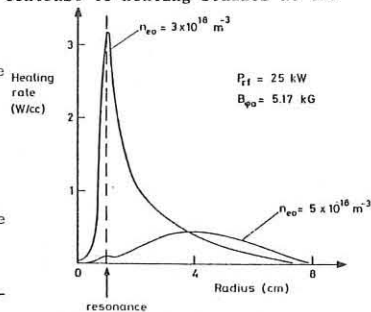of harmonic overlap and
the initial emission in Fig.2 is

correlated with the presence of high energy electrons, as
observed on a Si(Li) detector. The soft X-ray emission ob-
served vertically at seven spatial positions simultaneously
indicated strong local heating close to the cyclotron
resonance as shown in Fig.3. The width of the heating zone
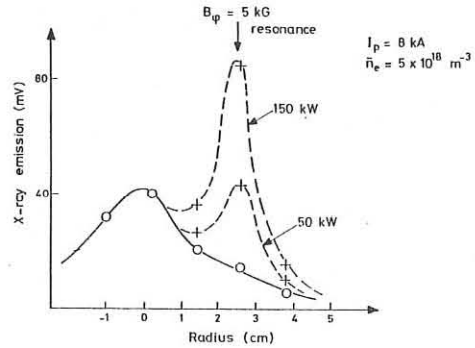is typically 20mm and the local heating is observed at

Fig.3 X-ray emission profile.
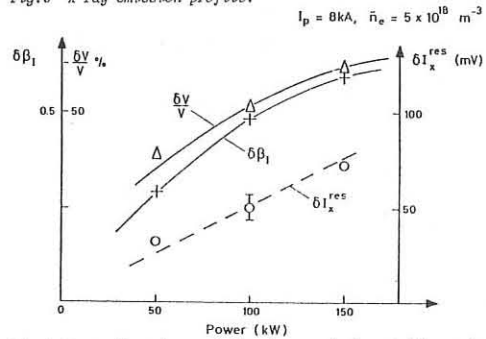
Fig.4 Power dependence of the changes in loop voltage, β_I and X-ray
emission.

densities both above and below the X-mode cut-off value, in
contrast to theoretical predictions which indicate that tunnel-
ling through the evanescent layer is not expected to be
significant. At these temperatures (~300eV) the emission signal
is approximately proportional to T^2 so that a substantial rise
in local temperature occurs. The power dependence of some of
the discharge characteristics is shown in Fig.4. The dependence
is clearly not linear for the diamagnetic conductivity and
local temperature and some form of saturation is indicated at
the higher power levels. Further details on the local heating
and the influence of the angle of the incident radiation are
described in an accompanying paper.

Preionisation using a pre-pulse from the gyrotron
reduces the initial loop voltage but unlike experiments at
the fundamental the V.sec consumption is increased. Scat-
tering by the heating waves off density fluctuations is
observed on the microwave interferometer at 1.4mm and at a
frequency of ~1MHz

CONCLUSIONS   Substantial bulk heating of the optically
thin plasma in the TOSCA device has been observed at the
second harmonic of the cyclotron frequency both above and
below the X-mode cut-off. Local absorption and current re-
distribution effects are observed.

REFERENCES
[1] McGUIRE K M, ROBINSON D C and WOOTTON A J, Proc. 7th
    Int. Conf. Plasma Physics and Controlled Nuclear
    Fusion Research, Innsbruck (1978), (IAEA Vienna, 1979),
    1, 335.

[2] ALIKAEV V V et al, Pisma ZhETF 15 (1972) 41.

[3] FIELDING P J, Culham Laboratory Report, CLM-PG15 (1980).

THE FIRST COMPRESSION EXPERIMENTS IN TUMAN-3 TOKAMAK

Vorobiev G.M.,Golant V.E.,Grigoriev A.V.,Gryaznevich M.P.,
Evtushenko T.P.,Ipatov V.A., Kislyakov A.I., Lebedev S.V.,
Lipin B.M., Litunovskij R.N.[*], Minyaev O.A.[*],
Rozhdestvenskij V.V., Sakharov N.V., Teplov P.P.[*],
Fedorov A.A., Shakhovetz K.G., Shchemelinin S.G.

A.F.Ioffe Physico-Technical Institute, Leningrad, USSR

[*]D.V.Efremov Scientific Research Institute for
Electrophysical Equipment, Leningrad, USSR

The first experiments on 2-fold plasma compression by increasing magnetic field were carried out. The initial conditions were B_t = 2.5÷4 kG, $\bar{n}_e$ = (0.7÷1.5)x10^{13}cm^{-3} and I_p = 70÷100 kA. The compression of density profile and the increase of ion temperature corresponded to adiabatic law. Plasma parameters obtained after compression did not change to the end of the discharge (t ≳ 10 ms).

The main purpose of the Tuman-3 tokamak is the investigation of plasma compression in minor radius and combined compression in minor and major radii. To increase plasma parameters before compression the RF-heating will be used in ohmic heating stage.[1]

In the first experiments plasma compression was investigated only in minor radius as the result of B_t increase. At present toroidal field magnitude in compression stage is limited by the strenght of vacuum vessel. The investigations of plasma compression were carried out in MHD stable ohmic regimes with relatively low magnetic fields (B_t^0 = 2.5÷4 kG, I_p= 70÷100 kA, $q_1 \sim$2÷2.7)[2]. These regimes were chosen to obtain maximum compression.

Adiabatic compression was carried out in the stationary stage of discharge (Fig.1). During $\tau_c \approx$3.7 ms toroidal field B_t was increased from the initial to the maximum value (compression coefficient α = B_t^c/B_t^0 = 2). After that passive "clamping" was used with time constant $\tau_{cl} \approx$ ≈55 ms (Fig.1, B_t). During this time plasma current was supported approximately constant (Fig.1, I_p). At the moment of compression the inductive rise of loop voltage was observed, confirming the current channel compression (Fig.1 U_p).[3] The timeprogrammed vertical field and feedback system confined plasma column near chamber axis during compression ($R - R_0 |\leq$ 0.5 cm, Fig.1).

An electron density was measured by 2-mm interferometer. Fig.1 shows the oscillogram of $n_e l$ which corresponds to the center of the column. The increase of $n_e l$ during compression approximates to the calculated value for the frozen plasma ($n_e l \approx 1.35 \sim \sqrt{\alpha}$).

We did not observe noticeable decrease of $\bar{n}_e$ after compression despite the B_t decrease. Sawtooth oscillations observed before compression increase their period, decrease amplitude and disappear during B_t growth and up to the end of the discharge. It should be noted, that effective compression was possible only in the limited range of initial plasma densities ($\bar{n}_e$=(1÷2)x10^{13} cm^{-3} for B_t^0 = 4 kG and $\bar{n}_e$ = (0.7÷1)x10^{13} cm^{-3} for B_t^0 = 2.5 kG). When density exceeds these magnitudes the intensive MHD oscillations start growing at the initial compression stage and prevent compression. Typical oscillations of $n_e l$ and $\tilde{B}_\varphi$ for these regimes are shown on Fig.2.

For different moments of compression the electron density profiles were obtained from measurement of $n_e l$ on different chords (Fig.3). The radial density distribution for the moment of the toroidal field maximum is more narrow than density profile before compression. The dotted line shows density profile for the compression of entirely frozen plasma. Some difference can be explained by plasma diffusion.

Ion temperature was defined according to the slope of energy spectrum of charge exchange neutrals in energy range from 500 to 1500 eV. The measurements show (Fig.4)

that in the plasma center ion heating corresponds to the adiabatic law ($T_i^c/T_i^0 \sim \alpha^{2/3} \sim$1.6). It should be noted,that ion temperature increase follows the increase of compressing toroidal field. It indicates, that the effect of additional heating is connected with compression so far as ion energy time τ_{Ei} exceeds noticeably τ_c . One can see from Fig.4, that there is no essential decrease of T_i after compression at time interval $t \gtrsim$ 10 ms, that also proves large τ_{Ei} value.

A qualitative estimation of electron temperature distribution in compressed plasma column can be made on the basis of spatial profiles of the intensity of spectral lines with different ionization potentials (Fig.5). One can see the strong burning out of ion CV (E_{cv}^i = 392 eV) in a central plasma region. The increase of radiation of ion OVII (E_{OVII}^i = 739 eV) was also observed (Fig.1).

Thus experiments showed that while the toroidal magnetic field is being increased 2-fold, the compression of density profile and the ion heating correspond to adiabatic law. Plasma parameters obtained during compression are retained approximately constant to the end of the discharge.

REFERENCES

1. Vorobiev G.M. et al. Proc. II Joint Grenoble-Varenna Int.Symp. on Heating in Toroidal Plasmas, Como Italy, 1980.
2. Golant V.E. et al., this conference.
3. Kaganskij M.G., Kalmykov S.G. Fizyka Plasmi, 1978, v.4, p.41.

Fig.1

Fig.2

Fig.3

Fig.4

Fig.5
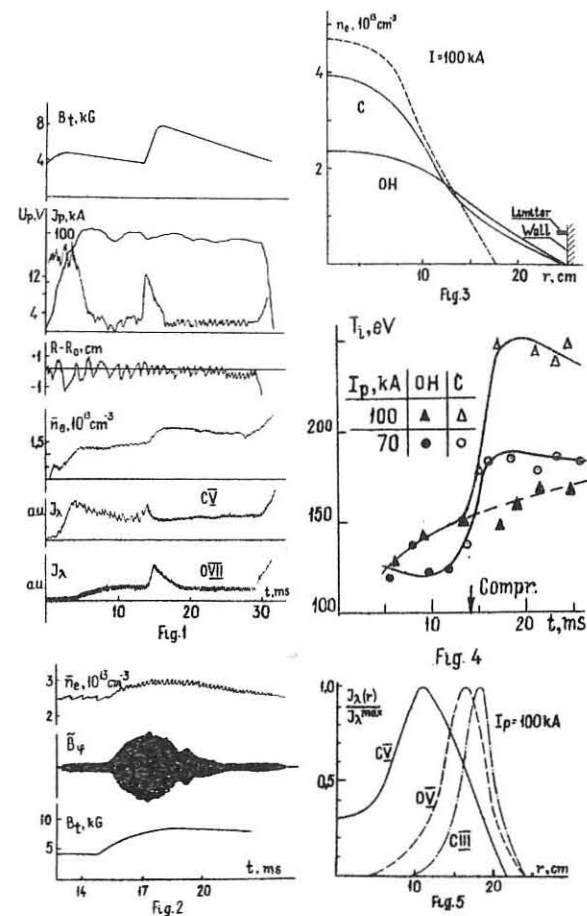
HEATING OF IONS BY MAGNETIC COMPRESSION OF THE PLASMA IN TUMAN-3 TOKAMAK

A.V.Grigoryev, A.I.Kislyakov, S.G.Shchemelinin

A.F.Ioffe Physico-Technical Institute, Leningrad, USSR

Experiments on the plasma compression by increasing toroidal magnetic field are carried out on TUMAN-3 tokamak[1]. To study the behaviour of the ions under compression, the charge exchange atomic flux was analyzed by a five-channel analyzer [2]. The analyzer detected the atoms emitted by plasma along the major radius. It was also possible to scan the plasma column cross section across its vertical axis within $\pm$ 15 cm or 0.6 a_L. The plasma to be compressed was produced by ohmic heating discharges [3,4] which were induced in rather small toroidal magnetic field B_t 3.0 kG and 4.5 kG. The plasma current was 70 and 100 kA, the safety factor at the limiter $q_L = 2.5$, the mean plasma density n_e 0.7 10^{13} and 1.5 10^{13} cm^{-3} respectively. During the compression the toroidal magnetic field increase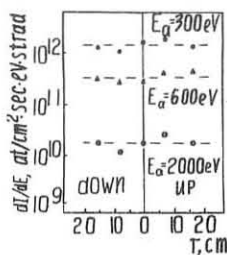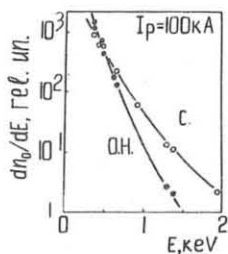d 2 times for τ_{compr} = 3.7 ms and then decreased exponentially with the time constant 55 ms. Fig.1 shows that the intensities of a flux of the charge exchange atoms with different energy are practically independent of the distance r between the discharge chamber axis and the line of sight of the analyzer. This feature is typical for both the ohmic heating and the compression stage. Ion temperature was derived from the slope of the spectra of the charge exchange atoms in the energy range above 500 eV. Typical spectra are shown in Fig.2. The atomic flux attenuation in plasma and the energy dependence of the charge exchange rate coefficients were not taken into account, but the estimates showed that the influence of these factors is less than 10 - 15 %. Profiles of the ion temperature are shown in Fig. 3 and 4 for the moment just before compression (T_{io}) and for the maximum of magnetic field ($T_{i\ compr}$). As is seen, the ion temperature does not vary within the scanned plasma region. One must bear
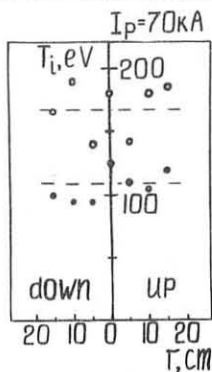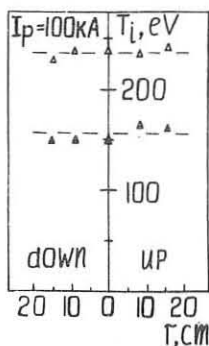

Fig.1

Fig.2

in mind that the real temperature profile may differ from the observed one due to the fact that the analyzer detected atoms produced from charge exchange of trapped ions and emitted by plasma in a meridional plane. The distribution function of these ions may be other than the Maxwellian one corresponding to the mean ion energy in the point where the charge exchange occurs. A further study is necessary for reconstruction of the real ion temperature profile. As to the measurements in the major radius direction, the distortion of the distribution function is the least in this case, and we assume that the ion temperature observed in the centre is near to the real one under the present experimental conditions.
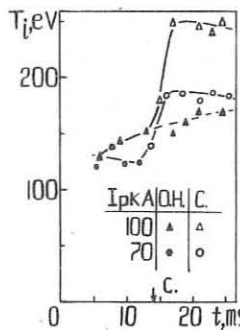
Fig.5

Fig.5 shows that during the compression the ion temperature increased 1.5 and 1.6 times (for I_p = 70 kA and I_p = 100 kA respectively) and remained at this level for a significant time.

From the absolute intensity value of charge exchange atoms it follows that the neutral atom density in the plasma centre is 1 10^9 and 0.7 10^9 cm^{-3} and decreases 2 - 3 times after the compression. This gives the ion lifetime for charge exchange $\tau_{cx} = I/n_a \langle \sigma_{cx} v \rangle$ which is equal to 18 and 26 ms in ohmic heating discharges. Further, since the plasma density n_e just before compression is stationary [3], it follows from the equilibrium between the atom ionization and ion diffusion processes at the middle region that the diffusion lifetime τ_D is equal to 28 and 45 ms. Taking diffusion into account the centre plasma density must increase under compression as $n_{e\ compr}/n_{eo} = B_{compr}/B_o \exp(-\tau_{compr}/\tau_D)$. This ratio is equal to 1.75 and 1.85 for the two regimes and qualitatively consistent with the interferometer plasma density measurements [4].

In the earlier TUMAN-2A experiments [5] the ion temperature during compression increased as $(n_{e\ compr}/n_{eo})^{2/3}$, which gives us 1.45 and 1.50 for the present experiment. Within the experiment accuracy these values are consistent with the ion temperature increase measurements under compression on TUMAN-3.

REFERENCES

1. Vorobiov G.M. et al., Proc. II Joint Grenoble-Varenna Int. Symp. on Heating in Toroidal Plasmas, Como, Italy, 1980.

2. Afrosimov V.V., Berezovsky E.L. et al., JETF, 45, 56 (1975).

3. Golant V.E., Gornostayev S.V. et al., this Conference.

4. Vorobiov G.M., Golant V.E. et al., this Conference.

5. Afrosimov V.V., Berezovsky E.L. et al., Fizika Plazmy, 5, 1251 (1979).

Fig.3

Fig.4

THE ECRH-EXPERIMENTS ON THE T-10 TOKAMAK

Alikaev V.V., Arsen'ev Yu.I., Berlizov A.B.,
Bobrovskii G.A., Buzankin V.V., Vasin N.L.,
Vertiporoch A.N., Vinogradova N.D., Vlasov S.N.,
Gegechkory N.M., Gorbunov E.P., Dochenkov A.S.,
Yesiptchuk Yu.V., Efremov S.L., Zaveryayev V.S.,
Il'in V.I., Kislov A.Ya., Kovrov P.E., Luk'yanov
S.Yu., Maximov Yu.S., Notkin G.E., Parail V.V.,
Pimenov A.B., Popov I.A., Razumova K.A., Rant-
sev-Kartinov V.A., Stepanenko M.M., Strelkov V.S.,
Tarakanov A.V., Usov V.G., Flyagin V.A., Fyach-
retdinov A.N., Chromkov I.N.

I.V.Kurchatov Institute of Atomic Energy,
Moscow, USSR

The experiments on plasma heating in the T-10 Tokamak at second harmonic of ECR are described in this paper. The HF-power was guided to plasma through four waveguides placed in the same cross-section. The wave was mainly ordinary ($\sim 70\%$) polarized and was put along the major radius from the outside. The wave length was 3.6 mm, the total power P_{HF} was up to 0.6 MW and the pulse duration Δt was up to 0.1s. Most of the results described here was performed at B_T=1.5 T, I_p = 200 kA, $q(a_L) \simeq 2$ with bottom carbon limiter in the three regimes illustrated in the Table:

Regime	$B_T(T)$	$I_p(kA)$	$q(a_L)$	$P_{HF}(MW)$	$\Delta t(s)$	$\bar{n}_e(10^{13}cm^{-3})$
I	1.5	200	$\simeq 2$	0.50	0.05	1.5
II	1.5	200	$\simeq 2$	0.30	0.05	1,8
III	1.5	200	$\simeq 2$	0.30	0.08	3

Under these conditions the ordinary wave absorption along a single path is not more than 1-2%; after reflection wave depolarization takes place. These features led to some peculiarities in the experimental results.

The main properties of the discharge in the regime I are shown in Fig.1.

The soft X-ray spectra give the evidence of the Maxwellian character of electron distribution both before and after the HF-pulse, at least, up to 8 keV (Fig.2). The T_{ex}-increase in the regime I was about 0.5 keV. The T_{ex}-profiles measured in the regime III are given in Fig.3. It is seen that the profiles did not sharpen during the HF-pulse. Neither the r_s-value, nor the sawtooth period changed within the experimental accuracy.

The increase of the plasma energy $\mathcal{E}$ measured by diamagnetic loops in all the three regimes is shown in Fig.4. It is clearly seen that the stationary stage was not reached on the course of the heating in the regime I. To calculate the HF-power absorbed in the plasma, W_{HF}, the balance equation was used:

$$ J_p U_{act} + W_{HF} = P_{rad} + \frac{\mathcal{E}}{\tau_E} + \frac{d}{dt}\mathcal{E} $$

The energy confinement time τ_E was calculated by the same equation with $W_{HF}=0$ just after the HF-pulse and was supposed to be constant during the pulse. The W_{HF}-value turned out to be 0.25$\pm$0.05, 0.11$\pm$0.02 and 0.17$\pm$0.075 MW in the regimes I,II and III,respectively.

The increase of the impurity ion line intensity (Fig.1) and of the P_{rad}-value gave the evidence of impurity influx increase with the ECRH; increase in neutral outflux was also observed. The impurity influx is believed to be the result of poor wall conditions and of the absorption of a considerable fraction of the HF-power in the chamber walls and at the plasma periphery. This supposition is supported by the experimental fact that the n_e-value was observed to increase at the column periphery, while the $n_e(o)$ was constant during ECRH,as a rule.

To locate a zone of HF-power absorption we estimated the local energy balance in the regime I, using the measured profiles of P_{rad} and T_e. The coefficient of heat conductivity, χ_e, was calculated just before HF-pulse and was supposed to be constant during the pulse. The results of the evaluation are shown in Fig.5.

The $\chi_e(T_e)$-function was estimated in regime II for r=15.5 cm. The heat conductivity coefficient appeared to be the same before and after ECRH-pulse and was equal to $(1,65\pm0,3)\times10^{17}cm^{-1}sec^{-1}$. It means that if $\chi_e(T_e)$-dependance is supposed to be $\chi_e \sim T_{ex}^{\alpha}$ follows $\alpha \leq 0.5$.

In conclusion: 1) the efficiency of ECRH increased with the increase of n_e and reached at least 50% for central regions at $\bar{n}_e=3.10^{13}cm^{-3}$ for the second harmonic; 2) the efficiency increased during HF-pulse at large HF-power ($P_{HF} \simeq 0,6$ MW) and reached $\sim$ 50%; 3) the α-value is not higher than 0.5 if χ_e is supposed to be proportional to T_e^{α}.

Fig.1
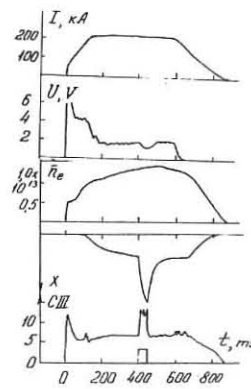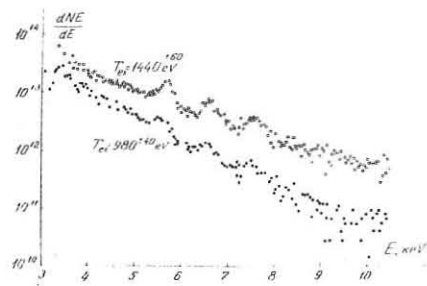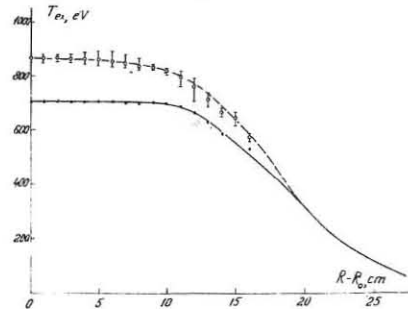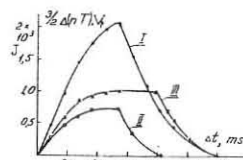

Fig.2

Fig.3

Fig.4

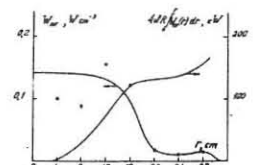

Fig.5

PRELIMINARY ALFVEN WAVE EXPERIMENTS IN THE TCA TOKAMAK

G. Bugmann, A. de Chambrier, A.D. Cheetham, A. Heym, F. Hofmann,
B. Joye, R. Keller, A. Lietti, J.B. Lister, A.Pochelon, A. Simik,
W.C. Simm, J.-L. Toninato and A. Tuszel

Centre de Recherches en Physique des Plasmas
Association Euratom - Confédération Suisse
Ecole Polytechnique Fédérale de Lausanne
CH-1007 Lausanne / Switzerland

The TCA tokamak is a new experiment which has been designed to study the excitation of Alfvén waves. The construction was completed and commissioning was begun during the latter half of 1980. The main parameters of the tokamak are as follows. The toroidal field has a maximum of 15 kG, and plasma operation has been at 8.2 and 12.2 kG so far. The major radius is 61 cm and the limiter radius is 17 cm (R/a $\sim$ 3.6). Plasma currents up to 125 kA have been obtained with pulse lengths typically 100 msec driven by an air-core transformer; the value of safety factor q_L during the current plateau can be varied between 6 and 2.2. Peak electron densities are in the range of $n_{eo} = 0.5-4.5 \; 10^{19} m^{-3}$ corresponding to values of $n_e R/B_\phi$ up to 1.9 10^{19} Weber^{-1}. The torus is not gettered and operation has been in both hydrogen and deuterium. A typical discharge is shown in Fig. 1 and detailed descriptions of the experiment can be found in Reference 1.

The principle of exciting Alfvén waves in a plasma discharge as one method of r.f. heating is not new and has been reviewed in Reference 2. Some experiments have already been carried out and are reviewed in Reference 4. Recent advances in theoretical understanding using both analytical (5) and numerical (3) approaches have been encouraging (see Reference 5 for full bibliography). At present, experiments are being carried out on the TCA tokamak at Lausanne, and on the Pretext tokamak at Austin.

Analytical calculations have shown that the excitation of the mode n = 2, |m| = 1 represents a good compromise between the antenna coupling efficiency and the depth of the Alfvén resonance surface in the plasma. We have, therefore, started our experiments with an antenna configuration which excites n = 2, m = + 1 modes. The considerable problem of inserting antennae of a fixed helicity into the torus is avoided by using purely poloidal antennae consisting of naked stainless steel plates. Figure 2 shows the antenna configuration which we have installed. The frequency of the mode excited, corresponding to the local Alfvén speed, is in the range 2 – 5 MHz and we have started operation at a frequency of 3.1 MHz. The inductance of the active part of a group of three antennae is 27 nH and we require therefore only $\sim$ 500 V across the antennae to excite a current of 1000 Ampères. The external circuit, including the current connections to the exterior of the torus, increases the impedance considerably. In order to maximize the power transfer to the antennae, each group of 3 plates forms part of a tuned circuit physically close to the torus. Considerable attention was necessary to ensure the correct tuning of all eight antenna circuits, especially considering their high Q when unloaded (150). The generator is an auto-oscillator using 4 high power triodes for industrial heating and is fed from a line generator which provides sufficient energy for a 30 msec r.f. pulse. Without plasma loading, the generator can at present provide 500 Ampères in each antenna group.

The r.f. supply was connected at the end of March this year, following which we have made some exploratory investigations and we describe briefly our observations. It is to be hoped that by the time of the conference we shall have made a complete study of this configuration.

When the antennae are excited, we measure effects both in the r.f. circuit and in the plasma at high antenna current. We observe considerable increase in electron density which confuses the interpretation of other observations. We see a large increase in the visible impurity line Fe_{II}, a small increase in the line 0_{II}, and large increases in both bolometer and soft X-ray signals. In addition, we observe a considerable increase in T_i. The plasma resistance is found to increase during the r.f. pulse causing a shortening of the plasma duration. Most of these effects can be roughly reproduced by a short gas-pulse. In general, they are not linear with antenna current or with its square, and seem to have a threshold. There is some indication that the density increase was reduced after particularly intensive discharge cleaning. Changing the antenna potentials by grounding them or letting them float had no effect. Finally, the density increase has been found to vary with plasma current, being smaller at low or high values of q_L, and to vary with plasma density, again being smaller at low or high values of n_e.

In contrast with these observations, the measurements on the loading of the antenna during a tokamak discharge have shown little dependence on the antenna current, suggesting that the effects discussed above are not the main sources of loading. We have varied the value of B_ϕ^2/ρ_o by a factor of 8 and observe a tripling of the antenna loading at low values, where we predict the greatest loading. The loading is small compared with that predicted by the theory, however. At large values of B_ϕ^2/ρ_o ,where our Alfvén mode is not present in the plasma, we still observe a small loading. Ohmic dissipation of the antenna image currents can explain the size of this absorption.

The nefarious effects of the r.f. pulse may be due to a direct interaction of the electrostatic r.f. potential with the plasma, possibly an r.f. glow. Since our antennae are shielded only in the toroidal direction by vertical screens, we are at present designing an electrostatic (or particle) screen to cover each antenna group completely. Tests on a prototype should have been carried out by the time of the conference.

To summarize, we have just begun tests on our antenna configuration, resulting in both positive (constant antenna loading) and negative (gas and impurity influx, small antenna loading) observations.

REFERENCES

(1) A. Cheetham et al., Proc. 11th Symposium on Fusion Technology, Oxford, September 1980
A. Lietti, ibid; R. Keller and A. Tuszel, ibid; J.B. Lister and A. Simik, ibid; F. Hofmann and J.M. Noterdaeme, ibid

(2) T.H. Stix, 2nd Joint Grenoble-Varenna International Symposium on Heating in Toroidal Plasmas, Como, Italy (1980)

(3) K. Appert, B. Balet, R. Gruber, F. Troyon, T. Tsunematsu and J. Vaclavik, ibid

(4) J.L. Shohet, Comments on Plasma Physics 4, 37 (1978)

(5) R. Keller, R. Gruber, F. Troyon, Joint Varenna-Grenoble International Symposium on Heating in Toroidal Plasmas, Grenoble, France (1978)
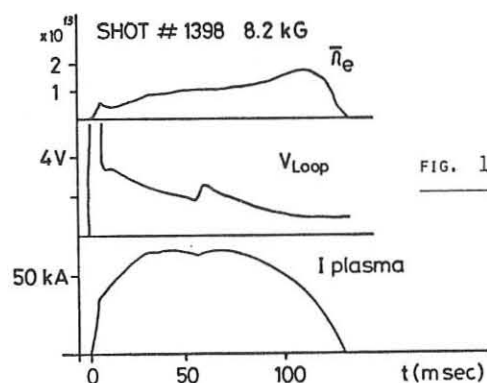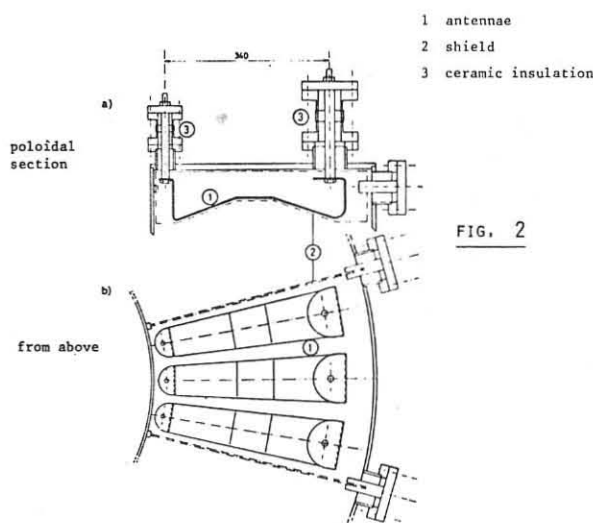
FIG. 1

SHOT # 1398   8.2 kG

1 antennae
2 shield
3 ceramic insulation

a) poloidal section

b) from above

FIG. 2

TURBULENT HEATING OF WELL-CONFINED PLASMA
IN THE TRIAM-1 TOKAMAK

S. Itoh, Y. Kawai, N. Hiraki, K. Nakamura, Y. Nakamura,

M. Kikuchi, O. Mitarai,[*] T. Watanabe

Research Institute for Applied Mechanics,

Kyushu University, Fukuoka, Japan

Abstract: Dispersion relation of low-frequency ion acoustic instability is observed and critical drift velocity is confirmed. Two-component ion energy spectrum formed by turbulent heating relaxes to single one within τ_{ii}.

Introduction

In high-field tokamak TRIAM-1 (B_t = 40 kG, R = 25.4 cm, a = 4 cm), a comparatively small toroidal electric field pulse ($\lesssim$ 10 V/cm) is applied to a well-confined high temperature tokamak plasma (T_{eo} = 200-450 eV, T_{io} = 80-200 eV). Efficient ion heating of the tokamak plasma is observed and the turbulently heated plasmas are well confined, without anomalous losses [1]. In order to investigate the mechanism of turbulent heating in this experiment, measurements of time evolution of electron and ion temperatures are performed by Thomson scattering system and neutral energy analyzer and the dispersion relation of instability which is excited by the turbulent heating current is measured by a 4 mm microwave scattering method.

Electron heating

Figure 1 shows the loop voltage (V_L^{TH}) and the plasma current (I_p^{TH}) induced by the heating pulse. The resistive hump, which is indicated by an arrow, is observed and the plasma current is slightly reduced at the same time.

By applying the heating pulse, the electron temperature increases only on the plasma surface and the skin structure with about 1 cm width exists for 0.5 msec after the pulse is turned off [2]. The time variation of the electron temperature at the skin layer (r = 3.4 cm) during the heating pulse is shown in Fig. 2. The abrupt increase of electron temperature coincides with the appearance of the resistive hump and the density fluctuation described later. The threshold current for the anomalous electron heating is about 7 kA and it follows that $v_d/v_{th} \sim$ 0.39 in our experimental conditions, where v_d/v_{th} is the ratio of the drift velocity to the electron thermal velocity. This value is comparable to the critical value of ion acoustic instability [3].

Ion heating

As the result of the turbulent heating, the bulk ion heating is observed all over the plasma cross section after 100 μsec from the triggering of heating pulse [2]. Within 100 μsec hot ion tails are clearly observed in energy spectrums of charge-exchange neutrals. The preferential heating of this hot ion tails may be explained by an ion acoustic turbulence model. The energy of hot ion component is gradually transferred to the bulk of plasma ions within τ_{ii} (ion-ion collision time) as shown in Fig. 3. According to one-dimensional Fokker-Planck equation, however, this energy transfer is performed within 10 τ_{ii}. The raised ion temperature returns to the initial temperature in 0.3-0.4 msec which is anticipated from the neoclassical theory. The hot ion tails are observed in the plasma center region already at 10 μsec. The wave transport to the plasma center will be investigated by a 2 mm microwave scattering.

Density fluctuation

In the 4 mm microwave scattering experiment, the scattering angles of 30°, 75°, 90° and 110° are selected to obtain the dispersion relation of instabilities and we measure waves propagating almost perpendicular to the toroidal magnetic field lines. Figure 4 shows the dispersion relation obtained from the power spectrums of density fluctuations for the various scattering angles. The observed dispersion relation is in good agreement with the theoretical curve (solid line) of the low-frequency ion acoustic instability, which is calculated numerically using the experimental parameters. The fluctuation levels increase with increase in the turbulent heating current. Moreover, from the analysis of the dispersion relation, it is shown that the low-frequency ion acoustic instability is always acompanied by the high-frequency ion acoustic instability. Therefore, ion acoustic turbulence plays an important role for the observed effective ion heating.

Concluding remarks

It is concluded that the effective ion heating is attributed to ion acoustic turbulence by confirming the critical drift velocity and the dispersion relation of ion acoustic instability. The energetic ions resulting by the turbulent heating are well confined and its energy is transfered to the bulk ions.

References

[1] K. Toi, N. Hiraki, K. Nakamura, O. Mitarai, Y. Kawai, S. Itoh, Nuclear Fusion 20, 1169 (1980)

[2] K. Toi, S. Itoh, Y. Kawai, N. Hiraki, K. Nakamura, O. Mitarai, Y. Nakamura et al., Proc. 8th Int. Conf. on Plasma Phys. and Contr. Nucl. Fusion Res., Brussels, 1980, IAEA-CN-38/X-4-3

[3] N. A. Krall, A. W. Trivelpiece, "Principles of Plasma Physics", McGraw-Hill, New York (1973)

* Present address: University of Saskatchewan, Saskatoon, Saskatchewan, Canada.
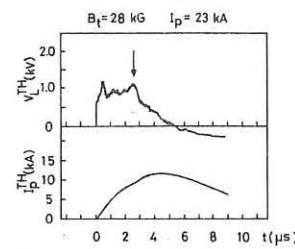
Fig. 1.
Voltage and current of the heating pulse. Resistive hump is indicated by an arrow. V_C^{TH} = 17.5 kV.
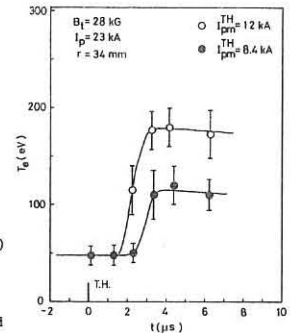
Fig. 2.
Temporal variation of electron temperature at the skin layer. (o): V_C^{TH} = 17.5 kV, (•): V_C^{TH} = 12 kV.
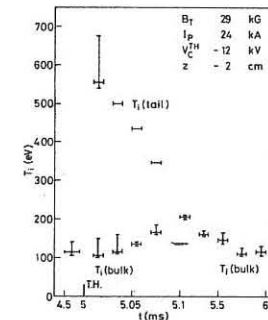
Fig. 3.
Time evolution of ion temperature (bulk and tail) at the vertical position z = -2 cm (below the torus midplane).
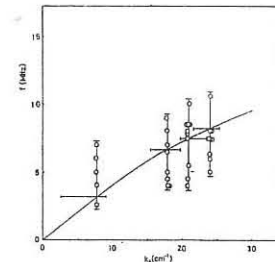
Fig. 4.
Open circles indicate peak frequencies of frequency spectrums. Solid line is a theoretical curve of low-frequency ion acoustic instability.

LOWER-HYBRID HEATING EXPERIMENT ON THE TM-1-MH TOKAMAK

Ďatlov J., Jakubka K., Kopecký V., Körbel Š., Kryška L.,
Magula P., Stöckel J., Žáček F.

Institute of Plasma Physics, Czechoslovak Academy of Sci.,
Pod vodárenskou věží 4, 182 11 Prague 8, Czechoslovakia

During preliminary experiments on the plasma heating in the LHR region in the TM-1-MH device HF power up to 100 kW at the frequency of 616 MHz has been injected into the tokamak by means of a loop fed by a coaxial line. The process of HF field-plasma interaction has been found strongly nonlinear in the whole 3-100 kW power range. It takes place predominantly at the periphery of the plasma column. Electron density increase during the heating process has been reduced by working at various temperatures of the liner up to 300°C.

The parameters of the TM-1-MH tokamak are as follows: $R=0,4m$; $a=0,075m$; $B_0 =$ up to $1,6T$; $I_p=15-30kA$; hydrogen. The results of our heating experiments at $f \approx 2f_{LH}=1,25$ GHz, $P_{HF}=40kW$ carried out on this tokamak have been reported [1]. Under such conditions the increase of the ion temperature up to $\Delta T_i/T_i \approx 1$ was measured. The nonlinear character of this process with a threshold power of 20kW has been found.

Recently we started the LHR heating experiments with the klystron power source up to 100kW at 616MHz ($P_{HF}=(1-3)$ P_{OH}). Due to small dimensions we could not use the waveguide grill [2,3,4]. A simple loop coupler with the front dimensions 4x1,5cm has been used, similarly to [5]. From this at 50 kW of HF power the power flow density of 5kW/cm^2 and vacuum electric field intensity of several kV/cm in the vicinity of the coupler can be estimated. The ratio of oscillating velocity to the thermal velocity of electrons $v_E/v_{Te} \gtrsim 5$, which gives the conditions for the highly nonlinear wave-plasma interaction. This is corroborated by the broad downshifted frequency spread of HF spectra (Fig. 1a,b). We suppose that the L.F. spectra are generated by
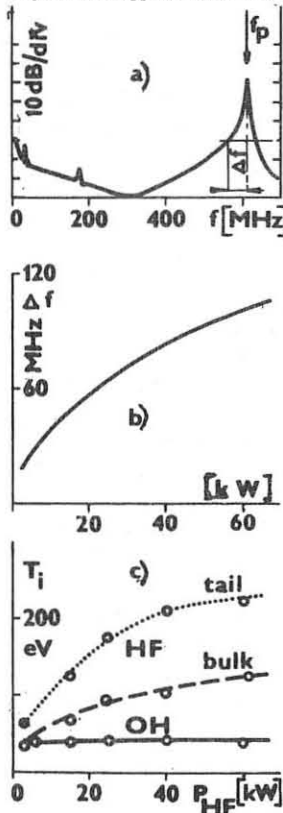

the decay parametric instabilities. The threshold power for this instabilities seems to be lower than 3kW (the lowest power used in our experiments). In Fig. 1c is shown the power dependence of the temperatures of the bulk part and tail of energy distribution function of ions as measured by C.X. 5-channel analyzer. The threshold power for the heating effect, if does exist, must be lower than the lowest power used.

The total energy of the plasma loop was evaluated from the diamagnetic measurements. In the Fig. 2a,b,c are given the time dependences of the kinetic pressure $\bar{p}_\perp$, of the radial shift ΔR of the plasma column in a typical tokamak discharge and of the electron density $n_e(0)$ on the axis. The dashed lines correspond to the OH regime, the full lines are the values during the HF heating. The picture 2 corresponds to the case in which a substantial increase of density during the HF pulse is the predominant cause of the increase of $\bar{p}_\perp$ and radial shift ΔR. The increase of T_i can be caused by the higher transport of energy from electrons to ions. The electron density in-

FIG. 1

crease is due to neutral gas release from liner walls under the intense bombardment by energetic particles during the HF-plasma interaction.

This density increase during the HF heating pulse has been removed by working with the liner at elevated temperature, up to 300°C. The effect of this procedure was similar to the gettering with titanium evaporation as used see e.g. [2]. The density does not increase in this case, as shown in Fig. 3. Than the resulting increase of the kinetic pressure can be interpreted as the increase of the temperature of the bulk ions of the plasma column with correspondence to C.X. neutral measurements. However, due to strong nonlinear absorption at the plasma periphery, the heating efficiency for the ion component of plasma remains also in this case relatively low, of the order of ten percent.

[1] Ďatlov J. et al.: Proc. of 9th Europ. Conf. on Contr. Fus. and Pl. Phys., Oxford 1979, vol. II, p. 539
[2] Suzuki N. et al.: Proc. of 8th Int. Conf. on Pl.Phys. and Contr.Nucl.Fus.Res., Brussels 1980, T-2-1
[3] Fujita J. et al.: Proc. of 8th Int. Conf. on Pl.Phys. and Contr.Nucl.Fus.Res., Brussels 1980, H-3-2
[4] Schuss J.J. et al.: Phys.Rev.Lett. 43 (1979), 274
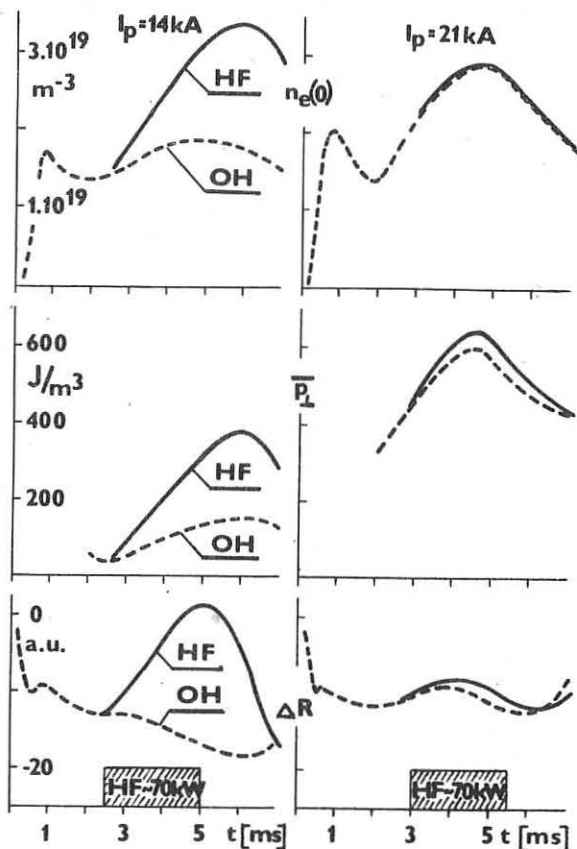[5] Gormezano C. et al.: EUR-CEA-FC 1045, July 1980

FIG. 2

FIG. 3

PLASMA HEATING BY WEAK TURBULENCE IN TORTUR II

A.W. Kolfschoten, H.J.B.M. Brocken, B. de Groot, T. Oyevaar,
H.J. van der Meiden, E.C. de Bruin, C.J. Barth, H. de Kluiver.
Association Euratom-FOM, FOM-Instituut voor Plasmafysica,
Rijnhuizen, Nieuwegein/Jutphaas, The Netherlands.

Abstract

The TORTUR II device is a small tokamak ($R_T = 0.46$ m, $a = 0.085$ m), which has been designed to study turbulent heating of a plasma. After a brief description of the device, the mode of operation to induce heating is discussed. For the heating of tokamaks by current-driven turbulence, up to now, high-frequency fields have been used [1,2,3], requiring high electric field strengths. Indications exist however for a proportionality of the induced electric field E with the characteristic frequency, f, of the heating pulse [4]. The use of the lowest possible frequency, necessary for provoking the anomalous dissipation, will reduce the loop voltage to acceptable values for large-sized devices. Anomalous heating effects for different values of the induced electric field and frequency will be presented.

The TORTUR II device and its operation

The main parameters of TORTUR II are given in the following table:

major radius	$R_T = 0.46$ m	working gas	H_2
copper shield radius	$a_s = 0.105$ m	peak magnetic field B_ϕ	= 3.5 T
liner minor radius	$a_L = 0.093$ m	densities (0.3-1.5) 10^{20} m^{-3}	
limiter radius	$a = 0.085$ m	max. plasma current I_{ELCO}	= 52 kA

The vacuum vessel consists of a thin (0.18 mm) inconel liner. A residual pressure of 10^{-8} torr is achieved by means of a 450 ℓ/s turbo-molecular pump. Preionization is brought about by a 2.7 MHz oscillator connected to the stainless steel limiters. A small fast capacitor (750 µF, 5 kV) induces a preionization plasma.

Toroidal currents are subsequently induced by an electrolytic capacitor bank of 1 Farad, 500 V, with a rise time of 1 ms and a total pulse length of 4.5 ms.

A Taylor discharge cleaning procedure is applied for a few hours before each run of discharges. Following Murakami's scaling, clean discharges are then produced with effective Z-values below 2. The discharge evolution is followed by a number of diagnostics:
a) Electrical measurements and external pick-up loops.
b) A CO_2-laser interferometer for plasma densities.
c) A ruby laser Thomson-scattering apparatus. It provides the values of electron density and temperature at $r = 0.005$ m and $r = 0.06$ m.
d) The ion temperature is measured passively by a time-of-flight energy analyzer.
e) An active ion beam probe for local ion temperature measurements.
. The neutral particles are detected by an 8-channel electrostatic analyzer.
f) Measurement of plasma oscillations.

A four-channel soft X-ray detector and a six-channel polychromator for e.c.e. measurements are in preparation completing the diagnostics.

At any preset time a fast capacitor bank (100 µF, 50 kV) can be fired, inducing extra plasma currents. Electric fields can be varied from 0.1 - 2 kV/m, with rise times variable from 5 - 25 µs. An example of the addition of the extra current on the existing toroidal plasma current is shown in Fig. 1.
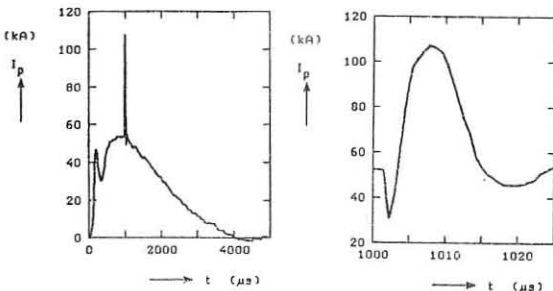

Fig. 1a. Toroidal currents vs time.

Fig. 1b. The additional current in detail.

Turbulent heating effects

Whenever the toroidal plasma current changes at a sufficiently high rate, weak turbulent instabilities of various nature can grow and be maintained at a marginal level during macroscopic times. During this quasi-stationary state rapid heating of the plasma occurs due to anomalously high resistivity.

With a turbulent heating current $I_{TH} = 2\pi a \delta (1-\delta/2a) e n_{ps} v_d$, where δ is the skin width, n_{ps} the plasma density in the skin and v_d the electron drift velocity, it can be shown that the following relations for the anomalous conductivity, σ, and the inducing electric field hold [3]:

$$\sigma = \frac{1}{\mu_0 \delta^2} \frac{I_{TH}}{\partial I_{TH}/\partial t} \ll \sigma_{classical} , \qquad (1)$$

$$E = \frac{\mu_0 \delta}{2\pi a} \frac{1}{(1-\delta/2a)} \frac{\partial I_{TH}}{\partial t} , \qquad (2)$$

for a sinusoidal pulse $\partial I_{TH}/\partial t = 2\pi f \, I_{TH}$.

Depending on the prevailing plasma parameters as T_e/T_i and f_{ce}/f_{pe}, several types of instabilities can be driven into a weakly turbulent state. For the parameters in TORTUR electrostatic instabilities of strongly magnetized plasmas ($f_{ce}/f_{pe} > 1$) with low ratios of T_e/T_i will occur [5]. They are various forms of oblique ion-acoustic and ion-

cyclotron instabilities depending on the precise parameters at stake.

Quite generally, regardless of the type of instability, during marginal stability, a slowly varying ratio, γ, exists between the drift velocity, v_d, and a characteristic velocity as e.g. c_s (c_s being the ion-acoustic velocity $c_s = (kT_e/m_i)^{\frac{1}{2}}$).

For the current-driven turbulent state to exist E/f should satisfy:

$$E/f \gtrsim \frac{6\pi \, 10^{-4}}{(\gamma-1)(1-\alpha)} T_e^{\frac{1}{2}} \quad [eV^{\frac{1}{2}}] \qquad (3)$$

for a hydrogen plasma, where α represents the fractional energy loss out of the skin during heating, to the wall as well as to the plasma centre.

The dissipated energy in the skin can be shown to be:

$$W(t) = \frac{1}{4} \mu_0 \delta \frac{R_T}{a} I_{TH}^2(t) \frac{1}{(1-\delta/2a)} . \qquad (4)$$

The increase of the electron and ion temperature in the skin follows to be:

$$\Delta(T_e+T_i)_{sk} = \frac{\mu_0 I_{TH}^2 (1-\alpha)}{24\pi^2 a^2 n_{ps} e} \frac{1}{(1-\delta/2a)^2} . \qquad (5)$$

The rapid heating of the TORTUR plasma in the current rising phase during the discharge of the electrolytic capacitor bank can be explained in terms of anomalous dissipation processes. The ambient electric field strength ($\bar{E} = 20$ V/m) and frequency (f = 250 Hz) yield a ratio E/f $\approx$ 0.08, which is high enough to ascertain a rapid plasma heating. Electron temperature measurements have been performed with Thomson scattering at the centre (r = 0.06 m) and near the centre (r = 0.005 m). Ion-temperature data are available throughout the entire plasma cross-section, deduced from time-of-flight measurements, and at various positions from an active beam probing technique.

The increase of T_e at 0.06 m and at the axis is shown in Fig. 2, reaching values up to 300 eV. The ion temperatures attain values of 180 eV near the edge and higher at the centre at a time rate almost undelayed as compared with the electrons. The rapid electron and ion heating can be explained in terms of current-driven electrostatic instabilities. For typical TORTUR parameters the electrolytic bank has $\bar{E} \approx 20$ V/m, f $\approx$ 250 Hz, $\bar{I} = 50$ kA; a = 0.085 m, yielding a skin area $\delta \approx 0.06$ m.
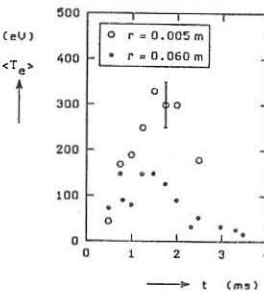
Fig. 2. T_e vs time at r = 0.06 m and r = 0.005 m. Thomson-light-scattering data.

According to Eq. (5), $\Delta(T_e+T_i)_{sk}$ can reach a value of 550 eV at $n_{ps} = 5\times10^{19}$ m^{-3}, taking $\alpha = 0$. The experimental data give $(T_e+T_i)_{sk} \approx 330$ eV at t = 1.0 ms and higher at the centre, indicating small wall losses.

In Fig. 3 the increase of T_e is shown at r = 0.06 m after application of a higher field strength, high-frequency current pulse as shown in Fig. 1. For the relevant parameters the anomalous heating should occur in a skin area $\delta \approx 0.015$ m ($\bar{E} \approx 700$ V/m; f $\approx$ 50 kHz, $I_{TH} \approx 50$ kA). The heating is transported inwards from the skin, arriving at r = 0.06 m after a delay of some 20 µs, which can be explained in terms of normal transverse heat conduction.

Fig. 3. The electron temperature evolution with and without the high-frequency heating pulse at r = 0.06 m.
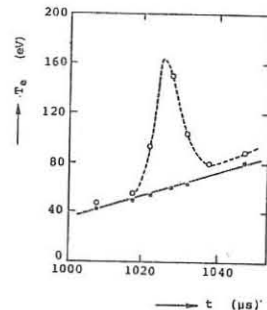
An MHD study on plasma equilibrium has been performed for various forms of concave current profiles [6]. One of the equilibrium cases is that corresponding with an almost shearless plasma. This situation is also realized in the experiment when the high-field current pulse is superimposed on the already flowing current ($q_a \approx q_0 \approx 2.4$). Gross instabilities have not been observed in that case.

References

1. Bengtson, R.D. et al., Phys. Fluids 18 (1975) 710.
2. Toi, K. et al., Nucl. Fusion 20 (1980) 1169.
3. De Kluiver, H. et al., Proc. 7th Int. Conf. on Plasma Phys. and Contr. Nucl. Fusion Res., Innsbruck, 1978, Vol. II, p. 639.
4. Piekaar, H.W. et al., Rijnhuizen Report 73-82 (1973).
5. TFR Group, EUR-CEA-FC-933 (1977).
6. Kolfschoten, A.W. et al., Proc. 2nd Joint Grenoble-Varenna International Symp. on Heating in Toroidal Plasmas, Como, 3-12 Sept. 1980.

ELECTRON CYCLOTRON HEATING IN FT-1 TOKAMAK ABOVE CRITICAL PLASMA DENSITY

Yu.F.Baranov, D.G.Bulyginsky, V.E.Golant, V.I.Ivanov,
M.M.Larionov, L.S.Levin, V.V.Rozhdestvensky, A.K.Sa-
lakhitdinov, A.I.Tokunov, V.I.Fedorov, N.V.Shustova.

A.F.Ioffe Physical-Technical Institute,Leningrad,USSR

Abstract: Additional heating in tokamak by gyrotron microwave generator is described. Energy input from the interior side of a torus allows to produce heating in rather dense plasma ($n_o \geqslant n_{cr}$). Numerical calculations of wave trajectories are consistent with experimental data obtained.

Electron cyclotron resonance heating (ECRH) in tokamak usually is supposed to be successful in a density range $n_o < n_{cr}$ (n_o - central electron density, n_{cr} - critical electron density for frequency ω , used for heating). If the wave is launched in an extraordinary mode from the stronger magnetic field side of a toroidal discharge, ECRH in a more dense plasma becomes possible. In this case the evanescense region for a wave appears only if $n_o > 2n_{cr}$, and two different mechanisms of wave absorbtion are of importance: a cyclotron absorbtion under gyroresonance condition, $\omega = \omega_{ce}$ / 1 / and a linear transformation into a plasma Bernstein wave under upper hybrid condition, $\omega^2 = \omega_{ce}^2 + \omega_{pe}^2$ / 2 /. In experiments described ECRH using the wave launching from internal and external sides of a torus was studied in a wide density range, $0,5 \, n_{cr} < n_o < 2,5 n_{cr}$. Previous results were published in / 3,4 /.

FT-1 tokamak (R= 62 cm, a= 15cm, I = 30kA) was provided by the gyrotron generator (f = 29,17 GHz, 2mS pulse, 80kW). Ohmic heating power also was about 60 - 80 kW. The microwave energy was fed by two circular waveguides, ∅ 32mm, operating at H_{02} mode of a wave. Ends of waveguides, properly shaped, served as antennas for wave launching into a plasma. External waveguide excited mainly the ordinary wave,directed normally to the magnetic field, while the internal one excited the wave,directed at 42° and polarised normally to the magnetic field. The arrangement of waveguides in a discharge chamber is shown in fig. 1.

The decrease of a loop voltage ΔU_1 and the increase of diamagnetic signal ΔnT during ECRH indicate the rise of electron temperature T_e. Fig.2 shows ECRH pulse and signals of U_1 and ΔnT. Discharge conditions are: B_o=9,7kG, n_o=1,3° $\cdot 10^{13}$cm^{-3}=1,2 n_{cr},internal waveguide. To obtain the data on T_e,soft X-ray radiation was analysed by the set of beryllium filters and microwave emission at $2\omega_{ce}$ was measured by the supergeterodyne radiometer,tunable over 44-67 GHz range.Oscyllograms of soft X-ray flux and microwave radiation temperature T_r are also shown in fig.2. Changes in U_1 and nT during ECRH are observed only if toroidal field B_o=8,7-12kG, when ω_{ce} resonance is inside a plasma volume,and if B_o=5-6kG, when $2\omega_{ce}$ resonance exist.In the last case,influence of ECRH is observed only in a low density plasma, $n_o < 0,6.10^{13}$ cm^{-3}. Fundamental ω_{ce} resonance heating is effective in a rather dense plasma, especially when the internal waveguide is used.Fig.3 shows the dependence of ΔnT on the mean electron density $\bar{n}_e$. ($\bar{n}_e$ = 0,6n_o) Diamagnetic signal is almost constant, $1,4 \div 2.10^{14}$ eV·cm^{-3}, although a density variation is large, $0,5 \, n_{cr} < n_o < 2,5 \, n_{cr}$. Loop voltage decrease during ECRH also is constant, ΔU_1= 0,5 - 0,6V, in all density range. Internal antenna is about 2 times more effective than external one.(fig.3). Large ΔnT and ΔU_1 effects of ECRH in a rather dense plasma, $n_o \geqslant n_{cr}$, distinguish our results from some former experiments, where external energy input was used / 5,6 /.

Time constants of ΔU_1 and ΔnT are about 1mSec and are close to the electron energy life time in ohmic heating. Probably, these signals represent bulk electron heating during ECRH. Soft X - ray signal increases strongly during ECRH, but its time constant is about 3 mSec (fig.2). So, it demonstrates the influence of ECRH on the tail of electron distribution, and measurement of T_e by X - ray energy spectrum is wrong. There is also a large increase of $2\omega_{ce}$ microwave radiation during ECRH, and this signal contains a com-

ponent with time constant of 3 mSec. But in many cases thermal component with τ = 1 mSec is also observed (fig. 2). In fig. 4 an example of radial profile of microwave temperature T_r during ohmic heating (O.H.) and ECRH is shown. It is deduced from measurements in 9 frequency points in 44 to 67 GHz range, at $\bar{n}_e = 7.10^{12}$ cm^{-3}. Low frequency part of a profile is distorted by a radiation of runaway electrons. Thermal and nonthermal components of ΔT_r are separated. Increase of T_e in the central part of a profile is about 50 eV. So far as ECRH power was 64 kW during this measurement, efficiency of ECRH is 0,8 eV/kW.

Data on T_e radial profiles enable us to evaluate the portion of total microwave power, which is spent for the plasma heating:
$$\eta = \frac{P_{oh}}{P_{ecrh}}\left(\frac{\Delta \bar{n}T}{\bar{n}T} + \frac{\Delta U_e}{U_e}\right) \cong 0,60$$
P_{oh}, P_{ecrh} are powers of ohmic and microwave heating, $\frac{\Delta U_1}{U_1}$ takes into account the decrease of P_{oh} during ECRH. Energy life time is supposed to be the same for O.H. and ECRH. (Of course, this assumption may be not correct).

Numerical simulation of ECRH in different density conditions was undertaken. Real radiation pattern of internal antenna, refraction in plasma, reflection and depolarisation at chamber walls were taken into account in calculation of the ray trajectories. Cyclotron absorbtion, transformation into a plasma wave and plasma wave absorbtion were included into a code. It was shown, that in a dense plasma ray trajectories reached cyclotron and upper hybrid surfaces after some reflections, and in real conditions of our experiment wave transformation plays the main part in energy absorbtion. Radial distribution of absorbed energy for n_o=0,6÷3 n_{cr} is presented at fig.5. A simulation shows, that if $n_o > n_{cr}$, zone of energy absorbtion moves to the periphery, but still remains at r/a = 0,7, when n_o= 3n_{cr}.

REFERENCES.
1. V.V.Alikaev et al. Fizika plasmy, 3, 2, 230, 1977.
2. V.E.Golant,A.D.Pilija.Uspechi Fiz. Nauk, 104, 413,1971.
3. D.G.Bulyginsky et al. 9 ECCFPP, Oxford, 1979,v.2 p.547.
4. D.G.Bulyginsky et al. 2 Int. Symp. on Heating in Toroidal Plasmas, Como, 1980.
5. V.V.Alikaev et al. JETP letters,15,1,41,1972.
6. V.E.Golant et al. 6 ECCFPP,Moscow, 1973, v.1 p.587.

Fig.1

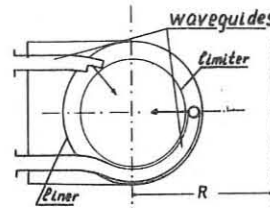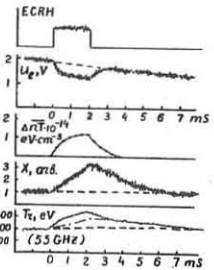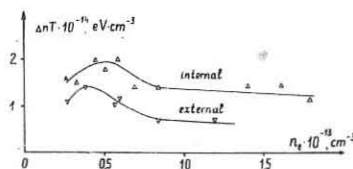

Fig.2

Fig.3
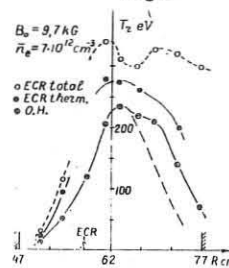

Fig.4

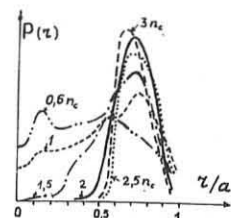

Fig.5

NUMERICAL SIMULATION OF ION-CYCLOTRON HEATING
In $D_2 + {}^3He^{++}$ MIXURE IN TOKAMAK

I.A.Kovan, N.V.Chudin, R.V.Shurygin

I.V.Kurchatov Institute of Atomic Energy,
Moscow, USSR

Abstract. This paper includes numerical calculations of antenna radiation resistance and dynamic of plasma heating in $D + {}^3He^{++}$ mixture with using fast wave.

Recently some successful experiments on r.f. power injection in tokamak plasma at cyclotron frequency of resonance minority ions. The analysis made in /1,2/ shows that a use of $D + {}^3He$ heating technique has some advantages over $D + H$ technique. These advantages are the following: the possibility of more efficient basic ions heating due to collisions; simple control of ${}^3He^{++}$ ion concentration, the possibility of antenna radiation resistance control, lack of charge-exchange, frequency reduction. This paper considers the possibility of supplementary plasma heating using ${}^3He^{++}$ ions in tokamak with adiabatic plasma compression /3/.

The calculation of antenna radiation resistance is made on the assumption of cylindrical geometry. It is considered that fast wave is excited in plasma contained in conducting sheath with radius $r=b$ by current layer located at $r=a$. Radiation resistance is determined as $R_a = 2P/I^2$ where P is power absorbed in plasma, I - is antenna current. To define plasma fields an equation for H_z^{1m} component is used:

$$\frac{1}{r}\frac{d}{dr} rA \frac{dH_z^{\ell m}}{dr} + \left(\frac{m}{r}\frac{dB}{dr} - \frac{m^2}{r^2}A - 1\right)H_z^{\ell m} = 0 \quad (1)$$

it is assumed that $\vec{H}(r,t) = \vec{H}^{1m}(r)e^{im\sigma + i\ell\varphi - i\omega t}$, where

$$A = \frac{\varepsilon - h_\shortparallel^2}{g^2 - (\varepsilon - h_\shortparallel^2)^2}, \quad B = \frac{g}{g^2 - (\varepsilon - h_\shortparallel^2)^2}, \quad n_\shortparallel = \frac{\kappa_\shortparallel c}{\omega}, \quad \kappa_\shortparallel = \frac{\ell}{R}$$

ε, g are the components of cold tensor. Using equation (1) with appropriate bound conditions we obtain:

$$H_z^{\ell m}(r) = \frac{4\pi}{c} j^{\ell m} h_1(r) \frac{h_2'(a) + \lambda h_2(a)}{\Delta_{\ell m}} \quad 0 < r < a$$
$$H_z^{\ell m}(r) = \frac{4\pi}{c} j^{\ell m} h_2(r) \frac{h_1'(a) - \lambda h_1(a)}{\Delta_{\ell m}} \quad a \leq r < b$$

where $\Delta_{\ell m} = h_2' h_1 - h_1' h_2 \big|_{r=a}$, $\lambda = + \frac{m}{a} B(a)/A(a)$
h_1, h_2 - functions which are determined by numerical integration of equation (1) in $0 < r < a$ and $a < r < b$ domains.

It should be noted that the above equations do not allow for absorbtion since Hermitian portions of tensor are used. Let us inject the absorbtion artificially, replacing $\Delta_{\ell m} \rightarrow \Delta_{\ell m} + i\delta_{\ell m}$. Value $\delta_{\ell m}$ remains the fields finite when resonance ($\Delta_{\ell m} = 0$) is reached and, also, a phase shift between antenna current and plasma field $E_\theta^{\ell m}$ appears. It makes it possible to determine the work which the antenna current makes over the plasma field:

$$P_{ant}^{\ell m} = \frac{1}{2} Re \int j_\theta^{\ell m} \cdot E_\theta^{\ell m} dV$$

Value $\delta_{\ell m}$ can be found from the energy conservation

$$P_{ant}^{\ell m} = \frac{\omega W_{\ell m}}{Q_\ell}$$

where $W_{\ell m}$ - avarage field energy, Q_1 - is quality.
Q_1 is determed by longitudinal damping λ_d /4/ taking into account r.f. power absorption in wave transit via ion-ion hybrid layer

$$Q_\ell = \frac{\lambda_d \cdot \omega}{2 V_{g\perp}}, \quad \lambda_d = -\frac{8a}{\ell_n F}\frac{V_{g\shortparallel}}{V_{g\perp}}, \quad F = \xi^2\left[(1-e^{-2\tau})^2 + e^{-4\tau}\right]$$

where $V_{g\shortparallel}$, $V_{g\perp}$ are fast wave group velocities, $2a$ is a distance between walls, $\xi = 0.9$ is coefficient of wall reflection. The parameter $\zeta = \frac{\pi}{2}\kappa_\perp^2 \cdot W$ derived from Buden's equation /5/. Assuming that l, m mode contribution is additive an expression for radiation resistance can be

$$R_a = \frac{16\pi^3}{c}\frac{a}{R} \, 9 \cdot 10^{11} \sum_{\ell,m} \gamma_{\ell m}^2 \, \psi_{\ell m} \frac{\delta_{\ell m}}{\Delta_{\ell m}^2 + \delta_{\ell m}^2} \, [ohm]$$

where $\gamma_{\ell m}$ is a factor in Fourrier series of antenna current $j_{\ell m} = \frac{1}{R}\gamma_{\ell m}$, $\psi_{\ell m} = \left[h_z'(a) - \frac{m}{a}h_z(a)\right]\left[A h_1'(a) + \frac{m}{a}h_1(a) B\right]$

For the purpose of this calculations the following parameters of initial tokamak stage are used /3/: C=32 cm - plasma radius, a=35,5 cm, b=37 cm, R=106 cm, $B_0 = 20$ kG, $W = 1.28 \times 10^8$ cm^{-1}. A parabolic profile of plasma density is assumed. Four half-loops are used as exciting structure. Fig.1 shows a radiation resistance of such structure as well as one antenna depending on plasma density. Four antenna structure produces discrete fast-wave eigenmodes more efficiently than one antenna structure.

To calculate the dynamics of plasma heating a system of balanced diffusion equations including source Q_{re} and Q_{ri} in equations for T_e and T_i is used. These sources are obtained by determining second moments from Coulomb collisional terms:

$$Q_{r\alpha} = \int \frac{m_r v^2}{2} St_{r\alpha}(v) d\vec{v}$$

where α is index of basic ions and electrons, r - is index of resonance particles. In this case resonance ion distribution functions are assumed to be as in /6/. Fig.2 shows the curves Q_{ri}/P_0 as a function of dimensionless power $\xi = P/P_0$ injected in plasma for ${}^3He^{++}$ and H^+ ions. The power supplied from resonance particles to electrons can be derived from the equality:

$$Q_{re} + Q_{ri} = \xi P_0, \quad P_0 = 8\pi n_e h_r Z_r^2 e^4 \ell_n \lambda / m_r V_i$$

where n_r, m_r and z_r are density, mass and charge of resonance ions respectively. Fig.3,4 shows T_i and T_e time evolution when 900 kW power is injected. It also shows temperature increase on plasma axis depending on the power injected. The heating rate is $\sim 6 \frac{ev}{kw \cdot cm^{-3}}$.

References

1. I.A.Kovan, Sposob nagreva plazmy, Author's certificate N. B N9 1981, p.234.
2. J.Adam, J.Jacquinot, H.Kuus, EUR-CEA-1065, 1980.
3. E.A.Azizov and al. 8-th Intern.conf. on plasma phys. and contr.nucl.fusion research, Brussel, 1980, V-3.
4. H.Kimura and al. 8-th Intern.conf. on plasma phys. and contr. nucl.fusion research, IAEA-CN-38/D-4.
5. J.Jacquinot and. al. Phys.Rev.Lett. 39 (1977), 88.
6. T.Stix, Nuclear Fusion, 15 (1975), 737.

FIG.1

FIG.2

FIG.4

FIG.3
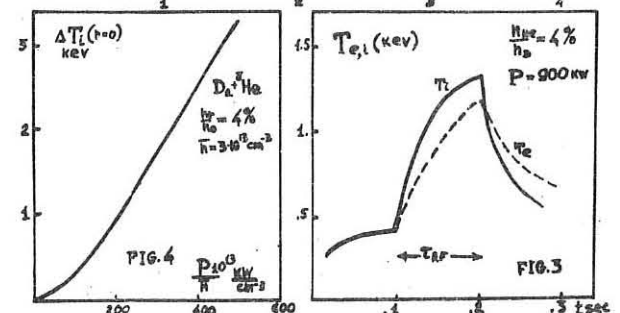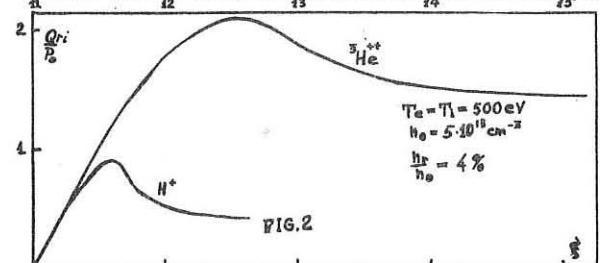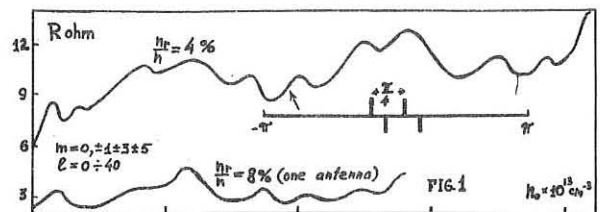
NUMERICAL CALCULATIONS OF PLASMA HF HEATING
WITHIN THE ALFVEN FREQUENCY RANGE IN A TOKAMAK

O.S.Boordo, V.V.Gorin, A.G.Dmitrenko (The Institute of Cybernetics of the Ukrainean Academy of Sciences) and A.G.Elfimov (Sukhumi Institute of Physics and Technology). The Union of Soviet Socialist Republics.

The Alfven frequency range $(\Omega \simeq k_z H_z (1-\frac{m}{nq})/\sqrt{4\pi m_i n} \ll \omega_{Hi})$ HF fields are used to achieve additional heating of tokamak and stellarator plasmas [1,2,3,4]. Works [2,3,4] represent qualitative results of studies on HF field distributions based on some analytical estimates in accordance with the geometric optics theory for the waves in an inhomogeneous plasmas. To use this method of heating in various-scale machines one needs more accurate data for heating and HF field distributions along the radius type in inhomogeneous plasma.

The present paper deals with calculations of boundary-value problem for HF fields in a plasma cylinder with a parabolic profile of density $n = n_0(1-\frac{r^2}{a^2})$ and temperature T in a uniform stationary magnetic field $H_z = H_o$. A set of equations

$$\text{rot rot } \vec{E} - \frac{\Omega^2}{C^2}\hat{\varepsilon}\vec{E} = 0 \qquad (I)$$

for the components $E_{r,\varphi,z}(r) = \exp i(k_z z + m\varphi - \Omega t)$

has been integrated where the dielectric constant tensor $\hat{\varepsilon}$ components are: $\varepsilon_{zz} = \frac{\omega_{pe}^2}{k_z^2 v_{Te}^2}\{1+\text{Re}[s_e Y(s_e)] + i\mu\text{Im}[s_e Y(s_e)]\}$; $\varepsilon_{r\varphi} = -\varepsilon_{\varphi r} = \frac{i\Omega}{\omega_{Hi}}\varepsilon_1$, $\varepsilon_{rr} = \varepsilon_{\varphi\varphi} = \varepsilon_1 = \frac{c^2}{C_A^2(r)}$; $\varepsilon_{rz} = \varepsilon_{zr} = \varepsilon_{\varphi z} = \varepsilon_{z\varphi} = 0$. Here $s_e = \frac{\Omega}{\sqrt{2}k_z v_{Te}}$; $Y(s) = -i\sqrt{\pi}W(s)$ is plasma dispersion function and the factor $0 < \mu \leq 1$ expresses plasma interaction attenuation with resonance electrons as a result of electron distribution function quasilinear relaxation. Tensor $\hat{\varepsilon}$ is valid if inhomogeneity scales for fields and plasma are much more than gyration radii for electrons and ions, and if the following conditions $\omega_e^* \ll k_z c_s \ll k_z C_A \sim \Omega \ll \omega_{Hi} \ll \omega_{pi}$; $T_e > T_i$ are met.

A launching system is represented by a thin helical HF circuit, r=b in radius, with the current surface density $\vec{j}_{\varphi,z} = \vec{j}_{\varphi,z}\exp i(k_z z + m\varphi - \Omega t)$; $m j_\varphi = k_z b j_z$. Solutions for vacuum fields have been sought via the magnetic $\vec{H} = \nabla\varphi$ and electric $\vec{E} = -\nabla\psi$ potential, where $(\mathscr{æ}^2 = k_z^2 - \frac{\Omega^2}{C^2})$ $\varphi = [\varphi_+ I_m(\mathscr{æ}r) + \varphi_- K_m(\mathscr{æ}r)] \exp i(k_z z + m\varphi - \Omega t)$; $a < r < b$.

The absorbed power (W) can be expressed via magnetic potentials φ_-, $\varphi_+ = \frac{4\pi b}{c}j_\varphi K_m(\mathscr{æ}b)$ amplitudes $W = \frac{b c r}{4}\text{Re}(E_\varphi H_z^*) = \frac{\Omega}{4}\varphi_+ j_\varphi\varphi_-^*$.

Equation (I) has been represented as a set of the 6th order ordinary linear differential equations. Boundary conditions at the plasma-vacuum interface have been determined by matching of the normal magnetic and tangential electric components of HF fields. In computation HF field amplitudes $E_{r,\varphi,z}(r)$, the absorbed power density $P = \text{Im}\varepsilon_{zz}|E_z|^2$ along the radius and the coefficient φ_- value versus the conversion point position $r_\ell^* = a\sqrt{1-\frac{(k_z c_A)^2}{\Omega^2}}$ (or Ω) have been defined. φ_- resonances at $\mu \ll 1$ (Fig.I shows the first three of them) coincide with natural frequencies of inhomogeneous plasma over the Alfven range [4]. The calculations have been performed for two series of dimensionless parameters $k_z a = 1; 1,5; \frac{k_z c_A}{\omega_{Hi}} = 0,32; 0,032; \frac{\text{Re}\varepsilon_{zz}}{\varepsilon_1} = 1,8\cdot10^3; 3\cdot10^5$. The first set of parameters is meant for (Fig.I;2) small-sized tokamaks, while the second set is for medium-sized ones (Fig.3), the values of $\mu = 0,03; 0,1;0,3;1; m=1;2$ and the conversion point ($0,1 \leq x_\ell = r_\ell/a \leq 0,9$) being varied.

SUMMARY. 1. For weak absorption $(\mu \ll 1)$ in inhomogeneous plasma there is a set of Alfven resonances corresponding to homogeneous plasma ones $\Omega^2 = k_z^2 C_A^2(0)(1 + k_\perp^2\rho_{AS}^2)$ [3,4].

2. The HF field structure qualitatively corresponds to the HF field convertion into a short-wave length mode theory [3,4].

3. For optimal absorption $(\mu \ll 1)$ frequency should be chosen within exact resonances values (absorbed power being released at the centre of plasma). The convertion point in the range of $r_\ell \simeq 0,8a$ is another condition for maximal absorption (the absorbed power will be concentrated in the vicinity of the point $r=r_\ell$). The best heating conditions are $r_\ell = 0,5a$ for small tokamaks and $r_\ell = 0,3a$ for medium ones.

4. The HF field rotation should be positively directed $\frac{\Omega}{m} > 0$. With the direction being opposite the absorbed power decreases by twenty times for small tokamaks as a result of convertion attenuation due to plasma gyrotropy.
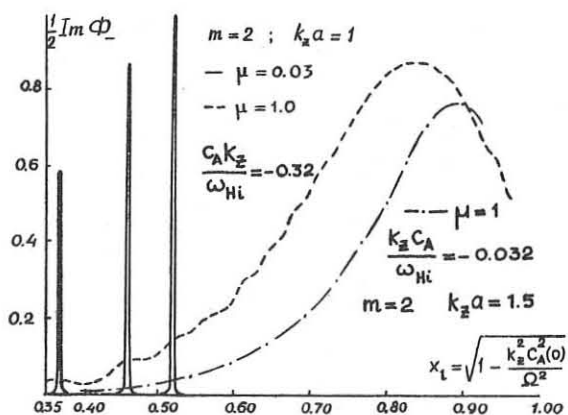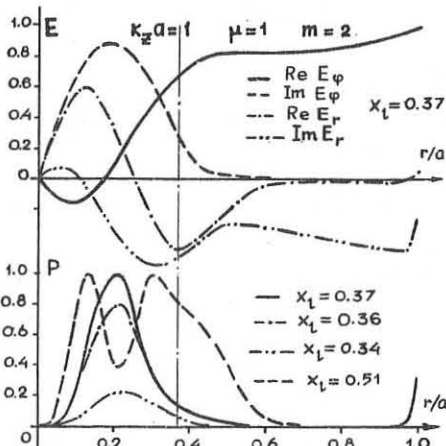
Fig. 1

Fig.2

REFERENCES

1. A.G.Kirov, L.F.Ruchko et al. AR 8 in Proc. of 9th European Conference on Plasma Phys. and CNF, Oxford, Sept.1980.
2. A.V.Longinov, K.G.Stepanov. Preprint KhFTI 72-I, Kharkov, 1972.
3. Akira Hasegawa, Liu Chen.Phys.Fluids, 19, 1924, 1976.
4. A.G.Elfimov. Report at the 2nd Int.Symp.on Heating in Toroidal Plasma, Como, Italy. 3-12 September, 1980.
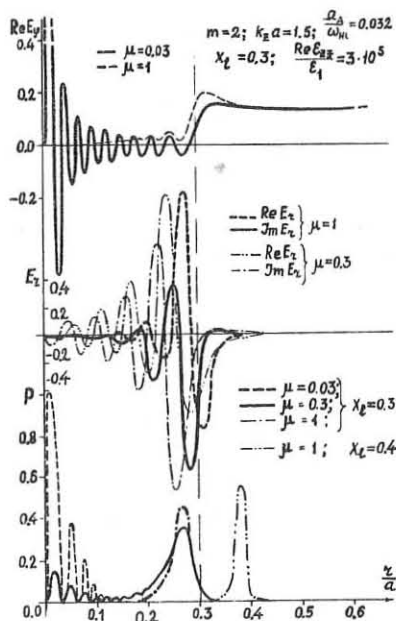
Fig.2

ANALYSIS OF THE FINITE-LENGTH ICRH ANTENNA

V.P. Bhatnagar, R. Koch[+], A.M. Messiaen[*], R.R. Weynants[°]

Laboratoire de Physique des Plasmas - Laboratorium voor Plasmafysica
Association "Euratom-Etat belge" - Associatie "Euratom-Belgische Staat"
Ecole Royale Militaire - B 1040 Brussels - Koninklijke Militaire School

Abstract : The impedance of a finite-length ICRH antenna of the "all metal" type is computed using the classical induced *emf* method, and properly describing the antenna end effects. In the case of broad and short antennae the results indicate a strong reduction of coupling with respect to the predictions of infinite antenna theory.

I. INTRODUCTION. The early work concerning the computation of the impedance of the present all metal ICRH antennae was done in the framework of infinite strip-line theory [1 - 4]. More recently, attempts [5, 6] have been made to account for the finiteness of the antenna length, i.e. the finite width of the k_y-spectrum as well as the antenna end effects (refer to Fig. 1 for the geometrical definitions). Whereas Ref. 5 expects only a slight decrease of the coupling resistance with respect to the infinite line analysis, Ref. 6 predicts possible increases of the same quantity of up to a factor of five. It is to be noted that the above conflicting results are obtained from models which only differ in the assumed plasma density and antenna current profiles. In the present paper, we outline how a consistent treatment of the finite-length antenna could be made, from which the correct expression of the antenna impedance can be derived and which allows to explain the above conflicting results.

In antenna theory, a consistent solution of the radiation problem is usually [7] arrived at by considering a voltage excitation across a gap, as the energy source, and applying the metallic boundary conditions on the antenna to determine the correct fields and the self-consistent surface current $\bar{J} = \nu_s \times \bar{H}$ at the antenna surface. Since such a treatment is very complicated, one frequently uses as an approximation the so-called induced *emf* method (see e.g. [8]) where one considers the excitation to be the antenna current itself - assumed approximately known - instead of the applied voltage. This method has been implicitly used in [1 - 6]. In the case of the ICRH antenna (Fig. 1), the excitation current induces a $TE/_z$ field ($/_z$ meaning that transversality is defined with respect to z, the $\bar{B}_o$ direction) which extends beyond the screen into the plasma. Always when the chosen current profile is such that $\nabla.\bar{J} \neq 0$ (i.e. when considering propagation effects or when neglecting the current feeders shown in Fig. 1), a $TM/_z$ field, of essentially electrostatic nature, exists which is intrinsicly linked to the $TE/_z$ field. It was shown in [2] that such a field is confined between the wall and the electrostatic screen which can be modeled by a layer of anisotropic conductivity ($\sigma_{yy} = 0$, $\sigma_{zz} = \infty$).

As in the induced *emf* method the current profile is assumed, one should look outside of its context for a consistency check of this assumption, in particular concerning the propagation constant β of the assumed sinusoidal current distribution. A possible means for doing so is examined in this paper and is based on the simultaneous consideration of the $TE/_z$ and $TM/_z$ fields. In the quasistatic limit they can be used to divide the reactive antenna energy in an inductive and capacitive part from which β can be derived.

II. MODEL. The geometrical configuration, including the plasma density variation, is shown in Fig. 1. The exciting current is defined as $\bar{J} = (J_x, J_y, 0)$ with $J_y(y,z) = \delta(x)(\gamma(y) - \gamma(y-2w_y))\cos \beta y \, J(z)$ (1)
$$J_x(y,z) = \gamma(x)(\delta(y-2w_y)\cos 2\beta w_y - \delta(y))J(z) \quad (2)$$
where $\gamma(x)$ and $\delta(x)$ are the usual step and delta functions. $J(z)$ is chosen according to previous theory[5]; propagation is neglected along the feeders. After Fourier analysis in the y and z directions the vacuum field can be derived from the components $B_z(TE/_z$ part) obeying $\frac{d^2 B_z}{dx^2} - p^2 B_z = \mu_o(ik_y J_x - \frac{dJ_y}{dx}) = -\mu_o (\nabla \times \bar{J})_z$,   (3)

and $E_z(TM/_z$ part) obeying $\frac{d^2 E_z}{dx^2} - p^2 E_z = \frac{k_{\parallel}}{\omega \varepsilon_o} \frac{dJ_x}{dx} + ik_y J_y) = \frac{k_{\parallel}}{\omega \varepsilon_o} \nabla.\bar{J}$ (4)
where $p^2 = k_y^2 + k_{\parallel}^2 - k_o^2$.

Metallic boundary conditions are applied at the wall and $E_z = 0$ on the screen. This last condition ensures that only the $TE/_z$ field passes through the screen so that only the magnetosonic wave has to be retained in the plasma where we assume that single pass absorption prevails [2, 9]. As can be easily seen from Poynting's theorem the work of the applied current on the field is given by
$$P = -\frac{1}{2} \int_V \bar{E}.\bar{J}^* \, dV \quad (5)$$
the integral being taken over the vacuum region and yielding both the active (real part) and reactive (imaginary part) power delivered to the medium. This expression can be identified $\frac{1}{2} Z_A I_A^2$, the power delivered to the system by the source, with $I_A = \int_{-\infty}^{\infty} J(d, 2w_y, z)dz$ thus providing a complete evaluation of the antenna input impedance. The above power integral can be computed from the Fourier spectra by means of the Parseval theorem. The consistency of the β value assumed in (1) and (2) can be checked after invoking,from transmission line theory[8],
$$\frac{1}{2} Z_A I_A^2 = \frac{1}{2} R \int_0^{2w_y} |I|^2 \, dy - \frac{i\omega L}{2} \int_0^{2w_y} |I|^2 dy - \frac{1}{2i\omega C} \int_0^{2w_y} |\frac{dI}{dy}|^2 dy \quad (6)$$
and making a term by term identification with the constitutive terms of (5). In particular the TE contribution to the reactive power is identified with the inductive term and the TM contribution with the capacitive term of (6). These equivalences allow also to define a specific(i.e. per unit length) resistance R, inductance L and capacitance C. β is then given by $\omega\sqrt{LC}$.

III. RESULTS. The evaluation of the power integral shows that as long as the current differs from zero at the antenna tips the feeder currents cannot be neglected. In [9] it is shown in detail that the consequence of such a neglect is an infinite value of the inductive energy and an overestimation of the loading resistance. This explains the results of [5]. If this model is used with a current that vanishes at the antenna tips, as in [6] , a reasonable value of the loading resistance can be obtained but such a current is of course not a realistic assumption in the case of the usual short-circuited antennae. In addition to a correct value of the loading resistance R under all conditions, the present model allows the computation of an equivalent specific inductance L and capacitance C. Preliminary results, analysed in detail in [9] obtained for $\beta = 0$ indicate that the overall effect of the finiteness of the antenna is a reduction of coupling : increase of L and and decrease of R. This is shown in Fig. 2 where, for a set of typical plasma and geometrical conditions, we compare the values of R and ωL with the corresponding values, denoted R_2 and ωL_2, obtained from the infinite antenna theory [2]. The strong dependence on antenna aspect ratio $\frac{w_y}{w_z}$ shows the correct asymptotic dependence in contrast with the puzzling results of [5]. The important reduction of R/L in the case of broad and short antennae will severely limit the rf power,for a given applied voltage, that can be transferred by such antennae.

REFERENCES.
[1] J. Adam, Eur-CEA-FC-1004 (1979).
[2] R.R. Weynants, A.M. Messiaen, C. Leblud, P.E. Vandenplas, Proc. 2d Joint Grenoble-Varenna Int. Symp. on Heating in Toroidal Plasmas, Invited paper, Como, Sept. 1980.
[3] Y. Lapierre, Ibid.,paper C(79).
[4] A.M. Messiaen, R.R. Weynants, L. Bral, R. Koch, Proc. IVth Topical Conference on R.F. plasma heating, paper A23, Austin, Feb. 1981.
[5] A. Bers, L.P. Harten, A. Ram, Ibid.,paper A16.
[6] J. Adam, J. Jacquinot, Y. Lapierre, D. Marty, Ibid.,paper A1.
[7] R.W.P.King,"The Theory of Linear Antennas",Harvard University Press Cambridge, Massachusetts, 1956.
[8] S. Ramo, J. Whinnery, T. Van Duzer, "Fields and waves in communication electronics", John Wiley & Sons, New York 1965.
[9] V.P. Bhatnagar, R. Koch, A.M. Messiaen, R.R. Weynants, to be publ.

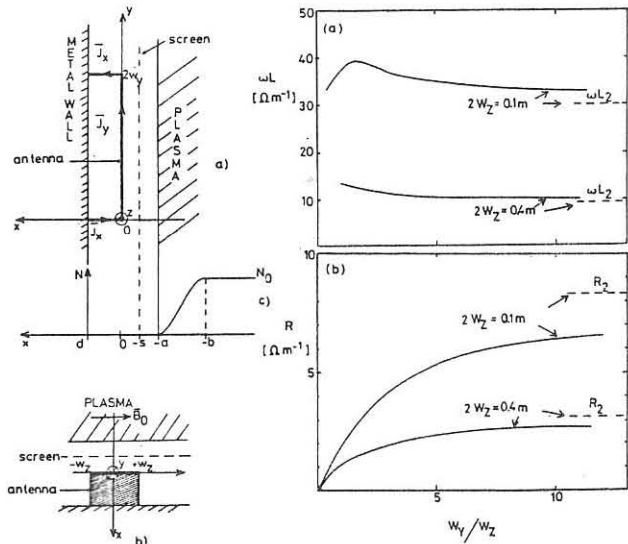+ Chercheur agréé IISN; *Maître de Recherches FNRS;°Bevoegdverklaard Navorser NFWO.
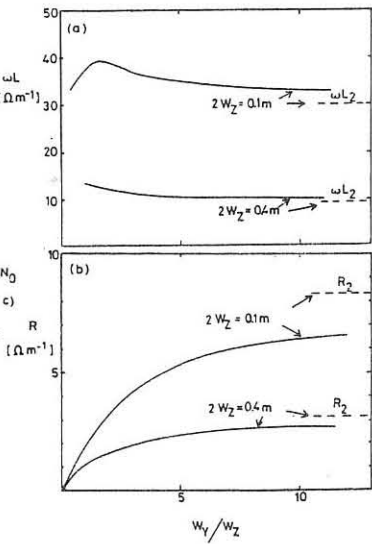
Fig.1. Model of the all-metal antenna.

Fig.2. R and L vs w_y/w_z for a=b=3cm,d=4cm, $N_{e,o}$=5 10^{13}cm^{-3}, f=2f_{cD}=27 MHz. R_2 and L_2 are for an infinite length antenna.

PARTICLE TRAPPING UNDER CYCLOTRON RESONANCE CONDITIONS

A.B. Kitsenko, I.M. Pankratov, K.N. Stepanov

Kharkov Institute of Physics & Technology, Ukr.Acad.Sci.,
Kharkov, USSR

In the present report it is shown that particle trapping by an electromagnetic wave under cyclotron resonance conditions $\omega \approx n\omega_B$ ($n=1,2$) may essentially influence wave absorption and RF plasma heating in up-to-date traps and tokamak reactors.

The resonant particle motion in a uniform magnetic field and electromagnetic wave field $\omega \exp i(\kappa_\perp x + \kappa_\parallel z - \omega t)$ at $\omega \approx n\omega_B$ is described by the equations (see also [1,2]):

$$\frac{dv_\parallel}{dt} = \frac{e}{m} \frac{\kappa_\parallel}{\kappa_\perp} \frac{a^n}{n 2^n} \, Re \, E_{eff} \, e^{i\Phi_n}$$

$$\frac{dv_\perp}{dt} = \frac{e}{m} \frac{a^{n-1}}{2^n} \, Re \, E_{eff} \, e^{i\Phi_n}$$

$$\frac{d\Phi_n}{dt} = n\omega_B - \omega + \kappa_\parallel v_\parallel + \frac{e n \kappa_\perp}{m\omega_B} \frac{a^{n-2}}{2^n} \, Re \, i E_{eff} \, e^{i\Phi_n} \quad (1)$$

where $\Phi_n = \kappa_\parallel z - \omega t + \kappa_\perp \xi - \epsilon n\theta$, $x = \xi - \epsilon v_\perp \sin\theta/\omega_B$,

$E_{eff} = E_x + i\epsilon E_y + E_\parallel v_\parallel \kappa_\perp/\omega_B$, $a = \kappa_\perp v_\perp/\omega_B \ll 1$, $\epsilon = sgn\,e$.

The ratio $E_{eff}/|E|$ depends strongly on the wave type and the parameter $\kappa_\parallel/\kappa_\perp \lesssim 1$. For the extraordinary wave ($\omega \approx \omega_{Be}$) and fast magnetosonic wave (at $\omega \approx \omega_{Bi}$, $i=d,t$) we have $E_{eff} \sim \kappa_\parallel v_\perp E$, for the ordinary wave ($\omega \approx \omega_{Be}$), $E_{eff} \sim \kappa_\parallel \varrho_L E \kappa_\perp/\kappa_\parallel$, while for the Alfven (ion-cyclotron) wave ($\omega \approx \omega_{Bi}$) and fast magnetosonic wave under proton minority cyclotron resonance $E_{eff} \sim E$ ($\varrho_L = v_T/\omega_B$, $v_T = \sqrt{T/m}$).

The particle motion in the vicinity of the centres ($\Phi_n = \Phi_c$) on the phase plane (a, Φ_n) is described by the equation $\ddot{\Phi}_n + \Omega_{tr}^2(\Phi_n - \Phi_c) = 0$ where Ω_{tr} is the trapped particle oscillation frequency determined by the relations ($\omega \approx \omega_B$):

$$\Omega_{tr} \sim \left(\frac{\kappa_\perp}{\kappa_\parallel}\right)^{2/3} \left(\frac{\kappa_\perp v_E}{\omega_B}\right)^{2/3} \omega_B, \quad \Delta a \sim \left(\frac{\kappa_\perp}{\kappa_\parallel}\right)^{2/3} \left(\frac{\kappa_\perp v_E}{\omega_B}\right)^{1/3}, \quad (2)$$

if $a \lesssim \left(\frac{\kappa_\perp}{\kappa_\parallel}\right)^{2/3} \left(\frac{\kappa_\perp v_E}{\omega_B}\right)^{1/3}$,

$$\Omega_{tr} \sim \frac{\kappa_\parallel}{\kappa_\perp} \left(\frac{\kappa_\perp v_E}{\omega_B}\right)^{1/2} (\kappa_\perp \varrho_L)^{1/2} \omega_B, \quad \Delta a \sim \frac{\kappa_\perp}{\kappa_\parallel} \left(\frac{v_E}{v_T}\right)^{1/2} \omega_B, \quad (3)$$

if $a \gtrsim \left(\frac{\kappa_\perp}{\kappa_\parallel}\right)^{2/3} \left(\frac{\kappa_\perp v_E}{\omega_B}\right)^{1/3}$.

For $\omega \approx 2\omega_B$ we have

$$\Omega_{tr} \sim \kappa_\parallel \varrho_L \left(\frac{\kappa_\perp v_E}{\omega_B}\right)^{1/2} \omega_B, \quad \Delta a \sim \frac{\kappa_\perp}{\kappa_\parallel} \left(\frac{\kappa_\perp v_E}{\omega_B}\right)^{1/2} \quad (4)$$

where $v_E = cE_{eff}/B_0$, Δa is the width of the particle trapping region in the variable a. The width of the trapping region in $v_\parallel$ is ($\Delta a = \kappa_\perp v_\perp \Delta v_\perp/\omega_B$)

$$\Delta v_\parallel \sim \kappa_\parallel v_\perp \Delta v_\perp/n\omega_B \ll \Delta v_\perp. \quad (5)$$

If $\eta \lesssim 1$, where

$$\eta = (\nu_{coll}/\Omega_{tr})(v_T/\Delta v_\parallel)^2, \quad (6)$$

the resonant particle trapping results in strong distortion of the distribution function in $v_\parallel$ in the region of width $\Delta v_\parallel$ near $v_\parallel = (\omega - n\omega_B)/\kappa_\parallel$. (At $\eta \gg 1$ the collisions

"maxwellize" the distribution function in this region). However, even at $\eta \gg 1$ nonlinear effects can influence the wave absorption due to considerable distortion of the distribution function in $v_\perp$. Using eqs.(2) to (6) we obtain for η the following estimates:

$$\eta \sim \frac{\nu_{coll}}{\omega_B} \left(\frac{v_T}{v_E}\right)^2, \quad a \lesssim \left(\frac{\kappa_\perp}{\kappa_\parallel}\right)^{2/3} \left(\frac{\kappa_\perp v_E}{\omega_B}\right)^{1/3} \quad (\omega \approx \omega_B)$$

$$\eta' \sim \frac{\nu_{coll}}{\omega_B} \left(\frac{v_T}{v_E}\right)^{3/2} (\kappa_\perp \varrho_L)^{-1}, \quad a \gtrsim \left(\frac{\kappa_\perp}{\kappa_\parallel}\right)^{2/3} \left(\frac{\kappa_\perp v_E}{\omega_B}\right)^{1/3} \quad (\omega \approx \omega_B)$$

$$\eta \sim \frac{\nu_{coll}}{\omega_B} \left(\frac{\omega_B}{\kappa_\perp v_E}\right)^{3/2} (\kappa_\parallel \varrho_L)^{-1} \quad (\omega \approx 2\omega_B) \quad (7)$$

When the plasma with reactor parameters ($n_0 \sim 3 \cdot 10^{14} cm^{-3}$, $T \sim 10 keV$, $B_0 \sim 50 kG$) at $\kappa_\parallel \sim 0.3\kappa_\perp$ is heated at $\omega \approx \omega_{Bo}$ ($E \sim 1 kV/cm$) by the extraordinary wave, we have $\eta \sim 30$, $\eta' \sim 4$, $\Delta v_\perp/v_{Te} \sim 0.1$; using the ordinary wave gives $\eta \sim 0.5$, $\eta' \sim 0.2$, $\Delta v_\perp \lesssim v_{Te}$; the second harmonic resonance $\omega \approx 2\omega_{Be}$ gives $\eta \sim 1$ and $\Delta v_\perp/v_{Te} \sim 0.1$.

Heating by the fast magnetosonic wave ($E \sim 300$ V/cm) at $\omega \approx \omega_{Bd}$ yields $\eta \sim \eta' \sim 5$ and $\Delta v_\perp \sim v_{Td}$; using the minority heating ($\omega \approx \omega_{Bp}$), $\eta \sim \eta' \sim 10^{-2}$ and $\Delta v_\perp \gtrsim v_{Tp}$; the second harmonic heating ($\omega \approx 2\omega_{Bd}$) gives $\eta \sim 1$ and $\Delta v_\perp \sim v_{Td}$.

When the plasma with $n_0 \sim 10^{13} cm^{-3}$, $B_0 \sim 20$ kG, $T \sim 300$ eV is heated by the ion cyclotron wave ($E \sim 300$ V/cm) we obtain $\eta \sim 10^{-4}$, $\eta' \sim 10^{-3}$ and $\Delta v_\perp > v_{Tp}$.

The above formulas obtained for the homogeneous magnetic field can also be applied to tokamaks if the difference $|\omega - \omega_B(R)|$ is smaller than Ω_{tr} while the resonant particle is moving along the magnetic line of force with $v_\parallel \sim v_T$ during the time Ω_{tr}^{-1}, i.e.

$$\Omega_{tr}^2 > \varepsilon_t \omega_\varrho \omega_B, \quad \left(\varepsilon_t = \frac{r}{R}, \; \omega_\varrho = \frac{v_T}{\varrho R}\right) \quad (8)$$

where ϱ is the safety factor.

Putting $\varrho \sim 2$, $\varepsilon_t \sim 0.1$, $R \sim 5$ m ($\varepsilon_t \sim 0.05$, $R \sim 1$ m for the Alfven wave) in the above examples we find that the condition (8) is met when the plasma is heated by the Alfven wave and the fast magnetosonic wave under the proton minority resonance; for $\omega \approx \omega_{Be}$, $\Omega_{tr}^2 \sim \varepsilon_t \omega_\varrho \omega_{Be}$ at the resonances $\omega \approx n\omega_{Bd}$ for the fast magnetosonic wave $\Omega_{tr}^2 \ll \varepsilon_t \omega_\varrho \omega_{Bd}$ with $\eta \gg 1$.

One can neglect the nonuniformity of the wave field amplitude in eqs.(1) if $Jm\,\kappa_\parallel v_T < \Omega_{tr}$. This inequality holds in the above examples for the Alfven wave and for the proton minority cyclotron resonance.

The examples presented show that the nonlinear effects are important for Alfven waves and fast magnetosonic waves when the proton minority resonance is involved, but they can be essential for the other waves under study as well.

REFERENCES

1. A.B. Kitsenko, I.M. Pankratov, K.N. Stepanov. Zh.Tekh. Fiz., 45, (1975), 912.

2. A.B. Kitsenko, I.M. Pankratov, K.N. Stepanov. Preprint KFTI 74-6, Kharkov (1974).

ELECTRON CYCLOTRON HEATING OF HIGH DENSITY PLASMAS
IN LARGE TOKAMAKS

Yu.F.Baranov, V.I.Fedorov

A.F.Ioffe Physico-Technical Institute, Leningrad, USSR

An efficient absorption of microwave power was observed in the experiments on the electron cyclotron heating (ECH) of a high density plasma ($n > n_{cr}$ – critical density) in FT-1 tokamak. For the interpretation of the experimental data we developed a numerical code which enabled us to calculate the energy deposition taking into account the real antenna directivity. We used toroidal coordinates r, θ, φ, where r is the radius in the minor cross-section, and are the poloidal and toroidal angles. The radial profiles of the plasma density n, electron temperature T_e, toroidal magnetic field $B^\bullet$ and current density j were chosen in the form

$$n = n_o (1 - r^2/a^2)^{1.1}, \qquad T_e = T_{eo}\, exp(-4r^2/a^2)$$

$$B_\varphi = B_{\varphi o}(1 + r\cos\theta/R_o), \qquad j = j_o\, exp(-6r^2/a^2)$$

roughly corresponding to the experimental data.

The ray trajectories and the absorption of the electromagnetic waves were calculated as in Ref. /1/, but in a vicinity of the upper hybrid resonance we used the "warm plasma" approximation /2/. The well known Bernstein's dispersion equation /2/ was used for the waves resulted from the linear mode conversion.

Because of the strong refraction the electromagnetic waves could reach ECR region in the high density plasma only after several reflections from the chamber wall. Since the wall was roughly homogeneous in θ -direction we considered the wave vector component k_θ to be constant during the reflection. A strong scattering of the waves occured in the φ -direction and we treated k_φ after the reflection as a random value, as well as the wave polarisation.

The calculation revealed high efficiency of the energy absorption in the FT-1 plasma for the case of the internal wave excitation (from the high field side of the torus). For example, 90% of the incident power was absorbed at $n_o = 2n_c$ and about 75% at $n_o = 3n_c$. But the heating was rather peripheral with the maximum of the absorption at r/a = 0.7. For the plasmas of large tokamaks (T-10 and T-15 types) the calculations gave also the peripheral absorption at $n_o > 2n_c$. At $n_o < 2n_c$ the heating of a central region of the plasma is possible if the wave is launched from the internal side of the torus. Fig.1 illustrates such a possibility for tokamak T-15 (R_o = 240 cm, a= 70 cm, B_φ = 35 kG, I_p = 1.4 mA, n_o = 1.6n_c, T_{eo} = 5 keV). We see projections of the ray trajectories onto the minor cross-section of the torus for the wave launched at various initial angles $\alpha_o = arctg \frac{k_{\theta o}}{k_{ro}}$ and the angle $\beta_o = arctg \frac{k_{\varphi o}}{k_{ro}}$ = 73°. In the case the energy is absorbed at r < 0.5a if $|\alpha_o| < 14°$.

Another possibility is based on the linear wave conversion and subsequent absorption of Bernstein waves. It is illustrated in Fig.2. Here the parameters of the discharge are as follows: n_o= 1.6n_c, $\omega_H(0)/\omega$ = 0.82, T_{eo} = 5 keV. The incident angle β_o is equal to 87° for all trajectories. The optical thickness of a plasma in the ECR region for extraordinary waves at $\beta_o = 90°$ can be evaluated from the formula

$$\mathcal{æ} = (2-V)^{3/2}\left(1 - \frac{V}{4} - \frac{5}{4V}\right)\frac{\pi R \omega T_e^2}{m^2 c^5}$$

Where $V = \omega_p^2/\omega^2/\omega = \omega_H$, R is major radius of the ECR layer. This formula was obtained in the WKB approximation in a model of a one-dimensional-inhomogeneous plasma. We used the well known dispersion equation with thermal corrections of the order $\left(\frac{k_\perp^2 v_T^2}{\omega_H^2}\right)^2$ (see, example Ref /3/) and carried out the integration shifting the contour in the complex plane.

In the case under consideration $\mathcal{æ}$ = 0.04, so that the main energy absorption was due to the Bernstein's mode. The parts of the trajectories in the region of a strong absorption are marked in Fig.2 by thick lines. We see that all the waves with $|\alpha_o| < 6°$ are absorbed at r < 0.5a. It is interesting that the picture of the wave propagation and absorption just described is rather insensitive to variation of the plasma temperature in the range 1 keV $\leqslant T_e \leqslant$ 10 keV. Thus, when plasma parameters are changing no adjustments of the antenna are necessary in this case.

It is advantageous from technological point of view to shift the antenna from the inner side of the torus toward the ECR layer (see Fig.3). But the optimal values of the angles α_o and β_o depend strongly on plasma parameters. As a consequence, an adjustable antenna is needed for the efficient plasma heating. For example, we can see from Fig.3 (β_o = 87°, n_o = 2n_c) that the Bernstein waves are absorbed on the plasma periphery, so the heating efficiency is connected with the cyclotron damping of the extraordinary wave, which is strongly influenced at $n \to 2n_c$ by the refraction.

In conclusion, we should like to point out that the internal excitation of the waves can reduce the density limitation of ECH.

REFERENCES

1. Litvak A.G., Permitin G.V., Suvorov E.V., Frajman A.A. Electron cyclotron heating of plasma in toroidal system., Nuclear Fusion, 1977, v.17, No 4, p.659.
2. Akhiezer A.I., Akhiezer I.A., Polovin R.V., Sitenko A.G., Stepanov K.N. Plasma Electrodynamics, Pergamon Press, 1975, Chap.5.
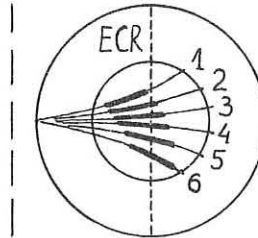3. Shkarofsky I.P. Dielectric Tensor in Vlasov Plasmas near Cyclotron Harmonics. Phys.Fluids, 1966, v.9, No 3, p.561.

Fig.1 β_o=73°
1 - α_o = 10°
2 - α_o = 4,3°
3 - α_o = 1,4°
4 - α_o = -1,4°
5 - α_o = -4,3°
6 - α_o = -10°
n_o = 1,6 n_c
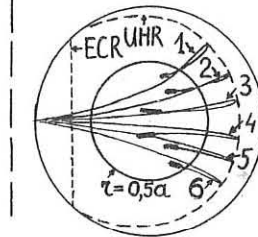
Fig.2 β_o = 87°
1 - α_o = 7°
2 - α_o = 4,3°
3 - α_o = 1,4°
4 - α_o = -1,4°
5 - α_o = -4,3°
6 - α_o = -7°
n_o = 1,6 n_c
$\omega_H(0)/\omega$ = 0,82

Fig.3 β_o = 87°
1 - α_o = 38°
2 - α_o = 33°
3 - α_o = 28°
4 - α_o = 22°
n_o = 2n_{cr}
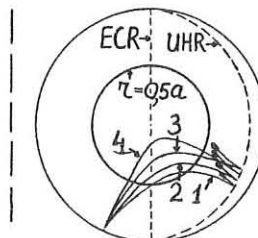
ABSORPTION OF A PLASMA OF FINITE DENSITY AROUND THE
ELECTRON-CYCLOTRON HARMONICS

M. Bornatici[a], F. Engelmann[b], V. Petrillo[c]

a) Istituto di Fisica e Matematica Applicata, Università di Pavia, Pavia, Italy.
b) FOM-Instituut voor Plasmafysica "Rijnhuizen" - Association Euratom-FOM - Nieuwegein, The Netherlands.
c) Istituto di Fisica, Università di Milano, Milano, Italy.

ABSTRACT. Analytical formulae for the absorption of a non-relativistic thermal plasma of finite density around the electron-cyclotron harmonics for oblique wave propagation are presented. The absorption coefficient is obtained from the energy balance, and finite-density effects are analysed in terms of wave dispersion and polarization. For a wide range of angles around perpendicular propagation the absorption of the fast extraordinary mode at the second harmonic is found to be stronger than what would follow from the tenuous-plasma limit, polarization effects being larger than dispersion effects.

INTRODUCTION. A simplified analytical treatment based on the use of the energy balance has been shown to provide physical insight in the absorption of electromagnetic waves around the electron-cyclotron frequency ω_c in a thermal plasma [1,2]. In particular, the significance of polarization effects, related with finite plasma density were displayed. Here this approach is used to evaluate the absorption coefficient at frequencies close to the n-th harmonic, $\omega \approx n\omega_c$, $n \geq 2$, for oblique propagation, i.e., at angles θ with respect to a static magnetic field $\underline{B}_0$ such that $N|\cos\theta| \gg (v_t/c)$ where N is the wave refractive index, $v_t = (T/m)^{\frac{1}{2}}$ is the electron thermal velocity and c the speed of light with $v_t \ll c$. This analytical study is complementary to numerical analyses performed earlier [3,4].

ABSORPTION COEFFICIENT. From the energy balance one obtains for the absorption coefficient

$$\alpha = 2\underline{k}'' \cdot \underline{S}/|\underline{S}| = \left[(\omega/4\pi)\underline{E}^* \cdot \underline{\varepsilon}_a \cdot \underline{E}\right]/|\underline{S}| , \tag{1}$$

with $\underline{k} = \underline{k}' + i\underline{k}''$ the wave vector ($|\underline{k}''| \ll |\underline{k}'|$), ω the (real) wave frequency, $\underline{E} \equiv \underline{E}(\underline{k}',\omega)$ the Fourier component of the wave electric field, $\underline{E}^*$ denoting the complex conjugate of $\underline{E}$. Furthermore, $i\underline{\varepsilon}_a \equiv i\underline{\varepsilon}_a(\underline{k}',\omega)$ is the anti-Hermitian part of the dielectric tensor and $\underline{S}$ is the (total) power flux density. Assuming propagation in the xz-plane with $\underline{B}_0 = \hat{z}|B_0|$, using the well-known expressions for the components of $\underline{\varepsilon}_a$ to lowest significant order in finite Larmor radius effects, and neglecting corrections of order $|\omega - n\omega_c|/\omega \lesssim (v_t/c)/N|\cos\theta|$ allows to write the absorption coefficient of the extraordinary (X) and ordinary (O) mode

$$\alpha_n^{(X,0)}(\omega,\theta) = \alpha_n(\theta)\, \phi_n(\omega,\theta)\, \mu_n^{(X,0)}(\theta) , \tag{2}$$

where

$$\alpha_n(\theta) \equiv \pi \frac{n^{2n-1}}{2^n(n-1)!} \frac{\omega_p^2}{c} \left(\frac{v_t}{c}\right)^{2(n-1)} (\sin\theta)^{2(n-1)}(1 + \cos^2\theta) , \tag{3}$$

$$\phi_n(\omega,\theta) \equiv \exp(-\zeta_n^2)/[\sqrt{2\pi}\,\omega N \cos\theta(v_t/c)] \tag{4}$$

with

$$\zeta_n \equiv \frac{1}{\sqrt{2}} \frac{\omega - n\omega_c}{\omega} \frac{c}{v_t} \frac{1}{N\cos\theta} , \tag{5}$$

and

$$\mu_n^{(X,0)}(\theta) \equiv \left[\frac{N^{2n-3}}{1 + \cos^2\theta} \frac{|E_x - iE_y|^2}{(4\pi\underline{S}/cN)}\right]_{N=N^{(X,0)}} . \tag{6}$$

The function μ_n describes the effects of wave dispersion and polarization. From (6) it is apparent that absorption is related with the deviations from circular, in the plane perpendicular to $\underline{B}_0$, of the wave polarization, the component E_z contributing via the power flux only.

Noting that for the case under consideration the contribution of $\underline{\varepsilon}_a$ to the dispersion relations is small, one can evaluate (6) considering just its real part, which furthermore can be taken in the cold approximation [5]. This implies

$$\frac{E_x - iE_y}{E_y} = i(n-1)\left(1 - \frac{n+1}{n} f_n^{(X,0)}\right) , \tag{7}$$

and

$$\left[N^{(X,0)}\right]^2 = 1 - \left(\frac{\omega_p}{n\omega_c}\right)^2 \frac{2[n^2 - (\omega_p/\omega_c)^2]}{2[n^2 - (\omega_p/\omega_c)^2] - \sin^2\theta \mp \rho_n} \equiv 1 - \left(\frac{\omega_p}{n\omega_c}\right)^2 f_n^{(X,0)} , \tag{8}$$

with

$$\rho_n^2 \equiv \sin^4\theta + \frac{4}{n^2}\left[n^2 - \left(\frac{\omega_p}{\omega_c}\right)^2\right]^2 \cos^2\theta ,$$

the functions f_n being defined by (8).

Using also the expression for the power flux which here, to lowest order, reduces to the Poynting vector, Eqs. (6) and (7) yield

$$\mu_n^{(X,0)}(\theta) = \frac{N^{(X,0)\,2n-3}}{1 + \cos^2\theta} \frac{(n-1)^2\left[1 - \frac{n+1}{n} f_n^{(X,0)}\right]^2}{[(a_n^2 + b_n^2)^{\frac{1}{2}}]_{N=N^{(X,0)}}} , \tag{9}$$

where

$$a_n^2 \equiv \left[1 + \frac{[1 - (\omega_p/n\omega_c)^2]N^2\cos^2\theta}{[1 - (\omega_p/n\omega_c)^2 - N^2\sin^2\theta]} n^2\left(1 - \frac{n^2-1}{n^2} f_n^{(X,0)}\right)^2\right]^2 \sin^2\theta , \tag{10}$$

$$b_n^2 \equiv \left[1 + \frac{1 - (\omega_p/n\omega_c)^2}{1 - (\omega_n/n\omega_c)^2 - N^2\sin^2\theta} n^2\left(1 - \frac{n^2-1}{n^2} f_n^{(X,0)}\right)^2\right]^2 \cos^2\theta . \tag{11}$$

DISCUSSION. The dispersion and polarization effects contained in the function $\mu_n^{(X,0)}(\theta)$, given by (9), account for the finite-density effects in the wave absorption. For simplicity, let us first consider quasi-perpendicular propagation, i.e., angles of propagation such that $\sin^4\theta \gg 4n^2[1 - (\omega_p/n\omega_c)^2]^2\cos^2\theta$, for which (9), to lowest significant order in $\cos^2\theta$, yields

$$\mu_n^{(X)}(\theta) = \left[N_\perp^{(X)}\right]^{2n-3}\left[1 + \frac{(\omega_p/\omega_c)^2}{n[n^2 - 1 - (\omega_p/\omega_c)^2]}\right]^2 \equiv \mu_n^{(X)}(\theta = \tfrac{\pi}{2}) , \tag{12}$$

with $N_\perp^{(X)} \equiv N^{(X)}(\theta = \pi/2)$ following from (8), while

$$\mu_n^{(0)}(\theta) = (n-1)^2\left[N_\perp^{(0)}\right]^{2n+1}\cos^2\theta . \tag{13}$$

From (12) it appears that for the fast X-mode, i.e., for $\omega_p^2 < n(n-1)\omega_c^2$, the term within the square brackets, which accounts for polarization effects, increases with density, in contrast to the factor $\left[N^{(X)}\right]^{2n-3}$, containing the dispersion effects, which decreases as the density increases. Thus, for the fast X-mode and quasi-perpendicular propagation, dispersion and polarization effects, as a function of density, introduce opposite tendencies (note that for the slow X-mode, i.e., for $(n^2 - 1)\omega_c^2 < \omega_p^2 < n(n+1)\omega_c^2$, polarization and dispersion both decrease $\mu_n^{(X)}(\theta = \pi/2)$ as density increases). For densities such that $\omega_p^2 \ll n(n-1)\omega_c^2$, Eq. (12) yields $\mu_n^{(X)}(\theta = \pi/2) = 1 - c_n(\omega_p/\omega_c)^2$, with $c_n \equiv (n - \tfrac{3}{2} - 2/n)/(n^2 - 1)$, the contribution $n - \tfrac{3}{2}$ accounting for dispersion and $-2/n$ for polarization. For the second harmonic, $c_2 = -\tfrac{1}{6}$, polarization prevailing with respect to dispersion, and, hence, $\mu_2^{(X)}(\theta = \pi/2) > 1$ and increasing with density. On the contrary, $c_n > 0$, for the harmonics $n \geq 3$, dispersion dominating over polarization so that $\mu_n^{(X)}(\theta = \pi/2) < 1$ and decreasing with density. Thus, for propagation close to perpendicular the absorption of the second harmonic (fast) X-mode is larger than obtained by using $\mu_n^{(X)} = 1$ as valid in the tenuous-plasma limit, while for the harmonics $n \geq 3$ the opposite is true. On the other hand, for quasi-parallel propagation, i.e., for $\sin^4\theta \ll 4n^2[1 - (\omega_p/n\omega_c)^2]^2\cos^2\theta$, one has, to lowest order in $\sin\theta$,

$$\mu_n^{(X)}(\theta) = \left[N^{(X)}(\theta \ll 1)\right]^{2n-3} = \left[1 - \frac{(\omega_p/\omega_c)^2}{n(n-1)}\right]^{n-\frac{3}{2}} \equiv \mu_n^{(X)}(\theta = 0) , \tag{14}$$

$\mu_n^{(X)}(\theta = 0) < 1$ being a decreasing function of density for all the harmonics $n \geq 2$. In this limit finite-density effects enter the wave absorption via dispersion only, which tends to reduce absorption with respect to an extrapolation of the tenuous-plasma limit $\mu_n^{(X)} = 1$. The case of the (fast) X-mode for arbitrary angles of propagation has been investigated numerically [5] and $\mu_2^{(X)}(\theta)$ is shown in Fig. 1 as a function of θ with $(\omega_p/\omega_c)^2$ as a parameter. It appears that $\mu_2^{(X)}(\theta)$ is larger than its value in the tenuous-plasma limit (dashed curve of Fig. 1) for a range of angles around 90°, which is the wider the smaller $(\omega_p/\omega_c)^2$ is. The dependence, on $(\omega_p/\omega_c)^2$, of the absorption coefficient of the X-mode for perpendicular propagation is shown in Fig. 2 for n = 2; 3. In the absorption of the O-mode finite-density effects are mostly due to dispersion (cf., e.g., (13) for quasi-perpendicular propagation). Hence, in general, the absorption is smaller than what would follow from extrapolating the tenuous-plasma limit, the only exception occurring for the second harmonic at small angles of propagation where absorption is weak [5]. Of course, the results obtained here agree with those found numerically [3,4,5].

REFERENCES.
1. Bornatici, M. and Engelmann, F. (1979) Absorption of Electromagnetic Waves around the Electron Cyclotron Frequency. *Proc. 9th Eur. Conf. on Contr. Fusion and Plasma Physics*, Oxford, 1, 67.
2. Bornatici, M. (1980) Electron Cyclotron Absorption in a Finite Density Plasma. *Proc. Joint Workshop on Electron Cyclotron Emission and Electron Cyclotron Resonance Heating*, Oxford.
3. Audenaerde, K. (1977) *Plasma Phys.* 19, 299.
4. Freund, H.P. and Wu, C.S. (1977) *Phys. Fluids* 20. 963.
5. Bornatici, M., Engelmann, F., Novak, S. and Petrillo, V. (1981) submitted to Plasma Phsyics.
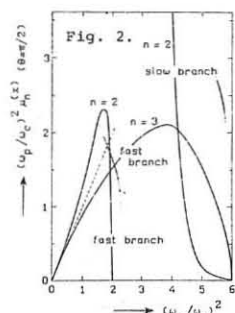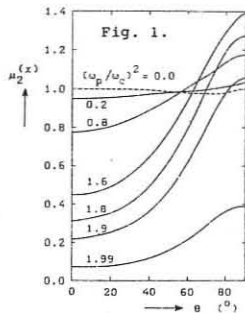
Dependence of the function $\mu_2^{(X)}$, defined by (10), on θ for n=2 and $(\omega_p/\omega_c)^2 = 0$ (dashed curve), 0.2, 0.8, 1.6, 1.8, 1.9, 1.99 (fast mode).

Dependence of $(\omega_p/\omega_c)^2 \mu_n^{(X)}(\theta = \pi/2)$, cf. (13), on $(\omega_p/\omega_c)^2$ for n=2 and 3. The dashed line refers to the tenuous-plasma limit $\mu_n^{(X)}(\theta = \pi/2) = 1$.

LOCAL HEATING AND CURRENT DRIVE INVESTIGATIONS ON TOSCA

M W Alcock, T Edlington, P A Gaisford*, T C Hender*,
B Lloyd** and D C Robinson

Culham Laboratory, Abingdon, Oxon, OX14 3DB, UK
(Euratom/UKAEA Fusion Association)

*Royal Holloway College, University of London
**University of Oxford

ABSTRACT   ECRH experiments at the second harmonic show local heating when the cyclotron resonance is on the outer flux surfaces. Above a critical power level this induces continuous m=1 activity in the heating zone. The local heat conduction coefficient is close to the INTOR value and the parallel heat conduction may be anomalous. Attempts to detect a wave driven current using a variable angled antenna (±50°) indicates that the current is less than 3A/kW in the plasmas used in these investigations.

INTRODUCTION   The resonance zone width for ECRH is generally much less than the plasma radius and localised heat-

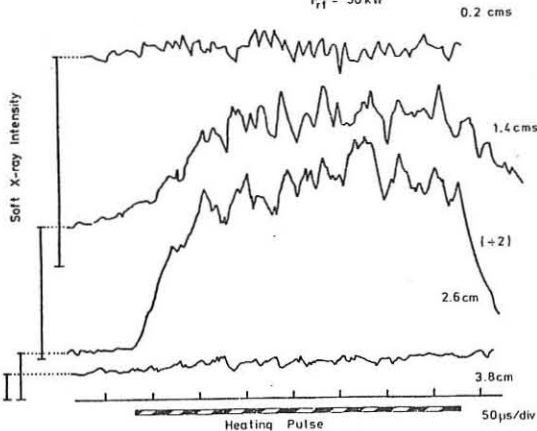$$\bar{n}_e = 7.5 \times 10^{18} \text{ m}^{-3}$$
$$P_{rf} = 50 \text{ kW}$$

Fig.1 Soft X-ray emission from four radii during the heating pulse.

ing is possible in an optically thick plasma, when the directionality of the injected radiation is controlled. This is important for current profile and instability control and heat conduction studies. Even in an optically thin plasma, when one must take account of reflections there is a geometrical effect[1] which permits strong local maxima in the heating profile thus allowing such investigations in small tokamaks. Theory[2] also indicates that cyclotron waves should be suitable for generating a current if the absorption is predominantly on one side of the resonance which is possible for the X-mode in a small tokamak at sufficiently high temperatures with the waves launched preferentially in one direction.

LOCAL HEATING EXPERIMENTS   The soft X-ray emission observed vertically from a seven channel diode array indicates that strong local heating occurs close to the cyclotron resonance both above and below the X-mode cut-off provided the resonance is on the outside of the magnetic surfaces. The emission associated with four different radii during the heating pulse is shown in Fig.1. The signal saturates in some 50μs and falls with a similar time constant. In the high temperature zone continuous fluctuations in the region of 50kHz are produced provided the input power is above some threshold dependent on the initial value of q. These fluctuations appear to be continuous m=1 activity associated with local heating and current concentration producing a small region with q<1. These discharges have $q_a \sim 7$ and before heating $q(0) \lesssim 2$. The new magnetic axis is thus close to the heating zone. Evidently the transport processes in this case do not permit sawtooth activity. The width of the heating zone is typically 20mm at a particular toroidal field. If the toroidal field is varied then heating is detected at a particular radius if the resonance zone moves approximately 30mm, - Fig.2. The existence of two sustained temperature maxima and the absence of a peak on the opposite side of the magnetic surface indicates the 2-D nature of the heat conduction process in the tokamak. We have used a 2D

anisotropic heat conduction and field diffusion code with a local heating source to simulate this behaviour. The experimental results can be reproduced by reducing the parallel heat conduction by 100 x as shown in Fig.3.
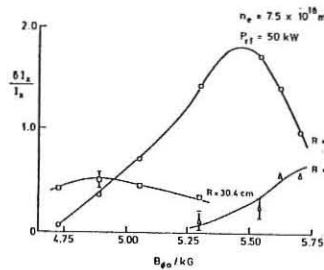

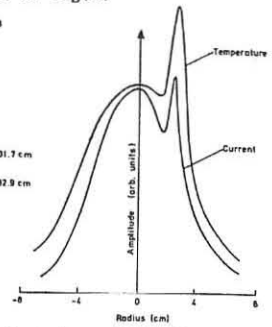Fig.2 Variation of soft X-ray emission at three radial positions with toroidal field.

Fig.3 Temperature and current profile associated with anomalous parallel heat conduction.

From the heating and decay times and the width of the heating zone we obtain a local average heat conduction coefficient of 0.5 $m^2 s^{-1}$ in the hot core of the plasma which is about six times smaller than the average INTOR value. An alternative explanation for the failure of the temperature to be uniform on a magnetic surface is that the ECRH produces perpendicular runaway and electrons with energies of ∿3keV become trapped with large banana orbits of width ∿1-2cm, which is in accord with the observed absence of local heating on the high field side of the plasma. No evidence for this non-thermal perpendicular electron distribution has however been obtained.

CURRENT DRIVE EXPERIMENTS   Theoretical ray tracing and absorption calculations for the X-mode in TOSCA at a central density of $4.5 \times 10^{18} m^{-3}$ and temperatures of 600eV indicate that a net current of some 30A/kW should be produced. The calculations suggest that the optimum angle of injection is less than 14° and that although the single pass absorption can be quite high (80%) the local current produced on one side of the resonant layer is approximately cancelled by that on the opposite side of the layer. This should produce a substantial change in the current profile and is likely to excite mode activity. The directed antenna in the experiments produces its power in two lobes (normally at ±20°), at +8° and +48° and can be rotated so that one lobe should be efficient for current drive.

Typical discharge waveforms for such an experiment are shown in Fig.4. The heating is not as efficient as for the usual ± 20° antenna and in general the soft X-ray emission is not fully sustained throughout the heating pulse. In both directions, the plasma current increases by typically 10% associated with the decrease in inductance, and resistance but there is a difference in the two directions of up to 300 amps for 100 kW input. As with the perpendicular antennae the high power ECRH does not produce run-away discharges.

CONCLUSIONS   The local heating on the outer flux surfaces may be associated with anomalous parallel heat conduction or with the presence of perpendicular electron runaway leading to a build up trapped electrons. The efficiency for current drive in these experiments appears to be low, possibly because the single pass absorption is low.

Fig.4 Discharge waveforms for a directed antenna.

REFERENCES
[1]   FIELDING P J, Culham Laboratory Report, CLM-P615 (1980).
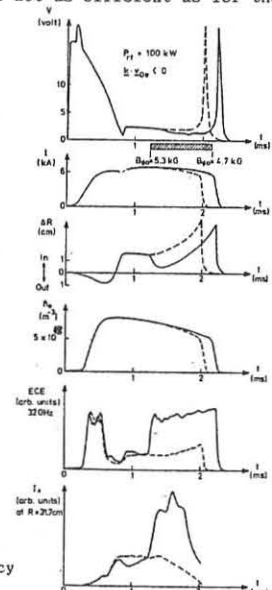[2]   CORDEY J G et al, Culham Laboratory Report, CLM-P636 (1981)

OBSERVATION OF CURRENTS DRIVEN BY RF WAVES AT THE ELECTRON CYCLOTRON RESONANCE IN THE CULHAM LEVITRON

D F H Start, N R Ainsworth, J G Cordey, T Edlington
W H Fletcher, M F Payne and T N Todd

Culham Laboratory, Abingdon, Oxfordshire, UK
(Euratom/UKAEA Fusion Association)

ABSTRACT   An observation of current generated by RF waves at the electron cyclotron resonance is reported. The current is found to flow in opposite directions on opposite sides of the non-Doppler shifted resonance position confirming that the current is driven by asymmetric heating of the electron distribution function by Doppler shifted waves. Scaling measurements show that the current ($\sim$30mA/W) is directly proportional to both the microwave power and electron temperature and inversely proportional to the density.

INTRODUCTION   During the last few years there has been growing interest in the possibility of driving the plasma current in a tokamak reactor continuously using RF waves. In 1980 Fisch and Boozer[1] proposed a scheme which relies on creating an asymmetric plasma resistivity. In this scheme an electron cyclotron wave, for example, is used to increase the perpendicular energy of resonant electrons moving in a particular direction along the magnetic field lines. The reduced collisionality of these electrons leads to an asymmetry of the electron distribution function which manifests itself as a current. The present experiments were designed to search for such a current.

EXPERIMENTAL METHOD AND RESULTS   The experiments were carried out using the Culham Levitron which is an axisymmetric toroidal system with a levitated superconducting ring of major radius 30cm and minor radius 4.5cm[2]. The ring current was 120kA and the current through the centre column providing the toroidal field was 65kA. The helium plasma was produced by ECRH using a 10GHz microwave source. Power levels of up to 120watts were used to form plasmas with temperature (T_e) and densities (n_e) in the range $1\times10^{11} < n_e < 3\times10^{11}$ and $3eV<T_e<18eV$. For each set of conditions the profiles of T_e and n_e were measured using a swept double probe. The microwave power was 100% square wave modulated at 2.88KHz and the total oscillating current flowing in the plasma was detected through the voltage induced in a 40 turn coil which looped the plasma in the poloidal direction. The coil signal was recorded digitally as was the signal from the microwave power monitor. The 2.88KHz component of each signal was then extracted by Fourier analysis. The observed coil signal consisted of a component due to the current flowing parallel to the field and a component arising from the modulation of the perpendicular diamagnetic current due to modulation of T_e and n_e. The diamagnetic component ($\sim$15% of the parallel current) was eliminated by making measurements with 'normal' and 'reversed' toroidal fields and averaging the results. Typical signals from the coil are displayed in the inset of Fig.1 showing that the current rises in about 15μs after the microwave power onset. This fast rise shows that the current is not carried by runaway electrons and is consistent with the skin-time of the plasma. The upper and lower coil signals show the reversal of the current when the poloidal direction of the microwave input power is reversed. Note that the principal field is the poloidal field in the Levitron.
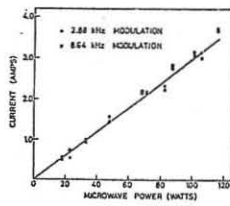
The radial position of the current was located using a floating probe which intercepted 3mm of the plasma in minor radius and 5cm in the toroidal direction and which served to inhibit the current. (The probe adjusts its floating potential to draw an essentially randomly directed current from the background plasma to cancel the intercepted wave driven current). Figure 1 shows the 2.88KHz component of the coil signal as a function of the probe position in minor radius. The electron cyclotron resonance is 1.65cm from the ring. The data are averaged over 'normal' and 'reversed' toroidal field conditions. As the probe moves inwards the current is unaffected until the resonance region is approached. At 2.1cm the net current begins to fall and reverses sign until the resonance is reached. At this point the net current swings positive again as the probe moves closer to the ring. Although the probe produces a large perturbation of n_e and T_e as it passes through the resonance region the results in Fig.1 clearly demonstrate that the current flows close to the electron cyclotron resonance and in opposite directions on either side of it. This behaviour is precisely that predicted by the current drive scheme based on asymmetric heating by a Doppler shifted wave[3].

The current was found to vary linearly with microwave power as shown in Fig.2. Inductive corrections for plasma-skin-time effects of typically 4% and 30% were made for the 2.88KHz and 8.64KHz data respectively. For these experiments a target plasma was formed using 63watts of unmodulated 10GHz microwave power in order to maintain T_e (7.5eV) and n_e (2.9×10^{11}cm^{-3}) constant as the modulated power was increased. The solid line is at least squares fit giving a current drive efficiency of 30mA/watt.

In Fig.3 the current per unit power times n_e is plotted against T_e. The observed linear dependence of the current per unit power on the ratio T_e/n_e is universally predicted by wave driven current theory provided the effective wave phase velocity (v_o) normalised to the electron thermal velocity (v_e) is constant. There is some evidence from numerical studies of the direct absorption of electron cyclotron waves that this is indeed the case and that v_o/v_e is close to unity[4]. However initial calculations suggest that direct ECRH by the Extraordinary wave is insufficient to explain the magnitude of the observed current. A more probable explanation is that the Extraordinary wave is first converted, at the upper hybrid resonance, to a Bernstein plasma wave which then propagates to, and is absorbed at, the electron cyclotron resonance.
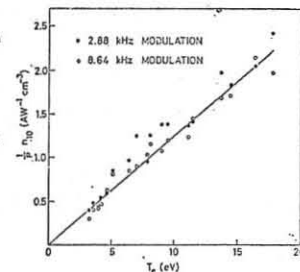
Fig.3 Current per unit power times density versus electron temperature.

SUMMARY   We have observed currents of a few tens of milli-amps per watt which are driven by the absorption of RF waves at the electron cyclotron resonance. The direction of the current was found to reverse on reversal of the microwave propagation direction. The currents on opposite sides of the resonance were found to flow in opposite directions consistent with the current being driven by asymmetric heating of the electrons by Doppler shifted waves. The current varies linearly both with microwave power and T_e/n_e. The latter result agrees with the general prediction of wave-driven current theory for constant ratio of wave phase velocity to electron thermal velocity.

REFERENCES

[1] N J Fisch and A H Boozer, Phys Rev Lett 45 (1980) 720.

[2] S Skellet, Cryogenics 15 (1975) 563.

[3] J G Cordey, T Edlington and D F H Start, Plasma Physics to be published.
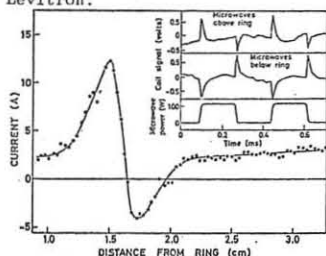
[4] T Edlington, private communication.

Fig.1 Current versus probe position. The inset shows the coil signal for microwave input above and below the ring.

Fig.2 Current versus microwave power.

STEADY-STATE CURRENT GENERATION BY CYCLOTRON
WAVES IN A TOKAMAK

V.V.Parail, G.V.Pereverzev

I.V.Kurchatov Institute of Atomic Energy,
Moscow, USSR

An idea of generating a steady-state current by cyclotron waves has been suggested in papers /1, 2/. It is known that these waves practically have no longitudinal momentum and they directly increase only the transverse energy of resonance particles. One can understand qualitatively the principle of generating the longitudinal current in the process on a basis of the following considerations. Assume that the cyclotron waves increase the transverse energy of all resonance particles with $v_z > 0$ (for clarity we shall speak about the heating of electrons). The frequency of electron-ion collisions $\mathcal{V}_{ei}$ drops as $\mathcal{V}_{ei} \propto \mathcal{V}^{-3}$. Thus after heating electrons with $v_z > 0$ collide with ions more seldom than electrons with $v_z < 0$, i.e. a non-compensated longitudinal momentum and, correspondingly, a longitudinal current emerge.

First, let's consider a steady-state electron current generation by the electron-cyclotron waves- (EC-wave). Assume that we have excited the electron-cyclotron oscillations which interact with electrons in a range of velocities $\mathcal{V}_0 \lesssim \mathcal{V}_z \lesssim C$ in plasma. The kinetic equation for electrons can be written in the following way:

$$\frac{\partial f}{\partial t} = St_{ee}(f) + St_{ei}(f) + \frac{1}{v_\perp} \frac{\partial}{\partial v_\perp} \left(v_\perp P(v_z) \frac{\partial f}{\partial v_\perp} \right) \quad (1)$$

where

$$P(v_z) = \begin{cases} P_0 & \text{at } v_z > v_0 \\ 0 & \text{at } v_z < v_0 \end{cases}$$

Now we analyze the most interesting case when $\mathcal{V}_0 \gg \mathcal{V}_{re}$ as it follows from the paper /1/, the current density can be expressed in the following way: $j \propto P(v_0/v_{re})^2$, where P is the specific EC-wave power. First of all, note that the operators $St_{ee}(f)$ and $St_{ei}(f)$ drop proportionally to $\mathcal{V}^{-3}$ with a rise in $\mathcal{V}$, the quasi-linear operator drops proportionally to $\mathcal{V}^{-2}$. If we didn't want to have a considerable amount of electrons with high velocities in the device, we should choose the EC-wave power and a velocity $\mathcal{V}_0$ so that the electron distribution function in a range $\mathcal{V} \sim \mathcal{V}_0$ would be quite a Maxwellian one. Let's consider this condition to be met. Then, a solution of the kinetic equation can be found as: $f_e = f_M(v)(1 + \varphi(v)\cos\theta)$ where $\varphi(v)$ is a small correction. We substitute f_e into (1) and take the integral over θ with a weight $\cos\theta$. After a linearization (we solve a kinetic equation for electron with $v \gg v_{re}$) we obtain

$$\frac{4 n_e e^{-v^3/v_{re}^2}}{3\sqrt{\pi}\, v_{re}^3} \frac{\partial \varphi}{\partial t} = \frac{1}{v^2} \frac{\partial}{\partial v}\left[v^2 \frac{n_e}{\hat{c}_e Z_i} \frac{v_{re}^3}{v^3}\left(v f_M \varphi + \frac{v_{re}^2}{2} \frac{\partial(f_M \varphi)}{\partial v}\right)\right] -$$
$$- \frac{n_e e^{-v^2/v_{re}^2}}{\hat{c}_e Z_i v^3}(1 + Z_i)\varphi + \frac{\pi P(v)}{2 v^3} \frac{\partial}{\partial v}\left[v^3 \left(1 - \frac{v_0^2}{v^2}\right)^2 \frac{\partial f_M}{\partial v}\right] \quad (2)$$

Here $\hat{c}_e = \frac{3 m_e T_e^{3/2}}{4\sqrt{2\pi} e^4 Z_i n_e \ln\lambda}$, Z_i is the effective charge of ions. Solving the differential equation obtained one finds:

$$\varphi(v) \sim \frac{C}{v^{2(1+Z_i)}} + \frac{P_0 \hat{c}_e Z_i}{\sqrt{\pi}\, v_{re}} \frac{1}{v^{2(1+Z_i)}} \int_{v_0}^{v} \frac{v^{2(1+Z_i)}}{v f_M(v)} \frac{\partial}{\partial v}\left[v^3\left(1 - \frac{v_0^2}{v^2}\right)^2 \frac{\partial f_M}{\partial v}\right] dv \quad (3)$$

The solution (3) should be joined to the solution for f_e in a range of thermal velocities. One can consider, as usually, that in a range where $\mathcal{V} \lesssim \mathcal{V}_{re}$

$$f_e \approx f_M\left(1 + \frac{2vu}{v_{re}^2}\cos\theta\right)$$

where u is the current velocity which is found from the law of conservation of momentum. The analysis shows that, when an inequality is met $(v_0/v_{re})^2 > 1 + Z_i$, the current is no longer dependent on $\mathcal{V}_0$ and can be found from

$$I = 100 \frac{T_e P}{R n_e} \quad (4)$$

where the current is given in kA, T_e - in keV, R - in M, n_e - in 10^{13}cm^{-3}, P - in MW.

Thus, the main difference between (4) and the relationships obtained previously, e.g. for the current generated by lower hybrid waves, is an absence of the dependence I on $\mathcal{V}_0$ in case of the current generation by EC-wave. This difference can be qualitatively understood from the following considerations (see, Fig.1).At a low power deposition, the distribution function slightly differs from a Maxwellian one in the region of RF interation. Therefore, only an exponentially small portion of electrons with the velocities $\mathcal{V}_0^2 \lesssim \mathcal{V}^2 \lesssim \mathcal{V}_0^2 + \mathcal{V}_{re}^2$ makes the main contribution into the current. The current is generated due to a collisional diffusion of particles into the hatched region in Fig.1 where $\mathcal{V} \gtrsim \mathcal{V}_0$. This diffusion should be compensated by a departure of particles from the region under discussion due to quasi-linear diffusion induced by the waves. From this an estimation follows: $\mathcal{V}_{ei} I \propto P (\Delta \mathcal{V})^2$, where $\Delta \mathcal{V}$ is a velocity interval necessary for electrons to leave the region where the current is generated. At the EC-wave heating $\Delta \mathcal{V} \sim \mathcal{V}_0$ at lower hybrid heating $\Delta \mathcal{V} \sim \mathcal{V}_{re}$. Therefore, $I_{LH}/I_{EC} \propto \propto (\mathcal{V}_0/\mathcal{V}_{re})^2$. There would be no difference if a strong distortion f_e took place in the region of interaction with the waves. But in difference from the lower hybrid waves, an interaction between the resonance superthermal electrons and the electron-cyclotron waves does not result in a reasonable steady-state distribution in velocities: electrons are accelerated up to the relativistic energies and that naturally, cannot be allowed in a tokamak-reactor.

Let's discuss now the problem of generation a steady-state current by the ion-cyclotron waves. The collisions between minority species ions which generate the current and the background majority ions, according to a law $\mathcal{V}_{zi} \propto \mathcal{V}^{-3}$, as well as those between the minority species and electrons, in accordance with a law $\mathcal{V}_{ze} \approx$ const, are the reason of the main difference between this approach and the previous one related to EC-waves. The ion-electron collisions independent of the ion velocity allows a non-Maxwellian distribution function of the resonance ions which, in its turn, is concluded by a relationship $I \propto (\mathcal{V}_0/\mathcal{V}_{ri})^2$. One can expect that the use of ion-cyclotron waves for generating the current by the minority species will result in a $(\mathcal{V}_0/\mathcal{V}_{ri})^2$ - fold increase in efficiency (i.e. in the ratio I/P), as from (1) it follows that the current does not depend on the mass of a current carrier in case of the heating by EC-waves. The maximum value of $\mathcal{V}_0$ can be found from the following conditions: at $\mathcal{V} = \mathcal{V}_0$ the frequency of collisions between the minority species ions and the majority ions is equal to the frequency of collisions between the minority species ions and electrons, hence $(v_0^{cr}/v_{ri})^2 \lesssim (M/m)^{1/3}$ (when $\mathcal{V}_0 > \mathcal{V}_0^{cr}$ the electron collisions will be the main ones; as a result, no current generation occurs).

References

1. N.J.Fisch, A.H.Boozer, Phys. Rev.Letters, 45, 720, 1980.
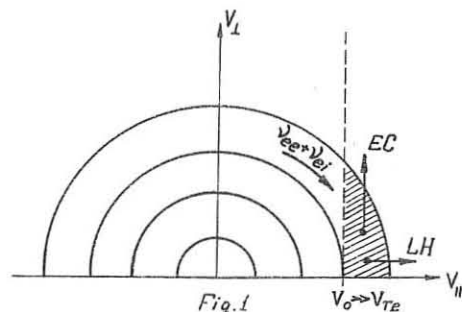2. N.J.Fisch, PPPL-1684, 1980.

Fig.1

TOROIDAL CURRENT DRIVE BY HELICAL SLOW WAVE STRUCTURE

S. Takamura, T. Kojima and T. Okuda

Department of Electrical Engineering , Faculty of Engineering,
Nagoya University, Nagoya 464, Japan

The current generation by the momentum of waves has been considered to allow tokamaks to run in the steady state. Lower hybrid waves are able to transfer their momentum to nearly collisionless electrons so that the power dissipation may be minimized. The experimental verification of current generation by lower hybrid waves has been tried in various devices. In the present study was employed a well-behaved slow wave antenna which allowed the toroidal plasma current to be driven in a quasi-tokamak machine[1].

The phased ring array has been employed in order to excite travelling lower hybrid waves in small devices, while the phased waveguide array will be more realistic in large tokamak machines. In this work helical slow wave structure has been employed as a slow wave antenna. The geometrical structure determines the longitudinal phase velocity which is given by the following formula without plasma loading, $v_{ph} = pc/(2\pi a)$, where a and p are the radius and the pitch of the helix, respectively, and c is the light speed[2]. When the plasma is loaded, the longitudinal retardation increases slightly. Its increment, up to 10 %, was found to be proportional to the normalized electron density, ω_{pe}^2/ω^2 where ω_{pe} is the electron plasma frequency. The numerical analysis on this loading effect will be reported elsewhere. Travelling lower hybrid waves were confirmed experimentally to be excited with the helical antenna wound around a glass vacuum chamber in a linear test device.

The experimental apparatus for the toroidal current generation is a simple toroidal machine with a vertical field winding and an air core transformer (CSTN-I). Its top view is shown in Fig. 1. The major and minor radii are R = 30 cm and a = 3.5 cm,

Fig. 1 Top view of experimental apparatus. Direction of propagation of waves is counterclockwise(C.W.).

respectively. Helical antennas with two different longitudinal wavelengths are wound around a glass vacuum chamber($\lambda_\parallel$ = 1.4 and 1.9 cm) over each quarter of toroidal circumference. The longitudinal phase velocity is 2.4 or 3.3 times as large as the electron thermal velocity, $(2T_e/m_e)^{1/2}$. The frequency is 289 MHz so that ω/ω_{LH} and $\omega/(\omega_{ce}\omega_{ci})^{1/2}$ may be much larger than unity. The toroidal magnetic field reaches up to 2 kG. The plasma was produced by the r.f. power fed to the helical antenna. The maximum available power is 35 kW at a pulse legth of 300 μs. The electron temperature obtained is around 10 eV, while the peak electron density is around 3×10^{11} cm^{-3}. They are measured with a Langmuir probe. The time evolutions of the loop voltage, the toroidal plasma current, the r.f. incident and reflected power, the electron saturation current, the visible light emission, the magnetic probe signals are shown in Fig. 2. The loop voltage appeared at the moments of the rise and the fall of the plasma current because of the electromotive force due to the magnetic flux change. The plasma current of 10 A was detected with Rogowskii coil.

The self-inductance of toroidal plasma column is given by, $L_p = \mu_o R(\ln(8R/a) + l_i - 2)$, where l_i is the internal part of the self-inductance which depends on the current distribution. It is assumed to be uniform (l_i = 0.5). The time derivative of the current 10 A/30μs gives the loop voltage of 0.31 V, which agrees roughly with the experimental observation, 0.1 ∼ 0.2 V.

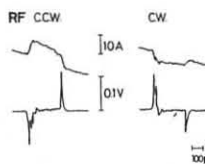It should be noted that the direction of the electron flow is

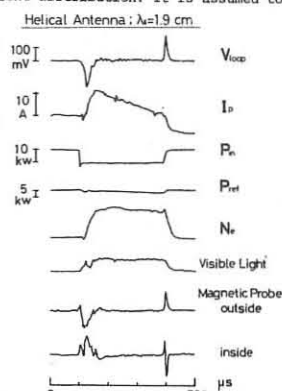Fig.3. Waveforms of plasma current and loop voltage when the direction of propagation was reversed. B_t = 1.3 kG.

Fig. 2 Discharge parameters. Ar pressure is 6×10^{-5} torr. B_t= 0.66kG.

the same as that of the propagation of travelling lower hybrid waves and is independent of the direction of the toroidal magnetic field. When the direction of propagation was reversed by changing the feed point of helical antenna, the direction of the current was also reversed as shown in Fig. 3.

Figure 2 shows that the signs of the magnetic probe signals are different for the inner and the outer probes. Poloidal field in a plasma due to the driven current was also examined by sweeping the magnetic probe across the plasma column. It showed that the current center is shifted inside with respect to the center of the chamber, and coincides with the position of the maximum of the electron density. It should be emphasized that the lower hybrid wave drives the plasma current not at the plasma surface but inside the plasma in the present experiment.

The above results have been obtained with each helical antenna. There is almost no difference between the shorter wavelength antenna and the longer one with respect to the magnitude of the driven current, while the quasi-linear effect is expected to give large difference if both antennas produce the same plasma. In addition, even if both antennas are excited simultaneously, the driven current was found to be nearly the same as in the case of the single antenna under the condition of the same input power.

The power dependence on the driven current was also examined. The driven current increases gradually as the input power increases. These above observations show that the non-resonant current drive (the collisional contribution) dominates over the resonant wave-particle interaction (the quasi-linear effect).
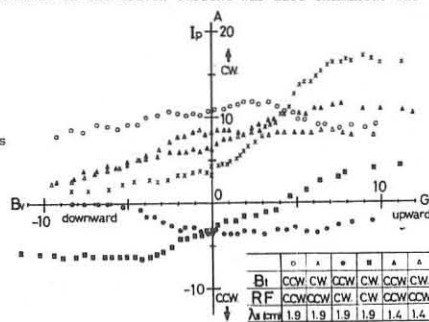

Fig. 4 Driven current as a function of the vertical magnetic field.

Figure 4 shows the influence of the vertical magnetic field on the driven current. It has been reported that the resonant electrons can be confined for longer time by cancelling the toroidal drift with the vertical magnetic field [3]. As shown in the figure the enhancement of the driven current was observed in some cases. However, the optimum magnetic field does not always corresponds to the value pridicted by the toroidal drift of resonant electrons(∼ 1 Gauss). Therefore we cannot say that the resonant wave-particle interaction is the main mechanism of the current generation although the toroidal magnetic field ripple is great in the present case.

Finally the superposition of the r.f. and the ohmic electromotive force has been examined. The additive property was demonstrated clearly because of the resistive plasma, while other experiments in high temperature plasmas show the voltage drop and the constancy of the plasma current rather than the current increase.

In conclusion the toroidal current generation was observed in a simple toroidal machine by exciting travelling lower hybrid waves with helical slow wave structures. The observed current may be due to the non-resonant wave particle interaction. The generated current is not localized at the plasma surface. A bulk current was obtained. The driven current was optimized in some cases by applying the vertical magnetic field, but its mechanism is not clear. The superposition of the currents driven by the ohmic field and the r.f. power is observed. The current drive due to the resonant wave-particle interaction may be expected to dominate the collisional one if the electron density and its temperature increase.

REFERENCES

[1] S. Takamura et al., The 2nd Joint Grenoble-Varenna Internatio al Symposium on Heating in Toroidal Plasmas, Como, 1980, C(114)10 ao.
[2] J. Musil et al., Czech. J. Phys. B29(1979)175.
[3] K.L. Wong et al., Phys. Rev. Letters 45(1980)117.

OPTIMIZATION OF NEGATIVE ION BEAM ACCELERATION SYSTEM
CONSIDERING INTERACTION WITH RESIDUAL GAS

Sveshnikov A.G., Yakunin S.A.,Moscow State University,USSR
Semashko N.N.,Kulygin V.M.,Institute of Atomic Energy,USSR.

Injection of the fast atom beams as a method of energy deposition into plasma has recived general recognition at the present time. The injectors are envisaged in the majority of big fusion facilities under design. The schemes of fast atoms generation in these facilities can be different dependent, e.g., on the required energy of particles. In particular, if one needs to obtain a beam of atoms with the energies greater than 160 – 200 keV the most effective scheme of the injector will be that which envisages the production of negative ion beam and its additional acceleration up to the necessary energy with the subsequent target stripping.

This paper deals with the mathematical method of optimizing an additional acceleration system, one of the possible parts of such injector. Initial assumptions for optimization are the limitations on the angle of beam divergens and a desire to have the best efficiency of the device dependent, among other things, on distribution of trajectories belonging to the secondary particles born in collisions between fast ions and a residual gas.

In the mathematical approach the optimization problem is reduced to a search for a minimum of some functional

$$F(\vec{P}) = C_\theta F_\theta + C_E F_E + C_L F_L + \alpha \Omega \qquad (1)$$

Here $\vec{P}=(P_1,\dots P_n)$ are the parameters of the additional acceleration system, F_θ is a term characterizing an angular distribution of the main ion flux at the outlet, F_E is an average energy which is acquired by secondary partticles, F_L is a term which imposes some limitations on the physical properties of the system, e.g., on the break-down voltage, Ω is a regularization functional which allows to stabilize the solution of the direct problem.

Computation of the functional is, in essence, a solu- of the direct problem on the particles dynamics in a given geometry when the distribution of potentials at the electrodes is known. The mathematical model of such problem is known [1]. Assume that G is the region in which the particles move, Γ is its boundary. Assume that

$$G = \{(x,y): x \in [0,\ell_1],\ y \in [-\ell_2,\ell_2]\},\ \Gamma = \Gamma_1 \cup \Gamma_2 \cup \Gamma_3 \cup \Gamma_4$$
$$\Gamma_1 = \{(x,y) \in G : x=0\},\ \Gamma_2 = \{(x,y) \in G : y=\ell_2\}$$
$$\Gamma_3 = \{(x,y) \in G : x=\ell_1\},\ \Gamma_4 = \{(x,y) \in G : y=-\ell_2\} \qquad (2)$$

A stationary flux of negative ions with the mass M_o charge q_o, energy W_o and with a given current density distribution $\vec{J}_o(y)$ is given to the boundary Γ_1. After acceleration ions leave the region G across the boundary Γ_3, the electric potential distribution $\Phi_o(x)$ is present on the Γ_2, Γ_4

$$\Phi_o(x) = \begin{cases} \Phi^B(x),\ y=\ell_2\ ,\ \Phi|_{\Gamma_1}=\Phi_o(0)\equiv\Phi_1 \\ \Phi^H(x),\ y=-\ell_2\ ,\ \Phi|_{\Gamma_3}=\Phi_o(\ell_1)\equiv\Phi_2 \end{cases} \qquad (3)$$

The charged particles dynamics in a system channel can be described by kinetic equations ($\alpha=0,1,2$)

$$\vec{V}\frac{\partial f_\alpha}{\partial \vec{r}} + \frac{q_\alpha}{M_\alpha}\vec{E}\frac{\partial f_\alpha}{\partial \vec{V}} = F_\alpha,\ n_\alpha=\int f_\alpha d\vec{V},\ \vec{J}_\alpha=\int f_\alpha \vec{V} d\vec{V} \qquad (4)$$

Here $\vec{E}$ is the electric field, q_α, M_α are the charge and the mass of a given sort of particles, F_α describes a volume ionization [2]. Let's consider that positive ions $\alpha=1$ and electrons $\alpha=2$ are born in the channel due to ionization of a residual gas (density of atoms n_a=const $\ll n_o$); negative ions $\alpha=0$ can decay into fast neutral atoms and electrons. Then $F_o = -\beta_o n_a n_o \delta(\vec{v}-\vec{v}_i)$, $F_1 = \beta_1 n_a n_o \delta(\vec{v})$,

$$F_2 = \beta_o n_a n_o \delta(\vec{v}-\vec{v}_i) + \beta_1 n_a n_o \delta(\vec{v})\ . \qquad (5)$$

An electric field is described by the Poisson equation with the boundary conditions (3)

$$\Delta\Phi = -4\pi q_o n_o\ ,\qquad \vec{E} = -\vec{\nabla}\Phi \qquad (6)$$

Here, one neglects the space charge of the secondary particles. A set of equations (2)-(6) is closed, self-consistent model which describes the dynamics of a stationary flux in a channel of the system of additional acceleration at the known dimentions of the region G, potential distribution Φ_o and the current density $\vec{J}_o$. The direct problem is solved with an iteration algorithm based on a combination of the stationary method of "large particles" and a finite difference method for solving the electric field equations. A structure of the functional has been chosen as $M(\theta)=\int f_o \theta|_{\Gamma_3} d\vec{v}$, $\sigma^2(\theta)=\int f_o [M(\theta)-\theta]^2_{\Gamma_3} d\vec{v}$, $\theta = arc\, tg\, \frac{V_y}{V_x}$,

$$F_\theta = C_{\theta 1}(M_\theta)^2 + C_{\theta 2}\sigma^2 + C_{\theta 3}(J_1+J_2+J_4)\ ,\ F_E = F_{E1} + F_{E2}\ ,$$
$$F_{E1} = \frac{1}{2}\int f_1 M_1 V^2|_{\Gamma} d\vec{v}\ ,\ F_{E2} = \frac{M_2}{2}\int f_2 V^2|_{\Gamma} d\vec{v}\ ,$$
$$F_L = C_{L1}\int\left(\frac{E_x}{E_o}\right)^5_{\Gamma_2} dx + C_{L2}\int\left(\frac{E_x}{E_o}\right)^5_{\Gamma_4} dx\ .$$

Here, J_1, J_2, J_4 are the negative ion fluxes on to the boundaries Γ_1, Γ_2, Γ_4, correspondently; E_o is the breakdown voltage, $C_{\theta i}, C_{Li}$ are weigt factors. The functional minimum search has been carried out by the method of conjugated directions. Three parameters: l_1 (length of the system), γ and μ (for potential distribution). $h_1 = const$, $h_2 = \mu h_1$, $\Delta\Phi = \Phi_2 - \Phi_1$, $x_1 = 1/2(\ell_1)-h_1$, $x_2 = \ell_1/2$, $x_3 = x_2+h_2$, $x_4 = \ell_1 - h_2$,

$$\Phi^B(x) = \begin{cases} \Phi_1,\ x \in [0,h_1] \\ \Phi_1 + \Delta\Phi\left(\frac{x-h_1}{x_4-h_1}\right)^\gamma,\ x \in [h_1,x_4] \\ \Phi_2,\ x \in [x_4,\ell_1] \end{cases} \Phi^H(x) = \begin{cases} \Phi^B(x-h),\ x \in [0,x_1] \\ \Phi^B(x_2),\ x \in [x_1,x_3] \\ \Phi^B(x-h,-h_2),\ x \in [x_3,\ell_1] \end{cases}$$

Equipotential lines and the paths of particles in the negative ion beam (an optimal solution for a characteristic variant of computation) are given in Fig.1. $\Phi_1 = 0.1$MeV, $\Phi_2 = 1$MeV, $\ell_1 = 15$cm, $J_o = 70$mA/cm^2, $\ell_1 = 35.9$cm, $\gamma = 1.8$, $h_1 = 6$cm, $\mu = 0.78$, $\sigma = 0.5°$, $F_{E1} = 0.08 \Delta\Phi$
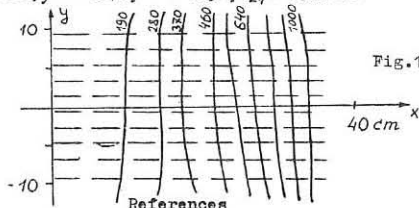

Fig.1.

References

1   Il'in V.P. Chislennye metody resheniya zadach electrooptiki. Novosibirsk, Nauka, (1974), s.127

2   Volkov B.I.,Sveshnikov A.G.,Yakunin S.A. K voprosu o matematicheskom modelirovanii fisicheskikh processov v plasmoopticheskikh sistemach. DAN, SSSR, 238, N2,(1978)

PRODUCTION OF NEGATIVE DEUTERIUM ION BEAMS BY MEANS OF NEGATIVE SURFACE IONIZATION

P. Massmann, P.J. v. Bommel, E.H.A. Granneman,
H.J. Hopman, J. Los, F. Siebenlist, J.N.M. v. Wunnik.

FOM-Institute for Atomic and Molecular Physics
Amsterdam, The Netherlands
Association EURATOM-FOM

ABSTRACT. We present a concept of ion source in which negative surface ionization of deuterium is used as a tool to produce a 20 keV, 50 mA cm^{-2}, 10 s negative ion beam. In this method deuterons impinge under grazing incidence on a low work function surface where they are specularly reflected and converted to negative ions. Conversion efficiencies up to 40% have been measured for single particles.

INTRODUCTION. It is commonly believed that neutralising D^--ions will be the more efficient option for the production of atomic hydrogen beams of several 100 keV needed in future fusion experiments. At the moment there are two main approaches to obtain a dense, (quasi)dc, negative hydrogen beam. One method uses the principle of double electron capture during interaction of the primary positive beam with an alkali jet [1]; in the other method the negative ions are directly extracted from a hydrogen discharge burning with a Cs admixture, the surface plasma source [1]. We present a modification of the latter approach in which the negatively ionizing surface is separated from the positive ion source. In order to obtain a dense beam the positive ions are extracted from the source plasma before impinging on a low work function surface, where they are converted to negative ions by negative surface ionization (Hopman et al. [1]). The idea is that in this way the surface conditions can be controlled and optimized better than in the surface plasma sources where surface and arc conditions are coupled. The results discussed in the present paper are based on reflection of hydrogen ions from a partially cesiated monocrystalline tungsten (110) surface. Compared to the first method of double capture our technique has the main advantage that no circulation of large amounts of Cs is needed. To test the feasability of the proposed concept two experiments have been set up. The first experiment, NIOBE (Negative Ion Beam Experiment), covers all fundamental aspects of the method. In the second experiment, DENISE (DEnse Negative Ion beam Surface Experiment), the principle of negative surface ionization is applied to develop a prototype D^--source with the aim to obtain a beam of 50 mA cm^{-2}.

THE FUNDAMENTAL EXPERIMENT (NIOBE). EXPERIMENTAL. A schematic of the experiment (Los et al. [1]) is shown in Fig. 1. The primary beam impinges under angles $\beta \lesssim 87°$ from normal on a monocrystalline tungsten ribbon (2×10 mm^2) which is partially cesiated by means of a dispenser (SAES-getters). The angular spread of the primary beam is $\lesssim 1°$. The ribbon and the detection system can be rotated independently about the ribbon's axis of symmetry. A parallel plate analyzer measures the energy distribution of either type of reflected ions and can detect H^-, H^0 and H^+ (or D^-, D^0, D^+) simultaneously with an angular resolution of $1°$. To

Fig. 1
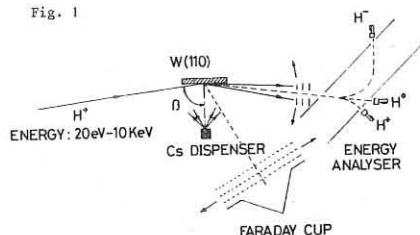
measure the total conversion efficiency a large opening Faraday cup is used. A special Faraday cup is used to measure the primary beam fraction impinging on the surface. Determination of the workfunction can be done with a Kelvin probe or by photo emission measurements. The vacuum during operation is 10^{-9} Torr.

RESULTS. The measurements are done at the minimum of the workfunction [2] which corresponds to about ½ monolayer of Cs-coverage. Measurements have shown that hydrogen is reflected specularly for sufficiently large angles of incidence. For primary beam energies between 150 eV and 2 keV and angles $75 \leq \beta \leq 85°$ the energy spread of the reflected ions varies between 4% ($\beta = 85°$) and 8% ($\beta = 75°$); the angular spread ranges between $5°$ ($\beta = 85°$) and $20°$ ($\beta = 75°$) around the specular direction. In the considered energy range practically all particles are reflected as neutrals or negative ions. The most important result is shown in Fig. 2, where the negative ionization efficiency is plotted for deuterium as a function of the velocity component $v_\perp$ normal to the surface. The maximum efficiency of nearly 40% occurs around $v_\perp = 4.2 \times 10^{14}$ $a_0/s = 2.2 \times 10^4$ ms^{-1} which is about 5 eV in energy terms. Up to 400 eV of pri-
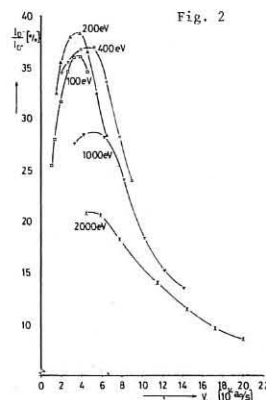

Fig. 2

mary beam energy the data fall nearly on a uniform curve. For low energies the dependence of the efficiency on $v_\perp$ is in agreement with the theory developed by Rasser [3]. This theory predicts an optimum distance or in other terms an optimum $v_\perp$ from the surface where the transition probably of the conduction electrons to the affinity level is maximum. Above 400 eV the absolute efficiency values drop off. This is attributed to the fact that at these energies the ion velocity becomes comparable to the maximum velocity of the metal electrons. This results in an effective decrease of the density of states of the metal electrons available to undergo resonant transitions to the hydrogen affinity level [4].

THE PROTOTYPE NEGATIVE ION SOURCE (DENISE). EXPERIMENTAL. A schematic of the set up is shown in Fig. 3. As a source of primary positive ions
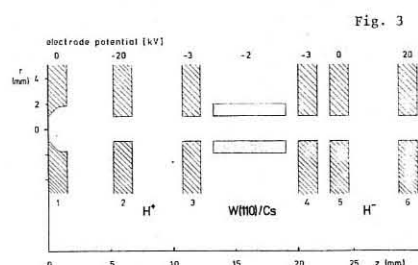

Fig. 3

we use a single slit (2×100 mm^2) bucket source. To obtain high current densities (250 mA cm^{-2}) the primary beam is extracted at potentials up to 20 kV. The maximum pulse length is 10 s. Since the optimum negative conversion efficiency is at low energies the beam is subsequently decelerated. This causes a divergence which has to provide that the major fraction of the primary beam is impinging under grazing incidence on a set of surfaces placed on either beam side. The negative ions are then accelerated to 20 keV. The potentials on the 3rd and 4th lens have to be optimized to cause both a suitable divergence and confinement of secondary electrons emerging from the surfaces. The 5th electrode prevents secondary electrons created at the backside of the 4th electrode from being accelerated to 20 kV. As can be seen from Fig. 3, the whole accel-decel-accel system has a total length of only 30 mm. Finally the beam is terminated by a collector permitting a 7 channel energy or current profile measurement. Different particles are discriminated by a mass spectrometer. The vacuum is performed by 2 refrigerator cryo pumps of 10^4 $1s^{-1}$ each, providing a background pressure of less than 10^{-8} Torr. Special attention is given to the construction of the surface configuration permitting easy variation of the following parameters. i) The surfaces can easily be displaced towards the source of the collector. ii) Various surface configurations and materials can be used. iii) Cs can be deposited on the surfaces during the beam pulse. The measurements will be started with 4 W(110) slabs of 100×5 mm^2. The cesiation will be provided by dispensers (SAES-getters) with active length corresponding to the slit and surface lengths of 100 mm. To optimise the ion optical system numerical ion trajectory calculations are done using the Herrmannsfeldt code [5]. First results are published in [1].

CONCLUSION. It has been shown that D^+-D^- conversion on surfaces is possible with efficiencies up to 40%. The fact that there exists an optimum $v_\perp$ which in energy terms is only 5 eV for D implies that for obtaining high efficiencies it is necessary to use low energy particles or to work under grazing incidence. From the viewpoint of high current densities which scale with $V^{3/2}$ the latter has to be preferred.

REFERENCES

[1] Proc. 2nd Int. Symp. Prod. Neutral. Neg. Hydrogen Ions and Beams, Brookhaven, USA (1980)
[2] V.M. Gavriluk et al. Sov. Phys. JETP 24 (1967) 899
[3] B. Rasser, J.N.M. v. Wunnik, J. Los, to be published
[4] J.N.M. v. Wunnik, B. Rasser, E.H.A. Granneman, J. Los, to be published
[5] W.B. Herrmannsfeldt, Report SLAC-166, Sept. (1973)

NUMERICAL MODEL FOR PLASMA HEATING BY NEUTRAL
INJECTION IN A HIGH FIELD TOKAMAK WITH
ADIABATIC COMPRESSION

V.M.Gribkov, D.H.Morozov, O.P.Pogutse,
N.V.Chudin

I.V.Kurchatov Institute of Atomic Energy,
Moscow, USSR

Abstract. In the paper a numerical model of plasma
heating by a neutral beam for tokamak with adiabatic
compression is performed with taking into account uni-
form distribution of fast trapped ion energy over the
banana width.

In the present paper a numerical study of plasma
heating by a fast neutral particle beam has been car-
ried out for a tokamak with a comparatively weak toro-
idal current. Similar calculations have been performed
for high toroidal current systems (see Ref.1 and its re-
ferences). In these systems the banana width of a fast
trapped ion resulting from the primary neutral beam par-
ticle ionization $\Delta \sim \frac{\rho_L q}{\sqrt{\varepsilon}}$ (ρ_L is the ion Larmor
radius, q the safety factor, ε the inverse aspect
ratio) is small compared with the system dimensions. Con-
sequently, one may approximately consider that the ion
energy is transfered to the plasma on the magnetic sur-
face where the ionization event has occured. In the low
current system, the banana width is of the order of the
system dimensions and the contribution of the fast trap-
ped ion energy is considerably redistributed along the
radius. To take this fact into account in the present
paper, we assume that the energy of the hot trapped ion
is distributed uniformly among the magnetic surfaces cros-
sing the banana. The untrapped ions were assumed to tran-
sfer all their energy to the plasma on the magnetic sur-
face on which they were born. The calculations of the
local factors of the energy transfer to the plasma ions
and electrons, the interaction cross sections and the
charge-exchange losses of fast ions are performed accor-
ding to Ref.1.

The neutral beam of a finite width $\Delta R_\ell = 10$ cm
and height 2h=40 cm is approximated by a set of 18
thin rays with conservation of the total current $I_o =$
=10-40A. The injector power is equal to 0.5÷1.5 MW
and each ray consists of particles with three ener-
gies E_o=20-40 keV, $E_o/2$ and $E_o/3$ and relative currents
0.63, 0.26 and 0.11, respectively. The beam impact para-
meter R_b=64-74 cm.

The beam density equation was solved along each
of the rays

$$\frac{dN}{ds} = I_o \sigma_c n(s) \exp\left\{-\sigma_c \int_{S_o}^{S} n(s') ds'\right\} \quad (1)$$

(here: dN is the number of fast ions born in the
interval ds, S is the running ray coordinate,
n (s) is the plasma density, σ_c is the beam capture
cross section, S_o is the point of the ray entry into
the plasma) and analysis of the integrals of the set of
the hot ion drift equations was performed.

Depending on the region they are formed, the beam
ions may be trapped or untrapped. The untrapped particle
power contribution Q_u on the magnetic surface with radi-
us z is defined as

$$\left(\frac{dQ_u}{dz}\right)_{e}^{i,e} \begin{cases} 0 & \text{when } z > z_{cz} \\ E \frac{dN}{dz} \eta_{i,e} & \text{when } z < z_{cz} \end{cases} \quad (2)$$

where E is the beam particle energy, z_{cz} is the bounda-
ry of region, where the formed ion is untrapped, determi-
ned from the integrals of the drift equation set, $\eta_{i,e}$
are the local energy transfer factors, defined in Ref.1.

The trapped particle contribution Q_t is considered to
be distributed uniformly over the banana, determined by
the maximum z_{max} and minimum z_{min} distances of the ion
orbit from the magnetic axis in the torus equatorial
plane. In this approximation Q_t is defined as

$$\left(\frac{dQ_t}{dz}\right)^{i,e} = \int_{z_{cz}}^{a} \Pi\left(z, z_{max}, z_{min}\right) \frac{dN}{dz}(z') \frac{E \eta_{i,e}}{z_{max} - z_{min}} dz' \quad (3)$$

a is the minor radius of the plasma column, the function
Π (z, z_{max}, z_{min})=1 only when $z_{min} < z < z_{max}$ and
vanishes outside this region.

The total neutral beam power contribution per unit
plasma volume is

$$\widetilde{Q}_\ell^{i,e} = \frac{1}{4\pi^2 R z}\left[\left(\frac{dQ_u}{dz}\right)^{i,e} + \left(\frac{dQ_t}{dz}\right)^{i,e}\right]$$

R is the torus major radius.

Radial $\widetilde{Q}_\ell^{i,e}$ profiles are shown in Fig.1. The exis-
tence of maximum at r/a ~ 0.35 and r/a ~ 0.65 is due
to the beam discreteness in height.

The calculated radial power profiles were used as
additional energy sources in the time-dependent transport
analysis code /2/. The results of calculations for a to-
kamak with adiabatic compression are plotted in Fig.2-3.

References
1. Yu.N.Dnestrovsky, D.P.Kostomarov, S.E.Lysenko.Preprint
   2978, I.V.Kurchatov Institute of Atomic Energy,1978.
2. V.V.Vikhrev, O.P.Pogutse, N.V.Chudin, E.I.Yurchenko,
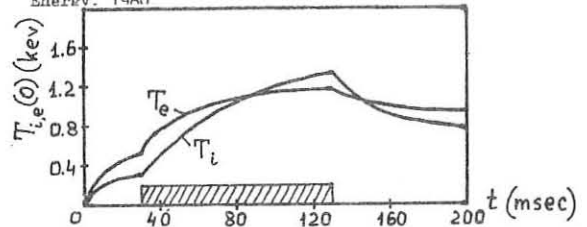   Preprint 3321/8, I.V.Kurchatov Institute of Atomic
   Energy, 1980.

Fig.2. Time evolution of central ion and electron
temperatures for the neutral injection with
I_o=30 A, E_o=40 keV. The average electron
density is $\bar{n}$=2.5x10^{13}cm^{-3}. The shaded area
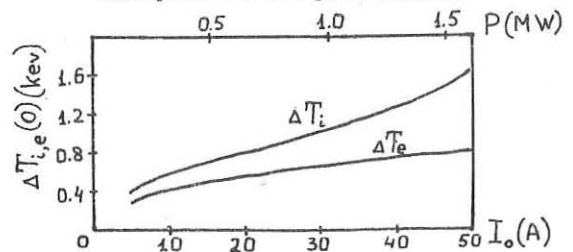corresponds to a beam pulse duration.

Fig.3. The increase of ion and electron tempera-
tures during the neutral injection vs.
beam current and injector power. The
neutral energy is E_o=40 keV, $\bar{n}$=2.5x10^{13}cm^{-3}.
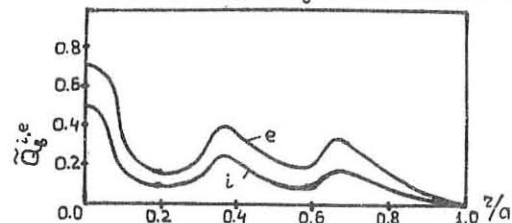

Fig.1. Radial profiles of the beam power input
into the ion (i) and electron (e) plasma
components per unit volume (arbitrary units).

ELIMINATION OF SURFACE WAVES IN LOWER HYBRID WAVE HEATING

K. Ushigusa, S. Takamura and T. Okuda

Department of Electrical Engineering, Faculty of Engineering,
Nagoya University, Nagoya 464, Japan

An analysis of the energy balance on lower hybrid wave heating[LH WH] has been pointing out that a considerable part of input energy is dissipated at the plasma surface through parametric instabilities[1]. Waves of small longitudinal retardation which are not accessible to plasma core localize at the plasma surface. These surface waves may enhance the impurity influx by the interaction with the vacuum wall. In order to improve a heating efficiency without unfavorable secondary effects during this heating, it is quite important to eliminate these waves. As is well known, a divertor can eliminates impurity ions and ash in nuclear fusion reactions. one of the objectives of the present paper is to check whether the divertor can eliminate these surface waves. Ray tracing technique based not on the electrostatic approximation but on the electromagnetic dispersion function is useful for this purpose. Such model is also available for examining the accessibility condition.

A tokamak with non-circular cross-section has been thought to be promising as a high β fusion reactor. The another objective of the present work is to study the propagation and other characteristics of LHW in such a tokamak anticipating that LHWH is employed as a heating scheme to ignition.

Since LHW is very sensitive to the distribution of plasma parameters, density, temperature and poloidal magnetic field B_θ, the care must be taken to introduce the non-circularity for the ray tracing calculation. The distribution of plasma parameters must be determined, being consistent with a MHD equilibrium. We can obtain easily the distributions of density and temperature with the value of β_p and with the relation of $p(\psi) = \sum_{e,i} n_\alpha(\psi) T_\alpha(\psi)$. Spatial derivatives of parameters are required for the calculation of ray tracing. In order to raise the accuracy of the computation, it is desirable to use the analytic form of ψ. For this reason, the technique in the formulation of MHD equilibrium reported in Ref.[2] was employed here. Machine and plasma parameters were chosen as shown in Table I, which are similar to those of JET. Figure a

Table I

Major radius of the chamber	R_0	2.8 m
Minor radii	a,b	0.82, 1.65 m
Plasma current	I_p	4 MA
Toroidal magnetic field	B_t	5 T
Electron density	n_{eo}	10^{14} cm^{-3}
Temperature	$T_{eo} = T_{io}$	1.5 keV
Ion		D$^+$
Frequency	f	1.35 GHz

shows magnetic surfaces obtained by the above mentioned code on MHD equilibrium(dashed curve). The plasma has an elliptic cross= section of a weak D-shape with elongation ratio of about 2. Several coils for shaping, vertical field and divertor were put in appropriate positions around the chamber to realize such a non-circular plasma. The present model includes automatically the parameter distributions on the scrape-off layer as well as on the divertor region. The Landau damping and the first order correction for thermal motion on both electrons and ions are also included in the present dispersion relation.

Figure c shows typical exemple of the propagation path projected on the poloidal plane taking the initial refractive index along the magnetic field, N_{11}, as a parameter. When N_{11} is greater than 1.8, the slow wave can penetrate into the core of plasma and convert to thermal modes near the plasma center where the ray trajectory is distorted. The turning point to the thermal mode approaches the magnetic axis as N_{11} reduces to 1.8. The slow waves of smaller N_{11} convert to fast waves at appropriate
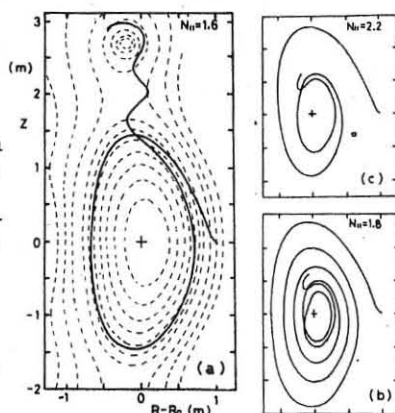
positions and come back to the plasma surface. These waves localize usually at the plasma surface after experiencing a mode conversion at the turning point to fast wave and reflecting at a cut-off layer. These are so-called surface waves which we concern in the present work. For the wave of critical N_{11} which equals to 1.8, there are regions where the mode identification, either slow or fast, is difficult. But they can penetrate into the center finally(Fig. b). The example for small N_{11} is shown in Fig. a. The wave turns around the plasma surface and goes away to the outside of the plasma through the mode conversion. Such a component of wave is not accessible to the plasma core. From a standpoint of one dimensional slab model, the slow wave whose N_{11} is smaller than $N_{11cr} = (1 - \omega^2/\omega_{ceo}\omega_{cio})^{-2} = 1.23$ will couple to a fast wave. The mode conversion to fast mode occurs here as shown in Fig. a even if $N_{11} = 1.6$ which is larger than the critical value mentioned above. Therefore the accessibility condition is severer than that given by one dimensional analysis. These results show that LHW can penetrate into the plasma deeply as long as the wave satisfies the local accessibility condition while their ray trajectories are deformed by the shape of the plasma cross-section.

We obtain the radial position of the ray from the magnetic axis R_p and the poloidal rotation angle θ_p of the ray as a function of the toroidal angle ϕ. The ratio of the group velocity parallel to the magnetic field to the perpendicular velocity is nearly equal to the so-called resonance cone angle. Therefore we can estimate roughly the relation between R_p and ϕ using this angle. In addition to this variation, our calculation shows another strong periodic structure which is caused from the effect B_θ distribution on the non-circular cross-section. Similarly, the poloidal rotation against the toroidal one for the ray satisfies the local safety factor q, in accordance with the prediction based on the electrostatic approximation. Our calculation confirms that the slow wave propagates along the magnetic field line with respect to the poloidal rotation with an accuracy of a few percents. The B_θ is weak where $\theta_p = \pm\pi/2$ and is strong where $\theta_p \approx$ 0 or π in the present model. The direction of group velocity tends to be along the poloidal direction in the latter region, and does to be along the toroidal direction in the former region, respectively. On the other hand, the electromagnetic computer code shows variations of N_{11}, $N_\perp$, the remaining power flux of wave, the damping rate and the ratio of the wave magnetic field $\tilde{B}$ to the wave electric field $\tilde{E}$. It has been known for a circular cross-section tokamak that N_{11} decreases as the wave penetrates radially, and that its change is accompanied by the oscillation that has the same periodicity as the poloidal rotation. In addition to these variations there appears the another oscillation due to the B_θ distribution on the non-circular cross-section. It should be noted that N_{11} becomes small where B_θ is weak and vice versa. This change causes the variations of the other wave properties. The damping rate and $N_\perp$ become considerably large and $c\tilde{B}/\tilde{E}$ becomes small when waves pass through the midplane. From these results, it can be concluded that the slow wave accessible to the plasma core becomes more electromagnetic on the region where B_θ is relatively weak, and more electrostatic where B_θ is strong. Therefore the heating occurs locally at the midplane. Theses behaviours characterize the wave kinetics in tokamaks with non-circular cross-section.

The final topic is an action of a poloidal divertor. As mentioned before, wave energy components of low N_{11} and not accessibel to the plasma core accumulate at the plasma surface through mode conversion to fast wave and the reflection near the wall. These waves are principal part of the surface waves that may have unfavorable effects on LHWH. As the first approximation, the ray trajectories of such surface waves were calculated using the WKB approximation that cannot be applied ro the wave trajectory in the strict sense when it has a long wavelengtn or receives a reflection due to the presence of cut-off layer. But it gives us the important suggestion concerning the fate of the accumulated energy of the surface wave. Figure a shows that a mode converted fast wave propagates toward the inner region away from the bulk plasma, and is reflected back at the cut-off point of fast wave in scrape-off layer, and finally enters into the divertor room. If some absorption mechanism of energy in the divertor are provided, these surface waves can be eliminated effectively. This function depends on the structure and the position of the divertor. The poloidal divertor may be more effective than other schemes, e.g. a bundle divertor. Although there are some open problems to construct an absorption layer in the divertor room, it must be pointed out that it is a new idea that has never been proposed.

[1] K. Uehara et al., J. Phys. Soc. Japan 49(1980)2364.

[2] K. Sakurai et al., J. Phys. Soc. Japan 37(1974)1108.

J

IMPURITY CONTROL
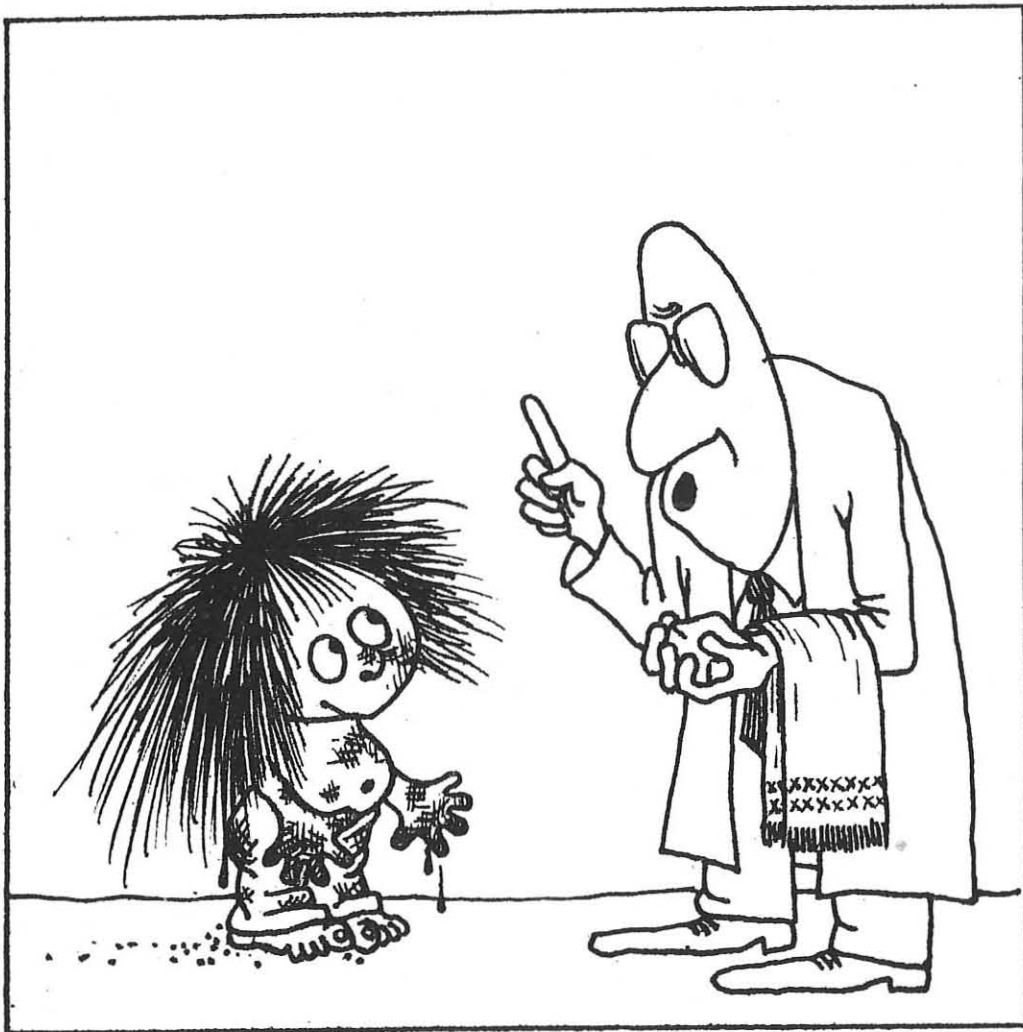
SUPPRESSION OF IMPURITY INFLUX, REMOTE RADIATIVE COOLING AND HELIUM ASH COMPRESSION WITH POLOIDAL DIVERTOR IN DOUBLET III

M. Shimada, K. Ioki, M. Nagami, H. Yokomizo, S. Izumi, M. Maeno,
K. Shinya, H. Yoshida, N. Brooks *, J. deGrassie *, and A. Kitsunezaki

Japan Atomic Energy Research Institute

Tokai, Ibaraki, JAPAN

at General Atomic Company

San Diego, California, USA

* General Atomic Company

Abstract: Three major advantages of a poloidal divertor are experimentally demonstrated:

1) Impurity influx (OV, NiXI, C IV) was reduced by 2 - 10.

2) Strong radiation cooling (50% of input power) at the divertor region resulted in the reduction of heat load to the divertor plate.

3) With helium content suppressed down to 1% of plasma density in the main plasma, helium partial pressure attained in the lower chamber was as high as 3.6×10^{-5} Torr, which means that helium ash exhaust is realistic in INTOR.

1) Reduction of Impurities: A single null poloidal divertor plasma was formed in the upper chamber of Doublet III (Ref. 1,2). Two of the 24 shaping coils are employed as divertor coils. Stable divertor operation was usually conducted in a condition of $I_D/I_p \simeq 0.58$ where I_D, and I_p are the current in both the two divertor coils and the plasma current. A typical divertor configuration is shown in Fig. 1. This magnetic configuration was confirmed by H_α - filtered TV camera, which shows that the plasma-wall interaction is transferred from the plasma-limiter interface to the remote divertor plate. As a result, a significant (by a factor of 2 - 10) reduction of impurity influx was observed in OV (624.7Å), NiXI (148.4Å) C IV (1548.2Å). The radiation loss from the main plasma was reduced by 20-50%.

2) Remote Radiative Cooling: A high density diverted discharge $(\bar{n}_e \simeq 5 \times 10^{13} \text{ cm}^{-3})$ in Doublet III is characterized by (Ref. 2):

a) concentrated recycling at the divertor region (H_α line intensity from the chord through the divertor region is ∿ 30 times as strong as that through the central chord).

b) high density (2mm μ wave interferometer looking through the divertor region implies that $\bar{n}_e \gtrsim 5 \times 10^{13} \text{ cm}^{-3}$).

c) remote radiative cooling at the divertor region.

The remote radiative cooling was studied by 5-channel and 21-channel bolometer array. The radiative power at the divertor increases with the increase of electron density (Fig. 2) and attains up to 50% of joule input power. The heat load measurement by thermocouples and infrared camera implies that the heat load on the divertor plate decreases down to 3% of input power as the electron density of the main plasma increases, due to strong remote cooling in high density discharges (Fig. 2). This remote cooling is particularly important since it possibly negates the engineering difficulties of using divertor plates in future diverted tokamaks.

3) Helium Ash Compression and Enrichment: The helium ash exhaustion function of a divertor has been experimentally demonstrated (Ref. 3). Helium was introduced into the vacuum vessel by a helium gas puff in a pulse of 5 ms duration. Both the hydrogen and helium pressure in the lower chamber increased with the increase in main plasma density (Fig. 3), while the helium density in the main plasma decreased (Fig. 4). Hydrogen and helium pressures were measured by a magnetically shielded ionization gauge, and a quadrupole mass-analyzer. Helium density in the plasma was measured by the increase of electron density. The maximum observed pressure was 3.6×10^{-5} Torr (He), 1.5×10^{-3} Torr (H_2) at $\bar{n}_e = 5 \times 10^{13} \text{ cm}^{-3}$. Helium density in the main plasma was ∿ $5 \times 10^{11} \text{ cm}^{-3}$, which was 1% of electron density. This result is sufficient to demonstrate the feasibility of using a poloidal divertor for ash exhaust in future alpha-heated tokamaks, since the INTOR design study (Ref. 4) showed that if helium partial pressure at the divertor plate is 1×10^{-5} Torr, the required pumping speed becomes 5×10^5 ℓ/s, which is an engineering possibility. Helium enrichment, defined by $\eta = (P_{He}/P_{H_2})_{\text{lower chamber}} / (n_{He}/n_e)_{\text{main plasma}}$ is also an increasing function of $\bar{n}_e$ and attains 2.4 at $\bar{n}_e = 5 \times 10^{13} \text{ cm}^{-3}$ (Fig. 4). Helium pressure in the lower chamber in non-diverted discharges was one order of magnitude lower than that in the diverted case.

References

[1] M. Nagami et al., Nucl. Fusion 20 (1980) 1325.

[2] M. Nagami et al., in Proceedings of the Eighth International Conference on Plasma Physics and Controlled Nuclear Fusion Research, Brussels, 1980, IAEAOCN/02.

[3] M. Shimada et al., JAPAN ATOMIC RESEARCH INSTITUTE REPORT, JAERI-M 9470, April 1981

[4] Y. Shimomura et al., JAERI-M 8294, June 1979, and Y. Seki er al., Nucl. Fusion 20, (1980) 1213.
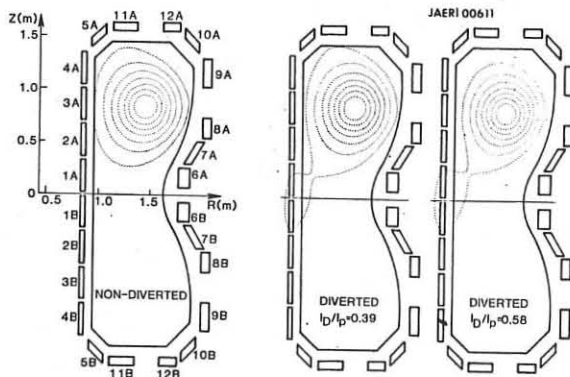
Fig. 1 Magnetic configurations with and without divertor.

Fig. 2 Reduction of heat load on the divertor plate by remote radiative cooling $P_{rad}(div)$ is the radiative power at the divertor region and ϕ_{div} is the heat load to the divertor plate ($I_p \simeq 500$kA)
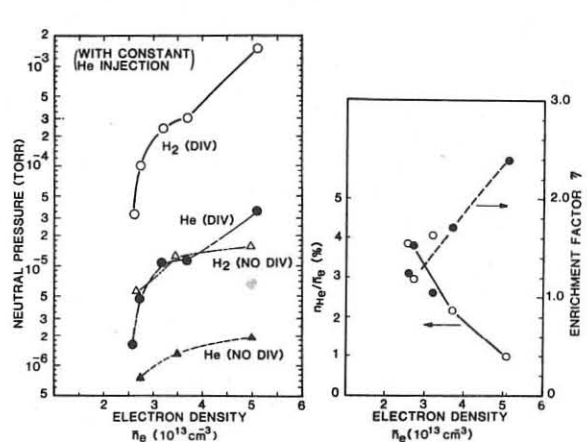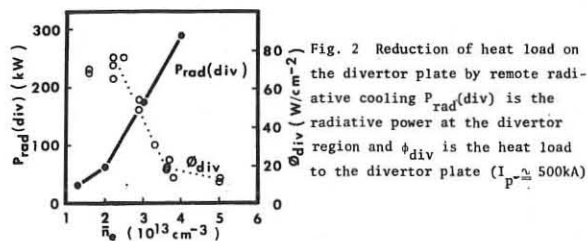

Fig. 3 Helium compression at the lower chamber vs. electron density of the main plasma. Note that this experiment was done with constant helium injection. ● helium pressure, ○ hydrogen pressure with divertor. ▲ helium pressure, △ hydrogen pressure without divertor.
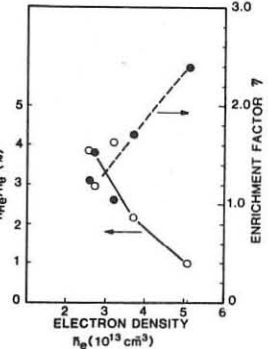
Fig. 4 Ratio of helium density to plasma density in the main plasma (○), and helium enrichment factor (●) vs. electron density in the main plasma.

$$\eta = \frac{(P_{He}/P_{H_2})_{\text{lower chamber}}}{(n_{He}/n_e)_{\text{main plasma}}}$$

FLUXES OF ENERGY AND PARTICLES IN THE T-12
TOKAMAK WITH DIVERTOR

Brevnov N.N., Vertiporokh A.N., Gera-
simov S.N. Khimchenko L.N.

Kurchatov Institute of Atomic Energy,
Moscow, USSR

Introduction. T-12 is a tokamak with two poloidal diver-
tors and with an elongated plasma column cross-section /1/.
The main parameters: R_o=36 cm, a·= 8 cm, elongation factor
K~2, toroidal magnetic field B_T=0.8 T, plasma current J_p=
10÷30 kA. The typical plasma parameters: electron tempera-
ture T_e(0) ~ 400 eV, T_i~110 eV, electron density $\bar{n}_e$(0)~
~ (2÷3).10^{13}cm^{-3}.

Magnetic configuration. Either the symmetric magnetic
configuration of a finger-ring tokamak with two poloidal
divertors (Fig.1a) or a drop-like magnetic configuration
with one poloidal divertor (Fig.1b), similar to the INTOR-
configuration, are formed dependent on the plasma column
position respective to an equatorial plane and on defi-
nite ratio between the plasma current and the current
through the windings of the quadrupole field. The advan-
tageous plasma transport into one divertor - instead of
two - is a criterion of a drop-like, one divertor configu-
ration formation. The ratio between the plasma flux into
the upper divertor and that into the lower one depending

the plasma column centre position respective to the
equatorial plane /2/ is given in Fig.1 c.

Flux of particles and energy into the divertor. The
column centre displacement by Δ Z ~ 1 cm along the ver-
tical results in a change in the ratio between the flux of
energy and particles into the upper divertor channel and
that into the lower one up to a value ~ 10 (Fig.2). An asym-
metry in fluxes of particles into the internal and exter-
nal divertor channels is observed in case of the drop-like
configuration, nevertheless, the energy fluxes are appro-
ximately the same. Distribution of fluxes of energy and
particles across the divertor channel is usually an asym-
metric one.

Out of the ratio of the energy fluxes to the divertor
(Fig.2) and to the wall, one can conclude that all the ener-
gy introduced into the discharge (except of the radiated
one) is transported into the divertors, i.e. efficiency of
the energy extraction into the divertor is close to 1.

Estimations of the flux of particles to the wall of a
discharge chamber /3/ show that a fraction ≤ 0.05 of
the flux of particles through the separatrix magnetic sur-
face reaches the wall. Therefore, the efficiency of the
particle extraction to the divertor is also close to 1.
The measured total flux of particles into the divertor
channels exceeds the flux of particles through the separa-
trix magnetic surface by ≈ 2 times, that points to the
fact that the recycling process occurs in the divertor
channels.

Radiation losses. In the transition from an ordinary li-
miter to the magnetic one, the relative radiation losses
decrease by 2÷3 times and equal ~ 20%. Power distribution
of the radiation losses across the plasma column for a dis-
charge with the limiter (dashed line) and with the divertor

(solid line) are given in Fig.3 b. The distributions have
been ontained from comparison of the experimental depen-
dences of the signal from a pyrodetector on its solid
angle of observation (Fig.3 a) with the calculated ones.

The model calculations based on /4/ have shown that
the profiles of radiated power (Fig.3 b) can be explai-
ned only by radiation of heavy impurities (e.g. iron).
If one takes into account that the profiles of T_e
and n_e are slightly changed when the plasma column is
limited with the limiter or with the separatrix, a de-
crease in the radiating power in a discharge with the
divertor will be dependent on a decrease in concentra-
tion of iron at the periphery of the plasma column that
also shows an effective plasma shielding from heavy im-
purities with the divertor layer /3/.

A level of radiation losses practically remains the
same in the central region of the plasma column. It is
likely to be dependent on the fact that any change in
concentration of impurities (which could emerge at the
initial stage of a discharge) has no time to occur in
the central region of the plasma column during the
discharge.

References

1. Bortnikov A.V. et al. Fizika Plasmy. v.4. N 2(1978)
   261.
2. Brevnov N.N., Gerasimov S.N. Preprint IAE-3184.Moscow,
   1979.
3. Bortnikov A.V. et al.in:Plasma Phys. and Contr.Nuclear
   Fusion Res. Brussel, 1980 IAEA-CN-38/X-2-2.
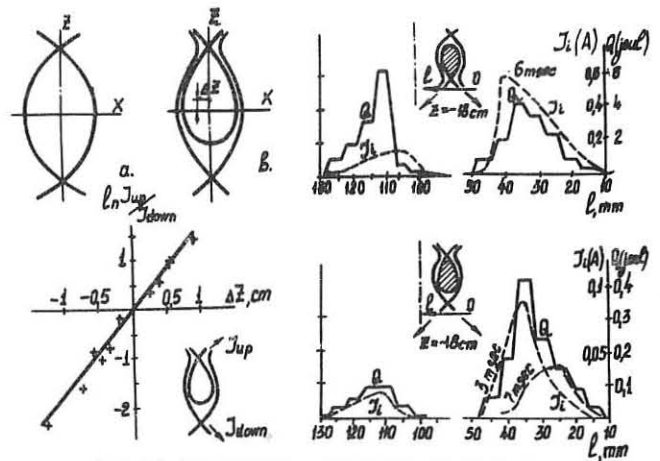4. Jensen R.V. et al. Nuclear Fusion. v.17, 1187, 1977.

Fig.1. Simmetric-(a)and "drop-like"-
(b) magnetic configuration Ratio
of the plasma fluxes to the diver-
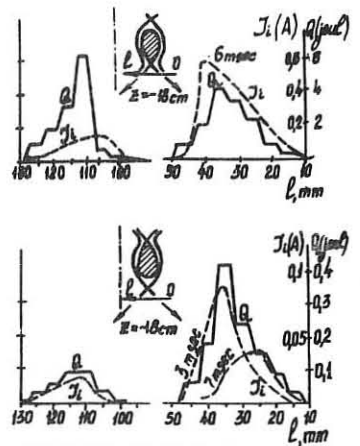tors vs vertical displacement
Δ Z-(c).

Fig 2 Energy flux-Q, par-
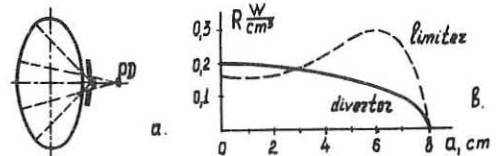ticle flux J_i - crosswise
the divertor channels

Fig 3 Scheme of experiments (a) and spatial distribution
of the radiated power (b), (- - limiter,— di-
vertor).

NONAMBIPOLAR PLASMA TRANSFER IN TV-1 TOKAMAK SCRAPE-OFF-LAYER

R.S. Ivanov, A.V. Nedospasov, G.N. Fideliman

Institute of High Temperatures of the USSR Academy of Sciences
Moscow, USSR

ABSTRACT The electric measurements in TV-1 scrape-off-layer are performed. Plasma transfer in the scrape-off-layer was found to be at least partialy nonambipolar. The "nonambipolar" diffusion coefficient was estimated. The effect of the external limiter-wall voltage on plasma parameters near the wall was observed.

INTRODUCTION In the experiments performed in T-5 |1| and T-11 |2| tokamak devices an electric current between a limiter and a vacuum vessel wall was observed with electrons from plasma escaping to the limiter and ions escaping to the wall. This phenomenon may be caused by existence of nonambipolar transfer similar to the processes in partly ionized plasma investigated earlier |3-5|.

The present paper describes the electric measurements performed in the scrape-off-layer of TV-1 device.

EXPERIMENTAL The TV-1 |6| is a small tokamak with major and minor radii of 23.5 and 4.1 cm, respectively. A single ss-aperture limiter with a minor radius of 3.5 cm was connected electrically with the ss-vacuum vessel. The insulated molibdenium rail-type limiters were introduced through the three horisontal diagnostic ports while the ports were disposed from the aperture limiter to the toroidal angles of 75°, 180° and 270°, respectively. The 1.5 cm high rail-type limiters were movable along the small radius of the torus. The typical discharge parameters observed in various sets of experiments were the following: the plasma current was 4-6 kA, the loop voltage was 2.0-4.5 V, the radial displacement of plasma column was 0.4-0.8 cm, the safety factor was 4-6, discharge duration varied between 5 and 8 ms. The toroidal magnetic field was 16 kG. The filling gas was hydrogen. The scrape-off-layer plasma parameters were measured by the movable double Langmuir probe, positioned at toroidal angle of 90° from the aperture limiter. The interpretation of the probe measurements were performed with no magnetic field taken into account using the well known exsspesions |7|. The electric current between the rail-type limiter and the wall was measured by the means of the current transformer.

RESULTS AND DISCUSSION The typical oscillogram of the limiter-wall current ("short current") is presented in Fig.1. As it was observed earlier |1, 2| the direction of this current everytime corresponded to the case when electrons escaped mainly to the rail-type limiter and ions escaped to the aperture limiter and to the wall. The current was of considerably oscillating type with oscillation amplitude being up to 40-50% of the mean current value and the oscillation frequency of 50-200 KHz. In all further results presented here the measured value of the "short current" was attached to the moment of time 3-4 ms after the start of discharge and averaged over the oscillations.

The dependence of the "short current" on the limiter position r_d is presented in Fig.2. A sharp current growth from zero to almost maximum value was observed when the movable rail-type limiter traveled past the aperture limiter edge. The current dropped to zero at $r_d=3.1$ cm when the additional rail-type limiter connected electrically with the wall was introduced to r=2.7 cm. These data seem to testify the following conclusion: electron and ion fluxes have been collected from separate along the minor radius areas of the conducting surface, i.e. electrons have been collected from the area disposed close to plasma edge and ions collected from more remote outwards areas.

Almost complete blocking of the current was observed when the negative potential of 50 V being applied to the rail limiter ($r_d=2.8$ cm). The current decreased twice when the external voltage was varied within 20-30 V interval, that is comparable with the electron temperature in the shadow region. Therefore one may conclude that the observed current at least was not caused by "run-away" electron flux.

The electron density and the temperature in the aperture

limiter shadow is presented in Fig.3. Fig.4 (curve 1) demonstrated the single probe current radial profile the probe being at the potential of the wall. The polarity of the probe current corresponded to the ion flux from plasma. The value of that current was 20-30% of the saturation ion current (see curve 2).

The diffusion coefficient estimated from the flux and gradient measurements for the conditions presented in Fig.3 was found to be $D_y=2\cdot10^3$ cm²/s, i.e. the diffusion coefficient is of Bohm order.

CONCLUSIONS The transport of plasma escaping the bulk becomes nonambipolar at least partialy in the scrape-off-layer . The electron flux is collected mainly from the area of limiter contacting plasma edge while the ion flux is collected from more outwards remote areas of the limiter and the chamber wall. The electric current is short circuited radially over the conducting surface.

The diffusion of ions separately from electrons may essentially cause the density radial profiles and transport properties in the scrape-off-layer plasma. Hence the effect of the external limiter-wall voltage on the plasm profiles may be supposed. Such influence was observed in certain experiments. While the expernal negative limiter-wall voltage (-45V) being applied plasma density near the wall reduced several times against the value measured at the same external voltage but of opposite polarity.

REFERENCES
1. Mukhovatov V.S. Plasma Phys. and Contr. Nucl. Fus. Res., IAEA, Vienna, 2, 577, 1966.
2. Leonov V.M. Preprint IAE-3232/7, Moscow, 1980.
3. Simon A. Phys. Rev., 98, 317, 1955.
4. Zharinov A.V. Atomnaya energiya, 7, 220, 1959.
5. Zhilinsky A.P., Tsendin L.D. Usp.Fiz.Nauk, 131, 343, 1980.
6. Ivanov R.S., Nedospasov A.V. Soviet American work-shop for plasma-wall interaction, Moscow, 1979.
7. Chen F. In: "Plasma diagnostic techniques". by R.H. Huddlestone and S. Leonard, Academic Press, 1965.
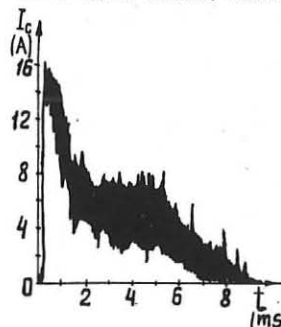
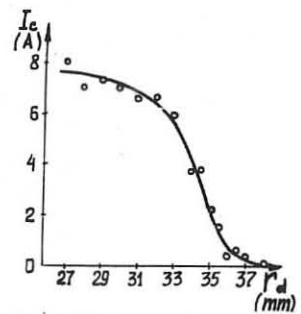Fig.1. Typical oscillogram trace of the "short current". $r_d=2.8$ cm P=12·10⁻⁴ torr.

Fig.2. "Short current" vs minor radial position of rail limiter P=4·10⁻⁴ torr.

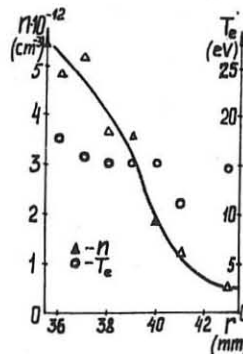

Fig.3. Radial dependence of electron density n and temperature T_e in the aperture limiter shadow. P=12·10⁻⁴ torr, $r_d=2.8$ cm, $I_c=5.5$ A, t=3 ms.
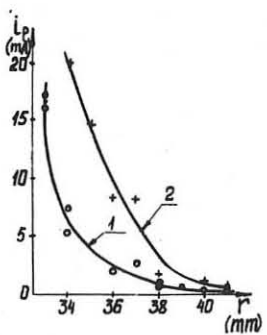
Fig.4. Radial dependences of the single probe current (1) and ion saturation current obtained by double probe (2), P=12·10⁻⁴torr, $r_d=2.8$ cm, t=3 ms.

ARCING STUDIES IN TOKAMAK TV-1

N.M.Zykova, R.S.Ivanov, V.N.Kabanov, T.S.Kurakina,
A.V.Nedospasov

Institute of High Temperature of the USSR Academy
of Sciences, Moscow, USSR

Measurements of currents between probes or limiters and vacuum vessel published earlier [1-6] show correlation between arcing and MHD-instability of the discharge. In tokamak TV-1 the measurements of currents between limiters were made in the condition of instable discharges and arc tracks on the limiter surface were observed to clear directions and paths of arc currents closing.

The TV-1 installation is a circular tokamak with R=235mm, r=41 mm, minor radius of constant limiter is a=35 mm. The experiments were performed in hydrogen under the following experimental conditions: $p=5 \cdot 10^{-4} - 1 \cdot 10^{-3}$ torr, $n_e = 1 \cdot 10^{13} cm^{-3}$, toroidal magnetic field $B_T = 14-16$ kG , plasma current $I_p = 3-12$ kA, minimum loop voltage $V_L = 2-4$ V, discharge duration 5-8 ms. The arc test probe and movable limiters were placed on 5 mm from unmovable limiter and actually served as plasma limiters.

The arc test probe position was fixed, but the limiters were shifted with respect to the probe. The probe and the limiters were insulated from vacuum vessel and were connected electrically via $1 \div 100 \Omega$ resistor. The current was measured with special 0.1Ω resistor or by current transformer with band $20 \div 10^6$ Hz. Limiters and probes surfaces were mechanically polished.

Two series of the experiment were carried out. In the first the currents between the arc probe and one of the limiters or between two limiters were measured. The material of limiters was molybdenum, the probe was made of stainless steel. The height of the probe and the limiters was 15 mm, their width along minor radius was 10 mm, and length of sides parallel to B_T were 24 and 2.5 mm respectively. The current pulses and the arc tracks were not observed in the stable discharges with $q \geqslant 3$. In the instable discharges the current pulses were observed with amplitude up to 100 A and duration up to 50 ms. The time of pulse occurance coincided with the abrupt displacement of plasma and with loop voltage spikes. The loop voltage spikes were positive in the first experimental series, but the current oscillograms recorded the pulses of both polarities. In the course of discharge several pulses with different amplitudes, occuring one after another, were seen.

Introduction of resistance into external circuit gave an opportunity to evaluate potential drop V_R, which correlated to the current amplitude.

Fig.1 presents dependence between maximum current values and respective V_R values under the identical discharge conditions.

The two current polarities in the external circuit may be caused by one of the reasons. First, currents in the plasma may flow in two opposite directions. Second, currents of the same direction flow by different paths. Since no cathode tracks on the electron side of the limiters and probes were observed the existence of predominant direction of the arc current may be supposed. The diagramm given in Fig.2 shows pulses of two polarities with the definite current direction and two paths of its closing - "short" and "long". In this case terms "short" and "long" mean the distance between the limiters, but not the length of the current path.

In the second series of the experiment an attempt was made to separate the currents closed along the different paths and to determine a correlation between current direction in the external circuit and the discharge parameters. For this purpose the arc probe was separated into two isolated parts. In the experiments a stainless steel limiter was used. The limiter was a part of a ring, the width of which was 7 mm and thickness 2 mm. The limiter subtended an angle of 135° at minor radius of 30 mm. The electron side of

the probe was connected via an external resistance with its ion side or the limiter. The probe and the limiter were placed in torus asymmetrically, an angle between the ion side and the limiter was 255°. The currents along "long" paths exceed 2-2.5 times the currents along "short" one. Maximum current and V_R were approximately 70 A and 150 V respectively. The current in external circuit flowed predominantly in one direction. The current polarity was the same as the polarity of plasma current, when loop voltage spikes were positive. While the disruption instability was observed loop voltage spikes reached -20 V (Fig.3) and the arc current polarity reversed.

Emf of a pure unipolar arc is plasma-wall potential drop, depended on plasma parameters [7]. Observed in TV-1 value of V_R considerably exceeded plasma-wall potential drop corresponding the electron temperature in the stable discharges. The arc current observed may have the predominant polarity if any additional polarised emf exists [8]. The source of the additional emf may be the loop voltage field, polarity of it depending on the instability type. The electric arcs observed in our experiments seem not to be exactly those unipolar arcs, that were proposed earlier in [7].

1. Goodall D.H.J., McCracken G.M., Nucl.Fus., 1979, 19, № 10, 1396-1401.
2. Goodall D.H.J., J.Nucl.Mater., 1980, 93&94, 154-160.
3. Mioduszewski P., Clausing R.E., Heatherly L., J.Nucl. Mater., 1979, 84&86, 963-966.
4. Clausing R.E., Emerson L.C., Heatherly L., J.Nucl. Mater., 1980, 93&94, 150-153.
5. Yamamoto S., Shimomuza Y., Ohasa K. et al., J.Phys.Soc. Jap., 1980, 48, № 3, 1053-1054.
6. Maeno M., Ohtsuka H., Yamamoto S. et al., Nucl.Fus., 1980, 20, № 11, 1415-1419.
7. Robson A.E., Thonemann P.C., Proc.Phys.Soc., 1959, 73, 508-512.
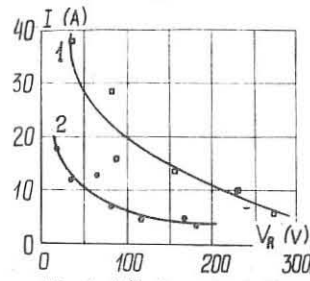8. Nedospasov A.V., Petrov V.G., J.Nucl.Mater., 1980, 93&94, 775-779.

Fig.1. V/A characteristics of arc external circuit:
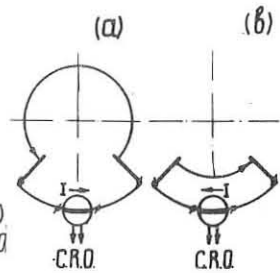1 - positive current pulses,
2 - negative current pulses

Fig.2. Possible paths of current closing between limiters:
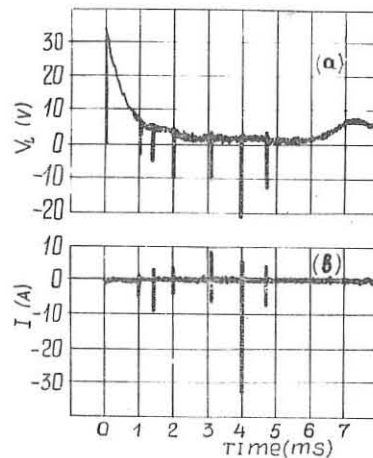(a) - "long",
(b) - "short"

Fig.3. Correlation between loop voltage (a) and current between electron side of probe and limiter (b)

THE INFLUENCE OF SURFACE CONDITIONS ON UNIPOLAR ARCS IN A TOKAMAK

K. Jakubka

Academy of Sciences of the CSSR, Institute of Plasma Physics, Prague, CSSR

B. Jüttner

Academy of Sciences of the GDR, Central Institute of Electron Physics, Berlin, GDR

1. Introduction

Unipolar arcs at inner surfaces of a tokamak are of interest as a possible source of plasma contamination /1, 2/. The conditions for their ignition as well as their elementary surface mechanism are not yet well understood. The present paper describes experiments with movable probes in a small tokamak (TM 1, Institute of Plasma Physics, Prague), the aim of which was a study with defined surface conditions.

2. Experimental

The TM 1-tokamak has a major radius of 0.4 m and a limiter radius of 0.075 m. The following parameters have been used: Toroidal field 1.4 T, discharge current 16-20 kA, discharge duration 6-8 ms, central values of electron density, electron temperature and ion temperature about $2-3.10^{19} m^{-3}$, 300 eV, 40-70 eV, respectively. The probes consisted of Mo. By single expositions an unambiguous interpretation of arc tracks was possible. The surface preparation was as follows:

a) Cleaning in situ by heating up to or beyond the melting point.

b) Cleaning as in case a), followed by a slight oxidation by a short exposition to air.

c) Applying a small dot of carbon

d) As case c), but degassed in situ by intense heating.

3. Results

With degassed probes according to a) and d) no arcing could be observed, even if the probes were immersed deeply into the plasma (causing their destruction by melting). In the quiet plasma phase the current signals of these probes indicated a positive floating voltage with respect to the liner, therefore the premises of the Robson-Thonemann-model of unipolar arcs /3, 4/ did not hold.

With weak oxide layers (case 6) arcing occurred during instabilities of the main discharge, generally 1-2 ms after beginning.

Carbon coated probes (case c) provoked arcs also during quiet plasma phases.

Fig. 1 shows oscillograms of probe currents for the latter case. Fig. 1a depicts the signal of a reference probe which was located at liner level. Fig. 1b shows the signal of the carbon-coated probe at the plasma boundary. About 1 ms after beginning there occurs an instability, presented by Fig. 1c in more detail. It is not necessarily connected with an arc, because it was shown also by the clean surface probes (without arc tracks), and because it was also indicated by the reference probe. About 3 ms after beginning, arc currents are to be seen (arrowed) which were accompanied by an increase of the CIII-radiation at the location of the probe.

Fig. 2 shows the erosion of the carbon dot. Here, and also

in other cases of thick contamination layers, arc tracks on the underlying metal are almost invisible. Fig. 3 shows arc tracks for the case b). The arc occurred during the starting instability (similar to Fig. 1), but it was shorter than the signal of this instability (<10 μs, deduced from the track length). The craters in Fig. 3 belong to two types: (i) large, overlapping craters (shown in more detail by Fig. 4 for another example) and small, dispersed ones (Fig. 5). We assume they reflect two arc spot modes which depend on the cleanliness of the surface.

We conclude: Arcing needs plasma instabilities as well as surface layers. Thick layers can provoke local instabilities by desorption processes. Different arc modes can occur in dependence on the surface state, in close analogy to spot modes of bipolar vacuum arcs.

References

/1/ G.M.McCracken, P.E.Stott, Nuclear Fusion 19, 1979, 889

/2/ R.Behrisch, J.Nucl.Mater. 85 & 86, 1979, 1047

/3/ A.E.Robson, P.C.Thonemann, Proc.Phys.Soc. 73, 1959, 508
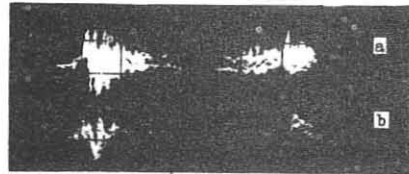
/4/ A.E.Robson, Radiotekhnika i Elektronika 4, 1959, 1299

Fig.1: Signals of probe currents
a) Reference probe. Horizontal 1 ms/div., vertical 0.08 A/div.
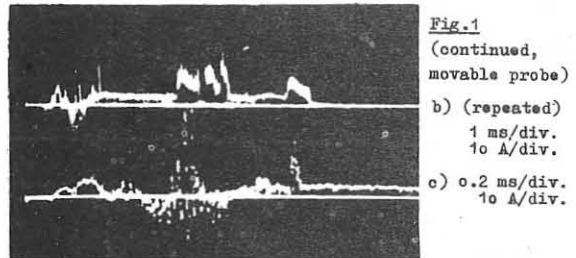b) Movable probe. Horizontal 1 ms/div., vertical 1o A/div.

Fig.1 (continued, movable probe)
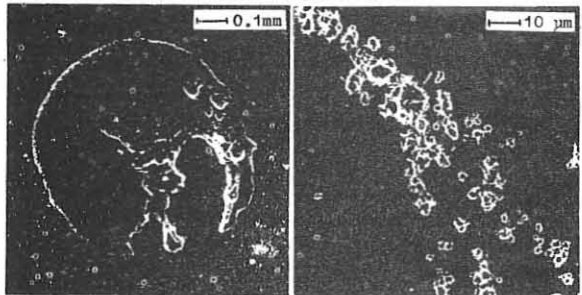b) (repeated) 1 ms/div. 1o A/div.
c) 0.2 ms/div. 1o A/div.

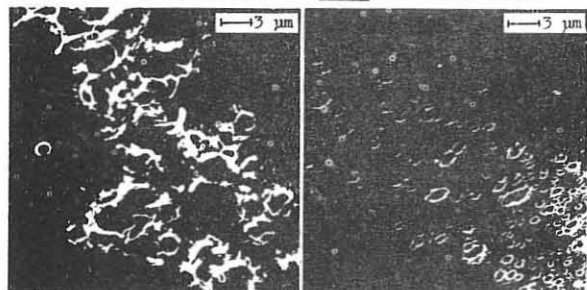Fig.2: Arcing on carbon   Fig.3: Arc track on Mo

Fig.4: Arc track on Mo   Fig.5: Arc track on Mo

THE EFFECT OF PARTICLE RECYCLING IN A TOKAMAK WITH HIGH PLASMA DENSITY

N.N.Vasiljev, V.K.Kolesnikov, V.Eh.Lukash,
A.V.Nedospasov
Institute of High Temperatures
USSR Academy of Sciences

A possibility of achieving "fusion" plasma parameters in a relatively small tokamak with dense plasma ($n \sim 10^{15} cm^{-3}$) confined by strong magnetic field is discussed in literature [1-3]. The objective of this paper is the simulation by onedimensional nonstationary model accounting for particle recycling near the wall, which mechanism automatically defines plasma temperature and density near the wall.

The algorithm used to solve the set of equations including electron and ion energy equations as well as plasma and magnetic field diffusion equations was described in [4].

In addition to equations mentioned the diffusion equation of impurity ion density was solved to estimate the radiation sponsored by impurities according to "coronal model". This equation describes neoclassical diffusion of "virtual ion" with the account for temperature screening as well as anomalous diffusion [5,6].

The coefficient in the term describing anomalous diffusion was assumed to be equal to the background plasma diffusion coefficient. Carbon was used as impurity in simulations.

Transport coefficients were calculated according to electron thermal conductivity and plasma diffusion empirical relations [7].

$$X_e = 9 \cdot 10^{18}/(n\sqrt{T_e})\, cm^2/s \quad , \quad \mathcal{D} = 10^3 \left[1 + g(r/a)^2\right] cm^2/s$$

where n_e is in cm^{-3} and T_e in eV, as well as by means of neoclassical relations for ion thermal conductivity.

All transport coefficients in simulations were limited by Bohm diffusion coefficient $D_B = \frac{1}{16}\left(\frac{cT}{eB}\right)$ in the following manner

$$X_{e,p} = \frac{1}{X_e^{-1} + \mathcal{D}_B^{-1}}\; ; \quad X_{i,p} = \frac{1}{X_i^{-1} + \mathcal{D}_B^{-1}}\; ; \quad \mathcal{D}_p = \frac{1}{\mathcal{D}^{-1} + \mathcal{D}_B^{-1}}$$

where index "p" denotes the calculated value of a coefficient. Plasma in the nearwall layer was described considering particial recycling similar to [8]. Cold neutral density value was defined solving integral equation: $n_H = N_o + N_1$

$$N_o = \frac{\Gamma_{Mo}}{V_M}\left\{\Phi(r,a,V_M) + \Phi(o,a,V_M) \cdot \Phi(o,r,V_M)\right\}$$

$$N_1 = \int_o^a \frac{\langle \mathcal{G}V\rangle_{cx}\, n_i n_H}{2V_i}\left\{\Phi(o,r,V_i)\cdot\Phi(o,x,V_i) + \left|\Phi(o,r,V_i) - \Phi(o,x,V_i)\right|\right\}dx$$

$$\Phi(\xi,\eta,V) = exp\left\{-\frac{1}{V}\int_\xi^\eta\left(\langle \mathcal{G}V\rangle_I + \langle \mathcal{G}V\rangle_{cx}\right) n_i dx\right\}$$

In this formulae $\langle \mathcal{G}V\rangle_{cx}$ and $\langle \mathcal{G}V\rangle_I$ are charge exchange and ionization rates correspondingly, Γ_{Mo} - neutral flux from the wall equal to ion and neutral flux to the wall (this simulation was conducted under zero-perforation assumption, i.e. the number of particles in plasma remained constant). The temperature of particles incoming to plasma from the wall T_m was determined with the account for the particle and energy reflection coefficients given in [9] for iron wall. The temperature of cold neutrals resulting from the dissociation of molecules desorbed from the walls was assumed to be 2 eV. The nearwall potential jump was neglected according to considerations similar to those described in [10]. Cold neutral temperature T_m was determined by the following relation

$$n_H T_H = T_M N_o + \int_o^a \frac{T_i\langle \mathcal{G}V\rangle_{cx}\, n_i n_H}{2V_i}\left\{\Phi(o,r,V_i)\cdot\Phi(o,x,V_i) + \left|\Phi(o,r,V_i) - \Phi(o,x,V_i)\right|\right\} dx$$

Heat transfer in the narrow nearwall region with a width of the ion Larmor radius order was realized by convection, thus zero electron and ion temperature gradients were assumed at the wall. Total plasma current conservation was used as a boundary condition for magnetic field diffusion equations. $n(a)$ equal to $10^{13} cm^{-3}$ was also taken

as a boundary condition. Initial profile of impurity density was chosen assuming $Z_{eff} = const \sim 1.3$, which corresponded to the total impurity content of about 1%.

The results of simulation for some initial profile are presented on Fig.1-3. Fig.1 shows that at 15th msec the plasma density levelling occurs, caused by the intensive ionization of neutrals near the wall. It can be also seen that a low temperature region forms near the wall, its width being defined by penetration depth of neutrals coming from the wall (Fig.2).

Time dependence of fusion power, main plasma energy losses as well as Q-value which is equal to the ratio of fusion power accounting for neutrons to the total power of all plasma energy losses. It must be noted that simulation presented was conducted without consideration for plasma heating by α-particles.

During the first five msec plasma main energy losses are determined by convection, since nearwall plasma temperature is relatively high at the initial moment (about 300 eV). Afterwards plasma temperature in the nearwall region decreases rapidly due to recycling of neutrals near the wall resulting in convection loss sharp decrease. This explains the existance of Q-value maximum at 5-6 msec when fusion power falls by a factor of two.

1. Coppy B, Comments Plasma Phys.Con.Fusion, 1977, v.3, M.2, p.47.
2. Cohn D.R., in Proc.Int.Conf., Cambridge, Mass., 18-20 Sept. 1978.
3. Brownmann U. et al., Tape-wounded toroidal (TF) magnet for ZEPHYR, IPP 1/176, 1979.
4. Васильев Н.Н., Лукаш В.Э., Препринт ИВТАН, № 7-017, М., 1977
5. Rutherford P.H., Phys. Fluids, 1974, 17, p.1782.
6. Duchs D.F. et al., Nucl.Fusion, 1977, 17, p.565.
7. Post D.E. et al., in Proc.of 7th IAEA Conf., Vienna, 1979, 1, p.471.
8. Васильев Н.Н. и др., Атомная энергия, 1978, 44, с.336
9. Oen O.S. et al., Nucl.Instr., 1976, 132, p.647.
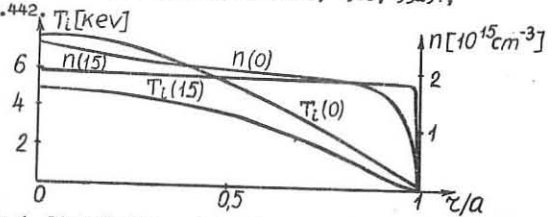10. Kotzlovski H. et al., J.Nucl.Mat., 1980, 93&94, p.442.

Fig.1. Distributions of ion temperature and plasma density at the initial moment (0) and after 15 msec (15) along the chamber radius
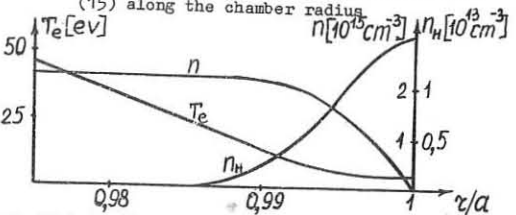

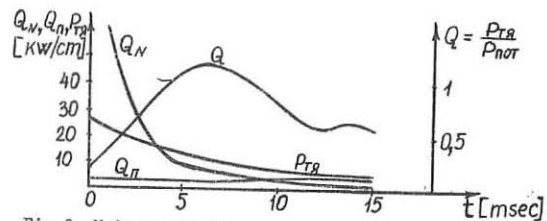Fig.2. Distribution of electron temperature, plasma and neutral density in the nearwall region after 15msec

Fig.3. Main energy losses

Q_N - energy loss due convection in kW per colomn unit length

Q_{π} - radiation sponsored by impurities

$P_{T_{\mathcal{A}}}$ - fusion reaction power

PLASMA DIFFUSION IN SYSTEMS WITH SEPARA-TRIX

V.M.Gribkov, D.Kh.Morozov, O.P.Pogutse

Kurchatov Institute of Atomic Energy,
Moscow, USSR

Abstract. The diffusion coefficient for a toroidal system with divertor is obtained. The depth of the region with destroyed magnetic surfaces near the separatrix is evaluated in a straight system. The diffusion flow in stochastic magnetic field is calculated.

The separatrix with an x-point, at which the poloidal field disappears, occurs in divertors, doublets and other configurations. The classical plasma diffusion was studied in /1/ for such systems with straight geometry.

We take into account two significant effects which can change the character of diffusion.

First, we investigate the classical diffusion in a toroidal system with separatrix and conserved magnetic surfaces. A diffusion flow across the magnetic surface ψ = const is obtained

$$\Gamma = \oint n\, \vec{v} \cdot \nabla \psi \, \frac{R\, d\varphi\, d\alpha}{B \cdot \nabla \alpha} \tag{1}$$

$$\vec{v} \cdot \nabla \psi = -\eta c^2 \frac{R^2}{R_o^2}\left(1 - \frac{B_\varphi^2}{\langle B^2\rangle}\right)P'$$

where, R is a distance from the point of observation to the axis of symmetry, R_o is the large radius of the torus, φ and α are the large and small azimuthal angles, η is the plasma resistivity.

$$\langle A \rangle = \oint \frac{A\, d\alpha}{B \cdot \nabla \alpha}\left(\oint \frac{d\alpha}{B \cdot \nabla \alpha}\right)^{-1}$$

For numerical calculations we use a model such as in /1/. Two coaxial thin coils, separated by a distance 2a, carry the current J. Fig.1 shows the results of calculations. In the straight model, the diffusion flow at the points along the separatrix vanishes, except the x-point /1/. In the torus, the plasma flows across the separatrix everywhere.

Second, if the magnetic field is perturbed, magnetic surfaces near the separatrix will be destroyed. The field line does not lie on the surface but occupies some volume. Using the results of /2/, we can evaluate the depth of the region with destroyed magnetic surfaces. In this case, we can neglect the toroidal effects. Perturbation of the field is caused by changing the form of one conductor. Its equations are: $x = a + x_1 \sin kz$, $y=o$. The other conductor is straight. For the unperturbed case, $\chi^2 = \left(\frac{x^2}{a^2} + \frac{y^2}{a^2} + 1\right)^2 - \frac{4x^2}{a^2}$ = const. The separatrix corresponds to $\chi = 1$. In the region $1 - \delta < \chi < 1 + \delta$, the magnetic surfaces are destroyed. The parameter is obtained from the equation

$$\ln^2 \delta = \frac{2\pi}{k\alpha} \frac{y}{c\, B_o x_1}\, \delta \tag{2}$$

In this region, the diffusion coefficient is greater than that in the system with conserved surfaces. The thermal conductivity in a stochastic field is considered in /3/. In the present paper, we obtain similar results for the diffusion flow in the two-liquid approximation as well as for the slab geometry.

$$\Gamma = \frac{3}{4} \frac{T\, \nu_{ii}}{m_i \omega_i^2} \int |b_\kappa|^2 \frac{\kappa_\perp^2\, d\vec{\kappa}}{\kappa_a^2 + 0{,}45\frac{\nu_{ii}^2}{\omega_i^2}\kappa_\perp^2}\, \frac{dn_o}{dx} \tag{3}$$

$$|b_\kappa|^2 = \int \langle b_x(0)b_x(\vec{\tau})\rangle e^{-i\vec{\kappa}\vec{\tau}}\, d\vec{\tau}\quad ; \quad \vec{b} = \frac{\vec{B}}{B_o}$$

Therefore, in the real systems with an x-point the diffusion flow may differ from the model in /1/. This difference is rather large near the separatrix in the case of destroyed magnetic surfaces.

References

/1/ S.P.Auerbach, A.H.Boozer. Phys.of Fluids, 23, 2396 (1980).

/2/ G.M.Zaslavsky. Statisticheskaja neobratimost v nelineinykh sistemakh, Nauka, M., 1970.

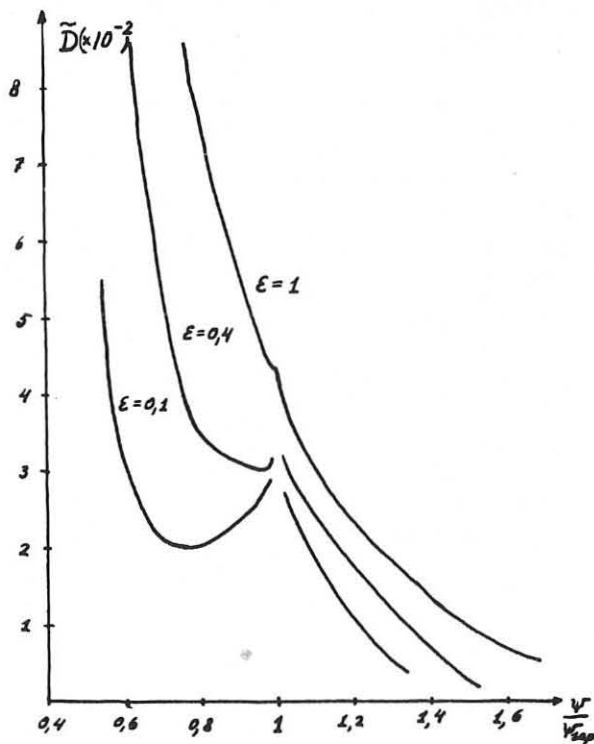/3/ B.B.Kadomtsev, O.P.Pogutse. Plasma Phys. and Contr. Nucl.Fusion Res., v.1, p.649, 1978, IAEA-CN-37/0-1.

Fig.1. Dimensionless diffusion coefficient $\tilde{D} = \frac{D\, \tilde{B}_P}{2\pi a\, \eta c^2 n}$

$$\tilde{B}_P = \frac{2y}{c\alpha}\quad ;\quad \frac{\Gamma}{\oint dS} = -D\frac{dP}{d\psi}\quad ;\quad \frac{\tilde{B}_P}{B_o} = 0{,}5$$

DIFFUSION OF IMPURITIES IN THE PRESENCE OF EXTERNAL FORCES AND ANOMALOUS PROCESSES IN A TOKAMAK PLASMA

S.V.Bazdenkov, P.N.Yushmanov

I.V.Kurchatov Institute of Atomic Energy,
Moscow, USSR

Abstract. An effect of the tokamak plasma impurity removal via the application of some external forces is theoretically studied when the anomalous longitudinal viscosity of electrons and some anomalous processes, like the magnetic field irregularities, are taken into account.

In the paper presented, one of the possible mechanisms responsible for the removal of α-particles and impurities from a tokamak with the external forces applied to plasma is discussed. These forces are produced by the same methods which are supposed to be used for the maintenance of a stationary current, i.e. by injection of neutral atoms and by RF oscillations. The method of cleaning, discussed previously in /1,2/ in the regimes with an ordinary neoclassical viscosity, is based on a change in velocities of the plasma motion along the magnetic surfaces under external forces as well as under friction between plasma and the wall, or a neutral gas, or the locally trapped ions. In its turn, this results in a change in friction between the components and, thus, in emergence of an additional drift of particles along the radial direction.

Some anomalous processes, which increase the electron viscosity and induce additional electron currents across the magnetic surfaces, are responsible for changes in the diamagnetic velocities of plasma. An increase in the electron longitudinal viscosity is equivalent, by its effect, to introduction of an additional damping of the poloidal momentum. Therefore, any mechanism which results in this effect, can be considered as viscosity.

Another type of anomalous processes under study is associated with the RF oscillations in plasma or with some irregularities in the magnetic field. Such processes provide an increased heat conduction of plasma due to appearance of an additional term in a kinetic equation /3/

$$\frac{\partial f}{\partial t} = \frac{\partial}{\partial z}\left(\chi \frac{\partial f}{\partial z}\right) \tag{1}$$

where, f is the distribution function in the particle velocities, χ depends on the nature of oscillations. Besides the heat fluxes, the equation (1) also will determine an additional flux of particles $\Gamma_{add.}$, which is proportional to a diamagnetic velocity, if one can neglect the temperature gradient,

$$\Gamma_{add.} = - L_e u_e \tag{2}$$

$$u_e = -\frac{c}{B_\vartheta}\cdot\left(\frac{1}{en_e}\frac{dP_e}{dr} + E_r\right)$$

The designations here are universally adopted ones, the coefficient L_e depends on the nature of anomality. Later, the flux (2) is taken into account for electrons only.

The particle fluxes provided by the external forces applied to plasma, with anomality of electrons taken into account, can be determined from the force equations for each plasma component. In the Pfirsch-Schlüter regime, the main portion of an additional flux of impurities is determined by a dependence of the external forces F_α on a poloidal angle. In this case,

$$\Delta\Gamma_z^{PS} \approx \frac{c}{ezB_\vartheta}\cdot\left[f_z + \frac{2\varepsilon^2\lambda_z}{L_e + 2\varepsilon^2(\lambda_i+\lambda_z)}\cdot\sum_\alpha f_\alpha\right] \tag{3}$$

$$f_\alpha = \langle F_\alpha\rangle\langle 1/h\rangle - \langle h F_\alpha\rangle\;;\quad \langle\cdot\rangle = \int_0^{2\pi}(\cdot)d\vartheta/2\pi$$

where, ε is the toroidicity parameter, $h = 1 + \varepsilon\cos\vartheta$, λ_α characterizes an efficiency of the "external" friction $R_{\alpha\,ext} = -\lambda_\alpha\cdot V_\alpha$. When the dependences F_α on ϑ are extremely asymmetric ones, the flux $\Delta\Gamma_z^{PS}$ will be proportional ε. As for the anomality of L_e, it is manifested in ε^2. But the radial electric field E_r dependent on L_e can change the sign and, in the case when $L_e \gg 2\varepsilon^2(\lambda_i+\lambda_z)$, is found to be equal $E_r = -\frac{dP_e}{dr}/en_e$.

In the "banana" regime, a change in the flux of impurities under external forces has different character dependent on L_e in comparison with $(\lambda_i + \lambda_z)$. Transition from a neoclassical electron viscosity to an anomalously large one does not affect the structure of the dependence $\Delta\Gamma_z$ on F_α, it changes only the numerical coefficients.

A peculiar feature of a given regime is a great quantitative difference between the flux of plasma and that of impurities, as $\mathcal{M}_z \ll \mathcal{M}_i$, there $\mathcal{M}_z, \mathcal{M}_i$ are the coefficients of viscosity for the impurities and for the main ions. Independently of L_e, the fluxes of the main ions and electrons considerably exceed the flux of impurity, so the effect of cleaning occurs due to the plasma pinching against the background of a slowly diffusing impurity.

References

1. V.V.Fomenko, Fiz.Plazmy, 3, 1390 (1977).

2. W.M.Stacey, Jr, D.J.Sigmar, Phys.Fluids, v.22, N 10 (1979), p.2000.

3. V.V.Parail, O.P.Pogutse, IAEA-CN-38/C-1, 1980.

IMPURITY FLOW REVERSAL IN TOKAMAK WITH HELICAL MAGNETIC FIELDS

A.A. Shishkin

Institute of Physics & Technology, the Ukrainian Academy of Sciences, Kharkov 310108, USSR

Abstract. Modification of the flow reversal effect is considered for a tokamak with externally applied helical magnetic fields and background ions injection, local in φ and multipole in ϑ. Magnetic fields from external helical currents split the rational magnetic surface giving rise to the chain of magnetic islands. The source of background ions acts on impurities due to a coupling of the source harmonic $(m + 1, n)$ with the magnetic perturbation (m,n) and the harmonic $(1,0)$ in the toroidal magnetic field.

1. As is known [1-3], the inward diffusion of impurity ions in plasma can be counteracted by particle and heat sources. In conventional tokamak with the magnetic field $\vec{B} = B_0 \left\{ 0, \frac{r}{R} t(r^2), 1 \right\} \left(1 + \frac{r}{R} \cos\vartheta \right)^{-1}$ and the magnetic surfaces $\Psi = \frac{r^2}{2}$ the particle source with the Fourier expansion in ϑ harmonics: $Q(r,\vartheta) = \left(1 + \frac{r}{R} \cos\vartheta \right)^{-1} \sum_n Q_n^c(r) \cos n\vartheta + Q_n^s(r) \sin n\vartheta$ results in the additional friction force acting on impurity ions on the side of background plasma ions. Below, in the Fourier expansion of $Q(r,\vartheta)$ we keep the harmonic $\sin\vartheta$ which is the only harmonic that makes a nonzero contribution to the averaged impurity flux. The friction force on the side of source ions $\left(\vec{F}_{iI\|} \right)_Q = \vec{B} \frac{m_i Q(r) R}{\tau_{iI} B_0 t(r^2)} \cos\vartheta$ compensates the action of the friction force which is proportional to the pressure gradients $\left(\vec{F}_{iI\|} \right) = \vec{B} \frac{m_i n_i}{\tau_{iI}} \frac{2 \cos\vartheta}{B_0^2 t(r^2)} \left(\frac{1}{z e n_I} \frac{\partial p_I}{\partial r} - \frac{1}{e n_i} \frac{\partial p_i}{\partial r} \right)$ for the proper choice of the longitudinal magnetic field direction (the sign of B_0) and of the source amplitude $Q = \left| \frac{2}{e B_0 R} \frac{\partial p_i}{\partial r} \right|$. The friction forces compensation ensures the transformation-to-zero of the impurity diffusion flux at a distance from the plasma edge. In experiments [4] the effect of the source on the impurities was realized by the injection of the background gas along the major perimeter of the toroidal device, i.e. at all values of φ $(0 \le \varphi \le 2\pi)$, and along one direction $\vartheta = const$; ϑ is the angle along the minor perimeter of the torus (Fig.1).

2. We consider in what way the scheme of the background gas injection may be simplified for a tokamak with externally applied helical magnetic fields $\vec{B} = B_0 \ell_m r^{m-1} \times \left\{ \sin\Theta, \cos\Theta, -\frac{nr}{m} \cos\Theta \right\}; \Theta = m\vartheta - n\varphi$, which split the rational magnetic surface with the radius $r = r_{mn}$ and rotational transform angle $t(r_{mn}^2) = \frac{n}{m}$ thereby forming the isolated chain of magnetic islands with the half-width Δr [5]. In this case the magnetic structure is described by equation $\Psi = const$, where $\Psi = \left[m t(0) - n \right] \frac{r^2}{2} + m \frac{dt}{dr^2} \frac{r^4}{4} + \ell_m R r^m \cos\Theta$. In a tokamak with such geometry the impurity reversal takes place if the Fourier expansion of the particle source has the helical harmonics $k\vartheta - \ell\varphi$, particularly, the harmonic $\sin\left[(m+1)\vartheta - n\varphi \right]$. The compensation of friction forces is not obvious as in the case of the poloidal injection (point 1). But it is not so difficult to verify that the coupling of the source helical harmonic $(m + 1, n)$ with

the magnetic perturbation harmonic (m,n) and toroidal magnetic field harmonic $(1, 0)$ ensures the reversal of the impurity flux $\left\langle n_I U_I \frac{\nabla \Psi}{|\nabla \Psi|} \right\rangle$ averaged over the magnetic surface. The source amplitude required to reverse the inward flux of impurities at the external boundary of the chain of the magnetic islands is $Q = \left| \frac{2}{e B_0 R} \frac{\partial p_i}{\partial r} \frac{r_{mn}}{\Delta r} \frac{1}{\alpha} \right|$ where $\alpha = \frac{2}{3\pi} \left[m+1 - \frac{d \ln Q(r)}{d \ln r} \Big|_{r = r_{mn}} + 4 (m+1) \frac{d \ln t(r^2)}{d \ln r^2} \Big|_{r_{mn}} \right]$ The presence of helical harmonics in the source corresponds to local-in-φ particle injection. Neutral particles injected in a certain plane $\varphi = const$ are ionized at a distance from the plasma edge; they occupy the field lines on the magnetic surfaces, including the rational ones, with an angle of rotational transform $t(r^2) = \frac{\ell}{k}$. In this case the Fourier expansion of the source Q should include the helical harmonics [6]. The form of the source $Q = Q(r) \sin\left[(m+1)\vartheta - n\varphi \right]$ means that the source background ions should be distributed on the rational magnetic surface with $t = \frac{n}{m+1}$ (Fig.2). In a tokamak $t(r^2)$ decreases with the radius from the centre, i.e., $t(0) > t(r^2)$, therefore the magnetic surface with $t = \frac{n}{m+1}$ is external with respect to the chain of the magnetic islands arising at the place of the magnetic surface with $t = \frac{n}{m}$ (Fig.3). Furthermore, the form of the source $Q = Q(r) \sin\left[(m+1)\vartheta - n\varphi \right]$ indicates that the injection should be realized with the $(m + 1)$ multipolarity along the minor perimeter of the torus. If the magnetic perturbation $(m = 2, n = 1)$ splits the surface with $t = \frac{1}{2}$, then the injection should be realized along three rays of $\vartheta = const$ in one plane $\varphi = const$ (Fig.4). The total number of background gas particles to be injected into the device per unit time is of the same order of magnitude for both types of injection: continuous in φ, local in ϑ (point 1) and local in φ, multipole in ϑ, as considered here.

References: 1. Burrell K.H., Phys.Fluids 19 (1976) 401.
2. Stacey W.M.,Jr., Phys.Fluids 21 (1978) 1404.
3. Wong S.K., Phys.Fluids 21 (1978) 299.
4. Burrell K.H. et al, Phys.Rev.Lett. 41 (1978) 1382.
5. Karger F., Lackner K., Phys.Lett. 61A (1977) 385.
6. Wobig H. Proc. 7-th Int.Conf. Innsbruck 1978, v.1 Vienna 1979, p.643.

Fig. 1

Fig. 2

Fig. 3

Fig. 4
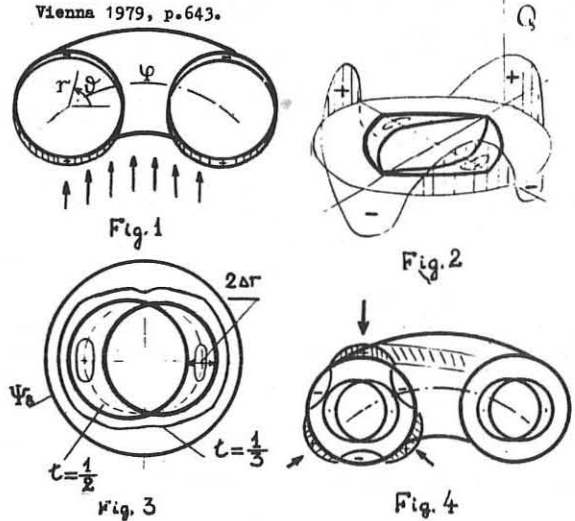
IMPURITY RADIATION FROM A PLASMA IN DIFFUSIVE EQUILIBRIUM

D E T F Ashby and M H Hughes
Culham Laboratory, Abingdon, Oxon, OX14 3DB, UK
(Euratom/UKAEA Fusion Association)

ABSTRACT   Impurity radiation from the peripheral region of a plasma is considered in the situation where diffusion affects the equilibrium distribution of the different charge states of the impurity. Numerical results are presented for oxygen in an idealised situation.

INTRODUCTION   Consider a hydrogen plasma in which power deposited in the central region is conducted to the edge region where it is lost by impurity radiation and transport to the boundary. In equilibrium the edge region satisfies

$$\frac{d}{dx}\left(\kappa \frac{dT}{dx}\right) = n_e n_z L(T) \qquad (1)$$

which on integration gives

$$\left(\kappa \frac{dT}{dx}\right)_1^2 - \left(\kappa \frac{dT}{dx}\right)_0^2 = 2 \int_{T_0}^{T_1} \kappa n_e n_z L(T) dT. \qquad (2)$$

Thus if the thermal flux from the central region is too small i.e.

$$\left(\kappa \frac{dT}{dx}\right)_1^2 < 2 \int_{T_0}^{T_1} \kappa n_e n_z L(T) dT \qquad (3)$$

equilibrium is not possible and the temperature profile collapses. Equation (3) can be simplified by assuming κ, n_e and n_z are constant giving

$$\left(\kappa \frac{dT}{dx}\right)_1^2 < 2\kappa n_e n_z \int_{T_0}^{T_1} L(T) dT \qquad (3a)$$

which shows the importance of the integral $\int L(T) dT$ in determining the effect of impurity radiation from the edge of a plasma[1]. This paper considers how $L(T)$ and its integral behave when diffusion affects the distribution of charge states so that 'coronal equilibrium' no longer applies.

BASIC THEORY   When individual charges states are considered eq(1) becomes

$$\frac{d}{dx}\left(\kappa \frac{dT}{dx}\right) = n_e n_z \tilde{L}.\tilde{m} \qquad (4)$$

where $n_z = \sum_{j=0}^{z} n_j$ is the impurity density and $m_j = n_j/n_z$ is the relative abundance of state j. The relative abundances $\tilde{m}$ are determined by the rate equations

$$\left\{\frac{\partial}{\partial t} + D\frac{\partial^2}{\partial x^2}\right\}\tilde{m} = n_e \tilde{\tilde{R}}.\tilde{m} \qquad (5)$$

where $\tilde{\tilde{R}}$ is a tridiagonal matrix since

$$\left\{\frac{\partial}{\partial t} + D\frac{\partial^2}{\partial x^2}\right\}m_j = n_e\left\{\alpha_{j-1} m_{j-1} - (\alpha_j+\beta_j)m_j + \beta_{j+1} m_{j+1}\right\} \qquad (5a)$$

and α and β are ionisation and recombination coefficients.

In coronal equilibrium the left hand side of eq(5) is zero; thus $\tilde{\tilde{R}}.\tilde{m}=0$ and the relative abundances are given by

$$\alpha_j m_j = \beta_{j+1} m_{j+1} \qquad (6)$$

Consider the case when the left hand side of eq(5) is non-zero. For simplicity assume that all charge states are subject to the same diffusivity namely $D_j=D$. Adding the equations of (5) gives

$$\left\{\frac{\partial}{\partial t} + D\frac{\partial^2}{\partial x^2}\right\}n_z = 0 \qquad (7)$$

so that in equilibrium (i.e. $\partial/\partial t \equiv 0$) n_z is constant in the absence of any internal sources. If n_e and κ are also assumed constant then eqs(4) and (5) become

$$\frac{\partial^2 T}{\partial s^2} = \tilde{L}.\tilde{m} \qquad (8)$$

and

$$\left(\frac{n_z D}{\kappa}\right)\frac{\partial^2 \tilde{m}}{\partial s^2} = \tilde{\tilde{R}}.\tilde{m} \qquad (9)$$

where $s^2 = x^2 n_e n_z/\kappa$.
Hence $\tilde{m}(T)$ and thus $L(T) = \tilde{L}.\tilde{m}$ depend only on the parameter $(n_z D/\kappa)$ and the boundary conditions chosen for eqs(8) and (9). An alternative and more convenient parameter of the problem is $(D/n_e)(dT/dx)_1^2$. This can be shown as follows:

$$\left(\frac{\partial T}{\partial x}\right)_1^2\left\{1 - \left(\frac{\partial T}{\partial x}\right)_0^2 \bigg/ \left(\frac{\partial T}{\partial x}\right)_1^2\right\} = \frac{n_e n_z}{\kappa} \int_{T_0}^{T_1} \tilde{L}.\tilde{m} dt = \frac{n_e n_z}{\kappa} f\left(\frac{n_z D}{\kappa}\right) \qquad (10)$$

$$\left\{\frac{D}{n_e}\left(\frac{\partial T}{\partial x}\right)_1^2\right\}\left\{1 - \left(\frac{\partial T}{\partial x}\right)_0^2 \bigg/ \left(\frac{\partial T}{\partial x}\right)_1^2\right\} = \frac{D n_z}{\kappa} f\left(\frac{n_z D}{\kappa}\right) = g\left(\frac{n_z D}{\kappa}\right) \qquad (11)$$

EVALUATION OF L(T) AND ITS INTEGRAL   Equations (8) and (9) were solved numerically using HELIOS, a 1-D time dependent code that follows individual charge states. Slab geometry was used with the following boundary conditions:

Inner Boundary
(a) dT/dx = constant, i.e. prescribed heat flux.
(b)   Zero flux of impurities which are fully-ionised.

Outer Boundary
(a) $T = 0$ (2 eV or less).
(b)   The flux of escaping impurities is balanced by a source of n_1 in the first computational cell. Neutrals are ignored by putting $\beta_1 = 0$.

RESULTS   Figure 1 shows how $\int L(T) dT$ varies with the diffusion parameter $(D/n_e)(dT/dx)_1^2$ for oxygen with three different constraints on the temperature profile.

(a) dT/dx = constant, i.e. $n_z \to 0$.
(b) $(dT/dx)_0 = 0$, $T_0 = 2$ eV.
(c) $(dT/dx)_0 = 0$, $T_0 < 2$ eV. The temperature profile is allowed to collapse until the impurity flux to the wall has time to recombine to the lowest charge state.

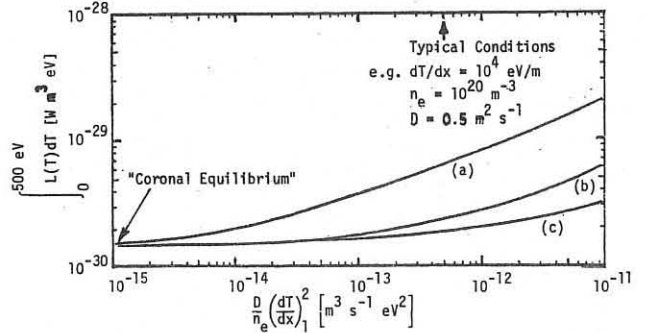These three equilibria were reached by varying the impurity concentration n_z.

Fig. 1 $\int L dT$ for oxygen as a function of $D/n_e (dT/dx)_1^2$.

Figure 2 compares $L(T)$ for the case of 'coronal equilibrium' (i.e. $D=0$) with the case where the diffusion parameter is large. The boundary condition on temperature is that labelled (c) in Fig.1. The effect of diffusion is to increase $L(T)$ at $T \gtrsim 50$ eV by a factor of ten or more but the associated reduction at low temperature results in the relatively small change in $\int L(T) dT$ shown in Fig.1.
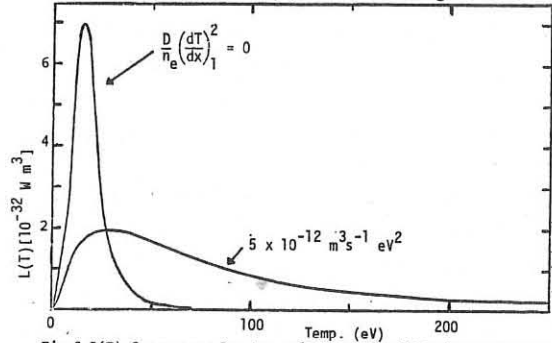

Fig.2 L(T) for oxygen for two values of the diffusion parameter.

CONCLUSIONS   The increase of $\int L dT$ with the diffusion parameter shows that the assumption of 'coronal equilibrium' underestimates the total power radiated by a hydrogen plasma containing oxygen as an impurity. However the change in the value of the integral is not large particularly when the level of radiated power is sufficient to substantially change the temperature profile (curves b and c in Fig.1) Hence in equilibrium the commonly used assumption of 'coronal equilibrium' should predict the total power radiated to within a factor of three or four provided that D_j, n_e and κ_e are constant over the region of interest.

REFERENCES
[1] ASHBY D E T F and HUGHES M H, "A Study of Impurity Radiation from the Peripheral Plasma of a Tokamak Reactor". Culham Laboratory Preprint CLM-P625. (Submitted to Nuclear Fusion.)

J-11

EXPERIMENTAL STUDY OF LIMITER EROSION MECHANISMS IN
THE MATERIALS TEST T-3M TOKAMAK FACILITY

D.G.Baratov, V.N.Demyanenko, S.V.Mirnov*, V.V.Myalton,
L.E.Demyanenko, T.B.Myalton, V.S.Semenov, V.P.Fokin.
"Energiya" Scientific-Manufacturing Association,
Moscow, USSR

It is known that limiter erosion is one of the main
sources of impurities in tokamak's plasma. Especially dangerous
are instability regimes of the discharge, when the intensity
of plasma-wall interaction higly increases. In particular, in-
stabilities, usually accompanying the initial phase of the dis-
charge, lead to the development of unipolar arcs and evaporat-
ion of significant quantities of limiter and wall materials
/1/. From energy measurements of hydrogen atoms, implanted in
the different sides of the limiter /2, 3/ it is possible to
suggest that the mechanism of unipolar arcs is not the only
one contributing to limiter erosion during instability regi-
mes. It was found that the limiter surface, looking at the
electron flow (i.e. the "electron" surface), and the opposite
surface (i.e. the "ion" surface) are bombarded differently.
The energy and number of hydrogen atoms, implanted from the
"ion" side is higher than that from the "electron" side. In
case of erosion, induced by unipolar arcs, this difference
either should not occur at all or would have been of opposite
sign, in case of erosion induced by accelerated electrons. One
of the possible explanations of this phenomenon is of electro-
dynamic character /4/. In the moment of instability (in par-
ticular, disruptive instability), plasma filaments with cur-
rent may easily reach the limiter . Each of these filaments
may be considered as a flexible conductor with electric cur-
rent, cut by the limiter , performing scissors' function. Mag-
netic flow within the filament cannot disappear abruptly; it
will cause overvoltage on the "ion" side of the limiter to
ensure the necessary electronic emission from the limiter sur-
face. It this is accompanied by arcing, then the voltage will
drop and the filament current will subside with skin time. Un-
til the arcing is not developed, the "ion" side will be bombar-
ded by ions, accelerated by the existing electric potential.
Simple estimate, made in Ref. /4/, shows that the necessary
difference of potentials of about 100 V will actually originate,
if the filaments contain currents up to 1 kA.

In this paper an attempt is made to determine experimen-
tally the real value of currents, passing through the limiter
during the disruption instability in conditions typical for
initial phase of tokamak's discharge.

Experiments were conducted on materials test T-3M toka-
mak facility of the USSR Ministry of Power and Electrification,
/5/. T-3M tokamak is a modification of T-3A tokamak, developed
earlier in Kurchatov's Atomic Energy Institute. Major radius
of the torus is 95 cm, minor radius of thin - wall discharge
chamber   of stainless steel being 20 cm. The longitu-
dinal magnetic field B_z of the first stage of the installation
is up to 1,2 T, longitudinal current Ip is up to 50 kA. Experi-
ments were performed with B_z = 0,8 ÷ 1 T and Ip = 20 ÷ 30 kA.
To limit the column size, three ring - shaped limiters were
inserted in the chamber /6/ with inner radius of 16 cm. The
limitters were placed at equal angular intervals of 120° along
the larger perimeter of the torus. In the firstseries of expe-
riments, relatively low -temperature plasma (Te ≤ 100 eV) was
obtained, which corresponds to the conditions of the initial
phase of dischargein tokamaks.

To study the limiter behaviour in such conditions, a
fourth plate-shaped graphite limiter (Fig. 1) was used, which
could be inserted into plasma behind the limiter shadow up to
4 cm deep. The limiter consisted of two plates (a) 8 cm high,
separated by insulator (B). Measuring the electrical current
through the shunt (c) which connects the plates, it was possi-
ble to determine the portion of plasma current Ip passing
through the limiter . On the other hand, for a "no shunt" case,
by measuring the voltage between the plates it was possible
to determine the typical electric voltages, originating in the
plasma - limiter layer during the disruption. Fig. 2 presents
the typical oscillograms of voltage along the torus perimeter
$V_p(t)$, of column horizontal shift Δ ; $I_p(t)$, current $I_p(t)$ and

current between the plates I_D for a case with plates inserted
into plasma 4 cm deep. It can be seen that the spike of the
current, passing through the limiter in the moment of disrup-
tion, reaches 1,6 kA, i.e. up to 5 ÷ 7% of I_p. The shift of the
moving limiter into the shadow of stationary limiters (Fig. 3)
reduces this current. Evidently the current is of the arc charac-
ter with the average density of 100 A/cm².

If we remove the shunt replacing it by large resistor
(1 kOhm), then in the moment of disruption a voltage pulse
of about several tens of volts is developed between the plates.
This voltage is enough for initiation of the arcs. It is abvious
that the pulse's nature is of electrodynamic character similar
to that suggested in /4/. Hydrogen ions, accelerated by this
potential, may be the reason for implantation anomalies, observed
in /2, 3/.

LITERATURE

1. Mioduszewski P., Clausing R.E., Heaterly L.   J. Nucl. Mat.,
1979, v. 85-86, N 3, p. 963.

2. Cohen S.A., Dylla H.F., Rossnagel et.al. Proc. 4 Int. Conf.
on Plasma Surface Interact. in Contr. Fus. Dev.
Garmish-Partenkirchen, 1980, A-1.

3. Staudenmaier G., Staib P., ibid. Paper A-3.

4. Mirnov S.V. Plasma Physics 1981, v. 6, N 3, p. 603.

5. Baratov D.G., Demyanenko V.N., Evsejev N.V. et.al. Report
at the Soviet-American meeting "Interaction of Plasma with
Tokamak Wall" , April 1978, Kurchatov's Atomic Energy In-
stitute, Moscow.

6. Vorobjev A.V., Mirnov S.V., Semenov I.B., Stepanchikov V.V.,
Plasma Physics, 1978, v. 4, N 5, p. 982.

Fig.1

Fig.2

Fig.3
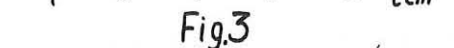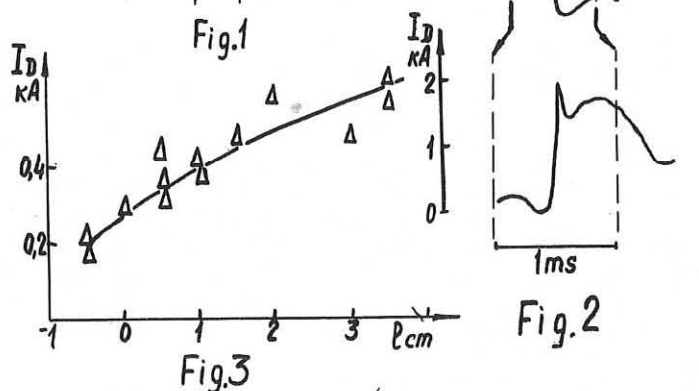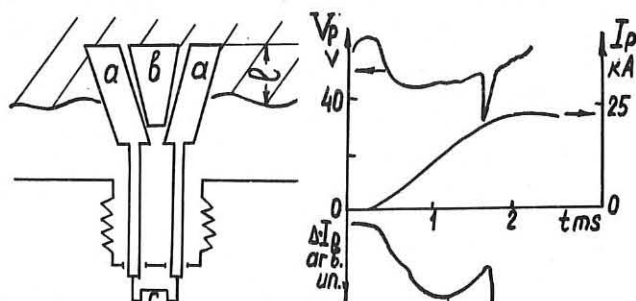
ANALYSIS OF A GRAPHITE LIMITER AFTER OPERATION
IN T-10

D. Hildebrandt, M. Laux, J. Lingertat, P. Pech,
H.-D.Reiner, H. Strusny, H. Wolff

Zentralinstitut für Elektronenphysik der Akademie
der Wissenschaften der DDR, 1080 Berlin, GDR

Introduction

It is well known that internal surfaces of a tokamak are
modified due to the interaction with the plasma. In order
to assess these modifications a graphite limiter used in
T-10 has been investigated. Erosion and deposition pheno-
mena were studied by morphological and elemental surface
analysis methods.

The graphite limiter had about 8000 discharges mainly in
deuterium. Typical discharge parameters were: plasma cur-
rent 230 kA, magnetic field 1.5 T, pulse duration 600 -
800 ms, electron temperature 1.1 keV, electron density
3.10^{19} m^{-3}. In addition to the high power discharges, the
vessel was routinely subjected to cleaning by heating,
glow discharges and low power pulse discharges of high re-
petition rate.

The construction of the limiter section is described in
/1/.

Results

Fig. 1 shows schematically the visible pattern of surface
phenomena observed on the graphite limiter after removal
from T-10. A thorough analysis of the surface revealed
that all parts of the limiter were modified in different
extent by deposition and erosion processes.

Common to the whole surface is a deposition of material
from internal components of T-10. Fig. 2 shows a typical
depth distribution of the atomic concentration measured
by AES-sputter technique. The source of the observed iron,
nickel and chromium is the liner, that of tungsten the
fixed limiter.

The depth distribution of all points analyzed shows a ma-
ximum near the surface and extends at least up to 3 μm
depth. We assume that the observed distribution is caused
by diffusion and by the competing action of erosion and
deposition. Micropores and cracks may also influence the
penetration depth of the metal atoms.

The total amount of metal deposited onto the limiter sur-
face is much higher than that estimated from the observed
metal deposition per discharge onto the probe of the ana-
lysis station WASA /2/ and from spectroscopic data of the
metal contamination of the T-10 plasma. Probably most of
the metal goes to the limiter during the pulse discharge
cleaning procedure. Measurements with the WASA device
have shown that after one cleaning cycle the probe sur-
face was contaminated up to 30 % by wall material.

In a region near the limiter edge heavy ablation and mul-
tiple cracking together with arc tracks could be observed.
It is obvious that the cracking is caused by severe ther-
mal stresses due to non-uniform heating and steep tempera-
ture gradients. The observed damage pattern may be the re-
sult of chemical sputtering, sublimation and macroscopic
disintegration of cracked areas. On the ion drift side the
damaged area is nearly at the centre of the limiter blade,
on the electron side it is considerably shifted towards
the centre of the torus. There is no explanation for this
shift which has been observed in a similar way on the SS
limiter of T-10 /1/ and on a SS limiter of PLT /3/.

The damaged area is bordered by a rather large region ap-
pearing bright, like a metal, in reflected light. No cor-
relation between the appearance of this region and the sur-
face concentration of deposited metal could be found. We
suppose that the bright region is mainly eroded by sput-
tering and the bright appearance is due to a polishing
effect.

Many arc tracks are spread over the bright area on the ion
drift side. No arc tracks were found on the electron drift
side of the limiter. This asymmetry of arcing probability

also observed on the stainless steel limiter of T-10 /1/,
is possibly an indication of an asymmetry of the parame-
ters of the limiter shadow plasma.

The bright region is bordered by a black one. Here deposi-
tion phenomena seem to prevail. Fig. 3 shows the depen-
dence of the iron and tungsten concentration in 1 μm depth
as a function of the distance from the limiter edge. Ero-
sion and deposition regions are clearly separated. The
analysis of the form of the black area shows that it cor-
responds to the shadow of the fixed limiter projected onto
the movable graphite limiter by the field lines.

The results discussed above allow us to divide the plasma
near the limiter into three regions: the edge of the hot
core with a temperature and density high enough to heat
the limiter surface to 2000 - 3000° K (heavy, macroscopic
damage), the limiter shadow region with a temperature and
density high enough to sputter effectively the limiter
surface and to ignite unipolar arcs (mainly microscopic
erosion, competing deposition) and the shadow region of
the fixed limiter with temperature and density so low that
no erosion is detectable (deposition). The near limiter
plasma shows a pronounced asymmetry comparing the electron
and the ion drift side.

References

/1/ D. Hildebrandt et al., Beitr. Plasmaphys. 20 (1980),313
/2/ V.M. Chicherov et al., Preprint 79-7 (1979), Zentral-
institut für Elektronenphysik, Berlin, DDR
/3/ S.A. Cohen et al., Nucl. Fusion 21 (1981),233

Figure Captions

Fig. 1: Map of the analyzed central part of the graphite
limiter of T-10 (size 225 x 75 mm^2)

Fig. 2: Depth profile of atomic composition measured by
AES-sputter technique (ion drift side)

Fig. 3: Concentration of iron and tungsten in a depth of
1 μm as a function of the distance from the limiter
edge measured by RBS (ion drift side)

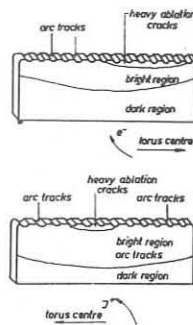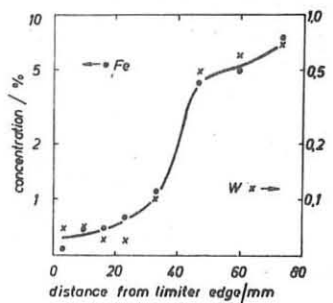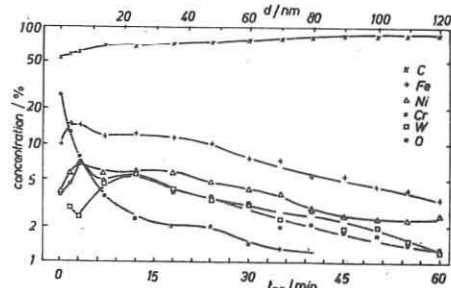Fig. 1

Fig. 3

Fig. 2

TIME RESOLVED MEASUREMENTS OF THE IMPURITY FLUX IN
THE LIMITER SHADOW OF THE T-10 TOKAMAK

V.M. Chicherov[x], D. Hildebrandt, M. Laux, J. Lingertat,
P. Pech, H.-D. Reiner, H. Wolff

Zentralinstitut für Elektronenphysik der AdW der DDR,
1080 Berlin, GDR

x) I.V. Kurchatov Institute for Atomic Energy, Moscow,
USSR

Introduction

In various tokamaks movable probes together with surface
analysis techniques are used to investigate impurity flu-
xes in the boundary layer /1-5/.

In this paper results of time resolved measurements of the
impurity flux in the limiter shadow of the T-10 tokamak
are presented. The surface analysis station used for in
situ analysis and its location at T-10 are described else-
where /4/. The aim of the present measurements was the es-
timation of the impurity flux in T-10 during low q-dis-
charges /q(a) $\cong$ 1.8/ free of disruptions, with additional
EC-heating and argon puffing.

Experimental

The position of the probe in T-10 with respect to the li-
miters and ECH-feeder is shown in fig. 1. The probe was
kept in liner position i.e. the centre of the exposure
slits in the Ta-shield was on the radius $r_p = 388$ mm. Du-
ring the discharge the probe was rotated by an angle of
60°.(The rotation frequency of the probe was 0.17 s^{-1},
with the slit width of 2 mm and a mean probe radius of
17 mm the exposure time was 0.11 s.) Five reproducible
discharges were superimposed. The following settings were
used: movable graphite limiter at $a = 290$ mm, fixed gra-
phite limiter at $a_f = 340$ mm, argon puffing at $t = 400$ ms
and ECH-pulse (50 ms duration and 140 kW power) at $t =$
700 ms.

Before exposure the probe was prepared by silver deposi-
tion. This deposited layer had a high carbon content (up
to 65 %) at the surface. After exposure the probe surface
showed no visible traces of arcing or surface damage due
to high power impact. Carbon and oxygen were analyzed by
AES while the very low metal concentrations were measured
by SIMS which was calibrated by AES.

Results and discussion

Fig. 2 and 3 show the changes of the surface densities of
the impurity atoms Fe + Cr + Ni and O on the probe during
the tokamak pulse. It is assumed that the atomic densities
found on the probe surface are proportional to the impu-
rity flux to the probe. On the electron and ion drift
side oxygen and metals show the same general behaviour
like in earlier measurements /5/. The course of the metal
deposition with time (fig. 2) resembles strongly the evo-
lution of the electron density.

The surface density of oxygen (fig. 3) shows an additional
maximum at the beginning of the discharge on the electron
drift side. The flux in poloidal direction estimated by
analyzing the atomic densities on the probe beneath the
upper and the lower slit differs considerably from the
fluxes in toroidal direction. While the metal flux to the
upper and lower slits is nearly constant during the dis-
charge, the oxygen flux has a wide maximum from about 100
to 400 ms. In all cases the detected atomic densities at
the upper slits are a factor of 2 to 3 higher than at the
lower slit.

It appeared that pulsed argon injection and the ECH-pulse
had no pronounced effect on the impurity flux in each di-
rection. The maximum of oxygen in e^- at $t = 0$ (fig. 3) is
ascribed to the special operating conditions of the ECH-
generator, which is emitting in the stand-by regime series
of short but full power pulses (1 ms, 140 kW). The RF-
power impings on the torus wall opposite to the RF-feeder,
desorbing oxygen within the line of sight of the e^--slit
of the surface analysis probe.

The impurity fluxes and the corresponding impurity densi-
ties in the limiter shadow estimated from the measured im-
purity densities on the probe surface are generally an or-
der of magnitude lower than in earlier measurements /5/.
Assuming an ion energy of 3 eV and taking the densities
at $t = 700$ ms for the ion drift side we get for oxygen
(one shot) $n_{imp_O} = 4.6 \cdot 10^8$ cm^{-3} and for the metals Fe +
Cr + Ni $n_{imp_M} = 3.3 \cdot 10^8$ cm^{-3}. This low impurity density
and the absence of peaks in poloidal direction at the
start of the pulse may be attributed to the action of the
additional carbon limiter at $a_F = 340$ mm.

References

/1/ P. Staib et al., Proc. 7th Europ. Conf. Contr. Fusion
       a. Plasma Phys., Lausanne 1975, Vol. 1, 133

/2/ S.A. Cohen, H.F. Dylla, J. Nucl. Mater. 76/77 (1978)
       425

/3/ G.M. McCracken et al., J. Nucl. Mater. 76/77 (1978) 431

/4/ V.M. Chicherov et al., Zentralinst. f. Elektronenphy-
       sik, Berlin, DDR, Preprint 79-7

/5/ V.M. Chicherov et al., J. Nucl. Mater. 93/94 (1980)
       133

Figure Captions

Fig. 1: Top view of the T-10 torus showing the position
of the deposition (WASA-)probe, the limiter and
the ECH-feeder

Fig. 2: Surface density of metals Fe + Cr + Ni vs. time
for 5 superimposed discharges (a = 29 cm, a_f =
34 cm, r_p = 38.8 cm) on the ion side (I^+), elec-
tron side (e^-), upper (U) and lower (L) side.
Ar: Ar-puffing, ECH: electron cyclotron heating
(50 ms)

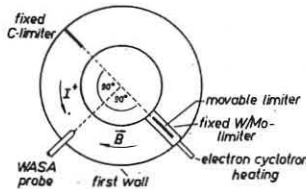Fig. 3: Surface density of oxygen vs. time (parameters
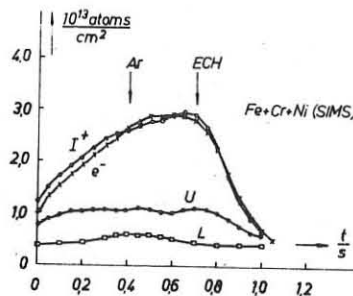equal to fig. 2)
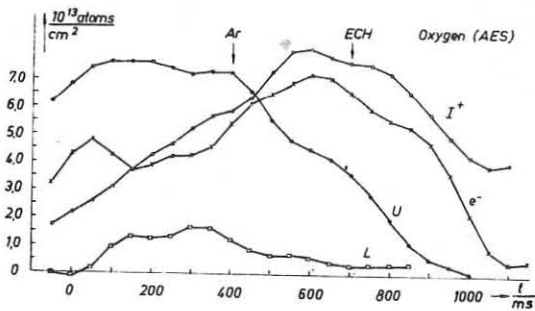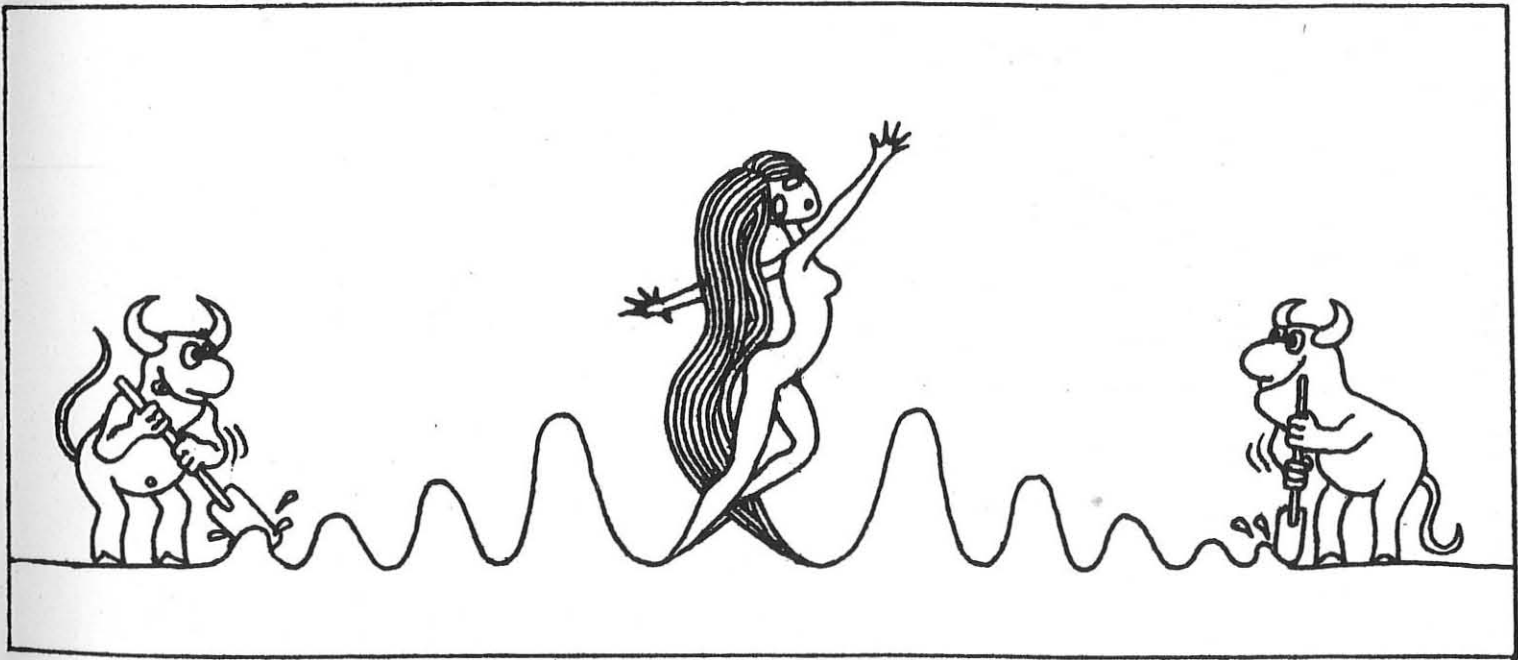

Fig. 1

Fig. 2

Fig. 3

K

WAVE-PLASMA INTERACTION

FULL-WAVE PROPAGATION ANALYSIS FOR THE X-MODE AT $2\omega_{ce}$.

E. Lazzaro, G. Ramponi and G. Giruzzi*

ISTITUTO DI FISICA DEL PLASMA, CNR, MILANO (ITALY)

The propagation of the extraordinary wave in the frequency range $\omega \simeq 2\omega_{ce}$ (ω_{ce} = electron cyclotron frequency) in a tokamak-like plasma slab may present some analogies with the behaviour of ion cyclotron waves at $\omega = n\omega_{ci}$ /1/,/2/.
Namely, from the analysis of the dispersion relation at $\omega = 2\omega_{ce}$ /3/ it is likely that waves incident from the high or low field side be subject to partial reflection and conversion into electrostatic waves, as well as cyclotron damping. To have a quantitative evaluation of these effects, keeping correctly into consideration the presence of the cyclotron damping given by the antihermitian part of the relativistic dielectric dyadic /4/, it is necessary to solve numerically the propagation equations, which, for incidence normal to the toroidal magnetic field, are:

$$(\varepsilon_{11} + \chi \frac{d^2}{d\xi^2}) E_x + (\varepsilon_{12} - i\chi \frac{d^2}{d\xi^2}) E_y = 0 \qquad (1)$$

$$-(\varepsilon_{12} - i\chi \frac{d^2}{d\xi^2}) E_x + (\varepsilon_{11} + (\chi+1) \frac{d^2}{d\xi^2}) E_y = 0$$

where: $\xi = (\omega/c)x$, ε_{ij} are the "cold" plasma dielectric tensor elements, and /4/:

$$\chi = \frac{\omega_p^2}{2\omega_{ce}^2} F_{\frac{3}{2}} (\frac{mc^2}{T}(1-2\frac{\omega_{ce}}{\omega}))$$

The numerical integration of system (1) is performed in various density regimes ($\omega_p^2/\omega^2 \gtrless 0.28$) /3/, for waves incident from the low (L.B.S.) or high (H.B.S.) magnetic field side.
In the high density regime ($\omega_p^2/\omega^2 = 0.33$) where a possible "warm" cutoff appears from the dispersion relation /3/, the typical behaviour of the longitudinal and transverse components of the electric field of the wave incident from the H.B.S. is shown in Figs. 1, 2. An enhancement of E_x in the region of strong interaction between the X-wave and the quasi-electrostatic wave is visible, superimposed to the effect of the cyclotron damping. Figs.3, 4 show the same quantities, but in the case of L.B.S. incidence.
Here the occurrence of partial reflection is evident; however there is sufficient transmission across the warm cutoff barrier, at least for low temperature cases (Fig. 7).
This tunnelling phenomenon is favoured by the complex nature of the refractive index due to the cyclotron damping.
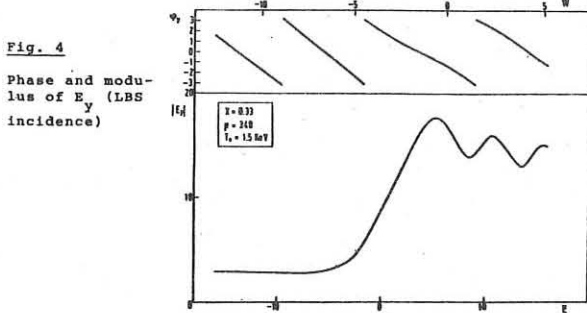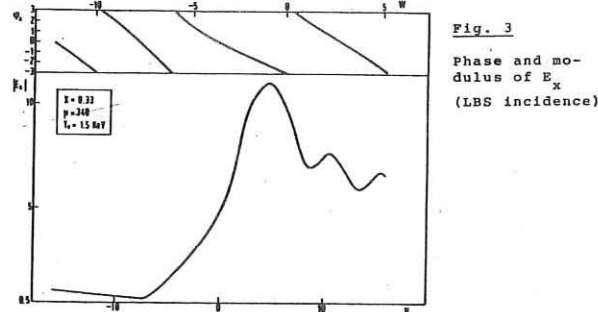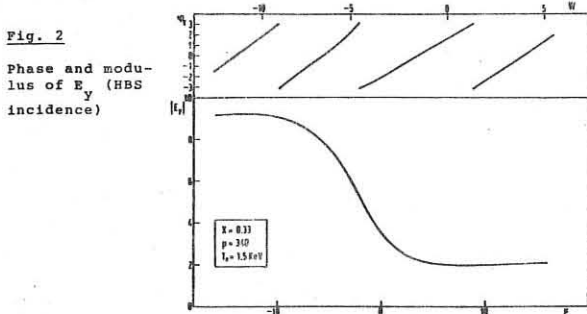
Figs.5, 6 show the behaviour of the x-component of the Poynting vector for L.B.S. and H.B.S. incidence, respectively. Figs.7, 8 show the reflection $|R|^2$ and transmission $|T|^2$ coefficients, defined as squared ratios of field amplitudes, versus temperature in the overcritical case.
A slight asymmetry in transmission for the two opposite incidences is visible. This suggests that the quasi-electrostatic branch plays a key role in determining the nature and the extent of the damping, as seen also in the ion cyclotron case /2/.
From a detailed analysis of these results it appears that the warm cutoff is not a serious obstacle to wave injection from the L.B.S., at least in a small scale device; on the contrary a possible asymmetry in transmission, due to interaction with the electrostatic branch, should be taken into account in a transmission and /or emission diagnostic experiment.

REFERENCES

/1/ R.R. Weynants, Phys. Rev. Lett. 33, 2 (1974)
/2/ P.L. Colestock et al., Proc. 2nd Grenoble -Varenna Int. Symp. on heating in toroidal plasmas, Como (1980)
/3/ E. Lazzaro, G. Ramponi, Plasma Phys. 23, 53 (1981)
/4/ Yu.N.Dnestrovski et al., Sov. Phys.-Tech.Phys. 8, 691 (1964).

Fig. 1

Tori aspect ratio a/R = 0.33
B_t = 10 Kgauss
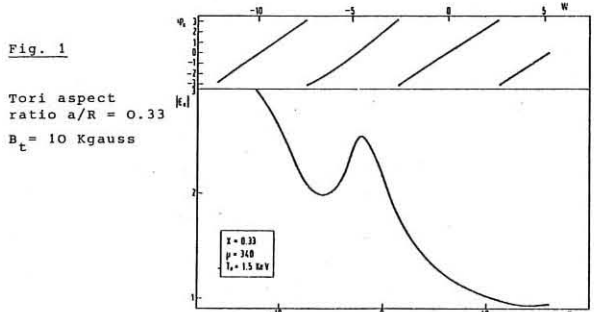
Phase and modulus of E_x (HBS incidence) vs. ξ; $\xi = 0$ position of coupling point.
$X = \omega_p^2/\omega^2$; $w = (mc^2/T)(1-2\omega_{ce}/\omega)$; $w = 0$ location of the second harmonic.

Fig. 2

Phase and modulus of E_y (HBS incidence)

Fig. 3

Phase and modulus of E_x (LBS incidence)

Fig. 4

Phase and modulus of E_y (LBS incidence)

Fig.5 (LBS)   Fig.6 (HBS)

Fig. 7

Fig. 8
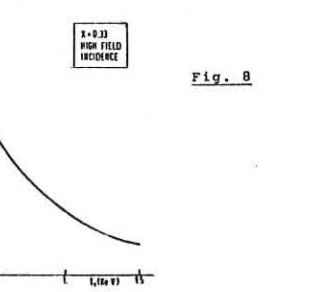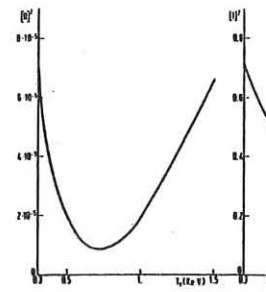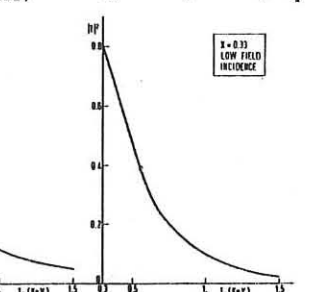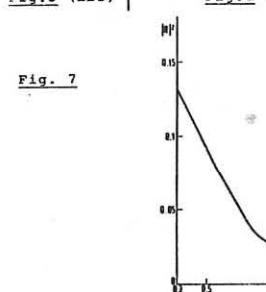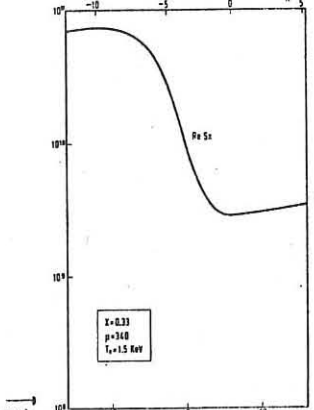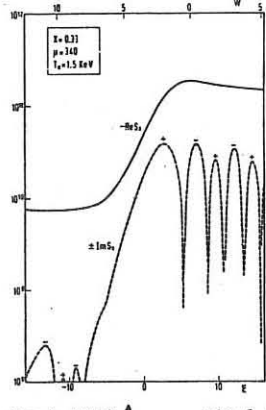
PROPAGATION OF KINETIC ALFVEN WAVE IN CYLINDRICAL TOKAMAK

Kimitaka Itoh

Division of Thermonuclear Fusion Research, Japan Atomic Energy
Research Institute, Tokai, Ibaraki, 319-11, Japan
and
Sanae-Inoue Itoh, Kyoji Nishikawa
Institute for Fusion Theory, Hiroshima University, Hiroshima,
730, Japan.

Abstract

Propagation and absorption of the kinetic Alfvén wave
are studied taking into account inhomogeneities of plasma
parameters, magnetic shear and kinetic wave-particle inter-
actions. The coupling coefficient with antenna is also
evaluated.

Alfvén waves have attracted much attention because of
their high potentialities of application to rf heating,
current-drive and flux control in thermonuclear plasmas. In
high temperature plasmas, the rf wave accessibility and propa-
gation analysis requires consideration of kinetic processes.
Moreover, the importance of these effects are strongly influ-
enced by the radial profiles of plasma parameters and magnetic
field configurations.

In this paper, we kinematically study the accessibility
and propagation of low frequency (ω < ion cyclotron frequen-
cy) shear Alfvén wave in a cylindrical tokamak. We solve
relevant propagation equation for the shear Alfvén wave,
correctly keeping the density and temperature inhomogeneities,
magnetic shear, ion gyroradius, plasma current and the col-
lisionless parallel conductivity. The coupling efficiency
is also obtained by using an antenna model, which is an os-
cillating current sheet placed in the vacuum region between
the plasma column and the conducting wall.

We take a cylindrical plasma column of radius a in a
conducting wall (radius b). Cylindrical coordinates (r,
θ, z) are used; z axis is coinciding the magnetic axis. We
choose an equilibrium distribution function f_0 as local Max-
wellian, $f_0(\vec{r},\vec{v}) = N(2\pi v_T^2)^{-3/2} \exp\{-(v^2-2uv_\theta+u^2)/v_T^2\}$ where N,
v_T^2 (=T/M) and u are in general functions of $Mr(v_\theta+r\Omega/2)$ (Ω:
cyclotron frequency).

We then obtain the density and current perturbations.
Since the equilibrium has axial and longitudinal symmetries,
$\partial/\partial\theta = \partial/\partial z = 0$, each Fourier component of the excited
perturbation is treated separately; $\tilde{n}(\vec{r},t) = \tilde{n}(r)\exp(im\theta-inz/R-i\omega t)$. Integrating the linearized Vlasov-Maxwell equ-
ations along the unperturbed orbit of particles, we obtain
the expressions for the density and current perturbations
$\tilde{n}$ and $\tilde{J}$. The charge neutrality condition and Ampère's law
yield a coupled equation of $\tilde{E}_\theta$ and $\tilde{B}_r$ for incompressible
shear Alfvén mode as

$$\{ \rho_i^2 \frac{1}{r}\frac{d}{dr} r \frac{d}{dr} - k^2\rho_i^2 - \beta_i \frac{u\omega_J}{k_\ell c_s^2} \} \psi = \beta_i \frac{c^2}{c_s^2} P \frac{\omega}{k_\ell c} \{ \phi + \frac{\omega}{k_\ell c}\psi \}. \quad (1)$$

$$\{ \rho_i^2 \frac{1}{r}\frac{d}{dr} r \frac{d}{dr} - k^2\rho_i^2 \} \phi = \frac{\omega}{\omega\tau+\omega_*} \frac{P}{\xi_i z(\xi_i)} \{ \phi + \frac{\omega}{k_\ell c}\psi \}, \quad (2)$$

$$P = \frac{\omega-\omega_*}{2\omega} Z'(\xi_e) + \frac{\omega_{Te}}{4\omega} \xi_e Z''(\xi_e) + \frac{\omega\tau+\omega_*}{2\omega} Z'(\xi_i)$$
$$+ [Z(\xi_e) + \frac{\omega-\omega_J}{\omega}\xi_e Z'(\xi_e) + \frac{\omega_{Te}}{2\omega}\{\xi_e Z'(\xi_e)\}'] \frac{k_\parallel u}{\sqrt{2}|k_\ell|v_e} \quad (3)$$

where $\phi = r\tilde{E}_\theta$, $\psi = r\tilde{B}_r$, $\omega_* = kcT_e\kappa/eB$, $\kappa = -\partial\ln N/\partial x$, $\omega_J/\omega_* =$
$-(dJ_0/dr)/J_0\kappa$, $\omega_{Te}/\omega_* = -(dT_e/dr)/T_e\kappa$, $k = m/r$, $\xi = \omega/\sqrt{2}|k_\parallel|v_T$,
$\tau = T_e/T_i$, $\beta_i = 4\pi n_i T_i/B^2$ and the other notation is standard.
The parallel wave number $k_\parallel$ is given by (m-nq)/qR. In the
presence of the magnetic shear, $dq/dr \neq 0$, P is a function of
r through $k_\parallel$. The propagation region, $\omega \lesssim |k_\parallel v_A|$, is localized
to the mode rational surface where $k_\parallel = 0$.

We next impose boundary conditions. The equations (1)
and (2) describe Alfvén mode as well as ion-sound like mode

(drift mode). The coupling is strong in the kinetic region
$|k_\parallel v_A| \lesssim \omega$ and near the plasma surface. When we consider
the low frequency mode, $\omega/\Omega_i \lesssim m\rho_i\hat{s}/Rq$ ($\hat{s} = |rq'/q|$), $k_\parallel v_i$
$\gtrsim \omega$ at r = a; the drift mode excited at the plasma surface is
subject to a strong ion Landau damping. Therefore, except
the thin layer near the surface, we demand that the excited
mode is composed of the shear Alfvén mode and out-going drift
mode. Another condition is that ϕ and ψ are regular at r = 0.
Imposing these conditions we solve Eqs.(1) - (3) to obtain
$\alpha \equiv B_r'/B_r|_{r=a}$ ($B_r' = dB_r/dr$). The information of the absop-
tion rate is included in the value $B_r'/B_r|_{r=a}$.

The coupling coefficient with the model antenna is then
presented as a function of α. We theoretically simulate the
antenna by an oscillating current sheet given by $\tilde{J} = (0,$
$-nr/Rm, 1) J_h \exp(im\theta-inz/R-i\omega t)\delta(r-d)$ (a < d < b). The oscil-
lating current $\tilde{I}_h$ is $2\pi\int r dr J_h \delta(r-d)$. We here consider the
transverse magnetic mode ($\tilde{B}_z = 0$), the solution in the vacuum
being given by use of modified Bessel functions as

$$r\tilde{B}_r = \left[\frac{K_m(\nu d)\{\nu I_m'(\nu a)+\alpha I_m(\nu a)\} - I_m(\nu d)\{\nu K_m'(\nu a)+\alpha K_m(\nu a)\}}{K_m(\nu b)\{\nu I_m'(\nu a)-\alpha I_m(\nu a)\} - I_m(\nu b)\{\nu K_m'(\nu a)-\alpha K_m(\nu a)\}} \right.$$
$$\times \{K_m(\nu b)I_m(\nu r) - I_m(\nu b)K_m(\nu r)\}$$
$$\left. - K_m(\nu d)I_m(\nu r) + I_m(\nu d)K_m(\nu r) \right] \times$$
$$\frac{2im\tilde{I}_h}{\nu\{K_m'(\nu d)I_m(\nu d)-K_m(\nu d)I_m'(\nu d)\}cd} \quad (a < r < d) \quad (4)$$

where $\nu^2 = n^2/R^2 - \omega^2/c^2$ and the condition, $(rB_r)'/rB_r|_{r=a} = \alpha$,
is used. From this vacuum solution, we can calculate the
coupling coefficient of the antenna. Let $\tilde{E}^{ext}$ be the electric
field which induces helical current $\tilde{I}_h$ in the antenna. The
impedance $\hat{Z}$ is given as $\hat{Z} = \tilde{E}^{ext}L/\tilde{I}_h$ (L is the length of the
antenna) and the power factor η is defined by $\eta \equiv \int-Re<\tilde{E}^{ext}$
$\tilde{J}_h>/|\tilde{E}^{ext}||\tilde{I}_h|$, where <> denotes time averaging. The applied
field is expressed in terms of $\tilde{B}_r$ as $r\tilde{E}_\theta = -cnr\tilde{B}_r/R\omega$ and $\tilde{E}_z =$
$m\omega r\tilde{B}_r/c(m^2+n^2r^2/R^2)$. Noting these relations we have

$$\eta = - Im[B_r^\dagger(d)\{B_r'(d-0) - B_r'(d+0)\}] / |B_r(d)|^2. \quad (5)$$

Substituting Eq.(4) into Eq.(5), we can express η as a function
of m, a, b, d and α. The energy absorbed is calculated from
the relation $\eta\tilde{E}^{ext}\tilde{I}_h$ or from Poynting vector $\vec{P} = c(\tilde{E}\times\tilde{B})/4\pi$.
Integrating $<-P_r>$ over the plasma column surface, we have

$$\int ds <-P_r> = - \frac{\omega}{2m} Im\alpha|\psi(a)|^2.$$

The energy absorbed does not depend on the antenna position
for given value of $\psi(a)$. α clearly shows the absorption rate.

Equations (1) and (2) are solved numerically. We
choose an equiribrium distribution as $N(r) = N_0\exp(-r^2/2L_n^2)$,
$T_e(r) = T_{e0}\exp(-r^2/2L_n^2)$ and u = const. For the typical para-
meters of large scale experiments, B = 4T, $T_{e0} \sim 4keV$, a =
0.5m and R = 2m, numerical solutions are obtained to give mode
structure and α. The figure shows typical wave form $\psi(r)$.
This figure shows that the angle $\theta \equiv \arctan(Im\psi/Re\psi)$ changes
most noticiablly in the kinetic region.
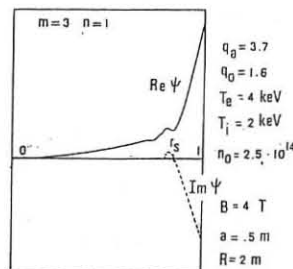
EVOLUTION OF THE UNSTABLE ALFVEN OSCILLATIONS IN THE INHOMOGENEOUS MAGNETIC FIELD

A.V.Timofeev

Kurchatov Institute of Atomic Energy,
Moscow, USSR

1. The frequency of the unstable ion-cyclotron waves, which were observed in the magnetic mirrors, is approximately equal to the minimum ion-cyclotron frequency, see e.g. /1/. This peculiarity can be explained by the effect of the magnetic field inhomogeneity on the ion-cyclotron waves. For example, the oscillation with $\omega \approx \omega_{i,min}$ have the maximum increment due to the loss-cone mechanism of the oscillation build up /2,3/. The magnetic field inhomogeneity effect on the anisotropic type instabilities is more efficient, while only the oscillations with $\omega \approx \omega_{i,min}$ can be unstable /4/. In this work we consider the anisotropic ion-cyclotron instability of the Alfven waves /5,6/. This instability is a serious danger for the confinement of a hot dense plasma in the magnetic mirrors, while it can emerge with large increment in the high pressure plasma $\left(\beta = \frac{8\pi p}{B^2} \sim 1\right)$. We want to show, that the unstable Alfven waves frequency tends to the minimum ion-cyclotron frequency in the magnetic mirrors.

2. First, let us consider natural oscillations. The unstable Alfven waves are described by the dispersion equation:

$$\left(\frac{Kc}{\omega}\right)^2 + \frac{\omega_{pi}^2}{\omega_i(\omega - \omega_i)} + \left(\frac{\omega_{pi}}{\omega_i}\right)^2 \left(\frac{K V_{\perp,T}}{\omega - \omega_i}\right)^2 = 0. \quad (1)$$

It is supposed here, that the magnetic field is a homogeneous one, the anisotropy of the ion velocity distribution is rather large $\left(\tau = \frac{T_\perp}{T_\parallel} \gg \sqrt{\beta_\perp}\right)$. If the magnetic field is an inhomogeneous one $\left(\nabla B \parallel \vec{B}_o\right)$ the following substitution can be made: $K \to -i \frac{\partial}{\partial \bar{z}}$ in Eq.(1) and the obtained operator will act upon the amplitude of the wave electric field - E(z). After this, let us multiply the wave equation by $E^*(z)$, integrate over z ($-\infty < z < \infty$) and single out the imaginary part

$$\gamma \omega_{pi}^2 \int d\bar{z} \left\{ -\frac{|E|^2}{\omega_i|\omega - \omega_i(\bar{z})|^2} + 2\left(\frac{V_{\perp,T}}{\omega_i}\right)^2 \frac{(\omega_i(\bar{z}) - Re\omega)}{|\omega - \omega_i(\bar{z})|^4} \left|\frac{\partial E}{\partial \bar{z}}\right|^2 \right\} = 0, \quad (2)$$

It follows from this equality that the natural oscillations with $Re\,\omega \geqslant \omega_i$ cannot exist.

The magnetic field can be approximated by the linear function ($B(\bar{z}) \approx B_o(1 + \frac{z}{L})$) in the regions located far off the extreme points of $B(\bar{z})$. If the magnetic field variation $\Delta B_o(\bar{z})$ exceeds $B_o \sqrt{\beta_\perp}$ we can neglect the last term in the wave equation, corresponding to Eq.(1), at $|\bar{z}-\bar{z}_s| \gg L\sqrt{\beta_\perp}$, where

$$\omega_i(\bar{z}_s) = \omega \qquad \text{Using the Landau bypass}$$

rule around the resonance region, we can show that the wave evanescent at $\bar{z} \to \infty$ is converted into a running wave at $\bar{z} \to -\infty$. Therefore, the localized natural oscillations are absent.

3. Let us consider the evolution of the unstable oscillations in the linear magnetic field. The frequency of the quasiclassical oscillations is determined by the equation /7/:

$$t = \int_{\bar{z}_o}^{\bar{z}} d\bar{z}' \frac{\partial}{\partial \omega} K(\bar{z}', \omega) \qquad (3)$$

Here, $\bar{z}_o$ is the perturbation emergence point, $\bar{z}$ is the point of observation after a time interval t. If $\omega_i t \gg 1$, the relation $\frac{\partial}{\partial \omega} = -\frac{L}{\omega_{io}} \frac{\partial}{\partial \bar{z}}$ is fulfilled, see Eq.(1). Using this relation in the Eq.(3), we obtain

$$t = \frac{L}{\omega_{io}} \left(K(\bar{z}_o, \omega) - K(\bar{z}, \omega) \right). \qquad (4)$$

If $t \ll (|\bar{z}-\bar{z}_o|L\tau\beta_\perp)^{1/2}/\omega_i\rho_i$, we can determine $K(\bar{z}, \omega)$ from the Eq.(1). The investigation of the Eqs.(1),(3) show, that $\omega(\bar{z}, t) \to \omega_i(\bar{z})(1 + i\sqrt{\beta_\perp})$ in time. The initial perturbation amplification factor at a time $t \sim (|\bar{z}-\bar{z}_o|L\tau\beta_\perp)^{1/2}/\omega_i\rho_i$ is equal $A \sim$ $\sim \exp(\beta_\perp \tau^{1/2} L/\rho_i)$.

If $t \gg (|\bar{z}-\bar{z}_o|L\tau\beta_\perp)^{1/2}/\omega_i\rho_i$, we can use a "kinetic" dispersion equation:

$$\left(\frac{Kc}{\omega}\right)^2 + \frac{\omega_{pi}^2}{\omega\,\omega_i} + \left(\frac{\omega_{pi}}{\omega_i}\right)^2 \left(1 - \tau + \left(\tau + \frac{\omega_i}{\omega - \omega_i}(-i\sqrt{\pi}\,\xi\,W(\xi))\right)\right) = 0 \quad (5)$$

Here, $W(\xi)$ is the plasma dispersion function, $\xi = (\omega - \omega_i)/KV_{\parallel,T}$. The analysis shows that at $K^2 \gg \sqrt{\tau}/\rho_i L$ the magnetic field inhomogeneity can be taken into account parametrically, i.e. one can consider ω_i as a function of the $\bar{z}$ -coordinate in the Eq.(5). We can use the asymptotic representation $W(\xi) \approx 2i\sqrt{\pi}\,\xi\, e^{-\xi^2} \left(|Im\xi| > |Re\xi|, Im\xi < 0\right)$ at $t \to \infty$. We obtain the damping decrement from the Eqs. (4), (5):

$$\gamma \approx \omega_{io} \frac{V_{\parallel,T}\,t}{L} \ln^{1/2}\left(\frac{V_{\parallel,T}\,t}{L\beta_\perp\tau}\right)$$

Therefore, the perturbation damping occurs in accordance with a law $\sim \exp(-Ct^2)$.

If the point of the magnetic field minimum lies between the points $\bar{z}$ and $\bar{z}_o$, the quantity $\frac{\partial K}{\partial \omega}$ in the Eq.(3) can go into the infinity at the finite $K(\bar{z}, \omega)$. In the result, we obtain $\omega \to \omega^* \approx \omega_{i,min}(1 + i\sqrt{\beta_\perp})$ and $\omega - \omega^* \sim \exp\left(-\frac{2^{9/2}\,3^{1/4}}{\tau^{1/2}\,\beta_\perp^{1/4}} \cdot \frac{\omega_i t\rho_i}{L}\right)$ at $t \to \infty$ from the Eqs.(1),(3). Such perturbations are converted into the natural oscillations, which have been studied in /8/.

References

1. F.H.Coensqen, W.F.Cummins, B.G.Logan et al., Phys.Rev.Lett., 35, 1501, 1975.

2. H.L.Berk, L.D.Pearlstein, J.G.Cordey. Phys.Fluids, 15, 891, 1972.

3. G.N.Chulkov, A.V.Timofeev. Nucl.Fusion, 20, 9, 1980.

4. A.V.Timofeev. Nucl.Fusion, 14, 165, 1974.

5. J.G.Cordey, R.J.Hastie, Phys.Fluids, 15, 2291, 1979.

6. D.E.Baldwin, H.L.Berk, J.A.Byers et al., Preprint UCID-17038, Lawrence Livermore Lab., 1976.

7. A.V.Timofeev. Plasma Phys., 14, 999, 1972.

8. T.Tajima, K.Mima. Phys.Fluids, 23, 577, 1980.

THE MAGNETO-PARAMETRIC INSTABILITIES

Miloš M. Škorić

Institute for Nuclear Sciences "Boris Kidrič"
Belgrade, Yugoslavia

Recently, several papers have been published on the possibility of the self-generation of a magnetic field in a collisionless plasma. This problem is of importance, in particular for the basic features of laser produced plasmas.

It was shown[1-4] that in the collisionless plasma the magnetic field generation is due to the nonlinear beating of high-frequency waves producing a low-frequency (l.f.) solenoidal electron current j given by the equation

$$j = - \frac{ie\omega_p^2}{16\pi m \omega_0^3} curl (E \times E^*) , \qquad (1)$$

where ω_p is the electron plasma frequency, m the electron mass, $-e$ the electron charge, and E the slowly varying complex amplitude of the high-frequency (ω_0) electric field

$$\bar{E} = \frac{1}{2} \{ E(k,t) exp(-i\gamma) + c.c. \} , \qquad (2)$$

where $\qquad \gamma = \omega_0 t - k_0 x$

In order to derive the basic generation equation, one takes the Ampère law, and by neglecting the displacement current and the ion contribution, one gets for the l.f. self-magnetic field[2-4]

$$- curl \, curl \, B = \nabla^2 B = \frac{ie\omega_p^2}{16\pi\omega_0^3} curl \, curl \, (E \times E^*) . \qquad (3)$$

However, it seems, that in these kinetic studies[1-4] a physical understanding was left somewhat obscured.

More recently, the general question of the ponderomotive force[5] in a plasma was discussed in some detail, and a novel formula was put forward[6].

It was argued, using both kinetic theory[4,7] and stress tensor formalism[6] arguments, that the complete form of the time-averaged ponderomotive force in a plasma without an external magnetic field, should read[6]

$$f = - \nabla p_0 - \frac{\omega_p^2}{16\pi\omega_0^3} \nabla |E|^2 + \frac{i\omega_p^2}{16\pi\omega_0^3} \frac{\partial}{\partial t} curl (E \times E^*) , \qquad (4)$$

where p_0 is the hydrostatic pressure, and where apart from the familiar potential force there is a new-solenoidal term, being consistent with the covariant formulation including both scalar and vector ponderomotive potentials[7-8].

In that way, an extra term in (4), in a straightforward manner leads to a solenoidal current given by (1), hence, offering a simple connexion with the magnetic self-generation process.

The present paper presents a further development of the above ponderomotive force formulation[6,10].

In contemporary plasma physics, it is widely recognized that the ponderomotive effects account for the fundamental nonlinear wave processes in both fusion and space plasmas. One can single the parametric excitation process as one of the simplest and most studied[9,11].

In what follows, we shall briefly discuss some of the parametric processes in an externally unmagnetized plasma. We should point out, that previously, in order to describe various parametric instabilities, a potential ponderomotive force formula was commonly used. In that way, one might attempt to extend the conventional parametric analysis according to expression (4), i.e. taking into account the self-generated magnetic field.

It appears, that the first step, in this direction was taken[3] in the investigation of the instability of a finite amplitude Langmuir wave in a hot collisionless unmagnetized plasma.

In these conditions, taking into account the l.f. self-magnetic field, the conventional modulational instability accompained by a novel- the so-called magneto-modulational instability was observed[3]. Subsequent studies of this problem concluded[10,12] that the l.f. magnetic field self-generation was expected to be a general feature of modulationally unstable plasmas.

More recently, an attempt[13] was taken, in order to study a parametric self-generation of the l.f. magnetic field in a collisionless plasma under the influence of strong dipole electromagnetic pump wave. In their terminology, the generation mechanism in question corresponds to a parametric excitation of the zero-harmonic of a solenoidal electric field. It is interesting to note that in that paper[13] formula (7) obtained in the framework of linear parametric theory[14], is just a linearized version of our equation (3). This fact seems to be the additional support for using the complete ponderomotive force (4) rather than just its potential part.

These authors[13] have investigated further the parametric instability development, under physical conditions corresponding to the conventional "oscillating two-stream "(OTS)-" purely growing " instability and they have calculated the corresponding growth rates for self-magnetic field excitation.

We feel that their result should be viewed as the generalization of the parametric analysis according to (4) and finding that, accordingly, that both conventional OTS as well as its novel (so-called) magneto-OTS counterpart can operate.

Let us add a few comments about what we feel might be more general feature of parametrically unstable plasmas. It is generally recognized, in conventional parametric theory, that the coupling between h.f. and l.f. modes commonly comes on the l.f. side, through the l.f. plasma density perturbations induced by the (potentional) ponderomotive force. In view of formula (4), it seems physically plausible to expect that the above effect should, in general, be accompained by the excitation of l.f. self-magnetic field perturbations driven by the solenoidal part of the ponderomotive force (4).

In conclusion, the previous discussion may be a reason for anticipating the possible existence of a number of new, so-called magneto-parametric instabilities encountered under different physical conditions. Accordingly, their implication in, for example, plasma heating schemes, should be studied. Finally, we feel that further investigations in this direction deserve more attention.

1. B.Bezzerides, D.F.DuBois,D.W.Forslund and E.L.Lindman, Phys. Rev. Lett. 38,495 (1977)
2. P.Mora and R.Pellat, Phys. Lett. 66A,28 (1978)
3. S.A.Belkov and V.N.Tsytovich, Zh. Eksp. Teor. Fiz.76,1293 (1979) (Sov. Phys. JETP 49,656 (1979))
4. M.Kono,M.M.Škorić and D.ter Haar, Phys. Lett. 77A,27 (1980)
5. L.D.Landau and E.M.Lifshitz, "Electrodynamics of Continuous Media", Pergamon Press, 1960
6. M.Kono.M.M.Škorić and D.ter Haar, Phys. Rev. Lett. 45,1629 (1980)
7. J.R.Cary, Lawrence Berkeley Laboratory Rept. No. 8185(1979) (unpublished)
8. S.Johnston,A.N.Kaufman and G.L.Johnston, J.Plasma Phys. 20, 365 (1978)
9. A.A.Galeev and R.Z.Sagdeev, Nucl. Fusion 13, 603 (1973)
10. M.M. Škorić, Ph.D. thesis (1980) (unpublished)
11. M.Porkolab and R.P.H.Chang, Rev. Mod. Phys. 50,745 (1978)
12. M.Kono.M.M.Škorić and D.ter Haar, J. Plasma Phys.(to appear)
13. Yu.M.Aliev and V.M.Bychenkov, Zh. Eksp. Teor. Fiz. 76,1586 (1979) (Sov. Phys. JETP 49,805 (1979))
14. L.M.Gorbunov and V.P.Silin, Zh. Eksp. Teor. Fiz.49,1973(1965) (Sov. Phys. JETP 22,1347 (1966))

PARTICLE TRAPPING IN STIMULATED BRILLOUIN AND RAMAN SCATTERING

S.J. Karttunen, J.A. Heikkinen and R.R.E. Salomaa

Technical Research Centre of Finland
Nuclear Engineering Laboratory
P.O.Box 169, Helsinki 18, Finland

Abstract: Particle trapping effects on stimulated Brillouin and Raman scattering have been investigated. A time and space dependent model assumes one-dimensional Maxwellian plasma which is taken to be homogeneous in the interaction region. Ion trapping has a rather weak effect on stimulated Brillouin scattering but stimulated Raman scattering is considerably reduced by electron trapping.

A nonlinear growth of parametric instabilities is extremely complex and it is not completely understood. A simple three-wave model for stimulated Brillouin (SBS) and Raman (SRS) scattering predicts too high reflectivities. Theoretical reflectivities can be reduced by introducing a heavy linear damping for a parametrically excited electrostatic wave [1]. However, relatively high levels of electrostatic fluctuations are generated by parametric processes which may favour nonlinear damping mechanisms rather than linear Landau-damping. At least nonlinear wave-wave and wave-particle interactions, which represent two basic types of nonlinear effects, are expected to play an important role. Recent studies [2,3] have shown that secondary wave-wave interactions (ion acoustic and Lagmuir wave decay) lead to efficient saturation of Brillouin and Raman reflectivities.

For a large amplitude electrostatic wave nonlinear wave-particle interaction leads to well known particle trapping phenomenon which has been observed in many computer simulations [1,4,5]. Except some 'waterbag'-calculations [6], analytical work of trapping effects on parametric instabilities has been rather limited.

In stimulated scattering process a large amplitude electromagnetic (EM) wave $E_0(k_o,\omega_o)$ decays to an electrostatic (ES) mode $E(k,\omega)$ and a (back)scattered electromagnetic wave $E_-(k_-,\omega_-)$. The interaction is strongest in the region, where the phase matching conditions ($\omega_o=\omega_- +\omega; k_o=k_-+k$) are satisfied. When the electrostatic amplitude E has grown large enough it starts to trap particles representing a nonlinear damping mechanisms for the excited ES-wave. Because of the particle flow into k-direction through the trapping, the resonance region has to be in thermal contact with larger surrounding plasma [6].

Our model assumes that all particles with a velocity between v_p-v_{tr} and v_p+v_{tr} will be trapped and accelerated (or decelerated) toward the phase velocity v_p of the electrostatic wave. The length of the resonance region is L and a Maxwellian plasma is taken to be homogeneous in the interaction region. The trapping width is $v_{tr}=(2|\delta n/n|)^{\frac{1}{2}}c_s$ for SBS and $v_{tr}=(2|\delta n/n|)^{\frac{1}{2}}v_e(k\lambda_D)^{-1}$ for SRS, where $\delta n/n$ is the electrostatic fluctuation level, c_s and v_e are ion sound speed and electron thermal velocity, respectively.

By evaluating the change in energy density and energy flux of particles in the trapping process we find corresponding loss terms to the equation of the parametrically excited electrostatic wave. After standard normalization [1] we obtain for slowly varying amplitudes

$$\frac{\partial e_o}{\partial \xi} = -e_- e, \tag{1}$$

$$\frac{\partial e_-}{\partial \xi} = -e_o e, \tag{2}$$

$$[1+f(e)]\frac{\partial e}{\partial \tau} + [1+g(e)]\frac{\partial e}{\partial \xi} = e_o e_-, \tag{3}$$

where $\xi=x/L_g$ and $\tau=v_p t/L_g$, L_g being the basic gain length [1]. The time scale of EM-modes $e_{o,-}$ is c/v_p-times faster than the electrostatic time scale which allows us to neglect time derivatives in Eqs. (1)-(2). The initial and boundary conditions for the scattering problem are: $e_o(0,\tau)=e_o(\xi,0)=1$, $e_-(\xi,0)=e_-(L/L_g,\tau)=0$ and $e(0,\tau)=e(\xi,0)=\epsilon$, where ϵ is the electrostatic amplitude at the onset of trapping. The reflectivity r is defined by the boundary condition $r(\tau)=(\omega_-/\omega_o)e_-^2(0,\tau)$. The trapping functions $f(e)$ and $g(e)$ for stimulated Brillouin scattering are

$$f(e) = (\tfrac{\theta}{2\pi})^{\frac{1}{2}}(\eta e)^{-1}\exp[-\tfrac{\theta}{2}(1+2\eta e)]\{2\sinh[\theta(2\eta e)^{\frac{1}{2}}] -(2\eta e)^{\frac{1}{2}}\cosh[\theta(2\eta e)^{\frac{1}{2}}]\}, \tag{4}$$

$$g(e) = (\tfrac{\theta}{2\pi})^{\frac{1}{2}}(\eta e)^{-1}\exp[-\tfrac{\theta}{2}(1+2\eta e)]\{(3+2\eta e)\sinh[\theta(2\eta e)^{\frac{1}{2}}] -3(2\eta e)^{\frac{1}{2}}\cosh[\theta(2\eta e)^{\frac{1}{2}}]\}, \tag{5}$$

where $\theta=ZT_e/T_i$ and $\eta=2(k_oc/\omega_p)(v_o/v_e)$; v_o being the electron quiver velocity. For Raman scattering the trapping functions are

$$f(e) = \frac{1}{\sqrt{2\pi}}(k\lambda_D\eta e)^{-1}\exp(-\frac{\Delta^2+2\eta e}{2k^2\lambda_D^2})\{2\Delta\sinh[\frac{\Delta(2\eta e)^{\frac{1}{2}}}{k^2\lambda_D^2}] -(2\eta e)^{\frac{1}{2}}\cosh[\Delta(2\eta e)^{\frac{1}{2}}/k^2\lambda_D^2]\} \tag{6}$$

$$g(e) = \frac{\Delta(k^3\lambda_D^3\eta e)^{-1}}{3\sqrt{2\pi}}\exp(-\frac{\Delta^2+2\eta e}{2k^2\lambda_D^2})\{(3\Delta^2+2\eta e)\sinh[\frac{\Delta(2\eta e)^{\frac{1}{2}}}{k^2\lambda_D^2}] -3\Delta(2\eta e)^{\frac{1}{2}}\cosh[\Delta(2\eta e)^{\frac{1}{2}}/k^2\lambda_D^2]\} \tag{7}$$

where $\Delta=(1+3k^2\lambda_D^2)^{\frac{1}{2}}$ and $\eta=(2/3)^{\frac{1}{2}}(k_oc/\omega_p)(k/k_o')^{\frac{1}{2}}(v_o/v_e)$.

We ignore detailed trapping dynamics assuming that the trapping starts from ϵ-level without delay. Then we obtain from Eqs. (2) and (3) ϵ-dependent threshold condition: $L/L_g>[1+g(\epsilon)]^{\frac{1}{2}}\pi/2$ which reduces to the familiar form $L/L_g>\pi/2$ in the limits: $\theta\to\infty$(SBS) and $k\lambda_D\to0$(SRS).

Numerical solutions of Eqs. (1)-(3) for steady-state Brillouin reflectivities as a function of normalized length L/L_g with various temperature ratios θ are seen in Figs. 1(a) and 1(b). The dotted curve is SBS-reflectivity without trapping. The threshold increases for smaller ZT_e/T_i and η according to the condition given above. At high pump intensities reflectivity curves are merging indicating that main part of the ions is trapped. Recall that $v_{tr}>c_s$ for $\delta n/n>0.5$. The temporal growth of Brillouin scattering, however, is considerably reduced by trapping. For instance, with the parameters $\theta=10$ and $\eta=0.4$ steady-state is reached at $t/t_g\approx50$.

Steady-state Raman reflectivities with different $k\lambda_D$-values are seen in Figs. 1(c) and 1(d). The effect of trapping is stronger than in SBS-case. Typically, 15-20 times higher laser intensities are required for $k\lambda_D>0.2$ to obtain same reflectivity levels than without trapping. On the other hand, the temporal growth is rather weakly reduced by electron trapping. Qualitatively the SRS-results for small $k\lambda_D$ are similar to the waterbag-calculations [6].

The simple trapping picture cannot explain experimentally observed saturation of Brillouin scattering or extremely low SRS-levels measured recently. However, a strong trapping modifies the particle distribution function and may affect indirectly through the processes like particle heating [7], short wavelength ion or electron turbulence or secondary decays [2,3].

References:

1. D.W. Forslund et al., Phys. Fluids 18, 1002; 1018(1975).
2. S.J. Karttunen and R.R.E. Salomaa, Phys. Lett. 72A, 336(1979).
3. S.J. Karttunen, Plasma Phys. 22, 151(1980).
4. W.L. Kruer et al., Phys. Rev. Lett. 35, 1076(1975).
5. H.H. Klein et al., Phys. Fluids, 18, 1031(1975).
6. W.M. Manheimer and H.H. Klein, Phys. Fluids 17, 1889(1974).
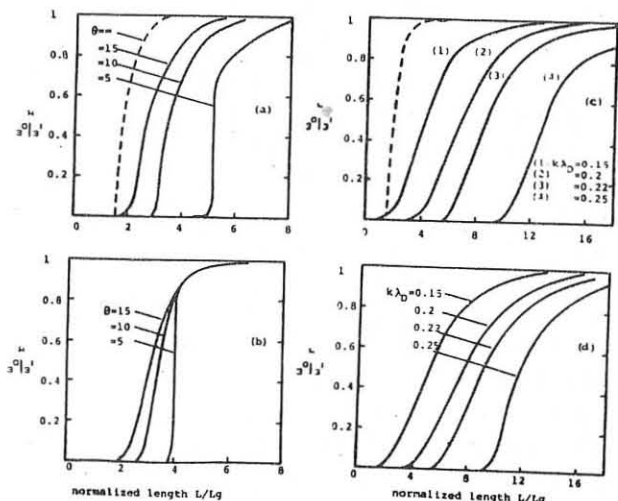7. D.W. Phillion et al. Phys. Rev. Lett, 39, 1529(1977).

Fig.1 Steady-state SBS- and SRS-reflectivities as a function of normalized length for ϵ = 0.01. SBS: (a) η = 0.4 and (b) η = 1.2. SRS: (c) η = 0.8 and (d) η = 1.2.

Nonlinear Interaction between Ion Beams and Electrostatic

Cyclotron Waves in an Ion Beam-Plasma System

M. Sugawa, R. Sugaya and T. Dodo

Department of Physics, Faculty of Science,

Ehime University, Matsuyama, Japan

Abstract: The amplitude oscilation of unstable electrostatic ion cyclotron waves in an ion beam-plasma system due to wave-particle interaction and its destruction have been studied experimentally and theoretically.

Electrostatic ion cyclotron waves (EIC-waves) can easily be destabilized by an ion beam [1]. Its linear limit of the wave growth occurs because the beam particles are electrostatically trapped in the potential thoughs of waves. In this paper, we show the results of the amplitude oscillation of the unstable EIC-wave due to nonlinear wave-particle interactions [2].

We derived the Poisson's equation and the equation of the motion of beam charge sheets for temporal evolutions based on a model of many waves [3]:

$$k^2 \phi_k [\frac{\partial \varepsilon_p}{\partial k} \delta k + \frac{\partial \varepsilon_p}{\partial \omega} \delta \omega + i \operatorname{Im}(\varepsilon_p)] = \frac{m_i}{e} \omega_b^2 \frac{1}{N}$$
$$\times \sum_{j=1}^{N} \exp[-i(k_{\shortparallel} z_j - \omega t)], \qquad (1)$$

$$\frac{d^2 z_j}{dt^2} = - \sum_k k \frac{e}{m_i} \phi_k \exp[i(k_{\shortparallel} z_j - \omega t)] + c.c. \qquad (2)$$

$$z_j(t=0) = (2\pi/k_{\shortparallel 0})(j/N), \qquad \frac{dz_j}{dt}\Big|_{t=0} = 0, \qquad (3)$$

where $j =, \cdots, N$, the sum of k is over the number of modes, and

$$\varepsilon_p = 1 + \frac{2\omega_{pe}^2}{k^2 v_{te}^2}[1 + \frac{\omega}{k_{\shortparallel} v_{te}} Z(\frac{\omega}{k_{\shortparallel} v_{te}})]$$

$$+ \frac{2\omega_{pi}^2}{k^2 v_{ti}^2}[1 + \frac{\omega}{k_{\shortparallel} v_{ti}} \sum_{n=-\infty}^{\infty} \exp(-\lambda) I_n(\lambda) Z(\frac{\omega - n \omega_{ci}}{k_{\shortparallel} v_{ti}})]. \qquad (4)$$

The experiments were performed in an ion beam-plasma system with the ion beam injected parallel to the magnetic field. The plasma has density $n_p = 10^8 \sim 10^9$ cm^{-3}, electron and ion temperatures $T_e \cong 5$ eV, $T_i \cong 0.5$ eV, the pressure of the neutral (H$_2$≅1mTorr. The ion has density $n_b = 10^7 \sim 5 \times 10^8$ cm^{-3}, energy $V_b = 200 \sim 300$ eV, energy spread $T_b \cong 0.5$ eV. In fig. 1, we show observed ω-$k_{\shortparallel}$ plots of the spontaneous emission of EIC=waves, where the solid and open circles correspond to the fastest growing EIC-wave (main wave) and the lower sideband wave. The curve A shows $\varepsilon_p = 0$, and the line B $\omega = k_{\shortparallel} v_b - \omega_{ci}$ ($v_b = \sqrt{2eV_b/m_i}$). Therefore, it is verified that the main wave is excited due to the cyclotron coupling between the space charge wave of the beam and EIC-wave, and occurred due to the absolute instability [2] as shown by the property of the curve A. In fig. 2, temporal evolutions of the output signal of the spontaneous emission are shown for various beam density ($\omega_{bt}^2/\omega_p^2 = 0.005$). As shown by curves. the wave amplitudes, after saturation, oscilates in time interval T_B and decays. Expected by $1/T_B = (1/2\pi)\sqrt{ek_{\shortparallel}E/m_i)}$, the bounce frequency $1/T_B$ of the temporal amplitude oscillation is proportional to $\sqrt{V_0}$ as shown by the inset in fig. 2, where V_0 estimates from the maximum

voltage of the unstable EIC-wave. Assuming that the beam ion oscilates back and forth in energy between V_b and V_{b1} as the main wave oscilates in amplitude, its bounce frequency $1/T_B$ is given by $(e/m_i)(V_b - V_{b1})k_{\shortparallel}/2\pi V_{ph}$. From observed $1/T_B = 29$ kHz, then we obtain $V_{b1} = 217$ eV. The line C in fig. 1 is $\omega = k_{\shortparallel} v_{b1} - \omega_{ci}$ for $V_{b1} = 217$ eV. Therefore, the sideband waves are excited by the beam with V_{b1} formed due to the beam energy loss according to the growth of the main wave. In fig. 3, we show theoretically temporal evolutions of wave amplitudes calculated by eqs. (1)∼(3), where k_0
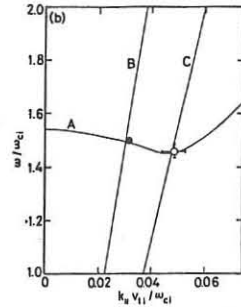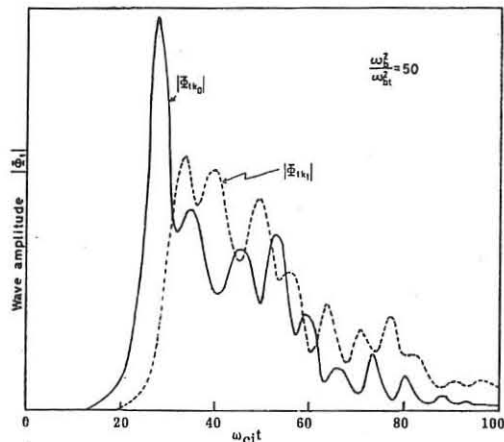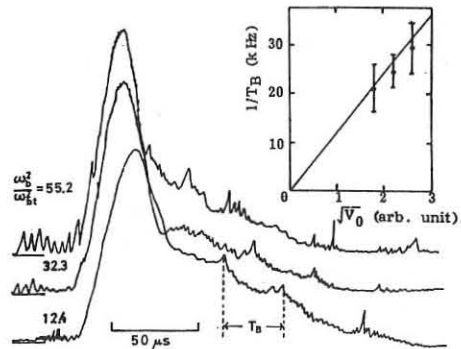
and k_1 correspond to main and sideband waves. The wave damping after saturation agrees qualitatively with theory. Therefore, the growth of many waves occurred due to slower beam destroy the nonlinear trapped particle oscilation of the main wave.

References

1. M. Sugawa, R. Sugaya and H. Nomoto, Phys. Lett. 63A, 321 (1977), and J. Phys. Soc. Jpn. 48, 983 (1980).

2. M. Sugawa and R. Sugaya, Phys. Lett. 79A, 74 (1981).

3. T. M. O'Neil, J. H. Winfrey and M. L. Malmberg, Phys. Fluids 14, 1204 (1971) and J. H. Winfrey and M. L. Dunlop, Plasma Phys. 19, 901 (1977).

NONRESONANT PARAMETRIC INTERACTION OF A HIGH-FREQUENCY,
NONMONOCHROMATIC DRIVER PUMP WITH MAGNETIZED PLASMA

V. Stefan

Boris Kidrič Institute of Nuclear Sciences-Vinča, Beograd
Yugoslavia

Parametric effects in magnetized plasma upon the action of a high-frequency nonmonochromatic driver pump are considered. It is shown that due to the nonmonochromaticity of a driver pump, a variety of parametric excitations is possible. In the case of monochromatic driver pump these effects do not occur.

In all actual experimental situations, signals of radio or laser radiation interacting with plasma are, principally, of finite time duration. For theoretical investigations of these situations the main quantities are pulse duration τ, interpulse spacing T characteristic time of processes in plasma T_c and carrier-frequency ω_0. Depending on the above listed quantities and their ratios, the processes in plasma could be strongly affected by nonmonochromaticity of driver pump and vice versa /1-6/. In this paper an investigation of the case when carrier-frequency ω_0 is much higher than all eigen-frequencies of magnetized plasma is presented, what is equivalent to the case of completely transparent plasma. The resonant case was considered in /7/.

A homogeneous magnetized plasma in interaction with the external field $E(t)=E_0(t)\sin\omega_0 t$ is considered. Generally, for the time-varying amplitude $E_0(t)$ dynamical /3,4,5,6/ or, stochastic /2/ dependence on t could be assumed. Here, a dynamical dependence is taken into consideration, namely:

$$E_0(t)=\begin{cases} E_{00} & nT \leq t \leq \tau+nT \\ 0 & \tau+nT \leq t \leq (n+1)T \end{cases} \qquad (1)$$

For the description of longitudinal plasma perturbations a system of kinetic equations for the function $\psi_\alpha(\vec{k},\vec{p},t)$ is used as an adding term of the equilibrium distribution function $f_\alpha(\vec{p_\alpha})$ /8/,

$$\frac{\partial\psi_\alpha}{\partial t}+ik\vec{V}_\alpha\psi_\alpha+\frac{e_\alpha}{c}\left(\vec{V}_\alpha\times\vec{B}_0\right)\frac{\partial\psi_\alpha}{\partial\vec{p}_\alpha}=ik\frac{\partial f_\alpha(\vec{p}_\alpha)}{\partial\vec{p}_\alpha}\sum_\beta\frac{4\pi e_\beta}{k^2}\int d\vec{p}_\beta\sum_{l=-\infty}^{+\infty}J_l[a_{\alpha\beta}]e^{-il\omega t}=0. \quad (2)$$

Here $J_l[a_{\alpha\beta}(t)]$ is the Bessel function of the order l and $a_{\alpha\beta}$ is the time dependent coupling coefficient $a_{\alpha\beta}^2=\frac{e^2 k^2 E_0^2(t)}{m_e^2\omega_0^4}\psi(t,\theta)$ where:

$$\psi(t,\theta)=\left[\frac{E_{0z}(t)}{E_0(t)}\cos\theta+\frac{\omega_0^2}{(\omega_0^2-\Omega_e^2)}\frac{E_{0y}(t)}{E_0(t)}\sin\theta\right]^2+\frac{E_{0x}^2(t)}{E_0^2(t)}\sin^2\theta\frac{\omega_0^2\Omega_e^2}{(\omega_0^2-\Omega_e^2)^2}. \quad (3)$$

The wave vector of longitudinal excitations is denoted by $\vec{k}$ and electron cyclotron frequency by Ω_e; e_α and m_α are charge and mass of α-sort particles. θ denotes the angle between $\vec{k}$ and the external magnetic field $\vec{B}_0$.

Assuming that carrier-frequency ω_0 is much higher than all eigen-frequencies of magnetized plasma $[\omega_0\gg\max(\Omega_e,\omega_{pe})]$ and also $\omega_0\gg k V_{T\alpha}$ $[V_{T\alpha}=(\frac{T_\alpha}{m_\alpha})^{1/2}]$ then, expanding ψ_α over harmonics of modulation frequency $\Omega=\frac{2\pi}{T}$, a system convenient for the investigation by the method of averaging /9,10/ could be obtained. After averaging eqs. (2) over the period $T_0=\frac{2\pi}{\omega_0}$ for the quantity $n_\alpha(t,\vec{k})=\frac{\omega_0}{2\pi}\int d\vec{p}\int\psi_\alpha(t,\vec{k},\vec{p})dt$ the following system of algebraic equations is obtained:

$$n_e(\omega,\vec{k})=R_e(\omega,\vec{k})\sum_{m=-\infty}^{+\infty}A_m n_i(\omega+m\Omega,\vec{k})=0,$$

$$n_i(\omega,\vec{k})=R_i(\omega,\vec{k})\sum_{m=-\infty}^{+\infty}A_m n_e(\omega+m\Omega,\vec{k})=0. \quad (4)$$

This system reduces to that one obtained in /8/ for the resonant case and monochromatic driver pump substituting $m\Omega$ by $m\omega_0$. In (4), $R_\alpha=\chi_\alpha(\omega,\vec{k})[1+\chi_e(\omega,\vec{k})]^{-1}$ where $\chi_\alpha(\omega,\vec{k})$ is linear susceptibility of α plasma component and,

$$A_0=1-\frac{\tau}{T}[1-J_0(a_0)],\quad A_{n\neq0}=-[1-J_0(a_0)]\frac{\sin n\pi\frac{\tau}{T}}{n\pi}\exp\left(-\frac{n\pi\frac{\tau}{T}}{T}\right). \quad (5)$$

The coupling coefficient a_0 could be easily obtained from $a_{\alpha\beta}(t)$ by putting E_{00} instead of $E_0(t)$. The analysis of the system (4) could be done for different cases depending on the ratio of $n\Omega$ and some of the plasma eigen-frequencies.

First, we shall consider the case of parametric excitations of two upper-hybrid waves, i.e., when $n\Omega\sim2\omega_{UH}$, $(\omega_{UH}^2=\omega_{pe}^2+\Omega_e^2)$ is satisfied. The dispersion relation derived from the system

(4) in the weak mode-coupling approximation reads:

$$\mathcal{E}(\omega,\vec{k})\mathcal{E}(\omega-n\Omega,\vec{k})=|A_n|^2\left(\frac{m_e}{m_i}\right)^2. \quad (6)$$

In the case $\gamma\gg\gamma_{UH}$ (γ_{UH} linear damping rate of upper-hybrid wave), for the parametric increment is obtained as:

$$\gamma=\frac{1}{8}\omega_{UH}\left(\frac{\omega_{pe}}{\omega_{UH}}\right)^2\left(\frac{m_e}{m_i}\right)(k^2 r_{De}^2)\left(\frac{\omega_{pe}}{\omega_0}\right)^4\psi(\theta)\left|\frac{\sin n\pi\frac{\tau}{T}}{n\pi}\right|\frac{E_0^2}{4\pi n_e\varkappa(T_e+T_i)}. \quad (7)$$

Minimum threshold value for this high-frequency modes parametric instability is obtained if $n=1$, $T=2\tau$ and reads:

$$\frac{E_{0,THR}^2}{4\pi n_e\varkappa(T_e+T_i)}=\frac{8\bar{u}}{k^2 r_{De}^2\psi(\theta)}\frac{\gamma_{UH}}{\omega_{UH}}\left(\frac{\omega_{UH}}{\omega_{pe}}\right)^2\frac{m_i}{m_e}\left(\frac{\omega_0}{\omega_{pe}}\right)^4. \quad (8)$$

With decrease of modulation frequency Ω, a situation when $n\Omega\sim\omega_{pe}$ could be reached. Then, parametric excitation of a high-frequency magnetized plasma mode coupled with low-frequency mode is possible. Corresponding dispersion relation has the form (weak coupling approximation),

$$\mathcal{E}(\omega,\vec{k})\mathcal{E}(\omega-n\Omega,\vec{k})=|A_n|^2\chi_i(\omega,\vec{k})[1+\chi_e(\omega,\vec{k})]. \quad (9)$$

From (9) for the increment of parametric excitation of upper-hybrid mode coupled with high-frequency ion-sound wave $(\omega_s=k V_s, V_s=(\frac{T_e}{m_i})^{1/2}; \omega_s\gg\Omega_i)$ could be obtained as:

$$\gamma=\frac{1}{8}(\omega_{UH}\omega_s)^{1/2}\left(\frac{\omega_{pe}}{\omega_{UH}}\right)^{1/2}\left|\frac{\sin n\pi\frac{\tau}{T}}{n\pi}\right|\left(\frac{\omega_{pe}}{\omega_0}\right)^2\psi(\theta)(k r_{De})\frac{E_0^2}{4\pi n_e\varkappa(T_e+T_i)} \quad (10)$$

The minimum threshold value is reached if $n=1$ and $T=2\tau$. It reads (γ_s linear damping rate of high-frequency ion sound wave):

$$\frac{E_{0,THR}^2}{4\pi n_e\varkappa(T_e+T_i)}=\frac{8\bar{u}}{(k r_{De})\psi(\theta)}\left(\frac{\omega_{UH}}{\omega_{pe}}\right)\left(\frac{\omega_0}{\omega_{pe}}\right)^4\left(\frac{\gamma_{UH}\gamma_s}{\omega_{UH}\omega_s}\right)^{1/2}. \quad (11)$$

Finally, if $n\Omega\sim2\omega_s$ parametric excitation of two ion-sound waves is possible. Dispersion relation describing evolution of this process in initial state has the form:

$$\mathcal{E}(\omega,\vec{k})\mathcal{E}(\omega-n\Omega,\vec{k})=4|A_n|^2\chi_e(\omega,\vec{k})\chi_e(\omega-n\Omega,\vec{k})\chi_i(\omega,\vec{k})\chi_i(\omega-n\Omega,\vec{k}). \quad (12)$$

For the parametric increment and minimum threshold value, the following expressions are obtained, respectively,

$$\gamma=\frac{1}{4}\omega_s\left(\frac{\omega_{pe}}{\omega_0}\right)^4\psi(\theta)\left|\frac{\sin n\pi\frac{\tau}{T}}{n\pi}\right|\frac{E_0^2}{4\pi n_e\varkappa(T_e+T_i)}-\gamma_s, \quad (13)$$

$$\frac{E_{0,THR}^2}{4\pi n_e\varkappa(T_e+T_i)}=\frac{4\bar{u}}{\psi(\theta)}\frac{\gamma_s}{\omega_s}\left(\frac{\omega_0}{\omega_{pe}}\right)^4. \quad (14)$$

In conclusion, let us say that due to the processes described above, a part of external electric field energy could be deposited in the regions of the magnetized plasma where without modulation of a driver pump nonlinear (as well as linear) absorption is impossible. On the other hand, by proper choice of the modulation frequency Ω these effects could be avoided.

REFERENCES:

1. D.Arnush, K.Nishikawa, P.D.Fried, C.F.Kennel, A.Y.Wong, Phys.Fluids, 16, (1973)2270

2. J.J.Thomson, Nucl.Fusion, 15, (1975)237

3. Yu.M.Aliev, A.A.Chernikov, O.M.Gradov, V.V.Pustovalov, V.P.Silin, V.Stefan, VIII European Conference on Controlled Fusion and Plasma Physics, Prague (1977) vol.1.

4. Yu.M.Aliev, O.M.Gradov, D.Sünder, Beiträge aus der Plasma Physik, band 17, heft 6, (1977).

5. V.V.Pustovalov, V.P.Silin, A.A.Chernikov, Sov.Phys. Quantum Electronics 5, (1978)1940

6. V.Stefan, Dissertation, Faculty for Electrical Engineering, University of Belgrade (1978), chapt.2.

7. Yu.M.Aliev, O.M.Gradov, V.Stefan, Journal de Physique, Coll.c.7, suppl.7, Tome 40, Julliet, (1979)

8. V.P.Silin, Parametric Action of a High-Power Radiation on Plasma, Nauka, Moscow 1973, chapt.3

9. N.N.Bogolyubov, Y.A.Mitropolsky, Asymptotic Methods in the Theory of Non-Linear Oscillations, Gordon and Breach, New York (1961) p.387.

10. L.D.Landau, E.M.Lifshitz, Mechanics, Moscow, (1958), p.102.

NONLINEAR DISSIPATION OF PARAMETRICALLY DRIVEN BERNSTEIN MODES IN PLASMA UPON THE ACTION OF NON-MONOCHROMATIC DRIVER PUMP

V. Stefan

Boris Kidrič Institute of Nuclear Sciences - Vinča, Beograd
Yugoslavia

Saturation of the parametrically induced turbulent plasma state by the secondary decays of the excited electron Bernstein modes is considered. It is shown that in the upper limit of the weak turbulence theory applicability, anomalous collision frequency significantly exceeds electron-ion collision frequency. As well, it is shown that the nonmonochromaticity of a driver pump leads to the reduction of the absorbed energy in the parametric resonance region.

The low-frequency RF heating of tokamak plasmas (e.g. lower-hybrid heating, ion-cyclotron resonance heating and so on) is considerably developed both theoretically and experimentally. Recently /1,2/, a high-frequency RF plasma heating at electron cyclotron resonance attracts a great attention due to the significant progress in continuous wave (CW) and pulsed operated (PO) gyrotrons technology /3/. The driver pump electric field intensities in contemporary experiments are such that plasma appears to be parametrically unstable and consequently nonlinear heating processes take place /4,5/.

A fully ionized homogeneous plasma interacting with the driver-pump electric field $E(t) = E_o(t) \sin \omega_o t$ is considered. The time-varying amplitude $E_o(t)$ is assumed to be in the form of rectangular pulse train with pulse duration $\mathcal{C}$ and interpulse spacing T. The carrier frequency ω_o is chosen so to be near electron cyclotron harmonics frequency $\omega_o \sim \omega_e^{(\ell)} + \omega_i$, where /6/,

$$\omega_e^{(\ell)} \sim \ell |\Omega_e| \left\{ 1 + \frac{1}{2} \frac{\ell_e^2}{\hbar_{\ell e}^2} \left(1 - k^2 \rho_e^2 \right) \right\}, \frac{\omega_{pe}}{\Omega_e} < 1, k^2 \rho_e^2 \ll 1 . \quad (1)$$

Here $\Omega_e, \omega_{pe}, \ell_e$ and $\hbar_{\ell e}$ are cyclotron and plasma frequency, Larmor and Debye radius of α-plasma component, respectively. The time-varying amplitude leads to the nonmonochromaticity of driver-pump what can be seen from Fourier expansion of $E_o(t)$. In ω-space, a frequency broadening appears with the width $\Delta \omega_o = 4\pi/\mathcal{C}$. Instead of the unique external field frequency a discrete frequency spectrum arises with the distance between lines $\Delta \omega = \frac{2\pi}{T} = \Omega$ and the total number of lines $2n^* = \frac{T}{\mathcal{C}}$. Then, plasma actually interacts with $2n^*$ independent monochromatic driver pumps with frequencies $\omega_o^x = \omega_o \pm n \Delta \omega$ $(n = 0, 1 \dots n^*)$ and corresponding amplitudes $E_o |f_n| \left(f_n = \frac{\sin n\alpha \mathcal{C}}{n\alpha} \right)$. Finally, because of $\omega_o \gg n^* \Omega$ it could be considered that plasma is in interaction with monochromatic driver pump of the amplitude $\sum_{n=-n^*} E_o f_n$.

In the frame of the above presented model of interaction, the anomalous collision frequency in the nonmonochromatic field $E(t)$ could be defined as:

$$\gamma_a^{NM} \sum_{n=-n^*}^{n^*} \left(E_o f_n \right)^2 \sim \sum_{n=-n^*}^{n^*} \gamma_a^{(n)} \left(E_o f_n \right)^2 . \quad (2)$$

The left-hand side of (2) represents nonlinearly converted non-monochromatic external field power and right-hand side the total power nonlinearly dissipated by $2n^*$ monochromatic driver pumps. $\gamma_a^{(n)}$ is the anomalous collision frequency corresponding to the n-th driver pump.

In order to evaluate $\gamma_a^{(n)}$ for saturation mechanism of parametrically excited Bernstein modes, cascading processes are considered. This saturation mechanism is based on the collisional dissipation of the excited waves and is effective for the Bernstein modes whose linear damping is just collisional. According to this mechanism, primary excited electron Bernstein mode further decays, transfering the energy from the domain of primary excitation to the domain of lower frequencies. A simple derivation in /8/ shows that in the weak turbulence theory one can write $\gamma_a^{(n)} \sim 2\gamma_n$ where γ_n is parametric increment corresponding to the n-th monochromatic driver pump.

Plasma parametric processes in the linear phase of development, upon the action of monochromatic driver pump with the amplitude $E_o f_n$ could be described using known procedure /9/. In the case of rather strong driver pumps $\left(\gamma_n > \gamma_{ce}, \gamma_{ci} ; \gamma_{ce}, \gamma_{ci} \right.$ linear damping rates of electron and ion Bernstein modes, respectively) parametric increment reads:

$$\gamma_n^2 = \frac{\mu_n^2}{4} \left[1 + Re \chi_i (\omega, \vec{k}) \right]^2 \left[\left(\frac{\partial Re \mathcal{E}_H(\omega)}{\partial \omega} \right)_{\omega = \omega_e^e} \left(\frac{\partial Re \mathcal{E}_L(\omega)}{\partial \omega} \right)_{\omega = \omega_i^{(\ell)}} \right]^{-1} . \quad (3)$$

Here $Re \mathcal{E}_H(\omega, \vec{k})$ and $Re \mathcal{E}_L(\omega, \vec{k})$ are real parts of the high and low-frequency dielectric permittivities of magnetized plasma /6/. The coupling coefficient of the parametrically excited electron and ion Bernstein mode by the extraordinary driver pump $\left(\vec{k}_o \perp \vec{B}_o \right)$ reads:

$$\mu_n^2 = \frac{e^2 (E_o f_n)^2 k^2}{4 m_e^2 \Omega_e^2} \left[(\ell-1) |\Omega_e| + \frac{\ell |\Omega_e|}{2\ell} \frac{\ell_e^2}{\hbar_{\ell e}^2} \left(\frac{k^2 \rho_e^2}{2} \right)^{\ell-1} \right]^{-2} \quad (4)$$

The external field wave vector $\vec{k}_o$ is oriented along x-axis, confining magnetic field vector $\vec{B}_o$ along y-axis and the wave vector of excitations $\vec{k}$ along z-axis. From (4) follows that the strongest coupling of the excited waves exists in the case of fundamental harmonic $(\ell=1)$ excitation.

In the long-wave length region $\left(k_i^2 \rho_i^2 \ll 1, k_e^2 \rho_e^2 \ll 1 \right)$ for the parametric increment,

$$\gamma_n^2 = \frac{\mu_n^2}{4 k_e^4 \rho_e^4} \frac{(\ell!)(\Omega_i \Omega_e)^3 (k^2 \rho_i^2)^{\ell+1} (k^2 \rho_e^2)^{\ell+1}}{(k^4 \rho_e^4)(\ell^2 \rho_e^2)(\omega_p \omega_{pe})^2 2^{\ell+5} \ell! S!} \quad (5)$$

is obtained. The maximum increment is possessed by the excitations with wave number k satisfying:

$$k \rho_e \sim \left\{ \ell \ell! \cdot \frac{\omega_o - \ell |\Omega_e|}{\omega_o} \frac{\Omega_e}{\omega_{pe}} \right\}^{\frac{1}{2\ell(\ell-1)}} \ell+1, \quad k \rho_e \sim \left\{ \frac{2(\omega_o - |\Omega_e|)}{\omega_{pe}} \frac{\Omega_e}{\omega_{pe}} \right\}^{\frac{1}{2}} \ell \neq 1. \quad (6)$$

Basing on (2) and (5) for anomalous collision frequency in the field of pulsed operated (nonmonochromatic) driver-pump could be written as:

$$\gamma_a^{NM} \sim \gamma_a^{CW} \left(\sum_{n=-n^*}^{n^*} |f_n|^3 \right) \left(\sum_{n=-n^*}^{n^*} f_n^2 \right)^{-1} . \quad (7)$$

Here γ_a^{CW} is anomalous collision frequency in the case of CW-operated (monochromatic) driver-pump $(T = \mathcal{C})$. The power absorbed by plasma per unit volume reads:

$$Q \sim \gamma_a^{NM} \sum_{n=-n^*}^{n^*} f_n^2 \frac{E_o^2}{4\pi} \quad (8)$$

In the case of strong nonmonochromaticity $\frac{\mathcal{C}}{T} \ll 1$, $\gamma_a^{NM} \sim 2\gamma_o \frac{\mathcal{C}}{T}$ and $Q \sim 2\gamma_o \frac{E_o^2}{4\pi} \left(\frac{\mathcal{C}}{T} \right)^2$. From here it could be seen that in the pulsed operation of driver-pumps a significant reduction of absorbed energy appears in comparison with (CW) operated driver-pumps.

It is to be noted that in the presented theory for modulation frequency $\Omega \gg \gamma_n$ is to be satisfied. In the opposite case, the saturation level is reached during one modulation period T and consequently, actually pulsed operated driver-pump appears to be CW operated in reference to the considered processes.

Finally, let us say that in the case of fundamental harmonic excitation $(\ell=1)$ and for typical tokamak plasma values $\left(n_e \sim 10^{14} \text{cm}^{-3}, T_e \sim 1-5 \text{keV}, B_o \sim 5 \sim 10 \text{ T} \right)$ anomalous collision frequency reaches the value of $10^3 - 10^4 \gamma_{ei}$. Accordingly, it could be concluded that the anomalous absorption due to the decay into Bernstein modes is effective mechanism of the external power absorption by tokamak plasma.

REFERENCES:

/1/. V.V.Alikaev, G.A.Bobrovskii, V.I.Poznyak, K.A.Razumova, V.V.Sannikov et al., Fizika Plazmi 2 (1976)212

/2/. T.H.Antonsen Jr., M.Porkolab in Physics of Plasma Close to Thermonuclear Conditions, Vol.1, CEC Brusseles (1980)

/3/. H.Jory, 2-nd Joint Grenoble-Varenna International Symposium on Heating in Toroidal Plasmas, vol.1, Grenoble (1978)

/4/. V.F.Kovalev, A.B.Romanov, Zh.Eksp.Teor.Fix. 77, 3(1979)913

/5/. V.Stefan, 1-st Joint Grenoble-Varenna International Symposium on Heating in Toroidal Plasmas, vol.1, Grenoble(1978) V.Stefan, 2-nd Joint Grenoble-Varenna International Symposium on Heating in Toroidal Plasmas, Como (1980) V.Stefan, Phys.Lett.A. to be published

/6/. A.I.Akhiezer et al., Plasma Electrodynamics, vol.1, p.278, Pergamon Press (1975)

/7/. W.L.Kruer, E.J.Valeo, Phys.Fluids 16(1973)675

/8/. V.Yu.Bychenkov, V.P.Silin, V.T.Tikhonchuk, Zh.Eksp.Teor.Fiz. Pis'ma 26(1977)309

/9/. V.P.Silin, Parametric Action of a High-Power Radiation on Plasma, Nauka, Moscow, chapt.3, (1973) in Russian.

ELECTRON CYCLOTRON ABSORPTION FOR A TWO-TEMPERATURE ELEC-
TRON DISTRIBUTION.

D. Farina, M. Lontano, R. Pozzoli

Istituto di Fisica del Plasma, Associazione CNR-EURATOM,
Milano, Italy.

At present, electron cyclotron resonant absorption se-
ems to be one of the most promising heating methods in ma-
gnetically confined plasmas (see, e. g., Refs. 1,2,3), owing
also to the availability of high frequency, high power sou-
rces. On the other hand, non maxwellian electron distribu-
tions are likely to occur in tokamak devices, due to diffe-
rent factors which can exploit the low collisionality of
high energy electrons. The absorption and spontaneous emis-
sion of electron cyclotron waves in presence of anisotropic
maxwellian distributions or a high energy component, descri-
bed by a shifted maxwellian have been analyzed in Refs. 4-9;
the electron cyclotron absorption for a Spitzer-Harm distri-
bution has been also treated in Ref. 10.

Here, we are interested in the absorption of electron
cyclotron waves in a plasma which is characterized by a
two-temperature electron distribution, since we would like
to emphasize the effect of the anisotropy of the main body
of the electron distribution. In addition, we investigate
plasma regimes with $\omega_p \sim \omega_c$, where $\omega_{p,c}$ are the electron
plasma and cyclotron frequencies, respectively. These re-
gimes are of interest for most of present-day tokamaks. We
note that the anisotropy effects in this case have not yet
fully investigated in the literature.

To exploit relativistic absorption we limit our ana-
lysis to the case of propagation perpendicular to the ma-
gnetic field. We have considered the relativistic dielect-
ric tensor expanded up to the fourth order in the electron
Larmor radius. This is consistent with the investigation of
a high density regime. The electron distribution function
is assumed with zero average velocity and different paral-
lel and perpendicular temperatures $T_{\parallel} \neq T_{\perp}$, modeling a dis-
charge regime with negligible suprathermal effects.

We report here (see Figs. 1,3) the absorption of ordi-
nary and extraordinary wave near the fundamental cyclotron
frequency for a plasma with $T = \frac{1}{3} (T_{\parallel} + 2T_{\perp}) = 1 \text{Kev}$, and dif-
ferent values of the ratio $R = T_{\parallel} / T_{\perp}$. We have chosen
$\omega_p^2/\omega_c^2 = 1$ for the case of extraordinary wave, and
$\omega_p^2/\omega_c^2 = 0.7$ for the case of ordinary wave. The two modes
show different behaviour as a function of R. We observe
(Fig.1) that for the extraordinary wave the absorption in-
creases as R decreases and this, generally speaking, is co-
nnected with the fact that the absorption mechanism is re-
lated to the perpendicular motion of the electrons. The co-
rresponding variations of the real part of the refractive
index are shown in Fig.2. The absorption of ordinary wave
is shown in Fig.3. We note in this case a behaviour, for
different R, opposite with respect to the previous case.
For ordinary waves, in fact, the elementary mechanism of
absorption is connected with the electron motion along the
magnetic field.

References

1 - D. G. Bulyginsky et al., Proceeding 2nd Joint Greno-
ble-Varenna Symposium on Heating in Toroidal Plasmas
Como (Italy), 1980;

2 - T. Cho et al., Proc. International Conference on Pla-
sma Physics, Vol. I, Nagoya (Japan) 1980;

3 - O. C. Eldridge et al., Proc. 2nd Joint Grenoble-Va-
renna Symposium on Heating in Toroidal Plasmas, Como
(Italy), 1980;

4 - I. Fidone, G. Granata, R. L. Meyer, G. Ramponi,
EUR-CEA-FC-956 (1978);

5 - H. P. Freund, C. S. Wu, L. C. Lee, D. Dillenburg,
Physics of Fluids, 21, 1502 (1978);

6 - S. Tamor, Nuclear Fusion, 19, 455 (1979);

7 - I. Fidone, G. Granata, R. L. Meyer, Plasma Physics,
22, 261, (1980);

8 - I. Fidone et al., Physics of Fluids, 23, 1336 (1980)

9 - M. Lontano, R. Pozzoli, E. V. Suvorov, in press on
Il Nuovo Cimento (1981);

10 - D. Farina, M. Lontano, R. Pozzoli, Proc. 2nd Joint
Grenoble-Varenna Symp. on Heat. in Toroidal Plasmas,
Como (Italy), 1980.
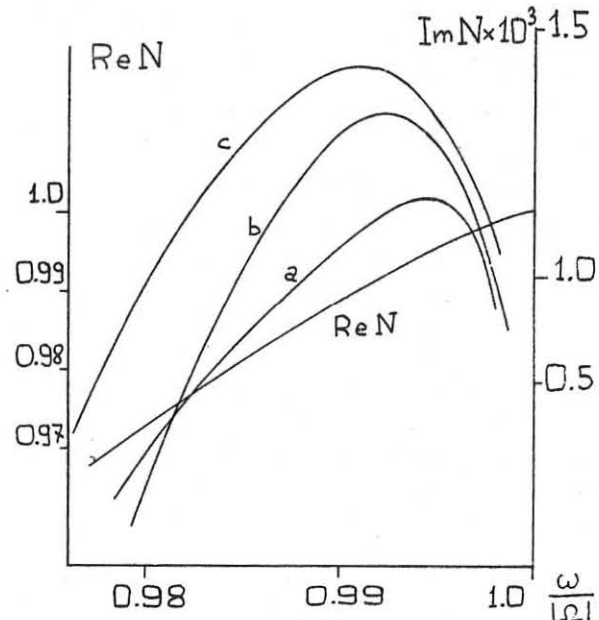
Fig.1 - Refractive index for extraordinary wave around the
cyclotron frequency, as a function of the frequency ω ,
for $\omega_p^2/\omega_c^2 = 1$. The cases a, b, c refers to the imagi-
nary part of N for R = 4, 1, 0.25, respectively; the real
part of the refractive index does not change appreciably
with R.
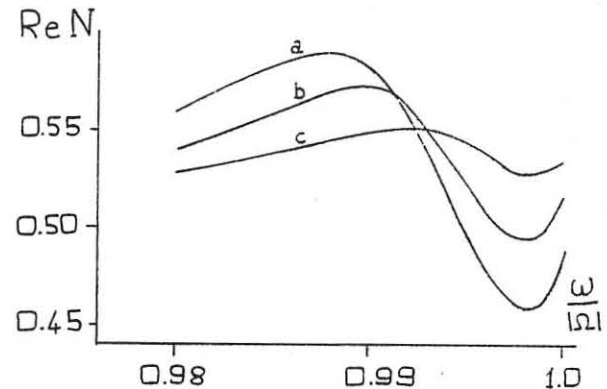
Fig.2 - Real part of N for ordinary wave around the cyclo-
tron frequency, as a function of the frequency ω , for
$\omega_p^2/\omega_c^2 = 0.7$. The cases a, b, c refers to the values
R = 4, 1, 0.25 respectively.
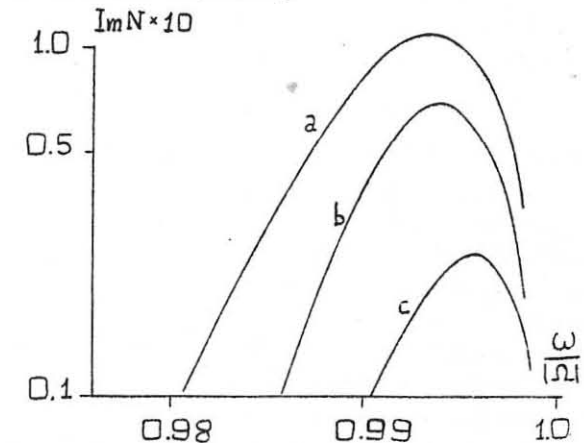
Fig.3 - The same as in Fig. 2 but for the imaginary part
of the refractive index.

ELECTRON HEATING OBSERVATION NEAR THE LOWER HYBRID
RESONANCE - WITH INDUCED l-s SCATTERING

Batanov G.M.,Kovrizhnykh L.M., Petrov A.E.,Sapozhnikov
A.V., Sarksian K.A., Skvortsova N.N.

P.N.Lebedev Physical Institute Academy of Sciences, USSR

1. The problem of physical mechanisms of nonlinear particle heating near the lower hybrid resonance has been discussed for about a decade.The process of the induced wave scattering on electrons with transformation into ion sound waves can play an important part in this type of heating. The matching condition for thermal magnetized electrons is

$$\left| (\omega_0 \pm \omega_s)/(\kappa_{oz} \pm \kappa_{sz}) \right| = |v_z| \approx v_{Te} \qquad (1)$$

where ω_0, κ_{oz}, ω_s, κ_{sz} - pump and sound frequences and longitudinal wave vector components, v_{Te}- thermal electron velocity, v_z - wave phase velocity along the magnetic field. For lower hybrid and oblique plasma waves $\omega_0 \ll \omega_{pe}$ and $\omega_s \ll \omega_0$, where ω_{pe} - electron plasma frequency. Supposing $\kappa_{sz} \gg \kappa_{oz}$ we have $\kappa_{sz} \approx \omega_s/v_{Te} \ll z_{de}^{-1}$. This condition leads to the increasing of quasilinear diffusion coefficient and, hence, heating efficiency.

2. Quasilinear diffusion coefficient and nonlinear wave growth rates can be estimated for electron Maxwell velocity distribution function with the direct electron velocity v_o, if we define $\kappa_{oz} \ll \kappa_{sz}$, $(m/M)^{1/2}\kappa_s/\kappa_{sz} \ll v_o/v_{Te}$ and $(\kappa_{oz}/\kappa_{sz})^2(\kappa_o z_{de})^{-1} \ll v_o/v_{Te}$. In this case the sound wave's growth rate reaches its maximum when $v_z/v_{Te} = 0$, $-\sqrt{3}$, hence,waves with $\kappa_{sz}/\kappa_s = 1$, $-\omega_0/\sqrt{3}\omega_{pe}$ are excited. The former is responsible for electron longitudinal impulse losses,the latter for the electron heating.Using the equation for quasilinear diffusion we can write equation for the electron heating and for the electron impulse loss rates, supposing the contributions of both types of waves are equal

$$\frac{d}{dt}(\ell n\, nT_e) \simeq \frac{\omega_{pe}}{4}\cdot\frac{\omega_{pe}^2}{\Omega_e^2}u_e u_s \quad (2), \quad \frac{d}{dt}(\ell n\, v_o') = -\sqrt{\frac{\pi}{2}}\frac{\omega_{pe}^2}{\omega_0}(1+\frac{\omega_{eo}^2}{\Omega_e^2})u_e u_s \quad (3)$$

where n , T_e , electron density and temperature respectiveky, Ω_e – electron cyclotron frequency, u_e , u_s – define the ration of wave energy (plasma or sound waves) to nT_e

3. The experiment was performed in the linear device, described earlier [1]. The plasma column was caused by hot cathode discharge in argon at a pressure of 3.10^{-4} torr. Magnetic field 0.08T, plasma density $1-2.10^{10} cm^{-3}$, $T_{eo} \approx$ $3-6$ ev,fluctuation level of sound noise $u_s = \left(\frac{\delta n}{n}\right)^2 = 10^{-3} \div 10^{-4}$ Oblique plasma wave (24 MHz) was used as the pump wave. Electron heating was measured with the flat probe, placed perpendicular to the magnetic field. The electron energy distribution of probe current. Ion sound waves spectrum was investigated by cylindrical Langmuir probe in the regime of ion current saturation.The information about wavenumbers was received from spatial correlation measurements selecting narrow frequency band from the broad turbulent spectrum.

Measurements of distribution function before surtching on the pump indicates that it is asymetrical; i.e. a longitudinal current with drift velocity $v_0 = 0.1 v_{Te}$ exists in plasma.This current is responsible for ion sound turbulence. Besides,a broad plateau is revealed on the electron dist-

ribution function for energies higher then $5T_e$.The plateau is due to kinetic instability of the initial electron beam. This instability induces a broad spectrum of Langmuir waves within frequency range 0.1-1 GHz. Energy density of Langmuir noise is $u_{\ell_0} \simeq 0.02 - 0.2$,estimated from the energy losses of electron beam.

Switching on pump leads to increase of temperature and sound noise(fig.1).However,Langmuir noise intensity,caused by the electron beam,remains constant. Increasing the drift velocity leads to increase of initial sound noise and ion temperature(fig.1b).Simultaneously,relative growth both of sound noise level and of temperature decreases.Correlation measurements demonstrate essential increase of longitudinal wave vectors of sound waves.At the same time relative intensity of short waves compared with long waves,increases, too.Besides,measurements of perpendicular wavenumbers shows that in strong pump fields($E_0 \simeq 10 V/cm$) $\kappa_{sz} \simeq \kappa_s$ .Correlation measurements results corroborate the condition of l-s scattering process going on: $\kappa_{sz} > \omega_0/v_{Te} \simeq 1 cm^{-1}$.

4. Using equations (2) and (3) the estimates of quantity and dependences of electron heating can be made,taking into consideration, that heating losses from plasma column are determined by electron heat-conductivity along magnetic field. The comparison of the comparative contributions of different parts in the heating balance equation shows that the main part of energy for electron heating is derived from the energy of Langmuir waves,excited by electron beam in the process of scattering electrons on neutral atoms. The meaning of l-s scattering in the heating processes is in decreasing longitudinal heat-conductivity

$$(nT_e)^3/mn\Lambda^2 \simeq \frac{E_\ell^2}{4\pi}v_{eo}\left[v_{eo}nT_e + 2\frac{\omega_{pe}^2}{\omega_0}\frac{E_0^2}{4\pi}\left(\frac{\delta n}{n}\right)^2\right] \qquad (4)$$

where Λ –characteristic heat-conductivity length, v_{eo} - electron-neutral collision frequency, m - electron mass, E_0, E_ℓ - pump wave and Langmuir noise intensity. The electron heating value and its dependence on the pump wave are in good agreement with equation(4).

The performed investigation demonstrate the significance l-s scattering in the process of nonlinear electron heating near the lower hybrid frequency.
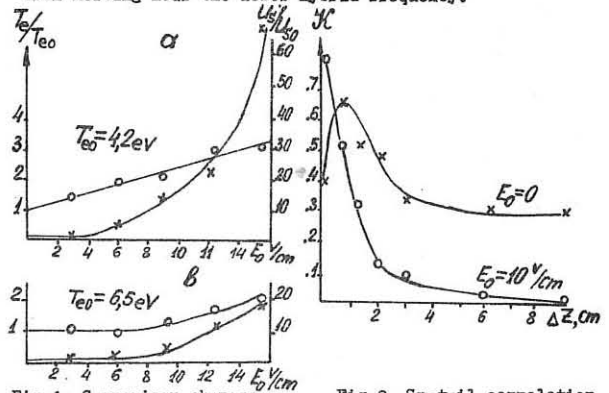
Fig.1. Comparison changes of the electron temperature and sound wave spectral density . The initial sound intensities ration for regimes "a" and "b" is $\left(\frac{\delta n}{\delta n_a}\right)^2 = 6$

Fig.2. Spatail correlation coefficient (along Z) of ion sound waves . $E_0 = 0$ and $E_0 = 10 V/cm$

References.

1. F.F.Assadulin, G.M.Batanov, A.V.Sapozhnikov, K.A.Sarksian Plasma Phisics , 1978 , vol. 4 , p.1104 .

MAGNETIC COMPRESSION, NON-ADIABATIC PARTICLE MOTION AND INTRINSIC STOCHASTICITY

Hans Persson

Studsvik Energiteknik AB, S-61182 Nyköping, Sweden

Introduction. This is a brief progress report from an ongoing study of magnetic compression and nonadiabatic particle motion; a more complete account is in preparation (Ref.1). The work started as an attempt to generalize, by including to some extent collective effects, some of the results by Krivets, Peregood and Wilhelmsson(Refs. 2,3), also used as a basis for plasma heating experiments (Ref.4). A particularly interesting question concerns the sensitivity to collective effects of the noteworthy time and space coherence of the energetic particles that was found by these authors.

The aim is also to contribute to the understanding of magnetic compression in general, with attention on shielding and induction effects between different parts of a plasma, the particles of which are more freely movable than in a fluid; the occurrence of nonadiabatic motion and the associated production of action; consideration of various model problems involving nonlinearly coupled oscillators, notably with onset of stochasticity; illuminating the interplay between magnetic flux and plasma rotation.

The theory of collisionless plasma is plagued by the formidable arbitrariness of the exact steady states, given by any function $f(W_i)$ of the constants of motion compatible with electromagnetic selfconsistency or other (Ref.5) considerations, and by the possible inadequacy of such a representation when the system is nonintegrable but not completely ergodic. Within the above framework, attempts are being made to search for and properly characterize asymptotic states evolving by nonlinear, transient processes from pertinent initial conditions.

Model. A cylindrically symmetric, quasistationary model is used, with a unidirectional magnetic field parallel to the axis and particle motion perpendicular to it. Magnetic field and induced electric field are selfconsistently included, emphasizing shielding and induction effects and free streaming of the collisionless particles, whereas electrostatic gradient fields are only included ad hoc; the requirement of quasineutrality is to some extent suppressed.

Neglect of the radial gradient field E_r has mostly been done, even if E_r can easily be included. The aim is to first analyse certain mechanisms, using the simplification to obtain qualitative insight required for the sharper problem definition necessary for a study of a complete plasma. One could say that the model so far either corresponds to a situation with an assumed, neutralizing background without appreciable azimuthal current, or in its discretized form to neutral, polarizable sheets of ions and electrons, provided that the geometric mean of the masses is taken. However, such polarizable sheets have limited application, especially with nonzero bias field.(Ref.1).

The initial state simulates (Ref.1) features of the plasma response to an applied magnetic field step: B_0 is kept constant, and the state at t=+0 corresponds to ordinary c/ω_p -shielding with a purely azimuthal velocity, having a radial variation consistent with Ampere's law, a spatially homogeneous density and the condition of zero canonical angular momentum L_φ imposed by zero temperature and bias field (Ref.6). Since there is no 2:1 betatron flux relation here, the radii will change and oscillations appear. Some cases of nonzero L_φ and time-varying B_0 have also been studied.

In the discrete model, the sheet radii are used as Lagrangian coordinates, L_φ relates v_φ and A_φ, particle density is obtained from area change, and the jump in B at a sheet is handled by taking the arithmetic mean. The equations of radial motion are complemented by expressing the vector potential at an arbitrary point in terms of the currents and locations of all the sheets, and the radius is then specialized to coincide with each of the sheet radii in succession. This leads to the following system of equations for the A_i:

$$\sum_{k=1}^{N}(\delta_{ik}+a_i)f\left(\frac{x_k}{x_i}\right)A_k = \frac{\mu_0 I_e \lambda}{2} x_i ; \quad (i=1,2,..,N)$$

where λ is a characteristic length, x_i the normalized sheet radii, and I_e is the current in the external loop. The constants a_i are measures of the "shielding strength" of the sheets, and $f(y)=y$ for $|y|\leqslant 1$; $f(y)=1/y$ for $|y|\geqslant 1$. Since the sheets will cross, track must be kept of their relative position during the motion. A constant-flux boundary condition can easily be accomodated.

A single sheet. The frequencies of azimuthal and radial motion of the particles of a single sheet are decreased by the shielding by factors $1/(1+a)$ and $1/\sqrt{1+a}$, respectively. With time-varying B_0 this splits up the magnetic moment into two distinct adiabatic invariants, and some classical results are reophained in a modified form. With constant B_0, the orbits are azimuthally compressed and precess, and the kinetic energy oscillates, as a result of the electric field induced by the variation of the size (not B) of the inner region.

Due to the phase singularity at the origin, the mean azimuthal motion is opposite to v_φ. This is better understood if nonzero L_φ, originating from a small bias field, are considered, conveniently expressed by a parameter ε. The equation of motion contains a factor $(1-\varepsilon^2/x^4)$, which shows the exceptional character of $\varepsilon=0$. A number of important quantities are discontinuous for this value of ε. (The magnetic flux is continuous, however.) :

Quantity (evaluated at inner turningpoint)	$\lim_{\varepsilon \uparrow 0}$	$\varepsilon=0$	$\lim_{\varepsilon \downarrow 0}$
v_φ	$\omega_g r_0/2(1+a) = v_{\varphi,0}$;	0 ;	$-\omega_g r_0/2(1+a)$
I_φ	$-\infty$;	$-aB_0/\mu_0(1+a)$;	$+\infty$
Magnetic energy in inner region	ζ_B ;	0 ;	ζ_B

Here, $\zeta_B = \frac{\pi\lambda^2}{2\mu_0}\cdot\left(B_0 a/(1+a)\right)^2$

The modulus of v_φ becomes the same as initially. Finite magnetic energy is enclosed in an arbitrarily small region, and this is connected with a kind of inversion: In the limit of zero thickness, the magnetic energy in the central rod becomes equal to that corresponding to the magnetic field initially excluded from the inner region by the shielding. The "boundary-layer" properties of the axis are not an effect of the coordinate system; the structure of the layer will certainly depend upon charge separation phenomena. With negative bias and $a>1$, magnetic field reversal will have taken place already outside the equilibrium radius, whereas smaller values of a require smaller radii.

Two sheets. The equations of motion for two equal magnetic sheets are

$\ddot{x}_1 = -x_1/4 \cdot F_1(x_1,x_2)$; $\ddot{x}_2 = -x_2/4 \cdot F_2(x_1,x_2)$, valid for $|x_1|>|x_2|$ and related expressions when the opposite inequality holds. Here

$$F_1 = \frac{[(1+a)x_1^2 - a x_2^2][(1+a)x_1^2 + a(1-a)x_2^2]}{[(1+a)^2 x_1^2 - a^2 x_2^2]^2} ; \quad F_2 = \frac{(1+a)x_1^4}{[(1+a)^2 x_1^2 - a^2 x_2^2]^2}$$

Clearly, $\ddot{x}_i$ are discontinuous for $x_1 = \pm x_2$, but x_i and $\dot{x}_i$ are continuous. The force is derivable from a potential, the equipotential lines of which are circles for a=0 but become flattened for a>0. Already for a=1 they are almost squares with vertices on the gradient discontinuity lines. The equations have been integrated in a number of cases. The solutions are sinus-like, oscillatory, with time-variable phase, amplitude and frequency. It is instructive to consider the action integrals $I_j = \int \dot{x}_j \, dx_j$, with the integration extended from the axis to an extremum or conversely.

The exchange of action (and energy) between the two oscillators becomes more pronounced as a grows. Fig.1 shows results for $x_1(0) = 1$, $x_2(0) = 0.5$, a=1. The points have been joined together with smooth curves. Two modes of variation have been found: In an asymmetric mode one or the other of the two oscillators stays at a high level of energy and action, and has about 20% higher frequency than the other (Fig.1a). There are also transitions to a symmetric mode, with a saw-teeth variation of I_1 and I_2 (Fig.1b). The oscillators are now frequency-locked, with an approximately constant phase shift, except during small time intervals around the knees of the curves, when the phase shift changes sign. The transitions between the modes appear to take place at random, but the data are insufficient to ensure this.

The Poincaré plots corresponding to $x_2=0$ show regular curves for small values of a, indicating that the system is then integrable or near-integrable (Fig.2a). Already very small values of a (.01) produce curves that extend well away from the points on the x_1-axis that results when a=0. Thus, even a minute amount of collective effects will strongly reduce the coherence found without such effects (Refs.1,2).
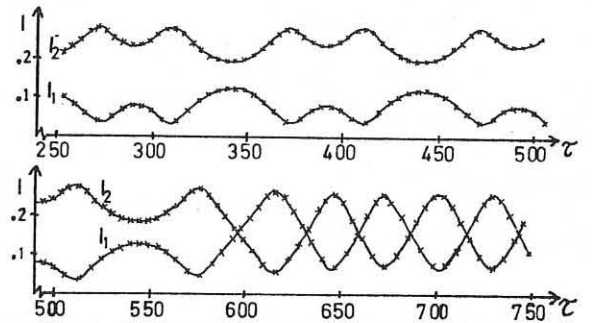

Fig.1. Action integrals versus normalized time. Fig.a shows the asymmetric mode, and b. a transition to the symmetric mode.
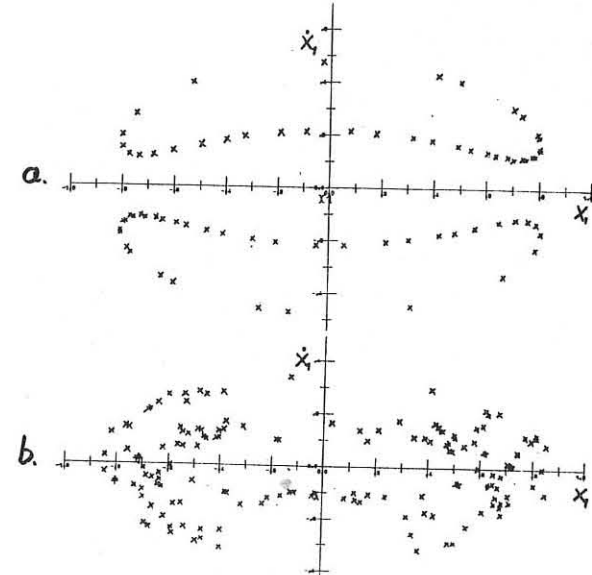

Fig.2. Poincaré plots with $x_2=0$ for the two-oscillator case with $x_1(0) = 1$, $x_2(0) = 0.5$: a.) a=0.1 ; b.) a=1

Fig 2b shows the Poincaré plot for a=1. Clearly, there is strong stochasticity, most of which occurs during the symmetric mode when the oscillators are frequency-locked.

Studies of the phase space divergence of near-by orbits have been initiated. Preliminary estimates indicate that the KS-entropy may be as high as $1/4\cdot\omega_{fast} = 1/8\cdot\omega_{gyro}$ in the symmetric mode. The asymmetric mode is less clear, but exponential growth does occur. Three-sheet calculations are underway, in order to study Arnold diffusion.

I wish to thank Mr. S. Linde for carrying out the numerical computations.

References. 1. Persson, H., to be published. 2. Krivets, V.P. and Peregood, B.P., Phys Lett. 31A (4) (1970)177, Ibid., Soviet Phys. - Techn. Phys. 16(6)(1971)928 ; 3. Wilhelmsson, H., Krivets, V.P. and Peregud, B.P., Ibid. 16(5)(1971)834 . 4. Abramova, K.B., Boshnyak, V.B., Krivets, V.P. and Peregood B.P., VII Int. Conf. Contr. Fus.& Plasma Phys., Lausanne 1-5 Sept. 1975, p.56. 5. Lovelace, R.V.,Larabee,D.A. and Fleischmann, H.H., Phys. Fluids 22(1979)701. 6. Lisak, M. private communication.

CUBIC LANGMUIR TURBULENCE

D. R. Nicholson

Department of Physics and Astronomy
The University of Iowa
Iowa City, Iowa 52242 U.S.A.

D. F. DuBois and H. A. Rose
University of California
Los Alamos National Laboratory
Los Alamos, New Mexico 87545 U.S.A.

Abstract: The properties of two statistical theories of the cubically nonlinear Schrödinger equation are considered.

1. Introduction

An important model of strong Langmuir turbulence is the Zakharov equations [1]

$$(i\partial_t + \partial_x^2)E(x,t) = n\,E \quad , \tag{1}$$

$$(\epsilon\partial_t^2 - \partial_x^2)n(x,t) = \partial_x^2|E|^2 \quad , \tag{2}$$

which are written here in dimensionless units for the one-dimensional case; usually, the parameter $\epsilon = 1$. The field $E(x,t)$ is the low-frequency envelope of the high-frequency Langmuir electric field, and $n(x,t)$ is the low-frequency density variation. Several statistical theories of these equations have been proposed [2-7].

Under certain circumstances, the time derivatives on the left of (2) can be ignored (formally, ϵ can be set equal to zero). Then (2) can be integrated in space whereupon (1) becomes the cubically non-linear Schrödinger equation

$$i\partial_t E + \partial_x^2 E + |E|^2 E - W E = 0 \tag{3}$$

where W is the spatial average of $|E|^2$. It is the purpose of this paper to discuss two possible statistical theories of (3). We do not discuss further the regime of validity of (3); this important subject has been discussed elsewhere [8,9] and deserves more work in the future.

2. Adiabatic Limit of a Statistical Theory
of the Zakharov Equations

The cubically nonlinear Schrödinger equation (3) is obtained from the quadratically nonlinear Zakharov equations (1) and (2) by taking the adiabatic limit $\epsilon \to 0$ whereupon the density becomes

$$n = W - |E|^2 \tag{4}$$

Thus, we could consider constructing a statistical theory of (3) by first constructing a statistical theory of (1) and (2), and then taking the adiabatic limit $\epsilon \to 0$. A statistical theory of (1) and (2) has been studied by DuBois and Rose [7], who apply Kraichnan's direct interaction approximation [10,11]. We have repeated their calculation, including the factor ϵ, and have then taken the adiabatic limit $\epsilon \to 0$. Some of the resulting formulas are found to differ by important factors of 2 from those to be obtained in the next section. This arises as follows. Kraichnan's direct interaction approximation [10,11] for quadratically nonlinear equations is an exact description of an associated random coupling model, provided that the initial value ensemble for the random coupling model is Gaussian. However, when $n(x)$ is related to $E(x)$ by (4) in the adiabatic limit, it is impossible to construct such an ensemble. This is the reason for the factors of 2. In the next section, we discuss an approach which avoids this.

3. Statistical Theory of the Cubically
Nonlinear Schrödinger Equation

There exists a statistical theory for cubically nonlinear equations [12-17] which is analogous to Kraichnan's direct interaction approximation for quadratically nonlinear equations; we call it the cubic direct interaction approximation. We have applied this theory to the cubically nonlinear Schrödinger equation, and have obtained the following results.

(a) The theory is realizable. It is only an approximation for (3), but it is exact for the cubic random coupling model, so that it can never yield such nonsensical results as negative energy spectra.

(b) Its spectrum has a Taylor series expansion in time which, to order t^2, is the same as that of (3) if the initial value ensemble is Gaussian. This is one of the places where the factors of 2 discussed in the previous section appear.

(c) It conserves the ensemble averages of

$$N \equiv \int dx \, |E|^2 \quad , \tag{5}$$

$$P \equiv \int dx \, (E\partial_x E^* - E^* \partial_x E) \quad , \tag{6}$$

$$H \equiv \int dx \, (|\partial_x E|^2 - \tfrac{1}{2}|E|^4) \quad , \tag{7}$$

which are conserved by each realization of (3).

(d) It correctly reduces in the small amplitude limit to the standard [1,18] weak turbulence theory of (3). This is another place where the factors of (2) discussed in the previous section enter.

4. Modulational Instability of a Narrow
Turbulent Spectrum

One of our long range goals is to compare the predictions of the various theories of cubic Langmuir turbulence with simulations of (3). As a first step in that direction we have considered a simplified model of (3) which is intended to mimic the evolution due to the modulational instability of a narrow turbulent spectrum. This will enable us to compare the various theoretical growth rates with those obtained from simulations of this model. In another publication [19], we will consider these subjects in greater detail.

References

[1] V. E. Zakharov, Zh. Eksp. Teor. Fiz. 62, 1745 (1972), [Sov. Phys.-JETP 35, 908 (1972)].
[2] V. N. Tsytovich, Zh. Eksp. Teor. Fiz. 57, 141 (1969), [Sov. Phys.-JETP 30, 83 (1970)].
[3] F. Kh. Khakimov and V. N. Tsytovich, Zh. Eksp. Teor. Fiz. 68, 95 (1975), [Sov. Phys.-JETP 41, 47 (1975)].
[4] A. A. Galeev, R. Z. Sagdeev, Yu. S. Sigov, V. D. Shapiro, and V. I. Shevchenko, Fiz. Plazmy 1, 10 (1975), [Plasma Phys. 1, 5 (1975)].
[5] G. Pelletier, J. Plasma Phys. 24, 287 (1980).
[6] G. Pelletier, J. Plasma Phys. 24, 421 (1980).
[7] D. F. DuBois and H. A. Rose, "Statistical Theories of Langmuir Turbulence I: Direct Interaction Approximation Responses", submitted to Phys. Rev. A, 1981.
[8] S. G. Thornhill and D. ter Haar, Phys. Rep. 43, 43 (1978).
[9] L. I. Rudakov and V. N. Tsytovich, Phys. Rep. 40, 1 (1978).
[10] R. H. Kraichnan, Phys. Rev. 113, 1181 (1958).
[11] R. H. Kraichnan, J. Fluid Mech. 5, 497 (1959).
[12] J. B. Morton and S. Corrsin, J. Stat. Phys. 2, 153 (1970).
[13] H. A. Rose, Ph.D. thesis, Harvard University, 1974.
[14] U. Deker and F. Haake, Phys. Rev. A11, 2043 (1975).
[15] U. Deker and F. Haake, Phys. Rev. A12, 1629 (1975).
[16] S. Gauthier, M. E. Brachet, and J. D. Fournier, "Field Theoretic Schemes for a Classical Cubic Equation with Stochastic Driving", preprint, 1981.
[17] P. J. Hansen and D. R. Nicholson, Phys. Fluids 24 (1981, in press).
[18] S. B. Pikelner and V. N. Tsytovich, Zh. Eksp. Teor. Fiz. 55, 977 (1969), [Sov. Phys.-JETP 28, 507 (1969)].
[19] D. F. DuBois, D. R. Nicholson, and H. A. Rose, "Statistical Theories of Langmuir Turbulence II: Theories of Cubic Langmuir Turbulence", in preparation.

SPATIALLY-TIME EVOLUTION OF FAST MAGNETOSONIC
WAVES OF HIGH AMPLITUDE

V. V. CHECHKIN, V. V. DEMCHENKO, V. E. D'YAKOV,

L. I. GRIGOR'EVA, V. I. PANCHENKO, A. V. PASHCHENKO,

B. I. SMERDOV

INSTITUTE OF PHYSICS & TECHNOLOGY,
UKR. ACAD. SCI., KHARKOV, USSR

In paper [1] by means of numerical integration one-dimensional magnetosonic waves of finite amplitude propagating along a radius of cylindrical plasma wavegude across static magnetic field became the subject of study. It was shown that in the course of time a profile of a propagating wave acquired the form of a solitary wave train with increasing amplitude.

In this report, in accordance with paper [1], the dynamics of FMS-waves of high amplitude was investigated analytically and numerically, the waves propagating in a homogeneous plasma waveguide at an angle to B_0. We consider the plasma gas-kinetic pressure to be low, as compared to magnetic field pressure, and suppose the frequency of excited FMS-wave Ω to be within $\omega_{ci} < \Omega < \sqrt{\omega_{ci}\omega_{ce}}$. For describing plasma dynamics in this case, use could be made of hydrodynamics equations with an addition of field equations. As a rule [2], in experimental conditions a longitudinal wave number of excited oscillations κ_z is much lower than $\kappa_\perp \sim a^{-1}$ (a — column radius), that allowing to use perturbation method while analyzing the results. To a zero approximation on the parameter $t = \kappa_z / \kappa_\perp$, plasma motion is one-dimensional and is described in Lagrange variables by the equations:

$$\frac{\partial^2 x}{\partial v^2} = -2 x h \frac{\partial h}{\partial a} + 4 x \left(\frac{\partial h}{\partial a}\right)^2, \quad \frac{\partial}{\partial v}\left(\frac{\partial x}{\partial a}\right) = 0, \quad (1),(2)$$

$$\frac{\partial}{\partial v}\left[h \frac{\partial(x^2)}{\partial a} - 4 \frac{\partial}{\partial a}\left(x^2 \frac{\partial h}{\partial a}\right)\right] = 4 v^* \frac{\partial}{\partial a}\left(x^2 \frac{\partial h}{\partial a}\right), \quad (3)$$

where v^* is the frequency of electron-ion collisions, $h = H/H_0$, $v = t(v_A \omega_{pe}/c)$, $x = r\omega_{pe}/c$. Equations (1)-(3) describe plasma radial motions at prescribing both the initial ($v = 0$) and boundary ($r = r_0$) conditions. In the first case the variable a is determined by the equation $da = r_0 n^{(0)}(r_0) dr_0$, in the second one — by $da = r(v_0) n^{(0)}(v_0) U(v_0)$, where r_0 and v_0 are initial values of a coordinate and time, $n = N / N_0$ — the density, $U = \frac{u}{v_A}$ — is plasma mass velocity. From eqns (1)-(3) in variables (r_0, v) we find solutions which take into account density and magnetic field distributions at an initial moment of time. In variables (v_0, v) solutions are determined by conditions at plasma column boundary. Let us notice that solutions of the sustem (1)-(3) parametrically depend on axial coordinate z, because of prescription of boundary conditions depending on z.

Analytical solution for eqns (1)-(3) could be find while using homogeneity property of these equations relative to variablers x and h. Assuming collision frequency to be a low one and $h(v,a) = T(v) S(a)$, $x = v(v) s(a)$, we derive from (1)-(3):

$$v^2 T(v) = c_1, \quad T(v) = \frac{c_2}{c_3(v - v_0)^2 \pm 1}, \quad (4)$$

where c_i ($i=1,2,3$) are constant values; minus complies with wave travel to the center, plus — from the centre.

For coordinate functions S, s we have the set of equations:

$$2(1 + v^*/D)(s^2 S')' = ss' S, \quad 2(s')^2 - ss' = B, \quad (5),(6)$$

where B and D are separation constants.

Numerical solution of eqns (1)-(3) was performed under the assumption that the magnetic field on the boundary of plasma column was changed according to the low: $h = 1 + A \sin(\kappa_z z) \sin v(1 - e^{-\frac{v}{v^*}})$, where $A = const$, $\Omega^* = \Omega\left[\frac{e B_0}{c\sqrt{\omega_{ce}\omega_{ci}}}\right]^{-1}$; a plasma is assumed to be a collisionless one. Fig. 1 shows spatially-time evolution of nonlinear FMS-wave under the fixed z. In the course of time, as the wave approaches the center, it is observed the release of a solitary pulse, the amplitude of which substantically rises at a simultaneous decrease of width. The time evolution of an amplitude of FMS-wave in point $r = a / 3$ at various z values, presented in fig. 2, is in accordance with the process of forming single pulse given in fig. 1. The results of numerical analysis are in qualitative agreement with the data obtained from experimrnts on the excitation of high-amplitude FMS-waves [2], that following from comparison of the graphs given in figs 1 and 2 of this work with the graphs of figs 4 and 5 of paper [2].

REFERENCES.

1. Yu. A. Berezin. Prikl. Mech. & Tech. Fiz. (USSR), No. 1, p. 107, 1966.

2. A. S. Bakai, V. A. Bashko, L. I. Grigor'eva et al. 8th IAEA Conference, Brussels, 1980, Book of Abstracts

REPORT CN-38/Z-5, p. 214.
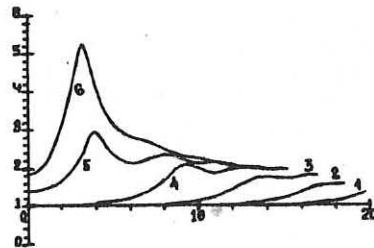
Fig. 1 Spatially-time evolution of nonlinear FMS-wave ($k_z z = 1.57$) 1) $v=3$, 2) $v=6$, 3) $v=9$, 4) $v=12$, 5) $v=15$, 6) $v=18$
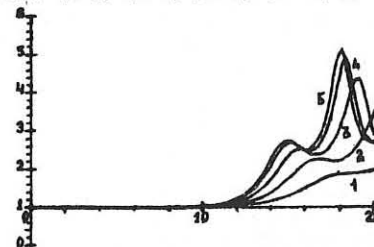
Fig. 2 Time evolution of FMS-wave at point $r=a/3$ 1) $k_z z = 0.00$, 2) $k_z z = 0.26$, 3) $k_z z = 0.52$, 4) $k_z z = 0.78$, 5) $k_z z = \pi$

LONG-TIME SBS OSCILLATIONS IN PLASMAS
WITH SUPERSONIC FLOW

K. Baumgärtel, K. Sauer and D. Sünder

Zentralinstitut für Elektronenphysik,
Akademie der Wissenschaften der DDR, Berlin, DDR

Abstract

Theoretical evidence of long-time oscillations of Stimulated Brillouin Backscatter from an underdense plasma with supersonic flow and a reflecting boundary is reported. For typical parameters of laser-plasma experiments the oscillation period is $\omega_s T \simeq 150$ where ω_s is the ion-sound frequency belonging to $2k_0$. Long-time SBS oscillations may be responsible for the observed burst-like behaviour of higher harmonic spectra /1-3/.

Theoretical background

In paper /4/ it was pointed out that a partially reflecting boundary can strongly influence the SBS by enhancement of the effective noise level. In this paper we study the temporal evolution of SBS in flowing plasmas and show that double reflection at both the boundaries and zero-frequency density perturbations can cause long-time SBS oscillations. Different levels of description are used: the full SBS equations and their reductions to mode-coupling equations.

1. Full SBS equations: The process of SBS is described by the standard system consisting of (1) the HF wave equation in modulational representation and (2) the fluid equations including the ponderomotive force term:

$$2i\alpha \frac{\partial A}{\partial t} + \frac{\partial^2 A}{\partial x^2} + \varepsilon A = 0 , \qquad (1)$$

$$\beta \frac{\partial n}{\partial t} + \frac{\partial}{\partial x}(nu) = 0, \quad \beta \frac{\partial u}{\partial t} + u \frac{\partial u}{\partial x} + \frac{1}{n} \frac{\partial n}{\partial x} = -\frac{1}{4} \frac{\partial}{\partial x} |A|^2 . \quad (2)$$

In these equations, A is the ratio of electron quiver velocity to electron thermal velocity, u is the fluid velocity normalized by the ion-sound velocity v_s and n is the plasma density; t and x are normalized by the ion-sound frequency $\omega_s = k_s v_s$ ($k_s = 2k_0 \sqrt{\varepsilon}$) and the vacuum wave number k_0, resp. Further, the following notations are used:

$$\alpha = 2\sqrt{\varepsilon} \, v_s/c \, , \quad \beta = 2\sqrt{\varepsilon} \, , \quad \varepsilon = 1 - n/n_c \, ,$$

where n_c is the critical density.

2. Linearized hydrodynamic theory: In a first step of approximation, small perturbations of the hydrodynamic quantities are assumed ($n/n_0 = 1 + \tilde{n}$, $u = M + \tilde{u}$ with $\tilde{n} = \delta n/n_0 \ll 1$, $\tilde{u} = \delta v/v_s \ll 1$; $M = v_0/v_s$ is the Mach number of the plasma flow).

3. Separation of "fast" spatial oscillations: According to the assumption that the Brillouin instability is localized at $k_s = 2k_0\sqrt{\varepsilon}$, the following representations can be used:

$$A(x,t) = A_+(x,t) e^{ikx} + A_-(x,t) e^{-ikx} , \quad k = \sqrt{\varepsilon} ,$$

$$\tilde{u}(x,t) = \text{Re}\left[p(x,t)e^{2ikx}\right] , \quad \tilde{n}(x,t) = \text{Re}\left\{q(x,t)e^{2ikx}\right\} .$$

As result, a coupled system of partial differential equations for the "slowly" varying amplitudes A_+, A_-, p and q is obtained.

4. Mode-coupling theory: In this approximation, temporal oscillations according to the dispersion relation of ion acoustic waves in flowing plasmas with $k = k_s$ are separated. With

$$A_- = i\tilde{A}_- \, e^{i(1+M)t}, \quad p = \tilde{p} e^{-i(1+M)t}, \quad q = \tilde{q} e^{-i(1+M)t}$$

we get the mode-coupling equations

$$\frac{\partial A_+}{\partial x} = -C \, \tilde{q} \, \tilde{A}_- , \quad \frac{\partial \tilde{A}_-}{\partial x} = -C \, \tilde{q} \, A_+ , \quad C = \frac{-1}{4\sqrt{\varepsilon}} \cdot \frac{n_0}{n_c} ,$$

$$\frac{\partial \tilde{q}}{\partial t} + \frac{(1+M)}{\beta} \frac{\partial \tilde{q}}{\partial x} = -\frac{1}{4} A_+ \tilde{A}_-$$

(time derivatives in the equations for A_+, $\tilde{A}_-$ neglected).

5. Plasma model and parameters: As initial state, an underdense homogeneous plasma layer covering the fixed region (0,L) is assumed. The supersonic flow is directed towards the incident radiation. The hydrodynamic perturbations at x=L are assumed to be zero. The parameters of our calculations are. $n_0/n_c = 0,3$, M=-2, L= $25\lambda_0$ ($\lambda_0 = 2\pi k_0/c$), incident field amplitude $A_0 = 0,3$.

Results and discussion

Fig. 1 shows results obtained by numerical solution of the full SBS equations. Besides of oscillations with ω_s, the reflection coefficient undergoes long-time oscillations with a period of $T \simeq 150 \omega_s^{-1}$. Both minimum and maximum reflectivity are characterized by typical spatial structures of electric field and plasma density (Fig. 1b-e). At mini-

mum reflectivity the density disturbance is seen to be composed of two separated phase-shifted parts whose scattering contributions match approximately to zero. In this case, the perturbed density profile acts as a resonator with a slightly enhanced field (Fig. 1d,e). Such configuration is created by the combined action of both the supersonic flow and a reflecting boundary. The mechanism is understood in the following way: owing to causality reasons, the evolution of SBS in the case of supersonic flow is sensitive to the conditions at the right boundary. A reflecting right boundary may strongly influence the temporal evolution of SBS when a portion of scattered radiation can reach it via reflection at zero-frequency density disturbances or at the left boundary. This part of scattered radiation is the source of phase-shifted density disturbances which penetrate into the plasma from the right boundary and compensate the SBS contributions from the region near the left boundary.

Long-time oscillations appear in all approximations in which the ion-acoustic dynamics is treated in second order in time (sec. 1-3), even without a second left boundary. Mode-coupling theory gives oscillating SBS when two reflecting boundaries are taken into account. Fig. 2 shows solutions, where the boundary condition

$$\tilde{A}_-(L) = f \, \tilde{A}_-(0)$$

with a reflection factor f= -0,01 has been used. The change in the sign of $\tilde{q}$ (Fig. 2c) indicates phase-shifted contributions of the density disturbance. $|R|^2 = 0$ is equivalent to $\int_0^L \tilde{q}(x)dx = 0$.

References

/1/ P.A. Jaanimagi et al., IEEE transactions on plasma
science Vol. PS-7, 166 (1979)

/2/ N.E. Andreev et al., Pisma Zh.Eksp.Teor.Fiz. 31 639
(1980)

/3/ P.D. Carter et al., Phys.Rev.Lett. 44 1407 (1980)

/4/ C.J. Randall et. al., Phys.Rev.Lett. 43 924 (1979)
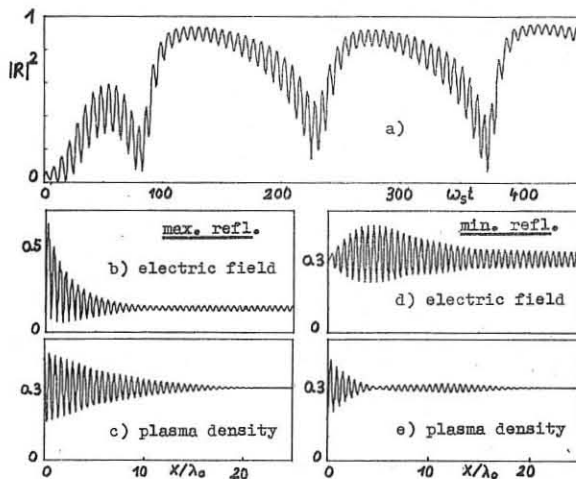
Fig. 1: Results of full SBS theory, sec. 1.
a) Time-evolution of $|R|^2$, b) - e) spatial structures.
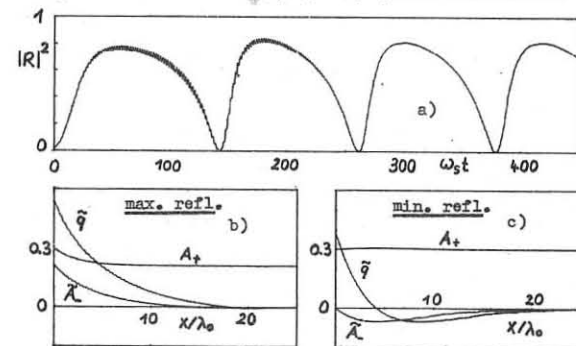
Fig. 2: Results of mode-coupling theory, sec. 4.
a) Time-evolution of $|R|^2$, b) + c) spatial structures.

RESONANCE ABSORPTION OF A STRONG EM WAVE AT SUPERSONIC PLASMA FLOW

N.E.Andreev, A.M.Sergeev, A.M.Feygin

Institute of Applied Physics, Academy of Sciences

of the USSR, Gorky, USSR

Recently there has been growing interest in theoretical studies of nonlinear processes which develop as laser radiation interacts with a plasma corona. At present more emphasis is placed on the influence of striction deformation of a plasma profile on the efficiency of resonance absorption of an EM wave. A possible approach to the analysis of the problem is associated with the use of a stationary model of the interaction of powerful EM radiation with an inhomogeneous plasma layer [1]. Simplicity and obvious results are not the only advantage of this model. Presently there is evidence for realizability of a stationary pattern of striction deformations occurring in the inhomogeneous plasma in the external quasi-static field [2]. Moreover, recent numerical studies of the dynamics of powerful EM wave absorption in a supersonic plasma flow [3] suggest that the system can arrive at a quasi-stationary regime with the resonance absorption coefficient slowly varying near some mean value.

The goal of the contribution is to study the stationary regime of resonance interaction of EM waves with a plasma moving with supersonic velocity.

The stationary approach assumes the presence of inhomogeneous plasma density profiles N and the plasma flow velocity u in the absence of an external EM wave. In the case of a supersonic plasma flow this condition is readily met for the spherically symmetrical model given by

$$(u^2 - u_c^2)/2 + \ln N/N_c = 0, \quad N u R^2 = N_c u_c R_c^2, \quad (1)$$

where u is the hydrodynamic velocity normalized to the sonic velocity; N_c, u_c, R_c are the plasma parameters at the critical point. Taking into account the ponderomotive action of a hf wave having the electric field $\vec{E} = \frac{1}{2}\{\vec{E} \exp(i\omega_0 t) + c.c\}$ the particle density is described by the equation

$$\frac{u_c^2}{2}\left[\frac{R_c^4 N_c^2}{R^4 N^2} - 1\right] + \ln \frac{N}{N_c} = -\frac{|\varepsilon|^2}{E_p^2} \quad (2)$$

$E_p^2 = 16\pi N_c(T_e + T_i)$ is the characteristic "plasma field" of collisionless nonlinear effects.

Further we shall use a simplified model assuming that the profile deformations are not too great and expanding the left-hand side of Eq. (2) over the smallness parameters $z = \frac{R}{R_c} - 1 \ll 1, \alpha = \frac{N}{N_c} \ll 1$. In this approximation an EM wave near the resonance region can be considered plane thus described by the known equation for the complex amplitude of a hf magnetic field $\vec{H} = \frac{1}{2}\{\frac{\mathcal{H}(k_0 z)}{E_p}\exp(i\omega_0 t - ihx) + c.c\}\vec{x}\vec{1}\vec{R}$

$$\mathcal{H}'' - \frac{\varepsilon'}{\varepsilon}\mathcal{H}' + (\varepsilon - \sin^2\theta)\mathcal{H} = 0, \quad (3)$$

where $\varepsilon = \alpha - i\mu$ is the dielectric permittivity of a cold plasma, $k = \frac{\omega_0}{c}, \sin\theta = \frac{h}{k_0}$. Equation (3) together with the relation for the real part of dielectric permittivity

$$(\alpha^2 + \mu^2)\left(\overline{R_c}\frac{u_c^2 - 1}{2u_c^2}\alpha - z\right) = -\frac{\overline{R_c}}{2u_c^2}\left(|\mathcal{H}|^2 + \sin^2\theta|\mathcal{H}|^2\right), \quad (4)$$
$$\overline{R_c} = k_0 R_c$$

comprises a complete system for the investigation of the interaction between an intense EM wave and a supersonic plasma flow.

Before passing over to the results of numerical integration (3)-(4) consider the dependence $\alpha(z)$ for the fixed values of tangential components of EM fields $\mathcal{H}_t \sim \mathcal{H}$ and

$E_t \sim \frac{\mathcal{H}'}{\varepsilon}$. Similarly for $E_t = 0$ the relation (4) was studied in [4] for determination of the dielectric permittivity of an isotropic plasma for the given electric displacement ($D \sim \mathcal{H}$). Specifically, it was shown that with the excess over some critical value $\mathcal{H} > \mathcal{H}_c$ the dependence $\alpha(z)$ becomes ambiguous and the transition from one branch to another corresponds to the parameter jump. In the presence of the additional factor $E_t \neq 0$ the coordinate of the jump is shifted. However, the statement on the possible ambiguity of the solution remains valid. Thus, for obtaining the jump the presence of the longitudinal component of the electric field $E_t \sim \mathcal{H}/\varepsilon$ is of principle.

In Fig.1 the characteristic structure of electric field and the deformed plasma density profile obtained are shown for $u_c = 2$, $\overline{R_c} = 80$ (the characteristic scale of the density inhomogeneity at the critical point $L \sim 30 k_0^{-1}$), $\sin^2\theta = 0.05$. For comparison in Fig.2 a similar pattern is given which is realized in a dynamic numerical model (note that for a neodymium laser the corresponding energy flows reach the value $2 \div 5 \; 10^{14} \; W/cm^2$).

The dependence of the absorption coefficient on the incident radiation flow is represented in Fig.3 for the parameters $u_c = 2$, $\overline{R_c} = 80$, $\mu = 10^{-3}$, $\sin^2\theta = 0.05$.

Note that the electrodynamic problem which lies in the solution of Eqs. (3)-(4) before and after the jump and meeting the relevant boundary conditions has a solution only up to a certain value of the incident energy flow [5]. This eliminates a possibility of matching the solutions at the "jump". Stress that the region of existence of stationary solutions diminishes with decreasing $k_0 L$.

This result enables one to assume that the quasi-static regime of plasma-wave interaction will break with the increase in power of the radiation flow in the nonstationary problem. This can lead to an essential redistribution of the absorbed energy between thermal and hot electrons.
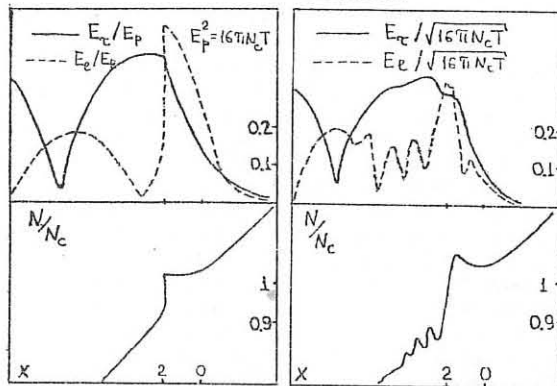
Fig.1

Fig.2
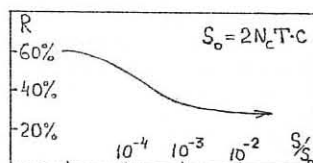
Fig.3

1. V.B.Gil'denburg, A.G.Litvak, A.M.Feygin, Fizika plazmy, 7, No.2, 198
2. A.Y.Wong. In: Laser Interaction and Related Plasma Phenomena, 4B, p.409, Plenum Press, 1978.
3. N.E.Andreev, V.P.Silin, G.L.Stenchikov. In: Interaction of Strong Electromagnetic Waves with Collisionless Plasma, p.156, Gorky, Institute of Applied Physics of AS USSR, 1980.
4. V.B.Gil'denburg, ZhETF, 46, 2156, 1964.
5. Ya.L.Bogomolov, A.M.Sergeev, Fizika plazmy, 7, No.3, 1981.

RAMAN BACK-SCATTERING IN AN INHOMOGENEOUS PLASMA

K. Baumgärtel, K. Sauer, D. Sünder

Zentralinstitut für Elektronenphysik,
Akademie der Wissenschaften der DDR, Berlin, DDR

Introduction

Recently experimental evidence was given for radiation at half the pump frequency ω_0 at laser-plasma interaction [1]. While radiation at three halves of the laser frequency can be attributed to both Raman scattering and two-plasmon-decay the $\omega_0/2$-radiation is directly produced only by Raman scattering. The paper draws attention again to the latter process and presents results concerning the growing period of the Raman instability in an inhomogeneous plasma.

Equations

The approach is mainly numerical and starts from a one-dimensional hydrodynamic plasma description. The basic equations are

$$2i\omega_L \frac{\partial E_L}{\partial t} + 3v_T^2 \frac{\partial^2 E_L}{\partial x^2} + (\omega_L^2 - \omega_p^2)E_L = \frac{v_E}{2}\frac{\omega_p^2}{\omega_T}\frac{\partial E_T^*}{\partial x}$$

$$2i\omega_T \frac{\partial E_T}{\partial t} + c^2 \frac{\partial^2 E_T}{\partial x^2} + (\omega_T^2 - \omega_p^2)E_T = -\frac{v_E}{2}\omega_T \frac{\partial E_L^*}{\partial x}$$

$$2i\omega_{TH} \frac{\partial E_{TH}}{\partial t} + c^2 \frac{\partial^2 E_{TH}}{\partial x^2} + (\omega_{TH}^2 - \omega_p^2)E_{TH} = \frac{v_E}{2}\omega_{TH}\frac{\partial E_L}{\partial x}$$

E_L, E_T, E_{TH} are the slowly time-varying amplitudes of the longitudinal (L-), the transverse (T-) and the three-halves (TH-) wave, respectively (normalized by $m\omega_0 c/e$). v_E is the pump quiver velocity, v_T is the electron thermal velocity. The frequency matching conditions are

$$\omega_0 = \omega_L + \omega_T, \quad \omega_{TH} = \omega_0 + \omega_L$$

(ω_0 - pump frequency). The second-order space derivatives are kept in the equations, that is, no use is made of the WKB approximation. Landau damping of the L-wave is included via an additional factor $(1+0,25i(\omega_L^2/\omega_p^2-1))^{-1}$ at v_T^2 as long as $\omega_L/\omega_p > 1$. A linear density profile is taken which varies from zero to about half of the critical density. The system has been solved by standard discretization schemes for a variety of parameter combinations v_E/c, v_T/c and L (density gradient scale length). A small initial field E_L is assumed to be present.

Results

Fig. 1 shows (a) the time evolution of the instability for a typical parameter set ($v_E/c=0,1$, $L/\lambda_0 = 50$; λ_0 pump vacuum wave length, $v_T/c= 0,05$) and (b) the spatial structure of the wave fields at $\omega_0 t = 500$. The "absolute" nature of the instability is obvious. The growing decay waves are confined to particular frequencies near $\omega_0/2$, independently of the frequency of the initial field. The shift against $\omega_0/2$ depends on the parameters. The L- and the TH-wave are generated in forward direction. After total reflection at its turning point the L-wave is Landau damped away before reaching the boundary. The backward generated T-wave is emitted into vacuum. The curves indicate that the instability operates in a narrow space region immediately adjacent to a quarter of the critical density towards lower density. Fig. 2 shows the growth rate γ as function of the pump intensity for different L. White et al. [2] predict somewhat higher growth rates, but both the plasma inhomogeneity and the Landau damping is treated in a too rough way in their calculations. Fig. 3 demonstrates the influence of the electron temperature on the frequency shift of the T-wave (a) and on the growth rate (b). Note the sharp drop of γ at $v_T/c \approx 0,15$. The frequency shift changes its sign with growing temperature. It turns from blue-shift to red-shift. The L- and the TH-wave have opposite shifts. These results are in good agreement with a WKB-

treatment (Fig. 4a). It predicts an absolute instability if both the mismatch of the wave vectors and its spatial derivative vanish [3,4]. Fig. 4b shows at which density the combined matching condition is fulfilled for different temperatures. This curve helps to interpret the drop of γ in Fig. 3b: as more the operation regime of the instability is shifted towards lower density, as more Landau damping of the up-shifted L-wave comes into play. Fig. 5 supports this view; it shows spatial profiles of both the L- and T-wave ($v_T/c = 0,2$, $L/\lambda_0 = 50$, $v_E/c= 0,1$). In contrast to Fig. 1, we see here a standing wave structure of the L-wave which indicates a significantly left-shifted operation region of the instability.

In addition the equations were solved with reflected pump wave. The effect was (i) a jump in the growth rate approximately by a factor $\sqrt{2}$ and (ii) a strong spatial modulation of the L-wave according to the standing wave pattern of the pump wave.

Also pump depletion due to the back action of the decay waves on the pump has been included. The instability saturates but the saturation levels turned out to be too high. Thus, saturation due to non-linear wave interaction is not effective enough to produce acceptable levels.

References

[1] Rutherford Lab. Report RL 8-80-026 (1980)

[2] R. White, P. Kaw, D. Pesme, M.N. Rosenbluth, G. Laval, R. Huff, R. Varma, Nuclear Fusion 14, 45 (1974).

[3] A.D. Pilia, Proc. of 11-th Conf. on Phenomena in Ionized Gases, Oxford, 320 (1971).

[4] M.N. Rosenbluth, Phys. Rev. Lett., 29, 565 (1972).

Fig. 1a $|E_L|_{max}$ $|E_T|_{max}$ $|E_{TH}|_{vacuum}$ $|E_T|_{vacuum}$

Fig. 1b $|E_L|$ $|E_T|$ $|E_{TH}|$

Fig. 2

Fig. 3

Fig. 4

Fig. 5
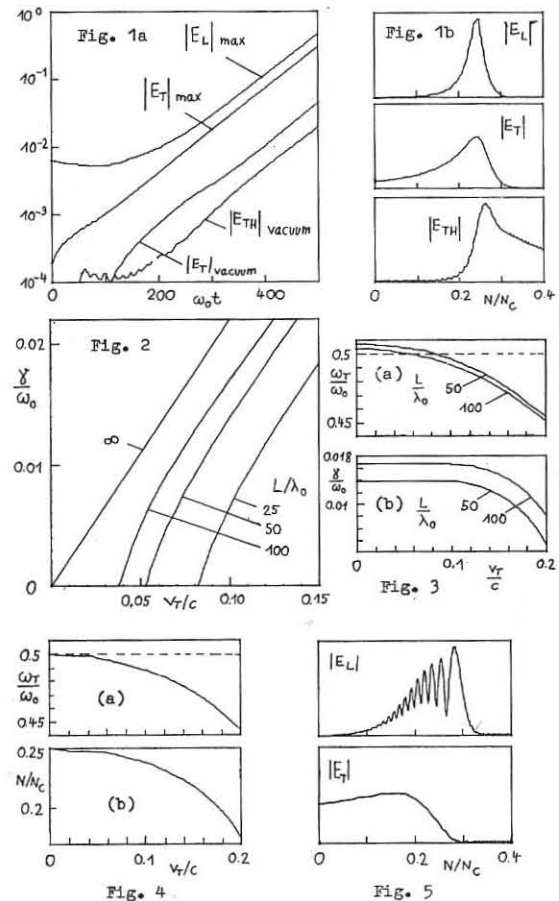
L

COMPACT TORI AND TOROIDAL PINCHES

EFFICIENCY AND PHYSICS OF COLLISIONLESS PLASMA HEATING
BY SHOCK COMPRESSION IN A CLOSED TRAP "COMPACT TORUS"

A.G.Es'kov, R.Kh.Kurtmullaev, Ya.N.Laukhin, A.I.Malutin, A.I. Markin, Yu.S.Martushov, O.L.Rostovtsev, V.N.Semenov, Yu.B.Sosunov

I.V.Kurchatov Institute of Atomic Energy, USSR

Generation and heating of compact toroid (CT) by an axial shock compression is the principal approach of the Soviet CT program [1]. It provides high efficiency of heating and is found to be one of the factors stabilizing CT [2].

1. The experiments have been carried out in a device with diameter $2r_w=40$ cm and magnetic field $B_{max}=11$ kG. Dynamics of the process is illustrated by the signals from a set of diamagnetic loops (Fig.1). The signal $D=B_e-\frac{1}{r_w^2}\int_0^{r_w}2B(r)rdr=B_e-\bar{B}$. The regime without crowbar (the 2nd half-cycle) is given. The process includes the following stages: reversal (1), establishment of a radial equilibrium ($D=D_{eq}$), the pulsed triggered reconnection, formation of a poloidal piston ($\tau\lesssim 10^{-6}s$) and a longitudinal plasma ploughing (2), an axial shock wave generation (3), its cumulation at the midplane (4), relaxation and the establishment of equilibrium (5). The relaxation time is $\tau\sim(2-3).10^{-6}s$.

2. The neutron yield (up to 5.10^7) correlates with the diamagnetic jump ratio D_{max}/D_{eq} (Fig.2). The temperature T_i found from the neutron radiation (1), as well as the sum T_i+T_e derived from the diamagnetic signals and a known density (interferometer) at two cross-sections: z=50 cm (2) and z=68 cm (3) are shown in Fig.3. The electron temperature T_e (4) found from the X-ray measurements by the method of foils is also shown. Comparison with T_i demonstrates a prevaling role of the shock heating. Oscillograms of impurity lines C1V (1) and CV (2) are shown in Fig.4. With the arrival of a shock wave (t=10mks) an abrupt decrease in the C1V intensity and an increase in the intensity of CV are observed. A downstream electron temperature $T_{e2}=180$ eV and an initial temperature in the neutral layer $T_{e1}=80-100$ eV have been determined from the observed time dependance of line intensities.

3. An evolution of $f_i(E)$ at the stage of compression is observed by a 9-channel neutral analyzer. A super-maxwellian high energy region E>0.8-1 keV appearing before arriving the main hydrodynamic perturbation, is registered together with the core of low energy particles (T=130-200 eV). A difference between the distribution function observed and the Maxwellian one for three instants corresponding to the initiation, development and to the completion of the shock process, is shown in Fig.5. The final shape of the distribution function is shown in Fig.6. A rise in the average energy of ions correlates with the shock front (Fig.7a). During this time interval the maxwellization occures (Fig7b). (ΔW is a rms deviation of the signals from the Maxwellian distribution curve). The results shown in Figs.5-7 correspond to the hydrogen plasma and $B_{max}=7$ kG. Comparison with the main regime ($B_{max}=11$ kG) confirm the expected scaling: $T\propto B^2$.

4. The time of ion-ion collisions $\tau_{ii}=1.5\cdot10^6\frac{T_i^{3/2}}{n}\sqrt{\frac{m_i}{m_p}}=30\mu s$ (n=$2\cdot10^{15}cm^{-3}$) exeeds the relaxation time by the order of magnitude. A collisionless thermalization obtained in these experiments gives physical grounds for extrapolating the applied method of heating up to the fusion parameters.

5. Observations show that the shock flow is accompanied by emergence of plasma streams running in the direction of shock compression with the double piston velocity $V_{||}=2V_p$. The accelerated flows are registered by a He-Ne interferometer (Fig.8). Characteristic pecularities (3) observed at the leading and trailing edges of a density pulse (Fig.8a) correspond to the particles running in front of the piston and from the opposite end. The dashed lines (1) represent the motion of the shock front, diamagnetic signal maximum and the piston. Thus, the characteristic energy acquired by ions corresponds to $2V_p$. This fact explains the relation between the final temperature (~1 keV) and the value $m_iV_p^2/2$.

6. After the axial compression the plasma parameters vary smoothly (adiabatically) in accordance with a variation in the external field. The curve 1 in Fig.9 shows the measured $\int ndl$, the dashed line (2) represents the same value calculated from the known initial density $n_o=2.3\cdot10^{14}$ cm^{-3} and from the CT geometry $r_s(t)$, $L_s(t)$. A good confinement of particles inside a separatrix is observed.

Thus, a high efficiency of the axial shock heating (T= 1 keV, rise time of shock field T/4=10 mks) is shown in this paper, some regularities in the development and relaxation of the shock flow are studied.

REFERENCES

1. A.G.Es'kov et al. 6th Europ. Conf. on Contr. Fusion and Plasma Phys., Moscow, 1973, p.599.

2. A.G.Es'kov et al. 7th International Conf. on Plasma Phys. and Contr. Nuclear Fus. Res., Innsbruck, 1978. IAEA-CN-37-U-4-1, 2, 1978, p.187.

Fig.1

Fig.3

Fig.4

Fig.5

Fig.2

Fig.6

Fig.8

Fig.9

Fig.7
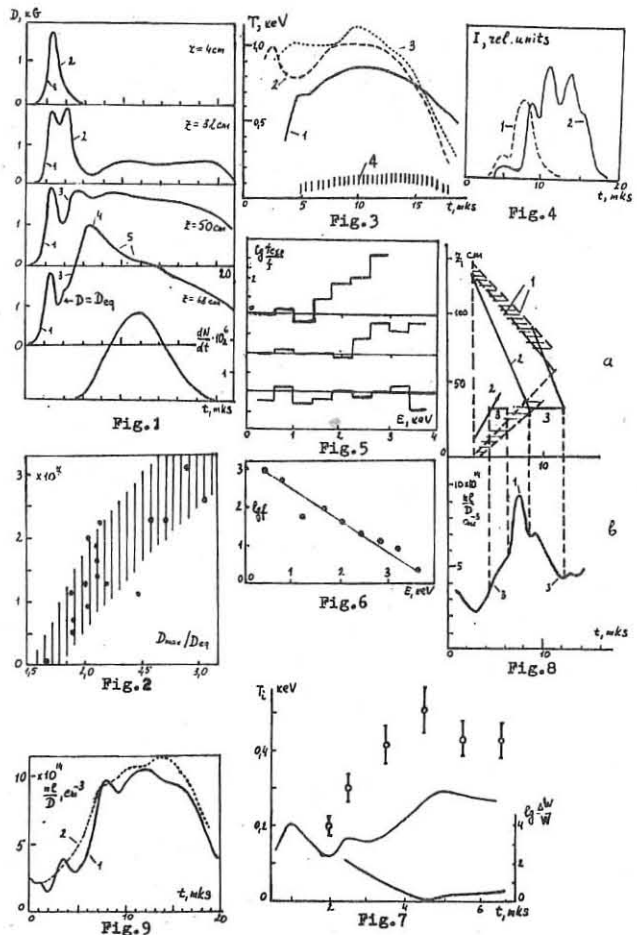
INITIAL RESULTS FROM THE HBTXIA
REVERSED FIELD PINCH EXPERIMENT

P G Carolan, L Firth, C W Gowers, G C H Haywood,
I H Hutchinson, A A Newton, V A Piotrowicz*,
M R C Watts, P D Wilcock and H A B Bodin

Culham Laboratory, Abingdon, Oxfordshire, UK
(Euratom/UKAEA Fusion Association)

*Oxford Polytechnic, Oxford, UK

ABSTRACT   Reversed field pinch plasmas with low fluctuation levels
have been set up using self reversal on its own and assisted by B_ϕ
field control at currents up to 300kA. The current and field rever-
sal are sustained for up to 5ms. The resistivity and density vari-
ations are discussed.

INTRODUCTION   The objective of HBTXIA (R/a = 0.8/0.26m, I = 400 -
500kA, pulse length = 5 - 10ms, rise time = 0.1 - 2.0ms) is to study
RFP [1] distributions set up with a slowly rising current using the
plasma self reversal effect assisted by external B_ϕ field control in
a metal walled toroidal vessel. It has been shown previously, origi-
nally in Zeta [2] and then on Eta Beta II [3] and TPE-1R(M) [4], that
confinement with T_e > 100eV can be obtained at currents of a few hun-
dred kA in such systems, which now include ZT-40(M) [5]. The minor
radius of HBTXIA is about twice that of Eta Beta II and TPE-1R(M) and
somewhat more than that of ZT-40(M). Here we report the results of
preliminary experiments using electrical measurements, an HCN laser
interferometer and a visible radiation spectrometer.

DESCRIPTION OF MACHINE [6,7,8]   The capacitor bank system using 8
and 40kV units of total energy 2.25MJ, is a flexible arrangement with
B_ϕ field control and power crowbars for both I_ϕ and I_θ circuits. The
vacuum vessel is of stainless steel bellows 0.3mm thick and has 42
pumping and diagnostic ports. The stabilising shell is of aluminium
alloy 25mm thick and split in the ϕ and θ directions. The B_ϕ wind-
ings, mounted directly on the shell, comprise 16 sets of 8 turns and
the I_ϕ windings, supported by the shell, are in 12 sets of 5 turns,
giving turns ratios from 5:1 to 60:1. The I_ϕ windings are displaced
inwards 40mm with respect to the concentric liner and shell. A 1Vs
iron core is used. Liner baking in situ at 150°C and glow discharge
cleaning [9] with a single electrode at 1A have been used. A biased
filament aids initial breakdown.

RESULTS IN DIFFERENT OPERATING MODES   Several modes of setting up
and sustaining distributions have been studied using different arran-
gements of the I_ϕ and B_ϕ circuits. These include self reversal on
its own (Zeta mode) and two variants of 'assisted reversal' in which
a negative B_ϕ is applied externally to control the evolution of the
discharge. In the Zeta mode the B_ϕ coils are short circuited to con-
serve toroidal flux after an initial B_ϕ has been established. In
the 'matched mode' the reversed B_ϕ inside the liner is produced by
the plasma and that outside by the circuit so that no flux crosses
the liner ($V_\theta = 0$). In 'aided reversal' the B_ϕ outside the liner is
driven negative faster than that produced inside by self reversal
($V_\theta < 0$) to increase the field reversal ratio. This mode has been
used in Eta Beta II. Examples of waveforms obtained are shown in
Fig 1(a)-(c) both without (solid line) and with (dashed line) power
crowbar to extend the current pulse. Electrical performance simu-
lations of V_ϕ, B_ϕ and $\bar{B}_\phi$ have been made with a code based on evolu-
tion through a series of instantaneously relaxed distributions. The
plasma acts as a four terminal element coupling the poloidal and
toroidal circuits [10] and the resistivity is chosen to fit $I_\phi(t)$.
Figure 1(b) shows results from this code (crosses) compared with
measurements. These calculations show that the flux consumption can
be reduced by field control. The normalised volt seconds parameter,
$\int V_\phi dt/I\theta R$, is calculated to be 1.08 for a self reversed case and
0.92 for a matched reversal case, compared with measured values of
1.2 - 1.35 and 0.9 - 1.2 respectively. The relation between the
field reversal (F) and the pinch parameter (θ), Fig 2, is similar to
the so-called 'universal' F-θ curve [1].

VARIATION OF BEHAVIOUR WITH PRESSURE   Figure 3 shows the plasma
resistance (R) and the current decay time (τ_I) as a function of
filling pressure (p_o). The plasma resistance is calculated from V
and I assuming an inductance as a function of θ. It is seen that
R increases and decreases as p_o is raised. The level of magnetic
field fluctuations at the edge of the discharge ($\delta B/B = 1\%$) shows
little variation with pressure. At lower filling pressures than
those shown, no reliable gas breakdown has yet been obtained and a
low pressure regime with increasing field fluctuations, as seen in
Eta Beta II, is not reached. Although low-Z impurities, particularly
oxygen and nitrogen, are clearly in evidence, calculations indicate
that these could only contribute significantly to the energy losses
at high filling pressures (> 3mtorr) and at low currents (< 100kA);
during the sustainment phase, when I/N reaches 10^{-13}Am, these losses
are insignificant. The principal energy loss in this phase could be
from turbulent convection or iron radiation; the iron concentration
has not been measured, but unipolar arc damage to the liner has been
observed.

PLASMA DENSITY   The line average density, $\bar{n}_e$, is measured with a
simple HCN laser interferometer whose plasma arm is a 25mm diameter
beam along a vertical minor diameter. In the absence of a phase
quadrature scheme there are ambiguities in interpreting the phase
shift; also the density variation during the early stages cannot be
resolved because of the large density fluctuations present in the
signal. After peak current these fluctuations decrease markedly,
falling to about $\delta n_e \sim 10^{17}$m^{-3}rms in the frequency band 5 to 100kHz
during the ensuing quiet period. During this period the density
decays steadily. The termination in the plasma current is usually
accompanied by an increase in density fluctuation, δn_e by a factor
of ~ 5. At this time the electron density is typically $\sim 10^{19}$m^{-3}.
Examples of the density evolution deduced tentatively from the
interferometer signal are shown in Fig 4, which illustrates the
observation that when the plasma current is sustained by positive V_ϕ

the density decays more slowly (recycling effects have not yet been
studied). In many conditions the plasma current terminates when the
reversed B_ϕ decays to approximately zero (Fig 1). In prolonged dis-
charges, however, termination can start before reversal is lost and
appears to be linked to the fall in density. During the decay phase
the streaming parameter, $v_D/v_{th\,e}$, can reach $\gtrsim 10\%$.

CONCLUSIONS   Reversed field pinches have been set up in HBTXIA with
currents up to 300kA and sustained up to 5ms with low magnetic field
fluctuations ($\delta B/B \sim 1\%$ rms). Initial studies of different setting
up modes (self, matched and aided reversal) have been made. The
gross behaviour and the plasma coupling of the I_ϕ and I_θ circuits
agree with predictions. Maintaining the plasma current sustains the
reversed B_ϕ, slows up the density decay and has little effect on the
level of magnetic field fluctuations. When the reversed B_ϕ is lost,
the plasma current decay rate always increases. In prolonged dis-
charges, current termination can occur before reversal is lost.

REFERENCES
[1] H A B BODIN and A A NEWTON: Nucl Fusion 20 (1980) 1255.
[2] D C ROBINSON and R E KING: Proc 3rd Int Conf on Plasma Physics
     and Nuclear Fusion Research, Novosibirsk, 1 (1968) 263.
[3] A BUFFA et al: Proc 8th Int Conf on Plasma Physics and Nuclear
     Fusion Research, Vol 2, IAEA Vienna (1981) to appear.
[4] Y HIRANO et al: Proc 8th Int Conf on Plasma Physics and Nuclear
     Fusion Research, Vol 2, IAEA Vienna (1981) to appear.
[5] D A BAKER et al: this Conference.
[6] G C H HEYWOOD et al: Proc 11th SOFT Conf, Oxford (1980).
[7] P D WILCOCK: Proc 10th SOFT Conf, Padua (1978) Pergamon Press,
     1 (1979) 55.
[8] P D WILCOCK et al: Proc 11th SOFT Conf, Oxford (1980).
[9] L FIRTH et al: Proc 10th SOFT Conf, Padua (1978) Pergamon
     Press, 2 (1979) 823.
[10] J W JOHNSTON: Plasma Physics 23 (1981) 187.
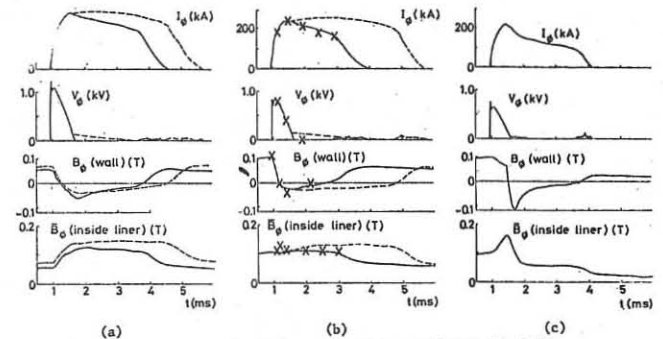
Fig 1   Plasma current, I_ϕ (kA), external loop voltage, V_ϕ (kV),
toroidal field at the wall, $B_\phi(a)$ (Tesla) and average
toroidal field, $\bar{B}_\phi$ (Tesla) obtained with (a) self reversal,
(b) matched mode, and (c) aided reversal. The dashed
waveforms illustrate cases where power crowbars were
applied to extend the current pulses. In 1(b) the x's
denote results from computer predictions (see text).

Fig 2   The reversal parameter F (= $B_\phi(a)/\bar{B}_\phi$),
as a function of the pinch parameter
θ (= $B_\theta(a)/\bar{B}_\phi$) for a typical shot.
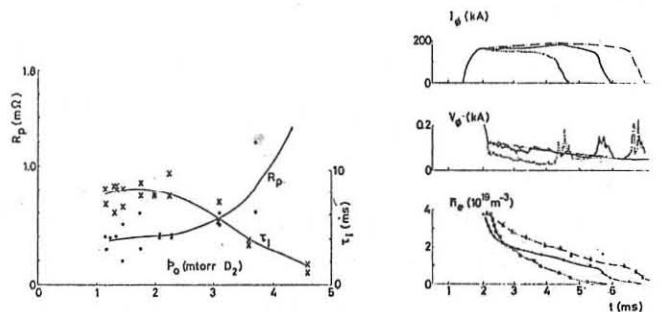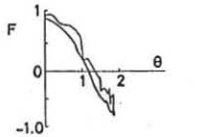
Fig 3   The plasma electrical resistance,
R_p(mΩ) and the current decay time,
τ_I(ms) as functions of the filling
pressure, p_o (mtorr D_2).

Fig 4   The average electron density,
$\bar{n}_e$ (x 10^{19}m^{-3}) for three cases
of differing external loop
voltage, V_ϕ (kV) and plasma
toroidal current, I_ϕ (kA).
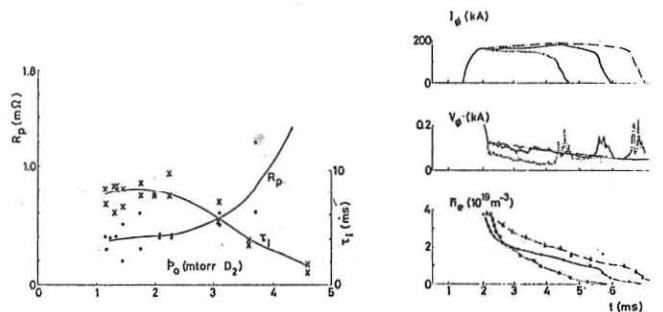
INITIAL REVERSED-FIELD PINCH EXPERIMENTS ON ZT-40M

WITH A METALLIC VACUUM LINER

D. A. Baker, C. J. Buchenauer, L. C. Burkhardt, J. N. DiMarco,
J. N. Downing, A. Haberstich, R. B. Howell, J. C. Ingraham,
A. R. Jacobson, K. A. Klare, E. M. Little, R. S. Massey, G. Miller,
J. A. Phillips, A. E. Schofield, K. F. Schoenberg, K. S. Thomas,
R. G. Watt, P. G. Weber, and R. Wilkins.

ABSTRACT: Recent reversed-field pinch (RFP) experiments with ZT-40M, operating with a metallic liner, have demonstrated improved plasma parameters compared to operation with a ceramic liner. Confinement of hot (150 eV) plasma in an RFP field configuration with toroidal current (I_ϕ) duration of ~ 8 ms at 200 kA has been achieved. Quiescent conditions have been obtained with both V_ϕ and I_ϕ positive. The total toroidal flux ($\phi \propto \langle B_\phi \rangle$) closely follows the time behavior of I_ϕ. With an initial toroidal magnetic field of ~ 0.15 T, "best" conditions are obtained for reversed fields of ~ 0.02 T.

INTRODUCTION: ZT-40M, a Reversed-Field Pinch (RFP) experiment,[1,2,3] recently started operating with a 0.38 mm thick Inconel vacuum liner, which replaced a ceramic liner. The liner is mounted inside a 22 mm thick toroidal Al shell that has an inner diameter of 0.44 m and a major diameter of 2.28 m. The initial D_2 filling pressure is in the range 1.0 to 10 mtorr. At this time experiments up to 250 kA (maximum design current 600 kA) have been carried out in the metal liner system. Passive or active (power) crowbars are available in the poloidal (B_θ) and toroidal (B_ϕ) field circuits. With passive crowbars and zero plasma resistance the B_ϕ and B_θ field circuits have field decay times of ~ 3 and ~ 5 ms, respectively. This is approximately five times greater than could be achieved with the circuits used with the ceramic liner system.

This paper will report on: a comparison between ceramic and metal liner operation; plasma parameters achieved in the metal liner system with passive crowbar; and operation with an active crowbar.

Comparison of Ceramic and Metal Liners: The pinch resistance under normal operation with the metal liner is less than 0.3 milliohm, an order of magnitude lower than with the ceramic liner. The difference in I_ϕ decay times (Fig. 1) is a measure of the improved conductance of the ZT-40M discharges compared to ZT-40 ceramic liner discharges.

The improved conductance of ZT-40M discharges is associated with a dramatically lower fluctuation level. The fractional root-mean-square fluctuations in interferometric phase, $\phi \sim \int n_e dl$, are profiled for a set of vertical interferometer chords, in Fig. 2. Except for the short quiescent periods, fluctuations observed in the ceramic liner system are large compared to the ~ 1% fluctuations measured in ZT-40M. Similarly the fluctuations in I_ϕ and ϕ are much reduced in ZT-40M.

The peak electron temperature (T_e) (measured by Thomson scattering on axis) in ceramic liner discharges varied approximately linearly with I_ϕ (at a given pressure) and required 480 kA to reach 100 eV. The peak T_e in ZT-40M also scales with I_ϕ and has already attained 100 eV at the relatively low current of 190 kA, as shown in Fig. 3. Also, the metal liner discharges maintain their on-axis peak T_e for the remainder of the current pulse, whereas the ceramic liner discharges cooled during the current pulse.

Metal Liner Operation (Passive Crowbar): The ZT-40M experiment has been operated in three modes: as a non-reversed pinch and two reversed field pinch modes, aided- and self-reversal. Measured plasma current and external toroidal magnetic field waveforms for the non-reversed pinch and aided-reversed pinch are shown in Fig. 4, where the current abruptly terminates at ~ 2.8 ms in the reversed field case. The differences indicated in Fig. 4 only occur in certain regimes of ZT-40M operation which, according to other diagnostics, corresponds to a "burnthrough" of OVI. It is found that the plasma current decay times are 0.2-0.4 ms at high (> 5 mtorr) initial D_2 gas pressure. In the non-reversed case, as the pressure is lowered, the decay time shows a sharp increase in the 3-5 mtorr range, and then decreases as the pressure is lowered further.

When ZT-40M is operated in an aided reversal mode, the same behavior is observed except that the decrease in the decay time at low pressures is not observed to occur down to ~ 1 mtorr below which gas breakdown limits operation.

Thomson scattering measurements on axis show that the increase in current decay time is associated with a rise in T_e. Figure 5 shows T_e, measured at 0.7 ms into the discharge, at three different current levels; at the lower currents, temperatures above 100 eV occur at lower fill pressures.

In summary, when ZT-40M is operated with passive crowbar, in a regime where the OVI burns through, current duration of ~ 3 ms and current decay times of ~ 3 ms are achieved.

Metal Liner Operation (Active Crowbar): The B_ϕ power crowbar circuit sustains the reversed field in the outer region of the discharge (see Fig. 6). (The magnitude of the reversed field varies due to plasma circuit interaction.) The reversed field at the wall which previously decayed in ~ 0.3 ms is extended to ~ 5 ms. Maintenance of the reversed field is accompanied by a corresponding lengthening of the I_ϕ duration. Activating the I_ϕ power crowbar results in a further extension of the I_ϕ pulse duration to ~ 8 ms. The toroidal flux closely follows the waveform of I_ϕ. With a proper choice of capacitor bank voltages, the I_ϕ can be programmed to be constant, to increase or decrease (Fig. 7). It is significant that the toroidal flux increases as I_ϕ increases indicating a possible dynamo effect. Total electron inventory at early times measured for passively and actively crowbarred operation obtained from the interferometer are shown in Fig. 8. Power crowbars improve the particle confinement.

Measurements indicate that T_e reaches the range of 150-200 eV for I_ϕ of 250 kA.

CONCLUSION: Use of a metallic vacuum liner wall improves RFP operation as follows: 1.) Plasma resistivity decreases by greater than an order of magnitude, probably because the (observed) fluctuation level is greatly reduced. 2.) Quiescent discharge durations up to ~ 8 ms have been achieved. Moreover quiescence is maintained even with positive toroidal voltage, contrary to earlier reports[4]. 3.) Electron temperatures of ≥ 150 eV have been achieved at 250 kA and are maintained in time. 4.) Toroidal flux and reversed toroidal fields are regenerated and maintained in power crowbar operation for times large compared to classical diffusion times. 5.) Application of power crowbar permits sustained quiescent operation. 6.) Particle decay times have increased up to 1.4 ms and particle loss rates decrease with increasing I_ϕ and power crowbar application.

REFERENCES:

1. D. A. Baker, et al., Proc. 8th Int. Conf. on Plasma Phys. and Contr. Nucl. Fusion Res. (IAEA, Vienna), Vol. 2 (1981) paper L-2-7.
2. A. Buffa, et al., Ibid., paper L-1.
3. Y. Hirano, et al., Ibid., paper L-2-2.
4. H. A. B. Bodin and A. A. Newton, Nuclear Fusion 20 (1980) 1291.
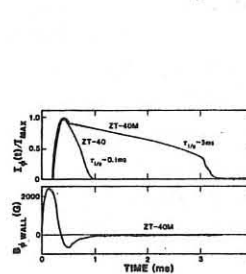
Fig. 1. A comparison of the toroidal currents for ZT-40M and ZT-40, showing the increased decay time for ZT-40M. Peak current was 250 kA for the ZT-40M discharge and 230 kA for the ZT-40.
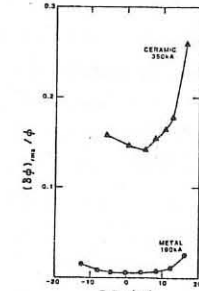
Fig. 2. Comparison of fluctuation levels for ZT-40 (ceramic liner) and ZT-40M (metal liner).
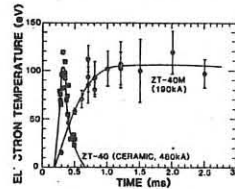
Fig. 3. A comparison of electron temperatures in ZT-40M and ZT-40. ZT-40M temperatures decayed in about 200 μs. ZT-40M temperatures are maintained for the duration of the discharge.
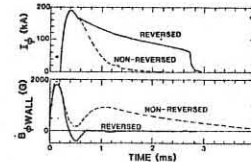
Fig. 4. A comparison of two ZT-40M discharges showing the effect of field reversal on toroidal current decay time.
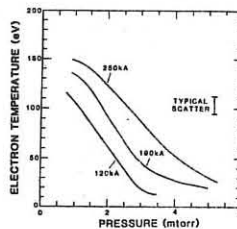
Fig. 5. Electron temperature at 0.7 ms.
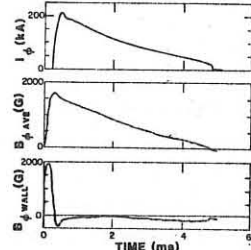
Fig. 6. Toroidal current, average toroidal field, and average toroidal field at the wall for ZT-40M operated with a power crowbar on the toroidal field circuit.
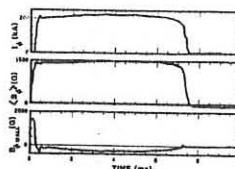
Fig. 7. Same traces as Fig. 6 but with power crowbars on both the toroidal and poloidal field circuit.
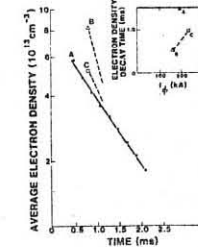
Fig. 8. Average density obtained in ZT-40M. (A) I_ϕ = 190 kA, fill pressure P_0 = 1.9 mt, power crowbars both circuits; (B) I_ϕ = 190 kA, P_0 = 1.9 mt, no power crowbars; (C) I_ϕ = 250 kA, P_0 = 1.5 mt, no power crowbars.

EXPERIMENTS IN THE "TOR-LINER" DEVICE

A.G.Es'kov, M.I.Kitaev, R.Kh.Kurtmullaev, V.M.Novikov,

V.I.Semenov, E.F.Strizhov

I.V.Kurchatov Institute of Atomic Energy, USSR

A quasi-spherical shape of a heavy shell and closed magnetic field structure are specific feature of the fusion Tor-Liner (TL) approach. It enables to reach breakeven at feasible parameters:

$$W_o = 25 \div 30 \text{ MJ}, \quad l = 100 \text{ cm}, \quad D = 50 \text{ cm}, \quad H_o = 20 \text{ kG}, \quad \text{[1]}$$
$$T_o = 100 \div 300 \text{ eV}, \quad r_o/r_f \sim 10, \quad V_{liner} \sim 10^5 \text{ cm/s},$$

In a given paper the results of the experiments on the compact toroid (CT) generation, its transportation, trapping in the liner are given. The experiments have been carried out in the TL-device shown in Fig.1. The TL-device includes a shock chamber where a compact toroidal plasma configuration is formed, heated and accelerated (1), transportation channel with a guiding magnetic field (2), driving coil and a profiled liner (3). Construction of a current-carrying conductors inserted into the driving coil is shown in Fig.2. The principal feature of this construction is the presence of only two slits, which are not greater than 0,3 mm wide. This results in a considerable decrease of ripple amplitudes which develop during liner acceleration.

Generation and heating of a compact toroid (CT) is performed in a scheme described elsewhere [2]. It includes triggered reconnection of magnetic fluxes at the tube ends by means of controling coils. Injection of the toroidal plasma configuration is provided by a proper synchronization of the controlling coils. Fig.3 shows a number of axial distributions of plasma diamagnetizm at various moments. A longitudinal motion of the topoidal configuration from left to right is clearly seen. A motion in the opposite direction can be achieved by a corresponding change in synchronization of the trigger coils.

Oscillograms obtained from two magnetic probes and from an interferometer which are located in the transport channel at a different distances from the shock coil are shown in Fig.4. The peak of a magnetic signal corresponds to the passage of a toroid middle cross-section by a probe. The low density plasma registered before the main CT-signal is explained by a particle leakage from the shock chamber at the first half-cycle. The typical parameters of the injected toroidal configuration:

$$l \sim 20 \div 40 \text{ cm}, \quad d \sim 10 \div 15 \text{ cm}, \quad P = (5 \div 7) \cdot 10^{17} \text{ eV/cm}^3,$$
$$V \sim (0,5 \div 1) \cdot 10^7 \text{ cm/s}$$

The inner CT structure, i.e. plasma pressure and current distrubution is of principle interest, in particular, it determines plasma stability to lines of force replacement.

Radial $B_z(r)$ distributions obtained from 10 probes located at different radii in the transport channel (z = 148 cm) are shown in Fig.5. Magnetic field measurements were performed inside the moving toroid, hence a duration of plasma-probe interaction as well as plasma perturbation were small. Similar measurements of the B_ψ component have shown that the pressure distribution at the central toroid cross-section $P(r)$ can be determined from the $B_z(r)$ profile with a 10-20% accuracy. Distribution $P(r)$ obtained in this way has been used to determine an equilibrium toroid structure and its further evolution at a quasi-spherical compression. The region unstable against convective plasma motions is shown to be reducing during compression [3].

Fig.6 demonstrates driving magnetic field in the coil-liner gap B(t) at the edge (2) and in the middle (1) during liner acceleration at U= 23 kV and W= 500 kJ. Total coil current (3) is shown too. The signal profiles confirms a quasi-spherical liner dynamics.

REFERENCES

1. Es'kov A.G. et al. Third Topical Conf. on Pulsed High Beta Plasmas Culham, 1975, p.37.

2. Es'kov A.G. et al. Proc. of the 7th Europ. Conf. on Cont. Fus. and Plasma Phys. v.1, p.55, 1975, Lausanne.

3. Беликов В.В. и др. Препринт ИАЭ–3391/16, Москва, 1981..

Fig.1

Fig.2

Fig.3

Fig.4

Fig.6

Fig.5
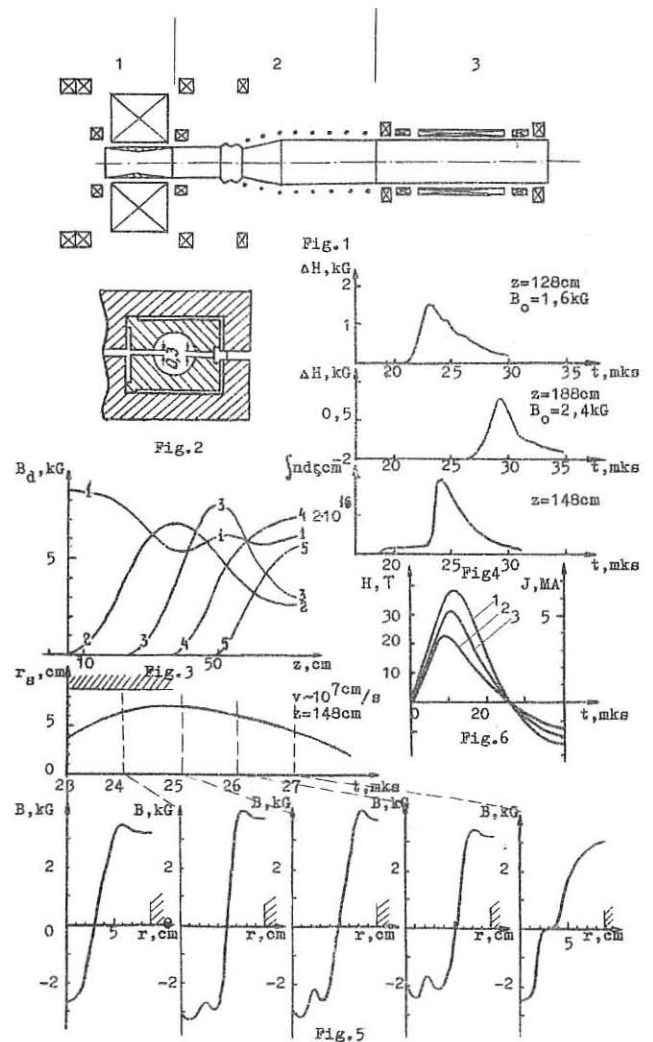
COMPACT TORUS: MHD STABILITY AND INNER STRUCTURE IN THE
PROCESS OF POWERFUL COMPRESSION

A.G.Kaligin, A.P.Kreschuk, R.Kh.Kurtmullaev, A.I.Malutin,
A.P.Proshletsov

I.V.Kurchatov Institute of Atomic Energy, USSR

The term of compact torus include the structure of clo-
sed magnetic trap ($A\sim 1$, $\beta\sim 1$) and all totality of the ex-
perimental methods and physical processes leading to the
establishment of the required final state (Fig. 1), that is
the triggering system, magnetic barrier, the system of po-
loidal and toroidal magnetic fields generation, the chamber
of stationary confinement (Fig.1)[1]. Controlled reconnec-
tion plays an impotant role having a drastic effect on the
evolution and parameters of the compact trap.

1. Development of the reconnection process under a
triggering coil (r$_w$=10 cm, B=15 kG) is shown in Fig.2.
Separatrix radius r_s is derived from a number of compensatid
loops. Evolution of the separatrix profile $r_s(z)$ indicates
localization of the reconnection process in the middle
plane of the triggering coil and its avalanche-like chara-
cter. The characteristic reconnection time is found to be
$\tau_{rc}\leqslant$ 0.3 mks ($\sim r_s/V_A$) when a radial inhomogeneity of B(r)
and an actual shape of $r_s(Z)$ (Fig.3) are taken into account.
The poloidal piston formed in this way have a diffuse B(r)
distribution and is localised in z-direction ($\Delta z\sim r_s$), so
that it satisfies requirments of both stability and effec-
tive shock compression. The similar result was obtained in
another magnetic structure of the reconnection zone (Fig.1)

2. Efficiency of plasma ploughing is shown by interfero-
metric measurements (He-Nelaser; λ=632,8 nm) (Fig.4). Cur-
ve 1 is an interferogram, curve 2a- diamagnetic signal at
the same cross-section. Amplitude and with of a density pul-
se are in a good agreement with assumtion of small particle
losses through the poloidal piston.

3. From the viewpint of plasma stability its radial expan-
sion and set of a diffuse magnetic field distribution B(r)
are important consequence of a compact torus shock formation.
The observations have been done with a set of 10 radially
distributed magnetic probes, 1,5mm in diameter. The transi-
tion from an unpertubed (narrow) neutrallayer (1,2) to a dif-
fuse magnetic field distribution in a shock heated plasma is
clearly seen (Fig.5). The regular stable contraction is wor-
tly of notice, especially because this stage is accompanied
by extremely strong perturbing factors, rapid changes in the
torus shape and structure.

4. An additional important information was obtained with
the aid of a framing image converter camera. It took four
end on photographs through a narrow radial slit with spatial
and spectral resolution. The registered spectral range was
equel to 1000Å. The separatrix moution and inner structure
evolution can be evaluated from the bremstrahlung omission
(Fig.6) (1,2 - radial compression, 3,4 - shock arrivel). The
axial plasma flow and its effective relaxation are registe-
red by the Doppler shift and broadennig of C$\overline{\text{III}}$ line emission
(Fig.6b); shock heating is accompanied by a regular change in
bremsstrahulung radiation and H$_\beta$ and C$\overline{\text{III}}$ intensities (Fig.6c,d).
Regularity and consistent evolution of different spectral

intervals as well as correlation with other diagnostic data
indicate MHD stability.

5. Similar behaviour reveals X-ray emission (Fig.7), which
correlates in detail with diamagnetic signal: rise of inten-
sity at radial compression and the main jump in the shock
wave. At the first stage which is characterised by a narrow
neutral layer a small group of hot electons with $T_e\sim$500-700 eV
is observed. The shock wave heats the whole mass of electrons
up to $T_e\sim$100-200 eV.

6. In conclusion it is necessary to emphasize that all
the dependences described are inherent precisely in the re-
gime of controlled shock generation by a triggering circuit.
A spontaneous reconnection (which takes place in an ordinary
reversed field θ-pinch) results in degradation and disappe-
arance of the shock wave, leads to a sharp rise of energy
and poloidal flux losses.

In the experiments described (B$\cong$10 kG, T$\sim$1 keV) a
collisionless mechanism of dissipation in a shok plasma
flow is ascertained. A most important fact is that a charac-
teristic time necessary for MHD instability development $\sim r/V_A$
appeared to be much smaller then a process duration; $\dfrac{T/2}{r/V_A}\sim$
30-50, though crowbar was not used.

REFERENCES

1.A.G.Es'kov et al. Proc. of the 7th Inter. Conf. on
Plasma Physics and Contr. Neuclear Fus. Res., Innsbruk,
1978, IAEA-3-U-4-1, Vienna, 1978, p.187.

Fig.1

Fig.2

Fig.3

Fig.4

Fig.5

Fig.6

Fig.7

FINITE-β MINIMUM ENERGY EQUILIBRIA IN THE SPICA SCREW PINCH
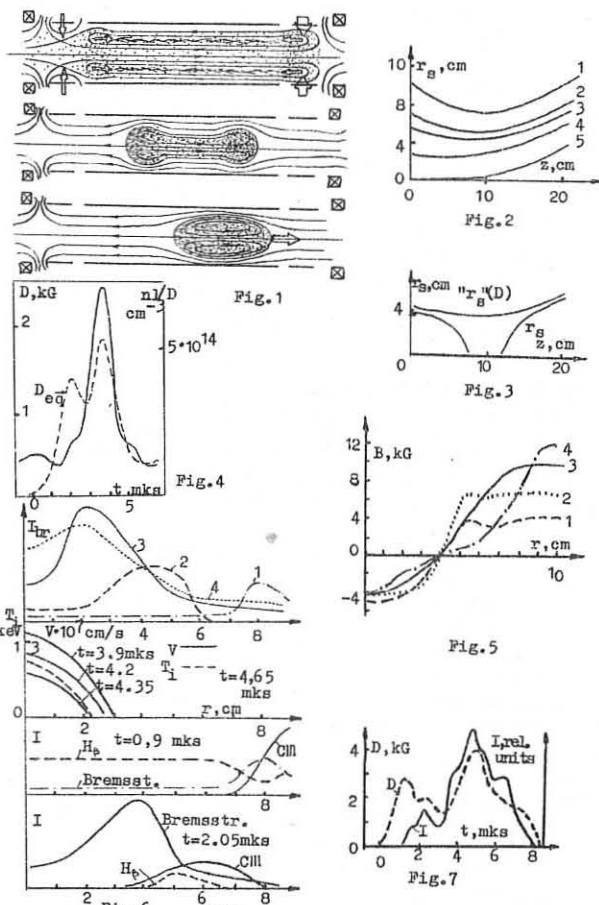
J.W.Edenstrasser
Institut für Theoretische Physik,University of Innsbruck,Austria

W.Schuurman
Instituut voor Plasmafysica,Rijnhuizen,Nieuwegein,The Netherlands

Introduction. A recent finite-beta theory on minimum energy states of symmetric MHD equilibria is applied to the equilibrium of the Rijnhuizen screw-pinch experiment SPICA.

Although the machine parameters and experimental conditions have been described elsewhere /1/,we give a brief summary here. In a toroidal vessel ($R = 0.6\,m$, $a = 0.2\,m$) a dense plasma column is formed and heated by fast implosion. During this implosion,heat conduction loss and resistive decay play a minor role and the flux conservation equation then leads to pitch conservation in time. The constant pitch applied at the wall thus creates a uniform pitch profile that extends to a few centimeters from the wall.

Since a small scrape-off region near the wall hardly influences the equilibrium position,this equilibrium can be maintained for times at least equal to the resistive decay time of force-free currents ($\approx 150\,\mu s$). This quiescent phase can be thought of as being a succession of minimum energy states. Due to a theory by Taylor /2/,these states are the force-free equilibria. Although this theory accounts for a number of phenomena occurring in the various pinch discharges,it cannot explain the observed pressure profiles in SPICA.

In a recent paper /3/ we have extended Taylor's variational principle to the finite-β case. Additional constraints imposed therein are the equilibrium equation,and the fixation of the pressure and of B_z at the axis and at the wall.

For a circular cylinder and for the case of a peaked current density profile the resulting equilibrium quantities are given by

$$B_r = 0 \; ; \; B_\theta = \frac{\lambda^2 x}{r_p v} C_1(v) \; ; \; B_z = \frac{\lambda\sqrt{2}}{r_p} C_0(v) \qquad (1)$$

$$j_r = 0 \; ; \; j_\theta = -\frac{\lambda\sqrt{2}}{\mu_0 r_p} B_\theta \; ; \; j_z = -\frac{\lambda^2}{\mu_0 r_p^2}\left\{2\,\frac{v_a^2}{v^3} C_1(v) + \left(1 - \frac{v_a^2}{v^2}\right)C_0(v)\right\} \quad (2)$$

$$p(v) = \frac{\lambda^2}{2\mu_0 r_p^2}\left\{3\left(C_0^2(v_p) - C_0^2(v)\right) - v_a^2\left[\left(\frac{C_1(v_p)}{v_p}\right)^2 - \left(\frac{C_1(v)}{v}\right)^2\right]\right\} \quad (3)$$

where we have defined (for $\rho > 0$)

$$C_0(v) = AI_0(v) + BK_0(v); \; C_1(v) = dC_0/dv; \; v = |\lambda|\sqrt{\rho + x^2}; \; x = r/r_p \, ,$$

I_0, K_0 are the modified Bessel functions, v_a and v_p the values of their argument at the magnetic axis and at the plasma-vacuum interface respectively, r_p is the plasma radius; A, B, λ and ρ are the four parameters to be determined from appropriate boundary conditions.

By taking into account the toroidal shift δ (see below),this solution is employed for the zero-order cylindrical approximation of SPICA.

Comparison with the experiment. The parameters used to fit the theory to the measurements are the poloidal flux between the magnetic axis and the wall ϕ_w, B_θ and B_z at the wall, and the pressure at the magnetic axis p_a. The toroidal shift δ , following from the experimental pressure profiles, was taken into account by approximating the torus (small radius a) by a cylinder with axis coinciding with the magnetic axis, and with radius $r_w = a - \delta$. The plasma radius r_p was found by subtracting from r_w the thickness of the vacuum region at the outer side of the torus. In this toroidal approximation, the radial dependence of B_θ in the vacuum (in the median plane) is difficult to calculate. To take into account the experimentally observed small decrease, we have assumed $B_{\theta V}$ to be constant and applied a B_θ (wall) slightly higher than the experimental value.

Fig. 1 shows the theoretical pressure profiles compared with averages over the measured ones at three different instants. The time dependence of the parameters on a coarse time scale is clearly seen. At the early time of 10 μs, the plasma-vacuum interface has been determined by accepting the expected constant-pitch configuration. Later times show the onset of magnetic field diffusion, leading to a region of small pressure gradient (with nearly force-free currents). Thus, at 50 and 100 μs, the theoretical curve found by prescribing a vanishing pressure gradient at the plasma boundary, consistent with experiments, gives a better agreement with the measurements than the curve following from constant-pitch matching (see Fig. 2 for t = 50 μs).

Fig. 3 shows the magnetic field profiles corresponding to the pressure profiles of Fig.1. In accordance with experimental observations and theoretical considerations,the equilibria at 10 μs are diamagnetic, whereas they become paramagnetic at later times. This is also concluded from the j_θ-profiles of Fig.4.
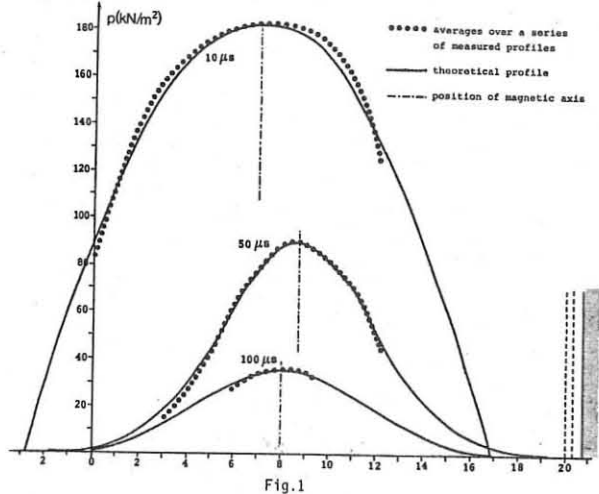
Fig.1

Conclusions. Pressure profiles found from density and temperature profiles measured during the equilibrium phase of the screw pinch SPICA have been compared with those obtained from axisymmetric equilibrium states derived by minimizing the total potential energy subject to certain constraints.

It has turned out that by prescribing (for each instant) a set of four parameters,theoretical pressure profiles can be obtained that agree satisfactorily with the measured ones. This justifies the assumption that the SPICA plasma evolves through a series of high-β minimum energy states where,on a timescale short compared to the plasma lifetime, the assumed invariants do really exist.Since the applied equilibrium theory is static, the time evolution of the assumed invariants (and hence of the four parameters determining the equilibrium) cannot be described.

While it is shown in another paper at this conference /4/ that high-β states with minimum potential energy are obtained in the quiescent phase of the slow RFP η-β-II, the same also seems to be true in fast pinches, like the SPICA screw pinch.

References
/1/ Bobeldijk,C.,et al.,Proc. 5th Conf.on Plasma Physics and Contr.Nucl. Fusion Res.Vol.III p.409
/2/ Taylor,J.B.. Proc. 3rd Topical Conf. on Pulsed High-Beta Plasmas, P.E.Evans Editor, pp. 59/67 (1975)
/3/ Edenstrasser,J.W.. "Minimum Energy States of Symmetric MHD Equilibria". Submitted to Journal of Plasma Physics.
/4/ Edenstrasser,J.W., and Nalesso,G.F. This conference, paper...
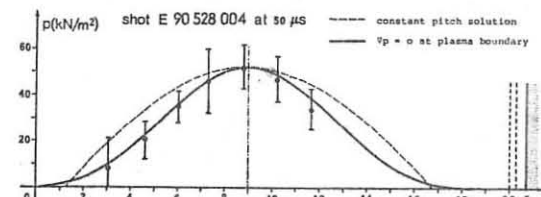
Fig. 2
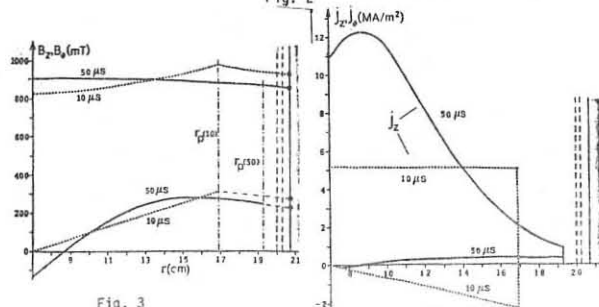
Fig. 3

Fig. 4

THE INFLUENCE OF A HELICAL FIELD ON THE START-UP

AND SUSTAINMENT OF A REVERSE FIELD PINCH

L J Barrow, P G Carolan, J J Ellis*, B A Foster, I H Hutchinson, D J Lees, B J Parham, M Protheroe[+], D C Robinson, P A Shatford and T N Todd

Culham Laboratory, Abingdon, Oxon, OX14 3DB, UK
(Euratom/UKAEA Fusion Association)

*University of Oxford, [+]Royal Holloway College, University of London.

ABSTRACT   The CLEO device has been used to investigate the production of helical pinch configurations. Slow start-up of a pinch and the influence of a helical field on self-reversal, stability and confinement have been investigated.

INTRODUCTION   Two crucial questions for the reverse field pinch, namely slow start-up and sustainment, have been investigated on the CLEO device (R=90 cm, a_p=13 cm), previously [1] operated as a stellarator and a tokamak. The OHTE concept, whereby the pitch reversal necessary in a reverse-field pinch is provided by the pitch associated with the helical windings, permits quasi-continuous operation of a pinch without requiring regenerative motions (and losses) which are necessary to sustain the reversed field. The ℓ=3, pitch 0.37m, winding has been used in an attempt to generate pitch reversal. The device possesses a 'conducting' shell (time constant 3.6 ms) which acts as the vacuum vessel and has two gaps in the toroidal direction which are screened by limiters. There is no bellows liner. Rise times between 0.5→5 ms, variable plasma position, gas puffing and gettering have been investigated.

SLOW START UP   With loop voltages limited to $\lesssim$80 V/turn pinches with currents of up to 8 kA for 8 ms with a toroidal field of 300 gauss have been obtained. To obtain such discharges, the operating density has to be carefully controlled. Too low a density results in excessive pump-out associated with instabilities and too high a density results in radiation cooling and a decrease in conductivity temperature. Optimal behaviour is obtained with gas puffing to counteract the influence of instabilities. Careful control of the vertical field is also required as the pulse length is longer than the shell time constant for these discharges. The current waveform is characterised by steps which are correlated with instabilities, Fig. 1. A multi-coil probe inserted into the discharge shows that it is tokamak-like with the safety factor q increasing with radius to a value of $\sim$ 1/4 at the current maximum. The cur-
rent steps are associated with helical mode activity with m=1, n=1, n=2, n=3, and n=4 as q passes through fractional values 1, 1/2, 1/3 and 1/4. They are reminiscent of 'magic numbers' observed on ZETA. The helical modes apparently saturate and rotate with frequencies 5-10kHz. This frequency is

Fig.1 Plasma current, voltage, density and internal poloidal field waveforms.

close to the electron diamagnetic drift frequency for such a plasma. The field perturbations are shown in Fig.2 and these compare well with those predicted from MHD resistive initial value calculations[2] provided that the observed average beta ($\sim$ 30%) is allowed for. The driving force for the instability comes from the current gradient at the edge of the plasma. The helical field does not influence the instabilities significantly but does increase the plasma resistance when the winding current is increased to a point where the separatrix appears in the vacuum vessel. The current steps are usually longer and the maximum current is reduced. Typical plasma parameters obtained under these conditions are $n_e \sim 5 \times 10^{13}$cm^{-3} $\bar{\beta} \sim 30\%$, $\tau_E \sim 50\mu s$, $\bar{T}_o \sim 6eV$. Gettering and gas puffing indicate

Fig.2 Comparison of measured and theoretical field perturbations.

that radiation does not represent the dominant energy loss process. At these limited loop voltages it was not possible to obtain discharges with q<1/4. The plasma activity was apparently too strong and produced too high a resistivity.

PRODUCTION OF A REVERSE FIELD PINCH   Increasing the loop voltage to $\gtrsim$300 V/turn and decreasing the rise time to $\lesssim$1ms has permitted the production of pinches with currents of up to 45kA and with pinch configuration parameters, θ, of up to 1.4 with the toroidal field close to zero at the 'conducting' wall. Again only a narrow range of operating densities was possible. Low densities lead to serious fast instability (few µs) activity and the development of high loop voltage transients (up to 1kV) together with a high plasma resistance. This phenomenum is not observed on pinch devices with metal liners[3]. Gas puffing was no longer effective because of the reduced pulse length and higher operating pressures (1-2mtorr). The higher loop voltages and filling pressures also lead to difficulties at the two main gaps, producing local breakdowns which short circuit the discharge via the conducting shell. This problem was aggravated by the initial loop voltage spike which has been overcome with a preionisation system, consisting of a tokamak discharge of $\sim$2kA, q$\sim$1 and $n_e \sim 5 \times 10^{12}$cm^{-3} for a few ms in one direction followed by the pinch discharge in the opposite direction. This reduces the initial loop voltage spike by almost a factor of two. The resultant field configuration shown in Fig.3 was measured with a multi-coil probe. Again slow helical oscillations were observed at a frequency of a few KHz. The discharge parameters were typically, $T_e \sim T_i \sim 20eV$, $n_e \sim 5 \times 10^{13}$cm^{-3} central beta $\sim$ 5%, $\tau_E \sim 10\mu s$. Though the current line density ratio was approximately correct for quiescence the plasma resistance remained relatively high ($\gtrsim$4mΩ). Reducing the oxygen level by gettering had little effect on the resistance. The influence of the helical field depends on the wall conditions but it can lower the plasma resistance slightly and the OII level significantly, however there is little effect on the fluctuations or magnetic configuration.
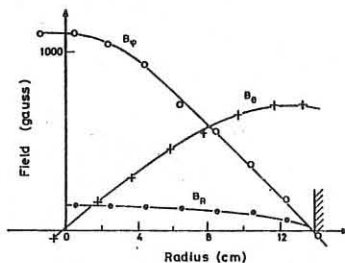
Fig.3 Field configuration in the vertical direction with θ=1.2 and helical field with I_h/I_p=0.1.

No strong effect on the initial start-up plasma is observed. The resultant pitch is calculated to be reversed close to the wall. Magnetic surface calculations indicate that the flux surfaces close to the separatrix are not closed, thus reducing the effective pitch of the winding.

CONCLUSIONS   Slow start-up of a pinch is characterised by strong instability activity at fractional q values. In CLEO the influence of the helical field on near reverse field pinches is observed to be small, however as no 'quiescent' behaviour is observed this does not represent a full test of the OHTE concept.

REFERENCES

[1]   OHKAWA T et al, Nuclear Fusion (1980) 20, 1464
[2]   CROW J E et al, 3rd EPS Conf. Moscow, (1973) 1, 269
[3]   CAROLAN P G et al, 10th EPS Conf. Moscow (1981)

THE INFLUENCE OF IMPURITIES ON THE DISCHARGE BEHAVIOUR IN SPICA

A.F.G. van der Meer, D. Oepts and A.A.M. Oomens.
Association Euratom-FOM, FOM-Instituut voor Plasmafysica,
Rijnhuizen, Nieuwegein/Jutphaas, The Netherlands.

Abstract. An investigation has been made of the time behaviour and intensity of oxygen impurity lines in SPICA, a high-β screw pinch with a quartz liner. An upper limit for the oxygen impurity concentration in standard discharges of 0.2% was established. Bolometric measurements of the total flux to the wall indicate a value that is considerably lower.

Introduction. In several machines, using an insulating liner, a rapid cooling of the plasma has been reported, due to a large impurity content (mainly oxygen) [1]. In SPICA such rapid cooling was not observed [2], in spite of plasma parameters for which even a small amount of oxygen would be critical. Therefore, a programme was started to measure the oxygen concentration directly, i.e. via absolute intensity measurements of oxygen lines in the visible part of the emission spectrum. Analysis of the spectrum shows that oxygen and silicon are the main impurity species in SPICA, indicating that wall contact during the predischarge is mainly responsible for the impurity content. It should be noted that at temperatures in the range from 30 to 70 eV, energy losses due to oxygen are much larger than losses due to silicon at comparable impurity concentrations.

Standard discharges may be characterized as follows:
- The plasma configuration is established by fast implosion (∼ 10 μs).
- A high density ($n_e = 3-7\times10^{21}$ m^{-3}) central column with a radius between 0.05 and 0.08 m, of moderate temperature ($T_e = T_i$: 30 - 70 eV) is surrounded by a low-density ($n_e = 1 - 3\times10^{20}$ m^{-3}) plasma, extending up to the wall, in which force-free currents provide a uniform q (∼ 1.5). (R = 0.6 m, a = 0.2 m; no limiter is used.)
- The plasma is in good equilibrium and the outward equilibrium shift, depending on β and q, is approximately 0.05 m.
- Beta-values in the central plasma are typically between 15 and 20%.
- Stable operation is obtained for over 100 μs, but the diameter of the column appears to decrease to 0.04 m at 100 μs.

Relevant diagnostics

- A ruby laser system measuring T_e- and n_e-profiles over a width of 0.12 m at one instant.
- A He-Ne-interferometer measuring $\int n_e d\ell$ as a function of time.
- A VUV 2-m grazing incidence spectrometer. Two emission lines in the spectral range from 2 - 110 nm can be recorded simultaneously as a function of time.
- A low resolution monochromator for the visible part of the spectrum.
- A platinum foil, preheated to 1000 °C, is used as a bolometer [3], with a rise time ≈ 1.5 μs, a decay time ≥ 90 ms and a detection limit ≈ 1 mJ/cm².

All observations are done in the equatorial plane, except for the bolometer which is positioned at a poloidal angle θ = π/2. Therefore, line-integrated intensities have to be used and an assumption about the emissivity profile has to be made. As this results in a large a priori uncertainty in the derived oxygen concentration, these measurements have been checked by adding 1% of oxygen to the working gas.

Measurements. At densities of 5×10^{21} m^{-3}, the rate of ionization is very fast as is shown in Fig. 1, where the time evolution of O V and O VI lines is given. At t = 10 - 13 μs, the intensity of the O V line is decreasing already while that of O VI is at its maximum.

In Fig. 2 the average temperature and density profile at t = 10 μs is shown. These profiles are rather flat, and we therefore assume that the O VI emissivity is uniform. Absolute intensity measurements of the 381.1 nm O VI (3s ^{2}S-3p $^2p^0$) line then lead to a value for $n_{OVI} \approx 2\times10^{18}$ m^{-3}. This value is derived using the Corona approximation. (Although the population of the excited 2p $^2p^0$ level is an important fraction of the ground state density at $n_e = 5\times10^{21}$ m^{-3}, the correction is estimated to be small.) Model calculations [2] for the ionization phase show that for a fairly large range of parameters about 50% of the total impurity content is in the O VI stage when the intensity of O VI lines is at its maximum, so a total oxygen content ≤ 0.1% results.

In discharges with 1% of oxygen added, all observed intensities of oxygen emission lines increase, however with different factors.
Although the O V 63.0 nm (2s² ^{1}S - 2s2p $^1p^0$) and O VI 103.2 nm (2s ^{2}S- 2p $^2p^0$) emission lines may well be optically thick at this impurity concentration (absorption lengths of half the plasma radius are computed) these intensities increase by a factor of 4 and 3 respectively, whereas the O VI 15.0 nm (2s ^{2}S - 3p $^2p^0$) line increases only by a factor of 2. This indicates that the discharge conditions have changed at t = 10 μs. However, no substantial difference in n_e- and T_e-profiles, as measured by Thomson scattering, was observed, which may well be due to the rather limited number of measurements and the large shot-to-shot variations.

Fig. 1. Oxygen line intensities as a function of time in standard discharges.

In Fig. 3 the time evolution of the emission lines is given for this case. A comparison with Fig. 1 shows that the time development during the first 8 μs hardly changes, but that the decay is rather different: The O V line decays less rapidly, whereas the O VI lines decay more rapidly (most substantially for the 15.0 nm line). This is interpreted as being due to rapid cooling when oxygen reaches the O V stage. Also in this case an estimate of the oxygen concentration is made from intensity measurements, resulting in a value of 0.25% when the profiles of Fig. 2 are used. This is low by a factor of 4 - 5, which, however, is not surprising in view of the fact that the increase of the 15.0 nm line is only half the increase of the 63.0 nm line, although the latter must be subject to substantial self-absorption. With 1% oxygen added, rapid cooling is also observed by means of Thomson scattering. At 50 μs temperatures as low as 10 eV are measured.
Moreover, discharges with oxygen added tend to be less stable, which is probably due to enhanced field diffusion. Measurements of (few) discharges with 0.3% of oxygen added show that a continuous transition exists between discharges with and without 1% of oxygen added.

Energy losses. With the fast bolometer, total power fluxes at the wall of 100 W/cm² (no oxygen added) and 500 W/cm² (1% of oxygen added) were measured (Fig. 4). This value of 500 W/cm² is, within a factor of 2, in agreement with the observed cooling of the plasma. (The power input by ohmic heating makes only a small contribution.) However, model calculations, assuming impurity concentrations of 0.2 and 1.0% respectively, yield loss rates that are at least a factor of 10 larger. For the 1% case this may be partly due to self-absorption of the resonance lines, which is not taken into account in the calculations.

Conclusion. An upper limit for the oxygen concentration under normal operating conditions of only 0.2% is well established. The low-energy loss rate to the wall, which is in fair agreement with the slow temperature decrease reported earlier [2], indicates a value that is at least a factor of 5 lower. So, in spite of the quartz liner and the critical electron temperature, the plasma is not radiation-dominated, with an energy-confinement time ≥ 100 μs.

Fig. 2. Electron temperature and density profile at t = 10 μs. (The plasma is shifted outward, r = 0 corresponds with the centre of the tube.)
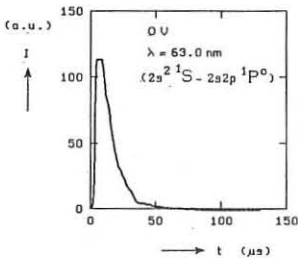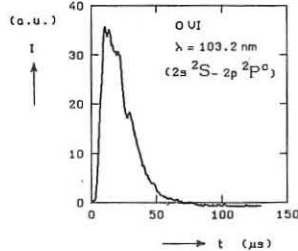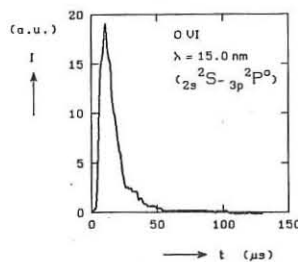
Fig. 3. Oxygen line intensities as a function of time with 1% of oxygen added. Each figure is plotted on the scale as used in Fig. 1.

References

1. J.N. di Marco, G.F. Nalesso, Proc. Workshop on the Reversed Field Pinch, Padua (1978) p.2.

   O. Grüber et al., Proc. 6th Int. Conf. on Plasma Phys. and Contr. Nucl. Fusion Res., Berchtesgaden 1976; Suppl. Nucl. Fusion (1977) Vol. 1, p. 311.

2. D. Oepts et al., Proc. 9th Eur. Conf. on Contr. Fusion and Plasma Phys., Oxford (1979) paper DP 9, p. 105.

3. Yu.G. Prokhorov et al., Plasma diagnostics, AEC-t2-6518 (1963).
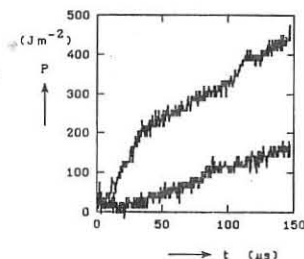
Fig. 4. Total power fluxes to the wall, measured by means of a fast bolometer. Upper trace: 1% oxygen added. Lower trace: no oxygen added.

CONFINEMENT AND MAGNETOACOUSTIC HEATING OF A LOW DENSITY BELT-PINCH PLASMA

V. Erckmann, G. Müller, J. Singethan, K. Schwörer, M. Thumm, R. Wilhelm
Institut für Plasmaforschung der Universität Stuttgart
D-7000 Stuttgart 80, Fed. Rep. of Germany

Abstract: Toroidal high-β -equilibria (β= 20-50 %) are investigated in a Belt-Pinch configuration. Operating in the low density regime ($n_e \leq 10^{20}$ m^{-3}) at temperatures around 200 eV the ion gyroradius becomes comparable with the typical gradient length. Under these conditions enhanced energy losses are observed. Applying magnetoacoustic wave excitation efficient energy coupling to the low density plasma has been found. In the special case of second cyclotron harmonic a pronounced increase of plasma-β is obtained. The central β-value has been raised from 25 to 45 %.

Introduction: In the Belt-Pinch device HECTOR heating and confinement of elongated high-β-equilibria are investigated. Recent results have been obtained in a density regime low compared with previous Belt-Pinch experiments /1, 2/. At these low densities (10^{19}-$10^{20} m^{-3}$) ion sound instability leads to an anomalous diffusion during shock compression resulting into a medium-β (β≈20 %) plasma equilibrium. Accordingly a weak gradient of magnetic field and pressure profile is observed. In terms of the ion gyroradius, however, the gradient length is very steep, i.e., a few gyroradii only. At these conditions the perpendicular ion heat loss should be modified compared with the classical value $K_\perp \propto r_i^2 \nu_{ii}$ at $\Delta \gg r_i$. Experimental observations on ion energy confinement are reported. Large ion gyroradii on the other hand favour the absorption of magnetoacoustic waves. First experiments with wave heating indicated high efficiency of energy conversion.

Plasma parameters and elongated equilibria: The HECTOR device has a toroidal coil system with a rectangular cross-section (height $2b_c$=1.2 m, inner radius R_i^c=0.37 m, outer radius R_a^c=0.87 m) /3/. The initial plasma for fast magnetic compression is generated in two stages: a h.f.-predischarge (f=85 MHz, U=40 kV, T=50 μs, P=1 MW) is used to ignite a toroidal preheating discharge (f=16 kHz, $B_t(0)$= 0.1 T, W= 65 kJ) which produces radially homogeneous plasmas with about 30 % ionization at p_0=0.1-0.2 Pa deuterium filling pressure. Magnetic shock heating is accomplished by a fast rising magnetic field generated by pulse-charged Blumlein transmission lines (U=200 kV, W=25 kJ, $B_t(0)$=1.6 T, risetime τ=0.5 μs, crowbar L/R-time τ_c=70 μs). Stability with respect to vertical displacement modes and a clear separation of the plasma ends from the wall is achieved by means of passive multipole windings. For additional plasma heating in the post compression phase, the magnetic field is strongly modulated (f=1 MHz, $\tilde{B}/B$=0.1-0.2) during a time interval of about 5 μs. Typical measured and calculated plasma parameters (p_0=0.1 Pa) at t=2.5μs are given in the following table:

Tor. magnetic field: $B_t(0)$= 0.11 T	Tor. plasma current: I_p =	80 kA
Plasma height : 2b = 0.95 m	Plasma beta (av.) : $\langle \beta \rangle$ =	0.2
Plasma width : 2a = 0.1 m	Pol. beta (av.) : $\langle \beta_p \rangle$ =	2.2
Major plasma radius: R(0)= 0.34 m	q-value (boundary) : q(a) =	2.7
Deg. of ionization : N/N_0 = 0.9	Plasma density (av.): $\langle n_e \rangle$ =	10^{20} m^{-3}
Impurity content : α_c = 0.4 %	Electron temp. : $T_e(0)$=	35 eV
α_0 = 0.3 %	Ion temperature : $T_i(0)$=	210 eV

Radial profiles of toroidal and poloidal magnetic field B_t, B_p, plasma pressure p and toroidal current density j_t were obtained from simultaneous measurements with internal multiple probes. The axial position and elongation of the plasma column was derived from external $B_{zi}(z)$ and $B_{za}(z)$-probe measurements. Electron temperature $T_e(r,t)$ was determined by 90°-Thomson scattering and by spectroscopic measurements (C_{II}, C_{III}, O_{II}-O_V). Electron density $n_e(r,t)$ was measured by end-on CO_2-laser interferometry and Thomson scattering. The ion temperature $T_i(r,t)$ was derived from pressure balance. In addition Rogowski loops, diamagnetic loops streak cameras and a neutron detector are installed for plasma diagnostics.

The plasma equilibria are studied by means of a free-boundary 2d-equilibrium code /4/. The experimental profiles have to be satisfied by an appropriate choice of input parameters, i.e., by the plasma surface shape and j_t. Fig. 1a shows the calculated poloidal flux surfaces of highly elongated equilibrium and Fig. 1b a comparison of calculated and experimental radial profiles of B_t, p, and j_t at t=2.5 μs. During the discharge the plasma cross-section gets more elliptical in agreement with Ref./1/.

Confinement and magnetoacoustic heating: For the measured electron temperature ($T_e(0) \approx 50$ eV) and average electron density of $\langle n_e \rangle$= 10^{20} m^{-3} ion-electron heat transfer can be neglected in the 10 μs time scale considered. Impurity content is low enough for radiation losses being negligible in comparison to cooling by plasma expansion due to the decaying magnetic field. In the post compression phase the ion temperature still

increases during the following 3 μs as shown in Fig. 2. This energy transfer to the ions is due to electromagnetic wave energy absorption in the plasma centre. Fig. 3 shows the time behaviour of the radial profile of the toroidal magnetic field. The wave is of the magnetoacoustic type ($k \perp B$) in the frequency range $\omega \geq 2\omega_{ci}$ with $kr_i \approx 1$. This means that kinetic effects e.g. Landau damping is expected to be an important absorption mechanism /5/. An estimate of power transferred by the wave shows a heating rate in the order of 10^8 W. In the high-β case the energy gain per particle reaches several eV/μs which is also observed in previous θ-Pinch experiments /6/. Approaching the condition $\omega = 2\omega_{ci}$ at medium β-values the energy gain is increased by one order of magnitude. The high values of ion heating power needed to raise β is a consequence of rapid loss of ion energy by radial transport. The energy confinement time, decreasing with rising ion temperature, is about 5 μs for $T_i \approx 200$eV. This is a result characteristic for shock heated high-β plasmas having ion gyroradii r_i comparable to plasma radius a. In our case the plasma centre is connected to the plasma edge by only one Larmor cycle. Using the formula $\tau_{Ei} \propto \tau_{ii} a^2/r_i^2$ for fully ionized plasmas with small values of r_i/a one obtains an energy confinement time exceeding the experimental data by a factor of ten. However, edge cooling by charge exchange with neutrals coming from the wall yields an energy confinement time $\tau_{Ei} \approx \tau_{in}$ The ion-neutral collision time for a neutral density at plasma boundary of $10^{19} m^{-3}$ at T_i=200 eV is of the order of the observed confinement time.

Conclusions: High-β experiments with very narrow profiles in terms of ion gyroradii indicate enhanced ion energy losses. These losses can be explained by the direct coupling of ions to the dilute plasma or neutrals near the surface. On the other hand large ion gyroradii make possible efficient absorption of magnetoacoustic waves. For the second cyclotron harmonic resonance a power flux of the order of 50 MW/m^2 and a pronounced increase of plasma β within a few μs has been measured under these conditions.

References: /1/ G. Becker et al., Nucl. Fusion 18, 1653 (1978)
/2/ C.K. Chu et al., IAEA-CN-38/L-4-2, Brussels, 1980
/3/ F. Söldner, Phys. Fluids 21, 1036 (1978)
/4/ G. Becker, K. Lackner, Nucl. Fusion 17, 903 (1977)
/5/ E. Canton, H.R. Lewis, Phys. Fluids 23, 109 (1980)
/6/ J.L. Shohet et al., IAEA-CN-37/Q-3, Innsbruck, 1978
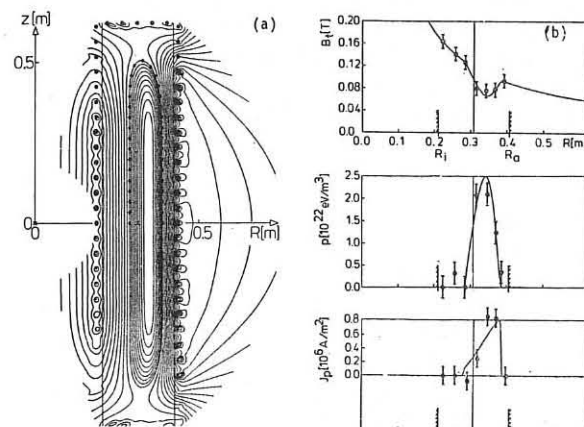
Fig. 1: Calculated poloidal flux surfaces (a) and comparison of calculated and experimental radial profiles of B_t, p, and j_t at t= 2.5 μs (b) for filling pressure p_0=0.1 Pa (D_2)
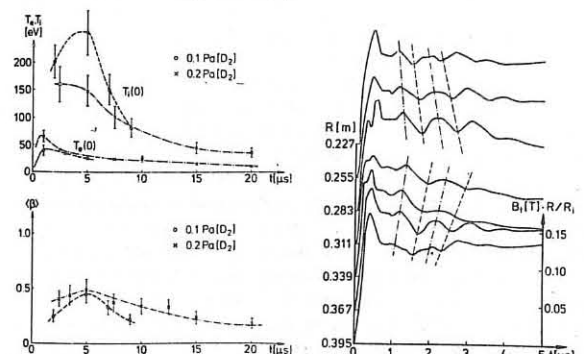
Fig. 2: Time dependance of ion- and electron temperatures in the plasma centre and $\langle \beta \rangle$

Fig. 3: Radial propagation of B_t-modulation. The dashed lines mark tajectories of constant phase.

THE NONLINEAR 'g' MODE

T C Hender* and D C Robinson
Culham Laboratory, Abingdon, Oxon, OX14 3DB, UK
(Euratom/UKAEA Fusion Association)

*Royal Holloway College, University of London

ABSTRACT   The nonlinear properties of the m=0 resistive
'g' mode have been studied for a wide range of magnetic
Reynolds numbers.   A quasi-linear saturation mechanism has
been found in which the pressure in the vicinity of the
singular surface is flattened. This saturation is however
counteracted by overheating of the plasma. The m=1 mode in
the core of the plasma has also been investigated and sim-
ilar mechanisms prevail. A field line tracing code has been
used to study the existence of magnetic surfaces when m=0
and m=1 modes interact. Ergodic field line behaviour has
been found for parameters typical of contemporary reverse
field pinches.

INTRODUCTION   In both the RFP and spheromak the most dan-
gerous instability is the 'g' mode. It is therefore import-
ant to understand its nonlinear behaviour.

To study the m=0 mode a simplified formalism is chosen;
a periodic cylindrical system is assumed, a 2D approxim-
ation made ($\frac{\partial}{\partial\theta} \equiv 0$), and the plasma is assumed to be incomp-
ressible. This allows the introduction of a flux function
and a velocity stream function. The resulting equations are
similar to the reduced tearing mode equations and an exten-
sion of the algorithm of Waddell et al[1] is used to solve
them. Recently a mixed helicity code has been developed. A
spectral method similar to the Oak Ridge code RSF[2] is used
to solve the full set of compressible resistive MHD equations.
This code has been used to make a study of the single helicity
m=1 mode.

RESULTS AND DISCUSSION   The equilibrium chosen for the
study is the tearing mode stable equilibrium developed by
Robinson[3]. This RFP equilibrium is stable to all ideal
MHD instabilities and to tearing modes. To model experi-
mental conditions more realistically this equilibrium
includes a vacuum region between the plasma and the wall.

The non-linear results for the m=0 mode show the domin-
ant nonlinear process to be the modification of the axial
current, J_{z0}. Figure 1 shows the alteration to ηJ_{z0} for a
case with a
magnetic
Reynolds
number, S =
5×10^4 (η be-
ing the plasma
resistivity).
The displace-
ment of E_{z0}
and ηJ_{z0} to
larger radii
is due to
resistive
diffusion
while the
behaviour in
the vicinity
of the sing-
ular surface
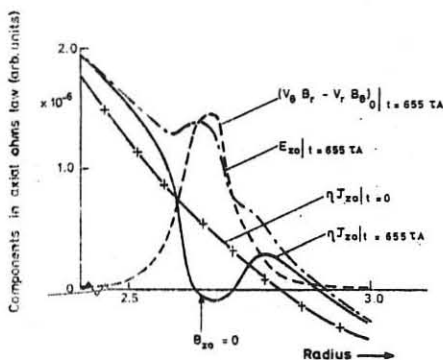
Fig.1 Components of Ohm's law at 655 Alfven transit
times for the m=0 'g' mode.

is due to the quasi-linear perturbation $(\chi_1 \times B_1)_{z0}$, to Ohm's
law. The modification to J_{z0} near the singular surface
causes a flattening of the equilibrium pressure in this
region, and since the 'g' mode is driven by pressure grad-
ient, represents a quasi-linear saturation mechanism. However
the resistive diffusion of the equilibrium results in ohmic
heating increasing the gross pressure and thus counteracting
the saturation process. The nonlinear behaviour observed
depends on the competition between these two mechanisms; our
calculations indicate that the S scaling of these two ef-
fects causes the saturation mechanism to become increasingly
dominant at high S. However at S $\sim 5 \times 10^4$ the growth rate
is only reduced to 40% of its linear value. It is likely
that by introducing physical energy loss mechanisms (ther-
mal conductivity, radiation etc) the saturation may be comp-

plete. Within the incompressible formalism used for the m=0
code this energy loss process can be represented by intro-
ducing a non-physical term in the resistive diffusion
equation to stop the fields resistively decaying. With this
term present saturation is obtained for S=1000.

The nonlinear behaviour of the m=0 leads to an enhance-
ment of the pressure gradient in the vicinity of the m=1
surfaces. Figure 2 shows the pressure gradient resulting
from the
presence of an
m=0 mode for
S=1000. The
positions of
some of the m=1
surfaces are
also recorded
on Fig.2. The
effect on the
linear growth
rates of the
m=1 modes due
to the alter-
ations to the
pressure pro-

Fig.2 Evolved pressure profile in the region of $B_z=0$

file have been investigated. In the centre of the plasma
the growth rates can double. The nonlinear behaviour of a
single helicity m=1 mode is found to be dominated by the
same mechanisms as for the m=0 mode.

To assist in a mixed helicity study a field line trac-
ing code has been used to study the result of the interaction
between the m=0 mode and the m=1, n=4 mode in the core of the
plasma. A linear code is used to produce the perturbations
to the magnetic fields and they are introduced at the smal-
lest amplitude at which saturation is likely to occur; the
results are therefore optimistic. At low magnetic Reynolds
numbers ergodic field line behaviour is found. Figure 3
shows the intersection of two different field lines with the
θ=0 plane, for S=5000 and a central beta of 5%. The closed
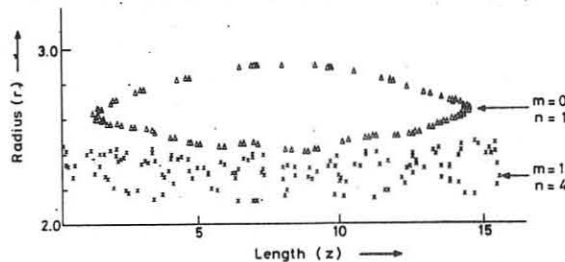
Fig.3 Magnetic surfaces in the r-z plane with m=0 and m=1 modes
present.

surface of the large m=0 island can be seen while field lines
forming the m=1 islands experience ergodic behaviour between
the two surfaces. At higher S the surfaces become closed if
only the two island structures are considered. However in-
creasing S causes the m=1 (and m=2) modes in the core with
n>4 (n>8) to become destabilised and so the surfaces do not
close. The effect of this non-closure on energy contain-
ment is being investigated.

CONCLUSIONS   The nonlinear behaviour of the m=0 mode
exhibits a quasi-linear saturation mechanism. This satur-
ation may be prevented by overheating of the plasma.

The m=1 mode possesses a similar nonlinear behaviour.
The m=1 modes are linearly destabilised by the presence of
the m=0 mode.

The interaction between the m=0 and m=1 modes leads to
ergodic field line behaviour.

REFERENCES

[1] WADDELL B, ROSENBLUTH M N and MONTICELLO D A, WHITE R B,
     CARRERAS B, "Nonlinear Numerical Algorithms", ITCP
     College (1977) 79.

[2] HICKS R, CARRERAS B, HOLMES J et al, Oak Ridge National
     Laboratory Report ORNL/TM7132, 1979.

[3] ROBINSON D C, Nuclear Fusion, 18 (1978) 939.

CTCC-I EXPERIMENT
- CT Plasma Collision and Compression -

K. Watanabe, K. Ikegami, A. Ozaki, N. Satomi, T. Uyama
Course of Electromagnetic Energy Engineering
Faculty of Engineering, Osaka University
Yamada-kami, Suita, Osaka 565, Japan

ABSTRACT. Compact toroidal plasma has been experimentally obtained in a drum-type copper vessel using a magnetized coaxial gun. Toroidal and poloidal magnetic fields of a toroid show a typical exponential decay with 110 μs and are described fairly well by a force-free configuration.

I. INTRODUCTION. This report presents an experimental result on the compact toroidal plasma with toroidal and poloidal magnetic fields, B_t and B_p, produced in a drum-type metal vessel by an injection of a magnetized coaxial gun plasma.[1][2] This experiment is the first phase to produce a stable high temperature plasma by means of CT plasma collision and compression. The experimental result is described very well by the model, which is the fundamental-mode state of the force-free equilibrium in a metal vessel and is easily estimated as a solution of the low-β limit Grad-Shafranov equation. Experimental apparatus consists of a magnetized coaxial plasma gun and a flux conserver for plasma confinement as shown in Fig. 1. The length of the coaxial gun is 0.8 m, and its inner and outer electrodes, which are made of 1.5 mm thick stainless steel cylinders, have radii of 0.1 m and 0.15 m, respectively. This is driven by a C=68 μF, V= 50 kV capacitor bank. Solenoidal coils installed outside and inside the electrodes are used for plasma magnetization. Hydrogen gas is puffed into the gun center region between electrodes by six fast valves. The gun plasma is injected through an entrance region into the oblate flux conserver having 0.75 m diameter and 0.4 m length. A vacuum chamber is evacuated to less than 1×10^{-7} Torr.

II. EXPERIMENTAL RESULTS. Typical axial magnetic field, $B_z(z)$, on symmetry axis measured with a array of five magnetic probes is shown in Fig. 2. Here, z denotes the distance between the probe and the gun muzzle. The midplane of the flux conserver is at z= 52 cm. About 50 μs after the gun firing, it starts to decay with the time constant 110 μs and lasts without any MHD instability longer than 200 μs in the region of z= 42 ~ 62 cm. In the entrance region, the magnetic field decays rapidly during about 30 μs as shown in the signal at z= 22 cm. These data indicate the occurrence of the elongation of field lines from the gun and the formation of the compact toroid due to the reconnection of field lines occurred in the entrance region. The reconnection time is about 20 μs in this case. According to this figure it is concluded that the compact toroid is just located on the midplane of the flux conserver after t= 30 μs. This is confirmed under the wide range of operating conditions.

Radial profiles of axial and azimuthal components of the magnetic field, $B_z(R, z= 52$ cm) and $B_\phi(R, z= 52$ cm), measured with a radial probe array are shown in Fig. 3. In these figures, crosses and closed circles are data obtained from two different shots. R denotes the distance between the probe and the symmetry axis. It is found in Fig. 3 (a) that the compact toroid with a magnetic axis at R= 25 cm is successfully produced after the reconnection and the position of the magnetic axis is not varried hereafter. The profiles of B_ϕ which corresponds to toroidal field is rather of flat top having its peak around a little inner than R= 25 cm after t=30 μs. A photographic measurement was also carried out using the image converter camera through the mesh-window. The maximum of observed light intensity distribution was located radially around the magnetic axis. These stable profiles of magnetic fields reveal that the compact toroid is free from any MHD instability.

The fundamental mode solution of the low-β limit Grad-Shafranov equation is given in cylindrical coordinate (ρ, ϕ, z) by

$$\psi = \frac{B_{p,max}}{3.83} \rho_o \, \rho \, J_1\left(3.83 \frac{\rho}{\rho_o} \right) \cos\left(\frac{\pi}{2} \frac{z}{z_o} \right) \qquad (1)$$

where $\psi= 0$ on the flux conserver wall ($\rho= \rho_o$ and $z= z_o$) and $I(\psi) \equiv \alpha\psi$ are assumed. The radial distributions of B_p and B_t on the flux conserver midplane deduced from above expression are shown by solid lines in the profiles at t= 30 μs of Fig. 3 (a) and Fig. 3 (b). Equation (1) is in good agreement with experimental results. If the observed field decay is only due to the homogeneous classical resistivity, $\eta(T_e)$, of the plasma, the model gives the average electron temperature of 6.5 eV. This value is considered reasonable according to the experimental evidence of the quiet decay of magnetic fields. A modified flux conserver with a tapered entrance region was installed to induce the faster reconnection, which may be expected to reduce the thermal conduction loss along field lines. The typical result obtained with this flux conserver is shown in Fig. 4. The reconnection time becomes considerably smaller but the decay time does not change appreciably. As a next step of this experiment, heating of the CT plasma has been carried out by means of the pulsed toroidal field produced by the poloidal current through the flux conserver and the center rod.

REFERENCES.

[1] I. Henins, H.W. Hoida, T.R. Jarboe, R.K. Linford, J. Marshall, K.F. McKenna, D.A. Plats and A.R. Sherwood, Proc. 3rd Symp. Phys. and Tech. of Compact Toroids in the Magnetic Fusion Energy Program, Los Alamos, 1980(Los Alamos Nat. Lab.,1980) P.113.

[2] K. Watanabe, K. Ikegami, A. Ozaki, N. Satomi and T. Uyama, Proc. Workshop on Compact Toroid, Osaka, 1981(Osaka Univ.,1981) P.66.
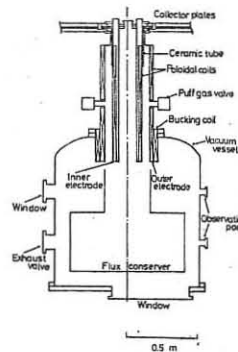
Fig. 1. Schematic diagram of CTCC-1.
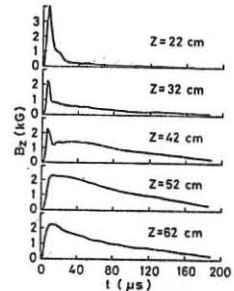
Fig. 2. Time evolutions of B_z at various positions on the axis.
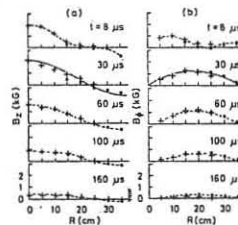
Fig. 3. Radial profiles of B_z (a) and B_ϕ (b) on the flux conserver midplane.
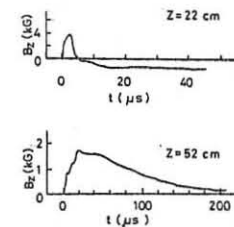
Fig. 4. Time evolution of B_z obtained with the modified flux conserver.

NUMERICAL SIMULATION OF THE COMPACT TOROID EVOLUTION TOWARDS THE EQUILIBRIUM STATE

V.V.Belicov, V.M.Goloviznin, V.K.Korshunov, A.I.Malutin,

V.N.Semenov

I.V.Kurchatov Institute of Atomic Energy, USSR

Generation and heating of a compact toroid occur due to a longitudinal shock compression of the initial non-equilibrium configuration with the strongly elongated loops of the magnetic field lines /1/ (Fig.1). Some preliminary results of simulating this stage of the toroid evolution towards equilibrium under the conditions close to the experimental ones are presented in this paper. The aim of this simulation is to find out an effect of the initial experimental conditions (size, density, current and plasma distribution) on the final steady-state characteristics. In particular, the conditions for a maximum effective plasma heating are of interest as well as the problem of the final state stability. Comparison of the computed and experimental results allow to make the more complete and precise interpretation of the experimental results and to obtain an information inaccessible in the direct measurements.

The simulation has been based on the 2-D MHD-code in which the field diffusion during the time of the MHD plasma relaxation /2/ is not taken into account.

Some consecutive stages of the toroid axial compression for one set of initial conditions are shown in Fig.1. Fig.1 demonstrates the propagation of a wave from the ends to the middle of the chamber. It is illustrated by the calculated oscillograms of a diamagnetic signal $\mathcal{D} = He - \frac{\varphi}{\pi R^2}$ and an optical thickness of plasma $n\ell$ (Fig.2a,3a). The comparison between the calculated and experimental data obtained under approximately similar conditions shows their qualitative agreement. A quantitative difference in a shock $n\ell$ and in the presence of oscillations in the experiment befor the wave passage is associated with a radial compression and plasma oscillations in the rising external field. A change in the external magnetic flux has not been taken into account in the calculations. The account of a 4-fold radial compression shows a quantitative agreement with the experiment. The characteristic pecularity of the compression is a strong cumulative convergence effect of the encountering waves at the central cross-section. This effect is manifested as steep spikes on the plasma parameters on the computed and experimental curves at that instant of time. After wave cumulation some 2-D oscillations of the plasma volume are observed. After their damping plasma comes to the equilibrium (Fig. 1). The plasma heating efficiency is illustrated in Fig. 4. Transition to the equilibrium is accompanied by the magnetic energy decrease and thermal energy increase within the region from the separatrix. A relative plasma volume with a low field and, consequently, with high presure (Fig. 5) steeply rises in this case. The equilibrium state characteristics are interesting from the point of view the plasma stability. For a computed variant, the stability of the compact toroid equilibrium configuration against the interchanges of the tubes of force (this configuration

is obtained as a result of the evolution described) has been studied. This configuration is found to be stable. One should note that a non-stationary 2-D shock wave differs from a stationary wave travelling along the plasma cylinder with the opposite fields inside it. The same can be said about the eqilibrium configuration.

References

1. Es'kov A.G., Zolotovsky O.A.,Kalygin A.G. et al. - In: Plasma Phys. and Contr. Nucl. Fus. Res., IAEA, Vienna, 1975, v.3, p.71.

   Es'kov A.G., Kurtmullaev R.Kh., Kreshuk A.P. et al. - In: Plasma Phis. and Contr. Nucl. Fus. Res., IAEA, Vienna, 1979, v.2, p.187.

2. Головизин В.М., Коршунов В.К.. Препринт ИПМ АНСССР, № 99,1980.

3. Семёнов В.Н., Соснин Н.В.. Физика плазмы, т.7, вып.2, стр.333, 1981.

Fig.1. Stages of evolution of compact toroid. Lines correspond to the magnetic lines of force.

Fig.2. Oscillograms of diamagnetic signal at different cross sections of chamber; Z=0 - middle of chamber; a - calculation, b - experiment.

Fig.3. Oscillograms of optical thikness of plasma, $n\ell$; a - calculation, b - experiment.

Fig.4. Time dependence of magnetic energy of reserved field (1), heat energy (2) and kinetic energy (3) of plasma.

Fig.5. Radial profiles of pressure before and after passage of wave (Z=0).

Fig. 1.

Fig. 2.

Fig. 3.

Fig. 4.

Fig. 5.
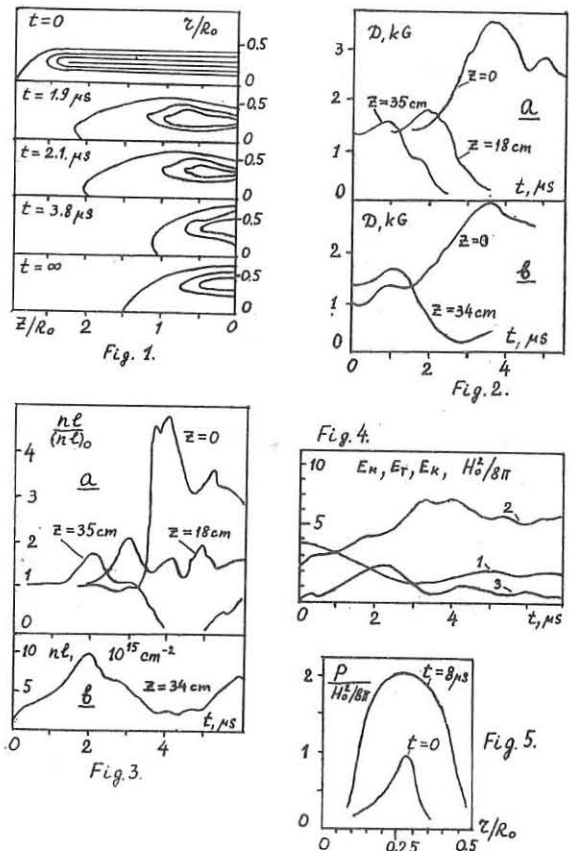
A STUDY OF THE EQUILIBRIUM AND DECAY OF COMPACT TOROIDS GENERATED BY A MAGNETIZED CO-AXIAL PLASMA GUN*

E. H. A. Granneman†, G. C. Goldenbaum‡, J. H. Hammer, C. W. Hartman, D. S. Prono, J. Taska, W. C. Turner

Lawrence Livermore National Laboratory, Livermore, California 94550

We have continued our earlier work on the co-axial gun production of compact toroidal plasmas that are contained in an oblate shaped cylindrically symmetrical flux conserver[1] (see Fig. 1). Following our observation that the magnetic structure produced by the gun is well described by force-free currents, the analysis of the data has been extended along the lines of J. B. Taylor's [2] theory of the reversed field pinch. Spatial magnetic field profiles are well represented by the lowest energy eigenmode solution to $\nabla \times \vec{B} = k\vec{B}$ with k = constant. Conservation of magnetic helicity during plasma formation leads to a scaling law that specifies an upper bound to the final state poloidal flux in terms of two plasma gun input quantities -- the magnetic flux superimposed on the inner electrode, and the number of volt-seconds input to the plasma gun discharge. The experimental data fall close to the upper bound predicted by the scaling law. This observation leads to the conclusions that magnetic helicity is fundamental to understanding compact torus formation and the plasma gun-flux conserver combination is remarkably efficient from the helicity viewpoint. The scaling law should prove useful in the design of future experiments and a similar law may be valid for the other spheromak formation schemes.[3][4] Aside from elucidating the formation process we have recently turned our attention to understanding the plasma lifetime. A dominant energy loss during the decay of the plasma magnetic fields is impurity radiation. The major impurities are carbon and oxygen. At present the plasma is apparently unable to burn through the low T_e radiation peaks of these impurities. A 20% increase in the magnetic field lifetime was observed after cleaning the gun electrodes and flux conserver in an argon glow discharge. Further work is needed to understand and control the plasma impurity influx. In order to reduce electron heat conduction losses and the possible influx of impurities along the initially open field lines, we have recently installed a pinching coil between the plasma gun and flux conserver to force reconnection of flux surfaces. Without the pinching coil, spontaneous reconnection occurs in a few tens of microseconds. With the pinching coil reconnection is complete about five microseconds after firing the coil current. Operation with the pinching coil has been too brief to allow any other definite conclusions to be reached regarding its operation.

Fig. 1 shows a schematic of the apparatus. The plasma gun injects into a cylindrically symmetrical copper flux conserver with wall thickness 0.16 cm. Typically the pulsed gas input ranges from 5 to 30 torr-liters deuterium, the magnetic flux in the inner electrode ranges from 600 to 2000 kG-cm², the outer electrode solenoid is shorted and 50 kJ electrical energy are input to the gun terminals producing a peak discharge current of 500 kA.

After an initial 20 to 40 μsec transient period profiles of magnetic field components in the flux conserver settle down to regular shapes that remain unchanged during the plasma decay. An example of radial profiles of B_z (poloidal) and B_x (toroidal) in the midplane of the flux conserver is shown in Fig. 2, 26 μsec after plasma initially left the plasma gun. The data have been fit with the lowest energy force-free eigenmode solution to $\nabla \times \vec{B} = k\vec{B}$, which for a flux conserving cylinder boundary with L/R ≤ 1.67 has been shown to be given by [5]

$$B_r = -B_0 \frac{k_z}{k_r} J_1(k_r r) \cos(k_z z)$$

$$B = B_0 \sqrt{1 + \frac{k_z^2}{k_r^2}} \ J_1(k_r r) \sin(k_z z) \qquad (1)$$

$$B_z = B_0 \ J_0(k_r r) \sin(k_z z)$$

where $k_z = \frac{\pi}{L}$, $k_r = \frac{3.83}{R}$, L = 40 cm is the length and R = 37.5 cm is the radius of the flux conserving wall. From Fig. 2 the poloidal field on the symmetry axis is seen to be about B_0 = 5 kG and from the fit we have estimated that the total magnetic energy is W_B = 4.5 kJ, and the toroidal current is I_{tor} = 225 kA. Auxiliary data with a He-Ne interferometer gives a chord average density $\bar{n}_e = 2 \times 10^{15}$ cm⁻³ for the data in Fig. 2. Since then we have operated with $\bar{n}_e$ as low as 1×10^{14} cm⁻³ and not observed any change in the magnetic profiles. Data with a quartz pressure probe inserted in the plasma give an upper limit to the local plasma beta ≤ 10%, in agreement with the force-free nature of the magnetic field.

The magnetic helicity $K = \int \vec{A} \cdot \vec{B} \, d^3x$, where $\vec{B} = \nabla \times \vec{A}$, can be computed from eqn. (1) as

$$K_{plasma} = \frac{\pi}{4} \frac{a_{11}^2 J_0^2(a_{11})}{a_{01} J_1(a_{01}) [1 - J_0(a_{11})]} \psi_{pol} \psi_{tor} = 1.07 \, \psi_{pol} \psi_{tor} \qquad (2)$$

$$\frac{\psi_{pol}}{\psi_{tor}} = \frac{\pi a_{01} k_z}{k} \frac{J_1(a_{01})}{1 - J_0(a_{11})}$$

where a_{01} = 2.40, a_{11} = 3.83 and ψ_{pol} = total poloidal flux, ψ_{tor} = total toroidal flux. The magnetic helicity input to the plasma gun terminals can be shown to be

$$K_{gun} = \left(\int_{t=0}^{V=0} V(t') \, dt' \right) \psi_{gun} \qquad (3)$$

where V(t') is the voltage applied across the gun insulator and ψ_{gun} is the inner electrode flux passing through the insulator. K_{gun} is an upper bound to K_{plasma} giving rise to the "flux amplification" inequality

$$\frac{\psi_{pol}}{\psi_{gun}} \leq 2 \sqrt{\frac{k_z}{k}} \frac{a_{01} J_1(a_{01})}{a_{11} J_0(a_{11})} \left[\frac{\int V dt}{\psi_{gun}} \right]^{\frac{1}{2}} \qquad (4)$$

where $k^2 = k_r^2 + k_z^2$. The data are compared with this inequality in Fig. 3 where it is seen that many shots lie close to the allowed upper bound, implying that for these shots $K_{plasma} = K_{gun}$. The flux amplification effect was first noted experimentally by Alfven, et al.[5]

In Fig. 4 we have plotted the time for magnetic field intensity to decay to 1/e of its initial value (τ_B) as a function of the initial plasma magnetic field energy (W_B). For this data all internal probes are removed from the plasma and τ_B and W_B are measured by a flux loop on the inside wall of the flux conserver. Data shown in Fig. 4 were taken before and after 14 hours of glow discharge cleaning with argon. In all cases the base vacuum pressure was maintained at ~ 1.5 (-7) Torr before a shot. The average decay time after discharge cleaning increased about 20 μsec, from 120 μsec to 140 μsec. The longest decay time observed to date is 170 μsec. The magnetic field decay is generally not pure exponential and the flux loop signal reaches zero after about 2 τ_B. Total radiated energy after plasma formation W_{rad} is compared with the initial magnetic energy W_B in Fig. 5. The radiation energy is computed by integrating the instantaneous power detected by a collimated, magnetically insulated pyroelectric detector. Although there is some scatter the data lie rather close to the line $W_{rad} = W_B$ indicating that radiation is an important plasma loss process in the present experiment, both before and after discharge cleaning.

A single turn theta pinch coil has been installed in the region between the plasma gun and flux conserver shown in Fig. 1 to force reconnection of flux surfaces. Fig. 6 shows a sequence of three shots with a magnetic probe positioned underneath the theta coil; pinching coil alone, plasma gun alone, and plasma gun plus pinching coil. The pinching coil is seen to quickly reverse the magnetic field on axis about 5 μsec after the coil is fired, implying forced reconnection of flux surfaces.

References

(1) W. C. Turner, G. C. Goldenbaum, E. H. A. Granneman, J. H. Hammer, C. W. Hartman, D. S. Prono, J. Taska, A. C. Smith, Jr., Proc 3rd Symposium on Physics and Technology of Compact Toroids, Los Alamos, New Mexico, LA-8700-C, pg. 113.

(2) J. B. Taylor, Phys. Rev. Lett., 33, 1139, 1974.

(3) G. C. Goldenbaum, J. H. Irby, Y. P. Chong, G. W. Hart, Phys. Rev. Lett., 44, 393, 1980.

(4) M. Yamada, H. P. Furth, W. Hsu, A. Janus, S. Jardin, M. Okabayashi, J. Sinnis, T. H. Stix, K. Yamazaki, Phys. Rev. Lett., 46, 188, 1981.

(5) Z. G. An, A. Bondeson, H. Bruhns, H. Chen, Y. P. Chong, J. M. Finn, G. C. Goldenbaum, H. R. Griem, G. W. Hart, R. Hess, J. H. Irby, Y. C. Lee, C. S. Lin, W. M. Manheimer, G. Marklin, E. Ott, Proc. of 8th Intl. Conf. on Plasma Phys. and Cont. Fusion, IAEA, Brussels, 1980.

(6) H. Alfven, L. Lindberg, P. Mitlid, J. Nucl. Energy, Part C, 1, 116, 1960. L. Lindberg, C. Jacobsen, Astro. Phys. Journal, 133, 1049, 1961.
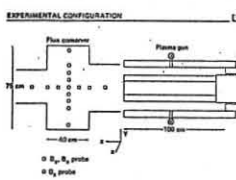
Fig. 1
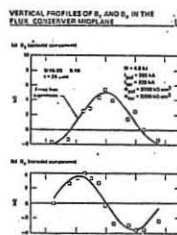
Fig. 4
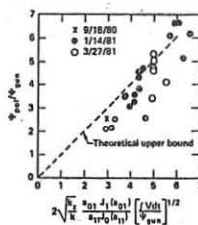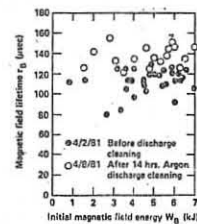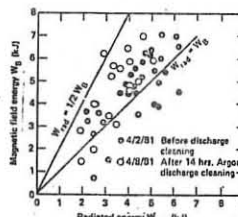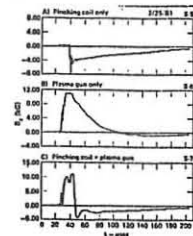
Fig. 2

Fig. 5

Fig. 3

Fig. 6

Experimental Studies on FRC plasma

S. Okada, M. Tanjyo, T. Minato, Y. Ito, S. Ohi,
T. Ishimura and H. Ito

Plasma Physics Laboratory, Faculty of Engineering
Osaka University
Yamada-Kami, Suita, Osaka 565, Japan

Experimental study to obtain a plasm with the ion temperature of a few keV had been done on PIACE.[1] The experiment has been extended to study on a confinement of high temperature plasma with field reversed configuration (FRC).

The apparatus consists of a main compression coil 1 m in length and a pair of theta pinch guns 20 cm in length equipped 5 cm apart from the main coil. Experiments were carried out on two types of the apparata. The inner radii of the main coil r_w and the tube r_{tube}, the maximum compression field B_{max}, and their rise and decay times τ_{rise} and τ_{decay} are shown below.

	r_w	r_{tube}	B_{max}	τ_{rise}	τ_{decay}
smaller bore exp.	50 mm	40 mm	20 kG	1.8 µs	45 µs
larger bore exp.	74	62	15	2.3	75

Two plasma streams from a pair of the guns flow along a guide field of 2 − 4 kG and make a collision. To this encounter plasma, main compression field is applied in the reverse bias mode.

A general feature of the FRC plasma is that its stable period terminates by the onset of n = 2 rotational instability and that the deformation by this instability grows gradually until the configuration disappears suddenly. It is thought at present that the diffusion of the particles across the magnetic field causes the rotation.[2] This idea indicates that the stable time can be increased by decreasing the density gradient near the separatrix around the FRC plasma. This is realized by increasing the value of x_s (=r_s/r_w, r_s ; the radius of the separatrix).

SMALLER BORE EXPERIMENTS

The stable time and the life time of the plasma are about 10 µs and 20 µs respectively. The separatrix radius r_s is about 1.5 cm (x_s = 0.3). The electron temperature T_e and density n_e are almost constant at 200 eV and 6×10^{15} cm^{-3}, respectively, for more than 10 µs. The radial profile of T_e is nearly uniform and that of n_e is nearly flat topped. The reverse flux in the plasma ϕ_i estimated by a rigid rotor model[2] is about 5 % ofthe initially applied reverse bias flux inside of the tube ϕ_0. The ion temperature T_i inferred from the Doppler profile of CV is 1 keV at 5 µs and the neutron emission from the deuterium plasma is also detected for up to 10 µs.[3]

LARGER BORE EXPERIMENTS

The enlargement of r_w and r_{tube} resulted in the increase of x_s as is shown in the following table. When the main compression field is crowbarred to be 7kG in its rising phase (low compression case), x_s increased further compared to the normal case (high cmpression case) as is shown in Fig.1. The length of the plasma also increased from 40 cm to 60 cm. The values of τ_s,

τ_l, r_s, x_s and T_i at 5 µs from the compression are shown as follows.

	τ_s	τ_l	r_s	x_s	T_i
high compression	15 µs	25 µs	2 cm	0.4	800 eV
low compression	25	40	4	0.5−0.6	400

For the low compression case, the reverse field along the axis of the FRC was directly observed by magnetic probes inserted along the axis, though the life time of the plasma became 15 µs due to the effects of probes. The ratio of the reverse field to the external one is about 70 % and remains nearly constant as long as the FRC is maintained. At 5 µs after the main compression, the estimated ϕ_i was about 20 % of ϕ_0.

These experimental results show a tendency that τ_s becomes larger as x_s is larger. In order to increase x_s by diminishing the loss of the reverse bias flux,[4] a quadrupole barrier field was added at the zero crossing phase of the main compression field. Preliminary results show that ϕ_i increased at the zero crossing phase. However, in the equilibrium stage, ϕ_i and x_s did not increase remarkably and also τ_l was not improved.

It is added that when a pair of gun coils are energized simultaneously with the main coil as in the case of the mirror compression, the diamagnetic signal lasted for about 75 µs.

REFERENCES

1) H. Ito et al. Proc. 5th Int. Conf. on Plasma Phys. and Contr. Nucl. Fus., Tokyo, 1974, volIII p.389
2) R. K. Linford et al. Proc. 7th Int. Conf. on Plasma Phys. and Contr. Nucl. Fus., Insbruck 1978, vol.II p.447
3) S. Ohi et al. Proc. Int. Conf. Symposium on Phys. in Open Ended Fus. Systems, Tsukuba, 1980, p.274
4) A. G. Es'kov et al. Proc. 7th Int. Conf. on Plasma Phys. and Contr. Nuc. Fus., Insbruck, 1978, volII p.187

Fig.1. Side-on streak photograph, diamagnetic flux signal, magnetic field at the coil wall (upper trace and the lower one is the signal with and without plasma respectively) and temporal variation of the separatrix radius r_s for the (a) high compression case and the (b) low compression case.
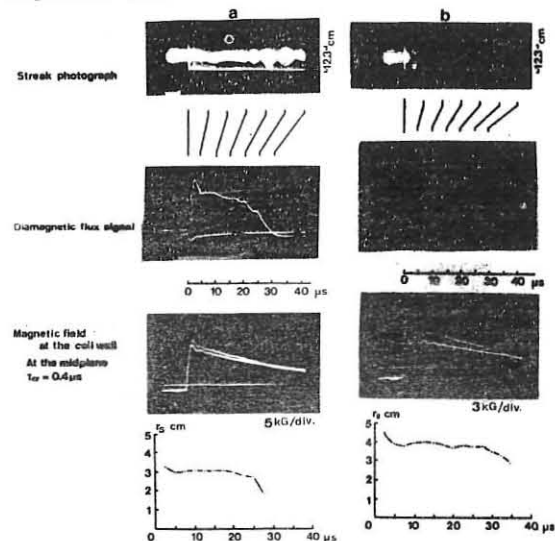
FINITE BETA MINIMUM ENERGY EQUILIBRIA OF ETA-BETA II RFPs

J.W. Edenstrasser

Institut für Theoretische Physik-University of Innsbruck, Austria

G.F. Nalesso

Centro di Studio sui Gas Ionizzati del Consiglio Nazionale delle
Ricerche e dell'Università di Padova, Italy

Introduction. A recent finite beta theory has been applied to describe the observed quiescent phase of RFPs in Eta-Beta II.

The main machine parameters and standard experimental conditions are described elsewhere [1]; here it is sufficient to recall that in Eta-Beta II, as well as in Zeta [2] and more recently in other experiments (TPE-1RM, Sakura-Mira [3], ZT-40M, Los Alamos, HBTX-1A, Culham) plasmas have been produced that after the setting-up phase show a characteristic period of reduced field fluctuations and reduced energy losses commonly known as "quiescence".

The observed improved confinement has been interpreted as due to a natural tendency of the plasma to relax through a series of relative minimum energy states. In a theory developed by J.B. Taylor [4], these turn out to be the force free equilibria. Although Taylor's theory deals only with the case of an incompressible plasma, it has attracted much attention, because it accounts for a number of phenomena occurring in toroidal discharges, as for example, field reversal in pinches. In a recent paper [5] we have extended Taylor's variational principle to the finite-β case. As additional constraints therein we have imposed the equilibrium equation (i.e. the comparison states must be neighbouring equilibria) and constancy of the pressure and of the longitudinal magnetic field at the axis and at the wall. For the circular cylinder and for the case of a peaked current density profile the resulting equilibrium quantities are (assuming for the specific heat ratio γ the value 5/3)

$$B_r = 0, \quad B_\Theta = \frac{\lambda^2}{r_w} \frac{x \, C_1(v)}{v}, \quad B_z = \frac{\sqrt{2}\lambda}{r_w} C_o(v) \tag{1}$$

$$j_r = 0; \quad j_\Theta = -\frac{\sqrt{2}\lambda}{\mu_o r_w} B_\Theta, \quad j_z = \frac{\lambda^2}{\mu_o r_w^2}\left[2\frac{v_a^2}{v^3}C_1(v) + \left[1 - \frac{v_a^2}{v^2}\right]C_o(v)\right] \tag{2}$$

$$p(v) = \frac{\lambda^2}{2\mu_o r_w^2}\left[3\left[C_o^2(v_w) - C_o^2(v)\right] - v_a^2\left[\left(\frac{C_1(v_w)}{v_w}\right)^2 - \left(\frac{C_1(v)}{v}\right)^2\right]\right] \tag{3}$$

where we have defined

$$C_o(v) = AI_o(v) + BK_o(v), \quad C_1(v) = dC_o/dv, \quad v = |\lambda|\sqrt{\varrho + x^2}, \quad x = r/r_w, \quad \varrho > 0$$

I_o, K_o are the modified Bessel functions, v_a and v_w the values of their argument at the magnetic axis and at the wall, r_w is the minor radius; A, B, λ, and ϱ are the four parameters to be determined from appropriate boundary conditions. In comparing the measured magnetic field profiles of Eta-Beta II (which have been obtained by inserting a set of magnetic coils in an equatorial plane from the geometric axis R_{ga} outwards) we apply a "half order" toroidal correction.

First the toroidal shift, δ, is taken into account in approximating the torus by a cylinder whose axis coincides (locally) with the magnetic axis $R_{ma} = R_{ga} + \delta$ and with radius $r_w = a - \delta$ (a being the minor radius). Then the second dominant toroidal effect, the 1/R dependence of the field is included in an approximation of the form

$$B_{pol} = \frac{B_\Theta}{1 + \varepsilon x}, \quad B_{tor} = \frac{B_z}{1 + \varepsilon x} \qquad (\varepsilon = r_w/R_{ma}) \tag{4}$$

with B_Θ and B_z given by (1) and similar expressions for the currents and pressure. These expressions may be easily derived if the magnetic field is expressed by the poloidal flux function $\emptyset$, and employing for $\emptyset$ its cylindrical approximation.

Comparison with the experiments. In figures 1 and 2 the measured magnetic field profiles (taken at three time instants during the quiescent phase) are shown and compared with the theoretical ones following from equations (4). The applied boundary conditions have been the values of B_{pol} and

B_{tor} at the metal wall (liner) B_{tor} at the torus axis and the toroidal flux ψ_{tor}. Note that to determine each equilibrium state it is necessary to fix a set of four parameters, as has been shown previously. From the figures it is clearly seen that the fitting of the experimental profiles with the calculated ones is quite satisfactory and well within the experimental errors. This agreement turns out even more clearly from figure 3 where the current densities are reported. Note that in evaluating these last quantities the errors due to the discreteness of the coils may be quite important. The kinetic pressure corresponding to one of the equilibrium states shown in figures 1, 2 is plotted also in figure 4 and is consistent with the experimental value on axis obtained with laser scattering. It must be pointed out, however, that the pressure profile is very sensitive to small variations of the magnetic field.

Conclusions. Magnetic field profiles (as well as current density and pressure profiles) measured during the quiescent phase of RFP plasmas produced in Eta-Beta II have been compared with those obtained from axisymmetric states derived by minimizing the total potential energy subject to certain constraints.

It has turned out that there is indeed a satisfactory agreement between the measured profiles and the theoretical ones obtained by prescribing (for each instant) a set of four parameters. However, since the applied theory is a static equilibrium theory it cannot describe the evolution of the plasma itself (i.e. describe the time dependence of the four parameters on such a time scale). In any case, the obtained results justify the assumption of a decaying of the plasma through a series of equilibrium states where, on a timescale short compared with the plasma lifetime, the assumed invariants may be thought to be strictly verified. It is important to note that the theory discussed here describes finite beta plasma equilibria and the observed agreement between the experimental and theoretical profiles increases the confidence that minimum energy high beta states are indeed obtained in the quiescent phase of slow pinches.

Fig. 1

Fig. 2

Fig. 3

Fig. 4
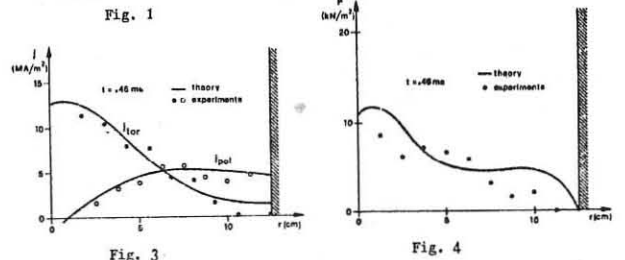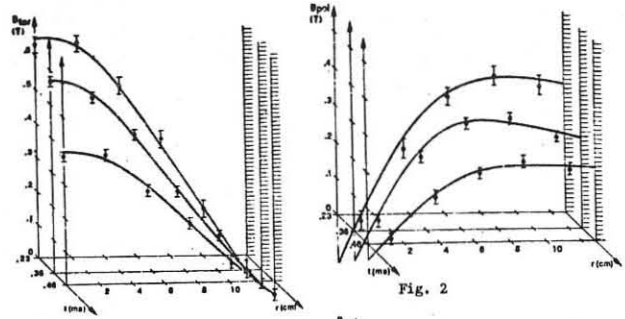
References

[1] Buffa A. et al.: Proc. 8th Conf. on Plasma Physics and Controlled Nuclear Fusion Research, Bruxelles 1980, paper IAEA-CN-38-L1.

[2] Newton A.A.: Proc. Int. Workshop on RFP 1979, Padova, UPee 78/08.

[3] Hirano Y. et al.: Proc. 8th Conf. on Plasma Physics and Controlled Nuclear Fusion Research, Bruxelles 1980, paper IAEA-CN-38-L-2-2.

[4] Taylor J.B.: 3rd Topical Conf. on Pulsed High Beta Plasmas, D.E. Evans Editor, pp. 59-67 (1975).

[5] Edenstrasser J.W.: "Minimum energy states of symmetric MHD equilibrium", submitted to Journal of Plasma Physics.

M

RELATIVISTIC PLASMA ELECTRONICS
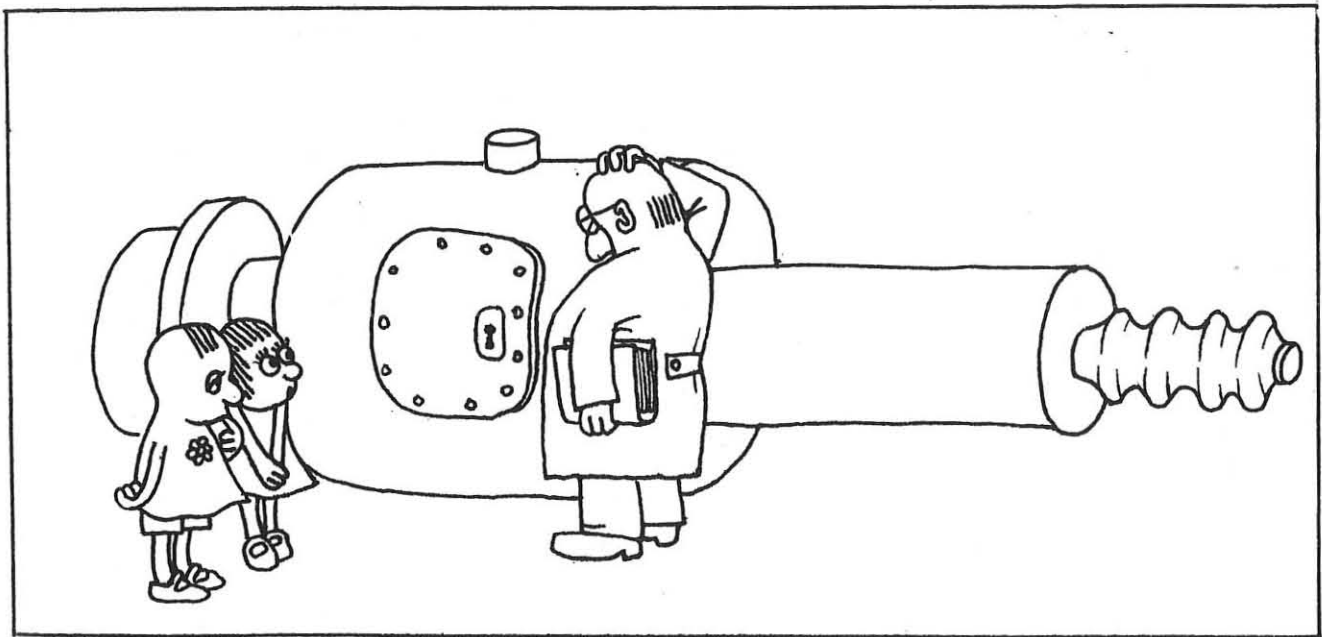
EXPERIMENTAL STUDY OF THE INFLUENCE OF CATHODE
AND COLLECTOR PLASMA DYNAMICS ON THE MICROWAVE
GENERATOR WITH A RELATIVISTIC ELECTRON BEAM

N.I.Zaitsev, N.F.Kovaljov, G.S.Korabljov, I.S.Kulagin

Institute of Applied Physics, Academy of
Sciences of the USSR, Gorky, USSR

To increase pulse duration of microwave radiation in relativistic generators one must solve a number of problems related to dynamics of a cathode plasma and a plasma formed on electrodes under intense electron beam bombardment.

Plasma with the electron density $N_e \sim 10^{15} cm^{-3}$ [1] is formed on the electron gun cathode and expands both transverse to and along the stationary magnetic field with the rate of the order of $10^5 cm/s$ and $10^7 cm/s$, respectively [1,2]. This results in the variation of the effective emitting surface of a plasma cathode during the pulse. Plasma from the bombarded surfaces may expand even with a higher rate. For example, when the origin threshold (150 J/g) was exceeded, on the stainless steel collector, plasma formed which was nontransparent to cm-waves and filled the beam transition channel with the rate higher than $3 \cdot 10^7 cm/s$ [2]. Therefore, most promising for generation of microwave radiation of enhanced duration are transit beam devices which have a cathode quite remote from the electrodynamic system and a collector with a sufficiently developed surface. A carcinotron with good adaptibility with respect to the variation of electron beam parameters, used in our experiments, is of most interest.
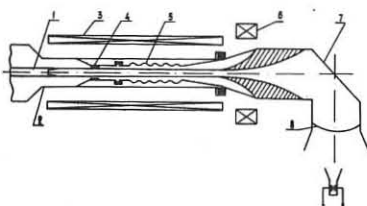
Fig.1. Scheme of experimental setup: 1 - cathode, 2 - anode, 3 - main solenoid, 4 - diaphragm, 5 - electrodynamic system, 6 - correcting solenoid, 7 - mirror, 8 - vacuum window

In this generator (Fig.1) electrons interacted with the first backward spatial harmonic of the TM_{01} type of a circular waveguide with a shallow-corrugated facet [1]. A coaxial diode with magnetic insulation was an electron source. A collimating diaphragm prevented elctron beam bombardment of the walls of the electrodynamic system. A drift tube between the diaphragm and the slowing-down system protected the latter from evaporation products of the cathode and diaphragm materials and enhanced the delay of plasma formation on the diaphragm in the active volume of the generator. The electron gun and the slowing-down system were placed into a uniform magnetic field H=1.3 T. The scheme and the measurement procedure for the parameters of the high-frequency radiation and of the electron beam were the same as in [1].

The configuration of the magnetic field in the collector region was chosen so as to obtain the density of the beam energy release on the collector lower than the threshold (150 J/g [2]). In this regime, generation cutoff was due to plasma formation on the collimating diaphragm. In all the instances duration of electromagnetic radiation was es-
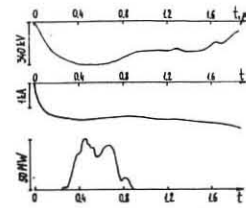
Fig.2. Voltage oscillogram on a diode (a); oscillograms of collector current (b) and of high-frequency power (c)

sentially lower than that of the electron current pulse.

The mean radiation power of $\sim$40 MW with the duration of 0.4 mcs was obtained in our experiments, which corresponds to the generator efficiency of $\sim$8% (see Fig.2). With respect to the peak power (50 MW) the generator efficiency was 11%, which is close to the calculated results. The wavelength and the radiation structure also corresponded to the results of calculations: λ =3.2 cm and TM_{01} of a circular waveguide.

In subsequent experiments we used an electron gun with beam compression by the magnetic field, similar to that described in [3]. It was found out, that in this system the expansion rate of the outer boundary of the beam in the transmission channel was two times lower than in the previous experiments. The magnetic field in the generator active volume was increased up to 1.7 T. The generator was intended for the wavelength λ =4 cm.

Fig.3 shows voltage oscillogram on a diode and oscillograms of an envelope of a high-frequency power pulse, which correspond to 3 coefficients of magnetic compression $\alpha = \frac{H}{H_K}$, where H is the magnetic field in the slowing-down system, and H_k is the cathode field (3; 3.6; 4.8). High-frequency generation delay depended only on the magnitude of magnetic
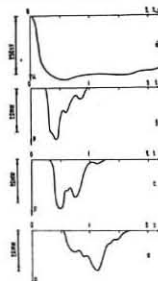
Fig.3. Voltage oscillogram on a diode (a) and oscillograms of a high-frequency power (b,c,d) at different compression, ($\alpha = \frac{H}{H_K}$) of electron beam: b) α =3, c) α =3.6, d) α =4.8.

compression, which is due to the variation of the initial diameter of the electron beam. The time of the generator cutoff also depended on the magnetic compression and, as in the previous generator, was conditioned by dense plasma formation on the collimating diaphragm.

Thus, decrease in the expansion rate of the outer boundary of the electron beam made it possible to obtain the generation duration up to 1 mcs. The peak output power was 20 MW, which corresponds to the generator efficiency of 15%.

REFERENCES

1. Proc. "Relativistic High-Frequency Electronics", ed.by Ac. A.V.Gaponov-Grekhov, Inst.Appl.Phys.,Acad.Sci.,USSR, 297 p. (1979).
2. N.I.Zaitsev et al. "Peculiarities of the High-Current Beam Formation for the Relativistic Microwave Oscillators", Proc. of the 3rd Intern.Top.Conf. on High-Power Electron and Ion Beam, Inst.Nucl.Phys., p.749, Novosibirsk, 1979.
3. V.A.Burov et al. "Accellerator of High-Current Beams of Microsecond Duration", Pribory i Tekhn.Eksp.,No.5,32,1979.

AUTOMODULATION AND STOCHASTIC OSCILLATION REGIMES IN
RESONANT RELATIVISTIC ELECTRON MASERS

N.S.Ginzburg, M.I.Petelin , M.A.Shapiro

Institute of Applied Physics, Academy of Sciences

of the USSR, Gorky, USSR

In high-power high-frequency generators electrodynamic
systems are often of quasi-optical type. Examples are
1) free electron laser (FEL) with two-mirror resonator;
2) gyrotron with whispering gallery modes; 3) magnetron
with large number of anode lamels.

Basic equations. In any of these systems, if the reso-
nator quality is high enough and the phase velocity disper-
sion is low, the wave envelope $A_n(\zeta, \bar{z})$ (here $\zeta = \bar{z} - V_{group}\bar{t}$)
is dimensionless wave variable, $\bar{z}$ is dimensionless longi-
tudinal coordinate) is of the "merry-go-round" structure
slowly altering from turn to turn. Changing the number of
a turn n by "slow" time τ and neglecting explicit depend-
ence of A_n on $\bar{z}$, the wave equation reduces to [1]

$$\frac{\partial A}{\partial \tau} + i\mu \frac{\partial^2 A}{\partial \zeta^2} + A = \int_0^L J \, \mathscr{x}(z) \, dz \qquad (1)$$

$$A(\zeta, \tau) = A(\zeta + T, \tau)$$

Here μ is the wave dispersion parameter, T is the wave
reversal period, $\mathscr{x}(\bar{z})$ is the electron-wave coupling coeffi-
cient, $J = \frac{1}{2\pi}\int_0^{2\pi} e^{-i\Theta} d\Theta_0$ is the electron current harmo-
nic synchronous to the wave, Θ_0 and Θ are initial and
current phases of an electron with respect to the wave. If
the force bunching of electrons is negligible compared to
the inertial one [2] (for the magnetron it is correct in
the weak magnetic field regime, when electrons are collect-
ed by the anode at the first cyclotron loop), the electron
motion equation reduces to the universal form

$$\left(\frac{\partial}{\partial \bar{z}} + \frac{\partial}{\partial \zeta}\right)^2 \Theta = \mathrm{Re}(A \, \mathscr{x} \, e^{i\Theta}) \qquad (2)$$

$$\Theta\big|_{\bar{z}=0} = \Theta_0 \in [0, 2\pi), \quad \left(\frac{\partial}{\partial \bar{z}} + \frac{\partial}{\partial \zeta}\right)\Theta\big|_{\bar{z}=0} = \delta$$

where δ is mismatch from electron-wave resonance. Sometimes
it is convenient to expand $A(\zeta,\tau)$ into the sum of modes
with space homogeneous amplitudes $A = \sum A_\delta(\tau) e^{i\Delta_\delta \zeta}$,
where $\Delta_\delta = \frac{2\pi}{T} s$.

Modulation instability. Some general properties of
generators under consideration can be revealed using the
"klystron" approximation of the coupling function:
$\mathscr{x}(\bar{z}) = \varepsilon\delta(\bar{z}) + \delta(\bar{z}-L)$ (electrons interact with the wave
in two narrow "gaps" separated by distance L). In this
case Eqs. (1)-(3) reduce to a delayed argument equation:

$$\frac{\partial a}{\partial \tau} + i\mu \frac{\partial^2 a}{\partial \zeta^2} + a = -iX\left\{\frac{a}{|a|} e^{-i\delta L} J_1(|a|)\right\}_{\zeta - L}$$

where a is proportional to A, $J_1(X)$ is the 1st order
Bessel function, X is parameter proportional to the electron
current.

Let the initial state be a stationary single-mode gene-
ration. Is it stable with respect to small arbitrary pertur-
bations? That depends on excess of electron current over
the threshold and on location of the primary mode in the
self-excitation band (Fig. 1). In particular, when $\mu \to 0$
(equidistant eigenfrequencies), perturbations grow, if

$$\mathcal{G}^2(2 - \rho - \rho R)(3 + R^2 - 4\rho R) < (1 + \rho)(1 + R - 2\rho R)^2, \text{ where}$$
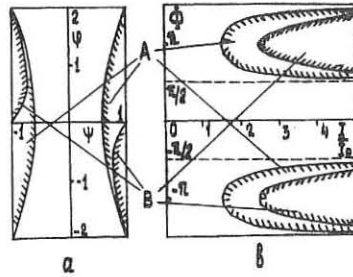
Fig. 1. Stability
diagrams: a) for small
excess over threshold;
b) for arbitrary
excesses over threshold
when the primary mode
frequency coincides
with the negative
absorption band center
ω_0. I is electron
current, I_0 is its mag-
nitude corresponding
to maximum frequency,
A and B are instability regions for weak ($\mu \to 0$) and
strong ($\mu \to \infty$) wave dispersions

$R = a_0 J_1'(a_0)/J_1(a_0)$, a_0 is amplitude of the primary
mode, $\rho = \cos\bar{\Phi}$, $\mathcal{G} = \cos\psi$, $\bar{\Phi} = \frac{\pi}{2}\frac{\bar{\omega}}{\omega}\varphi$, $\psi = \frac{\pi}{2}\frac{\bar{\omega}}{\omega}\psi$
$\varphi = \frac{\omega_\tau - \omega_p}{\bar{\omega}}$, $\psi = \frac{\omega_p - \omega_0}{\bar{\omega}}$, $\bar{\omega}$ and $\widetilde{\omega}$ are widths of the
negative absorption and self-excitation bands.

At moderate excesses over the threshold (Fig. 1a),
the primary mode is unstable only if its eigenfrequency ω_p
is shifted at a certain distance from position correspond-
ing to the maximum efficiency, i.e. the weaker is the mode,
the broader is the range of eigenfrequencies ω_τ of rival
modes able to withstand and suppress it. Finally, as nume-
rical solutions of Eqs. (1), (2) show, single-frequency
oscillations settle at a mode in the middle of the self-
excitation band.

At a large excess over the threshold, the stability
of the most efficient mode vanishes, satellite modes arising
in the positive absorption band of the electron beam
(Fig. 1b). This process (four-photon decay), according to
numerical calculations, results in phase-locking of modes,
i.e. in automodulation. The latter is periodic at moderate
I/I_0 and stochastic at large I/I_0 [3].

Quasi-linear approach to stochastic multimode regime
in FEL. For the FEL, where the high-Q two-mirror resonator
is excited by ultrarelativistic electron beam with finite
velocity dispersion, the stochastic regime can be described
by the following quasi-linear equations

$$\frac{\partial w_\kappa}{\partial \tau} + \frac{\omega}{Q} w_\kappa = \frac{1}{L}\int_0^L \Gamma \, dz \qquad w_\kappa\big|_{\tau=0} = w_0(\kappa)$$

$$\frac{\partial f}{\partial \bar{z}} = \frac{\partial}{\partial \gamma}\left(D \frac{\partial f}{\partial \gamma}\right) \qquad f\big|_{\bar{z}=0} = f_0(\gamma)$$

Here $f(\gamma, \bar{z}, \tau)$ is electron energy distribution function,
w_κ is spectral density of electromagnetic oscillations,
$\Gamma = \frac{\pi}{4}\frac{\omega\beta^2 \mathscr{x}^2}{\Omega}\gamma \frac{\partial f}{\partial \gamma}\big|_{\gamma = \sqrt{\frac{\kappa c}{2\Omega}}}$ is kinetic instability incre-
ment, $D = (8\pi^2 c^2 \mathscr{x}^2/m^2 c^4) w_\kappa$ is diffusion coefficient, $\mathscr{x}$ is
electron-wave coupling coefficient, Ω is electron oscilla-
tion frequency ($\kappa = 2\frac{\Omega}{c}\gamma^2$).

At large excesses over the threshold $\Gamma\frac{\omega}{Q} \gg 1$ in
the stationary generation regime $(\partial w_\kappa/\partial\tau) = 0$, the distri-
bution function at the resonator exit $f(\gamma, L)$ has the form
of a plateau stretching to energies small compared with
those at the entrance. So, a half of the electron beam
power converts into electromagnetic radiation.

1. V.L.Bratman, N.S.Ginzburg, M.I.Petelin. Izv. AN SSSR,
   ser. fiz. 44, 1595, 1980.
2. V.L.Bratman et al. Relativistic high-frequency electro-
   nics, Gorky, 1979, p.249.
3. Ya.L.Bogomolov et al. Optics Commun., p.209, 36, 1981.

RELATIVISTIC PLASMA GENERATORS WITH EFFECTIVE RADIATION OUTPUT

V.L.Bratman, N.S.Ginzburg, N.F.Kovaljov, M.A.Shapiro

Institute of Applied Physics, Academy of Sciences

of the USSR, Gorky, USSR

Numerous investigations (see, for example, [1,2]) show that it is rather easy to excite waves in plasma-beam systems, but it is difficult to provide single-frequency generation and extract radiation from plasma. The report deals with new possibilities of solving the problem on radiation extraction, arising as the result of excitation of plasma oscillations by a relativistic electron beam.

In the case when plasma is assumed to be a linear medium, the theory of plasma generators can be formulated by analogy with the theory of vacuum Cerenkov devices (see, for example, [3]). Such an approach permits to reduce the problem of the design to the electrodynamic one, i.e. to the choice of plasma configuration and density providing the necessary dispersive features of the wave, the coefficient of its coupling with the beam as well as matching to the output paths.

1. Relativistic plasma traveling wave amplifier.

Consider the case of magnetized plasma filling a cylindrical waveguide. From the dispersion diagram for this system (fig.1) it is seen that as the electron velocity increases, the phase velocity of the excited wave (curve a) increases as well and approaches the velocity of the wave propagating in a vacuum waveguide (curve c). When radiation is extracted from the system through the sharp cutoff between plasma and vacuum waveguides, the wave reflection coefficient from the cutoff is minimum $|r|_{min} =$

$$= \left(\frac{\kappa_\perp c}{\omega}\right)^2$$ at the frequency $\omega = \sqrt{(\omega_p^2 + \kappa_\perp^2 c^2)/2}$ where ω_p is the plasma frequency,
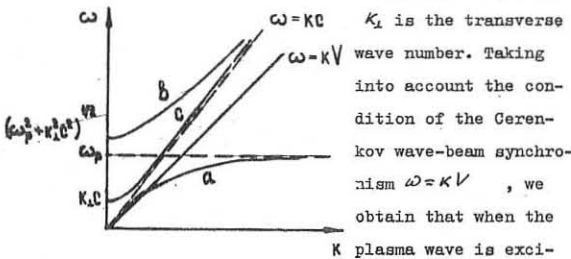
$\kappa_\perp$ is the transverse wave number. Taking into account the condition of the Cerenkov wave-beam synchronism $\omega = \kappa V$, we obtain that when the plasma wave is excited by ultrarelativistic electrons (the relativistic factor $\gamma = \left(1 - \frac{V^2}{c^2}\right)^{-1/2} \gg 1$ the reflection coefficient can be small $|r|_{min} \simeq \frac{1}{2}\gamma^{-2}$ Such value of $|r|$ is realized in the matching condition

Fig.1

$\omega_p \simeq \sqrt{2}\,\omega$, $a = \gamma\mu c/\omega$, where a is the waveguide radius, μ is the Bessel function root.

Application of results [3] to a plasma TWA shows that under the conditions of the optimum matching, the operating current proves to be a low one. A more favourable situation takes place in a waveguide with a gradually varying radius to the optimum value at the interface.

2. Relativistic plasma backward wave oscillator.

Another possibility is associated with radiation output through the lateral face of the waveguide. The possibility is realized at excitation of waves with anomalous dispersion (BWO). Waves with such dispersion exist, in gyrotropic plasma [2,4] and in a free layer of isotropic plasma [5] . In the latter case, however, only slow waves, which are not excited by the relativistic beam, possess anomalous dispersion. Necessary dispersion takes place in the tubular layer of isotropic plasma confined by a metal jacket (fig.2). In such a system, the
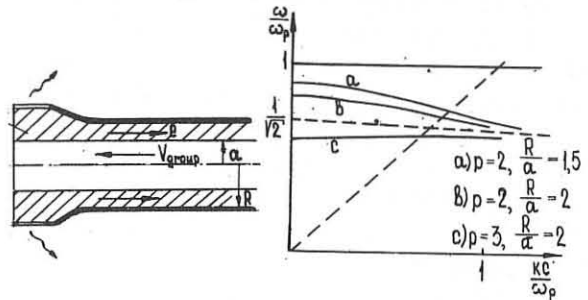
Fig.2   Fig.3

dispersion curve for the lowest mode crosses the light cone without changing the derivative sign. Due to this, rather a gradual variation of the waveguide geometry (of radius R in fig.2) permits to transform the wave phase velocity to a superlight value. Then, it is easy to radiate a wave through a free lateral face. Such a device is similar to an effluent-wave antenna. An optimum matching to the antenna is achieved for the lowest mode of the waveguide with parameters $\omega_p \simeq 1.5\,\omega$, $p = \frac{\omega_p a}{c} \simeq 2$, $R/a \simeq 1.5$.

REFERENCES

1. A.I.Akhiezer, Ya.B.Fainberg. DAN SSSR, 1949, 69, 555; D.Bohm, E.P.Gross. Phys.Rev., 1949, 75, 1851.

2. B.I.Aronov, L.S.Bogdankevich, A.A.Rukhadze. Plasma Phys., 1976, 18, 101.

3. N.F.Kovaljov, V.I.Petrukhina, A.V.Smorgonsky. Radiotekhnika i elektronika, 1975, 20, 1305, 1547.

4. A.W.Trivelpiece, R.W.Gould, J.Appl.Phys., 1959, 30, 1784.

5. T.Tamir, A.A.Oliner. Proc.IEEE, 1963, 51, 341.

STATES OF THE THIN-WALLED BEAM OF RELATIVISTIC
ELECTRONS IN LIMITED CHANNELS

M.I.Fuchs, N.F.Kovaljov

Institute of Applied Physics, Academy of Sciences
of the USSR, Gorky, USSR

The present report deals with results of the boundary value problem of formation and transportation of the thin-walled magnetized relativistic electron beam (REB) in a limited channel with an arbitrary profile $R(z)$ slightly varying along Z-axis. For slow variation of REB parameters $(2L_{//}/R)^2 \gg 1$ ($L_{//}$ is the variation scale) the Laplace equation for potential φ taking account of the condition $\varphi = V$ at the channel wall, the condition for the electrostatic field at the beam $\left(\frac{\partial \varphi}{\partial r}\right)_{\delta + 0} - \left(\frac{\partial \varphi}{\partial r}\right)_{\delta - 0} = 4\pi G$ (V is the anode voltage, G is the surface density) and the energy conservation law $\gamma(z) = 1 + \varphi(\delta, z)$, is reduced to the ordinary differential equation [1] :

$$\frac{d^2 \gamma}{d\varsigma^2} + (\gamma_R - \gamma)f - g\frac{\varkappa \gamma}{\sqrt{\gamma^2 - 1}} = 0 \qquad (1)$$

In (1) $\varsigma = \sqrt{2}\, z/R_0$, R_0 is transverse scale of the system, $\gamma_R = 1 + V$, $\varkappa$ is proportional to the beam current $\bar{I}$. For the plane channel with a beam propagating along the plane of symmetry $\varkappa = 2\pi \bar{I} R_0$, ($\bar{I}$ is the linear current density), $f(\varsigma) = g^2$, $g(\varkappa) = R_0/R$. For a cylindrical channel $\varkappa = 2\bar{I} \ln \frac{R_0}{R}$, $f(\varsigma) = g \ln \frac{R_0}{\delta}/\ln \frac{R}{\delta}$, $g(\varsigma) = (1 + \ln \frac{R_0}{\delta})/(1 + \ln \frac{R}{\delta})$ Here the potential is normalized to 0.5 MV, the current - to 17 kA. For the regular channel eq.(1) has an integral

$$C = F_1(\gamma) + F_2(\gamma') . \qquad (2)$$

The first function $F_1 = (2\gamma_R - \gamma)\gamma - 2\varkappa \sqrt{\gamma^2 - 1}$ depends on the beam energy, the second one $F_2 = (\gamma')^2 = \left(\frac{d\gamma}{d\varsigma}\right)^2$ depends on the electrostatic field only. Hence, the constant C is similar to Hamiltonian of the conservative mechanical system which is a sum of potential and kinetic energies. Such a representation permits to formulate a qualitative theory. Consider, for example, the injection of REB in a channel limited by planes with fixed potential γ_R . In the case $\frac{d}{d\varsigma} = 0$ possible states are described by the dependence $\bar{\varkappa} = (\gamma_R - \gamma)\sqrt{\gamma^2 - 1}/\gamma$ maximum current $\bar{\varkappa}_{cr} = (\gamma_R^{2/3} - 1)^{3/2}$ is reached at $\gamma = \gamma_R^{1/3}$ For limited systems this dependence $\bar{\varkappa}(\gamma)$ determines the geometrical location of extremal points of the two-humped curve $F_1(\gamma)$ only, whose first maximum is at $\gamma = 1$, the second one corresponds to the high-energy $(\gamma_2 \geq \gamma_R^{1/3})$ branch, while its minimum conforms to the low-energy $(\gamma_3 \leq \gamma_R^{1/3})$ branch (fig. 1a,b). With increase in current
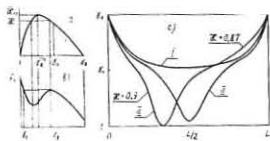
Fig.1. Geometric location of extremal points of function $F_1(\gamma)$ b) its profile for fixed $\varkappa$ c) distribution $\gamma(z)$.

$\varkappa > \varkappa_0 = \bar{\varkappa}(\gamma)$ the second maximum becomes less than the first one, and at $\varkappa > \varkappa_{cr}$ the second maximum vanishes completely and the function $F_1(\gamma)$ becomes monotonic. Here $\gamma_0 = -\frac{1}{2} + \sqrt{2\varkappa + \frac{1}{4}}$ coincides with the REB potential obtained in [2] for a homogeneous channel with the cathode having the emission limited by the space charge. So, for $\varkappa > \varkappa_0$ in the system three REB states are possible (fig.1c) with

various values of the electrostatic field γ' in the injection plane $\varsigma = 0$ (the value $\gamma'_{\varsigma=0}$ for the given current $\varkappa$ can be chosen as an eigenvalue of the investigated problem). State I has minimum energy $\gamma_{min} < \gamma_2$. In the state II $1 \leq \gamma_{min} \leq \gamma_1$ where is the energy at which $F_1(\gamma_1) = F_1(\gamma_2)$ (fig.1a). One more physically realized state is possible - state III with a virtual cathode $\gamma = 1, \gamma' = 0$ in some point of distribution $\gamma(z)$. With injection enhancement the reflected part of the electron beam grows and the virtual cathode itself shifts towards the injection plane. Beginning with the same current $\varkappa > \varkappa_{cr}$ only one state III remains.

Realization of a state depends on $\varkappa$ determined by the total space charge in the injection plane and on the method of beam formation. Fig.2 displays the dependences γ_{min} and the collector current $\varkappa_{col}$ on $\varkappa$. With increase in $\varkappa$ the REB potential in the state I gradually decreases and at $\varkappa = (\gamma^2 - 1)^{3/2}$ the REB jumps to state III. For
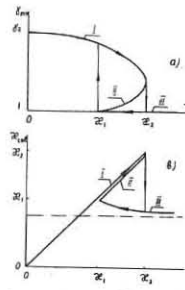
Fig.2. Dependences a) γ_{min} of distributions $\gamma(z)$ and b) collector current $\varkappa_{col}$ on electron beam density $\varkappa$ in the injection plane.

inverse direction of the current the virtual cathode vanishes at another current value (for an infinitely long channel - at $\varkappa = \varkappa_0$). Similar hysteresis phenomena occur with the channel length variation at the fixed parameter $\varkappa$. Two characteristic points of bifurcation are, evidently, the general feature of a straight electron flux penetrating the space limited by an equipotential surface of an arbitrary shape. For a thorough investigation of the system behavior near these points one needs to consider a nonstationary problem, in particular, the problem on stability of states I-III.

In the same approximation as for (1) it is easy to obtain the equation for slowly varying processes. Thus, for a plane regular system these equations have the form:

$$\frac{\partial^2 E}{\partial \varsigma^2} = E + \frac{\partial \varphi}{\partial \tau} , \quad \frac{\partial^2 \varphi}{\partial \varsigma^2} = \varphi - (\gamma_R - 1) - G , \quad \varkappa = \beta \delta ,$$
$$\frac{\partial \beta}{\partial \tau} + \beta \frac{\partial \beta}{\partial \varsigma} = \frac{1}{\gamma^3}\left(E - \frac{\partial \varphi}{\partial \varsigma}\right), \quad \frac{\partial G}{\partial \tau} + \frac{\partial \varkappa}{\partial \varsigma} = 0 . \qquad (3)$$

Here E is the electric field induced by the internal magnetic field of the beam, φ is potential related to the space charge, $\tau = \sqrt{2}\, ct/R_0$ From eq.(3) follows the instability of the state II. Such an absolute instability is associated with occurrence of a wave at $h_\rho^2 = \varkappa/(\gamma^2 - 1)^{3/2} > 1$ transmitting the energy in the (Z)-direction and insuring back coupling in the system. The instability of state II for REB propagating in a limited vacuum channel is of the same nature as the Pierce instability known for limited systems with a compensated electron beam.

1. N.F.Kovaljov, M.I.Fuchs. Preprint No.13 IPF AN SSSR, Gorky, 1980.

2. A.I.Fedosov et al. Izv.VUZov, Fizika, 1977, 10, 134.

AUTHOR INDEX

AUTHOR INDEX

Name	Ref	Name	Ref
Lysenko S. E.	B—15, G—6	Morris W. A.	H—1
Lysyansky P. B.	C—7	Moser F.	D—23
Ma C. H.	A—4	Motojima O.	E—1
Maddaluno G.	A—2	Mozer A.	D—1
Maeno M.	A—7, J—1	Mukhin P. A.	A—18
Magula P.	H—6	Mukhin V. V.	F—1
Malutin A. I.	L—1, L—6, L—13	Mukhovatov V. S.	A—17
Malyavina T. B.	F—17	Müller G.	L—10
Mandache N.	D—4	Murakami M.	A—4
Manuaba A.	A—8a	Murray L. E.	A—4
de Marco F.	A—2	Muton T.	E—1
DiMarco J. N.	L—3	Myalton T. B.	J—11
Marcus F. B.	A—6	Myalton V. V.	J—11
Markin A. I.	L—1	Nagami M.	A—7, J—1
Markov Yu. A.	F—2b	Nagao S.	E—3, E—14, G—14
Martushov Yu. S.	L—1	Nagraba S.	F—10
Maslow V. A.	C—15	Nakamura K.	H—5
Massey R. S.	L—3	Nakamura Y.	H—5
Massmann P.	H—20	Nakashima Y.	E—1
Matsunaga K.	E—6	Nakazawa M.	E—3
Matsuoka K.	E—5	Nalesso G. F.	L—16
Matsuura K.	E—5	Naumenkov P. A.	A—14
Matveev V. V.	D—8	Nawrot W.	D—15
Matveev Yu. V.	D—18	Nedospasov A. V.	G—10, J—3, J—4, J—6
Maximov Yu. S.	H—3	Neilson G. H.	A—4
Maxon S.	F—14	Nemchinov I. V.	F—17
Mazzitelli G.	A—2	Nesterov S. A.	G—17
Meddens B. J. H.	A—5	Neudatchin S. V.	B—15
van der Meer A. F. G.	L—9	Newton A. A.	L—2
van der Meiden H. J.	H—7	Nicholson D. R.	K—12
Meladze R. D.	D—17	Nielsen P. D.	F—14
Melikhov P. I.	A—18	Nikiforov V. A.	A—3a, A—3b
Merezhkin V. G.	A—17	Nikolskij	D—7
Mescherkin A. P.	F—7	Nishikara K.	F—21
Meskhi G. O.	C—13	Nishikawa K.	K—2
Messiaen A. M.	H—11	Nishito N.	E—1
Mészáros Z.	A—8b	Noda N.	E—5
Mezey G.	A—8a	Nogi Y.	E—13
Mihalczo J. T.	A—4	Notkin G. E.	A—9, H—3
Mikhailov A. P.	F—15	Novikov V. E.	F—1
Mikhailov M. I.	E—9	Novikov V. M.	L—5
Mikjailovskii A. B.	B—11	Nowikowsky J.	D—20
Mikheikin S. S.	A—3a	Nozdrachev M. G.	C—15
Miklaszewski R.	D—16	Obiki T.	E—1
Miller G.	L—3	Odnjov A. N.	A—9
Minato T.	C—20, L—15	Oepts D.	L—9
Mineev A. B.	G—12	Ogura Y.	E—13
Minyaev O. A.	A—12, H—2a	Ohi S.	C—20, L—15
Mirnov S. V.	J—11	Ohkubo K.	E—5
Mirnov V. V.	C—6	Oka Y.	E—5
Misakov P. Ya.	A—14	Okada S.	L—15
Mitarai O.	H—5	Okada T.	C—4
Mitrishkin Yu. V.	B—16	Okamura S.	C—4
Mittal K. C.	F—9	Okubo Y.	C—4
Miura Y.	E—3	Okuda T.	H—18, H—22
Miyamoto K.	E—5	Oomens A. A. M.	L—9
Miyoshi S.	C—1	Orlov V. V.	G—12
Mizui J.	F—21	Ornstein L. Th. M.	A—5
Mizuuchi T.	E—1	Osanai Y.	E—13
Moiseev S. S.	F—1	Osipov M. V.	F—18
Molvik A. W.	C—18	Overbey D. R.	A—4
Montvai A.	A—8b	Ovsjannikov V. A.	D—12
Morimoto S.	E—1	Oyevaar T.	H—7
Morozov D. Kh.	H—21, J—7	Ozaki A.	L—12
Morris A. W.	H—1	Paduch M.	D—16

C O R R I G E N D U M

Location	Delete	Insert
CONTENTS		
A-1a	tokamaks	tokamak
page 1	MAGNETIC CONFINEMENT	MAGNETIC CONFINEMENT THEORY
page 2	Q-PINCHES	θ-PINCHES
D-10	reximplo	REXIMPLO
D-17	sustem	system
D-21	mather's type	Mather's type
D-23	Absorbtion	Absorption
E-5	stellarotor	stellarator
E-10	stellarotr	stellarator
E-13	BETA	beta
G-7	T.E.Volkov	T.F.Volkov
G-7	scrape-eff	scrape-off
G-13	Yu.K.Kalmikov.	Yu.K.Kalmikov et al.
H-2a	G.M.Voroviev	G.M.Vorobiev
H-11	lenkth	length
J-2	particlesin	particles in
K-1	at 2ω	at $2\omega_{ce}$
K-5	brillouin	Brillouin
K-8	bernstein	Bernstein
L-2	reserved	reversed
L-3	reserved-field	reversed-field
L-3	linear	liner
L-16	S.Okada... L-16	S.Okada... L-15
M-1	Dynamics	dynamics
AUTHOR INDEX	Derepovsij N.T. D-7	Derepovskij N.T. D-7
	Ishimura T. C-20,L-15	Ishimura T. L-15
	Ito H. C-20,L-15	Ito H. L-15
	Ito Y. C-20,L-15	Ito Y. L-15
	Mikjailovskii A.B. B-11	Mikhailovskii A.B. B-11
	Minato T. C-20,L-15	Minato T. L-15
	Ohi S. C-20,L-1 5	Ohi S. L-15
	Vesiptchuk Yu.V. H-3	Yesiptchuk Yu.V. H-3

Seko E. V.	G—12	Stefan V.	K—7, K—8
Semashko N. N.	H—19	Steinmetz K.	D—2, D—3
Semenov V. I.	L—5	Stenchikov G. L.	F—5
Semenov V. N.	L—1, L—13	Stepanenko I. A.	C—15
Semenov V. S.	J—11	Stepanenko M. M.	H—3
Semenov V. V.	A—13, A—14	Stepanov K. N.	H—12
Sen A.	C—19, D—19	Sherwood A. R.	L—4
Sergeev A. M.	K—15	Stewart K. A.	A—4
Sestero A.	G—15	Stöckel J.	H—6
Shafranov V. D.	E—8, E—9	Stover E. K.	F—12
Shakhovetz K. G.	A—12, H—2a	Strand O. T.	C—18
Shapiro M. A.	M—2, M—3	Strelkov V. S.	H—3
Sharma A. S.	D—19	Strizhov E. F.	L—5
Sharp L. E.	E—4a	Strizhov V. F.	A—11
Shashkov A. Yu.	F—2b	Strusny H.	J—12
Shatford P. A.	L—8	Stupakov G. V.	C—8
Shchemelinin S. G.	A—12, H—2a, H—2b	Sudo S.	E—1
Shchepetov S. V.	E—10, E—11	Sugawa M.	K—6
Shchur L. N.	F—4	Sugawara M.	C—4
Shider R. T.	A—6	Sugaya R.	K—6
Shüna. S.	E—13	Sukachov A. V.	E—7
Shikanov A. S.	F—18, F—19	Suladze K. V.	D—17
Shimada M.	A—7, J—1	Sulwinski L.	F—10
Shinagawa Y.	C—1	Sundaram A. K.	C—19, D—19
Shinya K.	A—7, J—1	Sünder D.	K—14, K—16
Shirokov A. S.	F—5	Sunka P.	C—13
Shishkin A. A.	J—9	Suprunenko V. A.	E—12
Shkvarunets A. G.	C—14	Lo Surdo C.	B—5
Shoji T.	E—6	Suzuki S.	C—1
Sholokhov Yu. I.	D—12	Sveshnikov A. G.	H—19
Shpigel' I. S.	E—2	Swain D. W.	A—4
Shprits L. D.	A—13	Sy W. N.—C.	E—4b
Shurygin R. V.	H—9	Szentpétery I.	A—8b
Shustova N. V.	H—8	Szpula W.	F—10
Sidelnikov Y. V.	D—6	Takagi S.	F—21
Siebenlist F.	H—20	Takahashi T.	E—3
Silin P. V.	F—5	Takamura S.	H—18, H—22
Silin V. P.	F—3, F—5, F—6	Takasugi K.	E—6
Simik A.	H—4	Tanahashi S.	E—5
Simm W. C.	H—4	Tanaka M.	E—6
Simonen T. C.	C—18	Tang F. L.	B—6
Singethan J.	L—10	Tanga A.	A—2
Sinman A.	D—14	Tanjyo M.	L—15
Sinman S.	D—14	Tarakanov A. V.	H—3
Skladnik-Sadowska E.	D—22	Tarasyan K. N.	G—6
Sklizkov G. V.	F—18, F—19	Taska J.	L—14
		Tchukbar K. V.	F—11
Skoric M. M.	K—4	Teplov P. P.	H—2a
Skoryupin V. A.	F—2b	Terasawa T.	E—3
Skovoroda A. A.	B—19	Thomas C. E.	A—4
Skrzeczanowski W.	D—15	Thomas K. S.	L—3
Skvortsova N. N.	K—10	Thomas P. R.	B—18
Slavny A. S.	E—12	Thumm H.	L—10
Śledziński S.	D—16	Tikhanov E. K.	C—17
Smerdov B. I.	K—13	Tikhonchuk V. T.	F—3, F—6
Smirnov A. I.	A—13	Timofeev A. V.	K—3
Smirnov A. P.	B—13	Tin S. K.	E—4, E—4a
Smirnov V. G.	D—12, G—17	Tishkin V. F.	F—19
Socha R.	D—15	Titov V. A.	D—12
Sokolov Yu. A.	A—15	Tiunov M. A.	C—7
Sosunov Yu. B.	L—1	Todd T. N.	H—16, L—8
Stallard B. W.	C—18	Todoroki J.	E—13
Stamp M. F.	A—1b	Tokar' M. Z.	G—10
Start D. F. H.	A—1b, H—16	Tokunov A. I.	H—8
		Tolok V. T.	G—17